

To be published 2016*

Fluid Structure Interactions

Modeling, Mathematical Analysis and Finite Elements

Thomas Richter †

January 11, 2016

*Special, preliminary edition exclusively for the participants of the *Winter School on Modeling, Adaptive Discretizations and Solvers for Fluid-Structure Interactions, Linz, 2016*

†Universität Erlangen Nürnberg, Department Mathematik, 91058 Erlangen, richter@math.fau.de

Contents

Preface	v
Acknowledgements	vii
1 Models	1
1.1 Continuum Mechanics	1
1.1.1 Coordinate systems	1
1.1.2 Deformation Gradient	3
1.1.3 Strain	6
1.1.4 Rate of deformation and strain rate	7
1.1.5 Stress	8
1.1.6 Conservation principles	10
1.1.7 Conservation principles in different coordinate systems	13
1.2 Material Laws	17
1.2.1 Linearizations	19
1.2.2 Incompressible materials	19
1.3 The Solid Problem	20
1.3.1 The Navier-Lamé equations	22
1.3.2 Theory of nonlinear hyper-elastic material	29
1.4 The Fluid Problem	29
1.4.1 Boundary and initial conditions	31
1.4.2 The “do-nothing” outflow condition	32
1.4.3 Reynolds Number	35
1.4.4 The linear Stokes Equations	36
1.4.5 Theory of incompressible Flows	36
1.5 Flow Problems on moving domains	45
1.5.1 Eulerian techniques for flow problems on moving domains	45
1.5.2 The Arbitrary Lagrangian Eulerian (ALE) formulation for moving domain problems	46
1.5.3 Construction of the ALE map	50
2 Coupled Fluid-Structure Interactions	55
2.1 Coupling Conditions	55
2.1.1 The kinematic condition	56
2.1.2 The dynamic condition	57
2.1.3 The geometric condition	58
2.1.4 Interface regularity and boundary conditions	58
2.1.5 Coupled fluid-structure interaction	59
2.2 The Added-Mass effect	60
2.3 Variational coupling techniques	64

2.4	Fluid-structure interactions in ALE coordinates	66
2.4.1	Definition of the ALE map	68
2.4.2	Coupled ALE formulation	70
2.5	Fully Eulerian formulation for the fluid-structure interaction problem	73
2.5.1	Elastic structures in Eulerian coordinates	74
2.5.2	Fluid-structure interaction in Eulerian coordinates	77
2.5.3	The Initial Point Set method	77
3	Discretization	83
3.1	Time discretization of partial differential equations	83
3.1.1	Numerical Stability	84
3.1.2	Numerical Dissipation and further stability concepts	89
3.1.3	Galerkin time discretization schemes	92
3.1.4	Time discretization of the Stokes and Navier-Stokes equations	97
3.2	Spatial Discretization	98
3.2.1	Finite Elements	101
3.2.2	Finite Element Analysis for Elliptic Problems	104
3.2.3	Finite Elements on Curved domains	105
3.3	Finite Elements for Saddle-Point Problems	111
3.3.1	inf-sup stable Finite Element pairs	114
3.3.2	Stabilization techniques for the Stokes equations	119
3.4	Finite Elements for the Navier-Stokes equations	122
3.4.1	Oseen fixed point linearization	123
3.4.2	Newton iteration	123
3.4.3	Discretization of transport dominant flows	125
3.5	Discretization of interface-problems	129
3.5.1	Parametric interface finite elements	131
3.5.2	Condition number analysis	136
3.5.3	Numerical examples	138
3.6	Temporal discretization of Interface-Problems with moving interfaces	141
4	ALE Formulation for Fluid-Structure Interactions	145
4.1	Time-discretization for the FSI problem in ALE-formulation	145
4.1.1	Non-stationary dynamics of fluid-structure interactions	146
4.1.2	Time-stepping schemes for fluid-structure interactions	148
4.1.3	Derivation of second order time-stepping schemes	149
4.1.4	Temporal stability	150
4.1.5	Stable time-discretization and damping	151
4.2	Linearizations of fluid-structure interactions in the ALE framework	152
4.2.1	Linearization by fixpoint-iterations	153
4.2.2	Newton linearization for fluid-structure interactions in Arbitrary Lagrangian Eulerian formulation	154
4.2.3	Numerical Study on Linearizations	161
4.3	Finite elements for fluid-structure interactions in ALE formulation	161
4.3.1	Finite element triangulations for fluid-structure interactions in ALE formulation	162
4.3.2	Inf-sup stable FE-spaces for fluid-structure interactions in ALE formulation	164
4.3.3	Stabilized finite elements for fluid-structure interactions	166

4.4	Practical aspects	168
4.4.1	Matrix formulation of the linear systems	168
4.4.2	Construction of the ALE map	171
5	Fully Eulerian Formulation for Fluid-Structure Interactions	185
5.1	Eulerian models for fluid-structure interactions	185
5.1.1	Elastic structures in Eulerian coordinates	186
5.1.2	Fluid-structure interaction in Eulerian coordinates	189
5.2	Interface Capturing and the Initial Point Set Method	190
5.3	Time-Discretization of the Fully Eulerian Framework	193
5.4	Linearizations of the Fully Eulerian coordinates	194
5.5	Finite Elements for the Fully Eulerian Framework	197
5.6	Numerical Study	197
5.6.1	Stationary structure benchmark problem	198
5.6.2	Stationary fluid-structure interaction problem	199
5.6.3	Contact problem	200
6	Linear Solvers for Fluid-Structure Interactions	205
6.1	Direct solution of linear systems	206
6.2	Analysis of benchmark-problems	207
6.2.1	Configuration of the benchmark problems	208
6.2.2	Condition number analysis of the system matrices	210
6.3	Krylov space solvers for fluid structure interactions	211
6.4	Multigrid solvers for the Arbitrary Lagrangian Eulerian formulation	213
6.4.1	GMRES multigrid iteration	214
6.4.2	Partitioned multigrid smoother	216
6.4.3	Approximation of the subproblems	219
6.4.4	Robustness versus problem parameters	222
6.4.5	Analysis of the iterative smoother	223
7	Error Estimation and Adaptivity	225
7.1	A posteriori error estimation	225
7.1.1	The Dual Weighted Residual Method	227
7.1.2	The DWR Method for Galerkin time-stepping schemes	238
7.2	Adaptivity	242
7.2.1	Localization of a posteriori error estimators	243
7.2.2	Techniques for spatial mesh refinement	248
7.3	Application to fluid-structure interactions in ALE formulation	249
7.3.1	Sensitivities for stationary fluid-structure interactions in ALE coordinates	249
7.3.2	Numerical examples: error estimation and adaptivity	251
7.3.3	Adaptivity for time-periodic fsi problems	258
7.3.4	Anisotropic mesh refinement	258
8	Applications	261
8.1	Optimization with fluid-structure interactions	261
8.1.1	The optimization problem	261
8.1.2	Reduced formulation of the optimization problem	264
8.1.3	Realization with fluid-structure interactions	266

Contents

8.1.4	Parameter identification test	266
8.1.5	Optimal control test	267
8.2	Mechano-chemical fluid structure interactions and active material growth . . .	272
8.2.1	Growth models	273
8.2.2	Mechano-chemical fluid-structure interactions	274
8.2.3	Monolithic schemes for the coupled problem	277
8.2.4	Numerical Tests	279
8.3	Simulation of high performance ball-bearings	282

Preface

Fluid-structure interactions

Fluid-structure interactions (FSI) play an important role in various application problems. The classical aerodynamical problem of predicting the aerodynamical properties of a flying airplane is a fluid-structure interaction problem, as the plane will deform under aeroelastic forces and the deformation will alter the shape, and hence the aeroelastic response of the plane. The pulsating flow of blood in big vessels causes significant deformation of the surrounding tissue that again alters the flow domain and pattern.

These two examples are classical FSI problems with a two-way coupling between the two involved physical models: fluid flow and elastic material. Each of the subproblems acts on the other. As this coupling is acting on the *interface* that is the surface between the two subproblems fluid and solid, such problems are called *surface-coupled multiphysics problems*.

Simulations involving fluid-structure interactions have a long history in technical disciplines such as aeroelasticity or ship design. Computational methods for performing such simulations are often ad hoc and based on coupling existing simulation tools for the two subproblems. In fact, the state of the art approach for computational fluid-structure interactions in real-world applications consists in the design of efficient coupling techniques, that reuse available tools for the fluid- and solid-problem. A mathematical analysis of the coupled fsi-system of equations describing the full fluid-structure interaction problem is still new. As these two subproblems are big mathematical challenges on their own, it is not surprisingly, that results for the coupled problem are rarely spread.

Scope of this book

This book aims at giving a mathematical introduction to modeling, analysis and simulation techniques for fluid-structure interactions. As the field of possible applications is huge, and as different applications will bring along different challenges that ask for adequate techniques each, we will focus our attention on problems involving a very strong coupling between the two sub systems fluid and solid. A prototypical example is the flow of blood in blood vessels.

For such problems, we will start by introducing the basic models of continuum mechanics and give an overview of different material laws used to describe solids and incompressible fluids. For these models and equations we will develop the fundamental mathematical theory that will give us answers on the existence, uniqueness and regularity of solutions. Given enough understanding of the two subproblems, we will be able to tackle coupled models for fluid-structure interactions. Both problems are coupled by means of boundary conditions on the common interface.

This book focusses on monolithic formulations for the coupled fluid-structure interaction problem: we will derive one mathematical formulation, that will cover the fluid-problem, the solid-problem and the interface conditions in between. Two different approaches are considered: First, we describe the *Arbitrary Lagrangian Eulerian* approach, a well-established technique to model fluid-structure interactions and that allows for very accurate discretization schemes. Second, we introduce the *Fully Eulerian* formulation of fluid-structure interactions, a novel modeling approach, that is able to cover a wide range of different application problems.

The second part of this books introduces the finite element discretization of partial differential equations. We start by gathering the essential, that are necessary to handle flow and structure problem. Afterwards, we turn the attention to the special needs of the coupled fluid-structure interaction problem, both in Arbitrary Lagrangian Eulerian and the Fully Eulerian Formulation.

A third part of this book deals with the solution of the algebraic systems of equations, that arise from discretization of the coupled system. The complex structure of the coupled fluid-structure interaction problem combines the difficulties of flow problems with those of elastic structures. The resulting systems of equations are huge, lack desirable structure (such as symmetry) and incorporate a very stiff coupling.

Finally, we will discuss some advanced topics regarding the efficient numerical treatment of complex fluid-structure interaction problems. With help of sensitivity analysis of the coupled systems, we will be able to design goal-oriented error estimators, that will help to significantly reduce the computational costs for large simulations. Further, these techniques can be applied to solve simple optimization problems with fluid-structure interactions.

Acknowledgements

This book would not have been possible without the scientific collaboration with various researchers working in the field of computational fluid dynamics and fluid-structure interactions. First of all, I wish to highlight the contributions of Thomas Wick [192, 242, 244, 245, 193, 194, 247, 248, 246, 195]. Some results within this book on the discretization of fluid-structure interactions in Arbitrary Eulerian Lagrangian and in Fully Eulerian coordinates, but in particular results regarding sensitivity techniques for adaptivity (Section 7.3) and optimization (Section 8.1) are joint effort with Thomas Wick. Furthermore, better understanding and efficient realization of the Fully Eulerian formulation of fluid-structure interactions was possible only in collaboration with Stefan Frei [101, 201, 202, 143], who made essential contributions in the field of interface problems (Section 3.5) and the accurate discretization of the Fully Eulerian formulation as presented in Chapter 5.

1 Models

1.1 Continuum Mechanics

In this chapter, we derive the equations that describe the dynamics of fluids and solids. These objects are made out of molecules, atoms and smaller particles, that interact with each other. A description of the dynamics of these micro-structure is possible by fundamental physical laws. Such a particle centered view-point is however not feasible, if large physical objects are considered, that consist of many atoms. To describe every particle in one liter of water, more than 10^{25} molecules must be considered. A description of every single molecule—or even every atom or subatomic particle—in a large scale hydrodynamical problem like the flow of water around a ship is completely out of bounds.

Instead, we consider a *continuum approach* for the description of the large scale dynamics. By a continuum, we denote a volume $V(t) \subset \mathbb{R}^3$ of (different) particles. Instead of describing every single particle, we only observe some few averaged properties of the complete volume. These properties are all considered as local density distributions. For instance by the velocity $\mathbf{v}(x, t)$ for some time t and point $x \in V(t)$, we denote the average velocity of the particles, that at time t are at location x . We assume, that all physical quantities, like velocity, temperature, density, and so on, have some smoothness.

In the following we will derive fundamental equations that describe the interplay of these averaged quantities. We will distinguish between basic physical principles, the called *conservation principles* that are assumed to be exact for all materials and *material laws*, that model the properties of the materials, in particular the reaction of the materials on acting forces. These material laws are usually simplifications, idealizations and derived by observation and measurements.

1.1.1 Coordinate systems

In the following, by $V(t) \subset \mathbb{R}^3$ we denote a *material volume*. We assume, that $V(t)$ is entirely occupied by some material. This material has physical properties like density $\rho : V(t) \rightarrow \mathbb{R}$, velocity $\mathbf{v} : V(t) \rightarrow \mathbb{R}^3$, which is a three dimensional vector-field, or pressure $p : V(t) \rightarrow \mathbb{R}$. We assume, that the volume is moving, and by $V_0 := V(t_0)$ we denote the *reference configuration* of the volume. Even though the reference time t_0 is arbitrary, we usually think of a system that is at rest and unstressed, e.g. a container filled with fluid that is at rest, or an elastic obstacle that is not deformed and where no stresses act. At time $t \geq t_0$, we denote by $V(t)$ the *current configuration*.

The volume $V(t)$ consists of particles, and we call $\hat{V} := V_0$ the material domain. For every particle $\hat{x} \in \hat{V}$, we denote by $x(\hat{x}, t) \in V(t)$ the location of the particle at time $t \geq t_0$. We

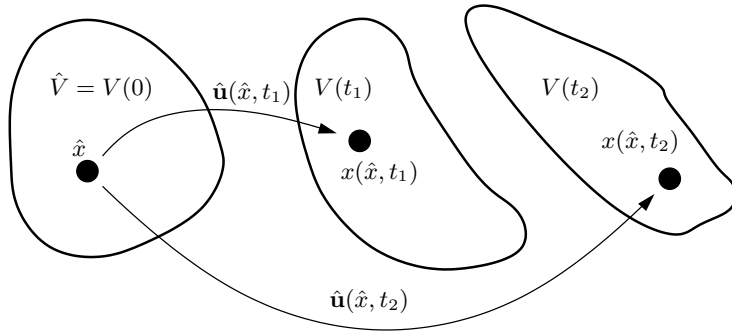


Figure 1.1: The Lagrangian reference system.

assume, that the path $\{x(\hat{x}, t), t \geq t_0\} \subset \mathbb{R}^3$ is continuous and that no two different particles $\hat{x}, \hat{x}' \in \hat{V}$ have the same position at any time $t \geq t_0$:

$$x(\hat{x}, t) = x(\hat{x}', t) \Leftrightarrow \hat{x} = \hat{x}'.$$

Hence, the mapping $\hat{T}(\hat{x}, t) := x(\hat{x}, t)$ is invertible and we define the inverse mapping $\hat{T}^{-1}(x, t) := \hat{x}(x, t)$, where $\hat{x}(x, t)$ relates the position $x \in V(t)$ with exactly that particle $\hat{x} \in \hat{V}$, that at time $t \geq t_0$ resides in this spatial location.

In a continuum, we assume that no particles are destroyed or created such that the moving volume $V(t)$ is given by all coordinates $x \in \mathbb{R}^3$ that are occupied by a particle $\hat{x} \in \hat{V}$:

$$V(t) = \{x(\hat{x}, t), \hat{x} \in \hat{V}\}.$$

The choice of the reference system V_0 is arbitrary and very often, we simple choose $V_0 = \hat{V}$, such that $\hat{T}(\cdot, t_0) = \text{id}$. Figure 1.1 shows this fundamental configuration.

For a particle $\hat{x} \in \hat{V}$, we define the *deformation* $\hat{\mathbf{u}}(\hat{x}, t)$ as

$$\hat{\mathbf{u}}(\hat{x}, t) = x(\hat{x}, t) - \hat{x}, \quad (1.1)$$

and its *material velocity* $\hat{\mathbf{v}}(\hat{x}, t)$ as

$$\hat{\mathbf{v}}(\hat{x}, t) := d_t x(\hat{x}, t) = d_t \hat{\mathbf{u}}(\hat{x}, t).$$

We call the particle system viewpoint for describing the dynamics of a continuum $V(t)$ as *Lagrangian coordinate system* or *Lagrangian framework*. This Lagrangian system is particle-centered. We observe single particles $\hat{x} \in \hat{V}$ and follow their paths $x(t) = \hat{x} + \hat{\mathbf{u}}(\hat{x}, t)$ over time. A Lagrangian viewpoint is the natural world for problems in solid mechanics, where the particles in the reference system are closely linked to each other, and where the continuum—in the case of elastic structures—comes back to the reference configuration, if the system is free of external forces

$$\begin{array}{c} \hat{V} = V_0 \\ \hat{x} = x(\hat{x}, 0) \end{array} \xrightarrow{\text{external forces act}} \begin{array}{c} V(t) \\ x(\hat{x}, t) \end{array} \xrightarrow{\text{absence of external forces}} \begin{array}{c} V(t_\infty) = \hat{V} \\ \hat{x} = x(\hat{x}, t_\infty) \end{array}$$

See Figure 1.1.

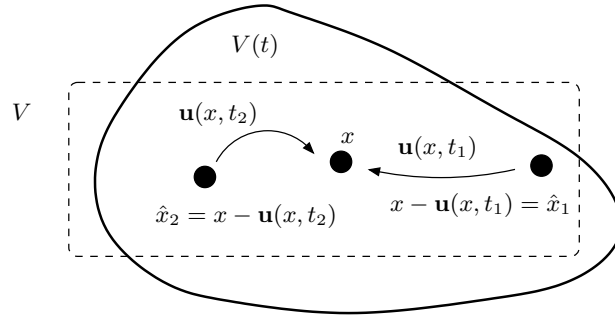


Figure 1.2: The Eulerian reference system. We observe one spatial coordinate $x \in V$. The view-point V is fixed, the continuum $V(t)$ is moving. Different particles \hat{x} have position x at different times.

We can define counterparts for deformation and velocity in the current configuration $V(t)$, that describe the behavior of those particles, that at a given time $t \geq t_0$ are in position $x \in V(t)$. By

$$x = \hat{x} + \hat{\mathbf{u}}(\hat{x}, t) \Leftrightarrow \mathbf{u}(x, t) := \hat{\mathbf{u}}(\hat{x}, t) = x - \hat{x},$$

we have an expression $\mathbf{u}(x, t)$ for the deformation at the spatial location $x \in V(t)$ of whatever particle $\hat{x} \in \hat{V}$ takes this position at time t . The difference is only given in the viewpoint: where $\hat{\mathbf{u}}(\hat{x}, t)$ denotes the deformation of the particle \hat{x} at time t , by $\mathbf{u}(x, t)$ we denote the deformation of whatever particle \hat{x} happens to be at location x at time t . If at time t it holds $x = x(\hat{x}, t)$, both concepts of deformation describe the same configuration. If we base the description of the continuum on the spatial coordinates $x \in V(t)$, we speak of the *Eulerian framework*, where the focus is set on a spatial domain $V \subset \mathbb{R}^3$ and all points $x \in V$, see Figure 1.2. This viewpoint is natural for fluid-dynamical problems. We consider the estimation of the drag-coefficient of a car. Here, the attention is on the flow around the car and we measure forces on the surface of the car, irrespective of the actual particle that just in time $t \geq 0$ interacts with the car. In fluid dynamics, we want to describe velocity and pressure at spatial points $x \in V$, we are not at all interested in the specific particle, that at a given time has this property.

The Eulerian velocity $\mathbf{v}(x, t)$ is defined as the velocity of that particle \hat{x} that at time $t \geq t_0$ is at position $x = x(\hat{x}, t)$:

$$\mathbf{v}(x, t) = \partial_t u(x, t) = \partial_t \hat{\mathbf{u}}(\hat{x}, t) = \hat{\mathbf{v}}(\hat{x}, t).$$

1.1.2 Deformation Gradient

In continuum mechanics, we study the behavior of moving and deforming continua $V(t)$ over time. In the following, we describe the relative change of positions $x(\hat{x}, t)$ and $x(\hat{y}, t)$ of two particles $\hat{x}, \hat{y} \in \hat{V}$ in a moving continuum. Relative change of location is called strain, and strain will show to be the most fundamental quantity that causes stress within the material. By stress, we denote the internal forces between the neighboring particles in a continuum.

Let \hat{x} and \hat{y} be two particles, that are close to each other, e.g. we consider the case $|\hat{y} - \hat{x}| \rightarrow 0$. Under deformation, these two particles have the position $x = \hat{x} + \hat{\mathbf{u}}(\hat{x})$ and $y = \hat{y} + \hat{\mathbf{u}}(\hat{y})$. We

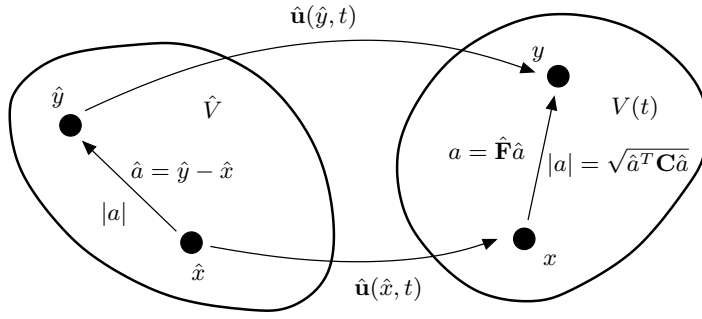


Figure 1.3: Transformation of infinitesimal line segment \hat{a} to a with $|\hat{a}| \rightarrow 0$. Deformation gradient $\hat{\mathbf{F}} = I + \hat{\nabla}\hat{\mathbf{u}}$ and squared length change $|a|^2 = \hat{a}^T \hat{\mathbf{C}} \hat{a}$ indicated by the right Cauchy-Green tensor $\hat{\mathbf{C}} = \hat{\mathbf{F}}^T \hat{\mathbf{F}}$.

measure the change in position $y - x$ in V with respect to $\hat{y} - \hat{x}$ in \hat{V} . By first order Taylor expansion we deduce

$$\begin{aligned} y - x &= \hat{y} + \hat{\mathbf{u}}(\hat{y}) - \hat{x} - \hat{\mathbf{u}}(\hat{x}) \\ &= \hat{y} - \hat{x} + \hat{\nabla}\hat{\mathbf{u}}(\hat{x})(\hat{y} - \hat{x}) + O(|\hat{y} - \hat{x}|^2). \end{aligned} \quad (1.2)$$

Hence, considering the relative change in position, it holds

$$\frac{y - x}{|\hat{y} - \hat{x}|} = [I + \hat{\nabla}\hat{\mathbf{u}}(\hat{x})] \frac{\hat{y} - \hat{x}}{|\hat{y} - \hat{x}|} + O(|\hat{y} - \hat{x}|). \quad (1.3)$$

We define

Definition 1 (Deformation Gradient). *Let $\hat{\mathbf{u}}$ be a differentiable deformation field in the material volume \hat{V} . The deformation gradient*

$$\hat{\mathbf{F}}(\hat{x}, t) := I + \hat{\nabla}\hat{\mathbf{u}}(\hat{x}, t),$$

denotes the local change of relative position under deformation.

The deformation gradient is the fundamental measure in structure dynamics.

Lemma 1 (Determinant of the deformation gradient). *Let \hat{V} be a reference volume and $\hat{\mathbf{u}} : \hat{V} \rightarrow \mathbb{R}^d$ be a differentiable deformation field. The determinant of the deformation gradient $\hat{J} := \det(\hat{\mathbf{F}})$ denotes the local change of volume:*

$$|V(t)| = \int_{\hat{V}} \hat{J} dx.$$

Proof. It holds by the transformation theorem

$$|V(t)| = \int_{V(t)} 1 dx = \int_{\hat{V}} \det(I + \hat{\nabla}\hat{\mathbf{u}}) d\hat{x} = \int_{\hat{V}} \hat{J} d\hat{x}.$$

□

The deformation gradient $\hat{\mathbf{F}}$ applies to the Lagrangian viewpoint. For an Eulerian description in $V(t)$, we can define the inverse deformation gradient \mathbf{F} in a similar way. For two spatial coordinates $x, y \in V$ belonging to particles \hat{x} and \hat{y} in \hat{V} it holds

$$\frac{\hat{y} - \hat{x}}{|y - x|} = \mathbf{F}(x) \frac{y - x}{|y - x|} + O(|y - x|),$$

with the *inverse deformation gradient* $\mathbf{F}(x, t) = I - \nabla \mathbf{u}(x, t)$. It holds $\mathbf{F} = \hat{\mathbf{F}}^{-1}$, see Problem 1.

Very often, it will be necessary to rapidly switch between different viewpoints on the same physical problem. Sometimes, it is appropriate to consider the material centered reference domain \hat{V} , while sometimes the Eulerian viewpoint of the current configuration $V(t)$ is better suited. Usually, we denote all entities in the material system with a hat “ $\hat{\cdot}$ ” and for every basic property like velocity and deformation, there is always a Eulerian counterpart to a Lagrangian symbol, e.g. $\mathbf{v}(x, t) = \hat{\mathbf{v}}(\hat{x}, t)$ and $\mathbf{u}(x, t) = \hat{\mathbf{u}}(\hat{x}, t)$, where for \hat{x} and x at a given time $t \geq t_0$ it always holds $x = \hat{x} + \hat{\mathbf{u}}(\hat{x}, t)$. When referring to derivatives of these basic quantities, a simple $\nabla \mathbf{u} = \hat{\nabla} \hat{\mathbf{u}}$ is usually wrong. Instead, we need to derive rules to map in between both coordinate frames:

Lemma 2 (Transformation between the reference and the current configuration). *Let \hat{V} be a reference domain and $\hat{\mathbf{u}} \in C^1(\overline{I \times \hat{V}})^3$. We assume, that $\text{id} + \hat{\mathbf{u}}$ defines a C^1 -diffeomorphism between \hat{V} and*

$$V(t) = \{\hat{x} + \hat{\mathbf{u}}(\hat{x}, t), \hat{x} \in \hat{V}\}.$$

Let $\hat{f} \in C^1(\overline{I \times \hat{V}})$ and $f(x, t) = f(x(\hat{x}, t), t) = \hat{f}(\hat{x}, t)$ be its counter-part in the current configuration. It holds

$$\hat{\nabla} \hat{f} = \hat{\mathbf{F}}^T \nabla f \quad (1.4)$$

and

$$d_t f = d_t \hat{f}, \quad \partial_t f = \partial_t \hat{f} - \hat{\mathbf{F}}^{-T} \hat{\nabla} \hat{f} \cdot \hat{\mathbf{v}}. \quad (1.5)$$

Let $\hat{\mathbf{w}} \in C^1(\overline{I \times \hat{V}})^3$ be given with counterpart $\mathbf{w}(x, t) = \hat{\mathbf{w}}(\hat{x}, t)$. It holds:

$$\hat{\nabla} \hat{\mathbf{w}} = \nabla \mathbf{w} \hat{\mathbf{F}} \quad (1.6)$$

Proof. For the spatial derivative of $f(x, t)$ it holds with $x(\hat{x}, t) = \hat{x} + \hat{\mathbf{u}}(\hat{x}, t)$:

$$\hat{\partial}_i \hat{f}(\hat{x}, t) = \hat{\partial}_i f(x(\hat{x}, t), t) = \sum_j \partial_j f(x, t) \hat{\partial}_i x^j(\hat{x}, t) = \sum_j \partial_j f(x, t) \hat{\mathbf{F}}_{ji}.$$

Hence

$$\hat{\nabla} \hat{f} = \hat{\mathbf{F}}^T \nabla f.$$

Then, for a vector field $\mathbf{w} = (\mathbf{w}_i)_i$ it follows

$$(\hat{\nabla} \hat{\mathbf{w}})_{ij} = \hat{\partial}_j \hat{\mathbf{w}}_i = \sum_k \partial_k \mathbf{w}_i \hat{\partial}_j x^k(x, t) = (\nabla \mathbf{w})_{ik} \hat{\mathbf{F}}_{kj} = (\nabla \mathbf{w} \hat{\mathbf{F}})_{ij}$$

For the total time derivative it holds with $\partial_t x(\hat{x}, t) = \hat{\mathbf{v}}(\hat{x}, t) = \hat{\mathbf{v}}(x)$

$$d_t f(x, t) = \partial_t f + \nabla f \cdot \mathbf{v}. \quad (1.7)$$

Then, with $\hat{x} = \hat{x}(x, t) = x - \mathbf{u}(x, t)$ and using 1.4:

$$\partial_t \hat{f}(\hat{x}, t) = \partial_t f(x(\hat{x}, t), t) = \partial_t f + \nabla f \cdot \partial_t x(\hat{x}, t) = \partial_t f + \hat{\mathbf{F}}^{-T} \hat{\nabla} \hat{f} \cdot \hat{\mathbf{v}}.$$

Finally, the last results follows together with (1.7). \square

1.1.3 Strain

Strain is defined as the relative length change of infinitesimal line-segments under deformation. Strain will be the basic quantity used to describe stresses in solid mechanics. A simple model is a spring, where change of length - the strain - will be proportional to a force.

Let $\hat{a} = \hat{y} - \hat{x}$ be the length of a line-segment between the two points $\hat{x}, \hat{y} \in \hat{V}$. Then, given a deformation field $\hat{\mathbf{u}} : \hat{V} \rightarrow \mathbb{R}^3$, let $x = \hat{x} + \hat{\mathbf{u}}(\hat{x})$ and $y = \hat{y} + \hat{\mathbf{u}}(\hat{y})$ and set $a := y - x$. It holds by using (1.3) that

$$a = y - x = \hat{\mathbf{F}}(\hat{x})\hat{a} + O(|\hat{a}|^2),$$

and for the length of such a line segment $a = y - x$

$$|a| = \sqrt{(\hat{\mathbf{F}}\hat{a}, \hat{\mathbf{F}}\hat{a}) + O(|\hat{a}|^3)} = \sqrt{(\hat{a}^T, \hat{\mathbf{F}}^T \hat{\mathbf{F}} \hat{a})} + O(|\hat{a}|^2).$$

For an illustration, see Figure 1.3. By $\hat{\mathbf{C}} = \hat{\mathbf{F}}^T \hat{\mathbf{F}}$ we denote the *right Cauchy-Green tensor* which is also denoted as the *Green deformation tensor*. This tensor is symmetric and positive definite, as

$$(\hat{\mathbf{C}}\hat{a}, \hat{a}) = (\hat{\mathbf{F}}\hat{a}, \hat{\mathbf{F}}\hat{a}) = \|\hat{\mathbf{F}}\hat{a}\|^2 > 0 \quad \forall \hat{x} \neq 0,$$

and it describes the (squared) length scaling of a line-segment in direction $\hat{a} = \hat{y} - \hat{x}$. A further commonly used strain measure is the *Green-Lagrange strain tensor* $\hat{\mathbf{E}} := \frac{1}{2}(\hat{\mathbf{C}} - I) = \frac{1}{2}(\hat{\mathbf{F}}^T \hat{\mathbf{F}} - I)$, that measures the (squared) length change of a line-segment $\hat{a} = \hat{y} - \hat{x}$ under deformation $a = y - x$:

$$\frac{1}{2}(|a|^2 - |\hat{a}|^2) = \frac{1}{2}(\hat{a}^T \hat{\mathbf{C}} \hat{a} - \hat{a}^T \hat{a}) + O(|\hat{a}|^3) = \hat{a}^T \left(\frac{1}{2}(\hat{\mathbf{F}}^T \hat{\mathbf{F}} - I) \right) \hat{a} + O(|\hat{a}|^3). \quad (1.8)$$

The tensors $\hat{\mathbf{C}} = \hat{\mathbf{F}}^T \hat{\mathbf{F}}$ and $\hat{\mathbf{E}} = \frac{1}{2}(\hat{\mathbf{C}} - I)$ are nonlinear functions in the deformation $\hat{\mathbf{u}}$:

$$\hat{\mathbf{C}} = I + \hat{\nabla} \hat{\mathbf{u}} + \hat{\nabla} \hat{\mathbf{u}}^T + \hat{\nabla} \hat{\mathbf{u}}^T \hat{\nabla} \hat{\mathbf{u}}, \quad \hat{\mathbf{E}} = \frac{1}{2} \left(\hat{\nabla} \hat{\mathbf{u}} + \hat{\nabla} \hat{\mathbf{u}}^T + \hat{\nabla} \hat{\mathbf{u}}^T \hat{\nabla} \hat{\mathbf{u}} \right).$$

Given a very small variation in deformation, i.e. $|\hat{\nabla} \hat{\mathbf{u}}| \ll 1$, one sometimes uses linearization of the strain tensors as an approximation:

$$\mathbf{c} = I + \hat{\nabla} \hat{\mathbf{u}} + \hat{\nabla} \hat{\mathbf{u}}^T, \quad \epsilon = \frac{1}{2} \left(\hat{\nabla} \hat{\mathbf{u}} + \hat{\nabla} \hat{\mathbf{u}}^T \right).$$

These approximations can be good approximations under certain conditions. One however has to be careful, as having a small deformation $\hat{\mathbf{u}}$ is not a sufficient condition for this linearization, see Problem 2.

The tensors $\hat{\mathbf{F}}$, $\hat{\mathbf{C}}$, $\hat{\mathbf{E}}$ and the linearized strain tensor ϵ all refer to the Lagrangian material coordinate system. They are called *material strain tensors*. Sometimes, we need to express strain in the spatial coordinate system, directly on the current frame $V(t)$. Hence, let $x, y \in V(t)$ be two spatial coordinates at time $t \geq t_0$, spanning the line-segment $a = y - x$. By $\hat{x}, \hat{y} \in \hat{V}$ we denote the material points corresponding to this line-segment. These span the material line-segment $\hat{a} = \hat{y} - \hat{x}$. Similar to (1.3) it holds using the Eulerian deformation $\mathbf{u}(x, t) = \hat{\mathbf{u}}(\hat{x}, t)$

$$\hat{y} - \hat{x} = y - \mathbf{u}(y) - (x - \mathbf{u}(x)) = [I - \nabla \mathbf{u}(x)](y - x) + O(|y - x|^2).$$

By $\mathbf{F}(x) = I - \nabla \mathbf{u}(x)$ we denote the *inverse deformation tensor*. It holds $\mathbf{F}(x) = \hat{\mathbf{F}}(\hat{x})^{-1}$ for $x = \hat{x} + \hat{\mathbf{u}}(\hat{x})$, see Problem 1. $\mathbf{F}(x)$ is the deformation gradient in the current configuration and it acts on the spatial coordinate system. With help of $\mathbf{F} = I - \nabla \mathbf{u}$ we can immediately analyze length changes in the spatial system. Let $a = y - x$ and $\hat{a} = \hat{y} - \hat{x}$. It holds

$$|\hat{a}|^2 = (\mathbf{F}a, \mathbf{F}a) + O(|a|^3) = a^T \mathbf{F}^T \mathbf{F}a + O(|a|^3) = a^T \hat{\mathbf{F}}^{-T} \hat{\mathbf{F}}^{-1} a + O(|a|^3).$$

The tensor $\mathbf{b}^{-1} := \hat{\mathbf{F}}^{-T} \hat{\mathbf{F}}^{-1} = \mathbf{F}^T \mathbf{F}$ is the inverse of the *left Cauchy-Green tensor* \mathbf{b}

$$\mathbf{b} = \hat{\mathbf{F}} \hat{\mathbf{F}}^T.$$

As $\hat{\mathbf{C}}$, \mathbf{b} is symmetric positive definite. Finally, we can define the spatial Eulerian counterpart $\mathbf{e} = \frac{1}{2}(I - \mathbf{F}^{-T} \mathbf{F}^{-1})$ to the Cauchy-Green strain tensor $\hat{\mathbf{E}}$. By (1.8), it holds

$$\frac{1}{2} (|a|^2 - |\hat{a}|^2) = \hat{a}^T \hat{\mathbf{E}} \hat{a} + O(|\hat{a}|^3),$$

and with

$$\hat{a}^T \hat{\mathbf{E}} \hat{a} = a^T \hat{\mathbf{F}}^{-1} \hat{\mathbf{E}} \hat{\mathbf{F}}^{-T} a + O(|\hat{a}|^3),$$

we introduce

$$\mathbf{e} := \frac{1}{2} (I - \mathbf{F} \mathbf{F}^T) = \frac{1}{2} (I - \hat{\mathbf{F}}^{-1} \hat{\mathbf{F}}^{-T}) = \hat{\mathbf{F}}^{-1} \hat{\mathbf{E}} \hat{\mathbf{F}}^{-T}$$

the symmetric *Euler-Almansi strain tensor* \mathbf{e} , that enables us to relate length changes to the Eulerian line segment a :

$$\frac{1}{2} (|a|^2 - |\hat{a}|^2) = a^T \mathbf{e} a + O(|a|^3).$$

If for a body \hat{V} it holds $\hat{\mathbf{C}} = I$, it follows that $\hat{\mathbf{E}} = 0$, and no relative changes in the position of material points \hat{x} and \hat{y} occur. Lengths and angles are maintained. A material body, that can only undergo motion with $\hat{\mathbf{E}} = 0$ is called a *rigid body*.

Remark 1 (Right Cauchy-Green or Green-Lagrange strain tensor). *We have two different strain measures at hand. The right Cauchy-Green strain tensor $\hat{\mathbf{C}}$ and the Green-Lagrange strain tensor $\hat{\mathbf{E}}$. Both are firmly linked and can be used to describe strains caused by deformation. For describing material laws, we will derive models, that characterize the materials reaction on strain. Most simple models will assume a linear dependency between strain and stress: if no strain is given, no stress is induced. Here, the Green-Lagrange strain tensor $\hat{\mathbf{E}}$ is the better basis, as $\hat{\mathbf{E}} = 0$ denotes a no-strain condition and a linear function $f(\hat{\mathbf{E}})$ can be consulted to model the strain-stress relationship.*

1.1.4 Rate of deformation and strain rate

The strain tensor is a fundamental quantity in solid mechanics, where we assume, that a finite force will cause a finite deformation. An ideal spring will linearly react on external forces by some finite extension, which directly refers to strain. In fluid-mechanics however, finite forces can lead to infinite deformation. Just think of the gravity-caused flow of water in a river. Here, not the deformation and the deformation gradient itself, but its temporal variation will be the key quantity to model the internal forces (stresses) of the material. We already discussed, that for fluid-dynamical observations, the Eulerian viewpoint is more meaningful. Hence, we will derive a measure for the rate of strain in the current system $V(t)$.

Figure 1.4: Traction vectors on a imaginary surface in the current system (left) and the reference system (right). Cauchy's stress theorem postulates a linear dependency of the traction vectors on the normals $\vec{t} = \sigma \vec{n}$ and $\hat{\vec{t}} = \hat{\mathbf{P}} \hat{\vec{n}}$.

By $\hat{x}, \hat{y} \in \hat{V}$ we denote two material points spanning the line-segment $\hat{a} = \hat{y} - \hat{x}$. We follow their positions $x(t) = \hat{x} + \hat{\mathbf{u}}(\hat{x}, t) \in V(t)$ and $y(t) = \hat{y} + \hat{\mathbf{u}}(\hat{y}, t) \in V(t)$ and the resulting line-segment $a(t) = y(t) - x(t)$ in the current configuration $V(t)$. With $a(t) = \hat{\mathbf{F}}(t)\hat{a}$ it holds

$$\partial_t a(t) = \partial_t \hat{\mathbf{F}}(t)\hat{a}, \quad (1.9)$$

and for the deformation gradient $\hat{\mathbf{F}}(t) = I + \hat{\nabla}\hat{\mathbf{u}}(t)$ we get

$$\partial_t \hat{\mathbf{F}} = \partial_t \hat{\nabla}\hat{\mathbf{u}} = \hat{\nabla}\hat{\mathbf{v}}.$$

where we assumed sufficient regularity to change the order of derivatives. By $\hat{\nabla}\hat{\mathbf{v}}$ we denote the *material velocity gradient*. The material velocity gradient $\hat{\nabla}\hat{\mathbf{v}}(\hat{x}, t)$ denotes the spatial change of the velocity as given in the Lagrangian material system. The *spatial velocity gradient* $\nabla\mathbf{v}(x, t)$ refers to the spatial change of the velocity of whatever particles are at location x at time t . For $\hat{\mathbf{v}}(\hat{x}) = \mathbf{v}(x)$ with $x = x(\hat{x}) = \hat{x} + \hat{\mathbf{u}}(\hat{x})$ it further holds

$$\partial_t \hat{\mathbf{F}} = \nabla\mathbf{v} \hat{\nabla}x = \nabla\mathbf{v} \hat{\mathbf{F}}.$$

Then, to continue with (1.9)

$$\partial_t a(t) = \nabla\mathbf{v} \hat{\mathbf{F}} \hat{a} = \nabla\mathbf{v} a(t),$$

and the rate of length change is given by

$$\partial_t |a(t)|^2 = (\nabla\mathbf{v} a(t), a(t)) + (a(t), \nabla\mathbf{v} a(t)) = 2 \left(\frac{1}{2} (\nabla\mathbf{v} + \nabla\mathbf{v}^T) a(t), a(t) \right).$$

Definition 2 (Strain rate tensor). *By*

$$\dot{\epsilon}(x, t) = \frac{1}{2} \{ \nabla\mathbf{v}(x, t) + \nabla\mathbf{v}(x, t)^T \}.$$

we denote the strain rate tensor or the rate of strain tensor. It denotes the local change of velocity in the current system.

1.1.5 Stress

Deformation, strain and strain rate are kinematic principles. They simply describe the relative motion of particles within a volume. As such, they are pure observations of the situations and do not depend on the model under consideration. We assume, that a material will react on strain of the strain rate. For expanding a spring, a certain force will be necessary.

By *stress* we denote the internal force that is acting on an imaginary surface within the volume $V(t)$. The unit of stress is force per area.

In Figure 1.4 we show a volume $V(t)$ that is cut at an inner surface $S \subset V(t)$. By $x \in S \subset V(t)$ we denote a point on this surface with normal \vec{n} . The average forces acting on a neighborhood

of $x \in S$ is denoted by the *Cauchy traction vector* \vec{t} . The right sketch of the figure shows this setting in the reference system, where by $\hat{x} \in \hat{S} \subset \hat{V}$ we denote point, surface and volume in reference state. Here, the normal vector is indicated by \hat{n} and the resulting *first Piola-Kirchhoff traction vector* $\hat{\vec{t}}$:

$$\vec{t} = \vec{t}(x, t, \vec{n}), \quad \hat{\vec{t}} = \hat{\vec{t}}(\hat{x}, t, \hat{n}).$$

By ds we denote a neighborhood of x on the surface $S \subset V(t)$ and by $d\hat{s}$ the corresponding neighborhood of \hat{x} on $\hat{S} \subset \hat{V}$. Then, it holds

$$\vec{t} ds = \hat{\vec{t}} d\hat{s},$$

such that both traction vectors refer to forces in the current configuration $V(t)$. While \vec{t} is a function in variables x, \vec{n} of the current configuration, the first Piola-Kirchhoff traction vector is a function of \hat{x} and \hat{n} in the Lagrangian reference system. Usually, it does not hold $|\vec{t}| = |\hat{\vec{t}}|$.

The traction vectors describe a *surface tension*. Such surface tensions arise from friction or contact. Another example for a surface tension is the pressure in a liquid or gas that pushes the particle to each other (or apart from each other).

The surface tensions depend on the normal vector \vec{n} of the imaginary surface. It holds

Theorem 1 (Cauchy's stress theorem). *There exist unique second order tensors σ and $\hat{\mathbf{P}}$, such that*

$$\vec{t}(x, t, \vec{n}) = \sigma(x, t)\vec{n}, \quad \hat{\vec{t}}(\hat{x}, t, \hat{n}) = \hat{\mathbf{P}}(\hat{x}, t)\hat{n}.$$

The tensor $\sigma = \sigma^T$ is symmetric and called the Cauchy stress tensor, the tensor field $\hat{\mathbf{P}}$ is called the first Piola-Kirchhoff stress tensor. $\hat{\mathbf{P}}$ is usually not symmetric.

Proof. For the proof, we refer to the literature [99]. □

One immediate consequence of Cauchy's stress theorem is that traction vectors for opposite normal vectors annihilate each other - Newton's law of action and reaction

$$\vec{t}(x, t, -\vec{n}) = \sigma(x, t)(-\vec{n}) = -\sigma(x, t)\vec{n} = -\vec{t}(x, t, \vec{n}).$$

As the Cauchy stress tensor must be symmetric, it consists of six independent components

$$\sigma = \begin{pmatrix} \sigma_{11} & \sigma_{12} & \sigma_{13} \\ \sigma_{12} & \sigma_{22} & \sigma_{23} \\ \sigma_{13} & \sigma_{23} & \sigma_{33} \end{pmatrix}.$$

The second order tensor $\hat{\mathbf{P}}$ is usually not symmetric and consists of nine independent entries. For the relation of σ and $\hat{\mathbf{P}}$ it holds

$$\sigma \vec{n} ds = \hat{\mathbf{P}} \hat{n} d\hat{s},$$

such that the two different traction vectors describe the transformation of a surface integral. We will get back to this relation in Section 1.1.7.

The components of the stress tensor are best understood by a decomposition of stresses into *normal stress* $\sigma \in \mathbb{R}$ and *shear stress* $\tau \in \mathbb{R}$. Let \vec{t} be a stress vector in $x \in V(t)$ on a imaginary

surface S with normal vector \vec{n} . The normal-stress σ is defined as the projection of the traction vector in normal direction

$$\sigma = \vec{t}^T \vec{n} = (\vec{n}, \sigma \vec{n}),$$

while the shear stress is defined as the tangential part of the stress

$$\tau = \vec{t}^T \vec{t}_1 = (\vec{t}_1, \sigma \vec{n}),$$

where \vec{t}_1 is the tangential vector that arises from projection of \vec{t} onto the surface

$$\vec{t}_1 = \frac{\vec{t} - \sigma \vec{n}}{\|\vec{t} - \sigma \vec{n}\|}.$$

Then, the stress vector can be decomposed into the normal stress σ and shear stress τ by

$$\vec{t} = (\vec{t}, \vec{n}) \vec{n} + (\vec{t}, \vec{t}_1) \vec{t}_1 = \sigma \vec{n} + \tau \vec{t}_1.$$

Here $\sigma, \tau \in \mathbb{R}$ are the lengths of the stress vectors in normal direction and tangential direction. Given the Cauchy stress tensor σ , it holds

$$\sigma = (\vec{n}, \sigma \vec{n}), \quad \tau = (\vec{t}, \sigma \vec{n}).$$

If for the normal stress it holds $\sigma < 0$, the material undergoes a compression, while for $\sigma > 0$ an expansion is given. Further, it holds

$$|\sigma \vec{n}|^2 = |\vec{t}|^2 = |n \cdot \sigma|^2 = \tau^2 + \sigma^2.$$

Next, let us assume, that the imaginary surface has normal vector $\vec{n} = \mathbf{e}_i$ with $(\mathbf{e}_i)_j = \delta_{ij}$. The normal stress is given

$$\sigma = (\mathbf{e}_i, \sigma \mathbf{e}_i) = \sigma_{ii},$$

by the diagonal entry of the Cauchy-stress tensor, while the shear stress in \mathbf{e}_k direction for $k \neq i$ gets

$$\tau = (\mathbf{e}_k, \sigma \mathbf{e}_i) = \sigma_{ki} = \sigma_{ki}.$$

Hence, the diagonal entries of σ refer to the normal stresses, while all off-diagonals refer to tangential shear stresses.

Remark 2 (Stress in the reference system). *Usually, only static stresses act in the initial reference state of a system at time $t = 0$. In case of a resting fluid, this stress can be caused by the hydrostatic pressure. Sometimes however, initial configurations cannot be considered to be stress-free. An example could be organic material like wood, where the undeformed reference system may be subject to stress caused by growth, see [141].*

1.1.6 Conservation principles

The most important physical conservation principles in the context of fluid-mechanics and structure-mechanics are conservation of mass, which says that “mass is neither created nor destroyed”, conservation of momentum, that says, that “the change in momentum is equivalent to the external forces” and conservation of angular momentum, saying that “the change in

angular momentum is equal to the torque". Using the notation derived in the previous section, conservation of mass reads

$$d_t m(V(t)) = 0, \quad (1.10)$$

where the volume's mass $m(V(t))$ is given by

$$m(V(t)) = \int_{V(t)} \rho(x, t) \, dx,$$

with a density ρ . Conservation of momentum gets

$$d_t I(V(t)) = K(V(t)) + K(\partial V(t)), \quad (1.11)$$

with the momentum $I(V(t))$

$$I(V(t)) = \int_{V(t)} \rho(x, t) \mathbf{v}(x, t) \, dx,$$

and volume- and surface forces $K(V(t))$ and $K(\partial V(t))$ given by:

$$K(V(t)) = \int_{V(t)} \rho(x, t) \mathbf{f}(x, t) \, dx, \quad K(\partial V(t)) = \int_{\partial V(t)} \vec{t} \, d.o.$$

Here, \mathbf{f} is a prescribed volume force density and \vec{t} denotes the surface stress in direction \vec{n} . As discussed, it holds by Cauchy's stress theorem 1 that this surface force linearly depends on the normal direction such that it can be expressed with help of a stress tensor $\sigma \in \mathbb{R}^{n \times n}$ as $\vec{t} = \sigma \vec{n}$. This way, the surface allows for a transformation to a volume integral

$$K(\partial V(t)) = \int_{\partial V(t)} \vec{n} \cdot \sigma \, d.o. = \int_{V(t)} \operatorname{div}(\sigma) \, dx.$$

Finally, conservation of angular momentum is given by

$$d_t L(V(t)) = D(V(t)), \quad (1.12)$$

where the angular momentum $L(V(t))$ with respect to the origin is given as

$$L(V(t)) = \int_{V(t)} x \times (\rho \mathbf{v}) \, dx,$$

and the torque $D(V(t))$ is defined by

$$D(V(t)) = \int_{V(t)} x \times (\rho \mathbf{f}) \, dx + \int_{\partial V(t)} x \times (\vec{n} \cdot \sigma) \, d.o.$$

Since the integration domain $V(t)$ in (1.10), (1.11) and (1.12) depends on the time t , evaluation of derivatives like $d_t m(V(t))$ is not straightforward and will be accomplished with help of the essential *Reynolds' Transport Theorem*:

Lemma 3 (Reynolds' Transport Theorem). *Let $V(t) \subset \mathbb{R}^d$ be a material volume. Further, let $\Phi(x, t)$ be a sufficiently smooth scalar function defined on $V(t)$. Then, it holds*

$$d_t \int_{V(t)} \Phi(x, t) \, dx = \int_{V(t)} (\partial_t \Phi(x, t) + \operatorname{div}(\Phi \mathbf{v})) \, dx.$$

Proof. The proof can be shown by elementary calculations using the transformation of $T(t) : \hat{V} \rightarrow V(t)$ to a fixed reference domain and requiring the derivatives of the transformations functional determinant $\det(\hat{\nabla}T(t))$ with respect to its entries $\hat{\nabla}\hat{T}_{ij}$. See also Lemma 30. \square

Applying this theorem to the scalar value $\Phi(x, t) := \rho(x, t)$ we derive the *Law of Mass Conservation*:

$$\int_{V(t)} \partial_t \rho + \operatorname{div}(\rho \mathbf{v}) \, d\mathbf{x} = 0.$$

This equation is valid for every volume $V(t)$. Assuming, that the expression $\partial_t \rho + \operatorname{div}(\rho \mathbf{v})$ is continuous (which is an assumption on the physical properties of the material), the equation of mass-conservation holds in a point-wise manner

$$\partial_t \rho + \operatorname{div}(\rho \mathbf{v}) = 0. \quad (1.13)$$

The second basic rule is *conservation of momentum*, derived by the scalar values $\Phi(x, t) := \rho(x, t)\mathbf{v}_i(x, t)$ for every component of the velocity field. With a column-wise representation of the stress-tensor $\sigma = (\sigma_1, \dots, \sigma_d)$ Reynolds transport theorem yields:

$$\int_{V(t)} \partial_t(\rho \mathbf{v}_i) + \operatorname{div}(\rho \mathbf{v}_i \mathbf{v}) \, d\mathbf{x} = \int_{V(t)} \rho \mathbf{f}_i + \operatorname{div}(\sigma_i) \, d\mathbf{x}, \quad i = 1, \dots, d.$$

Given continuity of the integrand we can again deduce a point-wise equation

$$\partial_t(\rho \mathbf{v}_i) + \operatorname{div}(\rho \mathbf{v}_i \mathbf{v}) = \rho \mathbf{f}_i + \operatorname{div}(\sigma_i), \quad i = 1, \dots, d.$$

By introducing the external product of two vectors

$$\mathbf{v} \otimes \mathbf{w} \in \mathbb{R}^{d \times d}, \quad (\mathbf{v} \otimes \mathbf{w})_{ij} := \mathbf{v}_i \mathbf{w}_j,$$

we can formulate the equation for the conservation of momentum in *conservative formulation*

$$\partial_t(\rho \mathbf{v}) + \operatorname{div}(\rho \mathbf{v} \otimes \mathbf{v}) = \rho \mathbf{f} + \operatorname{div}(\sigma).$$

Combining this equation with the mass-conservation, we can further deduce the equation for conservation of momentum in the *non-conservative formulation*

$$\rho \partial_t \mathbf{v} + \rho(\mathbf{v} \cdot \nabla) \mathbf{v} = \rho \mathbf{f} + \operatorname{div}(\sigma). \quad (1.14)$$

The equation for the *conservation of angular momentum* is given by

$$d_t \int_{V(t)} \mathbf{x} \times (\rho \mathbf{v}) \, d\mathbf{x} = \int_{V(t)} \mathbf{x} \times (\rho \mathbf{f}) \, d\mathbf{x} + \int_{\partial V(t)} \mathbf{x} \times (\vec{n} \cdot \sigma) \, d\mathbf{o}.$$

Applying Reynolds transport theorem (with the help of the Levi-Cicita symbol $[\cdot]$), we can deduce the following three equations

$$\begin{aligned} i = 1 \quad & \sigma_{23} - \sigma_{32} = 0 \\ i = 2 \quad & \sigma_{13} - \sigma_{31} = 0 \\ i = 3 \quad & \sigma_{12} - \sigma_{21} = 0, \end{aligned}$$

that impose the symmetry of the Cauchy stress tensor:

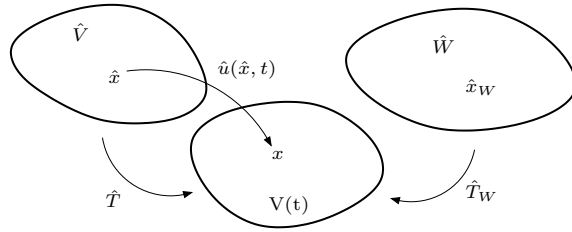


Figure 1.5: Moving Eulerian volume $V(t)$ with Lagrangian reference \hat{V} and third arbitrary reference volume \hat{W} .

$$\sigma = \sigma^T. \quad (1.15)$$

Further conservation principles are important if physical properties like entropy, energy and temperature are taken into consideration. Since we will deal with isentropic materials only, where all dynamical processes will take place without change of entropy, the three fundamental principles of mass-, momentum- and angular momentum-conservation will be sufficient to describe all desired behavior.

It remains to describe the tensor of surface-forces σ . This tensor will heavily depend on the material under consideration, whether it is a fluid or a solid, whether the fluid is water, air or blood, the solid may be elastic or plastic or have properties of both. Here, physical modeling comes into place, exact laws for the dependence of this tensor on quantities like velocity and density usually do not exist. Since we know that σ is symmetric, six additional equations are required for its description.

1.1.7 Conservation principles in different coordinate systems

In this section, we discuss the transformation of the conservation equations, which have been derived in the Eulerian framework, to different coordinate frameworks. The conservation principles are universal, however we already have discussed that for structure dynamics a Lagrangian view-point is more natural.

Let $V(t)$ be the moving Eulerian framework and let \hat{V} be the Lagrangian reference system. Further, by \hat{W} we denote an arbitrary second fixed reference system, see Figure 1.5. While the case $\hat{W} = \hat{V}$ is possible, we will allow for arbitrary systems without physical meaning. However, we assume that \hat{W} is fixed in time and that there exists an invertible mapping $\hat{T}_W(t) : \hat{W} \rightarrow V(t)$ with gradient $\hat{\mathbf{F}}_W := \hat{\nabla} \hat{T}_W$ and determinant $\hat{J}_W := \det(\hat{\mathbf{F}}_W)$. $\hat{\mathbf{F}}_W$ and \hat{J}_W have the same properties as the Lagrangian deformation gradient, see Definition 1 and Lemma 1.

By allowing for arbitrary reference systems \hat{W} we have to deal with three different reference systems, the Lagrangian particles, $\hat{x} \in \hat{V}$, their Eulerian path $x(\hat{x}, t) \in V(t)$ and further $\hat{x}_W \in \hat{W}$ with $\hat{T}_W(\hat{x}_W, t) = x = \hat{T}(\hat{x}, t)$. Note, that it does not hold $\partial_t \hat{T}_W = \hat{\mathbf{v}}$, as we have to distinguish between the physical velocity $\hat{\mathbf{v}}$ and the velocity of the arbitrary coordinate system motion.

We start by describing basic properties used to map between the two systems \hat{W} and $V(t)$. First, we introduce the inverse mapping $T_W(t) : V(t) \mapsto \hat{W}$. It holds:

Lemma 4 (Inverse mapping). *By $T_W(t) : V(t) \rightarrow \hat{W}$ we denote the inverse mapping, by $\mathbf{F}_W := \nabla T_W$ its gradient and by $J_W := \det(\mathbf{F}_W)$ its determinant. It holds*

$$\mathbf{F}_W = \hat{\mathbf{F}}_W^{-1}, \quad J_W := \hat{J}_W^{-1}, \quad \partial_t T_W = -\hat{\mathbf{F}}_W^{-1} \partial_t \hat{T}_W.$$

Proof. It holds

$$T_W \circ \hat{T}_W = \text{id} \Rightarrow \mathbf{F}_W \hat{\mathbf{F}}_W = I \Rightarrow \mathbf{F}_W = \hat{\mathbf{F}}_W^{-1}.$$

By taking the determinant of both sides, we immediately get $J_W = \hat{J}_W^{-1}$. Finally,

$$T_W \circ \hat{T}_W = \text{id} \Rightarrow 0 = d_t T_W(\hat{T}_W(\hat{x}, t), t) = \partial_t T_W + \nabla T_W \partial_t \hat{T}_W.$$

Using $\nabla T_W = \mathbf{F}_W = \hat{\mathbf{F}}_W^{-1}$ we obtain the relation $\partial_t T_W = -\hat{\mathbf{F}}_W^{-1} \partial_t \hat{T}_W$. \square

In Lemma 2 we have already considered the transformation of spatial and temporal derivatives between the Eulerian and the Lagrangian coordinate system. Likewise, it holds for a scalar function $f : V(t) \rightarrow \mathbb{R}$ and a vector field $\mathbf{w} : V(t) \rightarrow \mathbb{R}^d$ with counter parts \hat{f} and $\hat{\mathbf{w}}$ on \hat{W} :

$$\nabla f = \hat{\mathbf{F}}_W^{-T} \hat{\nabla} \hat{f}, \quad \nabla \mathbf{w} = \hat{\nabla} \hat{\mathbf{w}} \hat{\mathbf{F}}_W^{-1}. \quad (1.16)$$

For temporal derivatives transformed to general coordinate systems W we must take care of two different velocities: the particle velocity $\hat{\mathbf{v}}$ and the domain velocity $\partial_t \hat{T}_W$, which do not coincide, if $\hat{W} \neq \hat{V}$:

Lemma 5 (Transformation of temporal derivatives). *Let $f : V(t) \rightarrow \mathbb{R}$ with counterpart $\hat{f}(\hat{x}_W, t) = f(x, t)$. It holds*

$$\partial_t f = \partial_t \hat{f} - (\hat{\mathbf{F}}_W^{-1} \partial_t \hat{T}_W \cdot \hat{\nabla}) \hat{f}, \quad d_t f = \partial_t \hat{f} + (\hat{\mathbf{F}}_W^{-1} (\hat{\mathbf{v}} - \partial_t \hat{T}_W) \cdot \hat{\nabla}) \hat{f}.$$

Proof. With $\hat{x}_W = T_W(x, t)$ it holds

$$\partial_t f(x, t) = d_t \hat{f}(\hat{x}_W, t) = d_t \hat{f}(T_W(x, t), t) = \partial_t \hat{f} + \hat{\nabla} \hat{f} \cdot \partial_t T_W.$$

The first result follows with help of Lemma 4. The relation for the material derivative is given by

$$d_t f(x, t) = \partial_t f(x, t) + \nabla f \cdot \partial_t x.$$

Here, $\partial_t x = \mathbf{v} = \hat{\mathbf{v}}$ refers to the trace of particles, where $\mathbf{v} = \hat{\mathbf{v}}$ is the velocity of the particle and not the velocity of the mapping \hat{T}_W ! Together with (1.16) and the transformation of the partial time derivative we get

$$d_t f = \partial_t \hat{f} - (\hat{\mathbf{F}}_W^{-1} \partial_t \hat{T}_W \cdot \hat{\nabla}) \hat{f} + \hat{\mathbf{F}}_W^{-T} \hat{\nabla} \hat{f} \cdot \hat{\mathbf{v}}.$$

\square

Remark 3 (Transformation between Lagrangian and Eulerian coordinates). *If $\hat{V} = \hat{W}$ it holds $\hat{T}_W = \hat{T}$ as well as $\hat{\mathbf{F}}_W = \hat{\mathbf{F}}$ and $\hat{J}_W = \hat{J}$. the statements of Lemma 5 simplify to*

$$\hat{W} = \hat{V} \Rightarrow \partial_t f = \partial_t \hat{f} - (\hat{\mathbf{F}}^{-1} \hat{\mathbf{v}} \cdot \hat{\nabla}) \hat{f}, \quad d_t f = \partial_t \hat{f}.$$

This results explains, why the convective term $(\mathbf{v} \cdot \nabla) \mathbf{v}$ will not appear in Lagrangian coordinates. See also Lemma 2.

In the following we discuss the transformation of the conservation principles to arbitrary coordinate reference systems \hat{W} . This transformation will be fundamental for solid mechanics, where the natural view-point is the Lagrangian one with $\hat{W} = \hat{V}$. Further, one of the standard approaches for coupling fluid-structure interactions relies on the mapping of the fluid problem onto a fixed reference system. Since this reference system will not be the Lagrangian one, we proceed without specifying the connotation of \hat{W} . The equation for conservation of momentum (1.14) is given by

$$\rho \partial_t \mathbf{v} + \rho (\mathbf{v} \cdot \nabla) \mathbf{v} = \rho \mathbf{f} + \operatorname{div}(\sigma) \text{ in } V(t),$$

with a density ρ , velocity \mathbf{v} , volume force \mathbf{f} and the Eulerian stress-tensor σ . The specific form of this stress-tensor will be discussed in later sections. Here, we only assume, that this stress tensor is symmetric $\sigma = \sigma^T$. By $\hat{\mathbf{v}}(\hat{x}_W, t) = \mathbf{v}(x, t)$, $\hat{\rho}(\hat{x}_W, t) = \rho(x, t)$, $\hat{\mathbf{f}}(\hat{x}_W, t) = \mathbf{f}(x, t)$ as well as $\hat{\sigma}(\hat{x}_W, t) = \sigma(x, t)$ we denote the counterparts of these quantities in the reference system \hat{W} . By (refmodel:spatialalderis) and 5 it holds:

$$\partial_t \mathbf{v} = \partial_t \hat{\mathbf{v}} - (\hat{\mathbf{F}}_W^{-1} \partial_t \hat{T}_W \cdot \hat{\nabla}) \hat{\mathbf{v}}, \quad (\mathbf{v} \cdot \nabla) \mathbf{v} = \nabla \mathbf{v} \mathbf{v} = \hat{\nabla} \hat{\mathbf{v}} \hat{\mathbf{F}}_W^{-1} \hat{\mathbf{v}} = (\hat{\mathbf{F}}_W^{-1} \hat{\mathbf{v}} \cdot \hat{\nabla}) \hat{\mathbf{v}},$$

and combined, we get:

$$\partial_t \mathbf{v} + (\mathbf{v} \cdot \nabla) \mathbf{v} = \partial_t \hat{\mathbf{v}} + (\hat{\mathbf{F}}_W^{-1} (\hat{\mathbf{v}} - \partial_t \hat{T}_W) \cdot \hat{\nabla}) \hat{\mathbf{v}}. \quad (1.17)$$

As discussed above, in the case of a mapping to the Lagrangian reference system, the mapping's temporal derivative is the velocity $\partial_t \hat{T} = \hat{\mathbf{v}}$ and the momentum terms simplify to

$$\hat{V} = \hat{W} \Rightarrow \partial_t \mathbf{v} + (\mathbf{v} \cdot \nabla) \mathbf{v} = \partial_t \hat{\mathbf{v}}. \quad (1.18)$$

It remains to transform the divergence of the stresses to the reference domain. Here, a simple transformation of $\operatorname{div}(\sigma)$ to the reference system is not sufficient. We need to keep the meaning of this stress-term in mind, indicating surface-forces in normal-direction. Since under deformation of the domains $\hat{V} \rightarrow V(t)$ these normal vectors are also transformed, we must base the mapping process on the correct representation of these surface forces. We need to find the exact form of the first Piola-Kirchhoff stress tensor $\hat{\mathbf{P}}$ in the reference system, such that it holds:

$$\int_{\partial \hat{W}} \hat{\mathbf{P}} \hat{n} d\hat{o} = \int_{\partial V(t)} \sigma \vec{n} do.$$

$\hat{\mathbf{P}}$ will be called the *Piola transformation* of σ . For the derivation of this transformation we first regard vector fields $\mathbf{w} : V(t) \rightarrow \mathbb{R}^d$ with reference counterpart $\hat{\mathbf{w}} : \hat{W} \rightarrow \mathbb{R}^d$.

Lemma 6 (Piola transformation). *Let $\mathbf{w} : V(t) \rightarrow \mathbb{R}^d$ be a differentiable vector field and $\hat{\mathbf{w}}$ its representation in the reference system \hat{W} . The Piola transformation of \mathbf{w} is given by*

$$\hat{J}_W \hat{\mathbf{F}}_W^{-1} \hat{\mathbf{w}}.$$

On every volume $V(t)$ with corresponding reference volume \hat{W} it holds

$$\int_{\partial V(t)} \vec{n} \cdot \mathbf{w} do = \int_{\partial \hat{W}} \hat{n} \cdot (\hat{J}_W \hat{\mathbf{F}}_W^{-1} \hat{\mathbf{w}}) d\hat{o}, \quad \int_{V(t)} \operatorname{div}(\mathbf{w}) dx = \int_{\hat{W}} \widehat{\operatorname{div}}(\hat{J}_W \hat{\mathbf{F}}_W^{-1} \hat{\mathbf{w}}) d\hat{x}.$$

Further, in a point-wise sense it holds

$$\hat{J}_W \operatorname{div}(\mathbf{w}) = \widehat{\operatorname{div}}(\hat{J}_W \hat{\mathbf{F}}_W^{-1} \hat{\mathbf{w}}).$$

Proof. We use a variational argument. Let ξ be differentiable on $V(t)$ with reference counterpart $\hat{\xi} \in \hat{W}$:

$$\int_{\partial V(t)} \vec{n} \cdot \mathbf{w} \xi \, d\sigma = \int_{V(t)} \operatorname{div}(\mathbf{w} \xi) \, dx = \int_{\hat{W}} \hat{J}_W \operatorname{div}(\mathbf{w} \xi) \, d\hat{x}. \quad (1.19)$$

Next, with (1.16) it holds for $\hat{\xi} = \xi$:

$$\int_{\hat{W}} \hat{J}_W \operatorname{div}(\mathbf{w} \xi) \, d\hat{x} = \int_{\hat{W}} \hat{J}_W \operatorname{div}(\mathbf{w}) \hat{\xi} \, d\hat{x} + \int_{\hat{W}} \hat{J}_W \hat{\mathbf{w}} \cdot \hat{\mathbf{F}}_W^{-T} \hat{\nabla} \hat{\xi} \, d\hat{x}. \quad (1.20)$$

With Green's formula, the second integral is transformed to

$$\begin{aligned} \int_{\hat{W}} \hat{J}_W \hat{\mathbf{w}} \cdot \hat{\mathbf{F}}_W^{-T} \hat{\nabla} \hat{\xi} \, d\hat{x} &= \int_{\hat{W}} \hat{J}_W \hat{\mathbf{F}}_W^{-1} \hat{\mathbf{w}} \cdot \hat{\nabla} \hat{\xi} \, d\hat{x} \\ &= - \int_{\hat{W}} \widehat{\operatorname{div}}(\hat{J}_W \hat{\mathbf{F}}_W^{-1} \hat{\mathbf{w}}) \hat{\xi} \, d\hat{x} + \int_{\partial \hat{W}} \hat{\vec{n}} \cdot (\hat{J}_W \hat{\mathbf{F}}_W^{-1} \hat{\mathbf{w}}) \hat{\xi} \, d\hat{o}. \end{aligned} \quad (1.21)$$

Combining (1.19), (1.20) and (1.21) gives

$$\begin{aligned} \int_{\partial V(t)} n \cdot \mathbf{w} \xi \, d\sigma - \int_{\hat{W}} \hat{J}_W \operatorname{div}(\mathbf{w}) \hat{\xi} \, d\hat{x} \\ = - \int_{\hat{W}} \widehat{\operatorname{div}}(\hat{J}_W \hat{\mathbf{F}}_W^{-1} \hat{\mathbf{w}}) \hat{\xi} \, d\hat{x} + \int_{\partial \hat{W}} \hat{\vec{n}} \cdot (\hat{J}_W \hat{\mathbf{F}}_W^{-1} \hat{\mathbf{w}}) \hat{\xi} \, d\hat{o}. \end{aligned}$$

By picking a Dirac sequence $\{\hat{\xi}_\epsilon^y\}_{\epsilon>0}$ where $\hat{\xi}_\epsilon^y \in C_0^\infty(\hat{W})$ with

$$\int_{\hat{W}} \hat{\xi}_\epsilon^y(\hat{x}) \hat{f}(\hat{x}) \, d\hat{x} \xrightarrow[\epsilon \rightarrow 0]{} \hat{f}(\hat{y}) \quad \forall \hat{f} \in C(\hat{W}),$$

we conclude for all inner points:

$$\hat{J}_W \operatorname{div}(\mathbf{w}) = \widehat{\operatorname{div}}(\hat{J}_W \hat{\mathbf{F}}_W^{-1} \hat{\mathbf{w}}).$$

Hence

$$\int_{V(t)} \operatorname{div}(\mathbf{w}) \, dx = \int_{\hat{W}} \hat{J}_W \operatorname{div}(\hat{\mathbf{w}}) \, d\hat{x} = \int_{\hat{W}} \widehat{\operatorname{div}}(\hat{J}_W \hat{\mathbf{F}}_W^{-1} \hat{\mathbf{w}}) \, d\hat{x}.$$

The relation for the surface integral follows by Gauss' divergence theorem. \square

This important result is used to transform the surface forces to the reference system. Let $\sigma = (\sigma_i)_{i=1}^d$ be the row-vectors (or the column-vectors since $\sigma = \sigma^T$ by the conservation of angular momentum). It holds:

$$F_i(\partial V(t)) := \int_{\partial V(t)} \vec{n} \cdot \sigma_i \, d\sigma = \int_{V(t)} \operatorname{div}(\sigma_i) \, dx$$

and with the just proven lemma we conclude

$$F_i(\partial V(t)) = \int_{\hat{W}} \widehat{\operatorname{div}}(\hat{J}_W \hat{\mathbf{F}}_W^{-1} \hat{\sigma}_i) \, d\hat{x} = \int_{\partial \hat{W}} \hat{\vec{n}} \cdot (\hat{J}_W \hat{\mathbf{F}}_W^{-1} \hat{\sigma}_i) \, d\hat{o}.$$

Reassembling the stress-tensor $\hat{\sigma} = (\hat{\sigma}_i)$ we get the reference presentation of the surface forces:

$$F(\partial V(t)) = \int_{\partial \hat{W}} (\hat{J}_W \hat{\sigma} \hat{\mathbf{F}}_W^{-T}) \hat{\vec{n}} \, d\hat{o} = \int_{\hat{W}} \widehat{\operatorname{div}}(\hat{J}_W \hat{\sigma} \hat{\mathbf{F}}_W^{-T}) \, d\hat{x}.$$

We define

Definition 3 (Piola Kirchhoff stress tensors). *The First Piola Kirchhoff stress tensor given by*

$$\hat{\mathbf{P}} := \hat{J}_W \hat{\sigma} \hat{\mathbf{F}}_W^{-T}.$$

It relates forces in the Eulerian coordinate framework with coordinates in a reference framework \hat{W} . The Second Piola Kirchhoff stress tensor given by

$$\hat{\Sigma} := \hat{\mathbf{F}}_W^{-1} \hat{\mathbf{P}} = \hat{J}_W \hat{\mathbf{F}}_W^{-1} \hat{\sigma} \hat{\mathbf{F}}_W^{-T}.$$

Unlike the Eulerian stress tensor σ , the 1st Piola Kirchhoff stress tensor $\hat{\mathbf{P}}$ is not symmetric. The 2nd Piola Kirchhoff stress tensor is symmetric but it does not have an immediate physical explanation.

Using the first Piola Kirchhoff stress tensor and relation (1.17) the momentum equation on arbitrary reference systems \hat{W} is given by:

$$\hat{J}_W \hat{\rho} (\partial_t \hat{\mathbf{v}} + (\hat{\mathbf{F}}_W^{-1} (\hat{\mathbf{v}} - \partial_t \hat{T}_W) \cdot \hat{\nabla}) \hat{\mathbf{v}}) = \hat{J}_W \hat{\rho} \hat{f} + \widehat{\operatorname{div}} (\hat{J}_W \hat{\sigma} \hat{\mathbf{F}}_W^{-T}). \quad (1.22)$$

1.2 Material Laws

The basic concepts of continuum mechanics introduced in the previous section are exact in a way, that they are based on fundamental physical principles. The conservation principles for mass, momentum and angular momentum form systems of four partial differential equations for 10 unknowns: density ρ , velocity field \vec{v} and the six unknowns of the symmetric stress tensor σ . This system is strongly under-determined and to close it, additional equations are required that rely the values of the stress tensor on other fundamental quantities like velocity, density or deformation.

In the following sections, we will derive such *material laws*, that describe the properties of the stress tensors, in the different formulations like σ , $\hat{\Sigma}$ or $\hat{\mathbf{P}}$. We assume, that these stress tensors will depend on strain or strain rate given as deformation gradient $\hat{\mathbf{F}}$, its inverse \mathbf{F} , or tensors like $\hat{\mathbf{C}}$, $\hat{\mathbf{E}}$, \mathbf{b} , \mathbf{e} or $\dot{\epsilon}$. We denote this relation by tensor-valued functions

$$\sigma = f(\dot{\epsilon}), \quad \hat{\mathbf{P}} = \hat{f}(\hat{\mathbf{F}}), \quad \hat{\Sigma} = \hat{f}(\hat{\mathbf{E}}),$$

or by similar expressions in $\hat{\mathbf{E}}$ or \mathbf{b} . We assume, that all materials are homogenous and do not explicitly depend on the location $x \in V(t)$.

We are not considering arbitrary material laws but postulate several assumption on the material's properties:

1. *Objectivity*: The material law is independent of the spectators viewpoint. This property will hold for every physical material.
2. *Homogeneity*: We assume, that the material is homogenous, i.e. the strain-stress relation will not explicitly depend on the location $x \in V(t)$.
3. *Isentropic and isothermal process*: We assume, that entropy and temperature do not play a role. There is no conversion between heat and kinetic energy. The temperature stays constant and does not affect the material law. This assumption is a simplification, as most elastic materials and also some fluids show a strong dependency on the temperature.

4. *Isotropy*: There is no distinct direction in the material. The response to strain or strain rate is the same in all directions. This assumption rules out anisotropic materials like fiber-reinforced composites or also biological tissue, where usually layers are directed anisotropically. Most fluids however are isotropic.

These assumptions lead to a strong simplification of possible material laws. The following *Rivlin-Ericksen Theorem* shows, that all possible material laws depend on symmetric strain tensors \mathbf{C} , \mathbf{E} or $\dot{\epsilon}$ only and that all material laws are quadratic polynomials in the invariants of these tensors:

Theorem 2 (Rivlin-Ericksen Theorem). *A stress response function $\tilde{f}(\hat{\mathbf{F}})$ is isotropic and indifferent with respect to the coordinate system, if and only if it depends on the symmetric strain tensors only*

$$\tilde{f}(\hat{\mathbf{F}}) = \hat{f}(\hat{\mathbf{F}}^T \hat{\mathbf{F}}) = \hat{f}(\hat{\mathbf{C}}),$$

and it is given as a quadratic polynomial

$$\hat{f}(\hat{\mathbf{C}}) = \beta_0(i(\hat{\mathbf{C}}))I + \beta_1(i(\hat{\mathbf{C}}))\hat{\mathbf{C}} + \beta_2(i(\hat{\mathbf{C}}))\hat{\mathbf{C}}^2, \quad (1.23)$$

with scalar coefficients β_i that depend on the invariants (under orthogonal transformation) of the symmetric tensors \mathbf{C} :

$$I_1(\vec{\mathbf{C}}) = \lambda_1 + \lambda_2 + \lambda_3, \quad I_2(\vec{\mathbf{C}}) = \lambda_1\lambda_2 + \lambda_2\lambda_3 + \lambda_1\lambda_3, \quad I_3(\vec{\mathbf{C}}) = \lambda_1\lambda_2\lambda_3,$$

where λ_1, λ_2 and λ_3 are the three eigenvalues of $\vec{\mathbf{C}}$.

Proof. For a proof, we refer to the literature [197] or to [227] for a modern presentation. \square

As a symmetric positive definite tensor, \mathbf{C} has three positive eigenvalues $\lambda_1, \lambda_2, \lambda_3$ and a system of orthogonal eigenvalues. We know, that eigenvalues are invariant to orthogonal transformation. To derive these invariants, we further cite the following Lemma:

Lemma 7. *Given a tensor $\vec{A} \in \mathbb{R}^{3 \times 3}$ it holds for every $\lambda \in \mathbb{R}$*

$$\det(\vec{A} - \lambda I) = -\lambda^3 + I_1(\vec{A})\lambda^2 + I_2(\vec{A})\lambda + I_3(\vec{A}),$$

with

$$I_1(\vec{A}) = \text{tr}(\vec{A}), \quad I_2(\vec{A}) = \frac{1}{2}(\text{tr}(\vec{A})^2 - \text{tr}(\vec{A}^2)), \quad I_3(\vec{A}) = \det(\vec{A}).$$

If \vec{A} is symmetric positive definite with eigenvalues $\lambda_1, \lambda_2, \lambda_3$, it further holds

$$I_1(\vec{A}) = \lambda_1 + \lambda_2 + \lambda_3, \quad I_2(\vec{A}) = \lambda_1\lambda_2 + \lambda_2\lambda_3 + \lambda_1\lambda_3, \quad I_3(\vec{A}) = \lambda_1\lambda_2\lambda_3.$$

Proof. See Problem 4 \square

The Rivlin-Ericksen Theorem 2 strongly limits possible material laws for homogenous and isotropic materials. All material laws - including fluids and solids - considered in the context of this book will fall under this theorem.

As every matrix satisfies its own characteristic polynomial, it holds for $\hat{\mathbf{C}} \in \mathbb{R}^{3 \times 3}$ that

$$\hat{\mathbf{C}}^3 = I_1(\hat{\mathbf{C}})\hat{\mathbf{C}}^2 + I_2(\hat{\mathbf{C}})\hat{\mathbf{C}} + I_3(\hat{\mathbf{C}}). \quad (1.24)$$

Using this relation, the material law (1.23) is equivalent to a second representation

$$\hat{f}(\hat{\mathbf{C}}) = \gamma_0(i(\hat{\mathbf{C}}))I + \gamma_1(i(\hat{\mathbf{C}}))\hat{\mathbf{C}} + \gamma_2(i(\hat{\mathbf{C}}))\hat{\mathbf{C}}^{-1}.$$

Remark 4. As the two tensors $\hat{\mathbf{E}} = \frac{1}{2}(\hat{\mathbf{C}} - I)$ are directly connected, every material law in $\hat{\mathbf{C}}$ can also be expressed in $\hat{\mathbf{E}}$, as

$$\alpha_0 I + \alpha_1 \hat{\mathbf{C}} + \alpha_2 \hat{\mathbf{C}}^2 = (\alpha_0 + \alpha_1 + \alpha_2)I + (2\alpha_1 + 4\alpha_2)\hat{\mathbf{E}} + 4\alpha_2 \hat{\mathbf{E}}^2.$$

Further, for the eigenvalues of $\hat{\mathbf{E}}$ and $\hat{\mathbf{C}}$ there holds a linear relation

$$\lambda_i w_i = \hat{\mathbf{C}} w_i = 2\hat{\mathbf{E}} w_i + w_i \quad \Leftrightarrow \quad \frac{1}{2}(\lambda_i - 1)w_i = \hat{\mathbf{E}} w_i.$$

1.2.1 Linearizations

For simplicity, we sometimes consider linear models. Two different types of nonlinearities must be considered: first, the material nonlinearity which denotes a nonlinear relation between stress and strain. Second, the geometric nonlinearity, which comes from the discrepancy between reference coordinate system and current system and which is expressed by the deformation gradient $\mathbf{e} = \hat{\mathbf{F}}\hat{\mathbf{e}}$.

Regarding the Rivlin-Ericksen Theorem 2, linearity of a material means that only the first invariant $I_1(\mathbf{E}) = \text{tr}(\mathbf{E})$ may enter the law and that no higher order terms may appear. Further, in geometrically linearized situations, the symmetric strain tensor and $\hat{\mathbf{E}}$ is approximated and linearized

$$\hat{\mathbf{E}} = \frac{1}{2}(\nabla \mathbf{u} + \nabla \mathbf{u}^T + \nabla \mathbf{u}^T \nabla \mathbf{u}) \approx \frac{1}{2}(\nabla \mathbf{u} + \nabla \mathbf{u}^T) =: \hat{\epsilon}.$$

Lemma 8 (Linear material law). *A stress response function $f(\cdot)$ for a linear, homogenous and isotropic material depends on the linearized strain $\hat{\epsilon} = \hat{\nabla} \hat{\mathbf{u}} + \hat{\nabla} \hat{\mathbf{u}}^T$ or on the strain rate tensor $\dot{\epsilon} = \nabla \mathbf{v} + \nabla \mathbf{v}^T$ and its first invariant only*

$$\hat{f}(\hat{\epsilon}) = \beta_0 \text{tr}(\hat{\epsilon})I + \beta_1 \hat{\epsilon}.$$

In fluid mechanics, the Navier-Stokes equations follow such a linear material law and in structure mechanics, the Navier-Lamé system considers these simplifications. While in fluid mechanics a fully linear material law - the Navier-Stokes model - is a very accurate model for many relevant fluids, linearization in solid mechanics is usually not feasible. Here, linear models only apply to very small deformations $|\hat{\mathbf{u}}| \ll 1$ and very small changes in deformation $|\hat{\nabla} \hat{\mathbf{u}}| \ll 1$. In particular, linearized solid models are no longer invariant with respect to fixed body rotations. In the context of fluid-structure interactions, this can significantly damp the dynamics.

1.2.2 Incompressible materials

Some materials have an incompressible behavior which means, that the volume

$$|V(t)| = \int_{V(t)} d\mathbf{x} \equiv \text{"const"},$$

does not change. For an incompressible material, there is no expansion or compression. Many fluids - like water - can be considered incompressible. Incompressibility further applies to many

1.3. The Solid Problem

biological structures. We can describe change of volume in the current system by Reynold's transport theorem

$$0 = d_t |V(t)| = d_t \int_{V(t)} 1 \, dx = \int_{V(t)} \nabla \cdot \mathbf{v} \, dx = \int_{\partial V(t)} n \cdot \mathbf{v} \, do, \quad (1.25)$$

but also in the reference configuration by transformation

$$0 = d_t |V(t)| = d_t \int_{V(t)} 1 \, dx = \int_{\hat{V}} d_t \hat{J} \, d\hat{x}. \quad (1.26)$$

For a fluid, modeled in the current configuration, (1.25) says, that the flow is “divergence-free” with $\operatorname{div} \mathbf{v} = 0$ and also, that the total normal flow over the volume’s boundary is zero. For a divergence free velocity field it holds

$$\operatorname{tr}(\dot{\epsilon}) = 0,$$

and in light of Lemma 8, the material law is even simplified to

$$f(\dot{\epsilon}) = \beta_1 \dot{\epsilon}.$$

To cope with isotropic expansion and compression forces, we introduce a pressure variable as part of the material law:

$$f(\dot{\epsilon}, p) = -pI + \beta_1 \dot{\epsilon}.$$

This pressure is required to enforce the incompressibility of the velocity field, see also Section 1.3.

Considering solid’s, incompressibility in terms of (1.26) means, that the determinant of the deformation gradient will be constant $d_t \hat{J} = 0$. As $\hat{\mathbf{F}} = I$ in the reference system, incompressibility simply says $\hat{J} = 1$ for all times $t \geq t_0$. Further, it then holds that

$$\det(\hat{\mathbf{C}}) = \det(\hat{\mathbf{F}})^2 = 1.$$

For the Green-Lagrange strain tensor $\hat{\mathbf{E}}$ it follows, that third and second invariant fall together, see Lemma 7, Remark 4 and Problem 6.

1.3 The Solid Problem

As discussed, we will usually describe the dynamics of elastic structures in the Lagrangian reference system. Hence, considering the conservation law (1.22) we choose $\hat{W} = \hat{V}$ as reference system. In light of Remark 3, the system of equations is given by

$$\hat{J} \hat{\rho} \partial_{tt} \hat{\mathbf{u}} = \hat{J} \hat{\rho} \hat{\mathbf{f}} + \widehat{\operatorname{div}}(\hat{\mathbf{F}} \hat{\Sigma}),$$

where we eliminated the velocity using $\partial_t \hat{\mathbf{u}} = \hat{\mathbf{v}}$. Considering a material law as introduced in the previous section, the stresses will depend on the strain, and hence on the displacement $\hat{\mathbf{u}}$. The density is known at initial time $\rho(x, 0) = \hat{\rho}^0(\hat{x})$. For $t \geq 0$ it must hold for the mass of the volume \hat{V} under motion:

$$m(\hat{V}) := \int_{\hat{V}} \hat{\rho}^0(\hat{x}) \, d\hat{x} \stackrel{!}{=} \int_{V(t)} \rho(x, t) \, dx = \int_{\hat{V}} \hat{J} \hat{\rho}(\hat{x}, t) \, d\hat{x} =: m(V(t)).$$

At time $t \geq 0$, the simple relation

$$\hat{\rho}(\hat{x}, t) = \hat{J}^{-1}(\hat{x}, t)\hat{\rho}^0(\hat{x}), \quad (1.27)$$

describes the mass in every point \hat{x} of the reference system. The full system of elastic structures formulated in the Lagrangian reference system \hat{V} is given by:

$$\hat{\rho}^0 \partial_{tt} \hat{\mathbf{u}} - \widehat{\operatorname{div}} (\hat{\mathbf{F}} \hat{\boldsymbol{\Sigma}}) = \hat{\rho}^0 \hat{\mathbf{f}} \quad (1.28)$$

It remains to complete this partial differential equation by appropriate boundary conditions and initial conditions. Let $\hat{\mathcal{S}} \subset \mathbb{R}^d$ be the solid domain in reference configuration. At time $t = 0$, we specify initial conditions for density, deformation and velocity

$$\hat{\rho}(\cdot, 0) = \hat{\rho}^0(\cdot), \quad \hat{\mathbf{u}}(\cdot, 0) = \hat{\mathbf{u}}^0(\cdot), \quad \partial_t \hat{\mathbf{u}}(\cdot, 0) = \hat{\mathbf{v}}^0(\cdot), \quad t = 0. \quad (1.29)$$

For all times $t \geq 0$, by $\hat{\mathbf{f}}(\hat{x}, t)$ we denote the acting volume force field. Note, that this force field is directed in the Eulerian framework, such that for example the gravity force field is given by $f = -9.81e_3$, with $e_3 = (0, 0, 1)^T$, independent of the reference framework. The boundary of the domain $\hat{\Gamma}_s := \partial \hat{\mathcal{S}}$ is split into a Dirichlet boundary part $\hat{\Gamma}_s^D$ and into a Neumann part $\hat{\Gamma}_s^N$. On the Dirichlet boundary, we specify matching boundary conditions for the deformation:

$$\hat{\mathbf{u}} = \hat{\mathbf{u}}^D \quad \text{on } \hat{\Gamma}_s^D \times [0, T]. \quad (1.30)$$

Note, that by $\hat{\mathbf{v}} = \partial_t \hat{\mathbf{u}}$ we also uniquely define the velocity on the boundary. The usual Neumann condition on $\hat{\Gamma}_s^N$ specifies the boundary stresses by

$$\vec{n} \cdot \hat{\mathbf{F}} \hat{\boldsymbol{\Sigma}} = \vec{n} \cdot \hat{J} \hat{\sigma}_s \hat{\mathbf{F}}^{-T} = \hat{\mathbf{g}}_s^{(\hat{n})} \text{ on } \hat{\Gamma}_s^N \times [0, T]. \quad (1.31)$$

If the external forces \mathbf{f} and the boundary data $\hat{\mathbf{g}}_s^{(\hat{n})}$ and $\hat{\mathbf{u}}^D$ do not explicitly depend on time, the solution can run into a stationary limit $\hat{\mathbf{u}}(\cdot, t) \rightarrow \hat{\mathbf{u}}(\cdot)$ that does not depend on time. In this case, it holds $\partial_t \hat{\mathbf{v}} = 0$ and hence $\partial_{tt} \hat{\mathbf{u}} = 0$. If such a stationary solution exists, we can directly consider the stationary set of equations:

$$-\widehat{\operatorname{div}} (\hat{\mathbf{F}} \hat{\boldsymbol{\Sigma}}) = \hat{\rho}^0 \hat{\mathbf{f}}. \quad (1.32)$$

Finally, it remains to provide material laws for specific solids. One of the most simple model is the *St. Venant Kirchhoff material*, that postulates a linear dependency between strain tensor $\hat{\mathbf{E}}$ and stresses:

Definition 4 (St. Venant Kirchhoff material). *The St. Venant Kirchhoff material follows the material law*

$$\hat{\boldsymbol{\Sigma}} = 2\mu_s \hat{\mathbf{E}} + \lambda_s \operatorname{tr}(\hat{\mathbf{E}}) I,$$

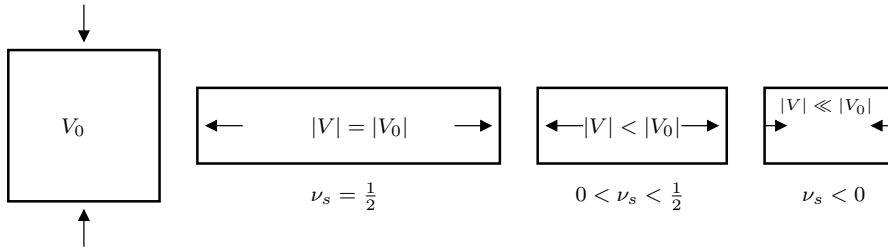


Figure 1.6: Material behavior under compression for different Poisson ratios. Left: incompressible material $\nu_s = \frac{1}{2}$. Middle: compressible material $0 < \nu_s < \frac{1}{2}$. Right: auxetic material with $\nu_s < 0$.

with the first λ_s and second μ_s (also referred to as the shear modulus) Lamé parameters. These two parameters are related to the Poisson ratio ν_s that describes the compressibility and Young's modulus E_s that describes the stiffness:

$$\nu_s = \frac{\lambda_s}{2(\lambda_s + \mu_s)}, \quad E_s = \frac{\mu_s(3\lambda_s + 2\mu_s)}{\lambda_s + \mu_s}.$$

The linear relation between strain and stress is called *Hooke's Law*. The Poisson ratio ν_s describes the compressibility of the system. It holds

$$\nu_s = \frac{1}{2} \left(\frac{1}{1 + \frac{\mu_s}{\lambda_s}} \right) < \frac{1}{2}.$$

The Poisson ratio $\nu_s = \frac{1}{2}$ refers to $\lambda_s \rightarrow \infty$ hence to incompressible materials. The Poisson ratio describes the reaction of the material on directional compression, see Figure 1.6. For a Poisson ratio $\nu_s = \frac{1}{2}$, the volume will stay constant, for $\nu_s < \frac{1}{2}$ the volume will decrease. There are some materials with negative Poisson ratio. Here, the material will react to the compression in one direction with compression in the orthogonal directions. Such materials play a greater role for computational means in the context of fluid-structure interactions, see Section 2.4.1. The St. Venant Kirchhoff model is a suitable approximation for metals at small deformations. Steel has a Poisson ratio of about $\nu_s \approx 0.3$.

Hooke's Law applied to an incompressible material leads to the incompressible Neo Hookean material law:

Definition 5 (Incompressible Neo-Hookean material). *The incompressible Neo-Hookean material law is given by*

$$\hat{\mathbf{P}} = \hat{\mathbf{F}} \hat{\boldsymbol{\Sigma}} = -p \hat{\mathbf{F}}^{-T} + 2\mu_s \hat{\mathbf{F}}^{-T} \hat{\mathbf{E}},$$

with the shear modulus μ_s and the Poisson ratio $\nu_s = \frac{1}{2}$. By p we denote the undetermined pressure.

1.3.1 The Navier-Lamé equations

The model for an elastic solid governed by one of the material laws is a system of nonlinear partial differential equations. Its analysis is difficult and theoretical results exist for small

deformation only. As a nonlinear set of equations, uniqueness cannot be expected in the general case.

To get at least some insight into the systems of equations, we will simplify the problem with the following assumptions:

- The deformation gradient $\hat{\mathbf{F}}$ is so small, that we can approximate $\hat{\mathbf{F}} = I$ and $\hat{J} = 1$. By this simplification, the concept of Eulerian and Lagrangian coordinates fall together. We will therefore also skip all hat's, that indicate reference variables.
- Further, the strains are so small, that we can linearize the Green-Lagrange strain tensor

$$\hat{\mathbf{E}} = \frac{1}{2}(\hat{\nabla}\mathbf{u} + \hat{\nabla}\mathbf{u}^T + \hat{\nabla}\hat{\mathbf{u}}^T\hat{\nabla}\hat{\mathbf{u}}) \approx \frac{1}{2}(\nabla\mathbf{u} + \nabla\mathbf{u}) =: \epsilon.$$

This simplification not only rules out very large elastic deformations, it also penalizes rigid body rotations, see Problem 2.

- Just for simplicity (this will not change the character of the equation), we set $\hat{\rho}^0 = 1$.

Considering the linear St. Venant Kirchhoff material (with these simplifications) the resulting set of equations are the

System 1 (Navier-Lamé equations). *Let $\Omega \subset \mathbb{R}^3$ be a bounded domain with a boundary split into Dirichlet- and Neumann-part $\partial\Omega = \Gamma^D \cup \Gamma^N$. On the time interval $I = (0, T)$ we search for solutions $\mathbf{u} : I \times \Omega \rightarrow \mathbb{R}^3$ such that*

$$\begin{aligned} \partial_{tt}\mathbf{u} - \operatorname{div} \sigma &= \mathbf{f} && \text{in } I \times \Omega \\ \mathbf{u} &= \mathbf{u}^0 && \text{for } \{0\} \times \Omega \\ \mathbf{u} &= \mathbf{u}^D && \text{on } I \times \Gamma^D \\ \sigma \vec{n} &= \mathbf{u}^\sigma && \text{on } I \times \Gamma^N, \end{aligned} \tag{1.33}$$

with the linearized material law

$$\sigma = 2\mu\epsilon + \lambda \operatorname{tr}(\epsilon)I, \quad \epsilon = \frac{1}{2}(\nabla\mathbf{u} + \nabla\mathbf{u}^T).$$

As a further simplification, we also consider the stationary limit of the Navier-Lamé equations:

System 2 (Stationary Navier-Lamé equations). *Find $\mathbf{u} \in C^2(\Omega)^3 \cap C(\Omega \cup \Gamma^D)^3 \cup C^1(\Omega \cup \Gamma^N)^3$ such that*

$$\begin{aligned} -\operatorname{div} \sigma &= \mathbf{f} && \text{in } \Omega \\ \mathbf{u} &= \mathbf{u}^D && \text{on } \Gamma^D \\ \sigma \vec{n} &= \mathbf{u}^\sigma && \text{on } \Gamma^N, \end{aligned} \tag{1.34}$$

with the linearized material law

$$\sigma = \mu(\nabla\mathbf{u} + \nabla\mathbf{u}^T) + \lambda \operatorname{tr}(\nabla\mathbf{u} + \nabla\mathbf{u}^T)I.$$

As usual, analysis of classical solutions is difficult. This is partly to the fact, that the solution \mathbf{u} often exhibits singularities in boundary nodes at the transition between Dirichlet and Neumann parts. The well known *Theorem of Cosserat* states, that classical solutions to the stationary

problem, System 2 are unique, if the Dirichlet boundary Γ^D contains at least three independent points and that—in the general case—they can differ by a rigid body motion only:

$$\mathbf{u}_1(x) - \mathbf{u}_2(x) = \mathbf{b} + \mathbf{B}x,$$

where $\mathbf{b} \in \mathbb{R}^3$ is a translation and $\mathbf{B} \in \mathbb{R}^{3 \times 3}$ is a skew-symmetric matrix, see e.g. [67].

For the following, we will introduce a weak formulation of the Navier-Lamé equations, that will offer an easy access to show existence and uniqueness of solutions:

Lemma 9 (Variational formulation). *Every classical solution to (1.34) is also solution to the variational formulation*

$$\mathbf{u} \in \mathbf{u}^D + H_0^1(\Omega; \Gamma^D)^3 : \quad (\sigma, \nabla\phi) = (\mathbf{f}, \phi) + \langle \mathbf{u}^\sigma, \phi \rangle_{\Gamma^N} \quad \forall \phi \in H_0^1(\Omega; \Gamma^D)^3. \quad (1.35)$$

Existence and uniqueness of solutions can be shown by standard arguments of elliptic equations. The difficulty however is to show ellipticity, i.e.

$$\mu(\nabla\mathbf{u} + \nabla\mathbf{u}^T, \nabla\mathbf{u}) + \lambda(\operatorname{tr}(\nabla\mathbf{u} + \nabla\mathbf{u}^T)I, \nabla\mathbf{u}) \geq c\|\nabla\mathbf{u}\|^2,$$

as $\nabla\mathbf{u} + \nabla\mathbf{u}^T = 0$ does not necessarily impose $\nabla\mathbf{u} = 0$. This is a consequence of *Korn's inequality*:

Theorem 3 (1st Korn's inequality). *Let $\Omega \subset \mathbb{R}^3$ be a domain. Then, it holds*

$$\|\nabla\mathbf{v}\| \leq c_{korn}\|\epsilon(\mathbf{v})\| \quad \forall \mathbf{v} \in H_0^1(\Omega)^3$$

with a constant $c_{korn} > 0$. This inequality corresponds to the case of Dirichlet boundary values on the complete boundary $\Gamma^D = \partial\Omega$.

Korn's first inequality deals with the case of homogenous Dirichlet conditions on the complete boundary $\partial\Omega$. In the context of structural mechanics, this limitation is severe, as no free boundary motion and deformation would be allowed. The case of general boundary conditions, with a Neumann part $\Gamma_N \subset \partial\Omega$ is less trivial and handled by Korn's second inequality:

Theorem 4 (2nd Korn's inequality). *Let $\Omega \subset \mathbb{R}^3$ be a domain with Lipschitz-boundary. Then, it holds*

$$\|\nabla\mathbf{v}\| \leq c_{korn}(\|\epsilon(\mathbf{v})\| + \|\mathbf{v}\|) \quad \forall \mathbf{v} \in H^1(\Omega)^3.$$

with a constant $c_{korn} > 0$.

Proof. The simple proof of 1st Korn's inequality is based on integration by parts and vanishing traces of \mathbf{v} on the complete boundary $\partial\Omega$. The proof of Korn's 2nd inequality is more involved and we refer to the literature, see e.g. [130, 68]. \square

Continuity and ellipticity of the bilinear form allows to apply the standard theory for linear elliptic problems to the Navier-Lamé equations:

Lemma 10 (Existence of unique solutions). *Let $\mathbf{f} \in L^2(\Omega)^3$, $\bar{\mathbf{u}}^D \in H^1(\Omega)^3$ be an extension of the Dirichlet data into the domain and $\mathbf{u}^\sigma \in H^1(\partial\Omega)^3$. There exists a unique solution $\mathbf{u} \in \bar{\mathbf{u}}^D + H_0^1(\Omega; \Gamma^D)^3$ to the linear Navier-Lamé equations and it holds*

$$\|\mathbf{u}\|_{H^1(\Omega)} \leq c \left(\|\mathbf{f}\|_{L^2(\Omega)} + \|\mathbf{u}^D\|_{L^2(\Gamma^D)} + \|\mathbf{u}^\sigma\|_{H^1(\Gamma^N)} \right),$$

with a constant $c > 0$.

Proof. We first show, that the variational formulation is bilinear, symmetric, continuous and elliptic. Further, the right hand side is continuous, such that existence of a unique solution follows by the Theorem of Lax-Milgram [200]. \square

Concerning the regularity of the solution, we cite the following lemma, see [67], which gives conditions that lead to classical solutions:

Lemma 11 (Strong regularity of the Navier-Lamé problem). *Let $\Omega \subset \mathbb{R}^3$ be a bounded domain of class $C^{2+\alpha}$ for $\alpha > 0$. Given, that the problem data has the regularity*

$$\mathbf{f} \in C^\alpha(\bar{\Omega})^3, \quad \bar{\mathbf{u}}^\sigma \in C^{1+\alpha}(\Omega)^{3 \times 3}_{sym}, \quad \bar{\mathbf{u}}^D \in C^{2+\alpha}(\bar{\Omega})^3,$$

the weak solution $\mathbf{u} \in H_0^1(\Omega; \Gamma^D)^3$ of (1.35) is also a classical solution

$$\mathbf{u} \in C^2(\Omega)^3 \cap C^1(\Omega \cup \Gamma^N)^3 \cap C(\Omega \cup \Gamma^D)^3.$$

A further regularity result with less strict assumption on the regularity of the domain and the problem data is given by Shi and Wright [211]:

Lemma 12 (Weak regularity of the Navier-Lamé problem). *Let $\Omega \subset \mathbb{R}^3$ be a domain with $W^{2,3}$ boundary. Further, let $\mathbf{f} \in L^2(\Omega)^d$. Then, for the solution of the stationary Navier-Lamé system with homogenous Dirichlet data $\mathbf{u}^D = 0$ it holds*

$$\|\mathbf{u}\|_{H^2(\Omega)^3 \cap H_0^1(\Omega)^3} \leq c \|\mathbf{f}\|_{L^2(\Omega)^3}.$$

Regularity of solutions is usually restricted at points, where Neumann and Dirichlet parts of the boundary come together. Here, we usually have singularities in the gradient of the solution and the stress tensor.

The incompressible Navier-Lamé equations

For incompressible linear materials with $\nu = \frac{1}{2}$, the stress tensor is reduced to

$$\boldsymbol{\sigma} = \mu(\nabla \mathbf{u} + \nabla \mathbf{u}^T),$$

as $\text{tr}(\boldsymbol{\epsilon}) = \text{div } \mathbf{u} = 0$. The material is no longer able to react on purely isotropic stresses. To formulate the incompressible Navier-Lamé equations, we consider the minimization form of Lemma 10, but minimize in the space of divergence free functions only:

$$\mathbf{u} \in V_0 : \quad E(\mathbf{u}) \leq E(\mathbf{v}) = \frac{1}{2}a(\mathbf{v}, \mathbf{v}) - l(\mathbf{v}) \quad \forall \mathbf{v} \in V_0,$$

where V_0 is the space of weakly divergence free functions

$$V_0 = \{\phi \in H_0^1(\Omega; \Gamma^D)^3, \quad (\text{div } \phi, \xi) = 0 \quad \forall \xi \in L^2(\Omega)\}. \quad (1.36)$$

The Hilbert space V_0 is a closed subspace of $H_0^1(\Omega; \Gamma^D)^3$, such that the existence of a unique solution follows as shown in Lemma 10. To derive a variational formulation, we use the Euler-Lagrange approach for constraint minimization problems and define the Lagrange functional

$$\mathcal{L}(\mathbf{u}, p) = \frac{1}{2}a(\mathbf{u}, \mathbf{u}) - l(\mathbf{u}) - (p, \text{div } \mathbf{u}),$$

with a Lagrange multiplier $p \in L^2(\Omega)$. A possible solution is given as stationary point of $\mathcal{L}(\mathbf{u}, p)$:

$$\begin{aligned} d_{\mathbf{u}} \mathcal{L}(\mathbf{u}, p)(\phi) &= a(\mathbf{u}, \phi) - l(\phi) - (p, \operatorname{div} \phi) \stackrel{!}{=} 0 \quad \forall \phi \in H_0^1(\Omega; \Gamma^D)^3 \\ d_p \mathcal{L}(\mathbf{u}, p)(\xi) &= -(\xi, \operatorname{div} \mathbf{u}) \stackrel{!}{=} 0 \quad \forall \xi \in L^2(\Omega). \end{aligned}$$

We include the Lagrange multiplier into the stress tensor and define

$$\sigma_I(\mathbf{u}, p) = -pI + \mu(\nabla \mathbf{u} + \nabla \mathbf{u}^T),$$

where we identify $p \in L^2(\Omega)$ with a *pressure function*. This identification is reasonable, as $-pI$ acts as isotropic stress in all directions. The problem is now to find $\{\mathbf{u}, p\} \in H_0^1(\Omega; \Gamma^D)^3 \times L^2(\Omega)$ such that

$$(\mu(\nabla \mathbf{u} + \nabla \mathbf{u}^T) - pI, \epsilon(\phi)) + (\operatorname{div} \mathbf{u}, \xi) = (\mathbf{f}, \phi) + \langle \mathbf{u}^\sigma, \phi \rangle_{\Gamma^N} \quad (1.37)$$

for all $\phi \in H_0^1(\Omega; \Gamma^D)^3$ and $\xi \in L^2(\Omega)$.

The incompressible Navier-Lamé equations, as a minimization problem with side condition is a *saddle-point system*. Existence and uniqueness theory cannot be based on ellipticity (in p). Instead, we split the proof for the existence of a well defined solution in two parts. We start by finding a suitable deformation field. Herefore, we restrict the space of admissible functions to those, that already fulfill the divergence condition in the space V_0 , see (1.36). Then, it holds

Lemma 13 (Incompressible Navier-Lamé - Existence of unique solutions (displacement)). *Let $\mathbf{f} \in L^2(\Omega)^3$, $\bar{\mathbf{u}}^D \in H^1(\Omega)^3$ be an extension of the Dirichlet data into the domain and $\mathbf{u}^\sigma \in H^1(\Gamma^N)^3$. There exists a unique solution $u \in \bar{\mathbf{u}}^D + H_0^1(\Omega; \Gamma^D)^d$ to the variational problem*

$$(2\mu\epsilon(\mathbf{u}), \epsilon(\phi)) = (\mathbf{f}, \phi) + \langle \mathbf{u}^\sigma, \phi \rangle_{\Gamma^N} \quad \forall \phi \in H_0^1(\Omega; \Gamma^D)^3$$

For this solution it holds

$$\|\mathbf{u}\|_{H^1(\Omega)} \leq c \left(\|\mathbf{f}\|_{L^2(\Omega)} + \|\mathbf{u}^D\|_{L^2(\Gamma^D)} + \|\mathbf{u}^\sigma\|_{H^1(\Gamma^N)} \right).$$

Finally, $\mathbf{u} \in V_0$ minimizes the energy function in the space V_0

$$E(\mathbf{u}) \leq E(\mathbf{v}) \quad \forall \mathbf{v} \in V_0.$$

Proof. The subspace $V_0 \subset H_0^1(\Omega; \Gamma_D)^3$ is a Hilbert-space. The variational formulation is V_0 -elliptic and the existence of a unique solution as well as the a priori estimate follow in the same way as shown in Lemma 10. \square

Next, given a deformation field $u \in V_0$ we find a corresponding pressure by analyzing the equation

$$p \in L^2(\Omega) : -(p, \nabla \phi) = (\mathbf{f}, \phi) + \langle \mathbf{u}^\sigma, \phi \rangle_{\Gamma^N} - (2\mu\epsilon(\phi), \nabla \phi) \quad \forall \phi \in H_0^1(\Omega; \Gamma^D)^3.$$

Existence of solutions to this system cannot be shown by simple variational arguments. Instead, we will define by

$$\langle \operatorname{grad} p, \phi \rangle := -(p, \nabla \cdot \phi) \quad \forall \phi \in H_0^1(\Omega; \Gamma^D)^3,$$

the weak gradient operator $-\operatorname{grad} = \operatorname{div}^* : L^2(\Omega) \rightarrow H^{-1}(\Omega)$ and show existence by proving surjectivity of $-\operatorname{grad}$ in appropriate function spaces. We postpone this discussion to Section 1.4.5, where we will come across the same pressure problem concerning the incompressible Stokes equations.

The non-stationary Navier-Lamé equations

The non-stationary system of Navier-Lamé equations as given in Definition 1 is a hyperbolic problem

$$\partial_{tt}\mathbf{u} - \operatorname{div}(\boldsymbol{\sigma}) = 0, \quad \mathbf{u}(0) = \mathbf{u}^0, \quad \partial_t\mathbf{u}(0) = \mathbf{v}^0.$$

For simplicity we will consider the case of homogenous Dirichlet data only and we will further assume, that $\mathbf{f} = 0$. We multiply the differential equation by $\phi = \partial_t\mathbf{u}$ and integrate over the spatial domain to get

$$0 = (\partial_{tt}\mathbf{u}, \partial_t\mathbf{u}) + (\boldsymbol{\sigma}(\mathbf{u}), \boldsymbol{\epsilon}(\partial_t\mathbf{u})) = \frac{d}{dt} \left(\underbrace{\frac{1}{2} \|\partial_t\mathbf{u}\|^2}_{=:E(t)} + \frac{1}{2} (\boldsymbol{\sigma}(\mathbf{u}), \boldsymbol{\epsilon}) \right),$$

where by $E(t)$ we denote the energy of the system. This energy does not change over time (remember, that we consider the homogenous problem only). Integration over the temporal domain $I = [0, T]$ yields the relation

$$E(t) = E(0) \quad t \geq 0, \quad E(0) = \frac{1}{2} \|\mathbf{v}^0\|^2 + \frac{1}{2} (\boldsymbol{\sigma}(\mathbf{u}^0), \boldsymbol{\epsilon}(\mathbf{u}^0)),$$

with the initial velocity $\mathbf{v}^0 = \partial_t\mathbf{u}^0$. Hence, a solution must be unique and it is bounded by the initial data.

The conservation of energy $d_t E(t) = 0$ fits to the close relation to the wave equation. Existence of solutions to this simple (linear, symmetric and positive) problem can be shown by the Fourier approach. The operator

$$\langle \mathcal{L}\mathbf{u}, \mathbf{v} \rangle := (\mathbf{C}\boldsymbol{\epsilon}(\mathbf{u}), \boldsymbol{\epsilon}(\mathbf{v}))$$

is symmetric, positive definite, selfadjoint and a bijection. Its inverse is bound and considered as operator $\mathcal{L}^{-1} : L^2(\Omega)^d \rightarrow L^2(\Omega)^d$ it is compact. Hence, \mathcal{L} has a spectrum of positive eigenvalues, with no finite accumulation point and further an orthonormal basis of eigenvectors. This allows to diagonalize the system of equations, such that it decomposes into a sequence of scalar initial values problems, that have a solution, that can be constructed by elementary principles. For the details on this construction, we refer to the literature [180].

A recent result on the regularity of the non-stationary Navier-Lamé system with homogenous Dirichlet data is given by Mitrea and Monniaux [166]. They basically show, that given sufficient regularity of the domain's boundary (Lipschitz), the solution of the non-stationary Navier-Lamé system with zero initial data and zero Dirichlet data satisfies $\mathbf{u} \in H^1(I; L^2(\Omega)^3)$ for every right hand side $\mathbf{f} \in L^2(I; L^2(\Omega)^3)$.

In the upcoming chapters, we will see, that the coupling of the solid equation to the fluid equations brings along further challenges for the analysis of the partial differential equations. The *kinematic coupling condition*, see Section 2.1 will ask for continuity of solid- and fluid-velocities on a common interface $\mathcal{I}(t) = \partial\mathcal{S}(t) \cap \partial\mathcal{F}(t)$:

$$\mathbf{v}_f = \mathbf{v}_s \text{ on } \mathcal{I}(t).$$

In the case of stationary problems, this kinematic coupling condition is just a usual no-slip boundary condition $\mathbf{v}_f = 0$ for the fluid's velocity. If however the problem is fully non-stationary, a real coupling between the two velocities is introduced. The solution of the Navier-Stokes equations is well defined for velocities with traces in

$$\mathbf{v}_f \Big|_{\partial\mathcal{F}} \in H^{\frac{1}{2}}(\partial\mathcal{F}),$$

which – as seen from the solid problem – will require

$$\mathbf{v}_f \Big|_{\mathcal{I}} = \mathbf{v}_s \Big|_{\mathcal{I}} \quad \Rightarrow \quad \mathbf{v}_s \in H^1(\mathcal{S}).$$

As seen in the previous analysis, we only have

$$\mathbf{u}_s \in L^2(I; H^1(\Omega)^3),$$

which by $\mathbf{v}_s = \partial_t \mathbf{u}_s$ only yields

$$\mathbf{v}_s \in L^2(I; L^2(\Omega)^3),$$

and which does not give us sufficient regularity. This dilemma has two possible solutions. First – and this will be our usual procedure – we can simply assume additional a priori knowledge on the regularity of \mathbf{u}_s and therefore \mathbf{v}_s . This can be guaranteed for small and regular problem data, if the boundaries of the coupled problem have very high regularity. Coutand and Shkoller show the existence of solutions for the coupling of linear solids with the Navier-Stokes equations, if the solid with boundary of class H^4 is completely embedded in a fluid-domain with boundary of class H^3 , see [73]. Further, very high regularity of the problem data is required. A second way to enforce sufficient regularity it to add damping terms to the solid equation. Gazzola and Squassina show the following result, see [104]:

Theorem 5 (Damped wave equation). *Let $\Omega \subset \mathbb{R}^d$ be a Lipschitz domain. The strongly damped wave equation*

$$\partial_{tt}u - \Delta u - \omega\Delta\partial_tu + \mu\partial_tu = 0 \text{ in } [0, T] \times \Omega,$$

with initial values

$$u(0, \cdot) = u_0 \in H^1(\Omega), \quad \partial_tu(0, \cdot) = u_1 \in L^2(\Omega),$$

and homogenous Dirichlet values on $\partial\Omega$ and the damping parameters

$$\omega > 0, \quad \mu > -\omega\lambda_1,$$

where λ_1 is the first eigenvalue of $-\Delta$ has a unique solution satisfying

$$u \in L^\infty([0, T], H_0^1(\Omega)) \cap W^{1,\infty}([0, T], L^2(\Omega)), \quad \partial_tu \in L^2([0, T], H_0^1(\Omega)).$$

For the proof, see [104].

By adding strong damping terms, we are able to assure sufficient regularity to realize the kinematic coupling condition between solid problem and fluid problem.

1.3.2 Theory of nonlinear hyper-elastic material

Tackling the existence and uniqueness problem of the full elastic structure equation (using the St. Venant Kirchhoff material law) is complicated by the nonlinearity of the system. Here, we will not give details on the complex proofs, but will simply cite some important results. A good overview on the theory of nonlinear elastic materials is given in the textbook of Ciarlet [67].

All approaches for the nonlinear problem will at some time use a linearization of the problem and will consult the theory, that has been derived for the linear Navier-Lamé system. Further, most approaches use variational techniques, such that the starting point for every analysis is the following weak formulation of the problem:

Lemma 14 (Weak formulation of the hyper-elastic structures). *Let $\bar{\mathbf{u}}^D \in H^1(\hat{\mathcal{S}})^d$ be an extension of the Dirichlet data on Γ^D into the domain Ω . If the solution*

$$\hat{\mathbf{u}}_f \in \bar{\mathbf{u}}_f^D + H_0^1(\hat{\Omega}; \Gamma^D)^d$$

of the variational formulation

$$(\hat{\mathbf{F}}\hat{\Sigma}_s, \hat{\nabla}\hat{\phi})_{\hat{\mathcal{S}}} = (\rho_s^0 \hat{\mathbf{f}}_s, \hat{\phi}), \quad \forall \hat{\phi} \in H_0^1(\hat{\Omega}; \Gamma^D)^d, \quad (1.38)$$

has sufficient regularity $\hat{\mathbf{u}} \in C^2(\hat{\Omega}) \cap C(\hat{\Omega} \cup \Gamma^D) \cap C^1(\hat{\Omega} \cup \Gamma^D)$, it is also a solution to the classical formulation of the elastic structure equations (1.32) with Dirichlet data on Γ_s^D .

Using the implicit function theorem, Ciarlet [67] proofs the following result for weak solutions of the elastic structure equation governed by the St. Venant Kirchhoff material:

Lemma 15 (Stationary St. Venant Kirchhoff material). *Let $\Omega \subset \mathbb{R}^3$ be a domain with C^2 -boundary. Then, for every $p > 3$ there exists a constant α such that for every $\mathbf{f} \in L^p(\Omega)^d$ with $\|\mathbf{f}\|_{L^p} \leq \alpha$ there exists a unique solution $\mathbf{u} \in W^{2,p}(\Omega)$ to the stationary elastic structure equation governed by the St. Venant Kirchhoff material.*

For the proof, we refer to the literature [67].

1.4 The Fluid Problem

In fluid-dynamics, we describe the flow of particles in the Eulerian framework. Looking at a fixed coordinate $x \in \mathbb{R}^d$ we observe that particle $\hat{x}(x, t)$, that at time t is in position x . The fate of a single particle is of no interest.

We will only consider incompressible fluids, i.e. a given moving volume $V(t)$ will not change its size under motion:

$$d_t |V(t)| = 0, \quad t \geq 0.$$

Applying Reynolds' Transport theorem, Lemma 3 to the scalar $\Phi \equiv 1$ yields:

$$d_t |V(t)| = d_t \int_{V(t)} 1 \, d\mathbf{x} = \int_{V(t)} \operatorname{div} \mathbf{v} \, d\mathbf{x}.$$

Hence, as $V(t)$ can be chosen arbitrarily, we deduce the point-wise equation for the incompressibility of a fluid, see also Section 1.2.2:

$$\operatorname{div} \mathbf{v} = 0. \quad (1.39)$$

Using this condition, conservation of mass (1.13) reduces to a transport equation for the fluid's density:

$$\partial_t \rho_f + (\mathbf{v} \cdot \nabla) \rho_f = 0. \quad (1.40)$$

For further simplification, we will restrict all our considerations to homogenous fluids, where the density at initial time $t = 0$ is constant in the complete volume $\rho_f(x, 0) = \rho_f^0(x) \equiv \rho_f$. Given (1.40) it hereby follows, that the density is homogenous at all times $t \geq 0$ and conservation of mass is reduced to the divergence condition (1.39).

To close the system of equations for incompressible fluids we must introduce material laws, that model the dependency of the stress tensor σ_f on velocity and pressure. We are considering *Navier-Stokes* fluids only, that linearly depend on the strain rate following Hooke's law

$$\sigma = 2\mu_f \dot{\epsilon} + \lambda \operatorname{tr}(\dot{\epsilon}) I.$$

As for an incompressible fluid it holds $\operatorname{div} \mathbf{v} = \operatorname{tr}(\dot{\epsilon}) = 0$, the stress tensor simplifies to

$$\sigma = -pI + \mu_f(\nabla \mathbf{v} + \nabla \mathbf{v}^T), \quad (1.41)$$

where again by p we denote the undetermined pressure, that will act as Lagrange multiplier to ensure the divergence condition $\operatorname{div} \mathbf{v} = 0$. By $\mu_f = \rho_f \nu_f$ we denote the dynamic viscosity of the fluid and by ν_f its kinematic viscosity. The complete set of the Navier-Stokes equations is given by

$$\rho_f(\partial_t \mathbf{v} + (\mathbf{v} \cdot \nabla) \mathbf{v}) - \operatorname{div} \sigma = \rho_f \mathbf{f}_f, \quad \operatorname{div} \mathbf{v} = 0,$$

or, using the material law for a Navier-Stokes fluid

$$\rho_f(\partial_t \mathbf{v} + (\mathbf{v} \cdot \nabla) \mathbf{v}) + \nabla p - \rho_f \nu_f \operatorname{div}(\nabla \mathbf{v} + \nabla \mathbf{v}^T) = \rho_f \mathbf{f}_f, \quad \operatorname{div} \mathbf{v} = 0. \quad (1.42)$$

Remark 5 (Symmetry of the stress-tensor). *For an incompressible fluid, the stress-tensor allows for a further simplification. It holds:*

$$[\operatorname{div}(\nabla \mathbf{v} + \nabla \mathbf{v}^T)]_i = \sum_j \partial_j(\partial_j \mathbf{v}_i + \partial_i \mathbf{v}_j) = \Delta \mathbf{v}_i + \partial_i \underbrace{\operatorname{div} \mathbf{v}}_{=0}, \quad \text{for } i = 1, 2, 3,$$

and equation (1.42) is equivalent to the reduced formulation

$$\rho_f(\partial_t \mathbf{v}_f + (\mathbf{v} \cdot \nabla) \mathbf{v}) - \rho_f \nu_f \Delta \mathbf{v} + \nabla p = \rho_f \mathbf{f}_f, \quad \operatorname{div} \mathbf{v} = 0.$$

Usually, this simplified set of equations is considered as the Navier-Stokes equations. However, while both equations yield the same solution (\mathbf{v}, p) , the value of boundary stresses is altered, if the reduced tensor $\tilde{\sigma}_f = \mu_f \nabla \mathbf{v} - pI$ would be considered:

$$\tilde{\sigma}_f n \neq \sigma_f n.$$

In the context of fluid-structure interactions, boundary stresses will be important to couple flow and structure problem. Out of this reason, we will always consider the full symmetric stress tensor σ_f . One of the coupling conditions will couple normal stresses of the fluid problem and the solid problem

$$\vec{n} \cdot \sigma_f = \vec{n} \sigma_s,$$

where by σ_s we denote the Cauchy stress tensor of the solid, i.e.

$$\sigma_s = \hat{J}^{-1} \mathbf{F} \hat{\Sigma}_s \hat{\mathbf{F}}^T.$$

Here, it will matter, whether it holds

$$-p\vec{n} + \rho_f \nu_f \vec{n} \cdot (\nabla \mathbf{v} + \nabla \mathbf{v}^T) = \vec{n} \sigma_s,$$

or

$$-p\vec{n} + \rho_f \nu_f \vec{n} \cdot \nabla \mathbf{v} = \vec{n} \sigma_s,$$

as usually

$$\vec{n} \cdot \nabla \mathbf{v}^T \neq 0.$$

1.4.1 Boundary and initial conditions

The system of equations is completed by adequate boundary and initial conditions. Let $\mathcal{F} \subset \mathbb{R}^d$ be the fluid-domain. At time $t = 0$ we prescribe an initial condition for the velocity

$$\mathbf{v}(x, 0) = \mathbf{v}^0(x) \quad x \in \mathcal{F}.$$

As the density is constant $\rho_f(x, t) \equiv \rho_f$ for all times (and homogenous in the domain), we do not need an initial condition here, but simply consider $\rho_f \in \mathbb{R}$ as a problem parameter. The boundary $\partial\mathcal{F}$ is split into a Dirichlet part Γ_f^D and into a Neumann part Γ_f^N . On Γ_f^D we prescribe Dirichlet conditions for the velocity

$$\mathbf{v}(x, t) = \mathbf{v}^D(x, t) \quad \text{on } \Gamma_f^D \times [0, T].$$

In the case $v^D = 0$, we denote this condition as the *no-slip condition*. Physical observation tells us, that viscosity will cause the fluid to stick to the boundary. This condition holds for the flow of water over elastic material (at usual velocities). The importance of viscous effects is lessened at high velocities, when e.g. considering the aerodynamical flow of air around a plane. Here, one often refers to the *slip condition*, that only prescribes the flow in normal direction

$$\vec{n} \cdot \mathbf{v}(x, t) = 0 \quad \text{on } \Gamma_f^D \times [0, T].$$

The slip boundary condition prevents the flow from entering the boundary, it however allows for tangential flow. All examples considered in this work will be in the viscous regime where no-slip condition are usually well-placed. Boundaries with non homogenous Dirichlet data are often *inflow boundaries*.

Neumann conditions model situations, where we do not know the velocity profile at the boundary, but where assumptions on the boundary stress are given:

$$\sigma_f(x, t)n(x, t) = g^\sigma(x, t) \quad \text{on } \Gamma_f^N \times [0, T].$$

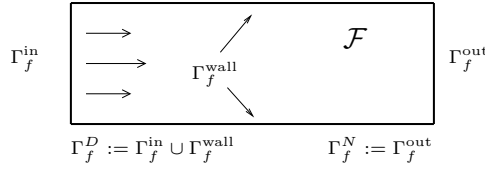


Figure 1.7: Typical configuration of a flow problem with Dirichlet inflow boundary Γ_f^{in} and Dirichlet no-slip boundary on the walls Γ_f^{wall} as well as an outflow boundary Γ_f^{out} of Neumann type.

The typical application of Neumann conditions are *outflow boundaries*, where the profile of the flow is not known and a Dirichlet condition cannot be prescribed. See Figure 1.7 for a typical configuration of a flow problem with different boundary parts. We will come back to outflow boundary conditions in Section 1.4.2, as the exact form will depend on the material law and the Cauchy stress tensor σ_f .

If only no-slip and outflow boundary conditions are taken into account, the complete set of incompressible flow equations on the (fixed) domain $\mathcal{F} \subset \mathbb{R}^d$ is given by

$$\begin{aligned} \operatorname{div} \mathbf{v} = 0, \quad \rho_f (\partial_t \mathbf{v} + (\mathbf{v} \cdot \nabla) \mathbf{v}) &= \rho_f f + \operatorname{div} \boldsymbol{\sigma}_f && \text{on } \mathcal{F} \times [0, T], \\ \mathbf{v}(\cdot, 0) &= \mathbf{v}^0(\cdot) && \text{on } \mathcal{F}, \\ \mathbf{v} &= \mathbf{v}^D && \text{on } \Gamma_f^D \times [0, T], \\ \boldsymbol{\sigma}_f \vec{n} &= g^\sigma && \text{on } \Gamma_f^N \times [0, T]. \end{aligned} \tag{1.43}$$

If boundary data v^D and g^σ as well as volume force f do not explicitly depend on time, the flow configurations can tend to a stationary limit, where it holds $\partial_t \mathbf{v} = 0$. Stationary in the context of fluid dynamics stands for a flow that at all times looks the same way, it does not imply that the fluid is at rest, which would mean $v = 0$. If we know, that the flow will reach a stationary limit, we can immediately consider the set of stationary equations, given as a boundary value problem:

$$\begin{aligned} \operatorname{div} \mathbf{v} = 0, \quad \rho_f (\mathbf{v} \cdot \nabla) \mathbf{v} &= \rho_f \mathbf{f}_f + \operatorname{div} \boldsymbol{\sigma}_f && \text{on } \mathcal{F}, \\ \mathbf{v} &= \mathbf{v}^D && \text{on } \Gamma_f^D, \\ \boldsymbol{\sigma}_f \vec{n} &= g^\sigma && \text{on } \Gamma_f^N, \end{aligned} \tag{1.44}$$

Not all autonomous flow problems have a stationary limit. This stems from the nonlinearity of the Navier-Stokes equations and whether a flow is stationary or instationary will depend on the problem data like density, viscosity, right hand side f and inflow velocity v^D .

1.4.2 The “do-nothing” outflow condition

Many problem configurations feature boundaries, where the flow has mainly an outflow-character. We will call this boundary Γ_f^{out} . Here, the solution is not known a priori and cannot be specified in terms of a Dirichlet condition. Any boundary condition that is enforced, will be a model for the flow at the outflow boundary. Hence, a common practice is to not describe a condition

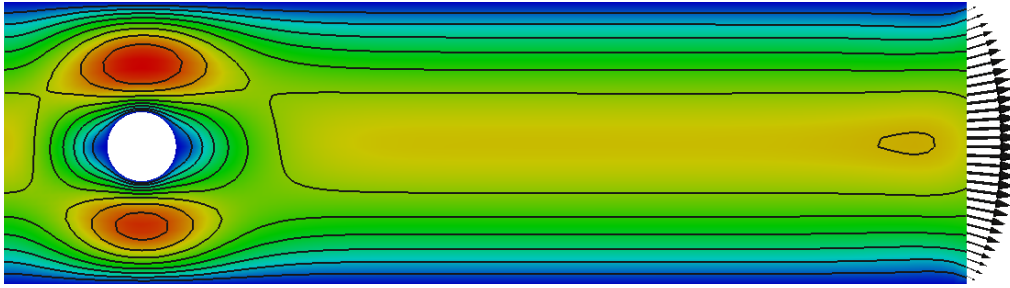


Figure 1.8: Channel flow with natural outflow condition $\sigma_f \vec{n} = 0$. The velocity field gets deflected and does not follow the Poiseuille flow.

at all, but simply use the “natural” boundary condition, that arises from integration by parts. We consider the stationary Stokes equations:

$$(\sigma_f, \nabla \phi)_{\mathcal{F}} = -(\operatorname{div} \sigma_f, \phi)_{\mathcal{F}} + \langle \sigma_f \vec{n}, \phi \rangle_{\Gamma_f^{\text{out}}},$$

from where we can deduce the “outflow-condition”

$$\sigma_f \vec{n} = 0 \text{ on } \Gamma_f^{\text{out}}.$$

In Figure 1.8, we show a solution to a “channel-flow” problem using this natural outflow-condition. The domain is a channel with length L and height H :

$$\mathcal{F} = (0, L) \times (0, H),$$

on the left boundary Γ_f^{in} we impose a Dirichlet inflow profile

$$\mathbf{v} = \mathbf{v}^D = \frac{4\bar{v}}{H^2} \begin{pmatrix} y(H-y) \\ 0 \end{pmatrix} \text{ on } \Gamma_f^{\text{in}} = 0 \times (0, H), \quad (1.45)$$

where \bar{v} is the peak velocity. On the horizontal lines Γ_f^{wall} we impose homogenous Dirichlet conditions

$$\mathbf{v} = 0 \text{ on } \Gamma_f^{\text{wall}} = (0, L) \times 0 \cup (0, L) \times H.$$

The outflow boundary is given as

$$\Gamma_f^{\text{out}} = L \times (0, H).$$

In Figure 1.8 we see, that the velocity vectors get deflected and sheer out of line. Considering the outflow model $\sigma_f \vec{n} = 0$, which simply states, that no external stresses act, this behavior can be interpreted as a duct, that ends in an open space, such that the fluid can expand in all directions.

Often, computational domains are chosen simply as a restriction of the real domain of interest to an area, where the interesting dynamics happen. Numerically, boundary lines often must be drawn to scale to problem down to a reasonable size. In such situations, a good outflow boundary should have as little influence on the solution as possible. Regarding Figure 1.8, the exact location of the outflow boundary should not change the flow pattern inside the domain. The natural condition does not satisfy this request.

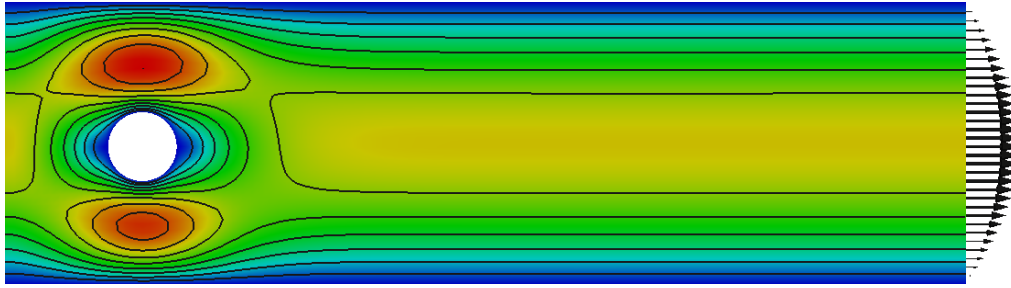


Figure 1.9: Channel flow with the *do-nothing outflow condition* $\rho_f \nu_f \nabla \mathbf{v} \cdot \vec{n} - pI = 0$ on Γ_f^{out} . The streamlines are not deflected on the right outflow boundary. Compare Figure 1.8.

One of the most simple analytical solutions to a channel problem is the *Poiseuille flow*. An extension of the inflow data (1.45) into the domain

$$\mathbf{v}(x, y) = \frac{4\bar{\mathbf{v}}}{H^2} \begin{pmatrix} y(H-y) \\ 0 \end{pmatrix},$$

satisfies the Navier-Stokes equations in channels (without obstacle) together with the pressure field

$$p(x, y) = \frac{8\bar{v}}{H^2} x + c,$$

for every $c \in \mathbb{R}$. In channel-like situations like shown in Figure 1.8, an outflow condition should allow for Poiseuille flow's without deterioration.

By a small modification of this outflow condition, we allow the Poiseuille flow to leave the domain without deflection. Using the reduced stress tensor introduced in Remark 5,

$$\tilde{\sigma}_f = \rho_f \nu_f \nabla \mathbf{v} - pI,$$

it holds for the Poiseuille flow that

$$\tilde{\sigma}_f \vec{n} = (\vec{n} \cdot \nabla) \mathbf{v} - p \vec{n} = 0 \text{ on } \Gamma_f^{\text{out}}.$$

This condition is called the *do-nothing outflow condition*, as it has as little impact on the flow as possible (or as it is the natural boundary condition, that arises without doing anything, when using the reduced tensor), see [124]. In Figure 1.9, we show the flow around a cylinder using this do-nothing condition. Here, the streamlines leave the domain in a straight way. Compare Figure 1.8.

Remark 6 (Outflow conditions). *We must stress, that the do-nothing outflow condition is not the better condition from a physical point of view. It is simply a model, that allows for some standard flow situations like Poiseuille flow or Couette flow to reduce the sensitivity of the solution on the position of artificial boundaries. From a good outflow condition we expect, that it has as little influence on the flow field as possible. If the outflow boundary is far away from a region of interest (e.g. from an obstacle) we expect that the flow close to the obstacle is not influenced by the position of the outflow boundary, if the outflow boundary condition does a good job. The do-nothing condition works excellent in several configurations. It does not only allow Poiseuille or Couette flows to leave the domain, it further allows vortices to leave the domain and has very small influence on these vortices, if the boundary is artificially cutting*

through them. However, many situations exist, where the analysis of outflow conditions is still not sufficiently developed: whenever the outflow boundary is not a single straight line normal to the main flow-direction, it will cause a deflection of the flow field. Further, if one considers more general material laws of non-Newtonian fluids, the do-nothing condition has an impact on the flow-field, see [237].

The *do-nothing* boundary condition brings along a further “hidden” boundary condition that normalizes the pressure. It can be shown [124], that on every straight outflow boundary-line segment $\Gamma_i \subset \partial\mathcal{F}$ that is enclosed by no-slip Dirichlet boundaries, it holds

$$\int_{\Gamma_i^{\text{out}}} p \, d\sigma = 0,$$

on all outflow boundaries Γ_i^{out} , such that the average outflow pressure is zero. This condition has two implications: first, whenever an outflow boundary of *do-nothing* type is given, no pressure-normalization has to be included in the trial-spaces. Second, the *do-nothing* condition can be used to prescribe pressure drops on boundary segments in order to drive the flow:

$$\int_{\Gamma_i} \{\rho_f \nu_f \vec{n} \cdot \nabla \mathbf{v} - p \vec{n}\} \, d\sigma = \int_{\Gamma_i} P_i \, d\sigma, \quad i = 1, \dots, N^{\text{out}}, \quad P_i \in \mathbb{R}.$$

This gets important, if the flow is driven by pressure differences and not by means of Dirichlet conditions. A frequently considered situation arises in hemodynamical simulations in which a flow in a part of the channel-system (i.e., the cardiovascular system) is investigated. This small part of the overall system can be coupled by prescribing pressure values, e.g. taken from the pressure profile as measured from the heart-beat.

1.4.3 Reynolds Number

Simulations with the incompressible Navier-Stokes equations help to gain better insight into flow configurations. They can be used to replace and complement experiments. For a better comparison of similar flow-configurations that for instance arise by scaling in wind tunnel experiments, we introduce a non-dimensional form of the incompressible Navier-Stokes equations. First, let L_f be a unit length and \bar{V}_f be a unit velocity. We define the non-dimensional values (without physical units)

$$x^* := \frac{1}{L_f} x, \quad \mathbf{v}^* := \frac{1}{\bar{V}_f} \mathbf{v}, \quad t^* := \frac{V_f}{L_f} t, \quad p^* := \frac{1}{V_f^2 \rho_f} p. \quad (1.46)$$

For these new values, it holds:

$$\begin{aligned} \frac{\partial \mathbf{v}^*}{\partial t^*} + (\mathbf{v}^* \cdot \nabla^*) \mathbf{v}^* &= \frac{L_f}{\bar{V}_f^2} \left\{ \frac{\partial \mathbf{v}}{\partial t} + (\mathbf{v} \cdot \nabla) \mathbf{v} \right\}, \\ \Delta^* \mathbf{v}^* &= \frac{L_f^2}{\bar{V}_f^2} \Delta \mathbf{v}, \quad \nabla^* p^* = \frac{L_f}{\bar{V}_f^2 \rho_f} \nabla p, \end{aligned}$$

and the Navier-Stokes equations in non-dimensional form (with homogenous right hand side) read

$$\begin{aligned} \frac{\partial \mathbf{v}^*}{\partial t^*} + (\mathbf{v}^* \cdot \nabla^*) \mathbf{v}^* - \frac{\nu_f}{V_f L_f} \operatorname{div}^* \{ \nabla^* \mathbf{v}^* + (\nabla^* \mathbf{v}^*)^T \} - \nabla^* p^* &= 0, \\ \nabla^* \cdot \mathbf{v}^* &= 0. \end{aligned}$$

The quantity

$$Re := \frac{V_f L_f}{\nu_f} = \frac{V_f L_f \rho_f}{\mu_f},$$

is called the *Reynolds number*. Scaled flow configurations with the same Reynolds number are equivalent. If the flow is known in the non-dimensional unit-system, it can be scaled to every equivalent configuration via (1.46). The Reynolds number is a good measure to describe the dynamical behavior of a flow configuration. Flows at low Reynolds number tend to have a stationary solution, while flows at higher Reynolds numbers have non-stationary or even turbulent solutions. The definition of the Reynolds number is somewhat arbitrary as fixing a reference velocity V_f and length L_f is usually not unique. The Reynolds number may therefore only be used to compare different flow situations for one configuration, e.g. the flow around a ship with length $L = 100m$ compared to a down-scaled model of the same ship with length $5m$.

1.4.4 The linear Stokes Equations

In flow situations where friction effects are very large compared to acceleration terms, the Navier-Stokes equations can be simplified by neglecting the convective term $(\mathbf{v} \cdot \nabla)\mathbf{v}$. This case is given, if the Reynolds number tends to zero $Re \rightarrow 0$. If the right hand side of the equation as well as boundary data does not depend on time, the flow field will be stationary and we end up with the stationary Stokes equations

$$-\rho_f \nu_f \Delta \mathbf{v} + \nabla p = \rho_f \mathbf{f}_f, \quad \operatorname{div} \mathbf{v} = 0 \text{ in } \mathcal{F},$$

with the usual Dirichlet or Neumann boundary conditions on $\partial\mathcal{F}$. By renormalizing pressure $\bar{p} = (\rho_f \nu_f)^{-1} p$ and volume force $\bar{\mathbf{f}} = \nu_f^{-1} \mathbf{f}$ all physical parameters can be omitted and we derive the equations in non-dimensionalized form:

$$-\Delta \mathbf{v} + \nabla \bar{p} = \bar{\mathbf{f}}, \quad \operatorname{div} \mathbf{v} = 0 \text{ in } \mathcal{F}. \quad (1.47)$$

Compared to the full incompressible Navier-Stokes equations, this equation is rather simple looking. As a saddle-point system it however still obtains one of the most important features of incompressible flows. While the physical relevance of the Stokes equations is very limited, it serves as entry-point to the mathematical analysis and the design of finite element discretizations for flow problems.

1.4.5 Theory of incompressible Flows

If there exists a unique solution $\{\mathbf{v}, p\}$ to the incompressible Navier-Stokes equations is still not known in all configuration. The stationary case is well understood, if we only consider Dirichlet boundary conditions. Here, a solution exists for small Reynolds numbers and it is unique, if the data is sufficiently small. When we consider general outflow conditions, we have no possibility to control the nonlinearity $(\mathbf{v} \cdot \nabla)\mathbf{v}$. In the instationary configuration there exists no proof for the existence of a unique solution under reasonable data assumptions. In three dimensions, the problem of proving the existence of a global smooth solution is considered open and one of the *Millenium Prize Problems*, see [61].

We start by deriving a weak formulation of the Navier-Stokes equations:

Lemma 16 (Weak formulation of the Navier-Stokes equations). *Let $\bar{\mathbf{v}}^D \in H^1(\mathcal{F})^d$ be an extension of the Dirichlet data on Γ_f^D into the domain \mathcal{F} . If the solution*

$$\mathbf{v} \in \bar{\mathbf{v}}^D + \mathcal{V}_f, \quad \mathcal{V}_f := H_0^1(\mathcal{F}; \Gamma_f^D)^d, \quad p \in \mathcal{L}_f, \quad \mathcal{L}_f := L^2(\mathcal{F}),$$

of the variational formulation

$$\begin{aligned} & (\rho_f(\partial_t \mathbf{v} + (\mathbf{v} \cdot \nabla) \mathbf{v}), \phi)_\mathcal{F} + (\sigma_f, \nabla \phi)_\mathcal{F} \\ & - \rho_f \nu_f \langle n \cdot \nabla \mathbf{v}^T, \phi \rangle_{\Gamma_f^{out}} = (\rho_f f, \phi)_\mathcal{F} \quad \forall \phi \in \mathcal{V}_f, \\ & (\operatorname{div} \mathbf{v}, \xi)_\mathcal{F} = 0 \quad \forall \xi \in \mathcal{L}_f, \end{aligned} \quad (1.48)$$

has sufficient regularity $v_f \in C^2(\mathcal{F}) \cap C(\mathcal{F} \cup \Gamma_f^D) \cap C^1(\mathcal{F} \cap \Gamma_f^{out})$ and $p \in C^1(\mathcal{F})$, it also solves the classical formulation of the Navier-Stokes equations (1.42) with Dirichlet data on Γ_f^D and the do-nothing outflow condition on Γ_f^{out} .

Proof. This follows by integration by parts and with basic variational principles. The boundary term on Γ_f^{out} is required as we use the full symmetric stress-tensor such that the solution of the variational formulation fulfills the *do-nothing* condition, see Section 1.4.2. \square

Remark 7 (Uniqueness of the pressure in Dirichlet problem). *If the configuration has Dirichlet boundaries all around the boundary $\Gamma_f^D = \partial\mathcal{F}$, a solution cannot be unique: let $\{\mathbf{v}, p\} \in \mathcal{V}_f \times \mathcal{L}_f$ be a solution. Then, it holds for $\{\mathbf{v}, p + c\}$ with $c \in \mathbb{R}$:*

$$\begin{aligned} (\sigma_f, \nabla \phi)_\mathcal{F} &= \rho_f \nu_f (\nabla \mathbf{v} + \nabla \mathbf{v}^T, \nabla \phi)_\mathcal{F} - (p_f + c, \nabla \cdot \phi)_\mathcal{F} \\ &= \rho_f \nu_f (\nabla \mathbf{v} + \nabla \mathbf{v}^T, \nabla \phi)_\mathcal{F} - (p_f, \nabla \cdot \phi)_\mathcal{F} + (\underbrace{\nabla c}_{=0}, \phi)_\mathcal{F} - \langle cn, \underbrace{\phi}_{=0} \rangle_{\partial\mathcal{F}}. \end{aligned}$$

If $\Gamma_f^D = \partial\mathcal{F}$ the pressure can only be unique up to a constant. In this case, we normalize the pressure-space

$$\mathcal{L}_f = L^2(\mathcal{F}) \setminus \mathbb{R}.$$

The Navier-Stokes equations brings along two characteristic difficulties for theoretical analysis and numerical discretization, the nonlinearity $(\mathbf{v} \cdot \nabla) \mathbf{v}$ and the side-condition of divergence freeness $\operatorname{div} \mathbf{v} = 0$. We will first focus on this second difficulty and consider the linear Stokes equations.

Existence and uniqueness of solutions to the Stokes equations

In the following, we consider the stationary Stokes equations

$$\begin{aligned} \mathbf{v}, p \in \mathcal{V}_f \times L_f, \quad \mathcal{V}_f := H_0^1(\mathcal{F}; \partial\mathcal{F})^d, \quad \mathcal{L}_f := L^2(\mathcal{F}) \setminus \mathbb{R} : \\ (\nabla \mathbf{v}, \nabla \phi)_\mathcal{F} - (p, \nabla \cdot \phi)_\mathcal{F} + (\nabla \cdot \mathbf{v}, \xi)_\mathcal{F} = (\mathbf{f}_f, \phi)_\mathcal{F} \quad \forall \{\phi, \xi\} \in \mathcal{V}_f \times \mathcal{L}_f. \end{aligned}$$

Here, we assume homogenous Dirichlet conditions on the complete boundary $\partial\mathcal{F}$ and further we consider the non-symmetric form of the stress tensor. Every solution $\mathbf{v} \in \mathcal{V}_f$ will be weakly divergence free in the space

$$\mathbf{v} \in \mathcal{V}_0 := \{\phi \in \mathcal{V}_f, (\operatorname{div} \phi, \xi)_\mathcal{F} = 0 \quad \forall \xi \in \mathcal{L}_f\} \subset \mathcal{V}_f.$$

By restricting the Stokes equations to this space, it remains to find

$$\mathbf{v} \in \mathcal{V}_0 : \quad (\nabla \mathbf{v}, \nabla \phi)_{\mathcal{F}} = (\mathbf{f}_f, \phi)_{\mathcal{F}} \quad \forall \phi \in \mathcal{V}_0. \quad (1.49)$$

Lemma 17 (Stokes velocity). *For every $\mathbf{f}_f \in H^{-1}(\mathcal{F})^d$ there exists a unique velocity $\mathbf{v} \in \mathcal{V}_0 \subset \mathcal{V}_f$ as solution of the Stokes equations. Further, it holds*

$$\|\nabla \mathbf{v}\| \leq \|\mathbf{f}_f\|_{-1}.$$

Proof. The space $\mathcal{V}_0 \subset \mathcal{V}_f$ is a Hilbert-space with the scalar product $(\nabla \cdot, \nabla \cdot)$. Riesz representation theorem guarantees the existence of a unique solution $\mathbf{v} \in \mathcal{V}_0$ to (1.49) and further gives the error estimate. \square

Existence and uniqueness of the pressure

Now, that we have shown the existence of a unique and divergence-free velocity field $\mathbf{v} \in \mathcal{V}_0 \subset \mathcal{V}_f$, the pressure is determined by the equation

$$p \in \mathcal{L}_f : \quad (p, \nabla \cdot \phi) = (\mathbf{f}_f, \phi) - (\nabla \mathbf{v}, \nabla \phi) \quad \forall \phi \in \mathcal{V}_f. \quad (1.50)$$

As this equation is not elliptic, we cannot proof existence with Riesz representation theorem or a generalization like Lax-Milgram. Instead, we reformulate this variational equation in operator notation as

$$-\operatorname{grad} p = l, \quad (1.51)$$

where $-\operatorname{grad} : \mathcal{L}_f \rightarrow H^{-1}$ is the weak gradient

$$-\langle \operatorname{grad} p, \phi \rangle = (p, \nabla \cdot \phi) \quad \forall \phi \in \mathcal{V}_f,$$

and $l \in H^{-1}$ a linear functional defined by

$$l(\phi) = (\mathbf{f}_f, \phi) - (\nabla \mathbf{v}, \nabla \phi) \quad \forall \phi \in \mathcal{V}_f.$$

Whether equation (1.50) or (1.51) has a solution depends on the surjectivity of the weak gradient operator. The difficulty of solution approaches to this equation is the low regularity of the problem. Two important results from the literature help up to answer the important questions of existence and uniqueness of solutions. It holds

Theorem 6 (de Rham). *Let $l \in H^{-1}$. The equation*

$$-\operatorname{grad} p = l,$$

has a unique solution $p \in \mathcal{L}_f$, if and only if

$$l \in \mathcal{V}_0^\circ,$$

where by \mathcal{V}_0° we denote the annihilator of \mathcal{V}_0 in H^{-1}

$$\mathcal{V}_0^\circ := \{f \in H^{-1}, f(\phi) = 0 \quad \forall \phi \in \mathcal{V}_0\} \subset H^{-1}.$$

And:

Theorem 7. Let \mathcal{F} be a bounded domain with Lipschitz boundary and $p \in L^2(\mathcal{F})$ be such, that $\text{grad } p \in H^{-1}(\mathcal{F})$. Then, it holds

$$\gamma \|p\|_{L^2(\mathcal{F}) \setminus \mathbb{R}} \leq \|\text{grad } p\|_{-1},$$

with a constant $\gamma = \gamma(\mathcal{F})$ that depends on the domain only.

Proof. For proofs on these essential theorems we refer to the literature. See Teman [221], de Rham [75] and Nečas [171]. \square

We will not be able to give proofs to these theorems, instead, we will show equivalence of Theorem 7 to further conditions, that will be handy in the context of the Stokes equations, both for proofing existence and uniqueness of the pressure, as well as for numerical error analysis:

Lemma 18 (Nečas). *The following three properties are equivalent*

- (i) *The weak gradient operator $-\text{grad} : \mathcal{L}_f \rightarrow \mathcal{V}_0^\circ$ is an isomorphism.*
- (ii) *For every $p \in L^2(\mathcal{F})$ it holds*

$$\|\text{grad } p\|_{-1} \geq \gamma \|p\| \quad \forall p \in \mathcal{L}_f, \quad (1.52)$$

where $\gamma > 0$ is a constant. (This is exactly Theorem 7).

- (iii) *The inf-sup condition holds*

$$\inf_{\xi \in \mathcal{L}_f} \sup_{\phi \in \mathcal{V}_f} \frac{(\xi, \nabla \cdot \phi)}{\|\xi\| \|\nabla \phi\|} \geq \gamma, \quad (1.53)$$

with a constant $\gamma > 0$.

Proof. Again, we refer to the literature [171, 221]. \square

All these preparations allow us to show the existence of a unique solution to the Stokes equations:

Lemma 19 (Stokes). *Let $\mathcal{F} \subset \mathbb{R}^d$ be a domain with Lipschitz boundary. The Stokes equation has a unique solution $\mathbf{v} \in \mathcal{V}_f$ and $p \in \mathcal{L}_f$ for every $f \in H^{-1}$. It holds*

$$\|\nabla \mathbf{v}\| + \gamma \|p\| \leq c \|f\|_{-1},$$

where $c > 0$ is a constant.

Proof. The existence of a unique $\mathbf{v} \in \mathcal{V}_0$ solving the velocity equation has already been shown. The functional

$$l(\phi) = (\nabla \mathbf{v}, \nabla \phi) - (\mathbf{f}_f, \phi)$$

is bound in $H^{-1}(\mathcal{F})$ and further, it holds $l \in \mathcal{V}_0^\circ$. Hence, existence of a unique weak pressure $p \in \mathcal{L}_f$ solving $-\text{grad } p = l$ follows by Lemma 18.

Finally, by using the inf-sup inequality we have

$$\begin{aligned}\gamma\|p\| &\leq \sup_{\phi \in \mathcal{V}_f} \frac{(p, \nabla \cdot \phi)}{\|\nabla \phi\|} = \sup_{\phi \in \mathcal{V}_f} \frac{(\mathbf{f}_f, \phi) - (\nabla \mathbf{v}, \nabla \phi)}{\|\nabla \phi\|} \\ &\leq \|f\|_{-1} + \|\nabla \mathbf{v}\| \leq 2\|f\|_{-1}.\end{aligned}$$

□

During the proof of this Lemma, we have used the following useful inequality for the divergence operator

Lemma 20 (Continuity of the divergence). *For $\mathbf{v} \in H^1(\mathcal{F})^d$ it holds*

$$\|\operatorname{div} \mathbf{v}\| \leq \sqrt{d}\|\nabla \mathbf{v}\|.$$

For $\mathbf{v} \in H_0^1(\mathcal{F})^d$ it even holds

$$\|\operatorname{div} \mathbf{v}\| \leq \|\nabla \mathbf{v}\|.$$

Proof. See Problem 16

□

Despite the special saddle-point character of the Stokes equations it shows, that we still get a unique solution that continuously depends on the right hand side \mathbf{f}_f . We only get L^2 -regularity for the pressure. The most important tool in the analysis of incompressible flows is the inf-sup condition. If the right hand side \mathbf{f}_f and the domain is sufficiently regular, we will get higher regularity of the solution. Here, the same rule of thumb holds as for the Laplace equation:

Lemma 21 (Regularity of the Stokes equations). *Let \mathcal{F} be a convex polygonal domain and $f \in L^2(\mathcal{F})$. Then, for the solution of the Stokes equations it holds*

$$\|\nabla^2 \mathbf{v}\| + \|\nabla p\| \leq c_s \|\mathbf{f}_f\|,$$

with a stability constant $c_s > 0$.

If $\mathcal{F} \subset \mathbb{R}^d$ is a domain with smooth C^{k+2} -boundary for $k \geq 0$ and $\mathbf{f}_f \in H^k(\mathcal{F})$ it holds

$$\|\mathbf{v}\|_{H^{k+2}(\mathcal{F})} + \|p\|_{H^{k+1}(\mathcal{F})} \leq c \|\mathbf{f}_f\|_{H^k(\mathcal{F})}.$$

Proof. For a proof to these results, we refer to the literature [221, 103].

□

The stationary Navier-Stokes equations

Next, we discuss the stationary Navier-Stokes equations including the nonlinearity

$$\begin{aligned}\mathbf{v}, p \in \mathcal{V}_f \times L_f, \quad \mathcal{V}_f := H_0^1(\mathcal{F}; \partial\mathcal{F})^d, \quad \mathcal{L}_f := L^2(\mathcal{F}) \setminus \mathbb{R} : \\ \frac{1}{Re}(\nabla \mathbf{v}, \nabla \phi) + (\mathbf{v} \cdot \nabla \mathbf{v}, \phi) - (p, \nabla \cdot \phi) + (\nabla \cdot \mathbf{v}, \xi) = (\mathbf{f}_f, \phi) \quad \forall \{\phi, \xi\} \in \mathcal{V}_f \times \mathcal{L}_f,\end{aligned}\tag{1.54}$$

again considering homogenous Dirichlet conditions only. Here, this restriction is essential not merely given for technical reasons, as the following Lemma shows:

Lemma 22 (Nonlinearity of the Navier-Stokes equations). *For $\mathbf{v}, \mathbf{w} \in H_0^1(\mathcal{F})^d$ with $\operatorname{div} \mathbf{v} = 0$ it holds:*

$$(\mathbf{v} \cdot \nabla \mathbf{w}, \mathbf{w}) = 0. \quad (1.55)$$

In the case of an outflow boundary $\Gamma_f^{out} \subset \partial\mathcal{F}$ it holds for all $\mathbf{v}, \mathbf{w} \in H_0^1(\mathcal{F}; \Gamma_f^D)^d$ with $\operatorname{div} \mathbf{v} = 0$

$$((\mathbf{v} \cdot \nabla) \mathbf{w}, \mathbf{w}) = \frac{1}{2} \int_{\Gamma_f^{out}} \vec{n} \cdot \mathbf{v} |\mathbf{w}|^2 \, do. \quad (1.56)$$

Proof. It holds (in the case of general boundary conditions):

$$\begin{aligned} ((\mathbf{v} \cdot \nabla) \mathbf{w}, \mathbf{w})_{\mathcal{F}} &= \sum_{i,j} (\mathbf{v}_j \partial_j \mathbf{w}_i, \mathbf{w}_i)_{\mathcal{F}} \\ &= \sum_{i,j} \left\{ \int_{\partial\mathcal{F}} \vec{n}_j \mathbf{w}_i \mathbf{v}_j \mathbf{w}_i \, do - (\mathbf{w}_i, \partial_j \mathbf{v}_j \mathbf{w}_i)_{\mathcal{F}} - (\mathbf{w}_i, \mathbf{v}_j \partial_j \mathbf{w}_i)_{\mathcal{F}} \right\} \\ &= - \underbrace{(\mathbf{w}, (\operatorname{div} \mathbf{v}) \mathbf{w})_{\mathcal{F}}}_{=0} - ((\mathbf{v} \cdot \nabla) \mathbf{w}, \mathbf{w})_{\mathcal{F}} + \int_{\partial\mathcal{F}} (\vec{n} \cdot \mathbf{v}) |\mathbf{w}|^2 \, do. \end{aligned}$$

This shows the two assertions. \square

This special structure of the nonlinearity will be the key to theoretical analysis of the incompressible Navier-Stokes equations. We directly get as a first result:

Lemma 23 (Stability estimate for the velocity). *Let $\mathbf{v} \in \mathcal{V}_0 \subset H_0^1(\mathcal{F})^d$ be a velocity field solving the Navier-Stokes equations. It holds for $\mathbf{f}_f \in L^2(\mathcal{F})^d$*

$$\|\nabla \mathbf{v}\| \leq \nu^{-1} \|\mathbf{f}_f\|_{-1}.$$

Proof. This results immediately follows using Lemma 22. \square

Remark 8 (Outflow conditions and stability estimates). *Lemma 22 shows, that the nonlinearity of the Navier-Stokes equations is only under control, if Dirichlet or at least no-penetration conditions*

$$\mathbf{v} \cdot \vec{n} = 0,$$

are given on all boundaries. For the do-nothing conditions but also for the no-stress condition introduced in Section 1.4.2 a boundary term remains. The problem of this remaining boundary term

$$\frac{1}{2} \int_{\Gamma_f^{out}} \vec{n} \cdot \vec{n} |\mathbf{w}|^2 \, do,$$

is the unknown sign. If there would be only outflow, i.e. $\vec{n} \cdot \mathbf{v} \geq 0$, we still get stability in the sense of Lemma 23. In the general setting, the boundary term however can be negative or positive. Braack and Mucha [46] introduced a modification of the do-nothing condition, denoted the directional do-nothing condition, that cancels the negative part of the boundary term and results in

$$-p\vec{n} \rho_f \nu_f \nabla \mathbf{v} - \frac{1}{2} (\mathbf{v} \cdot \vec{n})_- \mathbf{v} = 0 \text{ on } \Gamma_f^{out},$$

where by $(\mathbf{v} \cdot \vec{n})_-$ we denote

$$(\mathbf{v} \cdot \vec{n})_- = \begin{cases} 0 & \mathbf{v} \cdot \vec{n} \geq 0, \\ \mathbf{v} \cdot \vec{n} & \mathbf{v} \cdot \vec{n} < 0. \end{cases}$$

This condition is easily realized by a modification of the variational formulation

$$(\mathbf{v} \cdot \nabla \mathbf{v}, \phi) + (\rho_f \nu_f \nabla \mathbf{v}, \nabla \phi) - (p, \nabla \cdot \phi) - \frac{1}{2} \int_{\Gamma_f^{out}} (\mathbf{v} \cdot \vec{n})_- \mathbf{v} \cdot \phi \, do = (\mathbf{f}, \phi).$$

Braack and Mucha can show existence and uniqueness of solutions (for small data). Furthermore, they report from better numerical stability when using this directional *do-nothing* condition. Finally, this modified condition still allows for Poiseuille and Couette flow as well as vortices to leave the domain with little impact. See [46] for details.

Like for the Stokes equations, proofs for existence and uniqueness are split into first finding the velocity (this is a nonlinear problem now) and second, finding an appropriate pressure. While this second part is exactly as for the linear Stokes problem, showing existence and uniqueness of a velocity requires careful treatment of the nonlinearity.

$$\nu(\nabla \mathbf{v}, \nabla \phi) + ((\mathbf{v} \cdot \nabla) \mathbf{v}, \phi) = (\mathbf{f}, \phi) \quad \forall \phi \in \mathcal{V}_0. \quad (1.57)$$

Lemma 24 (Solutions for the Navier-Stokes equations). *Let $\mathcal{F} \subset \mathbb{R}^d$ be a domain with Lipschitz boundary. Further, let $\mathbf{f}_f \in H^{-1}(\mathcal{F})$. There exists a solution $\{\mathbf{v}, p\} \in \mathcal{V}_f \times \mathcal{L}_f$ to the Navier-Stokes equations (1.54) for every Reynolds number. It holds*

$$\|\nabla \mathbf{v}\| + \|p\| \leq c \|\mathbf{f}_f\|_{-1}.$$

This solution is unique, if

$$c^2 \nu^{-2} \|\mathbf{f}_f\|_{-1} \leq 1,$$

where $c > 0$ is a constant depending on the domain \mathcal{F} .

Proof. For the proof, we again refer to the literature [221, 171]. \square

The incompressible Navier-Stokes problem with homogenous Dirichlet values has a solution $\{\mathbf{v}, p\} \in \mathcal{V}_f \times \mathcal{L}_f$ for all Reynolds numbers and all right hand sides $\mathbf{f}_f \in H^{-1}(\mathcal{F})$. This solution is unique only if the Reynolds number is very small:

$$Re \leq \sqrt{\frac{1}{c^2 \|\mathbf{f}_f\|_{-1}}}.$$

Most application problems however deal with high Reynolds numbers $Re \gg 1000$ and a unique solution cannot be guaranteed. As we know that flows at very high Reynolds numbers get turbulent, we cannot expect a unique result for arbitrary Reynolds numbers. The gap between theory and observation however is still very large.

Nearly no theoretical results are known for different boundary conditions, in particular for outflow conditions like the *do-nothing* condition. Here, it is even unknown, whether the homogenous problem

$$-\frac{1}{Re} \Delta \mathbf{v} + (\mathbf{v} \cdot \nabla) \mathbf{v} + \nabla p = 0, \quad \nabla \cdot \mathbf{v} = 0,$$

with homogenous boundary conditions

$$\mathbf{v} = 0 \text{ on } \Gamma_f^D, \quad \frac{1}{Re} \partial_n \mathbf{v} - p \vec{n} = 0 \text{ on } \Gamma_f^{out}$$

only has the trivial solution $\mathbf{v} = 0$ and $p = 0$ or if other non-trivial solutions exist.

Finally, we cite a regularity result for the stationary Navier-Stokes equations which is in agreement to the expectation:

Lemma 25 (Regularity of the Navier-Stokes solution). *Let $\mathcal{F} \subset \mathbb{R}^d$ be a convex polygonal or smooth domain of class $C^{2,1}$. Further, let $\bar{\mathbf{v}}^D \in H^2(\mathcal{F})^d$ be a smooth extension of the Dirichlet data \mathbf{v}^D on $\partial\mathcal{F}$ into the domain. Finally, let $\mathbf{f}_f \in L^2(\mathcal{F})^d$. The solution to the Navier-Stokes equations has the regularity $\mathbf{v} \in H^2(\mathcal{F}) \cap \mathcal{V}_f$ and $p \in H^1(\mathcal{F}) \cap \mathcal{L}_f$ and it holds*

$$\|\nabla^2 \mathbf{v}\| + \|\nabla p\| \leq c_s \{\|\mathbf{f}_f\| + \|\nabla^2 \bar{\mathbf{v}}^D\|\},$$

where the stability constant is related to the Reynolds number $c_s \sim Re$.

Next, let \mathcal{F} be a C^{k+2} -domain and $\mathbf{f}_f \in H^k(\mathcal{F})^d$. Then, every solution $\mathbf{v} \in H_0^1(\mathcal{F})^d$ and $p \in L^2(\mathcal{F})$ of the stationary Navier-Stokes equations has the regularity

$$\|\mathbf{v}\|_{H^{k+2}(\mathcal{F})} + \|p\|_{H^{k+1}(\mathcal{F})} \leq c \|\mathbf{f}_f\|_{H^k(\mathcal{F})}.$$

Proof. For a proof of this result we refer to the literature, see Girault and Raviart [107] or Sohr [215]. \square

The non-stationary Navier-Stokes equations

Finally, we discuss the instationary Navier-Stokes equations

$$\begin{aligned} \mathbf{v} &= \mathbf{v}^{\text{in}} & t = 0, \\ (\partial_t \mathbf{v}, \phi) + ((\mathbf{v} \cdot \nabla) \mathbf{v}, \phi) + \nu(\nabla \mathbf{v}, \nabla \phi) - (p, \nabla \cdot \phi) &= (\mathbf{f}_f, \phi) \quad \forall \phi \in \mathcal{V}_f, \\ (\nabla \cdot \mathbf{v}, \xi) &= 0 \quad \forall \xi \in \mathcal{L}_f. \end{aligned}$$

Like in the stationary case, we can restrict the problem to the space of divergence free functions $\mathcal{V}_0 \subset \mathcal{V}$. Integration of the variational formulation over the time-interval $I = [0, T]$ gives

$$\int_I \{(\partial_t \mathbf{v}, \phi) + ((\mathbf{v} \cdot \nabla) \mathbf{v}, \phi) + \nu(\nabla \mathbf{v}, \nabla \phi)\} dt = \int_I (\mathbf{f}_f, \phi) dt.$$

To analyze this variational formulation, we must first specify suitable function spaces. For the viscous part, natural choices for \mathbf{v} and \mathbf{f}_f are

$$\mathbf{v}, \phi \in L^2(I; \mathcal{V}_0),$$

the space of square-integrable functions in time that map into \mathcal{V}_0 . For the time-derivative, we further ask for

$$\partial_t \mathbf{v} \in L^2(I; H^{-1}(\mathcal{F})).$$

We denote this space by $W(0, T)$:

$$W(0, T) := \{\phi \in L^2(I; \mathcal{V}_0), \partial_t \phi \in L^2(I; H^{-1}(\mathcal{F}))\}.$$

As

$$\mathcal{V}_0 \subset H_0^1(\Omega)^d \subset L^2(\Omega)^d \cong [L^2(\Omega)^d]^* \subset H^{-1}(\Omega)$$

it holds (see [221])

$$W(0, T) \hookrightarrow C(\bar{I}; L^2(\Omega)^d).$$

Every function $\mathbf{v} \in W(0, T)$ is almost everywhere equal to a continuous function in time that maps into $L^2(\Omega)^d$. It remains to discuss the nonlinearity: does for functions $\mathbf{v}, \phi \in W(0, T)$ hold, that

$$\int_I ((\mathbf{v} \cdot \nabla) \mathbf{v}, \phi) dt < \infty?$$

An answer is given by the following result:

Lemma 26. *Let $\Omega \subset \mathbb{R}^d$ be an open set. For $d = 2$ it holds*

$$\|\mathbf{v}\|_{L^4(\Omega)} \leq c \|\mathbf{v}\|^{\frac{1}{2}} \|\nabla \mathbf{v}\|^{\frac{1}{2}}.$$

In the case $d = 3$ it holds

$$\|\mathbf{v}\|_{L^4(\Omega)} \leq c \|\mathbf{v}\|^{\frac{1}{2}} \|\nabla \mathbf{v}\|^{\frac{3}{2}}.$$

Proof. A proof is given by Temam [221]. \square

We consider the two-dimensional case. It holds with Hölder's inequality ($1 = \frac{1}{4} + \frac{1}{2} + \frac{1}{4}$) and this Lemma, that

$$((\mathbf{v} \cdot \nabla) \mathbf{v}, \phi) \leq c \|\mathbf{v}\|_{L^4} \|\nabla \mathbf{v}\| \|\phi\|_{L^4} \leq c \|\mathbf{v}\|^{\frac{1}{2}} \|\nabla \mathbf{v}\|^{\frac{3}{2}} \|\phi\|^{\frac{1}{2}} \|\nabla \phi\|^{\frac{1}{2}}.$$

Using the embedding $W(0, T) \hookrightarrow C(\bar{I}; L^2(\Omega))$ it follows for the temporal integral by using Hölder's inequality (in time)

$$\begin{aligned} \int_I ((\mathbf{v} \cdot \nabla) \mathbf{v}, \phi) dt \\ &\leq c \|\phi\|_{C(\bar{I}; L^2(\Omega))}^{\frac{1}{2}} \|\mathbf{v}\|_{C(\bar{I}; L^2(\Omega))}^{\frac{1}{2}} \int_I \|\nabla \mathbf{v}\|^{\frac{3}{2}} \|\nabla \phi\|^{\frac{1}{2}} dt \\ &\leq c \|\phi\|_{W(0,T)}^{\frac{1}{2}} \|\mathbf{v}\|_{W(0,T)}^{\frac{1}{2}} \|\mathbf{v}\|_{W(0,T)}^{\frac{3}{2}} \|\phi\|_{W(0,T)}^{\frac{1}{2}} \\ &\leq c \|\mathbf{v}\|_{W(0,T)}^2 \|\phi\|_{W(0,T)}. \end{aligned}$$

This is exactly the desired stability result for the variational formulation. The nonlinearity is not bound in the three-dimensional case, if we ask for $\mathbf{v}, \phi \in W(0, T)$. We cite the following results, that can be found in Temam [221]:

Lemma 27 (Instationary Navier-Stokes equations). *Let $\mathcal{F} \subset \mathbb{R}^d$ be a Lipschitz domain and*

$$\mathbf{f}_f \in L^2(I; H^{-1}(\mathcal{F})), \quad \mathbf{v}^0 \in \mathcal{V}_0.$$

Then, the instationary Navier-Stokes equation has at least one solution for arbitrary Reynolds numbers. This solution is unique in the two dimensional case (for arbitrary Reynolds numbers) and it holds

$$\mathbf{v} \in L^2(\mathcal{F}; \mathcal{V}_0), \quad \partial_t \mathbf{v} \in L^2(I; H^{-1}(\mathcal{F})).$$

In the three-dimensional case, unity is usually not given, and the solution has the reduced regularity

$$\mathbf{v} \in L^{\frac{8}{3}}(I; L^4(\Omega)), \quad \partial_t \mathbf{v} \in L^{\frac{4}{3}}(I; H^{-1}(\Omega)).$$

It is remarkable, that the non-stationary solution is unique for all Reynolds numbers, if we look at the two-dimensional system. Directly working on the stationary equations asked for smallness of the data to guarantee uniqueness.

To prove existence of global solutions, uniqueness and regularity of the three dimensional problem is one of big open problems in applied mathematics, see [61].

1.5 Flow Problems on moving domains

In this section, we discuss models for the flows on a moving domain $\mathcal{F}(t) \subset \mathbb{R}^d$. Find

$$v(t) \in \mathcal{V}_f(t), \quad p(t) \in \mathcal{L}_f(t),$$

so that

$$(\partial_t \mathbf{v} + (\mathbf{v} \cdot \nabla) \mathbf{v}, \phi)_{\mathcal{F}(t)} + (\sigma_f, \nabla \phi)_{\mathcal{F}(t)} + (\operatorname{div} \mathbf{v}, \xi)_{\mathcal{F}(t)} = (\mathbf{f}_f, \phi)_{\mathcal{F}(t)} \quad (1.58)$$

for all $\phi \in \mathcal{V}_f(t)$ and $\xi \in \mathcal{L}_f(t)$. First we assume, that the domain motion is given by a mapping

$$t \mapsto \mathcal{F}(t).$$

Later on, when analyzing fluid-structure interactions, this mapping will be an unknown part of the solution. For simplicity, let $\hat{\mathcal{F}}$ be a fixed reference domain and let

$$\hat{T}(t) : \hat{\mathcal{F}} \rightarrow \mathcal{F}(t),$$

be a regular and invertible mapping to the moving domain. We will discuss the necessary regularity of this mapping in detail. Note however, that the mapping \hat{T} is not intended to be the mapping between Lagrangian and Eulerian coordinates. The motion described by $\mathcal{F}(t)$ is arbitrary and not following the particles.

1.5.1 Eulerian techniques for flow problems on moving domains

Discretization of partial differential equations is difficult if the domain is in motion. Usually, every discretization consists of first discretizing the domain $\mathcal{F}(t)$ by a mesh $\mathcal{F}_h(t)$. Here, if $\mathcal{F}(t)$ is moving, the meshes also cannot be fixed.

We consider time-stepping methods, where the solution in the time-interval $I = [0, T]$ is searched at discrete time-steps only

$$0 = t_0 < t_1 < \dots < t_M = T.$$

By $\mathbf{v}^m := \mathbf{v}(t_m)$ and by $p^m := p(t_m)$ we denote velocity and pressure at time t_m . Then, in a discrete setting, approximations \mathbf{v}_{kh}^m and \mathbf{v}_{kh}^{m-1} will live on different meshes - or in the context of finite elements - in different function spaces V_{kh}^m and V_{kh}^{m-1} . Usual time-discretization schemes approximate the temporal derivative by finite differences

$$\partial_t \mathbf{v}_h(t_m) \approx \frac{\mathbf{v}_{kh}^m - \mathbf{v}_{kh}^{m-1}}{t_m - t_{m-1}}.$$

Now we assume, that $\mathbf{v}_{kh}^m \in V_{kh}^m$ and $\mathbf{v}_{kh}^{m-1} \in V_{kh}^{m-1}$ are element of different finite element spaces. In this case, $\mathbf{v}_{kh}^m - \mathbf{v}_{kh}^{m-1}$ will most likely neither belong to V_{kh}^m or V_{kh}^{m-1} .

This problem gets even more severe, if we consider a spatial coordinate $x \in \mathcal{F}(t_m)$ that is not part of the domain at the last time-step $x \notin \mathcal{F}(t_{m-1})$. Here, the expression $\mathbf{v}_{kh}^m(x) - \mathbf{v}_{kh}^{m-1}(x)$ is not defined at all.

Eulerian schemes for moving domain problems will require non-standard discretization techniques. We will pick up this discussion at a later point and first continue with approaches that are based on fixed reference domains.

1.5.2 The Arbitrary Lagrangian Eulerian (ALE) formulation for moving domain problems

One possibility to deal with the motion of the fluid-domain is to introduce a fixed reference domain $\hat{\mathcal{F}} \subset \mathbb{R}^d$ and a mapping

$$\hat{T}_f(t) : \hat{\mathcal{F}} \rightarrow \mathcal{F}(t).$$

We can use this mapping to transform the Navier-Stokes equations onto the reference domain $\hat{\mathcal{F}}$ and to define velocity and pressure in the reference system

$$\hat{\mathbf{v}}(\hat{x}, t) := \mathbf{v}(\hat{T}_f(\hat{x}, t), t), \quad \hat{p}(\hat{x}, t) := p(\hat{T}_f(\hat{x}, t), t) \quad \forall \hat{x} \in \hat{\mathcal{F}}. \quad (1.59)$$

If the mapping \hat{T}_f is a C^1 -diffeomorphism, it can be used to transform the Navier-Stokes equations onto $\hat{\mathcal{F}}$ using $\hat{\mathbf{v}}$ and \hat{p} as principle variables. All relations required for this transformation have already been derived in Section 1.1.7. By (1.22) and with Definition 3 it holds by (1.59)

$$\begin{aligned} \rho_f (\partial_t \mathbf{v} + (\mathbf{v} \cdot \nabla) \mathbf{v}, \phi)_{\mathcal{F}(t)} &= \rho_f (\hat{J}_f (\partial_t \hat{\mathbf{v}} + \hat{\mathbf{F}}_f^{-1} (\hat{\mathbf{v}} - \partial_t \hat{T}_f) \cdot \nabla \hat{\mathbf{v}}), \hat{\phi})_{\hat{\mathcal{F}}}, \\ (\sigma_f, \nabla \phi)_{\mathcal{F}(t)} &= (\hat{J}_f \hat{\sigma}_f \hat{\mathbf{F}}_f^{-T}, \hat{\nabla} \hat{\phi})_{\hat{\mathcal{F}}}, \\ (\operatorname{div} \mathbf{v}, \xi)_{\mathcal{F}(t)} &= (\widehat{\operatorname{div}} (\hat{J}_f \hat{\mathbf{F}}_f^{-1} \hat{\mathbf{v}}), \hat{\xi})_{\hat{\mathcal{F}}}. \end{aligned} \quad (1.60)$$

The Cauchy stress tensor $\hat{\sigma}(\hat{x})$ expressed in the reference system is derived with help of (1.16)

$$\hat{\sigma}_f := -\hat{p}I + \rho_f \nu_f (\hat{\nabla} \hat{\mathbf{v}} \hat{\mathbf{F}}_f^{-1} + \hat{\mathbf{F}}_f^{-T} \hat{\nabla} \hat{\mathbf{v}}^T). \quad (1.61)$$

By these transformations, the Navier-Stokes equations on the ALE reference system $\hat{\mathcal{F}}$ are given by finding $\hat{\mathbf{v}} \in \hat{\mathcal{V}}_f$ and $\hat{p} \in \hat{\mathcal{L}}_f$ such that

$$\begin{aligned} \rho_f (\hat{J}_f (\partial_t \hat{\mathbf{v}} + \hat{\mathbf{F}}_f^{-1} (\hat{\mathbf{v}} - \partial_t \hat{T}_f) \cdot \nabla \hat{\mathbf{v}}), \hat{\phi})_{\hat{\mathcal{F}}} + (\hat{J}_f \hat{\sigma}_f \hat{\mathbf{F}}_f^{-T}, \hat{\nabla} \hat{\phi})_{\hat{\mathcal{F}}} &= (\rho_f \hat{J}_f \hat{\mathbf{f}}_f, \hat{\phi})_{\hat{\mathcal{F}}} \\ (\widehat{\operatorname{div}} (\hat{J}_f \hat{\mathbf{F}}_f^{-1} \hat{\mathbf{v}}), \hat{\xi})_{\hat{\mathcal{F}}} &= 0, \end{aligned} \quad (1.62)$$

for all $\hat{\phi} \in \hat{\mathcal{V}}_f$ and $\hat{\xi} \in \hat{\mathcal{L}}_f$. The domain $\hat{\mathcal{F}}$ is fixed and the test- and trial-spaces are defined as

$$\hat{\mathcal{V}}_f := H_0^1(\hat{\mathcal{F}}; \Gamma_f^D)^d, \quad \hat{\mathcal{L}}_f := L^2(\hat{\mathcal{F}}). \quad (1.63)$$

It holds

Lemma 28 (Navier-Stokes in ALE coordinates). *Let $\hat{\mathcal{F}} \subset \mathbb{R}^d$ be a smooth domain and $\hat{T}_f : \hat{\mathcal{F}} \rightarrow \mathcal{F}(t)$ be a C^2 -diffeomorphism. Then, for every solution $(\hat{\mathbf{v}}, \hat{p}) \in \hat{\mathcal{V}}_f \times \hat{\mathcal{L}}_f$ of (1.62) there exists a solution $(\mathbf{v}, p) \in \mathcal{V}_f(t) \times \mathcal{L}_f(t)$ of (1.58) with $\hat{\mathbf{v}}(\hat{x}, t) = \mathbf{v}(\hat{T}_f(\hat{x}, t), t)$ and $\hat{p}(\hat{x}, t) = p(\hat{T}_f(\hat{x}, t), t)$ almost everywhere.*

Proof. This directly follows by mapping between the two different formulation of the Navier-Stokes equations and using equivalence of the test-spaces given by the following Lemma 29. \square

Lemma 29 (Transformation of Sobolev-spaces). *Let Ω and $\hat{\Omega}$ be two domains in \mathbb{R}^d and let $\hat{T} \in C^{k,1}(\hat{\Omega})^d$ be a diffeomorphism with $\hat{T}(\hat{\Omega}) = \Omega$ and $\hat{T}^{-1}(\Omega) = \hat{\Omega}$. Then, the composition operators*

$$\phi := \hat{\phi} \circ \hat{T}^{-1} \quad \forall \hat{\phi} \in H^{k+1}(\hat{\Omega}) \text{ and } \hat{\phi} := \phi \circ \hat{T} \quad \forall \phi \in H^{k+1}(\Omega),$$

are continuous. Hence, the Sobolev spaces $H^{k+1}(\Omega)$ and $H^{k+1}(\hat{\Omega})$ are equivalent

$$H^{k+1}(\hat{\Omega}) \cong H^{k+1}(\Omega),$$

such that there exist constants $c_1, c_2 > 0$ such that

$$c_1 \|\hat{v}\|_{H^{k+1}(\hat{\Omega})} \leq \|\hat{v} \circ T\|_{H^{k+1}(\Omega)} \leq c_2 \|\hat{v}\|_{H^{k+1}(\hat{\Omega})} \quad \forall \hat{v} \in H^{k+1}(\hat{\Omega}).$$

Proof. We refer to the literature [249]. \square

The variational formulation (1.62) has the benefit, that the domain $\hat{\mathcal{F}}$ is fixed and that the function spaces $\hat{\mathcal{V}}_f$ and $\hat{\mathcal{L}}_f$ do not change in time. A standard finite element triangulation $\hat{\mathcal{F}}_h$ of $\hat{\mathcal{F}}$ can be constructed and used for defining discrete function spaces. The removal of the domain motion comes at the price of additional nonlinearities introduced in the equation. These nonlinearities all depend on the domain map \hat{T}_f .

The equivalence of the Eulerian and the ALE formulation of the Navier-Stokes equations strictly depends on the regularity of the mapping \hat{T}_f . If this mapping loses its regularity, the equivalence is also lost.

Remark 9 (Divergence in ALE coordinates). *On first sight, the divergence condition in ALE coordinates*

$$\widehat{\operatorname{div}} \left(\hat{J} \hat{\mathbf{F}}^{-1} \hat{\mathbf{v}} \right) = 0,$$

calls for the evaluation of $\hat{\mathbf{u}}$'s second derivatives. It turns however out, that all these second derivatives cancel out, if $\hat{\mathbf{u}} \in C^2(\hat{\mathcal{F}})^d$.

The following two technical lemma show this relation. First, we derive a rule for the partial derivatives of a matrices inverse and for the determinant of a matrix:

Lemma 30 (Partial derivatives of inverse and determinant). *Let $\hat{\mathbf{F}} : \mathbb{R}^{n \times n} \rightarrow \mathbb{R}$ be differentiable and invertible, $\hat{J} = \det(\hat{\mathbf{F}})$. By $\hat{\partial}_k \hat{\mathbf{F}} = (\hat{\partial}_k \hat{\mathbf{F}}_{ij})_{ij}$ and $\hat{\partial}_k \hat{\mathbf{F}}^{-1} = (\hat{\partial}_k \hat{\mathbf{F}}_{ij}^{-1})_{ij}$ we denote matrices of partial derivatives of $\hat{\mathbf{F}}$ and its inverse. It holds*

$$\hat{\partial}_k \hat{\mathbf{F}}^{-1} = -\hat{\mathbf{F}}^{-1} \hat{\partial}_k \hat{\mathbf{F}} \hat{\mathbf{F}}^{-1}, \quad \hat{\partial}_k \hat{J} = \hat{J} \operatorname{tr}(\hat{\mathbf{F}}^{-1} \hat{\partial}_k \hat{\mathbf{F}}) \quad (1.64)$$

Proof. (i) By $\hat{\mathbf{F}}^{-1} \hat{\mathbf{F}} = I$ we get for $k = 1, \dots, n$

$$0 = \sum_{l=1}^n \hat{\partial}_k \hat{\mathbf{F}}_{il}^{-1} \hat{\mathbf{F}}_{lj} + \hat{\mathbf{F}}_{il}^{-1} \hat{\partial}_k \hat{\mathbf{F}}_{lj} \quad \Rightarrow \quad \hat{\partial}_k \hat{\mathbf{F}}^{-1} \hat{\mathbf{F}} + \hat{\mathbf{F}}^{-1} \hat{\partial}_k \hat{\mathbf{F}} = 0,$$

such that the first result follows by multiplication with $\hat{\mathbf{F}}^{-1}$. Likewise, the inverse relation holds (we need it later on)

$$\hat{\partial}_k \hat{\mathbf{F}} = -\hat{\mathbf{F}} \hat{\partial}_k \hat{\mathbf{F}}^{-1} \hat{\mathbf{F}}. \quad (1.65)$$

(ii) We denote by Δ_{ij} the cofactor of $\hat{\mathbf{F}}$

$$\Delta_{ij} := (-1)^{i+j} \det(\hat{\mathbf{F}}_{kl})_{k \neq i, l \neq j},$$

Then, the determinant j can be given as

$$\delta_{ik}\hat{J} = \sum_{l=1}^n \Delta_{il}\hat{\mathbf{F}}_{kl}, \quad i = 1, \dots, n. \quad (1.66)$$

Differentiation of this formula ($k = i$) w.r.t. the entries $\hat{\mathbf{F}}_{ij}$ gives

$$\frac{\partial \hat{J}}{\partial \hat{\mathbf{F}}_{ij}} = \sum_{l=1}^n \underbrace{\frac{\partial \Delta_{il}}{\partial \hat{\mathbf{F}}_{ij}}}_{=0} \hat{\mathbf{F}}_{il} + \Delta_{il} \underbrace{\frac{\partial \hat{\mathbf{F}}_{il}}{\partial \hat{\mathbf{F}}_{ij}}}_{=\delta_{lj}} = \Delta_{ij}, \quad (1.67)$$

as Δ_{il} does not depend on $\hat{\mathbf{F}}_{ij}$. Hereby, we get with (1.65) and (1.67) and (1.66)

$$\begin{aligned} \hat{\partial}_k \hat{J} &= \sum_{ij} \frac{\hat{\partial} \hat{J}}{\hat{\mathbf{F}}_{ij}} \hat{\partial}_k \hat{\mathbf{F}}_{ij} = - \sum_{ij} \Delta_{ij} (\hat{\mathbf{F}} \hat{\partial}_k \hat{\mathbf{F}}^{-1} \hat{\mathbf{F}})_{ij} \\ &= - \sum_{jrs} \underbrace{\left(\sum_i \Delta_{ij} \hat{\mathbf{F}}_{ir} \right)}_{=\delta_{jr}\hat{J}} \hat{\partial}_k \hat{\mathbf{F}}_{rs}^{-1} \hat{\mathbf{F}}_{sj} = -\hat{J} \sum_{rs} \hat{\partial}_k \hat{\mathbf{F}}_{rs}^{-1} \hat{\mathbf{F}}_{sr}, \end{aligned}$$

and hence, using $A : B = \text{tr}(AB^T)$:

$$\begin{aligned} \hat{\partial}_k \hat{J} &= -\hat{J} \hat{\partial}_k \hat{\mathbf{F}}^{-1} : \hat{\mathbf{F}}^T = \hat{J} \hat{\mathbf{F}}^{-1} \hat{\partial}_k \hat{\mathbf{F}} \hat{\mathbf{F}}^{-1} : \hat{\mathbf{F}}^T \\ &= \hat{J} \text{tr}(\hat{\mathbf{F}}^{-1} \hat{\partial}_k \hat{\mathbf{F}} \hat{\mathbf{F}}^{-1} \hat{\mathbf{F}}) = \hat{J} \text{tr}(\hat{\mathbf{F}}^{-1} \hat{\partial}_k \hat{\mathbf{F}}) \end{aligned}$$

□

With help of these differentiation rules we can reformulate the divergence in ALE coordinates

Lemma 31 (Divergence in ALE coordinates). *Let $\hat{\mathbf{u}} \in C^2(\Omega)^d$, $\hat{\mathbf{F}} = I + \hat{\nabla} \hat{\mathbf{u}}$ be invertible and $\hat{J} = \det(\hat{\mathbf{F}})$. It holds*

$$\text{div}(\hat{J} \hat{\mathbf{F}}^{-1} \hat{\mathbf{v}}) = \sum_{kl} \hat{J} \hat{\mathbf{F}}_{kl}^{-1} \hat{\partial}_k \hat{\mathbf{v}}_l = \hat{J} \hat{\mathbf{F}}^{-1} : \nabla \hat{\mathbf{v}}^T = \hat{J} \text{tr}(\hat{\mathbf{F}}^{-1} \nabla \hat{\mathbf{v}}).$$

Proof. We start by component-wise differentiation

$$\text{div}(\hat{J} \hat{\mathbf{F}}^{-1} \hat{\mathbf{v}}) = \sum_k \hat{\partial}_k (\hat{J} \hat{\mathbf{F}}^{-1} \hat{\mathbf{v}})_k = \sum_{kl} \left\{ \hat{\partial}_k \hat{J} \hat{\mathbf{F}}_{kl}^{-1} \hat{\mathbf{v}}_l + \hat{J} \hat{\partial}_k \hat{\mathbf{F}}_{kl}^{-1} \hat{\mathbf{v}}_l + \hat{J} \hat{\mathbf{F}}^{-1} \hat{\partial}_k \hat{\mathbf{v}}_l \right\}.$$

While the third term already has the final form, we will show, that the first two parts cancel out. Using the two parts of Lemma 30, we get

$$\begin{aligned} \text{div}(\hat{J} \hat{\mathbf{F}}^{-1} \hat{\mathbf{v}}) &= \hat{J} \hat{\mathbf{F}}^{-1} : \nabla \hat{\mathbf{v}}^T + \hat{J} \sum_l \mathbf{v}_l \left(\sum_k \left(\text{tr}(\hat{\mathbf{F}}^{-1} \hat{\partial}_k \hat{\mathbf{F}}) \hat{\mathbf{F}}_{kl}^{-1} - (\hat{\mathbf{F}}^{-1} \hat{\partial}_k \hat{\mathbf{F}} \hat{\mathbf{F}}^{-1})_{kl} \right) \right) \\ &= \hat{J} \sum_l \mathbf{v}_l \sum_{kij} \left(\hat{\mathbf{F}}_{ij}^{-1} \hat{\partial}_k \hat{\mathbf{F}}_{ji} \hat{\mathbf{F}}_{kl}^{-1} - \hat{\mathbf{F}}_{kj}^{-1} \hat{\partial}_k \hat{\mathbf{F}}_{ji} \hat{\mathbf{F}}_{il}^{-1} \right) \end{aligned}$$

Next, we use the specific form $\hat{\mathbf{F}} = I + \hat{\nabla}\hat{\mathbf{u}}$ and the symmetry of the second derivatives $\hat{\partial}_{ij}\hat{\mathbf{u}} = \hat{\partial}_{ij}\hat{\mathbf{u}}$. Then,

$$\begin{aligned} \operatorname{div}(\hat{J}\hat{\mathbf{F}}^{-1}\mathbf{v}) &= \hat{J}\hat{\mathbf{F}}^{-1} : \nabla\mathbf{v}^T + \hat{J}\sum_l \mathbf{v}_l \sum_{kij} \left(\hat{\mathbf{F}}_{ij}^{-1}\hat{\partial}_i\hat{\mathbf{F}}_{jk}\hat{\mathbf{F}}_{kl}^{-1} - \hat{\mathbf{F}}_{kj}^{-1}\hat{\partial}_k\hat{\mathbf{F}}_{ji}\hat{\mathbf{F}}_{il}^{-1} \right) \\ &= \hat{J}\sum_l \mathbf{v}_l \sum_{kij} \left(\hat{\mathbf{F}}_{kj}^{-1}\hat{\partial}_k\hat{\mathbf{F}}_{ji}\hat{\mathbf{F}}_{il}^{-1} - \hat{\mathbf{F}}_{kj}^{-1}\hat{\partial}_k\hat{\mathbf{F}}_{ji}\hat{\mathbf{F}}_{il}^{-1} \right) = 0, \end{aligned}$$

where we switched the indices i and k in the first part. \square

The equivalence of two different representations of the Navier-Stokes equations in ALE and in Eulerian coordinates also states, that both formulations allow for the same solution concept: if the Eulerian formulation of the Navier-Stokes equations has a unique solution $(\mathbf{v}(t), p(t))$, for suitable mappings \hat{T}_f , the ALE formulation will have a corresponding unique solution $(\hat{\mathbf{v}}, \hat{p})$ and it holds:

$$\begin{aligned} c(\hat{T}_f(t))^{-1} \{ \|\nabla\mathbf{v}(t)\|_{\mathcal{F}(t)} + \|p(t)\|_{\mathcal{F}(t)} \} &\leq \|\hat{\nabla}\hat{\mathbf{v}}\|_{\hat{\mathcal{F}}} + \|\hat{p}\|_{\hat{\mathcal{F}}} \leq \\ &c(\hat{T}_f(t)) \{ \|\nabla\mathbf{v}(t)\|_{\mathcal{F}(t)} + \|p(t)\|_{\mathcal{F}(t)} \} \quad (1.68) \end{aligned}$$

The constant $c(\hat{T}_f(t))$ will depend on the deformation and if \hat{T}_f loses its regularity $c(\hat{T}_f(t)) \rightarrow 0$ or $c(\hat{T}_f(t)) \rightarrow \infty$ is possible.

Lemma 32. *Let $\mathcal{F}(t) \subset \mathbb{R}^d$ be such that the Navier-Stokes equations have a solution*

$$\|\nabla\mathbf{v}(t)\|_{\mathcal{F}(t)} + \|p(t)\|_{\mathcal{F}(t)} < \infty \quad t \in [0, T].$$

Further, let $\hat{T}_f : \hat{\mathcal{F}} \rightarrow \mathcal{F}(t)$ be a C^2 -diffeomorphism. There exist constants $c, C > 0$ so that relation (1.68) holds with

$$c \leq c(\hat{T}_f(t)) \leq C \quad t \in [0, T].$$

Proof. This result follows, as the two variational formulations are equivalent under these strong assumptions on the mapping. \square

The crucial inequality for the analysis of the Navier-Stokes and Stokes equations is the inf-sup condition (1.53). We assume, that on $\hat{\mathcal{F}}$ it holds:

$$\inf_{\hat{\xi} \in L^2(\hat{\mathcal{F}})} \sup_{\hat{\phi} \in H_0^1(\hat{\mathcal{F}})^d} \frac{(\widehat{\operatorname{div}} \hat{\phi}, \hat{\xi})}{\|\hat{\nabla}\hat{\phi}\|_{\hat{\mathcal{F}}} \|\hat{\xi}\|_{\hat{\mathcal{F}}}} \geq \hat{\gamma} > 0.$$

Next, let $\hat{T}_f(t) : \hat{\mathcal{F}} \rightarrow \mathcal{F}(t)$ be a C^2 -diffeomorphism with $\hat{T}_f(\hat{\mathcal{F}}, 0) = \hat{\mathcal{F}}$. In light of Lemma 29, the Sobolev-spaces on $\mathcal{F}(t)$ and $\hat{\mathcal{F}}$ are equivalent

$$H^1(\mathcal{F}(t)) \cong H^1(\hat{\mathcal{F}}), \quad L^2(\mathcal{F}(t)) \cong L^2(\hat{\mathcal{F}}).$$

On $\mathcal{F}(t)$ it holds

$$\frac{(\operatorname{div} \phi, \xi)_{\mathcal{F}(t)}}{\|\xi\|_{\mathcal{F}(t)} \|\nabla\phi\|_{\mathcal{F}(t)}} = \frac{(\widehat{\operatorname{div}} (\hat{T}_f \hat{\mathbf{F}}_f^{-1} \hat{\phi}), \hat{\xi})_{\hat{\mathcal{F}}}}{\|\hat{T}_f^{\frac{1}{2}} \hat{\xi}\|_{\hat{\mathcal{F}}} \|\hat{T}_f^{\frac{1}{2}} \hat{\nabla}\hat{\phi}\hat{\mathbf{F}}_f^{-T}\|_{\hat{\mathcal{F}}}},$$

where

$$\xi(\hat{T}_f(\hat{x}, t)) = \hat{\xi}(\hat{x}), \quad \phi(\hat{T}_f(\hat{x}, t)) = \hat{\phi}(\hat{x}).$$

We substitute

$$\tilde{\phi} := \hat{J}_f \hat{\mathbf{F}}_f^{-1} \hat{\phi} \quad \Rightarrow \quad \hat{\phi} = \hat{J}_f^{-1} \hat{\mathbf{F}}_f \tilde{\phi}.$$

Due to the strong regularity of $\hat{T}_f \in C^2$ it holds for every $\tilde{\phi} \in H^1(\hat{\mathcal{F}})^d$

$$\|\hat{\nabla} \tilde{\phi}\|_{\hat{\mathcal{F}}} \leq \|\hat{J}_f \hat{\mathbf{F}}_f^{-1}\|_{W^{1,\infty}(\hat{\mathcal{F}})} \|\tilde{\phi}\|_{H^1(\hat{\mathcal{F}})},$$

that $\tilde{\phi} \in H^1(\hat{\mathcal{F}})$ and with Poincaré's inequality we get the estimate

$$\|\hat{\nabla} \hat{\phi}\|_{\hat{\mathcal{F}}} \leq \|\hat{J}_f^{-1} \hat{\mathbf{F}}_f\|_{W^{1,\infty}(\hat{\mathcal{F}})} \|\tilde{\phi}\|_{H^1(\hat{\mathcal{F}})} \leq c_P \|\hat{J}_f^{-1} \hat{\mathbf{F}}_f\|_{W^{1,\infty}(\hat{\mathcal{F}})} \|\hat{\nabla} \tilde{\phi}\|_{\hat{\mathcal{F}}}.$$

With these preparations, we can carry over the inf-sup condition from $\hat{\mathcal{F}} = \mathcal{F}(0)$ to $\mathcal{F}(t)$:

$$\begin{aligned} & \inf_{\xi \in L^2(\mathcal{F}(t))} \sup_{\phi \in H^1(\mathcal{F}(t))^d} \frac{(\operatorname{div} \phi, \xi)_{\mathcal{F}(t)}}{\|\xi\|_{\mathcal{F}(t)} \|\nabla \phi\|_{\mathcal{F}(t)}} \\ &= \inf_{\hat{\xi} \in L^2(\hat{\mathcal{F}})} \sup_{\hat{\phi} \in H^1(\hat{\mathcal{F}})^d} \frac{(\widehat{\operatorname{div}}(\hat{J}_f \hat{\mathbf{F}}_f^{-1} \hat{\phi}), \hat{\xi})_{\hat{\mathcal{F}}}}{\|\hat{J}_f^{\frac{1}{2}} \hat{\xi}\|_{\hat{\mathcal{F}}} \|\hat{J}_f^{\frac{1}{2}} \hat{\mathbf{F}}_f^{-T} \hat{\nabla} \hat{\phi}\|_{\hat{\mathcal{F}}}} \\ &= \inf_{\hat{\xi} \in L^2(\hat{\mathcal{F}})} \sup_{\tilde{\phi} \in H^1(\hat{\mathcal{F}})^d} \frac{(\widehat{\operatorname{div}} \tilde{\phi}, \hat{\xi})_{\mathcal{F}(t)}}{\|\hat{J}_f^{\frac{1}{2}} \hat{\xi}\|_{\hat{\mathcal{F}}} \|\hat{J}_f^{\frac{1}{2}} \hat{\mathbf{F}}_f^{-T} \hat{\nabla}(\hat{J}_f^{-1} \hat{\mathbf{F}}_f \tilde{\phi})\|_{\hat{\mathcal{F}}}} \\ &\geq c_P^{-1} \|\hat{J}_f^{\frac{1}{2}}\|_{L^\infty}^{-1} \|\hat{J}_f^{\frac{1}{2}} \hat{\mathbf{F}}_f^{-T}\|_{L^\infty}^{-1} \|\hat{J}_f^{-1} \hat{\mathbf{F}}_f\|_{W^{1,\infty}}^{-1} \inf_{\hat{\xi} \in L^2(\hat{\mathcal{F}})} \sup_{\tilde{\phi} \in H^1(\hat{\mathcal{F}})^d} \frac{(\widehat{\operatorname{div}} \tilde{\phi}, \hat{\xi})_{\mathcal{F}(t)}}{\|\hat{\xi}\|_{\hat{\mathcal{F}}} \|\hat{\nabla} \tilde{\phi}\|_{\hat{\mathcal{F}}}} \\ &\geq c(\hat{T}_f(t)) \hat{\gamma} =: \gamma(t) \geq \gamma_0 > 0. \end{aligned}$$

Depending on the regularity of the transformation \hat{T}_f , the inf-sup constant $\gamma(t)$ can be significantly closer to zero than $\hat{\gamma}$. See [168] for a study on the stability of the Stokes system on moving and strongly deformed domains.

1.5.3 Construction of the ALE map

The ALE formulation of the Navier-Stokes equations carries an arbitrariness, as for a given moving domain $\mathcal{F}(t)$ different reference domains $\hat{\mathcal{F}}$ and different mappings $\hat{T}_f(t) : \hat{\mathcal{F}} \rightarrow \mathcal{F}(t)$ can be taken into account. While a straightforward choice for the reference domain is $\hat{\mathcal{F}} = \mathcal{F}(0)$, other choices are still possible. However, even for one reference domain, we can still choose between different mappings $\hat{T}_f(t) : \hat{\mathcal{F}} \rightarrow \mathcal{F}(t)$. Usually, these ALE-maps must be constructed with help of auxiliary problems. Assuming, that the motion of the boundary $\partial\mathcal{F}(t)$ is known, and that $\hat{\mathcal{F}} = \mathcal{F}(0)$, we can construct the mapping by

$$\hat{T}_f(\hat{x}, t) := \hat{x} + \hat{\mathbf{u}}_f(\hat{x}, t),$$

where by $\hat{\mathbf{u}}_f$ we denote a *deformation* of the fluid domain. The constraint $\partial\hat{\mathcal{F}} \rightarrow \partial\mathcal{F}(t)$ can be used as boundary values for the mapping $\hat{\mathbf{u}}_f$. In the interior of $\hat{\mathcal{F}}$ the deformation $\hat{\mathbf{u}}_f$ is

constructed by solving a partial differential equation. The most simple approach is to define $\hat{\mathbf{u}}_f$ as the harmonic extension of the boundary values to the fluid domain

$$-\hat{\Delta}\hat{\mathbf{u}}_f = 0 \text{ in } \hat{\mathcal{F}}, \quad \hat{\mathbf{u}}_f(t) = \hat{\mathbf{u}}_f^D(t) \text{ on } \partial\hat{\mathcal{F}}, \quad (1.69)$$

where $\hat{\mathbf{u}}_f^D(t)$ is the deformation of the boundary points. The crucial point is the regularity of this deformation \mathbf{u}_f that will define the regularity of the domain mapping. We know, that for strict equivalence between the ALE formulation and the Eulerian formulation of the incompressible Navier-Stokes problem, very high regularity is required. In the interior of the fluid domain $\hat{\mathcal{F}}$, qualitative regularity is given by the smoothing property of the Laplace-operator, as the right hand side is zero in (1.69). At the boundaries however, the regularity of \mathbf{u}_f is limited by the regularity of \mathbf{u}_s and further by the shape of the boundary. If the solid domain imposes edges entering the fluid-domain, we must expect corner singularities. Even on convex domains, we cannot expect more than $\hat{\mathbf{u}}_f \in H^2(\hat{\mathcal{F}})$ and on concave domains we even loose H^2 -regularity. Some remedy is given by choosing the biharmonic operator for extending the deformation to the fluid-domain, e.g., by the equation

$$\hat{\Delta}^2\hat{\mathbf{u}}_f = 0 \text{ in } \hat{\mathcal{F}},$$

with the interface boundary conditions

$$\hat{\mathbf{u}}_f = \hat{\mathbf{u}}_s \text{ and } \nabla\hat{\mathbf{u}}_f = \nabla\hat{\mathbf{u}}_s \text{ on } \hat{\mathcal{I}}.$$

The biharmonic operator has better regularity properties and yields a smooth transition from fluid- to solid domain. Numerical experiments show, that the case of solid domains, that enter the fluid domain with sharp edges imposes strong regularity problems, if large deformation appears. To be precise, it is not a large bending of the solid domain, that causes problems, but a large deformation of the fluid domain, that can also be due to fixed body translation or rotation of the solid.

A drawback of the biharmonic extension is the large computational effort, that is necessary to discretize fourth order equations. One either has to use finite elements with global differentiability or one has to use mixed methods, that require the introduction of artificial variables, blowing up the complexity of the overall system. Yet another method for constructing the ALE map is by means of a pseudo-elasticity problem, governed by the linear Navier-Lamé system

$$-\widehat{\operatorname{div}}\left(\mu(\hat{\nabla}\hat{\mathbf{u}}_f + \hat{\nabla}\hat{\mathbf{u}}_f^T) + \lambda_e\widehat{\operatorname{div}}\hat{\mathbf{u}}_f I\right) = 0 \text{ in } \hat{\mathcal{F}}, \quad \hat{\mathbf{u}}_f = \hat{\mathbf{u}}_s \text{ on } \hat{\mathcal{I}}.$$

The “material parameters” μ_e, λ_e can be chosen in such a way, that a stiff mapping with little deformation is constructed close to the interface.

In Section 4.4.2, we will discuss the quantitative regularity properties of different extension techniques and analyze their performance on simple benchmark problems.

Problem 1. Show, that for deformation gradient $\hat{\mathbf{F}} = I + \hat{\nabla} \hat{\mathbf{u}}$ and inverse deformation gradient $\mathbf{F} = I - \nabla \mathbf{u}$ it holds

$$\hat{\mathbf{F}}(\hat{x}, t) = \mathbf{F}^{-1}(x, t).$$

Problem 2. Show, that if $\hat{\mathbf{u}}$ is a rotational deformation field, the relative change of length $\sqrt{1 + 2(\hat{\mathbf{E}}\hat{e}, \hat{e})} - 1$ is zero in all directions \hat{e} . What happens, if the linear approximation ϵ is considered instead of $\hat{\mathbf{E}}$?

Problem 3. Show, that the principle of mass-conservation says “The change of mass in a fixed volume $V \subset \mathbb{R}^d$ is equivalent to the amount of mass that is flowing through the boundaries of V ”.

Problem 4. Proof Lemma 7.

Problem 5. Show, that every material law

$$f(\hat{\mathbf{C}}) = \gamma_0(i(\hat{\mathbf{C}}))I + \gamma_1(i(\hat{\mathbf{C}}))\hat{\mathbf{C}} + \gamma_2(i(\hat{\mathbf{C}}))\hat{\mathbf{C}}^2$$

allows for an alternative representation of the type

$$f(\hat{\mathbf{C}}) = \alpha_0(i(\hat{\mathbf{C}}))I + \alpha_1(i(\hat{\mathbf{C}}))\hat{\mathbf{C}} + \alpha_{-1}(i(\hat{\mathbf{C}}))\hat{\mathbf{C}}^{-1}$$

Hint: use, that every matrix satisfies its own characteristic polynomial.

Problem 6. Show, that for an incompressible structure with $\det(\hat{\mathbf{C}}) = 1$ the third invariant of the Green-Lagrange strain tensor $I_3(\mathbf{E})$ can be expressed by the first $I_1(\hat{\mathbf{E}})$ and second one $I_2(\hat{\mathbf{E}})$.

Problem 7. Show, that the Stokes equations also have a unique solution if the boundary of the domain \mathcal{F} is split into a Dirichlet part Γ_f^D and an outflow part Γ_f^{out} where the do-nothing condition is given.

Problem 8. Try to proof existence for a solution $\mathbf{v} \in \mathcal{V}_f$ and $p \in \mathcal{L}_f$ of the incompressible Stokes equations (using homogenous Dirichlet conditions) using the full symmetric tensor:

$$(\nabla \mathbf{v} + \nabla \mathbf{v}^T, \nabla \phi) - (p, \nabla \cdot \phi) + (\nabla \cdot \mathbf{v}, \xi) = (\mathbf{f}_f, \phi) \quad \forall \phi, \xi \in \mathcal{V}_f \times \mathcal{L}_f.$$

Hint: you'll need Korn's inequality to proof existence of a unique velocity solution!

Problem 9. Modify the proof of Lemma 24 to the case of the full symmetric tensor

$$\begin{aligned} \frac{1}{Re}(\nabla \mathbf{v} + \nabla \mathbf{v}^T, \nabla \phi) + ((\mathbf{v} \cdot \nabla) \mathbf{v}, \phi) - (p, \nabla \cdot \phi) &= (\mathbf{f}_f, \phi) \quad \forall \phi \in \mathcal{V}_f \\ (\nabla \cdot \mathbf{v}, \xi) &= 0 \quad \forall \xi \in \mathcal{L}_f. \end{aligned}$$

Problem 10. Try to extend the proof of Lemma 24 to a configuration including the do-nothing boundary part. Where does the proof fail?

Problem 11. Let $\hat{\mathcal{F}} = (-1, 1)^2$ be a unit square and $\mathcal{F} = \{x \in \mathbb{R}^2, |x| < 1\}$ be the unit ball. Show, that there exists no C^1 -diffeomorphism $\hat{T}_f : \hat{\mathcal{F}} \rightarrow \mathcal{F}$.

Problem 12. Let $\hat{\mathcal{F}} = (0, 1)^2$. At time $t = 0$, let

$$\mathcal{F}(t) = \left\{ (x, y) \in \mathbb{R}^2, 0 < x < 1, \frac{\sin(t) \cos(\pi x)}{2} < y < 1 \right\}.$$

Construct a C^2 -diffeomorphism $\hat{T}_f(t) : \hat{\mathcal{F}} \rightarrow \mathcal{F}(t)$ and compute

$$\max_t \|\hat{T}_f\|_{C^2(\hat{\mathcal{F}})}, \quad \max_t \|\hat{T}_f^{-1}\|_{C^2(\mathcal{F}(t))}.$$

Problem 13. Show, that if \hat{T}_f is a C^2 -diffeomorphism, all second derivatives appearing in

$$\widehat{\operatorname{div}}(\hat{J}_f \hat{\mathbf{F}}_f \hat{\mathbf{v}})$$

will cancel out.

Problem 14. Let $\hat{\mathcal{F}} = (0, 1)^2$. Consider the mapping $\hat{T}_f(t) : \hat{\mathcal{F}} \rightarrow \mathcal{F}(t)$, given by

$$\hat{T}_f(\hat{x}, \hat{y}, t) = \begin{pmatrix} \cos(t)\hat{x} - \sin(t)\hat{y} \\ \sin(t)\hat{x} + \cos(t)\hat{y} \end{pmatrix}$$

Give a sketch of $\mathcal{F}(\pi/2) = \hat{T}_f(\hat{\mathcal{F}}, \pi/2)$ and give an estimate for $c(\hat{T}_f(t))$.

Problem 15. We assume, that the inf-sup constant on the domain $\hat{\mathcal{F}} = (0, 1)^2$ is given by $\hat{\gamma} > 0$. Try to give an accurate bound for the inf-sup constant on the domains $\mathcal{F}(t) = (0, t)^2$ and $\mathcal{F}(t) = (0, t) \times (0, 1)$.

The dependency of the inf-sup constant on the aspect ratio of the domain is a well-known property, see Dobrowolski [80].

Problem 16 (Continuity of the divergence). *Proof Lemma .*

2 Coupled Fluid-Structure Interactions

In Figure 2.1 we show a typical configuration of fluid-structure interactions. Here, at time $t = 0$, the domain $\Omega \subset \mathbb{R}^2$ is split into a fluid-part $\hat{\mathcal{F}}$ and a solid-part $\hat{\mathcal{S}}$. This configuration is called the reference configuration and we assume, that the system is at rest, $\mathbf{v}_f = p_f = \mathbf{u}_s = 0$. The situation in Figure 2.1 shows a case, where an elastic obstacle is attached to the bottom of a flow container at Γ_s^D . The fluid is driven by an inflow boundary data on Γ_f^D and the fluid's stresses on the obstacle cause a deformation. Here we assume, that the outer boundary of the computational domain does not change in time. The interface boundary between fluid- and solid-domain is denoted by $\mathcal{I}(t) = \partial\mathcal{F}(t) \cap \partial\mathcal{S}(t)$. Figure 2.2 shows a typical configuration arising in hemodynamics. Here, the fluid flow is surrounded by elastic walls (e.g. by blood vessels). The coupled dynamic may either be driven by the fluid or by active contraction of the elastic walls (or by a combination of both). Here, the fluid-structure interface $\mathcal{I}(t)$ as well as the outer structure boundary $\Gamma_s(t)$ is subject to motion. Whatever configuration is considered, we assume, that for the partitioning it will hold at all times, that

$$\Omega(t) = \mathcal{F}(t) \cup \mathcal{I}(t) \cup \mathcal{S}(t), \quad \mathcal{F}(t) \cap \mathcal{S}(t) = \emptyset.$$

This condition will be called the *geometric coupling condition*. The two subdomains for fluid $\mathcal{F}(t)$ and solid $\mathcal{S}(t)$ are governed by the incompressible Navier-Stokes equations and by an hyper-elastic material law. In the following section, we will describe the coupling of these two sets of equations and finally, we will derive the complete system for the fluid-structure interaction problem.

2.1 Coupling Conditions

Coupling of fluid- and solid-problem is achieved by boundary conditions on the common interface $\mathcal{I}(t)$ which all stem from simple physical principles:

1. *Kinematic condition:* The velocity of the fluid and the velocity of the solid particles are continuous on the interface.
2. *Dynamic condition:* The normal stresses of fluid and solid are continuous on the interface.
3. *Geometric condition:* Fluid- and solid-domain always match, no holes appear on the interface and the domains do not overlap.

These three coupling conditions describe the interaction between the fluid-phase and the solid-problem. All of these conditions can be described as boundary conditions for the subproblems. Hence, fluid-structure interaction is called a *surface coupled multiphysics problem*, as opposed to *volume coupled multiphysics problems*, where two (or more) subproblems all live in the same

2.1. Coupling Conditions

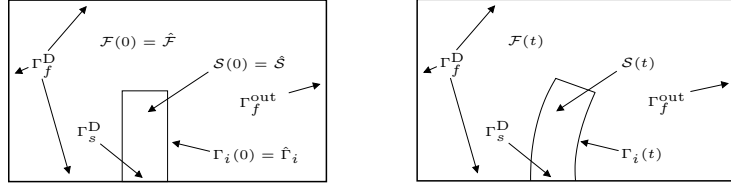


Figure 2.1: Typical configuration of a fluid-structure interaction problem. The domain is split into fluid- and solid-domain $\Omega = \mathcal{F}(t) \cup \mathcal{S}(t)$. Here, we assume, that the outer boundary of the domain is fixed. The left sketch shows the reference configuration at $t = 0$, the right one the configuration after some time $t > 0$.

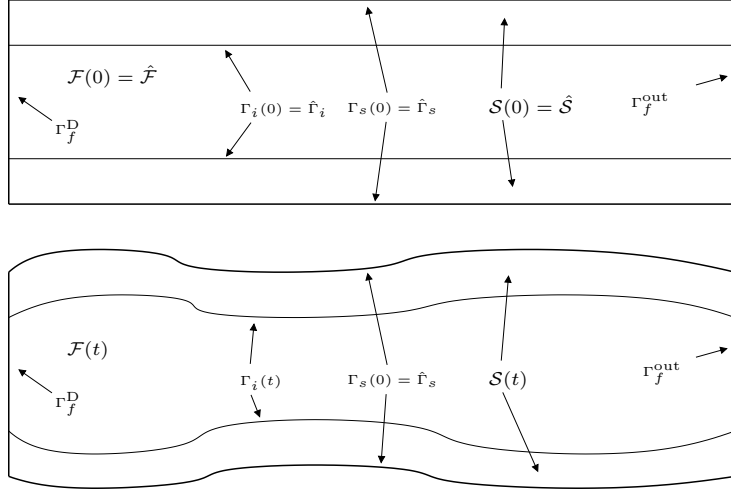


Figure 2.2: Typical configuration for the flow of blood in a vessel. Here, the fluid is embedded in elastic structures and the outer boundary is subject to motion.

domain Ω . A typical example for such volume coupled problems are chemically reactive flows, where the chemical reaction interacts with a flow problem.

In the following, we describe the three coupling conditions for fluid-structure interactions in detail.

2.1.1 The kinematic condition

The kinematic coupling condition stems from the observation, that a viscous fluid will stick at the boundary. Continuity of the velocities on the (moving) interface is simply an extension of the typical no-slip boundary condition known in fluid-dynamics. Hence, on the interface it holds

$$\mathbf{v}_f(x, t) = \mathbf{v}_s(x, t) \text{ on } \mathcal{I}(t).$$

This simple looking boundary condition reveals the great dilemma of fluid-structure interactions, as we usually model both subsystems in different coordinate systems, and as the solid's velocity is usually not available in the Eulerian configuration. Instead, we must link the fluid's velocity $\mathbf{v}_f(x_i, t)$ in an interface point $x_i \in \mathcal{I}(t)$ to the solid's velocity $\hat{\mathbf{v}}_s(\hat{x}_i, t) = d_t \hat{\mathbf{u}}_s(\hat{x}_i, t)$ in

a corresponding interface material point $\hat{x}_i \in \hat{\mathcal{I}}$. The relation between these two coordinates is given by the mapping property of the solid's deformation $x_i = \hat{\mathbf{u}}_s(\hat{x}_i, t)$, that defines a mapping between the Lagrangian and the Eulerian coordinate framework. We denote this mapping as $\hat{T}_s(\hat{x}, t) := \hat{x} + \hat{\mathbf{u}}_s(\hat{x}, t)$ and formulate the kinematic coupling condition in the reference system

$$\mathbf{v}_f \circ \hat{T}_s = \hat{\mathbf{v}}_s \text{ on } \hat{\mathcal{I}},$$

as well as in the current configuration

$$\mathbf{v}_f = \hat{\mathbf{v}}_s \circ \hat{T}_s^{-1} \text{ on } \mathcal{I}(t). \quad (2.1)$$

Hence, for every $\hat{x}_i \in \hat{\mathcal{I}}$, it must holds

$$\mathbf{v}_f(\hat{x}_i + \hat{\mathbf{u}}_s(\hat{x}_i, t), t) = \hat{\mathbf{v}}_s(\hat{x}_i, t).$$

This notation reveals the nonlinear character of the kinematic coupling condition.

If one considers the interaction between a non-viscid fluid with a solid, as appropriate for some applications in aerodynamics, instead of enforcing strong continuity at the interface, only a non-penetration condition is required

$$\vec{n} \cdot (\mathbf{v}_f \circ \hat{T}_s) = \vec{n} \cdot \hat{\mathbf{v}}_s \text{ on } \hat{\mathcal{I}}.$$

Continuity of the velocities in normal direction prohibits one phase entering the other, it however allows for free slipping of the fluid along the interface.

The kinematic coupling condition has the type of a Dirichlet boundary condition. Usually, one ascribes this condition to the fluid-problem: if the boundary of the fluid-domain is in motion, the fluid must move along.

2.1.2 The dynamic condition

The dynamic coupling condition relates to Newton's third law of action and reaction: the normal stresses, i.e. the forces per area acting on the interface are balanced:

$$\vec{n}_f \cdot \sigma_f = -\vec{n}_s \cdot \sigma_s \text{ on } \mathcal{I}(t),$$

or, using either $\vec{n} = \vec{n}_f$ or $\vec{n} = \vec{n}_s$

$$\vec{n} \cdot \sigma_f = \vec{n} \cdot \sigma_s \text{ on } \mathcal{I}(t). \quad (2.2)$$

Here, we noted this condition in the Eulerian coordinate framework. To realize the dynamic condition, we must however consider the Lagrangian setting used to formulate the structure system. With the Piola transformation, see Definition 3 it holds

$$\hat{\mathbf{F}} \hat{\Sigma}_s = \hat{\mathbf{P}} = \hat{J} \hat{\sigma}_s \hat{\mathbf{F}}^{-T},$$

such that (2.2) may be reformulated as

$$\vec{n} \cdot \sigma_f = \vec{n} \cdot (\hat{J}^{-1} \hat{\mathbf{F}} \hat{\Sigma}_s \hat{\mathbf{F}}^T) = \vec{n} \cdot (\hat{J}^{-1} \hat{\mathbf{P}}_s \hat{\mathbf{F}}^T),$$

using the Piola-Kirchhoff stress tensors.

2.1. Coupling Conditions

By physical reasoning one may want to add this coupling condition to the solid problem, as the fluid's forces on the interface will cause a deformation. Hence, we aim at reformulating the dynamic condition in the Lagrangian reference framework. As already discussed, a Lagrangian reference system does not make sense for flow problems. Instead, we will inherit the idea of an arbitrary reference system, as introduced in Section 1.5.2 for the modeling of flow problems on moving domains. Hence, let $\hat{\mathcal{F}}$ be a fixed domain that shares the common interface with $\hat{\mathcal{S}}$ and let $\hat{T}_f(t) : \hat{\mathcal{F}} \rightarrow \mathcal{F}(t)$ be a C^1 -diffeomorphism that satisfies

$$\hat{x}_i \in \hat{\mathcal{I}} \quad \hat{T}_f(\hat{x}_i, t) = \hat{T}_s(\hat{x}_i, t) = \hat{x}_i + \hat{\mathbf{u}}_s(\hat{x}_i, t) \in \mathcal{I}(t).$$

The mapping of the fluid domain and the mapping for the solid domain coincide on the common interface. In the inside of the fluid domain, the map $\hat{T}_f(t) : \hat{\mathcal{F}} \rightarrow \mathcal{F}(t)$ is arbitrary. Then, let

$$\hat{\mathbf{F}}_f := \hat{\nabla} \hat{T}_f, \quad \hat{J}_f := \det(\hat{\mathbf{F}}_f).$$

Following Section 1.5.2 we can define the stresses in the reference framework

$$\hat{\mathbf{P}}_f := \hat{J}_f \hat{\sigma}_f \hat{\mathbf{F}}_f^{-T},$$

and base the dynamic coupling condition on the Piola-Kirchhoff traction:

$$\hat{n} \cdot \hat{\mathbf{F}} \hat{\Sigma}_s = \hat{n} \cdot (\hat{J}_f \hat{\sigma}_f \hat{\mathbf{F}}_f^{-T}). \quad (2.3)$$

By $\hat{\sigma}_f(\hat{x}, t) := \sigma_f(x, t)$ we denote the Lagrangian representation of the fluid's Cauchy stress tensor.

The dynamic coupling condition is a Neumann boundary condition and here, we usually ascribe it to the solid-problem, even though all conditions are in the strict sense to be seen symmetric and belong to the coupled system of both subproblems.

2.1.3 The geometric condition

The final coupling condition prevents the two subdomains to separate or overlap. This condition describes the domain motion along the interface. It is a consequence of the physical principle, that the path of a particle $x = x(\hat{x}, t)$ and its inverse $\hat{x} = \hat{x}(x, t)$ are both continuous functions together with the condition, that the normal velocities of fluid $\vec{n} \cdot \mathbf{v}_f$ and solid $\vec{n} \cdot \mathbf{v}_s$ are continuous along the common interface. See also Problem 17.

2.1.4 Interface regularity and boundary conditions

The kinematic coupling condition (2.1) already reveals a regularity problem. This condition can be regarded as a Dirichlet condition for the fluid's velocity on $\mathcal{I}(t)$. The standard analysis, asks for Dirichlet boundary data \mathbf{v}_f^D being the trace of an $H^1(\mathcal{F}(t))^3$ -function, e.g.

$$\mathbf{v}_f^D \in H^{\frac{1}{2}}(\partial \mathcal{F})^3,$$

such that the trace inequality as well as the inverse inequality hold. Hence, for the solid's velocity we need the regularity

$$\hat{\mathbf{v}}_s = d_t \hat{\mathbf{u}}_s|_{\mathcal{I}(t)} \in H^{\frac{1}{2}}(\hat{\mathcal{I}})^3,$$

which is given for velocities

$$\hat{\mathbf{v}}_s = d_t \hat{\mathbf{u}}_s \in H^1(\hat{\mathcal{S}})^3.$$

In general, we can however only expect $u_s \in H^1(\mathcal{S})$ and $v_s \in L^2(\mathcal{S})$ which is not sufficient [166]. We know however, that if smoothing terms are added to the structure equations, sufficient regularity will be given, see Theorem 5.

For the following, we will always assume, that sufficient interface regularity will be given, e.g. by including strong smoothing of the solid problem.

Further, the interface conditions (2.1) and (2.3) live in two different coordinate frameworks and it will be required, that the two trace-spaces

$$H^{\frac{1}{2}}(\hat{\mathcal{I}}) \cong H^{\frac{1}{2}}(\mathcal{I}(t)),$$

are equivalent, which is given, if in turn

$$H^1(\hat{\mathcal{S}}) \cong H^1(\mathcal{S}(t)) \text{ and } H^1(\hat{\mathcal{F}}) \cong H^1(\mathcal{F}(t)),$$

are equivalent, see Lemma 29. For this equivalence to hold, the transformation $\hat{T}_s(t) : \hat{\mathcal{S}} \rightarrow \mathcal{S}(t)$ and its inverse must be Lipschitz. Usually, this high regularity (at the interface) can only be guaranteed on very regular domains, and it is usually not given for technical application problems.

2.1.5 Coupled fluid-structure interaction

In the following, we couple the incompressible Navier-Stokes equations (1.42) and the elastic structure equation (1.28) with the kinematic (2.1) and dynamic (2.3) interface condition. **Irgendwann mal die wesentlichen Gleichungen im vorherigen Kapitel in dieser Umgebung**

System 3 (Coupled Fluid-Structure Interaction). *Find fluid's velocity \mathbf{v}_f and pressure p_f , as well as the solid's deformation $\hat{\mathbf{u}}_s$ and velocity $\hat{\mathbf{v}}_s$, such that*

$$\begin{aligned} \rho_f (\partial_t \mathbf{v}_f + (\mathbf{v}_f \cdot \nabla) \mathbf{v}_f) - \operatorname{div} \boldsymbol{\sigma}_f &= \rho_f \mathbf{f}, \\ \operatorname{div} \mathbf{v}_f &= 0 && \text{in } \mathcal{F}(t), \\ \hat{\rho}_s^0 \partial_t \hat{\mathbf{v}}_s - \widehat{\operatorname{div}}(\hat{\mathbf{F}}_s \hat{\boldsymbol{\sigma}}_s) &= \hat{\rho}_s^0 \hat{\mathbf{f}}_s, \\ d_t \hat{\mathbf{u}}_s &= \hat{\mathbf{v}}_s && \text{in } \hat{\mathcal{S}}, \\ \mathbf{v}_f &= \hat{\mathbf{v}}_s \circ \hat{T}_s^{-1} && \text{on } \mathcal{I}(t), \\ \hat{\vec{n}} \cdot (\hat{J}_f \hat{\boldsymbol{\sigma}}_f \hat{\mathbf{F}}_f^{-T}) &= \hat{\vec{n}} \cdot \hat{\mathbf{F}} \hat{\boldsymbol{\Sigma}}_s && \text{on } \hat{\mathcal{I}}. \end{aligned} \tag{2.4}$$

System (2.4) is written in a monolithic coupled formulation. However, as fluid-problem and solid-problem live in different coordinate frameworks, the interface conditions somehow stand in between both sub-problems, one of them being defined in the Lagrangian framework, one in the Eulerian. Further we know, that this assignment is arbitrary as we could also state the coupling conditions in the other frameworks.

This system of partial differential equations is not amenable for a standard discretization in a straightforward way, as the motion of the fluid domain and the transformation between both frameworks at the interface must be incorporated.

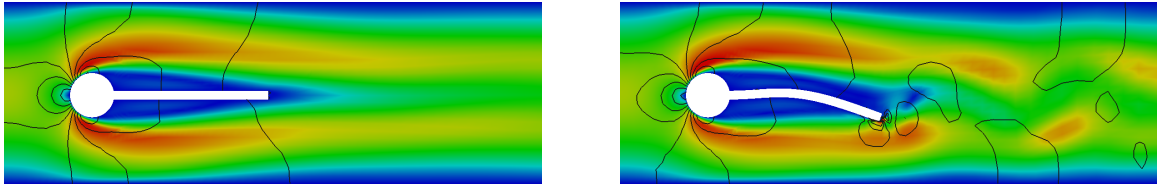


Figure 2.3: Flow around an elastic obstacle. Left: rigid obstacle with stationary solution, right: elastic obstacle with non-stationary solution. Both flows are at the low Reynolds number $Re = 20$.

The coupled fluid-structure interaction problem is a nonlinear system. By coupling of the two subdomains a non-local nonlinearity is introduced, as motion of the interface will influence the complete domain and hence also the solution in parts distant to the interface. This nonlinearity is difficult to grab, as it is only hidden in the definition of the domains. Even the coupling of fully linear problems like the Stokes equations 1.47 with the linear Navier-Lamé problem 1.33 results in a nonlinear coupled interaction problem.

2.2 The Added-Mass effect

A proper description of the dynamics that arise in the coupled fluid-structure interaction problem (2.4) is cumbersome. In the discussion on non-dimensionalization of the Navier-Stokes equations in Section 1.4.3 we have identified the Reynolds number

$$Re = \frac{\rho_f L_f V_f}{\mu_f},$$

as the key quantity to describe the property of a flow configuration. Here, by L_f we denote a characteristic length and by \bar{V}_f a characteristic velocity, by $\mu_f = \rho_f \nu_f$ the dynamic viscosity. Flows at low Reynolds numbers usually have stationary solutions (if the problem data does not explicitly depend on time). In the context of fluid-structure interactions, the overall dynamic can dramatically change. In Figure 2.3 we show the configuration of the flow around an obstacle. In the left sketch, we assume the obstacle to be rigid, where in the right sketch, the obstacle is considered to be elastic. In both situations, we consider a flow at Reynolds number $Re = 20$. While the pure flow problem with a rigid fixed beam shows a stationary solution, the elastic fluid-structure interaction problem has a time-periodic non-stationary solution if the attached beam is considered to be elastic. The Reynolds number alone is not sufficient to describe the dynamics of the coupled problem.

In the following, we will analyze the interaction of the coupled system at the interface. For this analysis we closely follow the concepts given by [64]. For the analysis we will strongly simplify system (2.4) by the following assumptions:

1. Deformation are so small that fully linear models are considered. Eulerian and Lagrangian coordinates coincide “ $\mathcal{S}(t) = \hat{\mathcal{S}}$ ” and linear material laws are taken into account, $\sigma_s = \mu_s \nabla \mathbf{u}_s$.
2. We neglect convective terms in the fluid.

3. We neglect viscous terms in the fluid, such that $\sigma_f = -pI$.
4. The deformation of the fluid domain is so small, that it can be neglected $\mathcal{F}(t) = \hat{\mathcal{F}}$.

The remaining system of equation is given by

$$\begin{aligned} \rho_f \partial_t \mathbf{v}_f - \nabla p_f &= g_s(\mathbf{u}_s), \\ \operatorname{div} \mathbf{v}_f &= 0 && \text{in } \mathcal{F} \\ \rho_s \partial_{tt} \mathbf{u}_s - \mu \Delta \mathbf{u}_s &= g_f(\mathbf{v}_f, p_f) && \text{in } \mathcal{S}. \end{aligned}$$

The system is coupled via boundary terms $g_s(\mathbf{u}_s)$ and $g_f(\mathbf{v}_f, p_f)$ coming from the other equation each. In the equilibrium it will hold $\mu_s \vec{n} \cdot \nabla \mathbf{u}_s = -p_f \vec{n}$ on the interface \mathcal{I} . Further, it holds $\mathbf{v}_f = \partial_t \mathbf{u}_s$ on \mathcal{I} . We will formulate this system of partial differential equations using an operator notation with mass \mathcal{M} , gradient \mathcal{B} , divergence \mathcal{B}^T and diffusion \mathcal{K} :

$$\rho_f \mathcal{M} \mathbf{v}'_f + \mathcal{B} p_f = g_s, \quad \mathcal{B}^T \mathbf{v}_f = 0, \quad \rho_s \mathcal{M} \mathbf{u}''_s + K \mathbf{u}_s = g_f,$$

where by $g_s \sim \mu_s \vec{n} \cdot \nabla \mathbf{u}_s$ and $g_f \sim -p_f \vec{n}$ we denote the boundary stresses, with $g_s = g_f$ in equilibrium. Due to the various simplifications, all operators are linear and by differentiation of the divergence equation $d_t \mathcal{B}^T \mathbf{v}_f = \mathcal{B}^T \mathbf{v}'_f = 0$ we can reformulate the fluid system as

$$\begin{pmatrix} \rho_f \mathcal{M}_{\mathcal{F}\mathcal{F}} & \rho_f \mathcal{M}_{\mathcal{F}\Gamma} & \mathcal{B}_{\mathcal{F}} \\ \rho_f \mathcal{M}_{\Gamma\mathcal{F}} & \rho_f \mathcal{M}_{\Gamma\Gamma} & \mathcal{B}_{\Gamma} \\ \mathcal{B}_{\mathcal{F}}^T & \mathcal{B}_{\Gamma}^T & 0 \end{pmatrix} \begin{pmatrix} \mathbf{v}'_{\mathcal{F}} \\ \mathbf{v}'_{\Gamma} \\ p_f \end{pmatrix} = \begin{pmatrix} 0 \\ g_s \\ 0 \end{pmatrix}.$$

Here, we have split the acceleration into inner $\mathbf{v}'_{\mathcal{F}}$ and interface acceleration \mathbf{v}'_{Γ} . Next, we simplify this equation by lumping the zeroth order mass operators $\mathcal{M} \sim |\mathcal{I}| \mathcal{F}|$ such that no coupling between inner and interface acceleration appears. By $|\mathcal{F}|$ we denote a fluid element's mass:

$$\begin{pmatrix} \rho_f |\mathcal{F}| & 0 & \mathcal{B}_{\mathcal{F}} \\ 0 & \rho_f |\mathcal{F}| & \mathcal{B}_{\Gamma} \\ \mathcal{B}_{\mathcal{F}}^T & \mathcal{B}_{\Gamma}^T & 0 \end{pmatrix} \begin{pmatrix} \mathbf{v}'_{\mathcal{F}} \\ \mathbf{v}'_{\Gamma} \\ p_f \end{pmatrix} = \begin{pmatrix} 0 \\ g_s \\ 0 \end{pmatrix}. \quad (2.5)$$

In the context of finite difference discretizations, the mass will always be diagonal, in the context of spatial finite element discretization, this process is given by integration of the mass-matrix with the trapezoidal rule. The solid problem is reformulated in a similar way:

$$\rho_s |\mathcal{S}| \begin{pmatrix} \mathcal{I} & 0 \\ 0 & \mathcal{I} \end{pmatrix} \begin{pmatrix} \mathbf{u}''_{\mathcal{S}} \\ \mathbf{u}''_{\Gamma} \end{pmatrix} + \begin{pmatrix} \mathcal{K}_{SS} & \mathcal{K}_{S\Gamma} \\ \mathcal{K}_{\Gamma S} & \mathcal{K}_{\Gamma\Gamma} \end{pmatrix} \begin{pmatrix} \mathbf{u}_S \\ \mathbf{u}_{\Gamma} \end{pmatrix} = \begin{pmatrix} 0 \\ g_f \end{pmatrix}. \quad (2.6)$$

For the solution of (2.5) and (2.6) we consider a partitioned approach:

1. We assume, that an interface acceleration \mathbf{v}'_{Γ} is given and we solve for $\mathbf{v}'_{\mathcal{F}}$ and p_f .
2. We use the resulting interface stresses $g_f(\mathbf{v}'_{\Gamma}, p_f)$ to solve for the new deformation \mathbf{u}_{Γ} on the interface.

Given \mathbf{v}'_{Γ} we can solve system (2.5) for $\mathbf{v}'_{\mathcal{F}}$ and p_f . First, it holds

$$\mathcal{B}_{\mathcal{F}}^T \mathcal{B}_{\mathcal{F}} p_f = -\rho_f |\mathcal{F}| \mathcal{B}_{\mathcal{F}}^T \mathbf{v}'_{\mathcal{F}} = \rho_f |\mathcal{F}| \mathcal{B}_{\Gamma}^T \mathbf{v}'_{\Gamma}.$$

2.2. The Added-Mass effect

We assume, that the operator $\mathcal{B}_{\mathcal{F}}^T \mathcal{B}_{\mathcal{F}}$ is positive. This is equivalent to the condition, that the flow problem has a unique solution (see Section 1.4.5 addressing the inf-sup condition). The pressure can be computed as

$$p_f = \rho_f |\mathcal{F}| (\mathcal{B}_{\mathcal{F}}^T \mathcal{B}_{\mathcal{F}})^{-1} \mathcal{B}_{\Gamma}^T \mathbf{v}'_{\Gamma}, \quad (2.7)$$

and for the inner acceleration $\mathbf{v}'_{\mathcal{F}}$ we get:

$$\mathbf{v}'_{\mathcal{F}} = -\frac{1}{\rho_f |\mathcal{F}|} \mathcal{B}_{\mathcal{F}} p_f = -\mathcal{B}_{\mathcal{F}} (\mathcal{B}_{\mathcal{F}}^T \mathcal{B}_{\mathcal{F}})^{-1} \mathcal{B}_{\Gamma}^T \mathbf{v}'_{\Gamma}. \quad (2.8)$$

With help of relations (2.7) and (2.8) we can use the second line of (2.5) to express the interface forces g_s by:

$$\begin{aligned} g_s &= \rho_f |\mathcal{F}| \mathbf{v}'_{\Gamma} + \mathcal{B}_{\Gamma} p_f \\ &= \rho_f |\mathcal{F}| \mathbf{v}'_{\Gamma} + \rho_f |\mathcal{F}| \mathcal{B}_{\Gamma} (\mathcal{B}_{\mathcal{F}}^T \mathcal{B}_{\mathcal{F}})^{-1} \mathcal{B}_{\Gamma}^T \mathbf{v}'_{\Gamma} \\ &= \rho_f |\mathcal{F}| \underbrace{\left(\mathcal{I} + \mathcal{B}_{\Gamma} (\mathcal{B}_{\mathcal{F}}^T \mathcal{B}_{\mathcal{F}})^{-1} \mathcal{B}_{\Gamma}^T \right)}_{=: \mathcal{M}_A} \mathbf{v}'_{\Gamma}. \end{aligned} \quad (2.9)$$

The operator \mathcal{M}_A is called the *added mass operator*. It is symmetric and positive (if the flow problem has a unique solution). It maps a given interface acceleration \mathbf{v}'_{Γ} onto a force-vector g_s at the interface. The eigenvalues of \mathcal{M}_A are all larger than one. The new interface stresses $g_s = g_f$ go as right hand side into the structure problem (2.6):

$$\rho_s |\mathcal{S}| \begin{pmatrix} \mathcal{I} & 0 \\ 0 & \mathcal{I} \end{pmatrix} \begin{pmatrix} \mathbf{u}''_{\mathcal{S}} \\ \mathbf{u}''_{\Gamma} \end{pmatrix} + \begin{pmatrix} \mathcal{K}_{SS} & \mathcal{K}_{S\Gamma} \\ \mathcal{K}_{\Gamma S} & \mathcal{K}_{\Gamma\Gamma} \end{pmatrix} \begin{pmatrix} \mathbf{u}_{\mathcal{S}} \\ \mathbf{u}_{\Gamma} \end{pmatrix} = \begin{pmatrix} 0 \\ \rho_f |\mathcal{F}| \mathcal{M}_A \mathbf{v}'_{\Gamma} \end{pmatrix}. \quad (2.10)$$

We assume little impact of diffusion such that we get a diagonal relation for the interface acceleration:

$$\rho_s |\mathcal{S}| \mathbf{u}''_{\Gamma} \approx \rho_f |\mathcal{F}| \mathcal{M}_A \mathbf{v}'_{\Gamma} = \rho_f |\mathcal{F}| \mathbf{v}'_{\Gamma} + \rho_f |\mathcal{F}| \mathcal{B}_{\Gamma} (\mathcal{B}_{\mathcal{F}}^T \mathcal{B}_{\mathcal{F}})^{-1} \mathcal{B}_{\Gamma}^T \mathbf{v}'_{\Gamma}. \quad (2.11)$$

By identifying $\mathbf{u}''_{\Gamma} = \mathbf{v}'_{\Gamma}$ we see, that the added mass operator \mathcal{M}_A acts as an additional mass on the common interface. This relation is typical for incompressible flows. Due to incompressibility, the fluid has to move along with the solid. The added mass operator is responsible for the special kind of coupling between the structure equation with incompressible flows.

We proceed with the stability analysis by considering a simple time-discretization of the interface system (2.11). By $t_0 < \dots < t_N$ we denote an equidistant partitioning of the time interval with $k := t_{n+1} - t_n$. The interface velocity at time t_n is denoted by \mathbf{v}'_{Γ} . We approximate by a simple backward difference formula:

$$\mathbf{u}''_{\Gamma}(t_n) = \mathbf{v}'_{\Gamma}(t_n) \approx \frac{\mathbf{v}^n_{\Gamma} - \mathbf{v}^{n-1}_{\Gamma}}{k}. \quad (2.12)$$

We apply this difference approximation to (2.11), where we assume, that a predictor for the interface velocity on the right hand side is given based on the old time-step $\mathbf{v}'_{\Gamma}(t_n)$. Then, the equation for approximating $\mathbf{v}'_{\Gamma}(t_{n+1})$ is given by the difference approximation

$$\frac{\rho_s |\mathcal{S}|}{k} (\mathbf{v}^{n+1}_{\Gamma} - \mathbf{v}^n_{\Gamma}) = \frac{\rho_f |\mathcal{F}|}{k} \mathcal{M}_A (\mathbf{v}^n_{\Gamma} - \mathbf{v}^{n-1}_{\Gamma}).$$

As the operator \mathcal{M}_A is symmetric and positive, there exists an orthogonal system of eigenvectors v_i and eigenvalues μ_i (larger than one) such that

$$\mathcal{M}_A \mathbf{v}_i = \mu_i \mathbf{v}_i, \quad \mu_i > 1, \quad i = 0, 1, \dots$$

We develop the unknown solution \mathbf{v}_Γ^n in the orthonormal eigenvector basis

$$\mathbf{v}_\Gamma^n = \sum_{i \geq 0} v_i^n \mathbf{v}_i, \quad (2.13)$$

with coefficients $v_i^n \in \mathbb{R}$. For each $i \geq 0$, the coefficient v_i^n satisfies a scalar difference equation:

$$(v_i^{n+1} - v_i^n) - \frac{\rho_f |\mathcal{F}|}{\rho_s |\mathcal{S}|} \mu_i (v_i^n - v_i^{n-1}), \quad i = 0, 1, \dots \quad (2.14)$$

To analyze the stability of the recurrence equation, we solve the difference equation (2.14) by the approach $v_i^n = \lambda_i^n$ to find the fundamental solutions. We get:

$$(\lambda_i^2 - \lambda_i) - \frac{\rho_f |\mathcal{F}|}{\rho_s |\mathcal{S}|} \mu_i (\lambda_i - 1) = 0.$$

This equation has a root at $\lambda_i = 1$ and is equivalent to

$$(\lambda_i - 1) \left(\lambda_i - \frac{\rho_f |\mathcal{F}|}{\rho_s |\mathcal{S}|} \mu_i \right) = 0,$$

revealing a second root at

$$\lambda_i = \frac{\rho_f |\mathcal{F}|}{\rho_s |\mathcal{S}|} \mu_i.$$

Every solution to the difference equation (2.14) is given by a combination of these two roots

$$v_i^n = a_i + b_i \lambda_i^n,$$

where by a_i and b_i we denote two constants.

Stability of the solution u_Γ^n represented in the eigenvalue basis (2.13) is given, if the absolute values of all roots are bounded by one:

$$|\lambda_i| \leq 1.$$

If this second root is larger than one, the solution is not stable. The added mass analysis reveals the important stability condition for the coupling of fluid-structure interactions:

$$\frac{\rho_f |\mathcal{F}|}{\rho_s |\mathcal{S}|} \mu_i \leq 1, \quad \text{where } \mu_i \geq 1. \quad (2.15)$$

Remark 10 (Stability of the solution). *The simplified stability analysis of the coupled fluid-structure interaction system is based on a partitioned iteration scheme, where first we find the solution of the fluid problem, use this solution to identify the new interface stresses and finally take these interface stresses to solve for the new deformation in the solid domain. Such a decoupled partitioned approach will only be stable, if condition (2.15) is fulfilled. If the density ratio condition is violated, we must use implicit solution approaches, that take the full fluid-structure interaction problem as one coupled unity, without partitioning.*

2.3. Variational coupling techniques

The density ratio (2.15) serves as a key quantity to describe the coupling behavior of fluid-structure interactions. In aerodynamical applications, where we usually couple the flow of air $\rho_f \approx 1 \text{ kg m}^{-3}$ with an elastic structure out of metal $\rho_s \approx 5000 \text{ kg m}^{-3}$ the density ratio is very small and partitioned approaches are well-suited for solving the coupled problem. In hemodynamics, both blood and surrounding tissue have similar densities $\rho_f \approx \rho_s \approx 1 \text{ g cm}^{-3}$. Here, partitioned approaches most often fail and implicit schemes with a monolithic view of the coupled problems must be taken into consideration. For a discussion on different solution procedures, whether monolithic or partitioned, see Chapter 6.

2.3 Variational coupling techniques

Equations (2.4) describe the coupled dynamics of the incompressible fluids in $\mathcal{F}(t)$ and the elastic structure in $\hat{\mathcal{S}}$. The coupling is realized with help of boundary conditions on the common interface \mathcal{I} . As preparation for the finite element discretization of the fluid-structure interaction system, we will derive a monolithic variational formulation of these coupled problem. The variational formulations of the incompressible Navier-Stokes equation and of hyper-elastic structures are given in Lemma 16 and Lemma 14. Here, we shortly recapitulate the two variational formulations given on the moving domain $\mathcal{F}(t)$ and the fixed structural domain $\hat{\mathcal{S}}$:

$$\begin{aligned} \mathbf{v}_f(t) \in \mathcal{V}_f(t), \quad p_f(t) \in \mathcal{L}_f(t) : \\ (\rho_f(\partial_t \mathbf{v}_f + (\mathbf{v}_f \cdot \nabla) \mathbf{v}_f), \phi_f)_{\mathcal{F}(t)} + (\sigma_f, \nabla \phi_f)_{\mathcal{F}(t)} = (\rho_f \mathbf{f}_f, \phi_f)_{\mathcal{F}(t)} \\ (\operatorname{div} \mathbf{v}_f, \xi_f)_{\mathcal{F}(t)} = 0 \end{aligned} \quad (2.16)$$

for all $\phi_f \in \mathcal{V}_f^{\text{test}}, \xi_f \in \mathcal{L}_f$, where the function spaces are defined as

$$\begin{aligned} \mathcal{V}_f(t) &:= \{\phi \in H^1(\mathcal{F}(t))^d, \phi = \mathbf{v}_f^D(t) \text{ on } \Gamma_f^D\}, \\ \mathcal{V}_f(t)^{\text{test}} &:= H_0^1(\mathcal{F}(t); \Gamma_f^D)^d, \\ \mathcal{L}_f(t) &:= L^2(\mathcal{F}(t)), \end{aligned}$$

and

$$\begin{aligned} \hat{\mathbf{u}}_s(t) \in \hat{\mathcal{V}}_s : \\ (\hat{\rho}_s^0 \partial_{tt} \hat{\mathbf{u}}_s, \hat{\phi}_s)_{\hat{\mathcal{S}}} + (\hat{\mathbf{F}}_s \hat{\boldsymbol{\Sigma}}_s, \hat{\nabla} \hat{\phi}_s)_{\hat{\mathcal{S}}} = (\hat{\rho}_s^0 \hat{\mathbf{f}}_s, \hat{\phi}_s)_{\hat{\mathcal{S}}} \quad \forall \hat{\phi}_s \in \hat{\mathcal{V}}_s^{\text{test}}, \end{aligned} \quad (2.17)$$

where test- and trial-space $\hat{\mathcal{V}}_s$ is given on the reference domain $\hat{\mathcal{S}}$:

$$\begin{aligned} \hat{\mathcal{V}}_s &:= \{\phi \in H^1(\hat{\mathcal{S}})^d, \phi = \hat{\mathbf{u}}_s^D \text{ on } \Gamma_s^D\}, \\ \hat{\mathcal{V}}_s^{\text{test}} &:= H_0^1(\hat{\mathcal{S}}; \Gamma_s^D)^d. \end{aligned}$$

Both equations are given with Dirichlet values on Γ_f^D and Γ_s^D , respectively. Here, we have embedded the Dirichlet data into the trial spaces.

This realization of Dirichlet data is the key for a realization of the kinematic coupling condition $\hat{\mathbf{v}}_f = \hat{\mathbf{v}}_s = d_t \hat{\mathbf{u}}_s$ on $\hat{\mathcal{I}}$. Of course, to realize this condition, we must implicitly map between Eulerian and Lagrangian coordinates. We modify the fluid's trial space to

$$\mathcal{V}_f(t, \hat{\mathbf{u}}_s(t), d_t \hat{\mathbf{u}}_s(t)) := \{\phi \in \mathcal{V}_f(t), \phi(\hat{x} + \hat{\mathbf{u}}_s(\hat{x}, t)) = \partial_t \hat{\mathbf{u}}_s(\hat{x}, t) \text{ on } \hat{\mathcal{I}}\}. \quad (2.18)$$

Then, it holds for every $\mathbf{v}_f(t) \in \mathcal{V}_f(t, \hat{\mathbf{u}}_s(t), d_t \hat{\mathbf{u}}_s(t))$, that $\mathbf{v}_f = \mathbf{v}_s$ on $\mathcal{I}(t)$. We are only looking for possible solutions to the incompressible Navier-Stokes equations that already satisfy the kinematic condition. Hence, it is realized in a strong way.

The dynamic coupling condition can be embedded into the test-space $\mathcal{V}_f^{\text{test}}(t)$ in a similar way by linking the fluid's and solid's test-functions:

$$\mathcal{V}_f^{\text{test}}(t, \hat{\mathbf{u}}_s(t), \hat{\phi}_s) := \{\phi_f \in \mathcal{V}_f(t), \phi_f(\hat{x} + \hat{\mathbf{u}}_s(\hat{x}, t)) = \hat{\phi}_s(\hat{x}) \text{ on } \hat{\mathcal{I}}\}. \quad (2.19)$$

The test-spaces are not independent of each other, instead, the fluid's test space depends on both the solid's deformation (required to cope with the domain motion) and a solid's test-function $\hat{\phi}_s$ to ensure continuity. By this restriction of test-functions it holds on the interface, that

$$\phi_f(\hat{x} + \hat{\mathbf{u}}_s(\hat{x}, t)) = \hat{\phi}_s(\hat{x}).$$

The dynamic coupling condition is recovered by variational principles using integration by parts:

Lemma 33 (Variational formulation of the fluid-structure interaction problem). *Let*

$$\hat{\mathbf{u}}_s(t) \in \hat{\mathcal{V}}_s, \quad \mathbf{v}_f(t) \in \mathcal{V}_f(t, \hat{\mathbf{u}}_s(t), d_t \hat{\mathbf{u}}_s(t)), \quad p_f(t) \in \mathcal{L}_f(t)$$

be the solution of

$$\begin{aligned} & (\rho_f(\partial_t \mathbf{v}_f + (\mathbf{v}_f \cdot \nabla) \mathbf{v}_f), \phi_f)_{\mathcal{F}(t)} + (\sigma_f, \nabla \phi_f)_{\mathcal{F}(t)} \\ & + (\hat{\rho}_s^0 \partial_{tt} \hat{\mathbf{u}}_s, \hat{\phi}_s)_{\hat{\mathcal{S}}} + (\hat{\mathbf{F}} \hat{\Sigma}_s, \hat{\nabla} \hat{\phi}_s)_{\hat{\mathcal{S}}} = (\rho_f \mathbf{f}_f, \phi_f)_{\mathcal{F}(t)} + (\hat{\rho}_s^0 \hat{\mathbf{f}}_s, \hat{\phi}_s)_{\hat{\mathcal{S}}} \\ & (\operatorname{div} \mathbf{v}_f, \xi_f)_{\mathcal{F}(t)} = 0 \end{aligned} \quad (2.20)$$

for all test-functions

$$\{\phi_f, \hat{\phi}_s\} \in \tilde{\mathcal{V}}_f^{\text{test}}(t, \hat{\mathbf{u}}_s(t), \hat{\phi}_s) \times \hat{\mathcal{V}}_s^{\text{test}}, \quad \forall \xi_f \in \mathcal{L}_f(t).$$

Given sufficient regularity $\hat{\mathbf{u}}_s(t) \in C^2(\hat{\mathcal{S}})^d \cap C^1(\bar{\mathcal{S}})^d$, $\mathbf{v}_f(t) \in C^2(\mathcal{F}(t))^d \cap C^1(\bar{\mathcal{F}}(t))^d$ and $p_f(t) \in C^1(\mathcal{F}(t))^d \cap C(\bar{\mathcal{F}}(t))^d$, the variational solution is also a classical solution to (2.4) and fulfills the strong interface conditions.

Proof. Let $\hat{\mathbf{u}}_s(t) \in \hat{\mathcal{V}}_s$, $\mathbf{v}_f(t) \in \mathcal{V}_f(t, \hat{\mathbf{u}}_s(t), d_t \hat{\mathbf{u}}_s(t))$ and $p_f(t) \in \mathcal{L}_f$ be solution to the variational formulation. Let $\hat{\phi}_s \in \hat{\mathcal{V}}_s^{\text{test}}$ and $\phi_f \in \mathcal{V}_f^{\text{test}}(t, \hat{\mathbf{u}}_s(t), \hat{\phi}_s)$ be arbitrary. Given sufficient regularity we can apply integration by parts to get

$$\begin{aligned} & (\rho_f \mathbf{f}_f, \phi_f)_{\mathcal{F}(t)} + (\hat{\rho}_s^0 \hat{\mathbf{f}}_s, \hat{\phi}_s)_{\hat{\mathcal{S}}} = (\rho_f(\partial_t \mathbf{v}_f + (\mathbf{v}_f \cdot \nabla) \mathbf{v}_f), \phi_f)_{\mathcal{F}(t)} + (\hat{\rho}_s^0 \partial_{tt} \hat{\mathbf{u}}_s, \hat{\phi}_s)_{\hat{\mathcal{S}}} \\ & - (\operatorname{div} \sigma_f, \phi_f)_{\mathcal{F}(t)} - (\widehat{\operatorname{div}}(\hat{\mathbf{F}}_s \hat{\Sigma}_s), \hat{\phi}_s)_{\hat{\mathcal{S}}} + (\operatorname{div} \mathbf{v}_f, \xi_f)_{\mathcal{F}(t)} \\ & + \int_{\mathcal{I}(t)} \vec{n}_f \cdot \sigma_f \phi_f \, d\omega + \int_{\hat{\mathcal{I}}} \hat{\vec{n}}_s \cdot (\hat{\mathbf{F}}_s \hat{\Sigma}_s) \hat{\phi}_s \, d\hat{\omega}. \end{aligned}$$

The classical solutions to fluid and solid problems are recovered by standard variational principles using Dirac series as test-functions in the interior of $\mathcal{F}(t)$ and $\hat{\mathcal{S}}$.

Using the Piola transformation, Lemma 6 and recalling Definition 3 for the different forms of the stress tensors it holds

$$\int_{\hat{\mathcal{I}}} \hat{\vec{n}}_s \cdot (\hat{\mathbf{F}}_s \hat{\Sigma}_s) \hat{\phi}_s \, d\hat{\omega} = \int_{\hat{\mathcal{I}}} \hat{\vec{n}}_s \cdot (\hat{J}_s \hat{\sigma}_s \hat{\mathbf{F}}_s^{-T}) \hat{\phi}_s \, d\hat{\omega} = \int_{\mathcal{I}(t)} \vec{n}_s \cdot \sigma_s \phi_s \, d\omega.$$

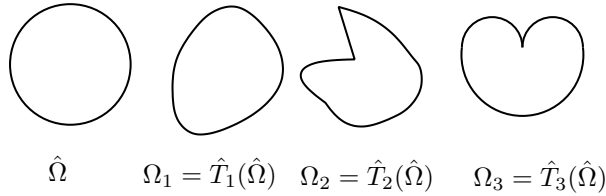


Figure 2.4: Three different transformations of a smooth domain $\hat{\Omega}$. $T_1 \in C^\infty$, $T_2 \in C^{0,1}$ and $T_3 \notin C^{0,1}$.

On $\mathcal{I}(t)$ the two test-functions ϕ_f and ϕ_s are continuous $\phi(x) := \phi_f(x) = \phi_s(x)$. Further, on $\mathcal{I}(t)$ it holds $\vec{n}_f = -\vec{n}_s$ and the dynamic coupling condition is recovered by choosing an appropriate Dirac series on the interface $\mathcal{I}(t)$. \square

This variational formulation is not standard in the following sense: test- and trial-spaces of the velocity spaces depend on the solution itself, as a mapping of coordinates on the interface is required

$$\mathbf{v}_f(\hat{x} + \hat{\mathbf{u}}(\hat{x}, t), t) = d_t \hat{\mathbf{u}}_s(\hat{x}, t), \quad \phi_f(\hat{x} + \hat{\mathbf{u}}_s(\hat{x}, t)) = \hat{\phi}_s(\hat{x}) \quad \forall \hat{x} \in \hat{\mathcal{I}}.$$

The dependency of the function spaces on the solution has big implications: if we think of finite element discretizations, the first starting step, the creation of a finite element mesh will fail, as the domain depends on the solution itself, which in turn is to be computed on the mesh! The domain $\mathcal{F}(t)$ is implicitly defined by the solution itself. At time $t \geq t_0$ it is bound by the location of the interface $\mathcal{I}(t)$, that itself is determined by the deformation of the solid.

Remark 11 (Regularity of the domain motion). *The motion of the domains must be given in such a way, that $\mathcal{F}(t)$ and $\mathcal{S}(t)$ still allow for the construction of well defined Sobolev spaces like $H^1(\mathcal{S}(t))$. Figure 2.4 shows different deformations of a reference domain $\hat{\Omega}$ with C^∞ regularity (a circle) arising from three different mappings $\hat{T}_i : \hat{\Omega} \rightarrow \Omega_i$. First, we consider a mapping that is highly regular and smooth, $T_1 \in C^\infty(\hat{\Omega})^d$, second, we choose a mapping that has slightly lower regularity but still is given in $C^{0,1}(\hat{\Omega})$. Here, the domain's boundary will loose its regularity. The cone-conditions however are still valid. Finally, we show a mapping $T_3 \notin C^{0,1}(\hat{\Omega})$. This mapping yields a domain Ω_3 that does not satisfy the cone-condition. Here, some of the important theorems for Sobolev spaces like the trace theorem do not hold any more.*

Remark 12 (Contact). *Contact and topology change is part of many application problems, think of closing heart valves or of sedimenting solids. It will be important to allow such contact scenarios. However, most theoretical results will ask for strong assumptions on the domains: first as a domain it must be connected. This condition is often violated in the case of contact, see Figure 2.5. Second, many important theorems from the theory of Sobolev spaces require all domains to fulfill the cone-condition. If a circular obstacle will touch a wall, this condition will most likely be hurt. Again, see Figure 2.5. See also Remark 36 in Section 5.6.3.*

2.4 Fluid-structure interactions in ALE coordinates

The variational coupling technique described in the last section still faces the problem of moving domains and requires coordinate transformations between fluid- and solid-problem. While the

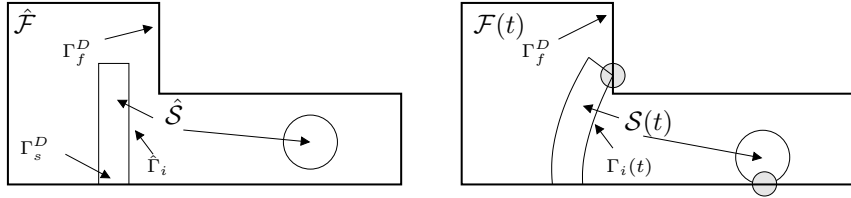


Figure 2.5: Contact of the elastic structure with the domain's boundary. The fluid-area $\mathcal{F}(t)$ is not connected and hence no domain in the strict sense. Further, by contact the cone-condition or other regularity conditions of the domain can be violated.

derived formulation can serve as basis for partitioned solution algorithms which switch between the two subproblems, it cannot be used for monolithic discretization and solution schemes in a strongly coupled way. To cope with the two different coordinate systems and the domain motion, we will couple the Lagrangian solid problem to the Navier-Stokes equations in ALE coordinates, such that the ALE reference configuration $\hat{\mathcal{F}}$ will match the Lagrangian solid configuration $\hat{\mathcal{S}}$. For the following, we assume, that by

$$\hat{T}_f(t) : \hat{\mathcal{F}} \rightarrow \mathcal{F}(t),$$

a map between reference configuration $\hat{\mathcal{F}}$ and the current configuration $\mathcal{F}(t)$ with sufficient regularity (in space and time) is given.

The ALE formulation of the Navier-Stokes equations have been introduced in Section 1.5.2, in particular, see Lemma 28. Coupling of test- and trial-spaces between the ALE formulation of the fluid problem and the Lagrangian solid problem is largely simplified compared to the Eulerian-Lagrangian coupling. Similar to (2.18) and (2.19), we modify the ALE velocity test- and trial spaces (1.63) to

$$\begin{aligned}\hat{\mathcal{V}}_f(\hat{d}_t \hat{\mathbf{u}}_s(t)) &= \{\hat{\phi} \in \hat{\mathcal{V}}_f, \hat{\phi} = d_t \hat{\mathbf{u}}_s \text{ on } \hat{\mathcal{I}}\}, \\ \hat{\mathcal{V}}_f^{\text{test}}(\hat{\phi}_s) &= \{\hat{\phi} \in \hat{\mathcal{V}}_f, \hat{\phi} = \hat{\phi}_s \text{ on } \hat{\mathcal{I}}\}.\end{aligned}$$

Function spaces on fluid and solid side are still coupled, but this coupling does not require a coordinate system transformation any more. Here however, we must again take notice of the regularity mismatch: while we require a $\gamma_{\hat{\mathcal{I}}} \mathbf{v}_f \in H^{\frac{1}{2}}(\hat{\mathcal{I}})^d$ trace on the interface, the solid's velocity usually only has limited $\hat{\mathbf{v}}_s = d_t \hat{\mathbf{u}}_s \in L^2(\hat{\mathcal{S}})^d$ regularity and no $H^{\frac{1}{2}}$ -trace. We will not be able to close this gap and will simply assume, that every solution of the solid problem will always satisfy the additional smoothness, such that we may define $\hat{\mathbf{v}}_s \in H^1(\hat{\mathcal{S}})^d$, e.g. by applying strong damping, see Lemma 5.

Next, let $\hat{\mathcal{S}}$ and $\hat{\mathcal{F}}$ be such, that trace inequality, and inverse trace inequality hold with respect to $\hat{\mathcal{I}}$. Then, it holds

Lemma 34 (Gluing of function spaces). *Let Ω be a domain of class $C^{0,1}$, split into $\Omega = \hat{\mathcal{F}} \cup \hat{\mathcal{S}}$, two domains with $C^{0,1}$ -boundary and common $C^{0,1}$ -interface $\hat{\mathcal{I}} = \partial \hat{\mathcal{F}} \cap \partial \hat{\mathcal{S}}$. (i) Let $\hat{\phi} \in H_0^1(\hat{\Omega})$. For the restrictions of $\hat{\phi}$ to the subdomains it holds*

$$\begin{aligned}\hat{\phi}_s &:= \hat{\phi} \Big|_{\hat{\mathcal{S}}} \in \mathcal{V}_s := H_0^1(\hat{\mathcal{S}}; \partial \mathcal{S} \setminus \hat{\mathcal{I}}), \\ \hat{\phi}_f &:= \hat{\phi} \Big|_{\hat{\mathcal{F}}} \in \mathcal{V}_f(\hat{\phi}_s) := \{\psi \in H_0^1(\hat{\mathcal{F}}; \partial \hat{\mathcal{F}} \setminus \hat{\mathcal{I}}), \psi = \hat{\phi}_s \text{ on } \hat{\mathcal{I}}\}.\end{aligned}$$

(ii) For every $\hat{\phi}_s \in \mathcal{V}_s$ and $\hat{\phi}_f \in \mathcal{V}_f(\hat{\phi}_s)$ it holds for the composed function

$$\hat{\phi} := \begin{cases} \hat{\phi}_s & \text{in } \hat{\mathcal{S}}, \\ \hat{\phi}_s & \text{on } \hat{\mathcal{I}}, \\ \hat{\phi}_f & \text{in } \hat{\mathcal{F}}, \end{cases}$$

that $\phi \in H_0^1(\Omega)$.

Proof. (i) directly follows from the usual results for the restriction of Sobolev spaces $W^{k,p}(\Omega)$ to subdomain $\Omega' \subset \Omega$ ([249]) and as $\phi \in H_0^1(\hat{\Omega})$ has identical traces in $H^{\frac{1}{2}}(\hat{\mathcal{I}})$ on the interface. (ii) follows, as $\hat{\phi}_f$ and $\hat{\phi}_s$ have the same trace on the common interface. \square

This simple Lemma allows for a further simplification of the coupling in ALE coordinates. Instead of searching for two velocities and using two different test-functions, we simply make the global approach

$$\hat{\mathbf{v}} \in \hat{\mathcal{V}} := \bar{\mathbf{v}} + H_0^1(\hat{\Omega}; \Gamma^D)^d, \quad \hat{\phi} \in \hat{\mathcal{V}},$$

where $\bar{\mathbf{v}} \in H^1(\hat{\Omega})^d$ is a suitable extension of the Dirichlet data. Then, trial- and test-functions on the two subdomains are given as restrictions

$$\hat{\mathbf{v}}_f := \hat{\mathbf{v}}|_{\hat{\mathcal{F}}}, \quad \hat{\mathbf{v}}_s := \hat{\mathbf{v}}|_{\hat{\mathcal{S}}}, \quad \hat{\phi}_f := \hat{\phi}|_{\hat{\mathcal{F}}}, \quad \hat{\phi}_s := \hat{\phi}|_{\hat{\mathcal{S}}}.$$

2.4.1 Definition of the ALE map

To derive a closed monolithic formulation, we must also indicate how to define the ALE map $\hat{T}_f(t) : \hat{\mathcal{F}} \rightarrow \mathcal{F}(t)$ as in the context of fluid-structure interactions, this map is not given as part of the problem data, but it depends implicitly on the solution.

The solid domain map $\hat{T}_s(t) : \hat{\mathcal{S}} \rightarrow \mathcal{S}(t)$ is defined as $\hat{T}_s(\hat{x}, t) = \hat{x} + \hat{\mathbf{u}}_s(\hat{x}, t)$ and based on the solid's deformation $\hat{\mathbf{u}}_s$. This map is physically motivated and describes the transformation between Lagrangian and Eulerian coordinates. Such map would not make sense for the flow problem, as a Lagrangian reference domain would not properly depict usual configurations. However, we will introduce a deformation $\hat{\mathbf{u}}_f$ of the fluid domain to define the ALE map

$$\hat{T}_f(\hat{x}, t) := \hat{x} + \hat{\mathbf{u}}_f(\hat{x}, t). \quad (2.21)$$

We note, that this deformation is not a physical deformation of particles. In particular, it holds $d_t \hat{\mathbf{u}}_f \neq \hat{\mathbf{v}}_f$. Deformation $\hat{\mathbf{u}}_f$ and velocity $\hat{\mathbf{v}}_f$ have no direct relationship.

Defining the ALE map via (2.21) has the benefit, that mapping, deformation gradient $\hat{\mathbf{F}}_f := I + \hat{\nabla} \hat{\mathbf{u}}_f$ and its determinant $\hat{J}_f := \det(\hat{\mathbf{F}}_f)$ are described as for the solid problem. Further, as one of the requirements of \hat{T}_f is a correct mapping of interface points

$$\hat{x} \in \hat{\mathcal{I}} \quad \Rightarrow \quad \hat{T}_f(\hat{x}, t) = \hat{T}_s(\hat{x}, t) \quad \Leftrightarrow \quad \hat{x} + \hat{\mathbf{u}}_f(\hat{x}, t) = \hat{x} + \hat{\mathbf{u}}_s(\hat{x}, t),$$

we must enforce deformations that have a continuous transition to the solid's deformation $\hat{\mathbf{u}}_f = \hat{\mathbf{u}}_s$ on $\hat{\mathcal{I}}$. On the outer boundaries of the domain (that does not move) $\Gamma_f^D \cup \Gamma_f^{\text{out}} = \partial \hat{\mathcal{F}} \setminus \hat{\mathcal{I}}$,

the ALE map may exhibit deformation in tangential direction, but no transformation in normal direction is allowed. Hence, $\hat{\mathbf{u}}_f$ must satisfy the boundary conditions

$$\hat{\mathbf{u}}_f = \hat{\mathbf{u}}_s \text{ on } \hat{\mathcal{I}}, \quad \hat{\mathbf{n}} \cdot \hat{\mathbf{u}}_f = 0 \text{ on } \partial\hat{\mathcal{F}} \setminus \hat{\mathcal{I}}. \quad (2.22)$$

Lemma 28 requires very high smoothness of the ALE map, such that solutions to the ALE formulation of the Navier-Stokes equations correspond to the standard weak solution of the Navier-Stokes equations. Namely, we require that \hat{T}_f is a $W^{1,\infty}$ -diffeomorphism. In light of (2.21) this calls for $\hat{\mathbf{u}}_f \in W^{1,\infty}$ such, that $\hat{x} + \hat{\mathbf{u}}_f$ is invertible, e.g. $\hat{J}_f > 0$.

We will define $\hat{\mathbf{u}}_f$ as an extension of $\hat{\mathbf{u}}_s$ from the interface $\hat{\mathcal{I}}$ into the fluid domain by using a differential operator $\mathcal{L} : \hat{\mathcal{F}} \rightarrow \mathbb{R}^d$:

$$\mathcal{L}(\hat{\mathbf{u}}_f) = 0, \quad \hat{\mathbf{u}}_f = \hat{\mathbf{u}}_s \text{ on } \hat{\mathcal{I}}, \quad \hat{\mathbf{n}} \cdot \hat{\mathbf{u}}_f = 0 \text{ on } \partial\hat{\mathcal{F}} \setminus \hat{\mathcal{I}}.$$

If we choose for \mathcal{L} an harmonic operator, the usual smoothing property will guarantee sufficient regularity in the interior of $\hat{\mathcal{F}}$ (as the right hand side is zero). Close to the boundaries $\partial\hat{\mathcal{F}}$ however, the regularity will be restricted. This restriction is one by means of the geometry, e.g. by edges of the domain, but also limited by the regularity of the boundary data $\hat{\mathbf{u}}_f = \hat{\mathbf{u}}_s$ on the interface $\hat{\mathcal{I}}$. In general, we cannot expect, that the extension procedure will give a fluid deformation field with satisfactory regularity. In Section 4.4.2 we will see, that regularity problems of this map are indeed a pitfall in implementations of the ALE method. In particular reentrant edges pose severe problems. Such edges appear, whenever the solid domain has sharp corners entering the surrounding fluid domain.

Besides regularity considerations, the extension operator \mathcal{L} should be such, that interior points $\hat{x} \in \hat{\mathcal{F}}$ are not mapped outside the fluid-domain $\hat{x} + \hat{\mathbf{u}}_f(\hat{x}, t) \notin \mathcal{F}(t)$. For this assumption to hold, the operator should for a start satisfy the maximum principle. In addition, the deformation $\hat{\mathbf{u}}_f$ must fulfill a certain smallness of growth. To illuminate this problem, we consider as example the one dimensional reference domain $\hat{\mathcal{F}} = (0, 2)$ and the Eulerian counterpart $\mathcal{F} = (0, 1)$. The deformation

$$\hat{\mathbf{u}}(\hat{x}) = -\frac{1}{2}\hat{x} \quad \Rightarrow \quad \hat{T}_f(\hat{x}) = \frac{1}{2}\hat{x},$$

will perfectly serve as ALE map, as $\hat{T}_f : \hat{\mathcal{F}} \rightarrow \mathcal{F}$. The map

$$\hat{\mathbf{u}}(\hat{x}) = -\frac{1}{2}\hat{x}^4 \quad \Rightarrow \quad \hat{T}_f(\hat{x}) = \hat{x} - \frac{1}{8}\hat{x}^4,$$

however satisfies $\hat{T}_f(0) = 0$ and $\hat{T}_f(2) = 1$, but $\hat{T}_f : \hat{\mathcal{F}} \not\rightarrow \mathcal{F}$, as $T_f(\frac{3}{2}) \approx 1.18 \notin \mathcal{F}$. The gradient of $\nabla \hat{\mathbf{u}}_f$ must be bound to prevent maps, that point out of the domain. It is difficult to guarantee this property by a priori limits, but we show in Section 4.4.2, that such problems frequently appear, in particular if we deal with reentrant edges.

The simplest choice for defining the extension operator \mathcal{L} is a harmonic extension of the solid deformation:

$$-\hat{\Delta} \hat{\mathbf{u}}_f = 0 \text{ in } \hat{\mathcal{F}}, \quad \hat{\mathbf{u}}_f = \hat{\mathbf{u}}_s \text{ on } \hat{\mathcal{I}}, \quad \hat{\mathbf{u}}_f = 0 \text{ on } \partial\hat{\mathcal{F}} \setminus \hat{\mathcal{I}},$$

or, as we have noted

$$\hat{\mathbf{n}} \cdot \hat{\mathbf{u}}_f = 0 \text{ on } \partial\hat{\mathcal{F}} \setminus \hat{\mathcal{I}}.$$

The drawback of such an harmonic extension is the limited regularity of the solution. If the fluid domain has reentrant edges, e.g. a solid with sharp edges entering into the fluid domain,

it will usually just hold $\hat{\mathbf{u}}_f \in H^1(\hat{\mathcal{F}})^d$, but $\hat{\mathbf{u}}_f \notin H^2(\hat{\mathcal{F}})$. Furthermore, even H^2 -regularity is not sufficient for the strict $W^{1,\infty}$ assumption, that is required to give equivalence of the H^1 -spaces on \mathcal{F} and $\hat{\mathcal{F}}$.

Another possibility for the definition of the deformation $\hat{\mathbf{u}}_f$ is by means of pseudo-elasticity problem

$$-\widehat{\operatorname{div}} \left(\mu_e (\hat{\nabla} \hat{\mathbf{u}}_f + \hat{\nabla} \hat{\mathbf{u}}_f^T) + \lambda_e \widehat{\operatorname{div}} \hat{\mathbf{u}}_f \right) = 0, \quad \hat{\mathbf{u}}_f = \hat{\mathbf{u}}_s \text{ on } \hat{\mathcal{I}}, \quad \hat{n} \cdot \hat{\mathbf{u}}_f = 0 \text{ on } \partial \hat{\mathcal{F}} \setminus \hat{\mathcal{I}}.$$

Depending on the specific type of boundary conditions, the solution suffers from similar regularity restrictions as the harmonic extension and we might again lose $\hat{\mathbf{u}}_f \in H^2(\hat{\mathcal{F}})$, if the fluid-domain has concave corners, see [199].

A further possibility for the definition of $\hat{\mathbf{u}}_f$ is a biharmonic extension of the solid's velocity:

$$\Delta^2 \mathbf{u}_f = 0 \text{ in } \hat{\mathcal{F}},$$

that – as a fourth order operator – asks for two boundary conditions. First, for satisfying the geometric coupling condition, we choose

$$\hat{\mathbf{u}}_f = \hat{\mathbf{u}}_s \text{ on } \hat{\mathcal{I}}, \quad \hat{n} \cdot \hat{\mathbf{u}}_f = 0 \text{ on } \partial \hat{\mathcal{F}} \setminus \hat{\mathcal{I}}.$$

Second, we can prescribe boundary conditions for the gradients or higher order derivatives of the solution. The choice

$$\hat{n} \cdot \hat{\nabla} \hat{\mathbf{u}}_f = \hat{n} \cdot \hat{\nabla} \hat{\mathbf{u}}_s \text{ on } \hat{\mathcal{I}}, \quad \hat{\Delta} \hat{\mathbf{u}}_f = 0 \text{ on } \partial \hat{\mathcal{F}} \setminus \hat{\mathcal{I}},$$

defines an extension of $\hat{\mathbf{u}}_s$, that is not only continuous but that has continuous normal derivatives. This construction will prevent rapid changes of $\hat{\mathbf{u}}_f$ close to the interface. The biharmonic extension has better regularity at edges, see e.g. [37].

In Section 4.4.2 we demonstrate a numerical study showing the performance of the different mesh motion models. We will see, that the biharmonic extension gives us the best quality for the ALE map. Numerical approximation of this fourth order equation is however very costly, so that we usually try to avoid it.

2.4.2 Coupled ALE formulation

By all these preparations, we can combine the variational coupling technique indicated by Lemma 34 with the different technique for an implicit construction of the ALE map. As fluid's and solid's deformation $\hat{\mathbf{u}}_f$ and $\hat{\mathbf{u}}_s$ both have the same H^1 -regularity and as they share a common trace on $\hat{\mathcal{I}}$, coupling will also be realized with help of Lemma 34. Instead of separating two deformations, we search for one global field $\hat{\mathbf{u}} \in \bar{\mathbf{u}}_s^D + H_0^1(\Omega; \Gamma^D)^d$.

It holds:

Lemma 35 (Variational formulation of the fluid-structure interaction problem in ALE coordinate). *Let*

$$\hat{\mathbf{u}}(t) \in \bar{\mathbf{u}}_s^D + \hat{\mathcal{W}}, \quad \hat{\mathbf{v}}(t) \in \bar{\mathbf{v}}^D(t) + \hat{\mathcal{V}}, \quad \hat{p}_f(t) \in \hat{\mathcal{L}}_f,$$

where

$$\hat{\mathcal{W}} := H_0^1(\hat{\Omega})^d, \quad \hat{\mathcal{V}} := H_0^1(\hat{\Omega}; \Gamma^D)^d, \quad \hat{\mathcal{L}}_f := L^2(\hat{\mathcal{F}}),$$

and where by $\bar{\mathbf{u}}_s^D(t) \in H_0^1(\hat{S}; \hat{\mathcal{I}})^d$ and $\bar{\mathbf{v}}^D(t) \in H_0^1(\hat{\Omega}; \Gamma_f^{out})^d$ extensions of the Dirichlet data are given. The solution of the coupled fluid-structure interaction system in ALE coordinates is given by

$$\begin{aligned} & \rho_f (\hat{J}_f (\partial_t \hat{\mathbf{v}} + (\hat{\mathbf{F}}_f^{-1}(\hat{\mathbf{v}} - \partial_t \mathbf{u}) \cdot \nabla) \hat{\mathbf{v}}, \hat{\phi})_{\hat{\mathcal{F}}} + (\hat{\rho}_s^0 \partial_t \hat{\mathbf{v}}, \hat{\phi})_{\hat{\mathcal{S}}}) \\ & + (\hat{J}_f \hat{\sigma}_f \hat{\mathbf{F}}_f^{-T}, \hat{\nabla} \hat{\phi})_{\hat{\mathcal{F}}} + (\hat{\mathbf{F}}_s \hat{\Sigma}_s, \hat{\nabla} \hat{\phi})_{\hat{\mathcal{S}}} = (\hat{J}_f \hat{\rho}_f \hat{\mathbf{f}}_f, \hat{\phi})_{\hat{\mathcal{F}}} + (\hat{\rho}_s^0 \hat{\mathbf{f}}_s, \hat{\phi})_{\hat{\mathcal{S}}} \\ & (\widehat{\operatorname{div}}(\hat{J}_f \hat{\mathbf{F}}_f^{-1} \hat{\mathbf{v}}), \hat{\xi})_{\hat{\mathcal{F}}} = 0, \\ & (\partial_t \hat{\mathbf{u}} - \hat{\mathbf{v}}, \hat{\psi}_s)_{\hat{\mathcal{S}}} = 0, \\ & (\hat{\nabla} \hat{\mathbf{u}}, \hat{\nabla} \hat{\psi}_f)_{\hat{\mathcal{F}}} = 0, \end{aligned} \quad (2.23)$$

for all test-functions

$$\hat{\phi} \in \hat{\mathcal{V}}, \quad \hat{\psi}_s \in \hat{\mathcal{L}}_s = L^2(\hat{S})^d, \quad \hat{\xi}_f \in \hat{\mathcal{L}}_f, \quad \hat{\psi}_f \in H_0^1(\hat{\mathcal{F}}).$$

Given sufficient regularity of $\hat{\mathbf{v}}, \hat{\mathbf{u}}, \hat{p}_f$, the variational solution is also a classical solution to (2.4) and fulfills the strong interface conditions.

Proof. Given sufficient regularity, the proof is a simple implication of Lemma 28 and Lemma 33. Here, for simplicity we have considered an harmonic extension of the deformation to the fluid domain. \square

Remark 13 (Test and trial spaces). *The variational formulation given in Lemma 35 uses different trial- and test-spaces, as the two equations for the extension of the deformation and the relationship between solid's deformation and velocity do not interact.*

Here, it is not appropriate to combine $\hat{\psi}_f$ and $\hat{\psi}_s$ to one global function, e.g. $\hat{\phi} \in H^1(\hat{\Omega})^d$. First, H^1 is the wrong regularity to define the L^2 -projection $\partial_t \hat{\mathbf{u}} \mapsto \hat{\mathbf{v}}$. Second, glueing of the test-spaces would result in an additional boundary condition of the extension operator on the interface:

$$(\hat{\nabla} \hat{\mathbf{u}}, \hat{\nabla} \hat{\psi})_{\hat{\mathcal{F}}} = -(\hat{\Delta} \hat{\mathbf{u}}, \hat{\psi})_{\hat{\mathcal{F}}} + \langle \vec{n} \cdot \hat{\nabla} \hat{\mathbf{u}}, \hat{\psi} \rangle_{\hat{\mathcal{I}}}.$$

This second condition $\vec{n} \cdot \hat{\nabla} \hat{\mathbf{u}}_f = 0$, in addition to $\hat{\nabla} \hat{\mathbf{u}}_f = \hat{\nabla} \hat{\mathbf{u}}_s$ would lead to a faulty feedback on the solid's deformation.

However, by defining

$$\mathcal{X} := \hat{\mathcal{W}} \times \hat{\mathcal{V}} \times \hat{\mathcal{L}}_f, \quad \mathcal{Y} := \hat{\mathcal{V}} \times \hat{\mathcal{L}}_f \times \hat{\mathcal{L}}_s \times H_0^1(\hat{\mathcal{F}}),$$

we can introduce a short notation and find $\hat{\vec{U}} := \{\hat{\mathbf{u}}, \hat{\mathbf{v}}, \hat{p}_f\}$ given as

$$\hat{\vec{U}}(t) = \vec{U}^D(t) + \mathcal{X},$$

such that

$$A(\hat{\vec{U}}, \hat{\vec{\Phi}}) = 0, \quad \forall \hat{\vec{\Phi}} = \{\hat{\phi}, \hat{\xi}_f, \hat{\psi}_s, \hat{\psi}_f\} \in \mathcal{Y},$$

where the semilinear form $A(\cdot)(\cdot)$ is given in accordance to the variational formulation (2.23).

Further, we point out, that the spaces \mathcal{V} and \mathcal{W} differ by boundary data only. On a fluid's outflow boundary Γ_f^{out} , functions in \mathcal{V} are free, where it holds $\hat{\phi} = 0$ on Γ_f^{out} for all $\hat{\phi} \in \mathcal{W}$.

A formulation of the fluid-structure interaction problem in Arbitrary Lagrangian Eulerian coordinates has the great advantage, that the domain motion can be captured in the deformation field $\hat{\mathbf{u}}$. The interface between fluid and solid will be fixed at all times. Thinking of finite element discretizations it will be easy to construct meshes $\hat{\mathcal{F}}_h$ of the fluid domain $\hat{\mathcal{F}}$ and $\hat{\mathcal{S}}_h$ of the solid domain $\hat{\mathcal{S}}$ and these meshes will always resolve the interface. Such methods are called *interface-tracking techniques*. The artificial fluid domain map \hat{T}_f and the fluid domain's deformation $\hat{\mathbf{u}}_f$ play the most important role. If the regularity of $\hat{x} + \hat{\mathbf{u}}_f$ is not sufficient, the ALE formulation in Lemma 35 will not be equivalent to the coupled formulation in physical coordinates. As the mapping \hat{T}_f is not given by physical motivation, it will be a purely numerical task to generate mapping of high regularity.

Further, as argued in Section 1.5, the regularity of the ALE map will also have impact on the inf-sup constant. This enters stability estimates for the solution of the Navier-Stokes equations and it will also be an important factor for error estimates in the context of the finite element method.

Finally, the ALE method has limits, if the domain motion is such, that a differentiable and invertible mapping does not exist at all. This can happen, if topology change occur due to contact of the structure with the domain's boundary or due to self-contact of the structure with other structural parts. Here, a fully monolithic ALE technique will not be suitable. In Section 2.5, we will introduce an alternative approach to derive a monolithic variationally coupled formulation for fluid-structure interactions. This will be able to also include problems with large motion or contact, but it will not be of *interface-tracking* type.

The ALE method is perhaps one of the most reliable and efficient techniques, if it comes to interaction problems with such a stiff coupling that monolithic approaches must be considered. It is well suited to handle large deformations. As the domains are fixed for all times, and as the interface is always properly defined, it is possible to use standard discretization and solver techniques in approximate settings.

Finally, to better understand the limits of the ALE approach we consider a simple configuration, where a solid structure $\mathcal{S}(t)$ is moving within the fluid domain. Here, we can assume, that this structure is rigid and at time $t = 0$ resting in the center of long channel, see Figure 2.6. The fluid is driven from left to right and the obstacle will start to move:

$$\hat{u}_s(\hat{x}) = \begin{pmatrix} \bar{v}t \\ 0 \end{pmatrix}.$$

For simplicity, we simply assume, that the problem reaches a stationary limit and that the structure is moving in the infinitely long channel with a fixed velocity \bar{v} in horizontal direction. We want to model this problem in ALE coordinates, hence we must find a deformation field $\hat{\mathbf{u}}_f$ that maps the reference state $\hat{\mathcal{F}} = \mathcal{F}(0)$ to the current configuration $\mathcal{F}(t)$. On the interface $\hat{\mathcal{I}}$ it must holds $\hat{\mathbf{u}}_f = \hat{u}_s$. Further, on the bottom on top boundary, it must hold $\hat{\mathbf{u}}_f = 0$, such that in between we can approximate the ALE map $\hat{T}_f(\hat{x}, t) = \hat{x} + \hat{\mathbf{u}}_f(\hat{x}, t)$ as (considering only the lower half of the domain)

$$\hat{T}_f(\hat{x}, t) \approx \begin{pmatrix} \hat{x}_1 + \hat{x}_2 \bar{v}t \\ \hat{x}_2 \end{pmatrix}, \quad \hat{\nabla} \hat{T}_f(\hat{x}, t) \approx \begin{pmatrix} 1 & \hat{x}_2 \bar{v}t \\ 0 & 1 \end{pmatrix},$$

with $\|\hat{\nabla} \hat{T}_f\| \rightarrow \infty$ for $t \rightarrow \infty$. For large times, the ALE mapping will loose regularity and the ALE formulation will not be stable. This result shows, that usually it is the motion of the

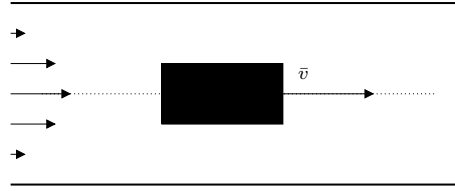


Figure 2.6: Flow around a moving rigid body in an infinitely long channel. Regardless of the bodies motion, the configuration looks similar for all times $t \geq 0$.

fluid-domain that will cause a break-down of ALE techniques and not a large deformation of the solid.

Here, relief could be given by the following approach: if for some time $t' \geq 0$ the derivatives of the mapping get too large, a new reference domain $\hat{\mathcal{F}}'$ together with a new mapping \hat{T}'_f is taken as basis of the ALE formulation. The solution $\hat{v}_f(t')$ must then be mapped onto the new reference framework and the formulation can be continued from here. In the context of discretized schemes, such an approach is called *remeshing* or *reinitialization*. It is extensively discussed in literature and part of most efficient implementations of the ALE technique. [218, 58].

2.5 Fully Eulerian formulation for the fluid-structure interaction problem

The success of the ALE formulation for fluid-structure interactions crucially depends on the quality of the fluid domain map \hat{T}_f . If this mapping loses its regularity, equivalence between the variational ALE formulation in Lemma 35 and the coupled formulation in Lemma 33 will not hold any more. Further, we have seen that bounds on $\hat{\nabla}\hat{T}_f$ and $\nabla\hat{T}_f^{-1}$ will enter basic inequalities like the trace inequality, Poincaré inequality and also the inf-sup inequality. Even if the derivatives of \hat{T}_f and \hat{T}_f^{-1} are bound, the constants, that will finally enter stability and error estimates can be very large.

In this section, we will introduce an alternative variational formulation for the coupled fluid-structure interaction problem that goes the opposite way: instead of mapping the moving fluid domain onto a fixed reference domain $\hat{T}_f(t) : \hat{\mathcal{F}} \rightarrow \mathcal{F}(t)$ we use an inverse map to transform the Lagrangian solid reference domain onto the Eulerian moving solid domain $\hat{T}_s(t) : \hat{\mathcal{S}} \rightarrow \mathcal{S}(t)$. Like the ALE map \hat{T}_f , this transformation is defined by the deformation $\hat{\mathbf{u}}_s$:

$$\hat{T}_s(\hat{x}, t) := \hat{x} + \hat{\mathbf{u}}_s(\hat{x}, t).$$

There is one fundamental difference between \hat{T}_s and \hat{T}_f . While the ALE map \hat{T}_f is based on the arbitrary deformation field $\hat{\mathbf{u}}_f$, and $\hat{\mathcal{F}}$ does not play a physical role, the solid domain map \hat{T}_s is given by physical principles. It maps the Lagrangian reference system onto the Eulerian system. By very basic assumptions, it holds

1. The mapping \hat{T}_s is a bijection between $\hat{\mathcal{S}}$ and $\mathcal{S}(t)$.
2. Mapping \hat{T}_s and inverse \hat{T}_s^{-1} are differentiable.

3. The determinants $\hat{J}_s := \det(\hat{\nabla}\hat{T}_s)$ and $\hat{J}_s^{-1} = \det(\nabla\hat{T}_s^{-1})$ are bound away from zero one infinity.

The well-posedness of an Eulerian formulation for fluid-structure interactions is obvious, since the Eulerian coordinates are the physical coordinates, where all governing equations (the conservation laws) have been derived. The transition to the Lagrangian reference system was mainly for practical reasons, as deformation stresses can be best modeled in a particle centered viewpoint. For structure mechanics both viewpoints, the Lagrangian and the Eulerian are physically relevant and the mapping between them is simply given by the deformation.

2.5.1 Elastic structures in Eulerian coordinates

In Section 1.1.6, we derived the basic conservation principles for moving volumes, that were based on conservation of mass, momentum and angular momentum. Here, we will derive the Eulerian formulation for the structure problem on the moving solid domain $\mathcal{S}(t)$, that is given by the Lagrangian deformation of $\hat{\mathcal{S}}$:

$$\mathcal{S}(t) = \{\hat{x} + \hat{\mathbf{u}}_s(\hat{x}, t), \hat{x} \in \hat{\mathcal{S}}\}.$$

By mass and momentum conservation, we derived the non-conservative formulation of the momentum equation (1.14)

$$\rho_s \partial_t \mathbf{v}_s + \rho_s \mathbf{v}_s \cdot \nabla \mathbf{v}_s - \nabla \cdot \sigma_s = \rho_s \mathbf{f} \text{ in } \mathcal{S}(t), \quad (2.24)$$

where $\rho_s(x, t)$ is the Eulerian density of the solid at time t in point $x \in \mathcal{S}(t)$, $\mathbf{v}_s(x, t)$ is the Eulerian velocity and σ_s the Eulerian Cauchy-Stress tensor of the solid problem, also given in the Eulerian coordinate system. Here, it is necessary to remember, that the transformation to the Lagrangian or to an arbitrary reference system (ALE) only touches the domain of functions $\mathcal{S}(t)$ and $\hat{\mathcal{S}}$, not the image, e.g. it holds

$$\mathbf{v}(x, t) = \hat{\mathbf{v}}(\hat{T}(\hat{x}, t), t) = \hat{\mathbf{v}}(\hat{x}, t)$$

for a pair $x = \hat{T}(\hat{x}, t)$. For defining a Eulerian representation σ_s of the Cauchy stress tensor, we must first introduce a Eulerian counterpart \mathbf{u}_s of the Lagrangian deformation $\hat{\mathbf{u}}_s$ by the relation

$$x = \hat{x} + \hat{\mathbf{u}}_s(\hat{x}, t), \quad \hat{x} = x - \mathbf{u}(x, t),$$

such that it holds

$$\mathbf{u}_s(x, t) = \mathbf{u}_s(\hat{x} + \hat{\mathbf{u}}_s(\hat{x}, t), t) = \hat{\mathbf{u}}_s(\hat{x}, t).$$

By $\mathbf{u}_s(x, t)$ we can define the inverse mapping $T_s(t) : \mathcal{S}(t) \rightarrow \hat{\mathcal{S}}$:

$$T_s(x, t) := x - u_s(x, t).$$

It holds

Lemma 36 (Inverse mapping). *Let $\hat{\mathbf{u}}(\hat{x})$ be a deformation field that defined a C^1 -diffeomorphism $\hat{T}(\hat{x}) := \hat{x} + \hat{\mathbf{u}}(\hat{x})$. Then, for the inverse mapping $T(x) := x - \mathbf{u}(x)$ with $\mathbf{u}(x) := \hat{\mathbf{u}}(\hat{x})$ for $x := \hat{x} + \hat{\mathbf{u}}(\hat{x})$ it holds*

$$T_s = \hat{T}_s^{-1}.$$

Proof. See Problem 21. \square

This Lemma shows, that by T_s we really defined the inverse of the Lagrange to Euler map \hat{T}_s . Further, considering Lemma 4, it holds

$$T_s \circ \hat{T}_s = \text{id} \quad \Rightarrow \quad \hat{T}_s =: \mathbf{F}_s = \mathbf{F}_s^{-1} = (\hat{\nabla} \hat{T}_s)^{-1}, \quad J_s = \hat{J}_s^{-1}. \quad (2.25)$$

And with $\hat{T}_s := \hat{x} + \hat{u}_s$ and $T_s := x - u_s$ it finally follows, that

$$[I - \nabla \mathbf{u}_s] = [I + \hat{\nabla} \hat{\mathbf{u}}_s]^{-1} \Leftrightarrow \nabla \mathbf{u}_s = I - [I + \hat{\nabla} \hat{\mathbf{u}}_s]^{-1} = I - \hat{\mathbf{F}}_s^{-1}.$$

By these relations, we can define the Cauchy stresses for different material laws like the St. Venant Kirchhoff model:

Lemma 37 (Cauchy stress tensor for the St. Venant Kirchhoff material in Eulerian coordinates). *The Eulerian Cauchy stress tensor σ_s of the St. Venant Kirchhoff material is given by*

$$\sigma_s = J_s \mathbf{F}_s^{-1} (2\mu \mathbf{E}_s + \lambda_s \text{tr}(\mathbf{E}_s) I) \mathbf{F}_s^{-T}, \quad \mathbf{E}_s := \frac{1}{2} (\mathbf{F}_s^{-T} \mathbf{F}_s^{-1} - I).$$

Proof. The second Piola Kirchhoff stress tensor $\hat{\Sigma}_s$ of the St. Venant Kirchhoff material is given by (see Definition 4):

$$\hat{\Sigma}_s = 2\mu_s \hat{\mathbf{E}}_s + \lambda_s \text{tr}(\hat{\mathbf{E}}_s) I,$$

with the Green-Lagrangian strain tensor

$$\hat{\mathbf{E}}_s := \frac{1}{2} (\hat{\mathbf{F}}_s^T \hat{\mathbf{F}}_s - I).$$

The relation between Cauchy stress tensor and 2nd Piola Kirchhoff stress tensor is given by the Piola transformation in Definition 3:

$$\hat{\mathbf{F}}_s \hat{\Sigma}_s = \hat{J}_s \hat{\sigma}_s \hat{\mathbf{F}}_s^{-T} \Leftrightarrow \hat{\sigma}_s = \hat{J}_s^{-1} \hat{\mathbf{F}}_s \hat{\Sigma}_s \hat{\mathbf{F}}_s^T.$$

This gives us a Lagrangian description of the Cauchy stresses. Finally, by (2.25), we can reformulate all quantities in the Eulerian system as

$$\sigma_s = J_s \mathbf{F}_s^{-1} \Sigma_s \mathbf{F}_s^{-T},$$

with the 2nd Piola Kirchhoff tensor in Eulerian coordinates

$$\Sigma_s = 2\mu_s \mathbf{E}_s + \lambda_s \text{tr}(\mathbf{E}_s) I,$$

where

$$\mathbf{E}_s := \frac{1}{2} (\mathbf{F}_s^{-T} \mathbf{F}_s^{-1} - I).$$

\square

The derivation of the Cauchy stress tensor σ_s in Eulerian coordinates completes the description of the momentum equation (2.24). It remains to derive a relation for the unknown Eulerian density $\rho_s(x, t)$. By defining $\rho_s(x, t) = \hat{\rho}_s(\hat{x}, t)$, and using (1.27), it holds

$$\rho_s(x, t) = J_s \hat{\rho}_s^0,$$

where $\hat{\rho}_s^0$ is the (homogenous) density of the solid at time $t = 0$.

Finally, for splitting the second order hyperbolic equation into a system of first order equations, we must transform the relation $d_t \hat{\mathbf{u}}_s = \hat{\mathbf{v}}_s$ to the Eulerian coordinate framework. By Lemma 5 we get

$$d_t \hat{\mathbf{u}}_s = \partial_t \mathbf{u}_s + \mathbf{v}_s \cdot \nabla \mathbf{u}_s, \quad d_t \hat{\mathbf{v}}_s = \partial_t \mathbf{v}_s + \mathbf{v}_s \cdot \nabla \mathbf{v}_s.$$

As outcome of the foregoing discussion it holds:

Lemma 38 (Solid problem in Eulerian coordinates). *Elastic deformation \mathbf{u}_s and velocity \mathbf{v}_s of a St. Venant Kirchhoff material in Eulerian coordinates are given by*

$$\begin{aligned} J_s \hat{\rho}_s^0 (\partial_t \mathbf{v}_s + \mathbf{v}_s \cdot \nabla \mathbf{v}_s) - \nabla \cdot \boldsymbol{\sigma}_s &= J_s \hat{\rho}_s^0 \mathbf{f}, & \text{in } \mathcal{S}(t), \\ \partial_t \mathbf{u}_s + \mathbf{v}_s \cdot \nabla \mathbf{u}_s &= \mathbf{v}_s, \end{aligned} \quad (2.26)$$

with the Eulerian formulation of the Cauchy stress tensor

$$\boldsymbol{\sigma}_s := J_s \mathbf{F}_s^{-1} (2\mu_s \mathbf{E}_s + \lambda_s \operatorname{tr}(\mathbf{E}_s) I) \mathbf{F}_s^{-T}, \quad \mathbf{E}_s := \frac{1}{2} (\mathbf{F}_s^{-T} \mathbf{F}_s^{-1} - I),$$

and where the domain $\mathcal{S}(t)$ is implicitly defined as

$$\mathcal{S}(t) := \{\hat{x} + \hat{\mathbf{u}}_s(\hat{x}, t), \forall \hat{x} \in \hat{\mathcal{S}} = \mathcal{S}(0)\}. \quad (2.27)$$

There are several immediate drawbacks of an Eulerian Eulerian of solid problems:

1. The problem is formulated on the moving domain $\mathcal{S}(t)$, that is a priori unknown and part of the solution. For simplicity, definition (2.27) for $\mathcal{S}(t)$ is formulated using the Lagrangian description of the deformation $\hat{\mathbf{u}}_s(\hat{x}, t) = \mathbf{u}_s(x, t)$. That however is not at hand in the Eulerian formulation. To be exact, the domain $\mathcal{S}(t)$ must implicitly be defined as the solution of a transport equation:

$$\mathcal{S} = \{x(t) \in \mathbb{R}^d : \partial_t x(t) + (\mathbf{v} \cdot \nabla) x(t) = 0, \forall x(0) = \hat{x} \in \hat{\mathcal{S}}\}. \quad (2.28)$$

Every realization of an Eulerian formulation must keep track of the domain. We will get back to this key point in Section 2.5.3.

2. By transformation to Eulerian coordinate, convective terms are introduced:

$$d_t \hat{\mathbf{v}} = \partial_t \mathbf{v} + (\mathbf{v} \cdot \nabla) \mathbf{v}, \quad d_t \hat{\mathbf{u}} = \partial_t \mathbf{u} + (\mathbf{v} \cdot \nabla) \mathbf{u}.$$

A discretization of this convective term will cause numerical stability problems, as known for the transport term in the Navier-Stokes equations. Numerical methods must introduce artificial stabilization terms that will cause loss of conservation principles.

A variational formulation of problem (2.26) is derived in the standard way by multiplication with test-functions and integration over the (moving) domain $\mathcal{S}(t)$.

Lemma 39 (Variational formulation of the solid problem in Eulerian coordinates). *Let*

$$\mathbf{u}_s(t) \in \bar{\mathbf{u}}_s^D(t) + H_0^1(\mathcal{S}(t))^d, \quad \mathbf{v}_s(t) \in \bar{\mathbf{v}}_s^D(t) + \mathcal{V}_s(t) \in H_0^1(\mathcal{S}(t))^d$$

be the solution of the variational problem

$$\begin{aligned} (J_s \hat{\rho}_s^0 (\partial_t \mathbf{v}_s + \mathbf{v}_s \cdot \nabla \mathbf{v}_s), \phi_s)_{\mathcal{S}(t)} + (\boldsymbol{\sigma}_s, \nabla \phi_s)_{\mathcal{S}(t)} &= (J_s \hat{\rho}_s^0 \mathbf{f}, \phi)_{\mathcal{S}(t)}, \\ (\partial_t \mathbf{u}_s + \mathbf{v}_s \cdot \nabla \mathbf{u}_s - \mathbf{v}_s, \psi_s)_{\mathcal{S}(t)} &= 0, \end{aligned} \quad (2.29)$$

for all $\phi_s \in H_0^1(\mathcal{S}(t))^d$ and $\psi_s \in L^2(\mathcal{S}(t))^d$ and where σ is defined as in Lemma 38. Given sufficient additional regularity, this solution is also a solution of the classical Eulerian formulation given in Lemma 38.

2.5.2 Fluid-structure interaction in Eulerian coordinates

One a variational formulation of the structure problem in Eulerian coordinates is given, coupling to the flow problem is straightforward. Again, we can just glue the two velocities \mathbf{v}_f and \mathbf{v}_s together and use one common test-function for the two momentum equations. See Lemma 34.

$$\begin{aligned} & (\rho_f(\partial_t \mathbf{v} + (\mathbf{v} \cdot \nabla) \mathbf{v}), \phi)_{\mathcal{F}(t)} + (\sigma_f, \nabla \phi)_{\mathcal{F}(t)} \\ & + (J_s \hat{\rho}_s^0(\partial_t \mathbf{v} + (\mathbf{v} \cdot \nabla) \mathbf{v}), \phi)_{\mathcal{S}(t)} + (\sigma_s, \nabla \phi)_{\mathcal{S}(t)} = (\rho_f \mathbf{f}, \phi_f)_{\mathcal{F}(t)} + (J_s \hat{\rho}_s^0 \mathbf{f}, \phi_s)_{\mathcal{S}(t)}. \\ & (\nabla \cdot \mathbf{v}_f, \xi_f)_{\mathcal{F}(t)} = 0, \\ & (\partial_t \mathbf{u}_s + (\mathbf{v} \cdot \nabla) \mathbf{u}_s - \mathbf{v}, \psi_s)_{\mathcal{S}(t)} = 0. \end{aligned} \quad (2.30)$$

The kinematic condition is embedded in the test-space

$$\mathbf{v}(t) \in \mathbf{v}^D(t) + H_0^1(\Omega; \Gamma_f^D)^d,$$

and the dynamic condition is realized by coupling the test-functions

$$\phi \in H_0^1(\Omega; \Gamma_f^D)^d.$$

Pressure and the solid's deformation are found in

$$p_f(t) \in L^2(\mathcal{F}(t)), \quad \mathbf{u}_s(t) \in \bar{\mathbf{u}}_s^D(t) + H_0^1(\mathcal{S}(t); \Gamma_s^D)^d.$$

Test-spaces for the divergence condition and the velocity deformation coupling are simply

$$\xi_f \in L^2(\mathcal{F}(t)), \quad \psi_s \in L^2(\mathcal{S}(t))^d.$$

Apparently, the Eulerian formulation of the fluid-structure interaction problem has a simpler structure than the ALE formulation. No mapping - at least no artificial mapping - between domains is necessary. Hence, there is no obvious reason, while the Eulerian formulation should show limits when treating problems with very large deformation, motion or even contact. All this is true, the simplicity of the variational formulation in (2.30) however conceals one essential vagueness: the domains $\mathcal{F}(t)$ and $\mathcal{S}(t)$ are given by the solution itself. For the solid domain, we have identified two possible definitions, given in (2.27) and (2.28). Both of them however are not well suited in a computational framework. In the following section, we will introduce a technique to resolve this last gap.

2.5.3 The Initial Point Set method

For realizing a computational methods based on (2.30), we must be able to determine, if a coordinate $x \in \Omega(t)$ at time $t \geq t_0$ belongs to the solid domain $x \in \mathcal{S}(t)$ or to the fluid domain $x \in \mathcal{F}(t)$. In contrast to the ALE realization, where we could deal with fixed subdomains, this partitioning will move. We must correctly capture the interface at all times. The Eulerian

formulation belongs to the class of *interface-capturing* techniques. One of the most prominent *interface-capturing* method is the *Level-Set method*, introduced Sethian [210]. Here, we introduce a scalar Level-Set function $\chi^0 : \hat{\mathcal{S}} \rightarrow \mathbb{R}$, that indicates the signed distance to the interface $\hat{\mathcal{I}} = \mathcal{I}(0)$, i.e.

$$\chi^0(\hat{x}) := \begin{cases} \text{dist}(\hat{x}, \hat{\mathcal{I}}) & \hat{x} \in \hat{\mathcal{S}}, \\ -\text{dist}(\hat{x}, \hat{\mathcal{I}}) & \hat{x} \in \hat{\mathcal{F}}, \end{cases}.$$

It holds $\chi(\hat{x}) = 0$ for all $\hat{x} \in \hat{\mathcal{I}}$ on the interface. For a given point $\hat{x} \in \hat{\Omega}$, the sign of $\chi^0(\hat{x})$ can be used to determine the domain affiliation. Further, the normalization with the distance can be used to express normal vectors of the interface. This is a very important feature for multiphase flow problems, where the curvature has an influence on the surface tension. Then, we simply use the velocity field \mathbf{v} to transport the Level-Set function over time:

$$\partial_t \chi + (\mathbf{v} \cdot \nabla) \chi = 0.$$

Then, $\chi(x, t)$ will at all times indicate whether a point x belongs to $\mathcal{S}(t)$ or $\mathcal{F}(t)$.

One immediate drawback of the Level-Set technique is the introduction of an additional unknown that will increase the complexity of the formulation. A greater challenge is the derivation of stable numerical routines to solve the transport equation. Usually, such a pure transport equation will call for stabilization techniques like upwinding or artificial diffusion, that will cause unphysical smoothing of the interface. In the context of fluid-structure interactions, this could mean, that points of the fluid problem will by fault be accounted to the solid domain, and vice versa.

Here, as an alternative, we describe the *Initial Point Set method* for capturing the interface between fluid- and solid-domain. This technique was first introduced by Dunne [84].

To be precise: instead of capturing the interface location, we will capture the complete reference coordinate system. The construction of the Initial Point Set is based on the following observation: if we know, that $x \in \Omega(t)$ at time $t \geq 0$ belongs to the solid domain, i.e. $x \in \mathcal{S}(t)$, it holds

$$T_s(x, t) = x - \mathbf{u}_s(x, t) \in \hat{\mathcal{S}}.$$

Coordinates $x \in \mathcal{S}(t)$ are deformed back to the Lagrangian system by the Eulerian deformation $\mathbf{u}_s(x, t)$. As the Lagrangian system is fixed and known, we could use the deformation \mathbf{u}_s to determine, if a point $x \in \Omega(t)$ is part of the solid domain.

The flaw of this construction is the absence of fluid domain's deformation \mathbf{u}_f , as \mathbf{u}_s is only defined in the (up to know) not accessible solid domain. A computational method however can easily be derived by an implicit extension of this deformation \mathbf{u}_f to the fluid domain. Hence, for the following, we assume, that $\mathbf{u}_f : \mathcal{F}(t) \rightarrow \mathbb{R}^d$ is given such, that

$$\mathbf{u}_f(x, t) = \mathbf{u}_s(x, t) \quad \forall x \in \mathcal{I}(t),$$

and such that if holds

$$x - \mathbf{u}_f(x, t) \notin \hat{\mathcal{S}}.$$

The extension should map every coordinate back to a coordinate at reference time. We do not expect, that $x - \mathbf{u}_f(x, t) \in \hat{\mathcal{F}}$ is part of the reference fluid domain, we are pleased, if $x - \mathbf{u}_f(x, t) \notin \hat{\mathcal{S}}$ is not part of the solid's reference domain. We will get back to this subtle (but

important) difference. As \mathbf{u}_f and \mathbf{u}_s are continuous on the interface and by assuming, that \mathbf{u}_f has sufficient regularity, we define a global deformation field $\mathbf{u}(t) : \Omega(t) \rightarrow \mathbb{R}^d$ and set

$$\mathbf{u}_s(t) := \mathbf{u}(t)\Big|_{\mathcal{S}(t)}, \quad \mathbf{u}_f(t) := \mathbf{u}(t)\Big|_{\mathcal{F}(t)}.$$

Based on this global deformation, we can finally define the *Initial Point Set* Φ_{IPS} as

$$\Phi_{IPS}(x, t) := x - \mathbf{u}(x, t),$$

and can use it to determine the domain affiliation for all coordinates $x \in \Omega(t)$:

$$x \in \Omega(t) \quad \Rightarrow \quad x \in \begin{cases} \mathcal{S}(t), & \text{if } \Phi_{IPS}(x, t) = x - \mathbf{u}(x, t) \in \hat{\mathcal{S}}, \\ \mathcal{F}(t), & \text{if } \Phi_{IPS}(x, t) = x - \mathbf{u}(x, t) \notin \hat{\mathcal{S}}. \end{cases}$$

The Initial Point Set allows to distinguish between the two subdomains.

We still have to provide a way to define suitable extensions \mathbf{u}_f in an implicit way. In principle, we can utilize the same techniques are discussed in the context of the ALE-map in Section 2.4.1. This effort however is not necessary, as the deformation \mathbf{u}_f will not be used to define a mapping between $\mathcal{F}(t)$ and $\hat{\mathcal{F}}$. We only require, that $x - \mathbf{u}_f(x, t)$ will be carried to a coordinate outside the solid domain. We not need any regularity of \mathbf{u}_f not do we need invertibility of the map $\text{id} - \mathbf{u}_f$.

Definition 6 (Initial Point Set). *A vector field $\Phi_{IPS} : \Omega((t) \rightarrow \mathbb{R}^d$ is called Initial Point Set, if for $x \in \Omega$ and $t \geq 0$ it holds:*

$$\begin{aligned} \Phi_{IPS}(x, t) &= x - \mathbf{u}_s(x, t) & x \in \bar{\mathcal{S}}(t) \\ \Phi_{IPS}(x, t) &\notin \hat{\mathcal{S}} & x \in \mathcal{F}(t) \end{aligned}$$

Finally, we can indicate some possibilities for the construction of \mathbf{u}_f . One simple option is to choose one more a harmonic extension of \mathbf{u}_s to the fluid domain:

$$-\Delta \mathbf{u}_f = 0 \text{ in } \mathcal{F}(t), \quad \mathbf{u}_f = \mathbf{u}_s \text{ on } \mathcal{I}(t), \quad \vec{n} \cdot \nabla \mathbf{u}_f = 0 \text{ on } \partial \mathcal{F}(t) \setminus \mathcal{I}(t).$$

Here, we have chosen homogenous Neumann boundary conditions on the outer boundary of the fluid-domain. This deformation \mathbf{u}_f will not define a mapping back to a reference domain, but as discussed, this property is not necessary. A Neumann condition will allow very large deformations, where $\mathcal{S}(t)$ (nearly) touches the outer boundary. We will focus our attention on the construction of the Initial Point Set in later sections dealing with the numerical realization.

Finally, we can close the formulation of the coupled fluid-structure interaction problem in Eulerian coordinate:

Lemma 40 (Initial Point Set formulation of the Eulerian fluid-structure interaction problem). *Let*

$$\begin{aligned} \mathbf{u}(t) &\in \bar{\mathbf{u}}^D(t) + H_0^1(\Omega(t); \Gamma_s^D)^d, \\ \mathbf{v}(t) &\in \bar{\mathbf{v}}^D(t) + H_0^1(\Omega(t); \Gamma^D)^d, \\ p_f(t) &\in L^2(\mathcal{F}(t)) \end{aligned}$$

be the solution of the variational system

$$\begin{aligned}
 & (\rho_f(\partial_t \mathbf{v} + (\mathbf{v} \cdot \nabla) \mathbf{v}), \phi)_{\mathcal{F}(t)} + (\sigma_f, \nabla \phi)_{\mathcal{F}(t)} \\
 & + (J_s \hat{\rho}_s^0(\partial_t \mathbf{v} + (\mathbf{v} \cdot \nabla) \mathbf{v}), \phi)_{\mathcal{S}(t)} + (\sigma_s, \nabla \phi)_{\mathcal{S}(t)} = (\rho_f \mathbf{f}, \phi)_{\mathcal{F}(t)} + (J_s \hat{\rho}_s^0 \mathbf{f}, \phi)_{\mathcal{S}(t)} \\
 & \quad (\nabla \cdot \mathbf{v}, \xi_f)_{\mathcal{F}(t)} = 0 \\
 & \quad (\partial_t \mathbf{u} + (\mathbf{v} \cdot \nabla) \mathbf{u} - \mathbf{v}, \psi_s)_{\mathcal{S}(t)} = 0 \\
 & \quad (\nabla \mathbf{u}, \nabla \psi_f)_{\mathcal{F}(t)} = 0,
 \end{aligned}$$

for all test-functions

$$\begin{aligned}
 \phi_f & \in H_0^1(\Omega(t); \Gamma^D)^d, \\
 \xi_f & \in L^2(\mathcal{F}(t)), \\
 \psi_s & \in L^2(\mathcal{S}(t))^d, \\
 \psi_f & \in H_0^1(\mathcal{F}(t); \mathcal{I}(t))^d.
 \end{aligned}$$

Given sufficient regularity, this solution also solves the fluid-structure interaction problem in classical formulation (2.4).

Proof. folgt???

□

Remark 14 (Similarity to multiphase flows). There are many similarities between the Eulerian formulation of fluid-structure interactions and multiphase flows, where two different fluids are coupled over a common (and moving) interface. To illustrate this analogy we first introduce global variables for the stress tensors and the densities

$$\sigma(x, t) := \begin{cases} \sigma_f(x, t) & x \in \mathcal{F}(t), \\ \sigma_s(x, t) & x \in \mathcal{S}(t), \end{cases} \quad \rho(x, t) := \begin{cases} \rho_f & x \in \mathcal{F}(t), \\ J_s \hat{\rho}_s^0 & x \in \mathcal{S}(t). \end{cases}$$

With help of this notation, we can specify the coupled problem in a shorter form as

$$\begin{aligned}
 & (\rho(\partial_t \mathbf{v} + (\mathbf{v} \cdot \nabla) \mathbf{v}), \phi) + (\sigma, \nabla \phi) = (\rho \mathbf{f}, \phi), \\
 & \quad (\nabla \cdot \mathbf{v}, \xi_f)_{\mathcal{F}(t)} = 0 \\
 & \quad (\partial_t \mathbf{u} + (\mathbf{v} \cdot \nabla) \mathbf{u} - \mathbf{v}, \psi_s)_{\mathcal{S}(t)} = 0 \\
 & \quad (\nabla \mathbf{u}, \nabla \psi_f)_{\mathcal{F}(t)} = 0,
 \end{aligned}$$

We however must notice, that fluid-structure interaction is not a simple change of problem parameters along an interface, instead, the complete setup of the stress tensors change, as $\sigma_f = \sigma_f(\mathbf{v})$ and $\sigma_s = \sigma_s(\mathbf{u})$ stand for a parabolic-type equation and one of hyperbolic type.

Problem 17. Show, that the geometric coupling condition follows by the kinematic condition and by the assumption, that the path of the particles is continuous and with a continuous inverse.

Problem 18. Show, that if \hat{T}_f and \hat{T}_s are $C^{0,1}$ -diffeomorphisms, contact in the following sense is not possible: let $\hat{x}_i \in \mathcal{I}(t)$ be a point of the interface and let $\hat{U}_\epsilon(\hat{x}_i)$ be a neighborhood of \hat{x}_i with $\hat{U}_\epsilon(\hat{x}_i) \cap \partial\Omega(t) = \emptyset$. At time $t > 0$ let $x_i = \hat{T}_f(\hat{x}_i) = \hat{T}_s(\hat{x}_i)$. For all neighborhoods $U_\delta(x_i)$ it holds $U_\delta(x_i) \cap \partial\Omega(t) \neq \emptyset$.

Problem 19. Let $\hat{V} = B_1(0) \subset \mathbb{R}^2$ be the unit ball. Let $\hat{T} : \hat{V} \rightarrow \mathbb{R}^2$ be an invertible mapping with $\hat{T}, \hat{T}^{-1} \in C^{1,1}(\hat{V})^2$. Show, that $\hat{T}(\hat{V})$ satisfies the cone conditions and that $\hat{T}(\hat{V})$ is a Lipschitz domain.

Problem 20. Motivate the three properties of \hat{T}_s and its inverse \hat{T}_s^{-1} given in Section 2.5 with physical reasoning.

Problem 21. Show Lemma 36.

3 Discretization

This chapter is devoted to discretization techniques for fluid-structure interaction problems. First however, we will focus on simple elliptic and parabolic partial differential equations and introduce methods for time-discretization as well as the basic finite element method.

3.1 Time discretization of partial differential equations

In this section, we discuss the time-discretization of parabolic differential equations given in variational formulation

$$u(t) \in \mathcal{V} : \quad (\partial_t u(t), \phi) + a(u(t), \phi) = (f(t), \phi) \quad \forall \phi \in \mathcal{V} =: H_0^1(\Omega), \quad (3.1)$$

with initial data

$$(u(0), \phi) = (u^0, \phi) \quad \forall \phi \in L^2(\Omega),$$

where $u^0 \in L^2(\Omega)$. Usually, three different approaches for the time-discretization of parabolic problems are considered, depending on the order, whether to first discretize in space or in time:

first space then time This approach is called *Method of Lines*. By space discretization, the parabolic equations is transformed into a system of ordinary differential equations that then can be tackled with usual single or multistep-methods.

first time then space This approach is referred to as *Rothe's Method*. By discretization in time with a single-step method, the parabolic equation is resolved into a sequence of quasi-stationary elliptic partial differential equations that then can be discretized in space. The advantage of this approach is the possible use of different discretizations (adaptive meshes) in different time steps.

simultaneously This approach is called a *Space-Time discretization*. By using a simultaneous Galerkin-discretization in space and time, the equation gets suitable for strong variational analysis techniques. This approach allows for the easy derivation of robust error estimators and adjoint optimization techniques. The effort for solving a space-time coupled problem however is immense, as the time acts as an additional dimension. Usually, space-time approaches are only considered for analysis purposes and Rothe's Method or the Method of Lines are used for solving.

It can be shown, that the Method of Lines and Rothe's method are equivalent, if uniform discretizations are considered. Further, it is possible to design space-time Galerkin methods that - at least for linear autonomous problems - correspond to certain time-stepping methods.

All time-discretizations are based on a subdivision of the time interval $I = [0, T]$ into discrete time-steps:

$$0 = t_0 < t_1 < \dots < t_M = T, \quad k_m := t_m - t_{m-1}, \quad k := \max_m k_m.$$

At every time-step t_m we denote by

$$u^m = u(t_m),$$

the solution at time t_m . One of the most basic time-stepping scheme used in the Method of Lines or Rothe's method is the one-step θ -scheme:

$$\begin{aligned} m = 1, \dots, M : \quad & (u^m, \phi) + \theta k_m a(u^m, \phi) = (u^{m-1}, \phi) \\ & - (1 - \theta) k_m a(u^{m-1}, \phi) + \theta k(f^m, \phi) + (1 - \theta) k(f^{m-1}, \phi) \quad \forall \phi \in \mathcal{V}. \end{aligned} \quad (3.2)$$

For $\theta = 1$, this is the implicit backward Euler method, for $\theta = 0$ the explicit forward Euler and for $\theta = \frac{1}{2}$ the Crank-Nicolson scheme. Error analysis for time-depending partial differential equations requires subtle techniques and even for the linear heat equation simple variational methods do not give general results. For insight into the analysis of Rothe's method applied to parabolic partial differential equations we refer to the literature [223]. Both implicit and explicit Euler scheme show first order accuracy in the time step k , the Crank-Nicolson scheme is second order accurate. Higher order accuracy can be reached by referring to Runge-Kutta methods or linear multistep schemes like the Backward Differentiation Formulas (BDF), see [78].

By discretization with a single-step method, the parabolic equation decouples into M pseudo-stationary problems of type (3.2) that can subsequently be discretized in space by appropriate Finite Element methods. Usually, it shows that choosing only first order accurate time-stepping schemes, the resulting discretization error is highly unbalanced and that very small time-steps (compared to the spatial discretization parameter h)

$$k \ll h$$

are required to yield a adequate overall error asymptotic. As however very high spatial approximation order is not easily obtained for complex problems like fluid-structure interactions, choosing second order accurate time-stepping schemes is a good compromise between approximation property and numerical effort.

3.1.1 Numerical Stability

Numerical stability is - next to approximation accuracy - the most important quality measure for time discretization schemes. For an analysis we consider the scalar ordinary differential equations

$$u'(t) = \lambda u(t), \quad t \geq 0, \quad u(0) = 1, \quad (3.3)$$

where $\lambda \in \mathbb{C}$ is a given complex parameter. The unique solution to this equation is given by

$$u(t) = e^{\lambda t},$$

and for all $Re(\lambda) \leq 0$ it holds

$$Re(\lambda) \leq 0 \quad \Rightarrow \quad |u(t)| \leq 1.$$

We define:

Definition 7 (Absolute Stability). A one-step method for the discretization of (3.3) is absolutely stable for a given $\lambda \in \mathbb{C}$ and time-step $k > 0$, if

$$|u^m| \leq 1, \quad m = 1, 2, \dots$$

A numerical scheme is usually stable for only some pairs of $\lambda \in \mathcal{C}$ and $k \in \mathbb{R}_+$. We consider the forward Euler method for the approximation of (3.3)

$$u^m = (1 + \lambda k)u^{m-1},$$

and we immediately get the relation:

$$|u^m| \leq |1 + \lambda k|u^{m-1} \leq \dots \leq |1 + \lambda k|^m |u^0| = |1 + \lambda k|^m.$$

Absolute stability is given, if

$$|1 + \lambda k| \leq 1 \Leftrightarrow \lambda k \in \bar{B}_1(-1) := \{z \in \mathbb{C} : |z + 1| \leq 1\}.$$

We define:

Definition 8 (Region of absolute stability). *The subset of the complex plane*

$$\mathcal{R}_S = \{z = \lambda k \in \mathbb{C} : \text{absolute stability for } \lambda, k\},$$

is called the region of absolute stability of the single-step method. A method with a stability region that contains the left complex half-plane is called A-stable

$$\{z \in \mathbb{C} : \operatorname{Re}(z) \leq 0\} \subset \mathcal{R}_S.$$

For the θ time-stepping method it holds:

Lemma 41 (Absolute stability of the one-step θ -method). *The region of stability for the implicit Euler scheme is given by:*

$$\mathcal{R}_S^{IE} = \mathbb{C} \setminus B_1(1),$$

for the explicitly Euler scheme

$$\mathcal{R}_S^{EE} = \bar{B}_1(-1),$$

and for the Crank-Nicolson scheme

$$\mathcal{R}_S^{CN} = \{z \in \mathbb{C} : \operatorname{Re}(z) \leq 0\}.$$

For all $\theta \in [\frac{1}{2}, 1]$ it holds

$$\mathcal{R}_s^{\theta \geq \frac{1}{2}} \supseteq \{z \in \mathbb{C} : \operatorname{Re}(z) \leq 0\}.$$

and for all $\theta \in [0, \frac{1}{2})$ it holds:

$$\mathcal{R}_s^{\theta < \frac{1}{2}} \cap \{z \in \mathbb{C} : \operatorname{Re}(z) \leq 0\} \neq \emptyset.$$

Proof. The θ -scheme is written with help of the *amplification factor*:

$$u^m = R(k, \lambda, \theta)u^{m-1}, \quad R(k, \lambda, \theta) = \frac{1 + (1 - \theta)k\lambda}{1 - \theta k\lambda}.$$

The region of stability is then calculated as the set of complex numbers $z = k\lambda$ that satisfy $|R(z, \theta)| \leq 1$. \square

Remark 15 (Amplification factor). *The amplification factors $R(z) = R(\lambda k)$ of a single-step method for solving the model-problem (3.3) are approximation to the complex exponential function*

$$R(z) \approx \exp(z).$$

For a single-step method with truncation error $O(k^\alpha)$ it holds

$$|R(\lambda k) - \exp(\lambda k)| = O(k^{\alpha+1}).$$

The amplification factor for implicit single-step methods is always a rational approximation to the exponential function. The best rational approximations to the exponential function are called Padé approximation. For increasing polynomial degree of denominator r and numerator s , the Padé approximations can be given in a Padé-table:

$s \setminus r$	1	2	3
1	$\frac{1}{1}$	$\frac{1+z}{1}$	$\frac{1+z+\frac{1}{2}z^2}{1}$
2	$\frac{1}{1-z}$	$\frac{1+\frac{1}{2}z}{1-\frac{1}{2}z}$	$\frac{1+\frac{2}{3}z+\frac{1}{6}z^2}{1-\frac{1}{3}z}$
3	$\frac{1}{1-z+\frac{1}{2}x^2}$	$\frac{1+\frac{1}{3}z}{1-\frac{2}{3}z+\frac{1}{6}z^2}$	$\frac{1+\frac{1}{2}z+\frac{1}{12}z^2}{1-\frac{1}{2}z+\frac{1}{12}x^2}$

It can be shown, that all diagonal Padé approximations correspond to A-stable time-stepping schemes, while all sub-diagonal Padé approximations correspond to a strongly A-stable scheme [112, 191, 217].

A method lacking numerical stability usually asks for restrictive time-step conditions. The forward Euler scheme requires

$$\lambda k \in B_1(-1),$$

and considering $\lambda \in \mathbb{R}$ with $\lambda < 0$ this refers to the condition:

$$0 \leq k|\lambda| \leq 2 \Leftrightarrow k \leq 2|\lambda|^{-1}.$$

For $|\lambda|$ large, this condition can be very restrictive. Next, we consider the heat-equation in variational formulation

$$(\partial_t u, \phi) + (\nabla u, \nabla \phi) = 0,$$

that we can write using an operator notation as

$$\mathcal{M}\partial_t u + \mathcal{A}u = 0,$$

where \mathcal{A} is the weak Laplace operator. We know, that \mathcal{A} is symmetric positive definite with an orthonormal basis of eigenvectors $\{w_i\}_{i \geq 0}$ and corresponding eigenvalues λ_i , where

$$0 < \lambda_1 \leq \lambda_2 \leq \dots, \quad \lambda_i \rightarrow \infty \quad (i \rightarrow \infty).$$

Using the eigenvector representation

$$u(t) = \sum_{i \geq 0} u^i(t) w_i,$$

the heat-equation decomposes into a set of scalar equations

$$\partial_t u^i(t) = -\lambda_i u^i(t),$$

each of the same type as the model problem (note the reversed sign). For numerical stable time-discretization of the heat equation it has to hold for all eigenvectors:

$$-\lambda_i k \in \mathcal{R}_S \quad \forall i \geq 0.$$

If a single-step method is strongly A-stable, it is unconditionally stable for discretizing the heat-equation for all step-sizes $k > 0$. We define:

Definition 9 (Stiff System). *A system of differential equations*

$$u'(t) = f(t, u(t)), \quad t \geq 0$$

is called stiff, if the ratio

$$\frac{\max |\lambda_-(f_u)|}{\min |\lambda_-(f_u)|} \gg 1,$$

where by $\lambda_-(f_u)$ we denote the Eigenvalues of

$$f_u := \frac{d}{du} f(t, u)$$

with negative real part.

A scalar equation $u' = \lambda u$ is never called stiff, even if $\text{Re}(\lambda) \ll 0$. Stiffness describes, that a small time-step k is required for reasons of numerical stability, but not simply for reasons of approximation accuracy. A vague, however perspicuous definition of a stiff problem is that of a problem, where the implicit Euler method yields an acceptable solution, where the explicit Euler method fails to give a good solution, when using the same time-step size.

Example 1 (Stiff problem). *We consider the scalar model problem*

$$u'(t) = -200u(t), \quad t \geq 0, \quad u(0) = 1,$$

with a large Lipschitz-constant $L = 200$. The solution is given by $u(t) = \exp(-200t)$. We discretize this problem by the forward and backward Euler method and measure the error at time $t_n = 1$

$$\frac{\|u(t_n) - u_n\|}{\|u(t_n)\|}.$$

In Table 3.1 we gather the results using different time-steps k .

Only very small time-steps $k = 2^{-11} \approx 0.0005$ give relative error smaller than 100% in both cases for implicit and explicit Euler scheme. This small time-step is well below the time-step condition $k < 2L^{-1} \approx 0.01$ of the explicit Euler scheme arising from the stability analysis, see Lemma 41.

The necessity for this small time-step is not by stability restrictions but simply due to the large Lipschitz constant of the problems that enters all error estimates.

3.1. Time discretization of partial differential equations

k	EE	IE	k	EE	IE
2^{-6}	∞	46594	2^{-10}	0.717	2.262
2^{-7}	0.999	2419	2^{-11}	0.462	0.823
2^{-8}	0.996	74.76	2^{-12}	0.265	0.354
2^{-9}	0.927	8.907	2^{-13}	0.142	0.164

Table 3.1: Example 1: discretization of the scalar model problem. Discretization with explicit Euler (EE) implicit Euler (IE) for decreasing time step sizes k .

k	EE	IE	k	EE	IE
2^{-4}	∞	0.0788	2^{-8}	0.2400	0.1063
2^{-5}	∞	0.1403	2^{-9}	0.0868	0.0624
2^{-6}	∞	0.2016	2^{-10}	0.0394	0.0333
2^{-7}	0.7781	0.1820	2^{-11}	0.0188	0.0173

Table 3.2: Example 1: discretization of the system of ode's. Discretization with explicit Euler (EE) implicit Euler (IE) for decreasing time step sizes k .

Next, we consider the system of initial value problems:

$$u'(t) = Au(t), \quad A := \frac{1}{3} \begin{pmatrix} -202 & -398 \\ -199 & -401 \end{pmatrix} u(t), \quad u(0) = \begin{pmatrix} 11 \\ -4 \end{pmatrix}.$$

The matrix A has the two eigenvalues $\lambda_1 = -200$ and $\lambda_2 = -1$. With $|\lambda_2|/|\lambda_1| = 200$ this problem can be considered stiff. It holds:

$$Q := \begin{pmatrix} 1 & -2 \\ 1 & 1 \end{pmatrix}, \quad Q^{-1}AQ = D = \begin{pmatrix} -200 & 0 \\ 0 & -1 \end{pmatrix},$$

and we define the diagonalized system for $\bar{u}(t) = Q^{-1}u(t)$

$$\bar{u}'(t) = D\bar{u}(t), \quad \bar{u}(0) = Q^{-1}u_0 = \begin{pmatrix} 1 \\ -5 \end{pmatrix},$$

with the solution

$$\bar{u}(t) = \begin{pmatrix} \exp(-200t) \\ -5 \exp(-t) \end{pmatrix}.$$

Table 3.2 shows the results for both implicit and explicit Euler scheme used for discretization of this system of equations. Again, we measure the relative error $\|\bar{u}(t_n) - \bar{u}_n\|_\infty / \|\bar{u}(t_n)\|_\infty$ at time $t_n = 1$.

Here, the explicit Euler method gives reasonable results starting from $k = 2^{-7} \approx 0.008 < 0.01$, where the the time-step first enters the region of absolute stability. The implicit Euler method also gives reasonable results for larger time-steps. If the time-step is small enough, both methods give results of similar accuracy.

This second problem is stiff, as it characterized by two different solution components with very different behavior. While one component quickly goes to zero, the second component governed

the absolute value of the solution. Combining the solutions of the diagonalized system we can estimate the original solution as:

$$u(t) = Q\bar{u}(t) = \begin{pmatrix} 10e^{-t} + e^{-200t} \\ -5e^{-t} + e^{-200t} \end{pmatrix}.$$

3.1.2 Numerical Dissipation and further stability concepts

Every A-stable time discretization scheme is robust for the discretization of stiff problems as solution components belonging to Eigenvalues with negative real part are quickly damped. This behavior is important for parabolic partial differential equations. Hyperbolic equations however have the property of energy conservation. We consider the following ODE as simple model for the wave equation

$$v''(t) + v(t) = 0, \quad v(0) = 1, \quad v'(0) = 0, \quad (3.4)$$

which has the solution

$$v(t) = \cos(t).$$

We introduce the notation $u_1(t) = v(t)$ and $u_2(t) = v'(t)$ to reformulate (3.4) as a system of first order equations

$$u'(t) = \begin{pmatrix} 0 & 1 \\ -1 & 0 \end{pmatrix} u(t), \quad u(0) = \begin{pmatrix} 1 \\ 0 \end{pmatrix}.$$

The matrix has two complex eigenvalues $\lambda = \pm i$. And for the vector-valued solution $u : I \rightarrow \mathbb{R}^2$ it holds $|u(t)| = 1$.

In the following, we consider the model problem (3.3) with complex eigenvalues

$$u'(t) = \lambda i u(t), \quad u(0) = 1,$$

with the solution

$$u(t) = e^{i\lambda t} = \cos(\lambda t) + i \sin(\lambda t).$$

It holds $|u(t)| = 1$ for all times $t \geq 0$ and the solution $u(t)$ has the frequency π/λ . The energy of the system is optimally conserved. We define

Definition 10 (Numerical dissipation). *A single-step method is said to have little numerical dissipation, if*

$$R(i) \approx 1.$$

For the θ -scheme, it holds:

$$R(i, \theta) = \frac{1 + (1 - \theta)i}{1 - \theta i} = 1 + \frac{1}{1 - \theta i}.$$

While the backward Euler method $\theta = 1$ is highly damping

$$|R(i, 1)| = \frac{1}{\sqrt{2}} \ll 1,$$

the forward Euler method $\theta = 0$ is very unstable and amplifies waves:

$$|R(i, 0)| = 2 \gg 1.$$

3.1. Time discretization of partial differential equations

The Crank-Nicolson method has perfect energy conservation and no numerical dissipation:

$$R\left(i, \frac{1}{2}\right) = \frac{1 + \frac{1}{2}i}{1 - \frac{1}{2}i} = 1.$$

The good stability (it is A-stable) and the excellent dissipation properties together with second order accuracy makes the Crank-Nicolson method for a nearly optimal discretization scheme for coupled problems like fluid-structure interactions, that involve both the very stiff system of flow equations and the elastic structure equation of hyperbolic type that calls for good energy conservation. It shows however, that A-stability of the Crank-Nicolson method is just not enough to cope with numerical truncation errors that are accumulated over time. Further, if the initial data for the heat-equation only has minimal regularity $u^0 \in L^2(\Omega)$, which is enough to guarantee a smooth solution, the numerical schemes may fail.

It hence remains to find a time-stepping scheme, that is at least second order accurate, has little numerical dissipation and better stability properties.

Shifted Crank-Nicolson methods

A popular discretization scheme with better stability properties as the Crank-Nicolson scheme is derived by an implicit shift, using

$$\theta = \frac{1}{2} + O(k).$$

The resulting scheme still is second order accurate but the stability region is slightly larger. It holds:

Lemma 42 (Shifted Crank-Nicolson). *The implicitly shifted Crank-Nicolson scheme is globally A-stable:*

$$\lim_{Re(\lambda) \rightarrow -\infty} \lim |\mathcal{R}_S^{\theta=\frac{1}{2}+O(k)}(\lambda, k)| = 1 - O(k).$$

Proof. It holds:

$$\begin{aligned} |\mathcal{R}_S| &= \left| \frac{1 + (1 - \frac{1}{2} - O(k)) \lambda k}{1 - (\frac{1}{2} + O(k)) \lambda k} \right| = \left| \frac{1 + (\frac{1}{2} - O(k)) \lambda k}{1 - (\frac{1}{2} + O(k)) \lambda k} \right| \\ &\xrightarrow[\lambda \rightarrow -\infty]{} \left| \frac{\frac{1}{2} - O(k)}{\frac{1}{2} + O(k)} \right| = 1 - O(k). \end{aligned}$$

□

A globally A-stable scheme has stronger damping properties. When discretized with a globally A-stable scheme, we can find global discrete solutions to parabolic equations. An even stronger stability concept is given by

Lemma 43 (Implicitly θ -schemes). *Given $\theta \in (\frac{1}{2}, 1]$, the θ -scheme is strongly A-stable:*

$$\lim_{Re(\lambda) \rightarrow -\infty} \lim |\mathcal{R}_S^{\theta>\frac{1}{2}}(\lambda, k)| \leq 1 - \delta < 0.$$

Proof. It holds:

$$|\mathcal{R}_S| = \left| \frac{1 + (1 - \theta)\lambda k}{1 - \theta\lambda k} \right| \xrightarrow{\lambda \rightarrow -\infty} \left| \frac{1 - \theta}{\theta} \right| = \left| 1 - \frac{1}{\theta} \right| =: |1 - \delta|$$

For $\theta > \frac{1}{2}$ it holds $|1 - \delta| < 1$ □

Methods with strong A-stability have damping properties for all time-step sizes and all eigenvalues. A time-stepping method with strong A-stability applied to the heat-equation will yield the full smoothing property of parabolic equations. Even for irregular initial data $u^0 \in L^2(\Omega)$, optimal order of convergence can be obtained. See [154, 179] for details on the analysis of smoothing properties of parabolic partial differential equations.

The fractional-step θ -method

For $\theta > \frac{1}{2}$ the θ -scheme is strongly A-stable, it however lacks second order accuracy. A simple idea to construct time-stepping schemes with higher accuracy and with strong A-stability is to combine multiple sub-steps of the θ -scheme into one new scheme. This idea goes back to Glowinski [108]. We perform three sub steps

$$t_{m-1} \rightarrow t_{m-1+\alpha} \rightarrow t_{m-\alpha} \rightarrow t_m, \quad k_m := t_m - t_{m-1},$$

with step-sizes

$$\alpha_1 k_m, \quad \alpha_2 k_m, \quad \alpha_3 k_m,$$

where $\alpha_i \in (0, 1)$ with $\alpha_1 + \alpha_2 + \alpha_3 = 1$. In each of these steps, we choose different values for $\theta_i \in [0, 1]$. To reduce the number of free parameters, we choose $\alpha_1 = \alpha_3 = \alpha \in (0, \frac{1}{2})$ and $\alpha_2 = 1 - 2\alpha$. Further we pick $\theta_1 = \theta_3 = \theta$ and $\theta_2 = 1 - \theta$. This results in the three-step method applied to (3.1):

$$\begin{aligned} (u^{m-1+\alpha}, \phi) + \alpha\theta k_m a(u^{m-1+\alpha}, \phi) &= (u^{m-1}, \phi) - \alpha(1 - \theta)k_m a(u^{m-1}, \phi) \\ (u^{m-\alpha}, \phi) + (1 - 2\alpha)(1 - \theta)k_m a(u^{m-\alpha}, \phi) &= (u^{m-1+\alpha}, \phi) - (1 - 2\alpha)\theta k_m a(u^{m-1+\alpha}, \phi) \\ (u^m, \phi) + \alpha\theta k_m a(u^m, \phi) &= (u^{m-\alpha}, \phi) - \alpha(1 - \theta)k_m a(u^{m-\alpha}, \phi). \end{aligned} \quad (3.5)$$

Applied to the model-problem (3.3), the amplification factor of the fractional-step θ -method is given as a combination of three θ -factors (note the reversed sign!)

$$R^{\text{fst}}(\theta, \alpha, z) = \frac{(1 + \alpha(1 - \theta)z)^2(1 + (1 - 2\alpha)\theta z)}{(1 - \alpha\theta z)^2(1 - (1 - 2\alpha)(1 - \theta)z)}$$

For small $z \in \mathbb{C}$, this amplification factor is an approximation to the exponential function and it holds:

$$|R^{\text{fst}}(\theta, \alpha, z) - \exp(z)| = (1 - 2\theta) \left(\alpha - \left(1 + \frac{1}{\sqrt{2}} \right) \right) \left(\alpha - \left(1 - \frac{1}{\sqrt{2}} \right) \right) |z|^2 + O(|z|^3).$$

Hence, for the choice $a = 1 - \frac{1}{\sqrt{2}} \approx 0.29289$ the resulting method is second order accurate for every $\theta \in (0, 1)$. For $z = \lambda k$ it holds in the limit $\lambda \rightarrow -\infty$:

$$R^{\text{fst}}(\theta, \alpha, k, \lambda) = \left| \frac{(1 + \alpha(1 - \theta)k\lambda)^2(1 + (1 - 2\alpha)\theta k\lambda)}{(1 - \alpha\theta k\lambda)^2(1 - (1 - 2\alpha)(1 - \theta)k\lambda)} \right| \xrightarrow{\lambda \rightarrow -\infty} \left| \frac{1 - \theta}{\theta} \right|,$$

and strong A-stability follows for every $\theta \in (\frac{1}{2}, 1]$.

Remark 16 (Choice of θ). One possible choice for θ is such that it holds:

$$\alpha\theta = (1 - 2\alpha)(1 - \theta) \Leftrightarrow \theta = \frac{1 - 2\alpha}{1 - \alpha} = 2 - \sqrt{2} \approx 0.5858.$$

This choice has the advantage, that when applying system (3.5) to a linear parabolic equation, the same system matrix

$$\mathcal{M} + \alpha\theta k\mathcal{A} \equiv \mathcal{M} + (1 - 2\alpha)(1 - \theta)k\mathcal{A}$$

must be inverted in each of the three sub-steps. Regarding nonlinear problems with nonlinear differential operators $\mathcal{A}(u)$, this advantage gets lessened as a system matrix must anyway be newly assembled in every sub-step.

Finally, it remains to analyze the dissipative character of the fractional-step θ -method. It holds for different values of θ :

$$|R(i, 1)| \approx 0.99687, \quad |R(i, 2 - \sqrt{2})| \approx 0.99970.$$

These properties make the fractional step θ -scheme to one of the most-used time-stepping methods for flow-problems. Second order accuracy is usually considered to be reasonable and the combination of strong A-stability with this nearly optimal dissipative character are well suited to represent the dynamics of fluid problems.

Many variants of the fractional step θ -scheme are possible, the choice of parameters $\theta, 1 - \theta, \theta$ as well as $\alpha k, (1 - 2\alpha)k, \alpha k$ is due to symmetry reasons but not strictly required. Glowinski et al. [230] introduced a modified fractional step theta scheme, that consists of only two implicit Euler like sub-steps and one purely explicit extrapolation step:

$$t_{m-1} \xrightarrow[\alpha k]{\theta=1} t_{m-1+\alpha} \xrightarrow[(1-2\alpha)k]{\text{linear extrapolation}} t_{m-\alpha} \xrightarrow[\alpha k]{\theta=1} t_m.$$

The choice $\alpha = 1 - 1/\sqrt{2}$ again results in a second order scheme. Like the original fractional step θ -scheme, this modification is strongly A-stable and has good dissipation properties. It is slightly more damping as the original scheme, but each time-step now consists of two implicit systems and one very cheap extrapolation step only. See [209] for a detailed discussion and comparison.

3.1.3 Galerkin time discretization schemes

Single step methods for time-stepping have the advantage of a very easy structure that makes an efficient implementation possible. As they are completely based on simple finite difference techniques, they are not accessible for rigorous error estimator methods known from Galerkin methods. Eriksson, Estep, Hansbo, and Johnson [86] as well as Thomée [223] derived Galerkin formulations of parabolic partial differential equations that are in some sense equivalent to the time-stepping scheme. Having Galerkin formulations at hand, error estimates can be established by standard residual techniques known from the finite element analysis. Again, we consider the parabolic differential equation given in (3.1), and a splitting of $I = [0, T]$, into M discrete time-steps t_i . In addition, we introduce half-open intervals

$$0 = t_0 < t_1 < \cdots < T_m = T, \quad I_m := (t_{m-1}, t_m],$$

and the function spaces

$$\begin{aligned} X^r &:= C^r(I; V) := \{\phi : I \times \Omega \rightarrow \mathbb{R}, \phi(t, \cdot) \in V, \phi(\cdot, x) \in C^r(I)\} \\ X_I^r &:= \{\phi : I \times \Omega \rightarrow \mathbb{R}, \phi(t, \cdot) \in V, \phi(\cdot, x) \in L^2(I), \\ &\quad \phi(\cdot, x)|_{I_m} \in C_c(I_m) \cap C^r(I_m), m = 1, \dots, M\}, \end{aligned}$$

where by $C_c(I_m)$ we denote the space of $C(I_m)$ functions that have a continuous extension to the left (open) boundary of I_m . Functions $u \in X_I^r$ allow for discontinuities at the discrete points in time t_m . We define:

$$u_m^+ := \lim_{t \searrow t_m} u_m(t, \cdot) \in V, \quad u_m^- := \lim_{t \nearrow t_m} u_m(t, \cdot) \in V, \quad [u]_m := u_m^+ - u_m^- \in V.$$

Starting point for all Galerkin formulations of the parabolic equation (3.1) is the following Lemma:

Lemma 44 (Galerkin formulation of parabolic equations). *Let $f \in C(I; L^2(\Omega))$. The following three formulations are equivalent:*

1. Find $u \in X^1$ such that

$$\begin{aligned} t \geq 0 : \quad (u'(t), \phi)_\Omega + a(u(t), \phi) &= (f(t), \phi)_\Omega \quad \forall \phi \in V, \\ (u(0) - u^0, \phi)_\Omega &= 0 \quad \forall \phi \in V. \end{aligned} \tag{3.6}$$

2. Find $u \in X^1$ such that:

$$\begin{aligned} \int_I \left\{ (u'(t), \phi(t))_\Omega + a(u(t), \phi(t)) \right\} dt &= \int_I (f(t), \phi(t))_\Omega dt \quad \forall \phi \in X^0, \\ (u(0) - u^0, \phi)_\Omega &= 0 \quad \forall \phi \in V. \end{aligned} \tag{3.7}$$

3. Find $u \in X_I^1$ such that:

$$\begin{aligned} \sum_{m=1}^M \int_{I_m} \left\{ (u'(t), \phi(t))_\Omega + a(u(t), \phi(t)) \right\} dt + ([u]_{m-1}, \phi_{m-1}^+)_\Omega \\ = \sum_{m=1}^M \int_{I_m} (f(t), \phi(t)) dt \quad \forall \phi \in X_I^0, \end{aligned} \tag{3.8}$$

where $u_0^- := u^0$.

Proof. (i) $1 \Rightarrow 2$: Let $\phi \in X$ be arbitrary. Then, $\phi(t, \cdot) \in V$ for every $t \geq 0$ and by integration of (3.6) over $I = [0, T]$, we get (3.7).

(ii) $1 \Rightarrow 3$: Let $\phi \in X_I^1$ be arbitrary. Then, $\phi(t, \cdot) \in V$ for every $t \neq t_m$. For $t = t_m$ it holds that $\phi(t_m, \cdot) = \phi_m^+ \in V$. Further, all jumps are zero $[u]_m = 0$ as $x \in X^1$. Now, (3.8) follows by the same argument as given in the previous step.

(iii) $2 \Rightarrow 1$: Let $u \in X^1$ be solution of (3.6). By $\xi_\epsilon^y \in C^\infty(I)$ we choose a Dirac sequence with the property

$$\int_I \xi_\epsilon^y(t) f(t) dt \xrightarrow[\epsilon \rightarrow 0]{} f(y).$$

By testing (3.7) with $\phi(x, t) := \xi_\epsilon^y(t)\phi(x)$ for a given $\phi \in V$ the results follows for $\epsilon \rightarrow 0$.

(iv) $3 \Rightarrow 1$: Let $t \in I_m$. By picking a Dirac sequence $\xi_\epsilon^y \in C_c(I_m)$ it follows (like in step (iii)) that (3.6) holds in a point-wise sense. Next, let $t = t_m$ for a given $m \in \mathbb{N}$. We choose a sequence $\xi_\epsilon^m \in C_c(I_m)$ such that:

$$\xi_\epsilon^m(t_{m-1}) = 1, \quad \xi_\epsilon^m(t) \xrightarrow[\epsilon \rightarrow 0]{} 0 \quad (t \neq t_{m-1}).$$

Then, by choosing $\phi(x, t) = \xi_\epsilon^m(t)\phi(x)$ it follows from (3.8) that

$$([u]_{m-1}, \phi)_\Omega = 0 \quad \forall \phi \in V,$$

and that $[u]_{m-1} = 0$ and hence $u \in C(I) \cap X_I^1$. **show that $u \in X^1$** . \square

Discontinuous Galerkin methods

Let $P^r(I; V)$ be the polynomial space of degree r in time with values in V :

$$P^r(I; V) := \{\phi : I \times \Omega \rightarrow \mathbb{R}, \phi = \sum_{s=0}^r \phi_s t^s, \phi_s \in V\}.$$

A conforming discontinuous Galerkin formulation of (3.8) is given by restricting test- and trial-spaces to

$$X_k^{r,\text{dc}} := \{\phi \in X_I^1, \phi|_{I_m} \in P^r(I_m; V)\},$$

and finding $u_k \in X_k^{r,\text{dc}}$ such that

$$\begin{aligned} \sum_{m=1}^M \int_{I_m} \left\{ (u'_k(t), \phi_k(t))_\Omega + a(u_k(t), \phi_k(t)) \right\} dt + ([u_k]_{m-1}, \phi_{m-1}^+)_\Omega \\ = \sum_{m=1}^M \int_{I_m} (f(t), \phi_k(t)) dt \quad \forall \phi_k \in X_k^{r,\text{dc}}. \end{aligned}$$

Since solution $u_k \in X_k^{r,\text{dc}}$ and test-function $\phi_k \in X_k^{r,\text{dc}}$ are discontinuous at every t_m , the equation decouples and can be written in form of a time-stepping scheme:

$$\begin{aligned} \text{for } m = 1, \dots, M \text{ find } u_k|_{I_m} \in P^r(I_m; V) \\ \int_{I_m} \left\{ (u'_k(t), \phi_k(t))_\Omega + a(u_k(t), \phi_k(t)) \right\} dt + ([u_k]_{m-1}, \phi_{k,m-1}^+)_\Omega \\ = \int_{I_m} (f(t), \phi_k(t))_\Omega dt \quad \forall \phi_k \in P^r(I_m; V). \quad (3.9) \end{aligned}$$

As example, we consider the most simple case of a dG(0)-discretization with piece-wise constant trial- and test-functions

$$u_k|_{I_m} =: u_k^m \in V, \quad \phi_k|_{I_m} =: \phi_k^m \in V,$$

where u_k and ϕ_k are piece-wise constant such that it holds:

$$\phi_{k,m-1}^+ = \phi_k^m, \quad [u_k]_{m-1} = u_k^m - u_k^{m-1}.$$

The time derivative $u'_k = 0$ is zero on every interval I_m , hence the Galerkin formulation is simplified to finding $u_k^m \in V$ such that for $m = 1, 2, \dots, M$ it holds

$$(u_k^m - u_k^{m-1}, \phi_k^m)_\Omega + k_m a(u_k^m, \phi_k^m) = \int_{I_m} (f(t), \phi_k^m) dt \quad \forall \phi_k^m \in V. \quad (3.10)$$

Apart from the integral over the right hand side function $f(t)$, this is exactly the implicit Euler scheme. By approximating the integral with the right-sided box scheme

$$\int_{I_m} (f(t), \phi_k^m)_\Omega dt = k_m (f(t_m), \phi_k^m)_\Omega + O(k_m^2),$$

we recover the implicit Euler method even for non-autonomous equations.

Remark 17 (Equivalence between Galerkin and time-stepping methods). *As shown, the dG(0)-Galerkin method is equivalent to the backward Euler scheme, if the equation, namely $a(\cdot, \cdot)$, is linear, and if the problem is autonomous without explicit dependency on the time t . For nonlinear equations or with time-depending right hand side $f(t)$ (or operator $a(t)(\cdot, \cdot)$) equivalency between the Galerkin scheme and the time-stepping scheme is only up to numerical quadrature error. In the case of the implicit Euler method, this quadrature error is of second order in k_m .*

Remark 18 (dG(r)-Galerkin formulations and Padé approximations). *It can be shown, that all dG(r) discretizations of the model problem correspond to a sub-diagonal ($r+2, r+1$) Padé approximation of the exponential function, see [191]. Hence, we know that these approximations have optimal order:*

$$|R(z) - \exp(z)| = O(k^{2r+2}).$$

This relation shows the optimal super-convergence order of discontinuous Galerkin methods when applied to linear autonomous problems. See [223] for the general proof of this super-convergence property. Further, it is well known, that for every $(r, r+1)$ Padé approximation there exists an implicit Runge-Kutta method with the same amplification factor $\|J\|$. This connection is guideline for the general approach: the parabolic equation is solved using an efficient time-stepping scheme (e.g. a Runge-Kutta method), the error estimate is derived by using the correspondence to a Galerkin method that allows for residual based techniques. If Galerkin method and time-stepping scheme differ by a numerical quadrature error, this additional error must taken into account. See Section 7.1.2 for details.

The effort for approximating a parabolic equation with a discontinuous Galerkin method is considerably larger than by using a single-step method. The local dG(r) solution has $r+1$ local degrees of freedom

$$u_k \Big|_{I_m} = \sum_{s=0}^r u_k^s t^s,$$

that all couple to each other in every time-step of (3.9). Considering parabolic equations (and not simple initial value problems) the spatial discretization has to be taken into account. $r+1$ degrees of freedom in time must be multiplied with $N := \text{div } V_h$ degrees of freedom in space coming from the finite element (or finite difference) discretization. Where the implicit Euler or θ -scheme asks for the solution of a $N \times N$ linear system, the dG(r) method requires to solve a coupled $(r+1)N \times (r+1)N$ linear system of equations. This huge effort - in terms of

computational time as well as memory - is usually not feasible. In [191], the authors describe an approximation scheme for splitting the large linear system into a sequence of small $N \times N$ systems.

Continuous Galerkin methods

Continuous Galerkin find the solution u_k in spaces of continuous functions:

$$X_k^r := \{\phi \in C(I; V), \phi|_{I_m} \in P^r(I_m; V)\}.$$

These functions are not globally differentiable, hence $u_k \notin X_f^1$ and even tho the approach yields a continuous solution, the discrete scheme is based on (3.8). However, for $u_k \in X_k^r$ it holds $[u_k]_m = 0$. We should not choose the space X_k^r as test-space, as this would result in a globally coupled system of equations for all time intervals I_m . Further, the discretization of a parabolic problem in times relates to a continuous Galerkin formulation of a transport equation, that is known to be numerically unstable, see Section 3.4.3.

Instead, we decouple the different time steps, by combining the continuous functions $u_k \in X_k^r$ with discontinuous test-functions $\phi_k \in X_k^{r-1,\text{dc}}$. Both spaces have the same number of degrees of freedom, as for u_k one freedom per interval is reserved to guarantee continuity. This coupled $X_k^r - X_k^{r-1,\text{dc}}$ approach will be called the cG(r)-discretization.

Due to global continuity of u_k , the minimal polynomial degree is one, combined with piece-wise constant test-functions. On I_m , we denote u_k and ϕ_k as:

$$u_k|_{I_m} = u_k^{m-1} \frac{t_m - t}{t_m - t_{m-1}} + u_k^m \frac{t - t_{m-1}}{t_m - t_{m-1}}, \quad \phi_k|_{I_m} =: \phi_k^m \in V,$$

where $u_k^m \in V$. As the trial-functions are piece-wise linear, the time-derivative is simply given by

$$\int_{I_m} (u'(t), \phi_k^m)_\Omega dt = (u_k^m - u_k^{m-1}, \phi_k^m)_\Omega.$$

Further, it holds

$$\int_{I_m} \frac{t_m - t}{t_m - t_{m-1}} dt = \frac{t_m - t_{m-1}}{2}, \quad \int_{I_m} \frac{t - t_{m-1}}{t_m - t_{m-1}} dt = \frac{t_m - t_{m-1}}{2}.$$

By these relations, the cG(1)-Version of (3.7) simplifies to solving for $m = 1, 2, \dots, M$

$$(u_k^m - u_k^{m-1}, \phi_k^m)_\Omega + \frac{k_m}{2} a(u_k^m, \phi_k^m) + \frac{k_m}{2} a(u_k^{m-1}, \phi_k^m) = \int_{I_m} (f(t), \phi_k^m)_\Omega dt,$$

for all test-function $\phi_k^m \in V$. If the right hand side $f(t)$ is piece-wise constant, or if we approximate the integral on the right hand side by the trapezoidal rule, we recover the Crank-Nicolson method for time-stepping.

Remark 19 (cG(r)-Galerkin formulations and Padé approximations). *The amplification factor of the Crank-Nicolson method is the diagonal (2, 2)-Padé approximation of the exponential function. It can be shown, that every cG(r)-Galerkin formulation applied to a linear autonomous problem is equivalent to a time-stepping method with amplification factor that corresponds to the $(r+1, r+1)$ Padé approximation. Hence, the nodal accuracy of the cG(r) formulation is $O(k^{2r})$.*

It shows, that it is also possible to derive Galerkin-formulation of non-standard discretization schemes, like the one-step θ method or even the fractional step θ scheme, see [160, 209]. Formally, the θ scheme can be derived by combining piece-wise linear and continuous trial-functions $u_k \in X_I^1$ with discontinuous θ -weighted test-functions:

$$\phi_k^\theta|_{I_m} = 1 + \frac{6}{k_m} (2\theta - 1) \left(t - \frac{t_{m-1} + t_m}{2} \right). \quad (3.11)$$

For $\theta = \frac{1}{2}$, it simply holds $\phi_\theta^m \equiv 1$ and we recover the Crank-Nicolson method. For arbitrary $\theta \in [0, 1]$ it holds for $u_k \in X_k^1$:

$$\begin{aligned} \int_{I_m} u'_k(t) \cdot \phi_k^\theta(t) dt &= u_k^m - u_k^{m-1}, \\ \int_{I_m} u_k(t) \cdot \phi_k^\theta(t) dt &= \theta k_m u_k^m + (1 - \theta) k_m u_k^{m-1}. \end{aligned}$$

This way, the θ time-stepping method can be reconstructed for linear autonomous problems. For the general non-linear case we must again rely on numerical quadrature. Here, the θ time-stepping method is obtained by approximating all integrals with the quadrature rule

$$\int_{I_m} f(t) \phi_k^\theta(t) dt = \theta k_m f(t_m) + (1 - \theta) k_m f(t_{m-1}) + O(k_m^3).$$

3.1.4 Time discretization of the Stokes and Navier-Stokes equations

The incompressible Stokes and Navier-Stokes equations are of saddle-point type, with a pressure variable $p \in L$, that has no physical role but serves as Lagrange-multiplier to guarantee the divergence condition. Given an initial value $v(0, \cdot) = v^0(\cdot)$, we find $\{v, p\} \in V \times L$ such that

$$(\partial_t v, \phi) + (\nabla v, \nabla \phi) - (p, \nabla \cdot \phi) + (\nabla \cdot v, \xi) = (f, \phi) \quad \forall \{\phi, \xi\} \in V \times L.$$

Again, by $0 = t_0 < \dots < t_M = T$ we denote the discrete time-steps. We aim at deriving the Crank-Nicolson (or general θ) method for this set of equations. The first obvious choice for defining the time-stepping method is to iterate:

$$\begin{aligned} (v_k^m - v_k^{m-1}, \phi) + \frac{k_m}{2} \{ (\nabla v_k^m, \nabla \phi) - (p_k^m, \nabla \cdot \phi) + (\nabla \cdot v_k^m, \xi) \} \\ + \frac{k_m}{2} \{ (\nabla v_k^{m-1}, \nabla \phi) - (p_k^{m-1}, \nabla \cdot \phi) + (\nabla \cdot v_k^{m-1}, \xi) \} \\ = \frac{k_m}{2} (f(t_{m-1}) + f(t_m), \phi). \end{aligned}$$

This formulation however does not properly reflect the role of the pressure as Lagrange multiplier. As the old pressure p^{m-1} enters each time-step, it will also influence the new solution. Since the continuous pressure usually comes without temporal regularity, such a relationship between old and new pressure could lead to unphysical solutions. Further, by testing with $\xi = \nabla \cdot v_k^{m-1}$ we get the relation:

$$\|\nabla \cdot v_k^{m-1}\|^2 = (\nabla \cdot v_k^m, \nabla \cdot v_k^{m-1}) \leq \|\nabla \cdot v_k^m\| \|\nabla \cdot v_k^{m-1}\|,$$

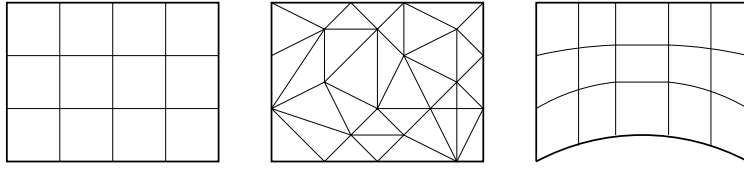


Figure 3.1: Different triangulations Ω_h for a domain $\Omega \subset \mathbb{R}^2$. From left to right: structured quadrilateral mesh, unstructured triangular mesh and structured quadrilateral mesh using curved parametric elements.

that turns to

$$\|\nabla \cdot v_k^m\| \geq \|\nabla \cdot v_k^{m-1}\|.$$

By testing with $\xi = \nabla \cdot v_k^m$ we obtain the estimate in the opposite direction, such that it holds:

$$\|\nabla \cdot v_k^m\| = \|\nabla \cdot v_k^{m-1}\|.$$

If the initial solution v^0 is not strictly divergence-free, this defect will be conserved for $m \rightarrow \infty$. Further, since we must expect truncation errors, there is no corrective that assures $\|\nabla \cdot v_k^m\| \rightarrow 0$. A remedy to both problems is given by first restricting the Stokes equations into the manifold of divergence free functions

$$V_0 := \{\phi \in V, \operatorname{div}(\phi) = 0\},$$

and by applying the Crank-Nicolson (or θ -scheme) on V_0 . Then, the pressure is added as Lagrange multiplier in every discrete time-step:

$$\begin{aligned} (v_k^m - v_k^{m-1}, \phi) + \frac{k_m}{2} (\nabla v_k^m, \nabla \phi) + \frac{k_m}{2} (\nabla v_k^{m-1}, \nabla \phi) \\ - (p_k^m, \nabla \cdot \phi) + (\nabla \cdot v_k^m, \xi) = k_m (\bar{f}, \phi). \end{aligned} \quad (3.12)$$

It is not possible to find a Galerkin scheme, that is equivalent to this time-stepping method. However, we get close to this formulation by using a mixed Galerkin method with continuous piece-wise linear velocities and a discontinuous, piece-wise constant pressure (of course without adding jump-terms to the discrete system). This formulation will prevent the old pressure p_k^{m-1} from entering the new time-step I_m , it however still does not strictly enforce divergence freeness in every interval.

3.2 Spatial Discretization

In this section, we introduce the necessary concepts of the finite element method for discretizing fluid-structure interactions. We start by describing finite elements for the Laplace equation

$$u \in \mathcal{V} = H_0^1(\Omega) : \quad (\nabla u, \nabla \phi)_\Omega = (f, \phi)_\Omega \quad \forall \phi \in \mathcal{V},$$

for a given right hand side $f \in H^{-1}(\Omega)$. The domain $\Omega \subset \mathbb{R}^d$ is two or three dimensional. First, we partition this domain into a triangulation (or mesh) Ω_h , consisting of open elements $K \subset \mathbb{R}^d$. These elements are simple geometric structures like triangles, quadrilaterals or tetrahedra. The boundary of each element K is piece-wise smooth with a finite number of edges $e \in K$ and nodes $x \in K$. The edges $e \in K$ are not necessarily straight, see Figure 3.1 for different triangulations. We define

Definition 11 (Structural regularity). A triangulation $\Omega_h = \{K_1, \dots, K_N\}$ of the domain $\Omega \subset \mathbb{R}^d$ is called structural regular, if the elements cover the domain

$$\bar{\Omega} = \bigcup_{n=1}^N \bar{K}_i,$$

and if each two elements different are disjoint

$$K_i \cap K_j = \emptyset \quad \forall i \neq j,$$

and if the intersection of the closure is either a common node, or a (complete) common edge

$$\bar{K}_i \cap \bar{K}_j = \begin{cases} \emptyset & \text{or,} \\ e \in K_i \text{ and } e \in K_j & \text{or,} \\ x \in K_i \text{ and } x \in K_j. \end{cases}$$

It is obvious, that a curved domain $\Omega \subset \mathbb{R}^d$ cannot be triangulated with geometric structures like triangles. Instead we must use meshes with curved elements, as shown in Figure 3.1 (right). A common approach for curved finite element meshes is to base every element $K \in \Omega_h$ on one common reference element \hat{K} :

Definition 12 (Parametric triangulation). Let $\hat{K} \in \mathbb{R}^d$ be the reference element. Further, let $\hat{P}(\hat{K})$ be a d -dimensional function space. A triangulation Ω_h is called parametric, if every element $K \in \Omega_h$ arises from the mapping of the reference element:

$$\forall K \in \Omega_h \text{ there exists a } T_K \in \hat{P}(\hat{K}) \text{ such that } K = T_K(\hat{K}).$$

Usually, for the reference element \hat{K} one chooses the unit triangle, the unit quad or the unit hex. If the space $\hat{P}(\hat{K})$ is the space of affine mappings, the parametric triangulation Ω_h will consist of standard elements with straight edges only. If we consider mappings $\hat{P}(\hat{K})$ of higher polynomial degree (or even rational functions), we can generate curved elements, that can be used to approximate domains with curved boundaries. Next, we define conditions on the shape of each element:

Definition 13 (Shape regularity of triangular meshes). A family of meshes Ω_h , $h > 0$ is called shape regular, if there exists a constant $c > 0$, independent on $h > 0$, such that

$$\max_{K \in \Omega_h} \frac{h_K}{\rho_K} \geq c,$$

where by $h_K := \text{diam}(K)$ we denote the diameter of K and by ρ_K the radius of the largest inscribed circle.

Shape regularity of a sequence of meshes describes that all triangles have approximately the same shape. It holds

Lemma 45 (Shape regularity of triangular meshes). For a family of triangular meshes Ω_h , $h > 0$ the following conditions are equivalent

1. The family of meshes is shape regular according to Definition 13.

3.2. Spatial Discretization

2. (Minimum angle condition) *There exists a constant $c > 0$ independent of $h > 0$, such that all interior angles are bound away from zero $\alpha \geq c$.*
3. (Maximum angle condition) *There exists a constant $c > 0$ independent of $h > 0$, such that all interior angles are bound away from π by $\alpha \leq \pi - c$.*

Proof. See Problem 31. □

Describing suitable shape regularity conditions for other types of finite element meshes is more complicated. Already for quadrilateral meshes one must combine minimum and maximum angle conditions to prevent that quadrilaterals can degenerate to triangles. Instead we introduce a more general concept of shape regularity, that can be applied to all kinds of parametric meshes (remember that triangular and quadrilateral meshes are also easy types of parametric meshes):

Definition 14 (Shape regularity of parametric meshes). *A family parametric mesh Ω_h , $h > 0$ with reference element \hat{K} is called shape regular, if there exists a constant $c > 0$, such that it holds independent on $h > 0$*

$$\|\nabla T_K\| \|(\nabla T_K)^{-1}\| \leq c \quad \forall K \in \Omega_h,$$

where $T_K : \hat{K} \rightarrow K$ is the reference map for element $K \in \Omega_h$.

This definition of shape regularity is less obvious, it however is directly usable for deriving interpolation estimates. These estimates are usually shown on fixed reference elements \hat{K} and then carried over to a specific $K \in \Omega_h$ by using this reference mapping. For triangular meshes, we can show that this general definition is equivalent to those given in Lemma 45:

Lemma 46. *Let Ω_h be a triangular mesh. The condition of Definition 14 is equivalent to those given in Lemma 45.*

Proof. Stimmt das? A triangular mesh can be considered as parametric mesh with affine transformation from the reference triangle $\hat{K} = \{(x, y), 0 < x + y < 1\}$. Let $z_i = (x_i, y_i)$, $i = 1, 2, 3$ be the three nodes of the triangle K in counter clock-wise sense, where $z_1 = (0, 0)$. Then, the mapping T_K is given by

$$T_K(x, y) = z_2x + z_3y, \quad \nabla T_K = \begin{pmatrix} x_2 & x_3 \\ y_2 & y_3 \end{pmatrix}, \quad \nabla T_K^{-1} = \frac{1}{x_2y_3 - x_3y_2} \begin{pmatrix} y_3 & -x_3 \\ -y_2 & x_2 \end{pmatrix}.$$

□

Remark 20 (Boundary approximation). *Most commonly, one considers polynomial spaces for the element maps T_K . Such a mapping allows for higher order representation of curved boundaries, see Figure 3.1. A more recent approach is the Isogeometric Analysis: the geometrical domains in application problems are usually designed with the help of CAD-programs. These programs use splines (NURBS) for representing the domain. The Isogeometric Analysis uses these splines for defining the finite element mesh and the discrete finite element spaces. By this construction, every geometrical error is eliminated, see Bazilevs et al. [17].*

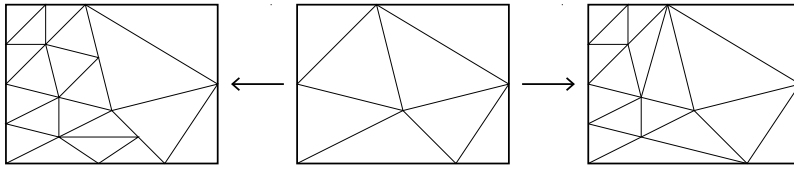


Figure 3.2: Different types of mesh-refinement. Left: refinement of a triangle into three triangles using hanging nodes. Right: using different refinement types such that no hanging nodes appear.

The quality and the resolution of the finite element mesh will determine the accuracy of the finite element approximation. Constructing a finite element mesh of a domain $\Omega \subset \mathbb{R}^d$ can be a very difficult task. In particular for complex technical structures, a mesh can consist of millions of elements just for resolving the complex geometry. Further, it is possible, that this complex mesh will not have the proper resolution at the correct spots to deliver good approximative solutions. In such cases, a mesh must be *refined*. Refining a mesh is either done by *remeshing* and constructing a completely new triangulation with better resolution in certain areas or by *mesh refinement*. Here, elements of a mesh are split into smaller elements. By mesh refinement, we usually must break the structural regularity assumption. In Figure 3.2, we show different procedures for mesh refinement. While the left sketch shows a refinement that does not satisfy the structural-regularity condition, it is simple as every triangle can be split in the same way. The right refinement type yields shape regular meshes, different types of refinement must however be used depending on the refinement topology of a triangle. If we consider quadrilateral meshes one always uses a simple refinement model, where each quad is split into four smaller quads. A shape-regular refinement is only possible, if quadrilateral elements are coupled with triangular elements.

If refinement techniques are used that generate non-shape regular meshes, nodes on the middle of edges appear. These nodes will be called *hanging nodes* and must be treated with special care when constructing finite element spaces. We will allow for meshes with one hanging node on an edge only. A mesh without hanging nodes and with element that all have approximately the same size is called a *uniform mesh*. A mesh with areas of mesh refinement is called a *locally refined mesh*.

If the boundaries Γ of the domain $\Omega \subset \mathbb{R}^d$ are not polygonal, a triangulation into simplices will not match the domain

$$\Omega \neq \bigcup_{K \in \Omega_h} K,$$

and a geometric error will occur. For better approximation of *curved domains*, the element mapping T_K must not be affine, but is allowed to have a higher degree. Figure 3.1 (right) shows the approximation of a circular domain with a quadrilateral mesh using affine mappings and a quadrilateral mesh using a piece-wise biquadratic mapping.

3.2.1 Finite Elements

Finite element spaces V_h are defined locally on the elements $K \in \Omega_h$ of the mesh Ω_h . The most basic finite element mesh on a triangular mesh is the space of piece-wise linear functions

$$V_h = \{\phi \in C(\bar{\Omega}), \phi|_K \in \text{span}\{1, x, y\} \forall K \in \Omega_h\}.$$

On every triangle $K \in \Omega_h$, the finite element space is locally constructed by three basis-functions $\phi_K^1, \phi_K^2, \phi_K^3$ such that for the three nodes x_K^1, x_K^2, x_K^3 it holds $\phi_K^j(x_K^i) = \delta_{ij}$. These basis functions are glued together with the basis functions of neighboring elements.

Such a local construction of finite element spaces is difficult on general elements, like quadrilaterals that arise from the transformation of a reference element. A more general approach uses parametric finite elements, where the basis is defined on the reference element \hat{K} . As reference elements, we consider the reference triangle or quad in two dimensions and the reference tetrahedra or hex in three dimensions. Let

$$\hat{P}^r := \text{span} \{x^\alpha, 0 \leq \alpha_i \leq r\}, \quad \hat{Q}^r := \text{span} \{x^\alpha, 0 \leq \alpha_i \leq r\}, \quad (3.13)$$

where $\alpha \in \mathbb{N}^d$ is a multi-index. By $\{\phi_1, \dots, \phi_n\}$ we denote a basis of these polynomial spaces. Besides the usual monomial basis functions $\phi_\alpha = x^\alpha$, we make use of nodal basis functions: let $\hat{x}_i \in \hat{K}$ be uniformly distributed piecewise distinct points in \hat{K} . Then, the nodal basis functions $\hat{\phi}_i \in \hat{P}^r$ (or $\hat{\phi}_i \in \hat{Q}^r$) are defined by the property

$$\hat{\phi}_i(\hat{x}_j) = \delta_{ij}, \quad i, j = 1, \dots, n.$$

In Figure ?? we show typical distributions of the nodes for different reference elements and indicate the corresponding polynomial space.

By this notation, we can define the nodal basis functions $\phi_i, i = 1, \dots, n$ for every mesh-element $K \in \Omega_h$ by using the domain-mapping:

$$\phi_i^K := \hat{\phi}_i \circ T_K^{-1}, \quad i = 1, \dots, n.$$

If the element map $T_K : \hat{K} \rightarrow K$ is affine, the resulting basis functions are polynomials in the same space as the reference basis. For general polynomial mapping however, the nodal basis usually consists of rational functions. In the mesh-nodes $x_i^K := T_K(\hat{x}_i^K)$ it holds $\phi_i^K(x_j) = \delta_{ij}$. The global finite element space of order r is then given by

$$V_h^r := \{\phi \in C^0(\bar{\Omega}) : \phi|_K \circ T_K \in P^r \text{ (or } Q^r)\} = \text{span}\{\phi_i, i = 1, \dots, N\},$$

where the basis functions ϕ_i are given by gluing the local basis functions ϕ_i^K together. Finite element spaces with global continuity are H^1 -conforming $V_h \subset \mathcal{V} = H^1(\Omega)$. Sometimes, we do not require this H^1 -conformity. Considering the Navier-Stokes equations, the pressure must only be discretized with L^2 -conforming finite elements, that are not necessarily continuous. Here, we introduce discontinuous finite element spaces:

$$V_h^{r,\text{dc}} := \{\phi \in L^2(\Omega) \rightarrow \mathbb{R} : \phi|_K \in P^r \text{ (or } Q^r), \forall K \in \Omega_h\}.$$

This space is not H^1 -conforming, but at least L^2 -conforming. Continuous finite element spaces using the element mapping T_K are called *parametric finite elements*. If the element-mapping is a polynomial from the same polynomial space P^r or Q^r as the reference space, the approach is called *iso-parametric*.

Interpolation operators $I_h : V \rightarrow V$ are the most important tool for finite element error analysis since due to their local construction they allow for a local analysis. Usually, we distinguish

between two types of interpolation operators. The nodal interpolant N_h of a function $u : K \rightarrow \mathbb{R}$ is constructed by a simple point-wise process on every element:

$$N_h u(x) = \sum_{i=1}^L u(x_i^K) \phi_i^K(x)$$

Nodal interpolants are completely local, only information on one element $K \in \Omega_h$ is required. They are however only well-defined for functions $u \in C(\bar{K})$. This is not the case for the Sobolev-space H^1 . Here, single point-values must not be finite. If we require interpolants of functions with such minimal regularity, we must replace the point-evaluation $u(x_i^K)$ by some kind of averages.

Lemma 47 (Nodal interpolation on $K \in \Omega_h$). *Let $K \in \Omega_h$ and $T_K : \hat{K} \rightarrow K$ and $u \in H^{r+1}(K)$. Then, it holds:*

$$\|\nabla^k(u - N_h u)\|_K \leq h^{r+1-k} \|\nabla^{r+1} u\|_K, \quad 0 \leq k \leq r,$$

and on the boundary of K :

$$\|u - N_h u\|_{\partial K} \leq h^{r+\frac{1}{2}} \|\nabla^{r+1} u\|_K.$$

Proof. For the proof, we refer to the literature []. □

The nodal interpolation operator $N_h : u \rightarrow N_h u$ is only well-defined, if $u \in C(\bar{\Omega})$. Point values of u must be accessible. For H^1 -functions, this regularity is not necessarily given, see Section 1 and the nodal interpolation can never be H^1 -stable. For $u \in H^1(\Omega)$, interpolation operators must be defined in terms of averages. The most famous H^1 -stable interpolation operator is the *Clement-Interpolation*:

Lemma 48 (Clement-Interpolation). *Let $u \in H^1(\Omega)$ and $V_h \subset H^1(\Omega)$ be a finite element space on the triangulation Ω_h . Then, there Clement-Interpolation $C_h u \in V_h$ is H^1 -stable*

$$\|\nabla C_h u\| \leq c \|\nabla u\| \quad \forall u \in H^1(\Omega),$$

where by $\chi_i(u)$ we denote the local patch-average of u :

$$\chi_i(u) := \frac{1}{|P_i|} \int_{P_i} u \, dx, \quad P_i := \bigcup_{K \in \Omega_h, x_i \in \bar{K}} K.$$

It holds:

$$\|\nabla C_h u\|_K \leq c_1 \|\nabla u\|_{P_K}, \quad P_K := \bigcup_{L \in \Omega_h, \bar{L} \cap \bar{K} \neq \emptyset} L.$$

Proof. The proof easily follows by showing stability of the node functionals $\xi_i(\cdot)$ and using Bramble-Hilbert Lemma. See [70]. □

Remark 21 (Interpolation on anisotropic meshes). *The Clement interpolation is an H^1 -stable operator*

$$\|\nabla C_h u\|_K \leq c \|\nabla u\|_{P_K},$$

3.2. Spatial Discretization

with a constant $c > 0$, that does not depend on $h > 0$. The Clement operator however fails, if the mesh-elements $K \in \Omega_h$ are anisotropic with $h_{\min}(K) \ll h_{\max}(K)$. On such elements, it only holds

$$\|\nabla C_h u\|_K \leq c \frac{h_{\max}(K)}{h_{\min}(K)} \|\nabla u\|_{P_K}.$$

An alternative to the Clement operator, that is H^1 stable also on anisotropic meshes is the Scott & Zhang operator. Here, the nodal values are also defined as averages, but averaging is only applied over edges of elements. This helps to avoid mixing of mesh-sizes in different directions. See [208] for basics on the Scott & Zhang interpolation operator, and [4] for an analysis of interpolation operators on anisotropic meshes.

3.2.2 Finite Element Analysis for Elliptic Problems

Let $\mathcal{V} = H_0^1(\Omega)$ and $V_h \subset \mathcal{V}$ be a finite element subspace. By $a(\cdot, \cdot) : \mathcal{V} \times \mathcal{V} \rightarrow \mathbb{R}$ we denote an elliptic and continuous bilinear-form, such that there exist constants $c_1, c_2 > 0$ such that

$$a(u, v) \leq c_1 \|\nabla u\|_\Omega \|\nabla v\|_\Omega, \quad a(u, u) \geq c_2 \|\nabla u\|^2.$$

This bilinear-form defines a the *energy norm*

Lemma 49 (Energy norm). *Let $a(\cdot, \cdot)$ be a \mathcal{V} -elliptic and continuous bilinear form. Then,*

$$\|u\|_a := \sqrt{a(u, u)},$$

defines a norm, that is equivalent to the \mathcal{V} -norm.

For $f \in H^{-1}(\Omega)$ we denote by $u \in \mathcal{V}$ and $u_h \in V_h$ solutions to

$$a(u, \phi) = (f, \phi) \quad \forall \phi \in \mathcal{V}, \quad a(u_h, \phi_h) = (f, \phi_h) \quad \forall \phi_h \in V_h. \quad (3.14)$$

It holds

Lemma 50 (Galerkin orthogonality). *For the solution $u \in \mathcal{V}$ and the conforming Galerkin-solution $u_h \in V_h \subset \mathcal{V}$ it holds*

$$a(u - u_h, \phi_h) = 0 \quad \forall \phi_h \in V_h.$$

Proof. This follows by $V_h \subset \mathcal{V}$. □

Using Galerkin orthogonality we can directly show the following important property:

Lemma 51 (Best approximation, Cea's Lemma). *The conforming finite element approximation is the best approximation in the energy norm $\|u\|_a := \sqrt{a(u, u)}$*

$$\|u - u_h\|_a = \min_{\phi \in V_h} \|u - \phi\|_a,$$

and it holds

$$\|\nabla(u - u_h)\| \leq$$

Proof. This essential results follows by use of Galerkin orthogonality

$$c_2^2 \|\nabla(u - u_h)\|^2 \leq a(u - u_h, u - u_h) = a(u - u_h, u - \phi_h) \leq c_1 \|u - u_h\|_a \|u - \phi_h\|$$

□

Using this best-approximation property, and choosing $\phi_h := I_h u \in V_h$ as interpolation, we get a first error estimate:

Lemma 52 (Energy norm a priori estimates). *Let $u \in H^{r+1}(\Omega) \cap V$ be the solution to (3.14), and $u_h \in V_h^r \subset V$ be the finite element solution. It holds:*

$$\|\nabla(u - u_h)\| \leq ch^r \|\nabla^{r+1}u\|.$$

Proof. This result follows by combining best approximation and interpolation estimates. □

Lemma 53 (L^2 -norm a priori error estimate). *Let $u \in H^{r+1}(\Omega) \cap V$ and $u_h \in V_h^r$ be solutions to (3.14). Then, it holds*

$$\|u - u_h\| \leq ch^{r+1} \|\nabla^{r+1}u\|.$$

Proof. Let $z \in V$ be the solution to the adjoint problem

$$a(\phi, z) = l(\phi) \quad \forall \phi \in V, \quad l(\phi) := \frac{(u - u_h, \phi)}{\|u - u_h\|}.$$

It holds, that $l : L^2(\Omega) \rightarrow \mathbb{R}$, hence given sufficient solution of the domain it holds $z \in H^2(\Omega) \cap V$ and

$$\|z\| \leq c_s \|l\| = c_s.$$

We choose $\phi = u - u_h$ to get by using Galerkin orthogonality:

$$\begin{aligned} \|u - u_h\| &= a(u - u_h, z) = a(u - u_h, z - I_h z) \leq cc \|\nabla(u - u_h)\| \|\nabla(z - I_h z)\| \\ &\leq ch^r \|\nabla^{r+1}u\| c_I h \|\nabla^2 z\| \leq ch^{r+1} \|\nabla^{r+1}u\|. \end{aligned}$$

□

3.2.3 Finite Elements on Curved domains

The standard finite element analysis is heavily depending on the conformity of the Galerkin approach $V_h \subset V$ which is essential for getting Galerkin-Orthogonality. If the domain Ω is curved and cannot be matched by the finite element mesh $\Omega_h \neq \Omega$, the finite element space will not be conforming. In this section, we shortly discuss the approximation of the Laplace problem

$$u \in H_0^1(\Omega) : \quad (\nabla u, \nabla \phi)_\Omega = (f, \phi)_\Omega \quad \forall \phi \in H_0^1(\Omega), \quad (3.15)$$

on a domain $\Omega \subset \mathbb{R}^d$ that is curved and smooth, i.e., the boundary $\partial\Omega$ locally allows for a C^{r+1} -parametrization, with $r \in \mathbb{N}_+$. Finite elements on curved domains must deal with two difficulties:

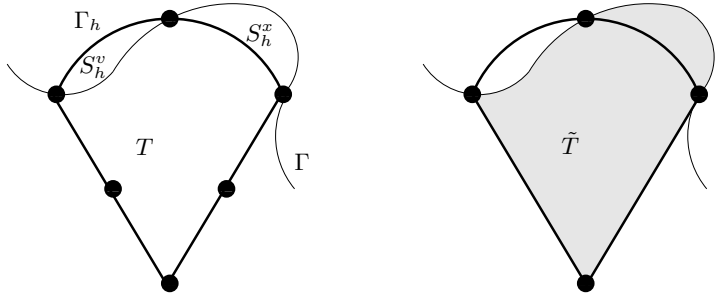


Figure 3.3: Left: geometric remainders for curved boundary approximation. Definition of the mesh snippets $S_h^v = \Omega_h \setminus \Omega$ and $S_h^x = \Omega \setminus \Omega_h$. Right: definition of the curved extended element \tilde{T} fitting the domain Ω . Exemplarily for quadratic iso-parametric elements.

1. A polygonal mesh will never exactly match the domain Ω . Hence, the discrete equation

$$u_h \in V_h : \quad (\nabla u_h, \nabla \phi_h)_{\Omega_h} = (\tilde{f}, \phi_h)_{\Omega_h} \quad \forall \phi_h \in V_h,$$

is given on a different domain. The right hand side f must not even be defined on all of Ω_h (this is the case, if the domain Ω has concave parts, where Ω_h stretches out of Ω). For details, we refer to Remark 22.

2. The boundary conditions cannot be exactly satisfied. Here, we consider homogenous Dirichlet conditions only. While $u \in H_0^1(\Omega)$ is zero on all of $\partial\Omega$, $u_h \in V_h$ is zero in the boundary nodes on $\partial\Omega$ but otherwise, it is zero on $\partial\Omega_h \neq \partial\Omega$.

Finite element analysis on curved domains is discussed in literature [50]. **Nochmal nachsehen:**

[@articleLenoir1986](#), author = M. Lenoir, title = Optimal Isoparametric Finite Elements and Error Estimates for Domains Involving Curved Boundaries, journal = SIAM Journal on Numerical Analysis, volume = 23, number = 3, pages = 562-580, year = 1986,

Nevertheless, we give details here, as these techniques will be required for an analysis of interface problems as the Fully Eulerian formulation, where the interior interface \mathcal{I} cannot be resolved by the mesh, see Section 3.5. Furthermore, we are not aware of a simple and general proof for optimal error estimates of isoparametric elements.

To cope with the two problems mentioned above, we will start by stating some definitions and lemma. Parts of the boundary can be convex or concave. We define the remainders by

$$S_h^x = \Omega \setminus \Omega_h, \quad S_h^v = \Omega_h \setminus \Omega, \quad S_h = S_h^x \cup S_h^v. \quad (3.16)$$

For a parametric triangulation Ω_h of Ω , see Definition 12, it holds

Lemma 54 (Isoparametric triangulation of Curved domains). *Let $\Omega \subset \mathbb{R}^d$ be a domain with smooth boundary allowing for a C^{r+1} -parametrization with $r \geq 1$. Let Ω_h be an isoparametric mesh of Ω with polynomial degree r . For the size of the mesh snippets S_h^x, S_h^v, S_h it holds*

$$|S_h^x| = |S_h^v| = |S_h| = O(h^r).$$

Proof. This follows by simple geometrical arguments. Let $T \in \Omega_h$ be an element at the boundary and (see Figure 3.3)

$$S = (T \setminus \Omega) \cup (\Omega \setminus T).$$

Further, let $e \in \partial T$ be the (curved) edge at the boundary Γ_h . Assume, that $\psi : [0, h] \rightarrow \mathbb{R}$ is the parametrization of $\partial\Omega$ over e (see again Figure 3.3). $\psi(s)$ has $r+1$ zero's along the edge. Hence,

$$\max_{[0,h]} |\psi| \leq ch^{r+1} \max_{[0,h]} |\psi^{r+1}|.$$

Therefore, as $|e| = O(h^{d-1})$, it holds

$$|S| = O(h^{r+d}) \quad \Rightarrow \quad |S_h| = O(h^{r+1}).$$

□

The previous lemma shows, that standard finite elements will always suffer from a geometrical error. By the use of isogeometric analysis [136], this error could be completely avoided (if the domain itself has a representation by splines).

One technical difficulty is, that $u \in H_0^1(\Omega)$ and $u_h \in V_h$ are defined on different domains, such that the expression $u - u_h$ must be carefully defined. The following lemma however will show, that we give $u_h \in V_h$ a meaning also on Ω :

Lemma 55 (Boundary extension of discrete functions). *Under the assumptions of Lemma 54, $h \leq h_0 \in \mathbb{R}$ and $T \in \Omega_h$ be an element at the boundary with boundary edge $e \in \partial T$. By \tilde{T} we denote the curved triangle fitting the domain's boundary, see Figure 3.3. For $u_h \in V_h$ we define by $\tilde{u}_h|_T$ the polynomial extension of $u_h|_T$ to \tilde{T} . It holds*

$$c_1 \|u_h\|_{H^s(T)} \leq \|\tilde{u}_h\|_{H^s(\tilde{T})} \leq c_2 \|u_h\|_{H^s(T)}, \quad s = 0, 1, 2,$$

with two constants $c_1, c_2 > 0$ that do not depend on T or h .

Proof. The proof follows by equivalence of norms and scaling and further, by using:

$$|T| = |\tilde{T}| = O(h^d), \quad |(T \setminus \tilde{T}) \cup (\tilde{T} \setminus T)| = O(h^{r+d}).$$

□

In the following, we will denote \tilde{u}_h simply by u_h .

For the analysis, we need on further - trace inequality-like - estimate:

Lemma 56 (Geometric boundary error). *Let $u \in H_0^1(\Omega)$. It holds for the convex remainder S_h^x , that*

$$\|u\|_{S_h^x} \leq ch^{\frac{r+1}{2}} \|u\|_{H^1(\Omega)}.$$

Further, let $u_h \in V_h$. It holds

$$\|u_h\|_{H^s(S_h)} \leq ch^{\frac{r}{2}} \|u_h\|_{H^s(\Omega)}, \quad s = 0, 1.$$

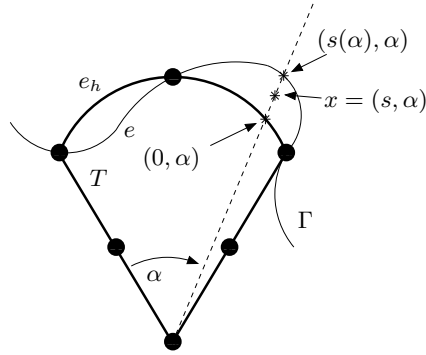


Figure 3.4: Local coordinate system on curved elements. Sketch for the proofs of Lemma 56 and 57.

Proof. For the proof, we refer to Sketch 3.4. Let $T \in \Omega_h$ be an element on the boundary, $e_h \in \partial T$ be the edge of the element, \tilde{T} the extended element and $e \in \tilde{T}$ be the edge at the boundary $\partial\Omega$. By S we denote the remainder between T and \tilde{T} .

(i) Let $x \in S$ be given as $x = (s, \alpha)$, where α is the angle and s the radial coordinate, see Figure 3.4. The local coordinate system is such, that $(0, \alpha) \in e_h \subset \Gamma_h$ is a point on the boundary of the (curved) triangle and $(s(\alpha), \alpha)$ is the corresponding point on the domain's boundary part $e \subset \Gamma$. It holds $|s(\alpha)| = O(h^{r+1})$, compare Lemma 54.

It holds

$$u(s, \alpha) = u(0, \alpha) + \int_0^s \partial_r u(t, \alpha) dt,$$

and hence

$$|u(s, \alpha)|^2 \leq c \left(|u(0, \alpha)|^2 + |s| \int_0^s |\partial_r u(t, \alpha)|^2 dt \right).$$

Integration over S (in s and α), noting, that $|s| \leq |s(\alpha)| \leq ch^{r+1}$, gives

$$\|u\|_S^2 \leq ch^{r+1} \|u\|_e^2 + h^{2r+1} \|\nabla u\|_S^2. \quad (3.17)$$

(ii) To proof the first estimate, we continue with (3.17) by summing over all boundary elements, using trace inequality and Poincaré and extending S_h^x to Ω :

$$\|u\|_{S_h} \leq ch^{\frac{r+1}{2}} \|\nabla u\|_\Omega.$$

(iii) For the second inequality, we apply the local trace inequality and extend from S to T :

$$\|u_h\|_S^2 \leq ch^{r+1} (h^{-1} \|u_h\|_T^2 + h \|\nabla u_h\|_T^2) + h^{2r+1} \|\nabla u_h\|_T^2.$$

Using the inverse inequality, we get

$$\|u_h\|_S^2 \leq ch^r \|u_h\|_T^2,$$

such that the result follows by summing over all boundary snippets. This argumentation is also valid for ∇u_h . \square

Discrete functions $\phi_h \in V_h$ are not zero on $\partial\Omega$. They are zero on $\partial\Omega_h$ and it holds:

Lemma 57 (Curved boundary error). *Let $\phi_h \in V_h$ be arbitrary. It holds*

$$\|\phi_h\|_{\partial\Omega} \leq ch^{r+\frac{1}{2}} \|\nabla\phi_h\|_{\Omega}$$

Proof. We again refer to Figure 3.4. Let $T \in \Omega_h$ and $(s(\alpha), \alpha) \in e$ be a point on the boundary of $\partial\Omega$. By $(0, \alpha) \in e_h \subset \partial T$ we denote the corresponding point on the boundary of the triangle. It holds for $\phi_h \in V_h$

$$\phi_h(s(\alpha), \alpha) = \phi_h(0, \alpha) + \int_0^{s(\alpha)} \partial_r \phi_h(t, \alpha) dt,$$

and hence by squaring and integration over α , noting, that $|s(\alpha)| = O(h^{r+1})$:

$$\|\phi_h\|_e^2 \leq \|\phi_h\|_{e_h}^2 + ch^{r+1} \|\nabla\phi_h\|_S^2. \quad (3.18)$$

Lemma 56 and noting, that $\phi_h = 0$ on e_h , gives

$$\|\phi_h\|_e^2 \leq ch^{2r+1} \|\nabla\phi_h\|_{\Omega}^2,$$

such that the result follows by summing over all boundary parts. \square

Remark 22. *Extension of the right hand side on concave domains* As discussed in the beginning of this section, problems already start with the definition of the discrete problem, as the right hand side $f : \Omega \rightarrow \mathbb{R}$ must not necessarily be defined on the discrete domain Ω_h . This issue is easily handled by defining a projection or interpolation $f_h \in V_h$ to be used as discrete right hand side. Additional terms of the type

$$(f - f_h, \phi)_{\Omega} \leq c \|f - f_h\|_{H^{-1}(\Omega)} \|\nabla\phi\|_{\Omega},$$

must be estimated. By exploiting the weak norm and some orthogonality of $f - f_h$ (w.r.t. piecewise constants) such estimates can be given with optimal order and without requiring additional regularity of $f \in H^{r-1}(\Omega)$:

$$\begin{aligned} \|f - f_h\|_{H^{-1}(\Omega)} &= \sup_{\phi \in H_0^1(\Omega)} \frac{(f - f_h, \phi)_{\Omega}}{\|\nabla\phi\|} \\ &= \sup_{\phi \in H_0^1(\Omega)} \frac{(f - f_h, \phi - \bar{\phi})_{\Omega}}{\|\nabla\phi\|} \\ &\leq ch^r \|\nabla^{r-1} f\|_{\Omega}. \end{aligned}$$

To shorten the proof of the following lemma, we will not give details on the approximation of the right hand side.

With these preparations, we can show the following essential theorem, that gives the a priori error estimate for the Laplace equation on smooth and curved domains:

Theorem 8 (A priori error on curved domains). *Let $r \in \mathbb{N}_+$. Let Ω be a domain with boundary that allows for parametrization of degree $r + 1$. Let $f \in H^{r-1}(\Omega) \cap L^2(\Omega)$. Let $u_h \in V_h$ be the isoparametric finite element solution of degree r . It holds*

$$\|u - u_h\|_{H^1(\Omega)} \leq ch^r \|f\|_{H^{r-1}(\Omega)}$$

and

$$\|u - u_h\| \leq ch^{r+1} \|f\|_{H^{r-1}(\Omega)}.$$

3.2. Spatial Discretization

Proof. (i) We start with the H^1 error estimate and derive a modified Galerkin orthogonality. For $\phi_h \in V_h$ it holds (where we use the extension $\tilde{\phi}_h = \phi_h$ defined by Lemma 55 without further notice)

$$(f, \phi_h)_\Omega = (-\Delta u, \phi_h)_\Omega = (\nabla u, \nabla \phi_h)_\Omega - \langle \partial_n u, \phi_h \rangle_{\partial\Omega}.$$

The discrete problem is defined on Ω_h with “ $\Omega_h = \Omega + S_h^v - S_h^x$. It holds

$$(f, \phi_h)_\Omega + (f, \phi_h)_{S_h^v} - (f, \phi_h)_{S_h^x} = (\nabla u_h, \nabla \phi_h)_\Omega + (\nabla u_h, \nabla \phi_h)_{S_h^v} - (\nabla u_h, \nabla \phi_h)_{S_h^x}.$$

Then, for the finite element error $e_h = u - u_h$, we get the following disturbed Galerkin orthogonality:

$$\begin{aligned} (\nabla e_h, \nabla \phi_h)_\Omega &= -(f, \phi_h)_{S_h^v} + (f, \phi_h)_{S_h^x} \\ &\quad + \langle \partial_n u, \phi_h \rangle_{\partial\Omega} + (\nabla u_h, \nabla \phi_h)_{S_h^v} - (\nabla u_h, \nabla \phi_h)_{S_h^x} \end{aligned} \tag{3.19}$$

(ii) Now, we can estimate the energy error by picking $\phi_h = I_h u - u_h$:

$$\begin{aligned} \|\nabla e_h\|_\Omega^2 &\leq \|\nabla e_h\|_\Omega \|\nabla(u - I_h u)\|_\Omega + \|f\|_S \|I_h u - u_h\|_S \\ &\quad + \|\nabla u_h\|_S \|\nabla(I_h u - u_h)\|_S + \|\partial_n u\|_{\partial\Omega} \|I_h u - u_h\|_{\partial\Omega}, \end{aligned} \tag{3.20}$$

where we enlarged S_h^x and S_h^v to S . The single terms can be estimated with help of Lemma 56 and 57 and the standard interpolation estimate. For example, we only discuss the boundary term. With Lemma 57

$$\|\partial_n u\|_{\partial\Omega} \|I_h u - u_h\|_{\partial\Omega} \leq c \|u\|_{H^2(\Omega)} ch^{\frac{r+1}{2}} \|\nabla(I_h u - u_h)\|_\Omega,$$

which again can be estimated into interpolation- and approximation error. The remaining terms can be handled in a similar fashion, such that combination with Young's inequality gives the final estimate.

(iii) For estimating the L^2 -error, we define the adjoint problem:

$$-\Delta z = \frac{e_h}{\|e_h\|}, \quad \|z\|_{H^2(\Omega)} \leq c_s,$$

for which it holds by multiplication with e_h

$$\|e_h\|_\Omega = (e_h, -\Delta z)_\Omega = (\nabla e_h, \nabla z)_\Omega + \langle u_h, \partial_n z \rangle_{\partial\Omega},$$

as $u = 0$ on $\partial\Omega$. Using (3.19) with $\phi_h = I_h z$, it follows

$$\begin{aligned} \|e_h\| &\leq \|\nabla e_h\|_\Omega \|\nabla(z - I_h z)\|_\Omega + \|u_h\|_{\partial\Omega} \|\partial_n z\|_{\partial\Omega} + \|\partial_n u\|_{\partial\Omega} \|I_h z\|_{\partial\Omega} \\ &\quad + \|f\|_S \|I_h z\|_S + \|\nabla u_h\|_S \|\nabla I_h z\|_S. \end{aligned}$$

The first term can be estimated with the energy error estimate and the interpolation estimate, followed by the stability of the adjoint solution $\|z\|_{H^2(\Omega)} \leq c_s$. For the second term, we first use (3.18) to get (with $\pm u$)

$$\begin{aligned} \|u_h\|_{\partial\Omega} &\leq ch^{\frac{r+1}{2}} \|\nabla u_h\|_S \leq ch^{\frac{r+1}{2}} (\|\nabla e_h\|_S + \|\nabla u\|_S) \\ &\leq ch^{\frac{r+1}{2}} \|\nabla e_h\| + ch^{r+1} \|u\|_{H^2(\Omega)}. \end{aligned}$$

This procedure will also be used for the third one. The fourth term

$$\|f\|_S \leq ch^{\frac{r}{2}} \|f\|_{H^1(\Omega)}$$

is estimated with Lemma 56 and the interpolation is bounded by using the intermediate result (3.17):

$$\|I_h z\|_S \leq \|z - I_h z\|_S + \|z\|_S \leq ch^{\frac{r+1}{2}} \|z - I_h z\|_{\partial\Omega} + ch^{r+\frac{1}{2}} \|z - I_h z\|_S + ch^{\frac{r+1}{2}} \|z\|_{H^1(\Omega)}.$$

This trick is also used in the final term to get

$$\|\nabla I_h z\|_S \leq ch^{\frac{r+1}{2}} \|\nabla(z - I_h z)\|_{\partial\Omega} + ch^{r+\frac{1}{2}} \|\nabla(z - I_h z)\|_{\Omega} + ch^{\frac{r+1}{2}} \|z\|_{H^2(\Omega)}$$

Together with

$$\|\nabla u_h\|_S \leq ch^{\frac{r}{2}} \|\nabla u_h\|_{\Omega} \leq ch^{\frac{r}{2}} \|f\|_{\Omega},$$

this gives the desired result. \square

Remark 23 (Further estimates on curved boundaries). *This type of estimate can directly be extended to the Stokes equations or to equations of solid-dynamics. Essential for all estimates are the lemmata given at the beginning of this section.*

It holds however, that it is not trivial to extend this general form of a priori estimate on curved domains to the case of non-Dirichlet boundary data. If we for example consider the Stokes equations with slip boundary data,

$$\vec{n} \cdot \mathbf{v} = 0 \text{ on } \partial\Omega,$$

the proof cannot be extended in the same spirit. Reason for difficulties is the Lemma 57. For the slip-condition, we can still show

$$\|\vec{n} \cdot \mathbf{v}_h\|_{\partial\Omega} \leq ch^{r+\frac{1}{2}} \|\nabla \mathbf{v}\|_{\Omega} + \|\vec{n} \cdot \mathbf{v}_h\|_{\partial\Omega_h},$$

we observe however, that $\vec{n} \cdot \mathbf{v}_h \neq 0$ on the discrete boundary $\partial\Omega_h$ (in the case of polynomial degree $r \geq 1$). One possible loophole is to define the reference map $T_T : \hat{T} \rightarrow T$ by means of the Piola transform, such that the basis functions on T are given by

$$\phi(x) = \frac{1}{\det(\nabla T_T)} \nabla T_T \hat{\phi}(\hat{x}).$$

For a discussion, we refer to the literature [33, 181]

3.3 Finite Elements for Saddle-Point Problems

In this section, we discuss the finite element discretization for problems of saddle-point type. We have come across such problems in the case of incompressible solids and the incompressible Stokes or Navier-Stokes system. Here, we will consider the incompressible Stokes equations exemplarily for all saddle-point systems. This saddle-point character causes various difficulties, like the need to satisfy the inf-sup condition, Lemma 18. When designing numerical algorithms,

this saddle-point character must be taken into account. The Stokes equations on a domain $\Omega \subset \mathbb{R}^d$ are given by

$$\begin{aligned} \{u, p\} \in \mathcal{V} \times \mathcal{L} : \quad (\nabla v, \nabla \phi) - (p, \nabla \cdot \phi) + (\nabla \cdot v, \xi) &= (f, \phi) \\ \forall \{\phi, \xi\} \in \mathcal{V} \times \mathcal{L}, \end{aligned}$$

where for simplicity we consider problems with homogenous Dirichlet conditions on the boundary $\partial\Omega$ only. Let $V_h \subset \mathcal{V}$ and $L_h \subset \mathcal{L}$ be two conforming finite element spaces. We note, that as $L = L^2(\Omega)$, conformity regarding the pressure does not ask for continuity. The discretized Stokes system is equivalent to a linear system of equations

$$\begin{pmatrix} \mathbf{A}_h & \mathbf{B}_h \\ -\mathbf{B}_h^T & 0 \end{pmatrix} \begin{pmatrix} \mathbf{v}_h \\ \mathbf{p}_h \end{pmatrix} = \begin{pmatrix} \mathbf{f}_h \\ 0 \end{pmatrix}, \quad (3.21)$$

where \mathbf{v}_h and \mathbf{p}_h are the coefficient vectors of the discrete solutions $v_h \in V_h$ and $p_h \in L_h$. The matrices are given by

$$(\mathbf{A}_h)_{ij} = (\nabla \phi_j, \nabla \phi_i), \quad (\mathbf{B}_h)_{ij} = -(\xi_j, \nabla \cdot \phi_i), \quad -(\mathbf{B}_h)_{ij}^T = (\nabla \cdot \phi_j, \xi_i),$$

where $V_h = \text{span}\{\phi_i, i = 1, \dots, \#V_h\}$ and $L_h = \text{span}\{\xi_i, i = 1, \dots, \#L_h\}$ is a basis of the finite element space. The matrix \mathbf{A}_h is symmetric and positive definite. The complete system matrix however reflects the saddle-point character of the Stokes equations. It holds:

Lemma 58 (Stokes solution). *Let $V_h \times L_h \subset \mathcal{V} \times \mathcal{L}$ be a conforming discretization of the incompressible Stokes equations. There exists a unique solution $\{v_h, p_h\} \in V_h \times L_h$, if the discrete inf-sup condition holds*

$$\inf_{\xi_h \in L_h} \sup_{\phi_h \in V_h} \frac{(\xi_h, \nabla \cdot \phi_h)}{\|\xi_h\| \|\nabla \phi_h\|} \geq \gamma_h \geq \gamma > 0.$$

The solution $\{v_h, p_h\}$ satisfies the a priori estimate

$$\|\nabla v_h\| + \gamma_h \|p_h\| \leq c \|f\|_{-1}.$$

Proof. (i) First, we define the subspace $W_h \subset V_h$ of weakly divergence free functions:

$$W_h := \{\phi_h \in V_h : (\nabla \cdot \phi_h, \xi_h) = 0 \quad \forall \xi_h \in L_h\}.$$

We assume, that $W_h \neq \emptyset$ and find $v_h \in W_h$ such that

$$(\nabla v_h, \nabla \phi_h) = (f, \phi_h) \quad \forall \phi_h \in W_h. \quad (3.22)$$

The existence of a unique solution $v_h \in W_h$ follows by linearity and ellipticity of the scalar product $(\nabla \cdot, \nabla \cdot)$ in $W_h \subset \mathcal{V} = H_0^1(\Omega)^d$. Further, it holds with Poincaré's inequality

$$\|\nabla v_h\|^2 = (\nabla v_h, \nabla v_h) = (f, v_h) \leq \|f\|_{-1} \|v_h\|_1 \leq (1 + c_P^2)^{\frac{1}{2}} \|f\|_{-1} \|\nabla v_h\|. \quad (3.23)$$

This solution v_h by construction fulfills the divergence condition.

(ii) Next, given $v_h \in W_h \subset V_h$ we find a pressure $p_h \in L_h$ as solution to

$$(p_h, \nabla \cdot \phi_h) = (\nabla v_h, \nabla \phi_h) - (f, \phi_h) \quad \forall \phi_h \in V_h.$$

This finite dimensional problem is equivalent to the linear system of equations:

$$\mathbf{B}_h \mathbf{p}_h = \mathbf{f}_h - \mathbf{A}_h \mathbf{v}_h. \quad (3.24)$$

As this problem is finite dimensional, it holds

$$\text{range}(\mathbf{B}_h) = \ker(\mathbf{B}_h^T)^\perp.$$

Hence, we find a solution, if the right hand side of (3.24) is orthogonal to the kernel of \mathbf{B}_h^T , the discrete divergence operator:

$$\langle \mathbf{A}_h \mathbf{v}_h - \mathbf{f}_h, \mathbf{z} \rangle = 0 \quad \forall \mathbf{z} \in \ker(\mathbf{B}_h^T).$$

First, we characterize the kernel of \mathbf{B}_h^T . It holds

$$\mathbf{B}_h^T \mathbf{z} = \left(\sum_{j=1}^{\#V_h} (\xi_h^i, \nabla \cdot \phi_h^j) \mathbf{z}_j \right)_{i=1}^{\#L_h} = (\nabla \cdot z_h, \xi_h^i)_{i=1}^{\#L_h},$$

and hence, $\ker(\mathbf{B}_h^T) = W_h$. In (i), we determined $v_h \in W_h$ as solution of (3.22):

$$(\nabla v_h, \nabla \phi_h) = (f, \phi_h) \quad \forall \phi_h \in W_h \quad \Leftrightarrow \quad \langle \mathbf{b}_h - \mathbf{A}_h \mathbf{v}_h, \mathbf{z} \rangle = 0 \quad \forall \mathbf{z} \in \ker(\mathbf{B}_h^T).$$

At least one pressure $p_h \in L_h$ exists.

(iii) The inf-sup condition is equivalent to the formulation

$$\gamma_h \|p_h\| \leq \sup_{\phi_h} \frac{(p_h, \nabla \cdot \phi_h)}{\|\nabla \phi_h\|} \quad \forall p_h \in L_h.$$

Let p_h^1 and p_h^2 be two solutions with corresponding velocity solution $v_h \in V_h$. For $q_h := p_h^1 - p_h^2 \in L_h$ is holds

$$\begin{aligned} (\nabla v_h, \nabla \phi_h) - (p_h^1, \nabla \cdot \phi_h) &= (f, \phi_h) \\ (\nabla v_h, \nabla \phi_h) - (p_h^2, \nabla \cdot \phi_h) &= (f, \phi_h) \end{aligned} \Rightarrow (q_h, \nabla \cdot \phi_h) = 0 \quad \forall \phi_h \in V_h.$$

Using the inf-sup condition, it holds, that $q_h = 0$, as

$$\gamma_h \|q_h\| \leq \sup_{\phi_h \in V_h} \frac{(q_h, \nabla \cdot \phi_h)}{\|\nabla \phi_h\|} = 0,$$

and it follows, that the pressure is unique. The a priori estimate is given using (3.23) with help of the inf-sup condition:

$$\begin{aligned} \gamma_h \|p_h\| &\leq \sup_{\phi_h \in V_h} \frac{(p_h, \nabla \cdot \phi_h)}{\|\nabla \phi_h\|} = \sup_{\phi_h \in V_h} \frac{(f, \phi_h) - (\nabla v_h, \nabla \phi_h)}{\|\nabla \phi_h\|} \\ &\leq (1 + c_p)^{\frac{1}{2}} \|f\|_{-1} + \|\nabla v_h\| \leq c \|f\|_{-1}. \end{aligned}$$

□

The inf-sup condition is required to get uniqueness of the pressure. Existence is given for every pair $V_h \times L_h$. At the beginning of the proof, we assumed, that the space

$$W_h = \{\phi_h \in V_h : (\nabla \cdot \phi_h, \xi_h) = 0 \quad \forall \xi_h \in L_h\},$$

is big enough to yield good approximation properties for $v \in \mathcal{V}$. By construction, the space W_h gets small, if L_h is large compared to V_h . For the most basic finite element pair, that consists of piece-wise linear velocities and a piece-wise constant pressure, the space W_h empty.

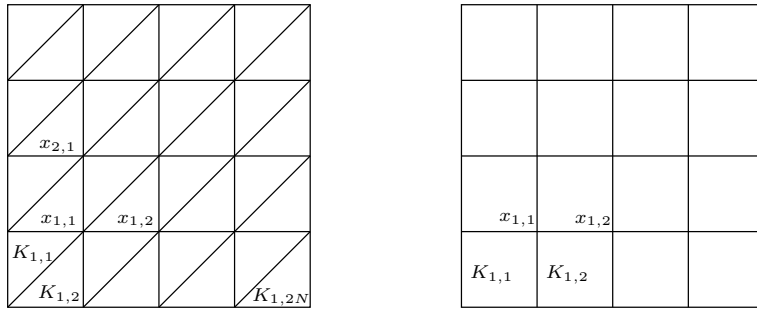


Figure 3.5: Meshes of tensor-product type. Left triangular and right quadrilateral.

3.3.1 inf-sup stable Finite Element pairs

Here, we discuss inf-sup stability for a given finite element pair $V_h \times L_h$. Proving the inf-sup condition is usually not easy and there exists not one approach that is usable for all different finite element pair. For details see the comprehensive text-books by Girault and Raviart [107] or Temam [221]. A conforming finite element space must consist of velocities, that are globally continuous, where the pressure space can be discontinuous.

We denote a finite element pair by $X - Y$, where X and Y are the finite element spaces used for velocity and pressure, respectively: by $P^2 - P^1$ we denote the pair consisting of piece-wise quadratic velocities and piece-wise linear pressure on triangles. This space is called the *Taylor-Hood element*. By $Q^2 - P^{1,\text{dc}}$ we denote the space of piece-wise quadratic velocities and discontinuous, piece-wise linear pressures on quadrilaterals. Spaces with discontinuous pressures have the advantage of local mass conservation. for the pair $Q^2 - P^{1,\text{dc}}$ we can choose the test-function $\xi_K \in L_h$ with $\xi_K \equiv 1$ on one $K \in \Omega_h$ and $\xi_K = 0$ for all $K' \neq K$. It holds:

$$\int_K \nabla \cdot v_h \, dx = (\nabla \cdot v_k, \xi_K) = 0.$$

Some very simple finite element pairs are not stable. The triangular $P^1 - P^{0,\text{dc}}$ element for instance is not usable, as $W_h = 0$, see [107]. Likewise, the quadrilateral $Q^1 - P^{0,\text{dc}}$ cannot be used, as the inf-sup condition is not fulfilled. Solutions on regular meshes will feature the so-called *checkerboard pattern* with oscillatory pressures.

After these negative results, we cite a Lemma that gives a simple criteria for showing inf-sup stability in certain cases, see [52]:

Lemma 59 (Fortin criteria). *Let $V_h \times L_h \subset \mathcal{V} \times \mathcal{L}$ be a finite element pair with $L_h \subset L$. Given a H^1 -stable projection operator $\pi_h : \mathcal{V} \rightarrow V_h$ satisfying*

$$\|\nabla \pi_h \phi\| \leq c_\pi \|\nabla \phi\| \quad \forall \phi \in V, \quad (\nabla \cdot (\phi - \pi_h \phi), \xi_h) = 0 \quad \forall \xi_h \in L_h,$$

it holds

$$\inf_{\xi_h \in L_h} \sup_{\phi_h \in V_h} \frac{(\xi_h, \nabla \cdot \phi_h)}{\|\nabla \phi_h\| \|\xi_h\|} \geq \gamma_h := \gamma c_\pi^{-1},$$

where $\gamma > 0$ is the continuous inf-sup constant in $\mathcal{V} \times \mathcal{L}$.

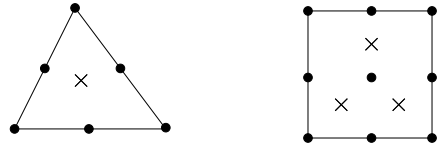


Figure 3.6: Modified Taylor-Hood elements $P^2 - P^{0,dc}$ (left) and $Q^2 - P^{1,dc}$ (right).

Proof. Let $p_h \in L_h \subset \mathcal{L}$. It holds with the continuous inf-sup condition

$$\gamma \|p_h\| \leq \sup_{\phi \in \mathcal{V}} \frac{(p_h, \nabla \cdot \phi)}{\|\nabla \phi\|} = \sup_{\phi \in \mathcal{V}} \frac{(p_h, \nabla \cdot (\phi - \pi_h \phi))}{\|\nabla \phi\|} + \sup_{\phi \in \mathcal{V}} \frac{(p_h, \nabla \cdot \pi_h \phi)}{\|\nabla \phi\|}.$$

As the first part is zero due to the orthogonality of the projection π_h it further follows with the stability of the projection

$$\gamma \|p_h\| \leq \sup_{\phi \in \mathcal{V}} \frac{(p_h, \nabla \cdot \pi_h \phi)}{\|\nabla \pi_h \phi\|} \sup_{\phi \in \mathcal{V}} \frac{\|\nabla \pi_h \phi\|}{\|\nabla \phi\|} \leq c_\pi \sup_{\phi_h \in V_h} \frac{(p_h, \nabla \cdot \phi_h)}{\|\nabla \phi_h\|},$$

as $\pi_h \phi \in V_h$.

□

For some elements this criteria helps to show inf-sup stability:

Lemma 60 (Modified Taylor-Hood elements with discontinuous pressure). *The $P^2 - P^{0,dc}$ and $Q^2 - P^{1,dc}$ elements are inf-sup stable.*

Proof. See Figure 3.6 for a sketch of these two element pairs. We construct a projection operator $\pi_h : \mathcal{V} \rightarrow V_h$ that has both properties, H^1 -stability and the required orthogonality.

(i) *The triangular element.* We construct π_h as $\pi_h := C_h + E_h$, where $C_h : \mathcal{V} \rightarrow V_h^1$ is the Clement operator into the space of piecewise linear functions. This space has three degrees of freedom (for every velocity component) and fixes the three nodal points of a triangle. This operator C_h satisfies

$$\|\nabla C_h v\|_K \leq c_C \|\nabla v\|_{P(K)},$$

where $P(K)$ is a patch of elements around K . See Lemma 48 for details. It remains to fulfill the orthogonality condition. As the pressure space is discontinuous, it holds on every K choosing by $\xi_h \equiv 1$ on K and $\xi_h = 0$ elsewhere:

$$(\nabla \cdot (v - \pi_h v), \xi_h) = \int_K \nabla \cdot (v - \pi_h v) \, dx = \int_{\partial K} n \cdot (v - \pi_h v) \, do.$$

For $\pi_h := C_h + E_h$ one condition is imposed on every edge $e \in \partial K$:

$$\int_e n \cdot E_h v \, do = \int_e n \cdot (v - C_h v) \, do.$$

This is easily established by the remaining degrees of freedom (two per edge).

(ii) *The quadrilateral element.* We define the projection as $\pi_h := C_h + E_h + B_h$, where C_h again is a H^1 -stable Clement interpolation, E_h takes care of the edges and B_h of the additional middle degree of freedom. For the orthogonality it holds for $\xi_K \in L_h$ with $\xi_K = 0$ for all $K' \neq K$:

$$(\nabla \cdot (v - \pi_h v), \xi_h)_K = -(v - \pi_h v, \nabla \xi_h)_K + \int_{\partial K} n \cdot (v - \pi_h v) \xi_h \, do.$$

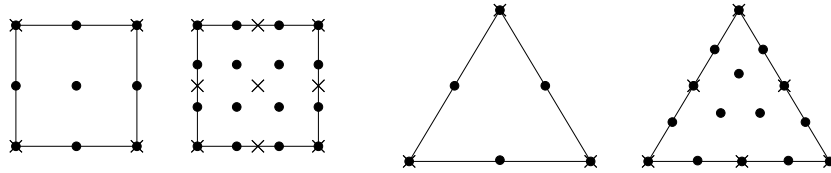


Figure 3.7: Different inf-sup stable finite element pairs: The $Q^2 - Q^1$ Taylor Hood element, a higher order $Q^3 - Q^2$ element, the classical $P^2 - P^1$ Taylor Hood element and a higher order $P^4 - P^2$ element.

As ξ_h is piecewise linear, $\nabla \xi_h \in \mathbb{R}^2$ is a constant vector on every element. The two inner degrees of freedom are used to define the operator B_h via

$$\int_K B_h v_i \, dx = \int_K v_i - \pi_h v_i \, dx, \quad i = 1, 2.$$

Finally, $\xi_h \in L_h$ is a linear function on every edge $e \in \partial K$, and the two remaining degrees of freedom are required for satisfying

$$\int_e n \cdot E_h v \xi_h \, do = \int_e n \cdot (v - \pi_h v) \xi_h \, do.$$

□

One of the most-often used finite element pairs for the discretization of the incompressible Stokes or Navier-Stokes equations is the Taylor-Hood element $P^2 - P^1$. Here, the Fortin criteria cannot be applied as easily.

Lemma 61 (Inf-sup stable finite element pairs). *The finite element pairs of Taylor Hood type $Q^2 - Q^1$ and $P^2 - P^1$ as well as the generalizations $Q^k - Q^{k-1}$ and $P^k - P^{k-2}$ for $k \geq 3$ are inf-sup stable. Further, the equal order spaces using a pressure on a coarser mesh $Q_h^k - Q_{2h}^k$ are inf-sup stable.*

Proof. Proofs for these and further element pairs are given in [52] and [107]. See Figure 3.7 for some inf-sup stable finite elements. □

For inf-sup stable and conforming finite element pairs $V_h \times L_h \subset \mathcal{V} \times \mathcal{L}$, a priori error analysis is possible by standard arguments. We start by showing a best-approximation results:

Lemma 62 (Stokes, best approximation). *Let $V_h \times L_h \subset \mathcal{V} \times \mathcal{L}$ be a inf-sup stable finite element space. It holds:*

$$\|\nabla(v - v_h)\| + \|p - p_h\| \leq c \left(\min_{\phi_h \in V_h} \|\nabla(v - \phi_h)\| + \min_{\xi_h \in L_h} \|p - \xi_h\| \right),$$

where the constant $c > 0$ depends on the inf-sup constant γ_h . Further, on convex or smooth domains, it holds

$$\|v - v_h\| \leq ch \left(\min_{\phi_h \in V_h} \|\nabla(v - \phi_h)\| + \min_{\xi_h \in L_h} \|p - \xi_h\| \right),$$

with constant $c = c(\gamma_h)$.

Proof. We define $e_v := v - v_h \in \mathcal{V}$ and $e_p := p - p_h \in \mathcal{L}$. It holds by Galerkin orthogonality

$$\begin{aligned} (\nabla e_v, \nabla \phi_h) &= (e_p, \nabla \cdot \phi_h) \quad \forall \phi_h \in V_h, \\ (\nabla \cdot e_v, \xi_h) &= 0 \quad \forall \xi_h \in L_h. \end{aligned} \tag{3.25}$$

(i) First, we start with an estimate of the velocity error:

$$\|\nabla e_v\|^2 = (\nabla e_v, \nabla e_v) - (e_p, \nabla \cdot e_v) + (e_p, \nabla \cdot e_v).$$

By Galerkin orthogonality, we get for arbitrary $\phi_h \in V_h$ and $\xi_h \in L_h$

$$\begin{aligned} \|\nabla e_v\|^2 &= (\nabla e_v, \nabla(v - \phi_h)) - (e_p, \nabla \cdot (v - \phi_h)) + (\nabla \cdot e_v, p - \xi_h) \\ &\leq \|\nabla e_v\| \|\nabla(v - \phi_h)\| + \|e_p\| \|\nabla(v - \phi_h)\| + \|\nabla e_v\| \|p - \xi_h\|. \end{aligned}$$

By Young's inequality, we get for $\epsilon > 0$:

$$\|\nabla e_v\| \leq (2 + \epsilon^{-1}) \|\nabla(v - \phi_h)\| + 2\|p - \xi_h\| + \epsilon \|e_p\|. \tag{3.26}$$

(ii) Next, we estimate the pressure error. Let $\xi_h \in L_h$ be arbitrary

$$\|p - p_h\| \leq \|p - \xi_h\| + \|p_h - \xi_h\|. \tag{3.27}$$

For $p_h - \xi_h \in L_h$ we use the discrete inf-sup inequality to get

$$\begin{aligned} \gamma_h \|p_h - \xi_h\| &\leq \sup_{\phi_h \in V_h} \frac{(p_h - \xi_h, \nabla \cdot \phi_h)}{\|\nabla \phi_h\|} \\ &= \sup_{\phi_h \in V_h} \frac{(p - p_h, \nabla \cdot \phi_h)}{\|\nabla \phi_h\|} + \sup_{\phi_h \in V_h} \frac{(p - \xi_h, \nabla \cdot \phi_h)}{\|\nabla \phi_h\|} \end{aligned} \tag{3.28}$$

We use (3.25) on the first part to replace the pressure error e_p by the velocity error e_v :

$$\sup_{\phi_h \in V_h} \frac{(e_p, \nabla \cdot \phi_h)}{\|\nabla \phi_h\|} = \sup_{\phi_h \in V_h} \frac{(\nabla e_v, \nabla \phi_h)}{\|\nabla \phi_h\|} \leq \|\nabla e_v\|.$$

Together with the second part of (3.28) we get the estimate

$$\gamma_h \|p_h - \xi_h\| \leq \|\nabla e_v\| + \|p - \xi_h\|,$$

and finally, with (3.27) for $\|p - p_h\|$

$$\|e_p\| \leq (1 + \gamma_h^{-1}) \|p - \xi_h\| + \gamma_h^{-1} \|\nabla e_v\|. \tag{3.29}$$

(iii) We insert this estimate into (3.26), using $\epsilon = \gamma_h/2$:

$$\|\nabla e_v\| \leq c(\gamma_h) (\|\nabla(v - \phi_h)\| + \|p - \xi_h\|).$$

Together with (3.29) we get the best-approximation property for the natural energy norm.

(iv) To derive the L^2 -estimate we define the adjoint problem

$$(\nabla \phi, \nabla z) - (\xi, \nabla \cdot z) + (\nabla \cdot \phi, q) = \|e_v\|^{-1} (e_v, \phi).$$

As $e_v/\|e_v\| \in L^2$ it holds by Lemma 21 (if the domain has a convex or smooth boundary) that

$$\|\nabla^2 z\| + \|\nabla q\| \leq c_s \left\| \frac{e_v}{\|e_v\|} \right\| = c_s.$$

By diagonal testing and using Galerkin orthogonality to insert the interpolants $I_h z \in V_h$ and $I_h q \in L_h$ it follows:

$$\begin{aligned} \|e_v\| &= (\nabla e_v, \nabla z) - (e_p, \nabla \cdot z) + (\nabla \cdot \phi, q) \\ &= (\nabla e_v, \nabla(z - \phi_h)) - (e_p, \nabla \cdot (z - \phi_h)) + (\nabla \cdot e_v, (q - \xi_h)) \\ &\leq \|\nabla e_v\| \|\nabla(z - I_h z)\| + \|\nabla e_p\| \|\nabla(z - I_h z)\| + \|\nabla e_v\| \|q - I_h q\| \end{aligned}$$

The result follows using the energy norm error estimate for $\|\nabla e_v\| + \|e_p\|$ and the interpolation estimate, Lemma 47:

$$\begin{aligned} \|e_v\| &\leq c_I h (\|\nabla e_v\| + \|e_p\|) (\|\nabla^2 z\| + \|\nabla q\|) \\ &\leq c(\gamma) c_{sh} \left(\min_{\phi_h \in V_h} \|\nabla(v - \phi_h)\| + \min_{\xi_h \in L_h} \|p - \xi_h\| \right). \end{aligned}$$

□

The approximation order of the Stokes element then depends on the polynomial degree of the finite element pair:

Lemma 63 (Stokes, a priori estimate). *Let $V_h \times L_h$ be an inf-sup stable finite element pair of order k for the velocity and l for the pressure. Further, let $u \in H^{k+1}(\Omega)^d$ and $p \in H^{l+1}(\Omega)$ be the solution to the incompressible Stokes equations. It holds*

$$\|\nabla(\mathbf{v} - \mathbf{v}_h)\| + \|p - p_h\| \leq ch^{\min\{k, l+1\}} (\|\nabla^{k+1}\mathbf{v}\| + \|\nabla^l p\|). \quad (3.30)$$

Proof. First, by Lemma 62 it holds

$$\|\nabla(\mathbf{v} - \mathbf{v}_h)\| + \|p - p_h\| \leq c(\gamma_h^{-1}) (\|\nabla(\mathbf{v} - I_h \mathbf{v})\| + \|p - I_h p\|),$$

where $I_h \mathbf{v} \in V_h$ and $I_h p \in L_h$ are the nodal interpolations. Given sufficient regularity it holds by Lemma 47

$$\|\nabla(\mathbf{v} - I_h \mathbf{v})\| \leq c_I h^k \|\nabla^{k+1} \mathbf{v}\|, \quad \|p - I_h p\| \leq c_I h^{l+1} \|\nabla^{l+1} p\|.$$

This completes the estimate. □

This lemma shows, that the optimal degree for velocity and pressure space differs by one. If $l = k - 1$, optimal order of convergence is given. Possible candidates for such finite element pairs are the Taylor-Hood element $P^2 - P^1$ or $Q^k - Q^{k-1}$ or the modified Taylor-Hood element with discontinuous pressure $Q^2 - P^{1,\text{dc}}$. This element has the further advantage of local mass conservation.

Remark 24. *Optimality of the a priori estimates In terms of mesh parameter $h > 0$, the estimates in Lemma 63 are optimal and represent the best-approximation property. They however exhibit two shortcomings which are severe under given circumstances.*

First, only coupled estimates for velocity and pressure are given. Assume, that the right hand side \mathbf{f} is such, that its divergence free part is zero with $\mathbf{f} = \nabla q$. Then, the Stokes equations have

the unique solution $\mathbf{v} = 0$ and $p = q$. Equation (3.30) gives an estimate for the velocity error depending on the pressure error. And indeed, most standard approaches elements like Taylor-Hood or the $Q^2-P^{1,d}$ element will show exactly this unsatisfactory behavior with very large errors. So called gradient-robust mixed methods are designed in such a way, that the velocity approximation is independent of the pressure. See [151] for details. In most applications, the right hand side \mathbf{f} itself is not critical, as it will be zero or a fixed gravity error. In large scale deformations however, Coriolis terms may have the same effect. In terms of fluid-structure interactions, the domain motion and the ALE map is a further source of such problems.

The second issue in Lemma 63 is the negative dependence of the error constant on the inf-sup constant. It is well known, that the inf-sup constant depends on the shape of the domain and that it goes to zero for strongly anisotropic domains, see [80]. For very long channels, this would suggest large error constants. Here however, numerical reality is in favor, such that usual finite element approaches do not see this issue. The proof of Lemma 63 can be modified in such a way, that Fortin's criteria is applied only locally, such that the bad behavior of the global inf-sup constant does impact the result. See [152, 157] for details.

3.3.2 Stabilization techniques for the Stokes equations

The most easy finite element pairs using equal-order finite elements for both velocity and pressure do not satisfy the inf-sup condition. Hence, they cannot be used for a robust discretization of saddle point problems like the Stokes equations. The use of such equal-order pairs is mainly attractive for implementation reasons. Further, equal order finite elements simplify the design of robust iterative solvers for saddle point problems. The proof of Fortin's Lemma 59 gives the following estimate that holds for every conforming finite element pair $V_h \times L_h \subset \mathcal{V} \times \mathcal{L}$, also for equal-order finite elements that are not inf-sup stable:

$$\gamma \|p_h\| \leq \sup_{\phi \in \mathcal{V}} \frac{(p_h, \nabla \cdot \phi_h)}{\|\nabla \phi\|} + \sup_{\phi \in \mathcal{V}} \frac{(p_h, \nabla \cdot (\phi - \phi_h))}{\|\nabla \phi\|} \quad \forall p_h \in L_h, \forall \phi_h \in V_h. \quad (3.31)$$

We choose $\phi_h := C_h \phi$ as the H^1 -stable Clement interpolation $C_h : \mathcal{V} \rightarrow V_h$, see Lemma 48. This interpolation does not satisfy any orthogonality condition like the projection operator π_h used in Fortin's criteria. However it holds for all $p_h \in L_h$ with help of Lemma 48 for the two terms in (3.31)

$$\begin{aligned} \sup_{\phi \in \mathcal{V}} \frac{(p_h, \nabla \cdot C_h \phi)}{\|\nabla C_h \phi\|} &\leq c \sup_{\phi_h \in V_h} \frac{(p_h, \nabla \cdot \phi_h)}{\|\nabla \phi_h\|} \\ \sup_{\phi \in \mathcal{V}} \frac{(p_h, \nabla \cdot (\phi - C_h \phi))}{\|\nabla C_h \phi\|} &= \sup_{\phi \in \mathcal{V}} \frac{\sum_{K \in \Omega_h} \langle p_h n, \phi - C_h \phi \rangle_{\partial K} - (\nabla p_h, \phi - C_h \phi)_K}{\|\nabla C_h \phi\|} \end{aligned}$$

3.3. Finite Elements for Saddle-Point Problems

We assume, that the pressure space $L_h \subset C(\Omega)$ is continuous such that the boundary integral vanishes. Then, using the error estimate for the Clement interpolation it follows, that

$$\begin{aligned} \sup_{\phi \in \mathcal{V}} \frac{(p_h, \nabla \cdot (\phi - C_h \phi))}{\|\nabla C_h \phi\|} &\leq c \sup_{\phi \in \mathcal{V}} \sum_{K \in \Omega_h} \frac{\|\nabla p_h\|_K h_K \|\nabla \phi\|_{P(K)}}{\|\nabla C_h \phi\|} \\ &\leq c' \left(\sum_{K \in \Omega_h} h_K^2 \|\nabla p_h\|_K^2 \right)^{\frac{1}{2}} \sup_{\phi \in \mathcal{V}} \left(\sum_{K \in \Omega_h} \frac{\|\nabla \phi\|_{P(K)}^2}{\|\nabla \phi\|_P^2} \right)^{\frac{1}{2}} \\ &\leq c'' \left(\sum_{K \in \Omega_h} h_K^2 \|\nabla p_h\|_K^2 \right). \end{aligned}$$

Altogether, it holds

Lemma 64 (Modified inf-sup condition). *Let $V_h \times L_h \subset \mathcal{V} \times \mathcal{L}$ be a finite element pair with continuous pressure $L_h \subset C(\Omega)$. Then, the modified inf-sup condition holds*

$$\gamma_h \|p_h\| \leq \sup_{\phi_h \in V_h} \frac{(p_h, \nabla \cdot \phi_h)}{\|\nabla \phi_h\|} + \left(\sum_{K \in \Omega_h} h_K^2 \|\nabla p_h\|_K^2 \right)^{\frac{1}{2}} \quad \forall p_h \in L_h.$$

This modified inf-sup condition gives rise to an alternative discretization technique for the Stokes equations that is based on modifications of the variational formulation. It holds

Lemma 65 (Pressure stabilized Stokes elements). *Let $V_h \times L_h$ be the equal order pair of continuous, piece-wise linear pressures and velocities. Let $f \in L^2(\Omega)^d$. For the solution $\{v_h, p_h\} \in V_h \times L_h$ of*

$$\begin{aligned} (\nabla v_h, \nabla \phi_h) - (p_h, \nabla \phi_h) &= (f, \phi_h) \quad \forall \phi_h \in V_h, \\ (\nabla \cdot v_h, \xi_h) + \sum_{K \in \Omega_h} h_K^2 (\nabla p_h, \nabla \xi_h) &= 0 \quad \forall \xi_h \in L_h, \end{aligned}$$

it holds

$$\|\nabla(v - v_h)\| + \|p - p_h\| + h_k \|\nabla(p - p_h)\| \leq ch \|f\|,$$

as well as the L^2 -estimate

$$\|v - v_h\| \leq ch^2 \|f\|.$$

Proof. See Problem 37. □

This first stabilized scheme for the Stokes equations has the disadvantage of a very low approximation order. Also for higher order finite elements, the additional stabilization term in the divergence equation will limit the scheme to first order accuracy. Hughes, Franca and Balestra [137] introduced a modification of this stabilization technique that can be generalized to higher order finite elements and that will give optimal error estimates:

Lemma 66 (Galerkin Least Squares stabilization). *Let $V_h \times L_h \subset \mathcal{V} \times \mathcal{L}$ be an equal order finite element pair with velocities and pressures of degree r . For the solution $\{v_h, p_h\} \in V_h \times L_h$ to*

$$\begin{aligned} (\nabla v_h, \nabla \phi_h) - (p_h, \nabla \phi_h) + (\nabla \cdot v_h, \xi_h) + & (-\Delta v_h + \nabla p_h, -\Delta \phi_h + \nabla \xi_h) \\ = (f, \phi_h) + (f, -\Delta \phi_h + \nabla \xi_h) & \quad \forall \phi_h \in V_h, \xi_h \in L_h. \end{aligned}$$

if holds

$$\| \dots \|$$

Proof. See Hughes et al. [137]. \square

Further developments of this stabilized formulation of the Stokes equations is one of the most-used discretization which is not based on inf-sup stable elements. It has the drawback of boundary layers in the pressure, introduced by the strong non-physical control of the pressure's gradient in the error estimate. The approximation properties of this stabilized scheme can be improved by further modifications, see Droux and Hughes [83].

An alternative to the GLS formulation and related residual based schemes is the Local Projection Stabilization method (LPS) that has been introduced by Becker and Braack [21]. Here, stability is given by projection of the solution to an inf-sup stable finite element space. It holds

Lemma 67 (Local Projection Stabilization). *Let $V_h \times L_h \subset \mathcal{V} \times \mathcal{L}$ be a conforming finite element space. Further, let $V_h \times \tilde{L}_h$ be an inf-sup stable finite element pair with inf-sup constant $\tilde{\gamma}_h$. By $\pi_h : L_h \rightarrow \tilde{L}_h$ we denote a projection operator and by $s(\cdot, \cdot) : L_h \times L_h \rightarrow \mathbb{R}$ a bilinear stabilization form. If it holds*

$$\|\pi_h p_h\| \leq c_1 \|p_h\|, \quad \|p_h - \pi_h p_h\|^2 \leq c_2 s(p_h, p_h) \quad \forall p_h \in L_h.$$

the stabilized Stokes equations

$$\begin{aligned} (\nabla v_h, \nabla \phi_h) - (p_h, \nabla \cdot \phi_h) &= (f, \phi_h) \quad \forall \phi_h \in V_h, \\ (\nabla \cdot v_h, \xi_h) + s(p_h, \xi_h) &= 0 \quad \forall \xi_h \in L_h \end{aligned}$$

is robust and it holds

$$\gamma_h \|p_h\| \leq \sup_{\phi_h \in V_h} \frac{(p_h, \nabla \cdot \phi_h)}{\|\nabla \phi_h\|} \quad \forall p_h \in L_h,$$

with the constant $\gamma_h \sim \tilde{\gamma}/c_1$.

Proof. See Becker & Braack [21]. \square

The Local Projection Stabilization method has the advantage of a very easy implementation. Opposed to the GLS method, no second derivatives are necessary in the variational formulations. Easy examples for the LPS method are based on the $Q^k - Q^{k-1}$ Taylor-Hood element for $k \geq 2$. Here, the projection operator $\pi_h : Q^k \rightarrow Q^{k-1}$ is simply the embedding and the stabilization form is given by

$$s(p_h, \xi_h) = \sum_{K \in \Omega_h} h_K^2 (\nabla(p_h - \pi_h p_h), \nabla(\xi_h - \pi_h \xi_h))_K. \quad (3.32)$$

3.4 Finite Elements for the Navier-Stokes equations

The incompressible Navier-Stokes equations

$$\begin{aligned} (\partial_t v + v \cdot \nabla v, \phi) + \frac{1}{Re} (\nabla v, \nabla \phi) - (p, \nabla \cdot \phi) &= (f, \phi) \quad \forall \phi \in \mathcal{V}_f, \\ (\nabla \cdot v, \xi) &= 0 \quad \forall \xi \in \mathcal{L}_f, \end{aligned}$$

differ from the Stokes equation by the nonlinearity only. We assume, that time-discretization is done by Rothe's method with a time-stepping method, such that in every time-step $t_{m-1} \rightarrow t_m$ a quasi-stationary problem must be solved

$$\begin{aligned} (\sigma v + v \cdot \nabla v, \phi) + \frac{1}{Re} (\nabla v, \nabla \phi) - (p, \nabla \cdot \phi) &= (g, \phi) \quad \forall \phi \in \mathcal{V}_f, \\ (\nabla \cdot v, \xi) &= 0 \quad \forall \xi \in \mathcal{L}_f, \end{aligned}$$

where $\sigma \sim k^{-1}$. A direct discretization with (an inf-sup stable) finite element pair $V_h \times L_h \subset \mathcal{V}_f \times \mathcal{L}_f$ leads to a finite dimensional - but nonlinear - system of algebraic equations

$$\begin{aligned} (\sigma v_h + v_h \cdot \nabla v_h, \phi_h) + \frac{1}{Re} (\nabla v_h, \nabla \phi_h) - (p_h, \nabla \cdot \phi_h) &= (g, \phi_h) \quad \forall \phi_h \in V_h, \\ (\nabla \cdot v_h, \xi_h) &= 0 \quad \forall \xi_h \in L_h, \end{aligned}$$

that can be written in operator-form as

$$\begin{pmatrix} \mathbf{A}(v_h) & \mathbf{B}_h \\ -\mathbf{B}_h^T & 0 \end{pmatrix} \begin{pmatrix} \mathbf{v}_h \\ \mathbf{p}_h \end{pmatrix} = \begin{pmatrix} \mathbf{f}_h \\ 0 \end{pmatrix},$$

where

$$(\mathbf{A}_h(v_h))_{ij} = (\sigma \phi_j, \phi_i) + \frac{1}{Re} (\nabla \phi_j, \nabla \phi_i) + (v_h \cdot \nabla \phi_j, \phi_i), \quad i, j = 1, \dots, N,$$

and \mathbf{B}_h is defined as in (3.21):

$$(\mathbf{B}_h)_{ij} = -(\xi_j, \nabla \cdot \phi_i), \quad i = 1, \dots, N, \quad j = 1, \dots, N_p.$$

This discrete operator could further be written as a third order tensor $\mathbf{A}_h^{(3)}$ independent of the transport direction v_h :

$$(\mathbf{A}_h^{(3)})_{ijk} = (\sigma \phi_j, \phi_i) + \frac{1}{Re} (\nabla \phi_j, \nabla \phi_i) + (\phi_k \cdot \nabla \phi_j, \phi_i), \quad i, j, k = 1, \dots, N.$$

The effort for assembling this tensor would however dominate the whole procedure and storing such a third order tensor would require vast amounts of memory. Instead of discretizing the nonlinear problem one usually first treats the nonlinearity by an outer iteration. Here, we discuss two common approaches for linearization.

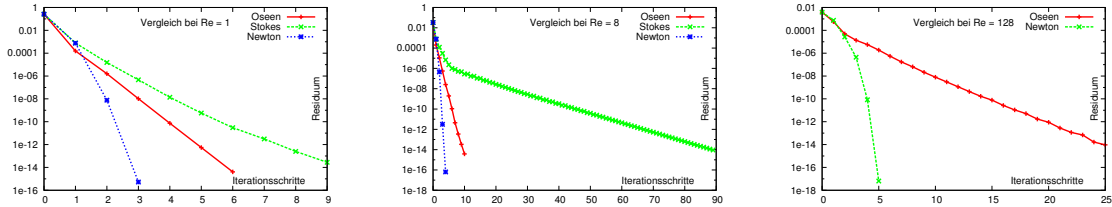


Figure 3.8: Comparison of different linearization techniques. We show the residual over the iteration count. From left to right: flow at Reynolds number $Re = 1, 8, 128$.

3.4.1 Oseen fixed point linearization

We iterate $v^l \rightarrow v \in \mathcal{V}_f$ by linearization of the nonlinearity at the old step v^{l-1} . Given $v^{l-1} \in \mathcal{V}_f$ find $\{v^l, p^l\} \in \mathcal{V}_f \times \mathcal{L}_f$ such that

$$\begin{aligned} (\sigma v^l + v^{l-1} \cdot \nabla v^l, \phi) + \frac{1}{Re} (\nabla v^l, \nabla \phi) - (p^l, \nabla \cdot \phi) &= (g, \phi) \quad \forall \phi \in \mathcal{V}_f, \\ (\nabla \cdot v^l, \xi) &= 0 \quad \forall \xi \in \mathcal{L}_f. \end{aligned}$$

In every step of this iteration a linear partial differential equation must be solved. This linear problem is called the *Oseen equation*. The same linearization has been used for proving existence of a Navier-Stokes solution in Lemma 24. It shows, that this iteration converges for small Reynolds numbers. The convergence $v^l \rightarrow v \in \mathcal{V}_f$ however is always only linear and the convergence rate will depend on Re . In Figure 3.8 we show the convergence history of the Oseen fixed point iteration for different Reynolds numbers.

In a further simplification of this linearization, we treat the nonlinearity completely explicitly and iterate $v^{l-1} \rightarrow v^l \in \mathcal{V}$ by solving

$$\begin{aligned} (\sigma v^l, \phi) + \frac{1}{Re} (\nabla v^l, \nabla \phi) - (p^l, \nabla \cdot \phi) &= (g, \phi) - (v^{l-1} \cdot \nabla v^{l-1}, \phi) \quad \forall \phi \in \mathcal{V}, \\ (\nabla \cdot v^l, \xi) &= 0 \quad \forall \xi \in \mathcal{L}. \end{aligned}$$

Every step of this iteration consists of solving a generalized (for $\sigma > 0$) Stokes equations. This *Stokes Linearization* can only be used for very small Reynolds numbers and converges very slowly. Again, see Figure 3.8 for the convergence behavior of this iteration compared to the Stokes linearization.

3.4.2 Newton iteration

The Newton method for solving nonlinear problems can also be defined in infinite dimensional Banach spaces. For the following, we assume, that the nonlinear partial differential equation is given in variational formulation by

$$u \in \mathcal{V} : A(u)(\phi) = F(\phi) \quad \forall \phi \in \mathcal{V}, \quad (3.33)$$

where $A(\cdot)(\cdot)$ is a semi-linear form, which is linear in the second argument and sufficiently differentiable. Here, by differentiability we consider the *Gâteaux derivative* as a generalization of the directional derivative to mappings between infinite dimensional spaces. By

$$A'(u)(w, \phi) := \frac{d}{ds} A(u + sw)(\phi) \Big|_{s=0},$$

we denote the derivative of $A(\cdot)(\cdot)$ in $u \in \mathcal{V}$ in direction $w \in \mathcal{V}$. The Newton iteration for solving (3.33) starts with an initial guess $u^0 \in \mathcal{V}$ and iterates for $l = 1, \dots$

$$w^l \in \mathcal{V} : \quad A'(u^{l-1})(w, \phi) = F(\phi) - A(u^{l-1})(\phi) \quad \forall \phi \in \mathcal{V},$$

$$u^l := u^{l-1} + w^l. \quad (3.34)$$

In every step of the Newton method a linear partial differential equation arises that can be discretized with the finite element method. The Newton iteration is usually considered in a defect correction way like (3.34). This allows for simple damping strategies that are necessary for complicated problems if no good initial guess $u^0 \in \mathcal{V}$ is known. As this is the usual case for complex problems arising in fluid-structure interaction we shortly introduce a common damping strategy:

Definition 15 (Damped Newton Iteration). *Start with $u^0 \in \mathcal{V}$ and compute $\rho^0 := \|F - A(u^0)\|$. Iterate for $l = 1, 2, \dots$:*

1. Solve Newton update $w^l \in \mathcal{V}$ by

$$w^l \in \mathcal{V} : \quad A'(u^{l-1})(w, \phi) = F(\phi) - A(u^{l-1})(\phi) \quad \forall \phi \in \mathcal{V}$$

2. Set $\omega^j = 1$ and iterate $j = 1, \dots$

- a) Update solution

$$u^{l,j} := u^{l-1} + \omega^j w^l.$$

- b) Compute residual

$$\rho^{l,j} := \|F - A(u^{l,j})\|.$$

- c) If $\rho^{l,j} < \rho^{l-1}$ set $u^l := u^{l,j}$ and continue with $l + 1$ at 1., otherwise set

$$\omega^{j+1} := \gamma \omega^j,$$

where $\gamma < 1$ and continue with $j + 1$ at 2.a.

Details on the nonlinear partial differential equations and the application of Newton's method is found in the literature [79].

For applying the Newton scheme to the Navier-Stokes equations we must compute the Gâteaux derivative of the variational formulation. For

$$A(v, p)(\phi, \xi) := (\sigma v, \phi) + (v \cdot \nabla v, \phi) + \frac{1}{Re}(\nabla v, \nabla \phi) - (p, \nabla \cdot \phi) + (\nabla \cdot v, \xi),$$

it holds for the search direction $\{w, q\} \in \mathcal{V}_f \times \mathcal{L}_f$:

$$A'(v, p)(w, q, \phi, \xi) = (\sigma w, \phi) + (v \cdot \nabla w + w \cdot \nabla v, \phi) + \frac{1}{Re}(\nabla w, \nabla \phi) - (q, \nabla \cdot \phi) + (\nabla \cdot w, \xi),$$

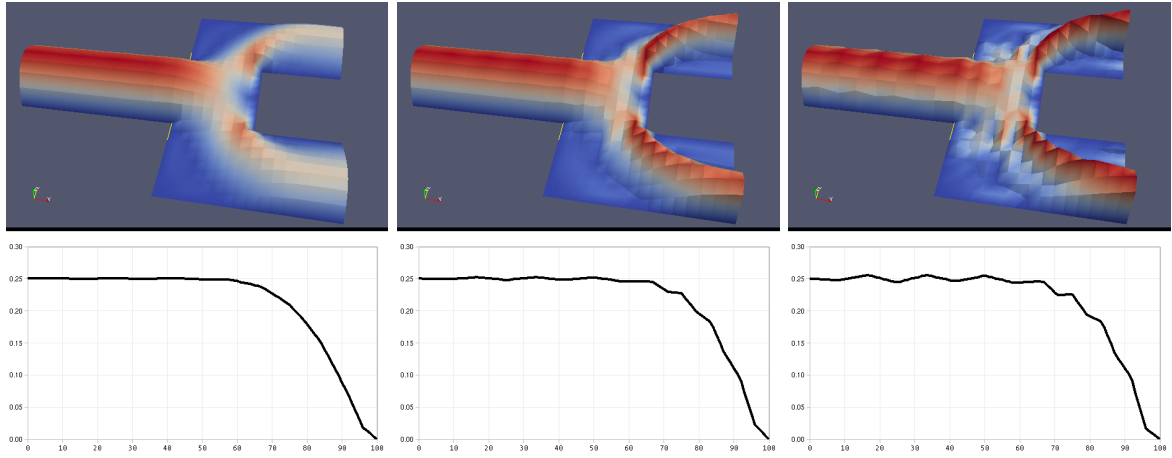


Figure 3.9: Galerkin approximation of a branching flow for increasing Reynolds numbers $Re = 100$, $Re = 500$ and $Re = 2500$.

Then, in every step of the Newton iteration a linear saddle-point problem must be solved for the update $w^l \in \mathcal{V}_f$ of velocity and $q^l \in \mathcal{L}_f$ of pressure:

$$\begin{aligned} (\sigma w^l, \phi) + (v^{l-1} \cdot \nabla w^l + w^l \cdot \nabla v^{l-1}, \phi) + \frac{1}{Re} (\nabla w^l, \nabla \phi) &= (f, \phi) \\ -(\sigma v^{l-1}, \phi) - (v^{l-1} \cdot \nabla v^{l-1}, \phi) - \frac{1}{Re} (\nabla v^{l-1}, \nabla \phi) \quad \forall \phi \in \mathcal{V}_f \\ (\nabla \cdot w^l, \xi) &= -(\nabla \cdot v^{l-1}, \xi) \quad \forall \xi \in \mathcal{L}_f. \end{aligned} \quad (3.35)$$

Remark 25 (Linearization of the Navier-Stokes equation by Newton's method). *In every step of the Newton method a linear saddle-point problem of Reaction-Diffusion-Transport type must be solved. This linear problem is difficult to solve as it is neither symmetric nor positive. The reaction part has the coefficient*

$$(\sigma w^l + w^l \cdot \nabla v^{l-1}, \phi) = ([\sigma I + \nabla v^{l-1}] w^l, \phi),$$

and depending on ∇v^{l-1} , it can be positive or negative. A negative sign can cause severe problems in the linear solver.

In terms of Problem 39, the sequence of discretization and linearization can be swapped. For a convergence analysis of the Newton iteration, one however always treats the non-discretized set of equations like discussed in this section. This approach allows to derive convergence estimates that are uniform in the mesh-size $h > 0$ and hold under mesh convergence $h \rightarrow 0$. See Deuflhard [79], or Rannacher ??.

3.4.3 Discretization of transport dominant flows

The Galerkin discretization of the Navier-Stokes equations sometimes shows spurious oscillations, if the Reynolds number is large. This numerical instability arises, if the convection term $v \cdot \nabla v$ gets dominant over the viscous term $-\nu \Delta v$. In Figure 3.9 we show the flow in a branching channel for increasing Reynolds numbers. In the top row of the figures we show the velocity

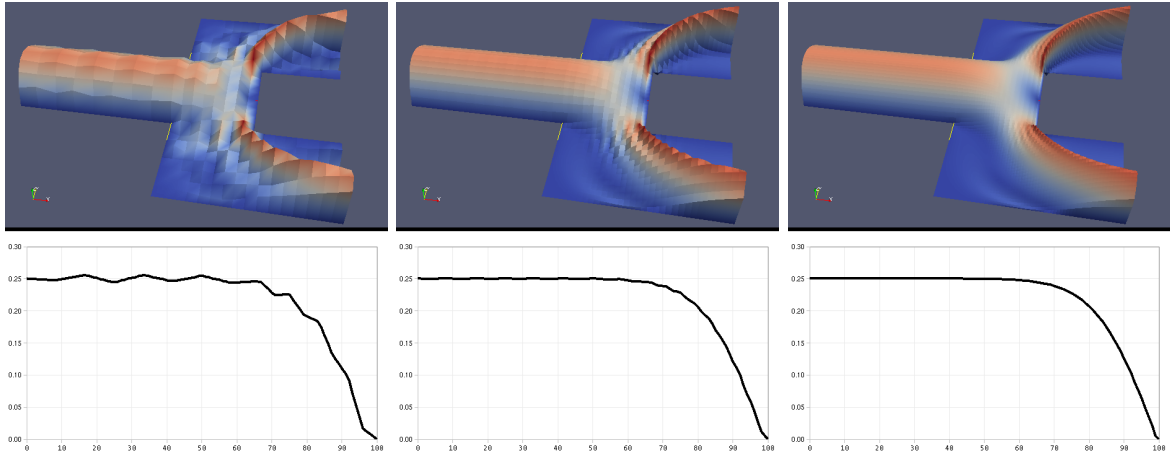


Figure 3.10: Galerkin approximation of a branching flow Reynolds number $Re = 2500$ under mesh refinement $h = 2^{-3}$, $h = 2^{-4}$ and $h = 2^{-5}$.

profile of the fluid, in the bottom row, we plot the value of the velocity at the center-line $y = 0$ of the domain, where the fluid hits the branching. For increasing Reynolds numbers, the velocity profile oscillated and does not look physical. The simulations in Figure 3.9 have all been carried out on a coarse mesh with mesh size $h = 2^{-3}$. In Figure 3.10 we repeat these simulations for Reynolds number $Re = 2500$ on a sequence of finer meshes. We observe, that the oscillations disappear for $h \rightarrow 0$.

These kind of transport instabilities can be analyzed with help of a simple one-dimensional model problem

$$-\epsilon u'' + u' = 0, \quad u(0) = 1, \quad u(1) = 0, \quad (3.36)$$

which has the exact solution

$$u(x) = \frac{\exp(\epsilon^{-1}) - \exp(x\epsilon^{-1})}{\exp(\epsilon^{-1}) - 1},$$

and features a boundary layer of width $O(\epsilon)$ at $x = 1$. For a Galerkin discretization of this problem with piece-wise linear finite elements - that corresponds to the standard central difference discretization - one discovers, that the system matrix loses its diagonal dominance, if $h < 2\epsilon$, see e.g. Johnson [139]. To tackle this problem, two different approaches are usually considered.

First, it is possible to use a Galerkin discretization, that does not contain such strong smoothness properties that make steep layer impossible. It shows that by discretization with discontinuous finite elements in space one can bypass stability problems caused by transport. Again, see Johnson [139] or Cockburn et al. [71]. The use of discontinuous finite elements however brings along the disadvantage of high computational effort, as the number of degrees of freedom is substantially bigger compared to a continuous finite element approach of the same degree.

The second approach consists in adding stability by modifying the variational formulation of the problem in such a way, that diffusion is added to the set of equations. This modification must be so significant, that it eliminates oscillations, it however must be small enough to still give good approximation results for the original problem. In particular, we expect that for $h \rightarrow 0$ the additional stabilization must vanish. The most simple approach, the *artificial*

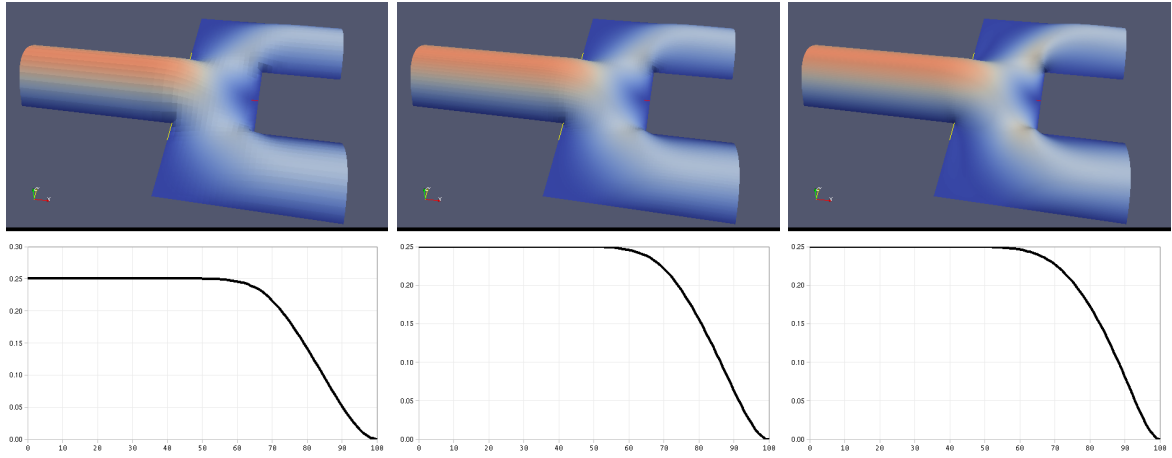


Figure 3.11: Artificial diffusion stabilization for a branching flow at Reynolds number $Re = 2500$ under mesh refinement $h = 2^{-3}$, $h = 2^{-4}$ and $h = 2^{-5}$.

diffusion method simply adds stability by increasing the viscosity in a h -depending way. The model problem (3.36) stabilized with the artificial diffusion method gets

$$-\tilde{\epsilon}(h)u'' + u' = 0, \quad u(0) = 1, \quad u(1) = 0, \quad \tilde{\epsilon}(h) := \epsilon + \frac{1}{2}h. \quad (3.37)$$

As for $\tilde{\epsilon}$ it holds $h < 2\tilde{\epsilon}(h) = 2\epsilon + h$ for all $h > 0$, a standard discretization of (3.37) will always be diagonally dominant and give monotone results. This simple artificial diffusion technique however limits the approximation accuracy of the resulting scheme to first order, see Problem 40. In Figure 3.11 we show the artificial diffusion stabilization for the branching flow example at Reynolds number $Re = 2500$. The result is stable and the velocity profile looks smooth. However, at $Re = 2500$ the solution is fully governed by the artificial viscosity, not by $\nu \sim Re^{-1}$. Comparing Figures 3.10 (right) and 3.11 a severe discrepancy between the stabilized and the physical profile gets visible.

Another stabilization technique falls into both approaches. The *Streamline Upwind Petrov Galerkin* method (SUPG) adds stability by introducing a Petrov Galerkin formulation of the model problem with a modified test-function $\phi + \delta_h\phi'$ where $\delta_h \sim h$:

$$\begin{aligned} (-\epsilon u_h'' + u'_h, \phi_h + \delta_h\phi'_h) &= (f, \phi_h + \delta_h\phi'_h) & \forall \phi_h \in V_h \\ &\Leftrightarrow \\ (\epsilon u'_h, \phi'_h) + (u'_h, \phi_h) + (\delta_h u'_h, \phi'_h) + (\delta_h(-\epsilon u_h'' - f), \phi'_h) &= (f, \phi_h) & \forall \phi_h \in V_h, \end{aligned}$$

While the term $(\delta_h u'_h, \phi'_h)$ adds diffusion to the equation and stabilizes the solution, the further term $(\delta_h(-\epsilon u_h'' - f), \phi'_h)$ assures consistency of the solution. It holds

Lemma 68 (Streamline Upwind Petrov Galerkin). *Let $u \in H^{r+1}(I)$ be the solution to the model problem (3.36) and $u_h \in V_h^r$ be the SUPG solution. It holds*

$$\|u - u_h\| + \sqrt{h}\|u' - u'_h\| \leq ch^{r+\frac{1}{2}}\|u\|_{r+1}.$$

Proof. See Johnson [139]. □

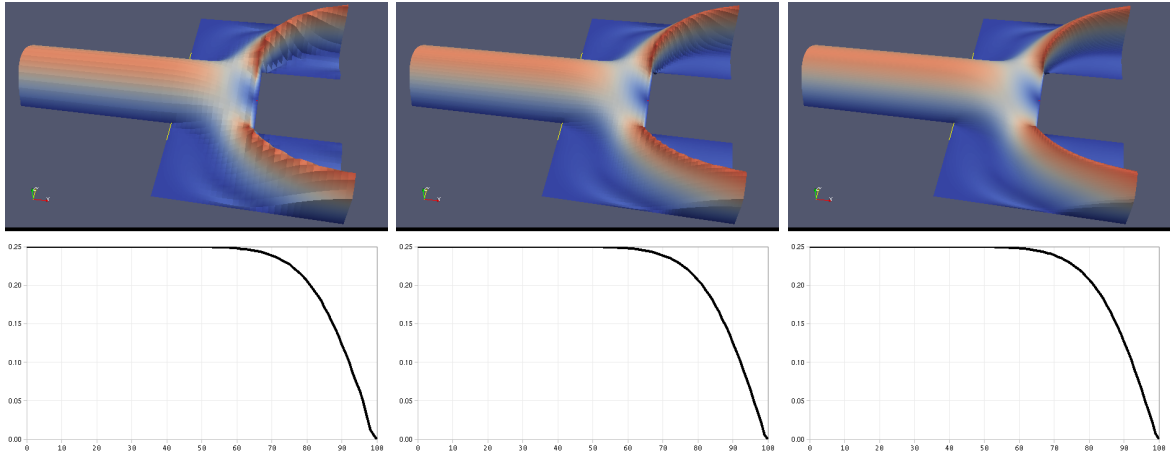


Figure 3.12: Local Projection Stabilization for a branching flow at Reynolds number $Re = 2500$ under mesh refinement $h = 2^{-3}$, $h = 2^{-4}$ and $h = 2^{-5}$.

The SUPG method can easily be applied to the Navier-Stokes equations. This has first been done by Brooks and Hughes [54]. We modify the test-space of the momentum equation to get

$$\begin{aligned} & (\partial_t v + v \cdot \nabla v, \phi) + \frac{1}{Re} (\nabla v, \nabla \phi) - (p, \nabla \cdot \phi) \\ & + (\partial_t v - Re^{-1} \Delta v + \nabla p - f, \delta_h v \cdot \nabla \phi) + (v \cdot \nabla v, \delta_h v \cdot \nabla \phi) = (f, \phi) \\ & (\nabla \cdot v, \xi) = 0. \end{aligned}$$

Again, stability is given by the term $(v \cdot \nabla v, \delta_h v \cdot \nabla \phi)$, where the second additional term stands for consistency only. The drawback of this technique is the introduction of a second order coupling in the pressure and a third order term regarding the velocity. Both terms give rise to boundary layers. Further, the SUPG technique couples the time derivative with spatial derivatives. A correct discretization of this term $(\partial_t v, \delta_h v \cdot \nabla \phi)$ is difficult to implement. For a discussion and analysis on transient problems, see [43, 59]. The SUPG method gives accurate and stable results for all polynomial degrees and apart from the Laplacian and the time-derivative in the consistency term, an implementation is straightforward. The SUPG stabilization can easily be combined with the PSPG pressure stabilization technique as introduced in Section 3.3.2. This combination of stabilization techniques is one of the most common discretization approaches for the incompressible Navier-Stokes equations.

The drawback of these consisting residual based stabilization techniques is the introduction of couplings between time-derivative, velocity and pressure. These couplings are not physical. Further, the implementation of these couplings can be complex and can have a negative impact on the behavior of iterative solvers. Another stabilization technique for convective flows is based on a projection of the solution to a subspace, similar to the Local Projection Stabilization for the inf-sup condition introduced in Section 3.3.2. The SUPG method introduces the stabilization term

$$s_{\text{SUPG}}(v, p)(\phi) = (\partial_t v - Re^{-1} \Delta v + \nabla p - f + v \cdot \nabla v, \phi).$$

For the solution $\{v, p\}$ it holds

$$v \cdot \nabla v = f - \partial_t v + Re^{-1} \Delta v - \nabla p.$$

Hence, we can replace the right hand side of this relation by an approximation of the left hand side, e.g. by a projection of $v \cdot \nabla v$ onto a coarser mesh. This is the idea of the Local Projection Stabilization (LPS) for convective flows, as introduced by Becker and Braack [22]:

$$s_{\text{LPS}}(v)(\phi) = (v \cdot \nabla v - \overline{v \cdot \nabla v}, \delta_h v \cdot \nabla \phi).$$

Different variants of the LPS method are discussed in the literature. One of the most simple variant uses a local projection to a mesh with double mesh-spacing $\pi_h : V_h \rightarrow V_{2h}$:

$$\begin{aligned} & (\partial_t v + v \cdot \nabla v, \phi) + \frac{1}{Re} (\nabla v, \nabla \phi) - (p, \nabla \cdot \phi) \\ & + (v_h \cdot \nabla v_h - v_{2h} \cdot \nabla v_{2h}, \delta_h (v_h \cdot \nabla \phi_h - v_{2h} \cdot \nabla \pi_{2h})) = (f, \phi) \\ & (\nabla \cdot v, \xi) = 0, \end{aligned}$$

where for abbreviation we used $v_{2h} := \pi_h v_h$ and $\phi_{2h} := \pi_h \phi_h$. In Figure 3.12 we present results for the Local Projection stabilization for the branching flow problem at Reynolds number $Re = 2500$. The results are less smooth as in the case of artificial diffusion stabilization shown in Figure 3.11, the layers however are clearly more accurate and close to the Galerkin discretization on fine meshes, indicated in Figure 3.10. The LPS method has the advantage, that it is diagonal in a sense, that no additional couplings are introduced. The LPS term stabilizing the convection will involve the velocity only, for LPS stabilization of the inf-sup condition only a pressure term is introduced. This diagonal setup will be of importance when considering complex coupled problems like fluid-structure interactions.

For comparison of these stabilization techniques, for numerical analysis and different variants see the overview articles by Braack et al. [43].

Remark 26. *Flux-Correction* A complete different approach for stabilizing transport equations is the technique of algebraic flux correction. As the name suggests, this method does not fall into the residual based Galerkin approaches. Instead, the system resulting matrix is modified by means of algebraic transformations with the goal to ensure the discrete maximum principle. This rather new technique is very successful and provides excellent results. For an overview, we refer to [148, 147] or [38] in the context of ALE schemes for moving domains.

3.5 Discretization of interface-problems

The Fully Eulerian formulation is what we call an *interface problem*, as the equation undergoes some changes across an internal interface $\mathcal{I} \subset \Omega$. Here, this interface is exactly the interface between fluid-problem and solid-problem, where the equation changes from the incompressible Navier-Stokes equations to a solid equation. Physical reasoning tells us, that deformation \mathbf{u} and velocity \mathbf{v} (at least in normal direction) are continuous at this interface, we however cannot expect higher regularity. In terms of regularity, it holds $\mathbf{u}, \mathbf{v} \in [H^1(\Omega)]^d$, however $\mathbf{u}, \mathbf{v} \notin [H^2(\Omega)]^d$. In each of the two parts, \mathcal{F} and \mathcal{S} , we can expect this higher regularity. When it comes to numerical approximation, convergence is assured by best approximation and interpolation estimates. These always locally require high regularity, see Section 3.2.1. If we are able to resolve the internal interface with the finite element mesh, interface problems do not pose an additional problem, as interpolation estimates only act locally and will work, as long as no mesh-element is cut by the interface.

For the Fully Eulerian formulation however, it will in general not be possible to choose a matching finite element mesh, as

- the location of the interface is a priori not known. Instead, it is implicitly given by the solution itself;
- the interface is usually not a polygonal, such that an exact resolution will not be possible;
- the interface is moving in time - if the problem is non-stationary - and new finite element meshes would be necessary in each time step. This is in principle possible, but would be very costly.

To explain efficient concepts of discretizing interface problems, we will focus on a very simple interface problem, the Laplace equation with a coefficient that has a jump within the domain $\Omega = \Omega_1 \cup \mathcal{I} \cup \Omega_2$:

$$-\nabla \cdot (\kappa_i \nabla u) = f \text{ on } \Omega_i, \quad i = 1, 2, \quad [u] = 0 = [\kappa \partial_n u] = 0 \text{ on } \mathcal{I}, \quad (3.38)$$

and with $u = 0$ on the outer boundary $\partial\Omega$. $\kappa_1, \kappa_2 > 0$ are diffusion parameters. By

$$[u](x) := \lim_{s \downarrow 0} u(x + ns) - \lim_{s \uparrow 0} u(x + ns), \quad x \in \mathcal{I},$$

we denote the jump of u at the interface \mathcal{I} . The variational formulation of this interface problem is given by

$$u \in H_0^1(\Omega) : \quad a(u, \phi) := \sum_{i=1}^2 (\kappa_i \nabla u, \nabla \phi) = (f, \phi) \quad \forall \phi \in H_0^1(\Omega),$$

and existence of solutions can be shown by standard arguments. We assume, that the partitioning of Ω into Ω_1 and Ω_2 is non-overlapping $\Omega_1 \cap \Omega_2 = \emptyset$ and that both subdomains Ω_i ($i = 1, 2$) have a boundary with sufficient regularity such that for smooth right hand sides it holds for the solution of (3.38), that

$$u \in H_0^1(\Omega) \cap H^{r+1}(\Omega_1 \cup \Omega_2),$$

for a given $r \in \mathbb{N}$, with $r \geq 1$. See Babuška [5] for an early work on such an interface problem.

Interface problems are elaborately discussed in literature []. If the interface \mathcal{I} cannot be resolved by the mesh, the overall error for a standard finite element ansatz will be bound by

$$\|\nabla(u - u_h)\|_\Omega = \mathcal{O}(h^{1/2}),$$

independent of the polynomial degree r of the finite element space, see the early work of Babuška [5] or MacKinnon and Carey [156]. In Figure 3.13, we show the H^1 and L^2 errors for a simple interface problem with curved interface that is not resolved by the finite element mesh. Both linear and quadratic finite elements only give $\mathcal{O}(h^{1/2})$ accuracy in the H^1 -seminorm and $\mathcal{O}(h)$ in the L^2 -norm. This is due to the limited regularity of the solution across the interface.

It has been shown, that for interface problems with jumping coefficients causing weak discontinuities, optimal convergence can be recovered by a harmonic averaging of the diffusion constants [224, 212]. Such an averaging procedure has been applied to multiphase flows, it is however not suitable for problems, where two entirely different types of differential equations are coupled on the interface, as it is the case for fluid-structure interactions.

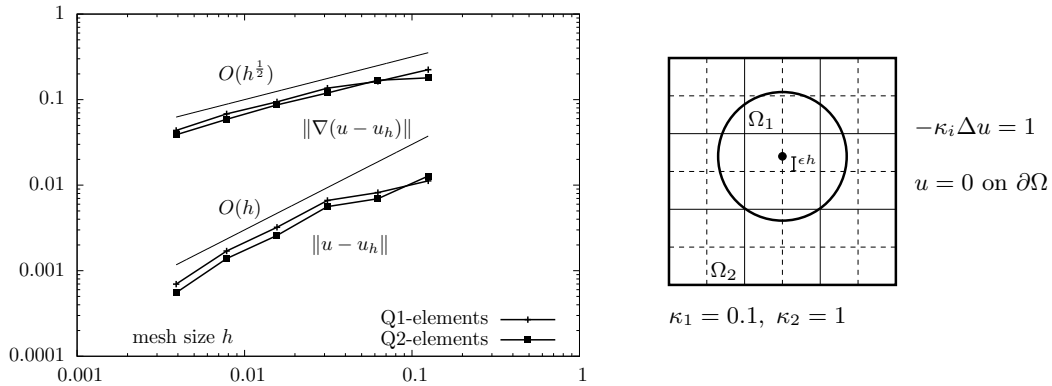


Figure 3.13: L^2 - and H^1 -error for a standard finite element simulation for a diffusion problem with a discontinuity in the diffusion coefficient. Configuration of the test-problem in the right sketch. Details on this problem are given in Section 3.5.3

Given a fitted finite element configuration, the optimal order of convergence is guaranteed [5, 90, 238, 51]. If the interface is moving, curved or has small scale features, the repeated generation of fitted finite element meshes can exceed the feasible effort. Further developments are based on local modifications of the finite element mesh, that only alter mesh elements close to the interface [39, 250]. By combining local mesh modifications close to the interface with an isoparametric approximation of curved interfaces, even higher order approximation could be shown [88].

An alternative approach is based on unfitted finite elements, where the mesh is fixed and does not resolve the interface. Here, proper accuracy is gained by local modifications or enrichment of the finite element basis. Prominent examples for these methods are the extended finite element method (XFEM) [167], the generalized finite element method [7] or the unfitted Nitsche method by Hansbo and Hansbo [113, 114], that casts the XFEM method into a new light. These enrichment methods are well analyzed and show the correct order of convergence. One drawback of all these methods is a complicated structure that requires local modifications in the finite element spaces leading to a variation in the connectivity of the system matrix and number of unknowns. In non-stationary computations, these methods can call for a change of the memory pattern in every time-step, a potentially costly operation.

Here, we propose a finite element technique for interface problems that fits both into the context of fitted methods and modified finite element schemes. Instead of resolving the interface by a motion of mesh nodes, we locally adapt the finite element in an implicit parametric way, such that the finite element bases can reflect weak discontinuities at the interface. This scheme requires neither an enrichment of the basis nor a modification of the mesh.

3.5.1 Parametric interface finite elements

Let Ω_h be a form and shape-regular triangulation of the domain $\Omega \subset \mathbb{R}^2$ into open quadrangles. The mesh Ω_h does not necessarily resolve the partitioning $\Omega = \Omega_1 \cup \Gamma \cup \Omega_2$ and the interface Γ can cut the elements $K \in \Omega_h$. For simplicity, we assume that the outer boundary $\partial\Omega$

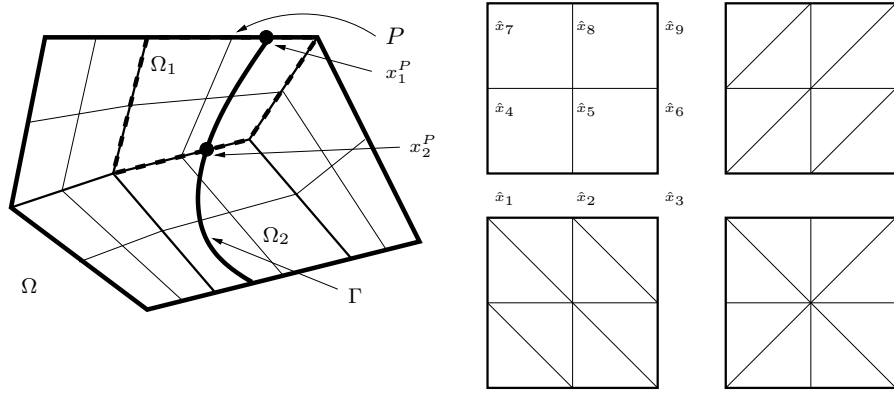


Figure 3.14: Left: triangulation Ω_h of a domain Ω , that split into Ω_1 and Ω_2 with interface Γ . The elements in Ω_h are arranged in a patched way. Patch P is cut by Γ at x_1^P and x_2^P . Right: subdivision of reference patches $\hat{P}_1, \hat{P}_2, \hat{P}_3, \hat{P}_4$ (top left to bottom right) into eight triangles each.

can be resolved by the mesh. Otherwise, the approximation of the curved boundary must be considered, see Section 3.2.3.

Next, we assume, that the mesh Ω_h has a patch-hierarchy in such a way, that each four adjacent quads arise from uniform refinement of one common father-element, see Figure 3.14. Such a mesh-hierarchy is naturally given for finite element methods based on adaptive mesh refinement and also commonly used for error estimation methods [29] or projection based stabilization schemes [21]. The interface Γ may cut the patches in the following way:

1. Each (open) patch $P \in \Omega_h$ is either not cut $P \cap \Gamma = \emptyset$ or cut in exactly two points on its boundary: $P \cap \Gamma \neq \emptyset$ and $\partial P \cap \Gamma = \{x_1^P, x_2^P\}$.
2. If a patch is cut, the two cut-points x_1^P and x_2^P may not be inner points of the same edge.

In principle, these assumptions only rule out two possibilities: a patch may not be cut multiple times and the interface may not enter and leave the patch at the same edge. Both situations can be avoided by refinement of the underlying mesh. If the interface is matched by an edge, the patch is not considered cut.

Modification of the finite element space

We define the finite element trial space $V_h \subset H_0^1(\Omega)$ as iso-parametric space on the triangulation Ω_h :

$$V_h = \left\{ \phi \in C(\bar{\Omega}), \phi \circ T_P^{-1} \Big|_P \in \hat{Q} \text{ for all patches } P \in \Omega_h \right\},$$

where $T_P \in [\hat{Q}]^2$ is the mapping between the reference patch $\hat{P} = (0, 1)^2$ and every patch $P \in \Omega_h$ such that

$$T_P(\hat{x}_i) = x_i^P, \quad i = 1, \dots, 9,$$

for the nine nodes x_1^P, \dots, x_9^P in every patch, see Figure 3.14 (left). The reference space \hat{Q} is a piecewise polynomial space of degree 1, that will depend on whether a patch P is cut by the

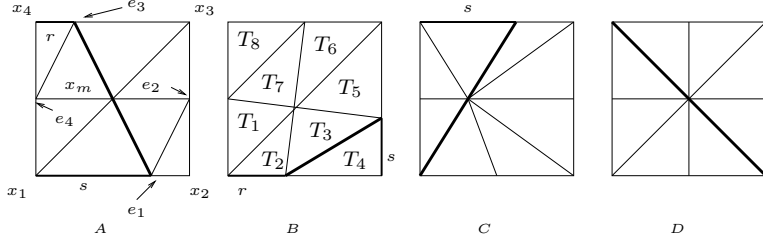


Figure 3.15: Different types of cut patches. The subdivision can be anisotropic with $r, s \in (0, 1)$ arbitrary.

interface or not. For patches $P \in \Omega_h$ not cut by the interface, we choose the standard space of piecewise bilinear functions:

$$\hat{Q} = \left\{ \phi \in C(\bar{P}), \phi|_{K_i} \in \text{span}\{1, x, y, xy\}, K_1, \dots, K_4 \in P \right\}.$$

If a patch $P \in \Omega_h$ is cut by the interface, we divide the reference patch into eight triangles T_1, \dots, T_8 and define

$$\hat{Q}_{\text{mod}} = \left\{ \phi \in C(\bar{P}), \phi|_{T_i} \in \text{span}\{1, x, y\}, T_1, \dots, T_8 \in P \right\}.$$

Depending on the position of the interface Γ in the patch P , three different reference configurations are considered, see the right sketch in Figure 3.14.

It is important to note, that the functions in \hat{Q} and \hat{Q}_{mod} are all piecewise linear on the edges ∂P , such that mixing different element types does not affect the continuity of the global finite element space. We denote by $\{\hat{\phi}^1, \dots, \hat{\phi}^9\}$ the standard Lagrange basis of \hat{Q} or \hat{Q}_{mod} with $\hat{\phi}^i(x_j) = \delta_{ij}$. The transformation T_P is given by

$$T_P(x) = \sum_{i=1}^9 x_i^P \hat{\phi}_i(x).$$

Next, we present the subdivision of interface patches P into eight triangles each. We distinguish four different types of interface cuts, see Figure 3.15:

Configuration A The patch is cut at the interior of two opposite edges.

Configuration B The patch is cut at the interior of two adjacent edges.

Configuration C The patch is cut at the interior of one edge and in one node.

Configuration D The patch is cut in two opposite nodes.

Configurations A and B are based on the reference patches \hat{P}_2 and \hat{P}_3 , configurations C and D use the reference patch \hat{P}_4 , see Figure 3.14. By $e_i \in \mathbb{R}^2$, $i = 1, 2, 3, 4$ we denote the vertices on the edges, by $x_m \in \mathbb{R}^2$ the midpoint of the patch. The parameters $r, s \in (0, 1)$ describe the relative position of the intersection points with the interface on the outer edges.

If an edge is intersected by the interface we move the corresponding point e_i on this edge to the point of intersection. The position of the midpoint x_m depends on the specific configuration, see [101] for details.

As the cut of the elements can be arbitrary with $r, s \rightarrow 0$ or $r, s \rightarrow 1$, the triangle's aspect ratio can be very large, considering $h \rightarrow 0$ it is not necessarily bound. We can however guarantee, that the maximum angles in all triangles will be well bound away from 180° :

Lemma 69 (Maximum angle condition). *All interior angles of the triangles shown in Figure 3.15 are bound by 144° independent of $r, s \in (0, 1)$.*

Proof. The proof follows by basic geometrical considerations, see [101]. \square

This maximum angle conditions allows us to define robust Lagrangian interpolation operators $I_h : H^2(T) \cap C(\bar{T}) \rightarrow V_h$ with accurate error estimates

$$\|\nabla^k(u - I_h u)\|_T \leq c_i h_{T,\max}^{2-k} \|\nabla^2 u\|_T, \quad k = 0, 1, \quad (3.39)$$

where $c_i > 0$ is a constant and $h_{T,\max}$ is the maximum diameter of a triangle $T \in P$ (see e.g. [4]). The interpolation error estimates are robust with respect to the maximum diameter $h_{T,\max} \approx h_P$ that is of the same order as the diameter of the patches P . We do not get (and will not depend on) an optimal interpolation result with respect to the anisotropic triangles in terms of short edges $h_{T,\min} \ll h_{T,\max}$.

In order to apply such an interpolation result at the interface, i.e. on triangles $T \in \Omega_h$, that belong to patches cut by the interface, we must take care of the fact, that the partitioning of the mesh $\Omega_h = \Omega_{1,h} \cup \Omega_{2,h}$ does not conform with the partitioning of the domain $\Omega = \Omega_1 \cup \mathcal{I} \cup \Omega_2$, i.e., $\Omega_{i,h}$ does not necessarily cover the same domain as Ω_i . This is always the case, if the interface \mathcal{I} is not a polygon. Then, if $T \in \Omega_{h,i}$ is an element on the interface, i.e. $\mathcal{I} \cap T \neq \emptyset$, the solution v is not smooth enough to locally apply the interpolation estimate (3.39).

The inverse trace inequality however, see [249] allows to extend $u_i \in H^2(\Omega_i)$ to $\tilde{u}_i \in H^2(\Omega)$ with

$$\|\tilde{u}_i - u_i\|_{H^2(\Omega_i)} = 0, \quad \|\tilde{u}_i\|_{H^2(\Omega)} \leq c \|u_i\|_{H^2(\Omega_i)}, \quad i = 1, 2, \quad (3.40)$$

if the interface \mathcal{I} is regular enough (having a $C^{1,1}$ boundary). This construction allows to use the interpolation estimates also on triangles, that are cut by the interface. Let $T \in \Omega_h$ be such an triangle and let $T \subset S$ be the small part, cut by the interface. It holds $|S| = O(h^2)$, see Lemma 54. Let $u \in H^1(\Omega) \cap H^2(\Omega_1 \cup \Omega_2)$ and $I_h u \in V_h$ be the interpolation. Further, let $\tilde{u} \in H^2(T)$ be the extension of $u|_{T \setminus S}$ to T . It holds

$$\begin{aligned} \|\nabla^k(u - I_h u)\|_T &= \|\nabla^k(u - \tilde{u})\|_T + \|\nabla^k(\tilde{u} - I_h u)\|_T \\ &= \|\nabla^K(u - \tilde{u})\|_S + \|\nabla^k(\tilde{u} - I_h \tilde{u})\|_T. \end{aligned}$$

The second part is now the standard interpolation

$$\|\nabla(\tilde{u} - I_h \tilde{u})\|_T \leq ch \|\nabla^2 \tilde{u}\|_T \leq ch \|\nabla^2 u\|_{T \setminus S},$$

while the first part can be estimated using Lemma 56:

$$\|\nabla(u - \tilde{u})\|_S \leq h \|u\|_{H^2(T)}.$$

Altogether, for the interpolation error at the interface, it holds

$$\|\nabla(u - I_h u)\|_T \leq ch \|u\|_T. \quad (3.41)$$

The parametric finite element approach is conforming, as $u_h \in V_h \subset H_0^1(\Omega)$, it is however not consistent, as the discrete solution u_h has its jump at \mathcal{I}_h and not at \mathcal{I} .

Theorem 9 (A priori estimate). *Let $\Omega \subset \mathbb{R}^2$ be a domain with convex polygonal boundary, split into $\Omega = \Omega_1 \cup \Gamma \cup \Omega_2$, where Γ is a smooth interface with C^2 -parametrization. We assume that Γ divides Ω in such a way that the solution $u \in H_0^1(\Omega)$ satisfies the stability estimate*

$$u \in H_0^1(\Omega) \cap H^2(\Omega_1 \cup \Omega_2), \quad \|u\|_{H^2(\Omega_1 \cup \Omega_2)} \leq c_s \|f\|.$$

For the corresponding modified finite element solution $u_h \in V_h$ it holds

$$\|\nabla(u - u_h)\|_\Omega \leq Ch\|f\|, \quad \|u - u_h\|_\Omega \leq Ch^2\|f\|$$

Proof. We repeat the proof from [101], as the original paper suffers from a small inaccuracy, evoked by neglecting, that $\Omega_{i,h}$ is not necessarily a triangulation of Ω_i for $i = 1, 2$. This directly touches the first step (i) of the proof:

(i) Let $e_h = u - u_h$. It holds

$$\begin{aligned} (\kappa \nabla e_h, \nabla \phi_h)_\Omega &= \sum_{i=1}^2 (\kappa_i \nabla e_h, \nabla \phi_h)_{\Omega_i} \\ &= \sum_{i=1}^2 (\kappa_i \nabla u, \nabla \phi_h)_{\Omega_i} - (\kappa_i \nabla u_h, \nabla \phi_h)_{\Omega_{i,h}} + (\delta \kappa_i \nabla u_h, \nabla \phi_h)_{\Omega_i \setminus \Omega_{i,h}} \\ &= \sum_{i=1}^2 (\delta \kappa_i \nabla u_h, \nabla \phi_h)_{\Omega_i \setminus \Omega_{i,h}}, \end{aligned}$$

where

$$\delta \kappa_i = \begin{cases} \kappa_1 - \kappa_2 & i = 1, \\ \kappa_2 - \kappa_1 & i = 2. \end{cases}$$

Hence, by picking $\phi_h = I_h u - u_h$, we get the following perturbed best-approximation property:

$$\|\nabla e_h\|^2 \leq c \|\nabla e_h\| \|\nabla(u - I_h u)\| + \sum_{i=1}^2 \|\delta \kappa_i \nabla u_h\|_{\Omega_i \setminus \Omega_{i,h}} \|\nabla(I_h u - u_h)\|_{\Omega_i \setminus \Omega_{i,h}}$$

For estimating these additional terms close to the interface, we use Lemma 56. It holds

$$\begin{aligned} \|\delta \kappa_i \nabla u_h\|_{\Omega_i \setminus \Omega_{i,h}} &\leq c(\kappa) h^{\frac{1}{2}} \|\nabla u_h\|_\Omega, \\ \|\nabla(I_h u - u_h)\|_{\Omega_i \setminus \Omega_{i,h}} &\leq ch^{\frac{1}{2}} \|\nabla(I_h u - u_h)\|_\Omega. \end{aligned}$$

Together with the interpolation estimate 3.41, the energy estimate follows.

(ii) Further, for the solution $z \in H_0^1(\Omega) \cap H^2(\Omega_1 \cup \Omega_2)$ of the adjoint problem

$$z \in H_0^1(\Omega) : (\kappa \nabla \phi, \nabla z)_\Omega = (e_h, \phi) \|e_h\|^{-1} \quad \forall \phi \in H_0^1(\Omega),$$

it holds $z \in H_0^1(\Omega) \cap H^2(\Omega_1 \cup \Omega_2)$ with $\|z\|_{H^2(\Omega_1 \cup \Omega_2)} \leq c_s$. Using the perturbed Galerkin orthogonality, the L^2 -error can be represented in the following way:

$$\|u - u_h\| = (\nabla e_h, \nabla(z - I_h z)) + \sum_{i=1}^2 (\delta \kappa_i \nabla u_h, \nabla I_h z)_{\Omega_i \setminus \Omega_{i,h}}.$$

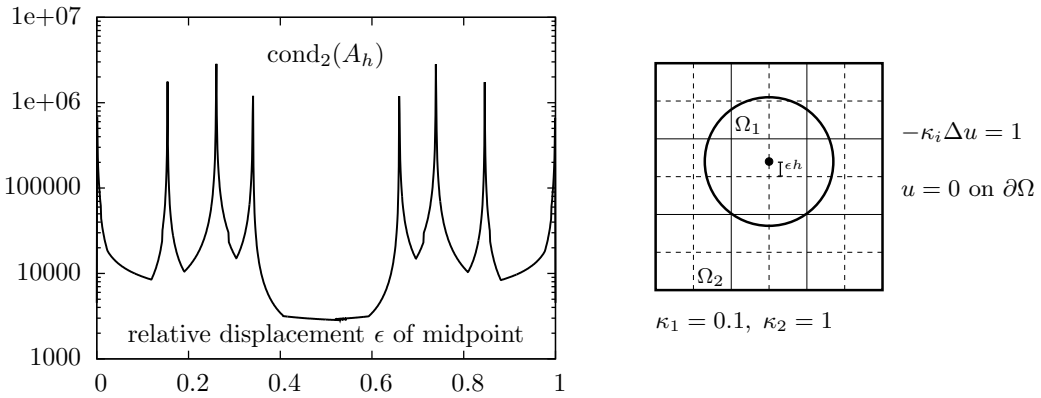


Figure 3.16: Condition number of the system matrix $\text{cond}_2(A_h)$ depending on the displacement of the circle Ω_1 .

Here, the argumentation for estimating the interface elements is more involved. Similar to the discussion in Section 3.2.3, we need to insert the solutions u and z to fully exploit Lemma 56. It holds

$$\begin{aligned}\|\nabla u_h\|_{\Omega_i \setminus \Omega_{i,h}} &\leq \|\nabla u\|_{\Omega_i \setminus \Omega_{i,h}} + \|\nabla(u - I_h u)\|_{\Omega_i \setminus \Omega_{i,h}} + \|\nabla(I_h u - u_h)\|_{\Omega_i \setminus \Omega_{i,h}} \\ &\leq ch\|u\|_{H^2(\Omega)} + ch^{\frac{1}{2}}\|\nabla(I_h u - u_h)\|_{\Omega}.\end{aligned}$$

By once more inserting $\pm u$, it follows, that

$$\|\nabla u_h\|_{\Omega_i \setminus \Omega_{i,h}} \leq ch\|f\|_{\Omega}.$$

Similarly, it holds for the adjoint interpolation by inserting $\pm z$

$$\|\nabla I_h z\|_{\Omega_i \setminus \Omega_{i,h}} \leq \|\nabla z\|_{\Omega_i \setminus \Omega_{i,h}} + \|\nabla(z - I_h z)\|_{\Omega_i \setminus \Omega_{i,h}} \leq ch\|z\|_{H^2(\Omega)}.$$

□

3.5.2 Condition number analysis

The modified finite element ansatz described above has one serious drawback. For certain anisotropies (e.g. $s, r \rightarrow 0$) the condition number of the stiffness matrix is not bounded. To illustrate this, we consider an interface problem where Ω_1 is a circle inside the unit square Ω (see Figure 3.16 right sketch). To study the sensitivity with respect to anisotropies, we move the circle in vertical direction by ϵ . We will give further details on this example in Section 3.5.3. In Figure 3.16 left sketch, we show how the condition number changes for different ϵ . For $\epsilon \rightarrow 0$, the condition number increases with order $\mathcal{O}(1/\epsilon)$.

In this section, we will present a scaled hierarchical finite element basis for the space V_h , that will yield system matrices A_h that satisfy the usual bound $\text{cond}_2(A_h) = \mathcal{O}(h^{-2})$ with a constant that does not depend on the position of the interface Γ relative to the mesh elements.

We split the finite element space V_h in a hierarchical manner

$$V_h = V_{2h} + V_b, \quad N := \dim(V_h) = \dim(V_{2h}) + \dim(V_b) =: N_{2h} + N_b.$$

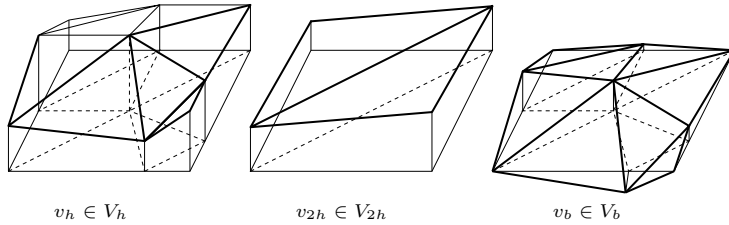


Figure 3.17: Example for a hierarchical splitting of a function $v_h \in V_h$ into coarse mesh part $v_{2h} \in V_{2h}$ and fine mesh fluctuation $v_b \in V_b$.

The space V_{2h} is the standard space of piecewise bilinear or linear functions on the patches $P \in \Omega_h$ equipped with the usual nodal Lagrange basis $V_{2h} = \text{span}\{\phi_{2h}^1, \dots, \phi_{2h}^{N_{2h}}\}$. Therefore, patches cut by the interface are split into two triangles.

The space $V_b = V_h \setminus V_{2h}$ collects all functions, that enrich V_{2h} to V_h . These functions are defined piecewise on T_1, \dots, T_8 in the remaining 5 degrees of freedom, see Figure 3.17 for an example. The basis is denoted by $V_b = \text{span}\{\phi_b^1, \dots, \phi_b^{N_b}\}$. The finite element space V_{2h} is fully isotropic and standard analysis holds. Functions in V_{2h} do not resolve the interface, while the basis functions $\phi_b^i \in V_b$ will depend on the interface location if $\Gamma \subset \text{supp } \phi_b^i$. For a function $v_h \in V_h$ we use the (unique) splitting

$$v_h = \sum_i \vec{v}_h^i \phi_h^i = \sum_{i=1}^{N_{2h}} \vec{v}_{2h}^i \phi_{2h}^i + \sum_{i=1}^{N_b} \vec{v}_b^i \phi_b^i = v_{2h} + v_b \in V_{2h} + V_b,$$

and for this splitting it holds:

Lemma 70 (Hierarchical finite element spaces). *For every $v_h = v_{2h} + v_b \in V_h$ it holds*

$$(i) \quad \|\nabla v_h\|^2 \leq 2\|\nabla v_{2h}\|^2 + 2\|\nabla v_b\|^2,$$

and further

$$(ii) \quad \|\nabla v_{2h}\|^2 + \|\nabla v_b\|^2 \leq C\|\nabla v_h\|^2,$$

with a constant $C > 0$.

Proof. See [101]. □

Using this hierachic splitting of the finite element space together with a diagonal scaling of the system matrix, we can proof the following result:

Theorem 10 (Condition number). *For the hierachic parametrized finite element space $V_h = V_{2h} + V_b$ together with a diagonal scaling of the system matrix \mathbf{A} , it holds*

$$\text{cond}_2(\mathbf{A}) \leq Ch^{-2},$$

with a constant $C > 0$ not depending on the interface location.

Proof. See [101]. □

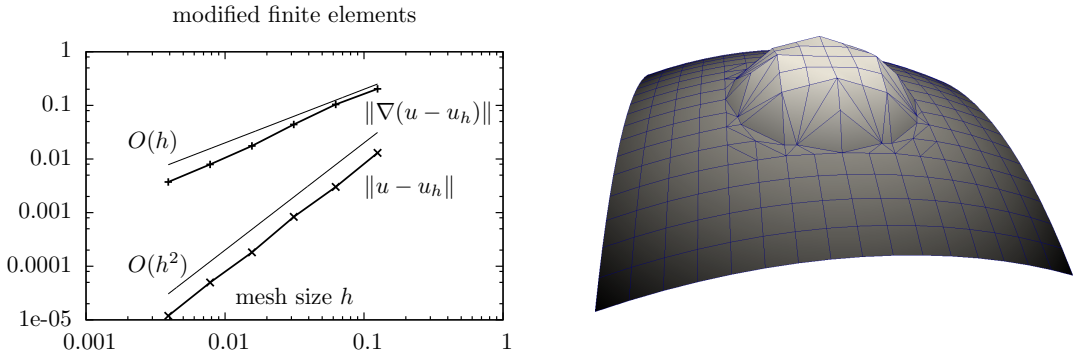


Figure 3.18: Example 1: H^1 - and L^2 -Error under mesh refinement. Right: sketch of the solution.

3.5.3 Numerical examples

In this section, design three different test-cases to validate the modified finite element technique introduced in Section 3.5.1. We will include all different types of interface cuts (configurations A to D) with arbitrary anisotropies including $r, s \rightarrow 0$ or 1.

Example 1: circular interface

This first example has already been considered to discuss the interface approximation in Section 3.5.1 and the dependency of the condition number on the interface in Section 3.5.2, see Figure 3.13 for a sketch of the configuration. The unit square $\Omega = (-1, 1)^2$ is split into a ball $\Omega_2 = B_R(x_m)$, where $R = 0.5$ and $x_m = (0, \epsilon h)$ for an $\epsilon \in [0, 1]$ and $\Omega_1 = \Omega \setminus \bar{\Omega}_2$. As diffusion parameters we choose $\kappa_1 = 0.1$ and $\kappa_2 = 1$ within the inner ball. We choose the analytical solution

$$u(x) = \begin{cases} -\kappa_1 \|x - x_m\|^2 + \frac{1}{4}\kappa_1 - \frac{1}{8}\kappa_2 & x \in \Omega_1, \\ -2\kappa_2 \|x - x_m\|^4, & x \in \Omega_2, \end{cases}$$

to define right hand side $f_i := -\kappa_i \Delta u$ and Dirichlet boundary data. After some steps of global refinement this simple example includes configurations A to C. In Figure 3.18, we plot the the H^1 - and L^2 -norm errors obtained on several levels of global mesh refinement. According to Theorem 9, we observe linear convergence in the H^1 -norm and quadratic convergence in the L^2 -norm. For comparison, Figure 3.13 shows the corresponding results using the standard non-fitting basis functions. A sketch of the solution is given in the right side of Figure 3.18.

Next, in Figure 3.19, we show a study of the condition number's dependency on the parameter $\epsilon \in [0, 1]$ used to shift the midpoint of the circle $x_m = (0, \epsilon h)$. The scaled hierarchical ansatz space shows optimal behavior $\mathcal{O}(h^{-2})$ with regard to mesh size h and no dependency on the shift ϵ , while the standard approach shows very large conditions numbers with $\text{cond}_2(A_h) \rightarrow \infty$ for $\epsilon \rightarrow 0$ and $\epsilon \rightarrow 1$.

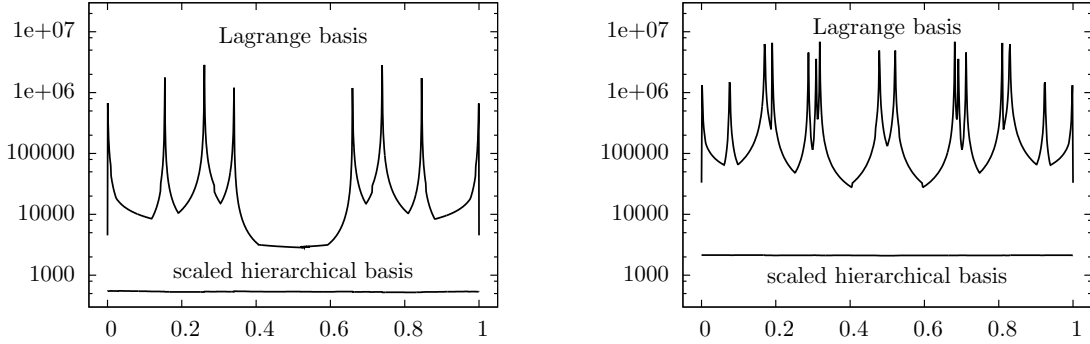


Figure 3.19: Example 1: condition number of the system matrix depending on the displacement of the circle Ω_1 by ϵh for $\epsilon \in [0, 1]$. Standard Lagrange basis versus the scaled hierarchical basis introduced in Section 3.5.2. Left $h = 1/16$, right $h = 1/32$.

Example 2: horizontal cuts

To study the different cuts of interface patches in more detail, let us next consider a the $\Omega = (-1, 1)^2$, cut horizontally into

$$\Omega_1(\epsilon) = \{x \in \Omega \mid x_2 < \epsilon h\}, \quad \Omega_2(\epsilon) = \{x \in \Omega \mid x_2 > \epsilon h\}.$$

By varying $\epsilon \in [0, 1]$ the interface patches of a Cartesian mesh will be split into rectangular with vertical edge lengths ϵh and $(1 - \epsilon)h$, $0 < \epsilon < 1$. We choose right hand side $f = -\kappa_i \Delta u$ and Dirichlet data according to the solution

$$u(x) = \begin{cases} \frac{\kappa_2}{\kappa_1} (x_2 - \epsilon) - (x_2 - \epsilon)^2 & x \in \Omega_1 \\ (x_2 - \epsilon) + (x_2 - \epsilon)^2 & x \in \Omega_2. \end{cases} \quad (3.42)$$

In Figure 3.20, we plot L^2 -norm and H^1 -norm error for $0 \leq \epsilon \leq 1$ on meshes with patch size $h = 1/16$ and $h = 1/32$. Both errors clearly depend on the position ϵ of the cut. As one would expect, we get the smallest errors for $\epsilon = 0$, $\epsilon = \frac{1}{2}$ and $\epsilon = 1$, where the mesh is perfectly uniform and resolves the cut. The largest error given for $\epsilon \rightarrow 0$ and $\epsilon \rightarrow 1$, where the anisotropy of the interface patches is maximal. Nevertheless, we see that the error remains bounded for all $\epsilon \in [0, 1]$. The variations get smaller on the finer mesh.

To explain these error variations we briefly analyze the interpolation error. The mesh consists of h^{-2} patches. Only h^{-1} patches are affected by the interface. These are cut into $2h^{-1}$ quads of size $h/2 \times \epsilon h$ and $2h^{-1}$ quads of size $h/2 \times (1-\epsilon)h$. The remaining $4h^{-2} - 4h^{-1}$ quads all have the size $h/2 \times h/2$. As the interface is a horizontal line, the modified mesh is still Cartesian and due to super-convergence effects the errors we observe are essentially the interpolation errors $\|u - I_h u\|$. The solution u only depends on x_2 , see (3.42). For the L^2 -norm, it holds on an element K of size $h_1 \times h_2$:

$$\|u - I_h u\|_K^2 \leq ch_2^4 \|\partial_{22} u\|_K^2 \approx ch_1 h_2^5.$$

summed over all elements $K \in \Omega_h$, we get the interpolation bound

$$\|u - L_h u\|_\Omega^2 \approx (4h^{-2} - 4h^{-1}) \frac{h^6}{64} + 2h^{-1}\epsilon^5 \frac{h^6}{2} + 2h^{-1}(1-\epsilon)^5 \frac{h^6}{2}.$$

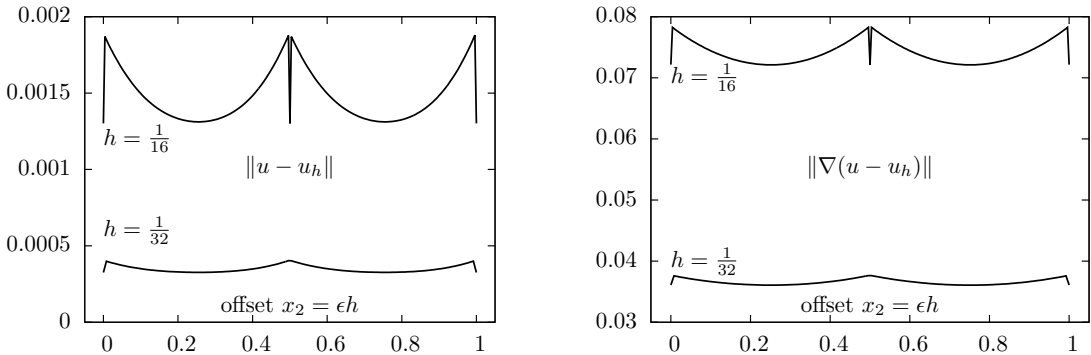


Figure 3.20: Example 2: L^2 - and H^1 -norm error depending on a vertical offset $x_2 = \epsilon h$ of the interface.

Table 3.3: Example 2: maximum and minimum error under vertical displacement ϵh of the interface line. Comparison of errors with the predicted error variation.

	H^1 -error		L^2 -error	
	$h = 1/16$	$h = 1/32$	$h = 1/16$	$h = 1/32$
Worst case ($\epsilon = 10^{-6}h$)	$7.864 \cdot 10^{-2}$	$3.774 \cdot 10^{-2}$	$1.904 \cdot 10^{-3}$	$4.077 \cdot 10^{-4}$
Best case ($\epsilon = h$)	$7.217 \cdot 10^{-2}$	$3.608 \cdot 10^{-2}$	$1.302 \cdot 10^{-3}$	$3.255 \cdot 10^{-4}$
Prediction	1.090	1.046	1.392	1.212
Variation	1.090	1.046	1.462	1.252

In the best case, for $\epsilon = \frac{1}{2}$, it holds

$$\|u - I_h u\|_{\Omega}^2 \approx \frac{h^4}{16},$$

while in the worst case for $\epsilon \rightarrow 0$ or $\epsilon \rightarrow 1$ we get

$$\|u - I_h u\|_{\Omega}^2 \approx \frac{h^4}{16} (1 + 15h)$$

Hence, the L^2 -norm error varies by a factor of $\sqrt{1 + 15h}$ which relates to approximately $\sqrt{2} \approx 1.4$ for $h = 1/16$ and $\sqrt{3/2} \approx 1.2$ for $h = 1/32$. For the H^1 -norm a similar analysis leads to a variation factor of $\sqrt{1 + 3h}$. In Table 3.3, we gather variation factors between maximum and minimum L^2 - and H^1 -norm on both meshes and find very good agreement to the prediction.

Example 3: tilted interface line

Next, we consider two subdomains that are separated by a straight interface line through the origin, which might be horizontal ($\alpha = 0$), vertical ($\alpha = \pi/2$) or inclined ($0 < \alpha < \pi/2$ or $\pi/2 < \alpha < \pi$). The interface Γ_i is defined by the relation $\cos(\alpha)x_2 = \sin(\alpha)x_1$ given the partitioning:

$$\begin{aligned}\Omega_1^\alpha &= \{x \in \Omega \mid \cos(\alpha)x_2 < \sin(\alpha)x_1\}, \\ \Omega_2^\alpha &= \{x \in \Omega \mid \cos(\alpha)x_2 > \sin(\alpha)x_1\}.\end{aligned}$$

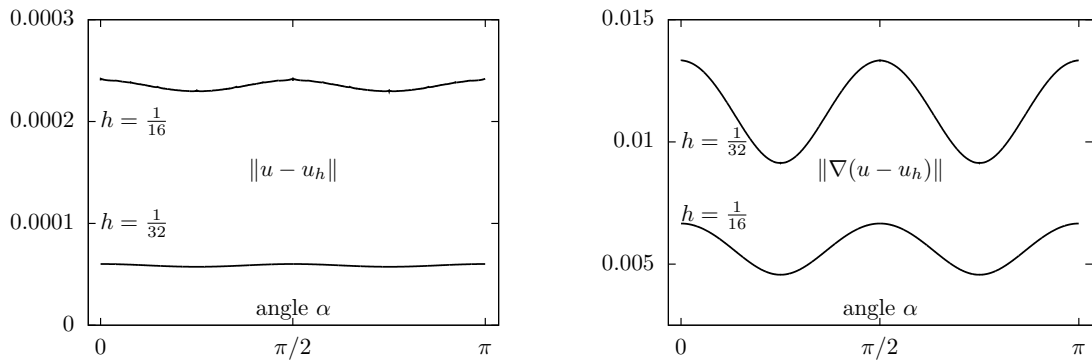


Figure 3.21: Example 3: L^2 - and H^1 -norm error for a line cutting at different angles $\alpha \in [0, \pi]$.

We choose right hand side $f = -\kappa_i \Delta u$ and Dirichlet data according to the given exact solution:

$$u(x) = \begin{cases} \sin\left(\frac{\kappa_2}{\kappa_1}(\cos(\alpha)x_2 - \sin(\alpha)x_1)\right), & x \in \Omega_1 \\ \sin(\cos(\alpha)x_2 - \sin(\alpha)x_1) & x \in \Omega_2. \end{cases}$$

In Figure 3.21 we plot the L^2 - and H^1 -norm error for angles $\alpha = 0 \dots \pi$ and two different refinement levels ($h = 1/16$ and $h = 1/32$). In the case $\alpha = \pi/2$ all the interface patches are of type D, while in the other cases types A to C appear with all kinds of anisotropies inside. Again, we observe linear convergence for the H^1 -norm error and quadratic convergence in the L^2 -norm. The error varies up to a factor of approximately $\sqrt{2}$ in the case of the H^1 -norm and about 1.05 in the L^2 -norm which can be explained similarly to the case of horizontal cuts. We emphasize that these variations are again bounded for all $\alpha \in [0, \pi]$.

3.6 Temporal discretization of Interface-Problems with moving interfaces

Hier ein wenig aus dem paper rein.

Exercises

Problem 22. Consider the ODE $u'(t) = f(t, u(t))$ for $t \geq 0$ and $u(0) = u^0$. Derive the amplification factor of Heun's method:

$$u^m = u^{m-1} + \frac{k}{2} \left(f(t_{m-1}, u^{m-1}) + f(t_m, t_{m-1} + kf(t_{m-1}, u^{m-1})) \right)$$

applied to the model problem (3.3). Show, that this amplification factor is an approximation to the exponential function and estimate its order.

Problem 23. Show that a single-step method with an amplification factor belonging to an over-diagonal Padé-approximation cannot be A-stable.

Problem 24. Show, that the $dG(1)$ -Galerkin scheme applied to the linear model problem

$$u'(t) + \lambda u(t) = 0 \quad t \geq 0, \quad u(0) = 1,$$

results in a time-stepping scheme with the same amplification factor of the subdiagonal (3,2) Padé approximation:

$$R(z) = \frac{1 + \frac{1}{3}z}{1 - \frac{2}{3}z + \frac{1}{6}z^2}.$$

Note: the dimension of the local solutions space for the $dG(1)$ scheme is 2. To derive the amplification factor, one has to solve a 2×2 linear system.

Problem 25. Let $I = [0, 1]$ and $t_i = ik$ for $i = 0, \dots, M$ and $k = 1/M$ be a uniform time-mesh. Detail the Galerkin discretization of the model problem

$$u'(t) + \lambda u(t) = 0 \quad t \geq 0, \quad u(0) = 1,$$

with piece-wise linear test-functions and piece-wise linear trial functions using the Lagrangian basis on every $I_m = (t_{m-1}, t_m]$. Further, assemble the system matrix and propose a solution scheme for the linear system.

Problem 26. Show, that if all integrals are approximated with the trapezoidal rule, the $cG(1)$ -Galerkin scheme for time-discretization is equivalent to the Crank-Nicolson method for general (nonlinear) parabolic problems

$$(u'(t), \phi) + a(u)(\phi) = (f(t), \phi), \quad t \geq 0, \quad (u(0) - u^0, \phi) = 0.$$

Give an estimate for the error due to numerical integration.

Problem 27. Derive the $cG(2)$ -Galerkin formulation for the linear model problem $u'(t) = \lambda u(t)$ and estimate the amplification factor.

Problem 28. Show the equivalence between the θ time-stepping method and the corresponding Galerkin scheme based on $u_k \in X_I^1$ using ϕ_k as given by (3.11) for linear autonomous initial values problems.

Problem 29. Show, that for $f \in C^2(I_m)$ and $\theta \in [0, 1]$ it holds:

$$\int_{I_m} f(t) \phi_k^\theta(t) dt = \theta k_m f(t_m) + (1 - \theta) k_m f(t_{m-1}) + O(k_m^3).$$

Problem 30. Derive the time-stepping scheme, that originates from the cG -formulation of the incompressible Stokes equations using

$$v_k \in [X_k^1]^d, \quad p_k \in X_k^{0,dc}, \quad \phi_k \in [X_k^{0,dc}]^d, \quad \xi_k \in X_k^{0,dc}.$$

Problem 31. Give a proof for Lemma 45.

Problem 32. Show that every continuous finite element space $V_h \subset C(\bar{\Omega})$ is H^1 -conforming.

Problem 33. Construct the nodal basis $Q^1(K)$ of the space of iso-parametric “bilinear” functions on the quadrilateral given by the four nodes $(0, 0), (1, 0), (2, 1), (0, 1)$. Note, that the resulting basis functions are not bilinear in the sense of (3.13).

Problem 34. Count the global degrees of freedom, $\dim(V_h^r)$ and $\dim(V_h^{r,dc})$ on a structured quadrilateral and structured triangular mesh.

Problem 35. Show, that the Mini-Element $P^{1,b} - P^1$ and the $P^{2,b} - P^{1,dc}$ bulb element is inf-sup stable, where

$$P^{r,b}|_K = P^r + \text{span}\{b_K\},$$

and where b_K is a cubic bulb on K with $b_K \in P^3(K)$ and $b_K = 0$ on ∂K . On the reference triangle $\hat{K} = \{(x, y) \in \mathbb{R}^2, 0 \leq x + y \leq 1\}$, this bulb function is given by

$$\hat{b}(x, y) = xy(h - x - y).$$

Problem 36. Determine the dimension of the different finite element pairs

$$Q^k - Q^{k-1}, \quad Q^2 - P^{1,dc}, \quad P^{1,b} - P^1,$$

on uniform meshes of tensor-product type as shown in Figure 3.5.

Problem 37. Prove Lemma 65.

Problem 38. Show that the embedding $\pi_h : Q^2 \rightarrow Q^1$ together with the stabilization form (3.32) satisfies the conditions of Lemma 67.

Problem 39. Show, that the following two approaches for solving the Navier-Stokes equations are equivalent:

1. First discretize the nonlinear Navier-Stokes equations by the finite element method, then solve this discretized set of equations in a Newton iteration.
2. First linearize the Navier-Stokes equations by a Newton iteration, then discretize the linear differential equation in every Newton step.

Problem 40. Let $u_h \in V_h^r$ be the finite element discretization of degree $r \geq 1$ of the model problem (3.37), stabilized with the artificial diffusion method. Show that - at best - it holds

$$\|\partial_x(u - u_h)\| = O(h),$$

as well as the L^2 -estimate

$$\|u - u_h\| \leq O(h),$$

for every polynomial degree $r \geq 1$.

4 ALE Formulation for Fluid-Structure Interactions

The following paragraphs will be devoted to the Arbitrary Lagrangian Eulerian method for modeling fluid-structure interactions. Based on the equations derived in Section 2.4, we describe methods for discretization in time and space. The basic techniques have already been introduced in Chapter 3, such that we can focus on the special characteristics of the Arbitrary Lagrangian Eulerian formulation of fluid-structure interaction problems. A third part, Section 4.2.2, we will consider the linearization of the algebraic systems, that arise from discretization in time and space.

In this chapter, we will focus on a very strict interpretation of the ALE formulation for the Navier-Stokes system

$$J\rho_f \left(\partial_t \mathbf{v} + \mathbf{F}^{-1}(\mathbf{v} - \partial_t \mathbf{u}) \cdot \nabla \mathbf{v} \right) - \operatorname{div} \left(J\sigma_f \mathbf{F}^{-T} \right) = J\rho_f \mathbf{f}, \quad \operatorname{div} \left(J\mathbf{F}^{-1}\mathbf{v} \right) = 0,$$

where the set of equations is completely mapped onto the reference coordinate system in $\hat{\mathcal{F}}$ [84, 134, 192, 135]. In literature [31, 81, 149, 119, 97, 92], mostly an alternative formulation is found, where the problem is mapped back into the Eulerian coordinate system and reads

$$\rho_f \left(\partial_t \mathbf{v} + (\mathbf{v} - \partial_t \mathbf{u}) \cdot \nabla \mathbf{v} \right) - \operatorname{div} \sigma_f = \rho_f \mathbf{f}, \quad \operatorname{div} \mathbf{v} = 0.$$

The domain mapping only enters via the additional transport term. The benefit of this presentation is the simplicity of formulation. After every time-step, the mesh must be updated. Considering time-stepping schemes, where the solution and the domain motion enters at two distinct points in time at once, the derivation of accurate higher order schemes is less obvious using this second formulation. From a technical point of view, both formulations are equivalent. Whether one uses a fixed and the reference formulation or a moving mesh and the Eulerian formulation. Considering strictly monolithically coupled schemes, the first ALE formulation is more natural, as it simply allows for a variational coupling of the two different sub-systems, see Section 2.4.

4.1 Time-discretization for the FSI problem in ALE-formulation

Time discretization of fluid-structure interactions is mainly governed by two specific complexities. First, the overall stiffness of the coupled problem is by far greater than that of the sub-problems. This is mainly due to the coupling of parabolic-type fluid equations with hyperbolic-type solid equations. Second, using a (most common) moving-mesh approach, due to implicit nonlinearities given by the motion of the underlying domains, time derivatives do not appear separated from spatial differential operators, but they depend nonlinearly on other

solution variables and there spatial derivatives. We start by repeating the coupled system of equations describing fluid-structure interactions in Arbitrary Lagrangian coordinates. Compare to System 35:

$$\begin{aligned} (J(\partial_t \mathbf{v} + (\mathbf{F}^{-1}(\mathbf{v} - \partial_t \mathbf{u}) \cdot \nabla) \mathbf{v}), \phi)_{\mathcal{F}} + (J\sigma_f \mathbf{F}^{-T}, \nabla \phi)_{\mathcal{F}} &= (J\rho_f \mathbf{f}, \phi)_{\mathcal{F}} \\ (J\mathbf{F}^{-1} : \nabla \mathbf{v}^T, \xi)_{\mathcal{F}} &= 0 \\ (\rho_s^0 \partial_t \mathbf{v}, \phi)_{\mathcal{S}} + (\mathbf{F} \boldsymbol{\Sigma}_s, \nabla \phi)_{\mathcal{S}} &= (\rho_s^0 \mathbf{f}, \phi)_{\mathcal{S}} \\ (\partial_t \mathbf{u} - \mathbf{v}, \psi_s)_{\mathcal{S}} &= 0 \\ (\nabla \mathbf{u}, \nabla \psi_s)_{\mathcal{F}} &= 0, \end{aligned} \quad (4.1)$$

where we have reformulated the divergence condition in the fluid equations by means of Lemma 31 to ease implementation and directly avoid the presence of second derivatives. For construction of the ALE map, we consider a simple harmonic extension, see Section 4.4.2 for variants. For simplicity of notation, we have skipped all hats, that usually indicate use of Lagrangian or ALE coordinates. Apart from the strong nonlinearities, this equation has some special feature with respect to the temporal derivatives, as in the fluid-domain they do not appear stand-alone, but nonlinearly mixed with further terms:

$$(J(\partial_t \mathbf{v} - (\mathbf{F}^{-1} \partial_t \mathbf{u} \cdot \nabla) \mathbf{v}), \phi)_{\mathcal{F}} + \dots \quad (4.2)$$

Detailed analysis for fluid flows on moving domains has been performed by Formaggia and Nobile [95, 96]. These studies already tackle several important aspects such as stability, order of convergence and the geometric conservation law. In fluid-structure interaction, the fluid-domain movement is caused by the solid deformation. Hence, the analysis of fully coupled fluid-structure interaction is similar but must also include detailed consideration of the solid discretization.

4.1.1 Non-stationary dynamics of fluid-structure interactions

We start the discussion on time-discretizations of fluid-structure interaction with a survey on results for two benchmark problems in fluid-dynamics and for fluid-structure interactions. In 1995, Schäfer and Turek [205] presented a benchmark configuration for incompressible laminar flows. Both problems use the geometric configuration given in Figure ??, where for the pure cfd benchmark problem the elastic beam \mathcal{S} with boundary \mathcal{I} is simply omitted and also part of the flow domain. Both problems are driven by a prescribed inflow profile \mathbf{v}^D on Γ_{in} . The full set of parameters for both problems is given by

$$\rho_f^{\text{cfd}} = 1, \quad \rho_f^{\text{fsi}} = 10^3, \quad \nu_f^{\text{cfd/fsi}} = 10^{-3}, \quad \mathbf{v}^D(0, y) = 1.5\omega(t) \frac{y(H-y)}{(H/2)^2} \bar{\mathbf{v}},$$

where $\omega(t) = (1 - \cos(\pi t/2))$ for $t < 2$ and $\omega(t) = 1$ for $t \geq 2$ is used for regularizing the initial data. As average velocity, we consider $\bar{\mathbf{v}} = 2$. In the original cfd benchmark problem, $\bar{\mathbf{v}}^{\text{cfd}} = 1$ was considered. With the radius of the obstacle $D = 0.1$, the Reynolds number is given by

$$Re = \frac{\bar{\mathbf{v}} D}{\nu} = 200.$$

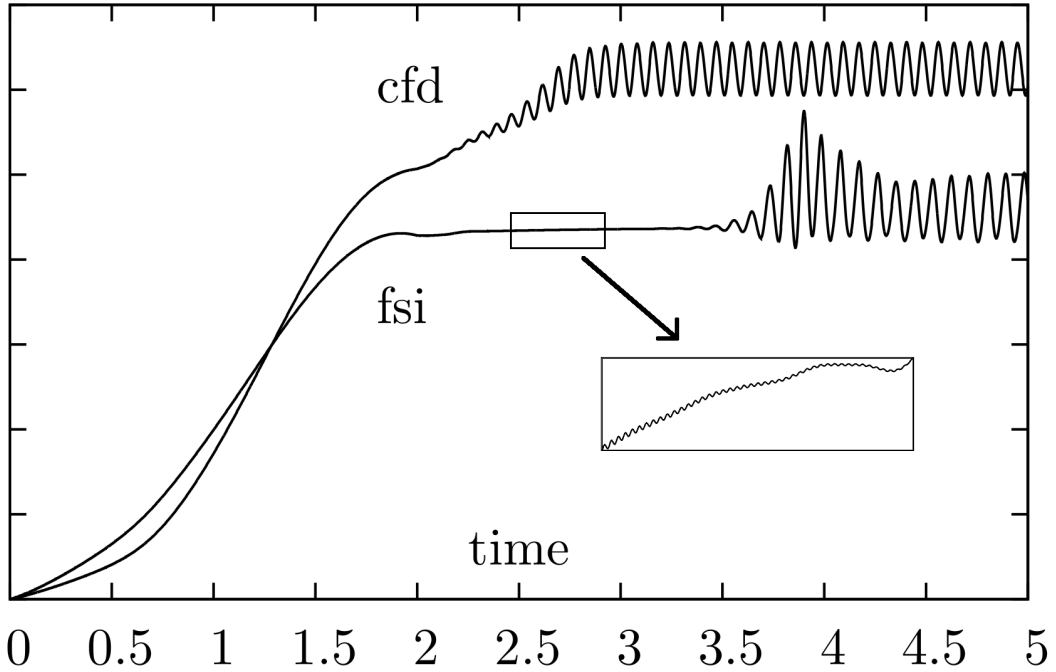


Figure 4.1: Comparison of the two benchmark problems cfd and fsi. We plot the drag coefficient as function over time. For the fsi-problem we show a detailed view of the transient oscillations revealing high frequent modes.

The description of the problem is closed by providing the material parameters of the elastic solid

$$\rho_s^{\text{fsi}} = 10^3, \quad \mu_s = 2 \cdot 10^6, \quad \lambda_s = 8 \cdot 10^6.$$

As quantity of interest, we consider principal boundary stresses in x - and y -direction on the obstacle with boundary Γ_{obs} :

$$J_{\text{drag}}(v, p) = \frac{2}{\bar{\mathbf{v}}^2 \rho_f L} \int_{\Gamma_{\text{obs}}} \sigma_f \vec{n} \vec{e}_x \, d\omega, \quad J_{\text{lift}}(v, p) = \frac{2}{\bar{\mathbf{v}}^2 \rho_f L} \int_{\Gamma_{\text{obs}}} \sigma_f \vec{n} \vec{e}_y \, d\omega.$$

By Γ_{obs} we denote the boundary of the circle with diameter in the case of the cfd-benchmark and the circle with attached beam in the case of the fsi-benchmark problem. Efficient ways for evaluating these functionals are shown in [47, 189].

Figure 4.1 shows the drag-coefficient as function over time $I = [0, 5]$ for the two benchmark problems. Both configurations show a similar behavior with a transient initial phase leading to a periodic oscillation with dominant frequencies $f_{\text{cfd}} = 13\text{Hz}$ for the cfd benchmark and $f_{\text{fsi}} \approx 11\text{Hz}$ for the fsi problem. The first obvious difference is the longer transient phase for the fsi benchmark problem. An insight look into the subinterval $I' = [2.5, 3]$ reveals high frequent oscillations $f_{\text{high}} \approx 100\text{Hz}$ in the drag-coefficient with a small amplitude $a \approx 10^{-4}$ that is not visible on the large scale. These high frequent oscillations are no numerical artifacts but remain stable under temporal and spatial mesh refinement.

Reviewing the results published by many research groups in the two surveys on the cfd benchmark problem [205] and the fsi benchmark [134, 135] a first surprising observation is the choice

of discretization parameters that have been necessary to obtain approximations with appropriate accuracy: even though more than a decade lies between both benchmark problems, the dimension of the spatial discretization is very similar. In both cases, about 300 000 spatial degrees of freedom are sufficient to result in output values of about 1% accuracy. The increased difficulty of the fsi benchmark problem has been accounted for by a general use of higher order finite elements, where most contributions to the original cfd benchmark problem relied on lowest order finite elements. However, observing the temporal discretization, it is found, that the fsi benchmark asks for significantly finer resolution in time. While less than 10 time-steps per period of the oscillation were sufficient in the cfd case, accurate results to the fsi benchmark problem required up to 100 time-steps per period of oscillation resulting in time-steps as small as 10^{-3} . One explanation for this difference in temporal discretization can be found in the high frequent oscillations that are present with small amplitude, see Figure 4.1.

Further insight is given by a discrete Fourier analysis of the output functional $J_{\text{drag}}(t)$ as function over time. A very fine temporal resolution (down to $k = 10^{-5}$) of some complete periods of the fully developed oscillation are analyzed in detail. Figure 4.2 reveals several dominant frequencies, at about 100 Hz (see also Figure 4.1, 500 Hz and 800 Hz. These modes are stable under mesh refinement and further decrease of the time step. The results in Figure 4.2 are scaled. The modes belonging to higher frequencies carry less energy. But even though the high frequent contributions take place on a much smaller scale as the dominant oscillation $f_{\text{fsi}} \approx 11$ Hz, they must be carefully resolved to capture the overall dynamics of the coupled benchmark problem. The key question in this respect is the origin of these micro-oscillations. They are not present in pure fluid-dynamical simulations. Further, they are no numerical artifact, but stable under discretization of both spatial and temporal discretization. Instead they stem from the coupling to the hyperbolic structure equations.

4.1.2 Time-stepping schemes for fluid-structure interactions

There is little theoretical background to monolithic time-discretizations of fluid-structure interactions. The main difficulty stems from the motion of the subdomains, that must either be modeled explicitly in partitioned approaches or that must be taken care of by implicit transformations of either the fluid-domain or the solid-domain. Concentrating first on pure fluid problems on moving domains, some crucial aspects with respect to stability and order of convergence are already identified [95, 96]. The equations presented therein can be directly employed in an implementation. In addition, [92] provided stability analysis of fluid-structure interaction problems. Several studies with qualitative comparisons of different time-stepping schemes and their long-time behavior has been reported in [242, 248]. In the primer study and additionally [247], we provide many details for the practical realization and implementation of time-stepping schemes for ALE fluid-structure interaction.

In the following, we focus the attention on the strict variant of the ALE method, that completely plays on fixed reference domains \mathcal{F} and \mathcal{S} , and where the complete set of equations is mapped.

Here, the domain motion is hidden in the ALE-map $T_f(x, t)$ and calls for the discretization of non-standard space-time coupled terms like, see (4.1) and (4.2):

$$(J(\mathbf{u})\nabla \mathbf{v}\mathbf{F}^{-1}(\mathbf{u})\partial_t \mathbf{u}, \phi)_{\mathcal{F}}. \quad (4.3)$$

Most approaches for the temporal discretization of this term are ad hoc and based on the experience with other types of equations as Navier-Stokes of multiphase fluids, see [133].

Remark 27. *An alternative approach to the monolithic formulation of fluid-structure interactions is given by an implicit transformation of the solid-domain to Eulerian coordinates resulting in the Fully Eulerian approach [84, 192]. This method of interface-capturing type must deal with subdomains that move freely through a fixed background mesh from time-step to time-step. We come back to this procedure in Section 5.3.*

4.1.3 Derivation of second order time-stepping schemes

The derivation of a second order stable time-stepping scheme is not obvious. Specifically, regarding (4.3), two immediate reasonable choices for are given by the secant version

$$\left(\left[\frac{J(\mathbf{u}^{m-1}) \nabla \mathbf{v}^{m-1} \mathbf{F}^{-1}(\mathbf{u}^{m-1})}{2} + \frac{J(\mathbf{u}^m) \nabla \mathbf{v}^m \mathbf{F}^{-1}(\mathbf{u}^m)}{2} \right] \frac{\mathbf{u}^m - \mathbf{u}^{m-1}}{k_m}, \phi \right),$$

and the midpoint-tangent version

$$\left(\left[J(\bar{\mathbf{u}}) \nabla \bar{\mathbf{v}} \mathbf{F}^{-1}(\bar{\mathbf{u}}) \right] \frac{\mathbf{u}^m - \mathbf{u}^{m-1}}{k_m}, \phi \right), \quad \bar{\mathbf{u}} := \frac{\mathbf{u}^{m-1} + \mathbf{u}^m}{2}, \quad \bar{\mathbf{v}} := \frac{\mathbf{v}^{m-1} + \mathbf{v}^m}{2},$$

of the trapezoidal rule. This idea is explored in [243, 248] A third version of a time-stepping scheme can be derived by using a temporal $cG(1)/dG(0)$ -Galerkin approach on (4.3) (see Section 3.1.3):

$$\left(\left[\frac{1}{6} J(\mathbf{u}^{m-1}) \nabla \mathbf{v}^{m-1} \mathbf{F}^{-1}(\mathbf{u}^{m-1}) + \frac{2}{3} J(\bar{\mathbf{u}}) \nabla \bar{\mathbf{v}} \mathbf{F}^{-1}(\bar{\mathbf{u}}) \right. \right. \\ \left. \left. + \frac{1}{6} J(\mathbf{u}^m) \nabla \mathbf{v}^m \mathbf{F}^{-1}(\mathbf{u}^m) \right] \frac{\mathbf{u}^m - \mathbf{u}^{m-1}}{k_m}, \phi \right),$$

where again by $\bar{\mathbf{u}}$ and $\bar{\mathbf{v}}$ we denote the average of old and new approximation. Such a Galerkin-derivation is also possible for more advanced time-stepping schemes like the fractional step theta method, see [160, 161].

Simple truncation error analysis shows second order convergence for $k \rightarrow 0$ in all three cases. The leading error constants slightly differ:

$$C_1 \approx \frac{11}{8}, \quad C_2 \approx \frac{3}{8}, \quad C_3 \approx \frac{3}{4}.$$

In numerical experiments, it is found, that all these variants show a very similar performance. Significant differences in temporal accuracy could not be found.

Finally, we point out, that the Crank-Nicolson scheme applied to the elastic structure equation in mixed formulation is closely related to the Newmark scheme [12], which is one of the most prominent time-discretization techniques in solid mechanics.

Mesh-Level	Time step size				Mesh-Level	$k = 0.005$	$0.003\bar{3}$
	0.025	0.02	0.004	0.003		1	$\gg 10$
1	×	✓	✓	✓	2	8.48	10.82
2	×	×	×	✓	3	6.04	12.54
3	×	×	×	✓	4	3.84	3.84

Table 4.1: Long-term stability of the Crank-Nicolson scheme. Left: combination of time-step k and mesh size h , such that the solution is stable in the interval $I = [0, 10]$. We cannot find a strict time-step relation $k \sim h^\alpha$. Right: maximum interval $I = [0, T_{\max}]$, where a solution could be found for $k = 0.005$ and $k = 0.003\bar{3}$, depending on the mesh-size. Here, we also cannot identify an obvious relationship.

4.1.4 Temporal stability

Issues of numerical stability are of utter importance for fluid-structure interaction problems, as they consist of the coupled consideration of two different types of equations: the incompressible Navier-Stokes equations which is of parabolic type and that comes with smoothing properties and the hyper-elastic solid equation of hyperbolic type, that calls for good conservation properties with very little numerical dissipation. By these considerations, the Crank-Nicolson scheme and its variants like shifted versions [154, 179] or the fractional step theta scheme [53, 230], appear to be ideal candidates that further show second order accuracy.

Motivated by [184, 123, 96], it is reported in [92, 248], that the discretization of the domain-motion term (4.3) introduces further stability issues. To investigate this stability problem, we again consult the fsi-3 benchmark problem introduced in the previous sections. Figure 4.3 shows the drag as functional over time for an unstable pair of spatial and temporal discretization parameters. Further, we also show the stable simulation using a damped version of the time-stepping scheme, see Section 4.1.5.

In a first test, we aim at obtaining a stable solution up to $T = 10$. On a sequence of uniform meshes, we identify the largest timestep k that is suited to generate a stable solution. The left part of Table 4.1 shows the results. Here, we see, that on the coarsest mesh, the large step size $k = 0.02$ is sufficient, while on finer meshes $k < 0.004$ is required. We however cannot identify a further relationship between mesh size and time step if we go to an even finer spatial mesh resolution.

In a second test-case, we consider the (relatively large) step size $k = 0.005$ and $k = 0.003\bar{3}$ and determine the point in time T_{\max} , where the solution gets unstable. Again, we carry out this test-case on different meshes. At first glance, the results in the right part of Table 4.1 for $k = 0.005$ suggest a stability relationship between time step and mesh size. The results concerning the second configuration with $k = 0.003\bar{3}$ however does not confirm this conjecture. Here, we can even reach a larger final point in time T_{\max} on finer meshes. Further, the simulations on the finest mesh do not cease due to stability problems but due to early failure of the Newton scheme. Altogether, it is not possible to numerically certify a strict time-step restriction. Instead, we find general stability problems for long-term simulation, if we consider the Crank-Nicolson scheme.

4.1.5 Stable time-discretization and damping

By analyzing the fsi benchmark problem, it seems, that time-step restrictions due to stability issues are too restrictive and not justified by the needs of approximation accuracy, see Sections 4.1.4 and 4.1.3. It is therefore nearby to search for accurate time-discretization schemes with better stability properties. Different possibilities are either to resort to A stable time-discretization schemes, or to apply modifications to the Crank-Nicolson schemes. Here, two possibilities are often discussed in literature: by slight implicit shifting of the discretization

$$(u^m - u^{m-1}, \phi) + \left(\frac{1}{2} + O(k) \right) a(u^m, \phi) + \left(\frac{1}{2} - O(k) \right) a(u^{m-1}, \phi) = 0,$$

global stability is recovered, see [122, 123, 154]. This is just sufficient for the damping of accumulated errors by truncation, quadrature or inexact solution of the algebraic systems. If the shift depends on the time-step size, the resulting scheme is still second order accurate in time. Similar results are recovered by applying some initial time-steps with the A-stable backward Euler method, see [179]. If these few (usually two are sufficient) backward Euler steps are introduced after every fixed time-interval, e.g. at every $t = j$ for $j = 0, 1, \dots$, we also recover sufficient stability for long term calculations. This scheme, also referred to as Rannacher time-marching, is second order accurate.

Higher stability, that is also able to cover non-smooth initial data is reached by applying strongly A-stable time-integration techniques. Here, the fractional-step theta method appears to be an optimal choice [53]. This time-stepping scheme consists of three sub-steps, that combined results in a second order, strongly A-stable scheme that further has very good dissipation properties. It is highly preferable to flow problems [230] and also frequently used in the analysis of fluid-structure interactions problems [133, 135, 242, 195].

An analysis of different damping strategies applied to the fsi-2 benchmark problem (a slightly more difficult test-case) is given in [248], which we briefly summarize in the following: There are only minor differences in the drag evaluation computed with the unstabilized Crank-Nicolson scheme using the different ALE convection term discretizations. Specifically, unstable behavior (blow-up) for computations over long-term intervals is observed. As expected, the shifted Crank-Nicolson scheme and the Fractional-Step- θ scheme do not show any stability problems in long-term computations, even for large time steps $k = 0.01$. This result indicates that the instabilities induced by the ALE convection term have minor consequences, and our observation is in agreement with the statement in [96].

In the following, we compare the three possibilities of a non-damped Crank-Nicolson scheme, with an implicitly shifted version using $\frac{1}{2} + k$ and the Rannacher time-marching algorithm with two steps of the backward Euler method at times $t = 0, t = 1, t = 2$ and so on. In Figure 4.4 we compare these three damping strategies. We show the drag-coefficient (see Figure 4.1 or 4.3 for a global view) in the sub-intervals $t \in [3.5, 4.2]$, $t \in [7.95, 8.15]$ and $t \in [9.3, 9.6]$. While all three versions are stable at initial time, Rannacher time-marching develops a first instability after two steps of backward Euler at time $t = 4$, see the left sketch in Figure 4.4. This instability will stay during the simulation, but it will not be further developed, as can be seen in the middle and right sketch of the figure. The undamped version of the Crank-Nicolson scheme delivers stable solutions up to a moderate time of about $t = 5$ but develops a strong instability that will finally lead to a break-down of the scheme, as can be seen in the middle and right

sketch. Finally, the implicitly shifted version of the Crank-Nicolson scheme gives stable and good result globally in time.

A systematic way for deriving a time-stepping scheme is the detour using a Galerkin formulation. Here, we exemplarily derive the cG(1)-method, that - for parabolic autonomous systems - is equivalent to the Crank-Nicolson scheme. We find $u_k, f_k, g_k \in X_I^1$ in the space of piece-wise linear, globally continuous functions and use $X_I^{0,\text{dc}}$ as test-space. On an interval I_m we write

$$f_k|_{I_m} = f_k^{m-1}\psi^{m-1} + f_k^m\psi^m, \quad g_k|_{I_m} = g_k^{m-1}\psi^{m-1} + g_k^m\psi^m,$$

where

$$\psi^{m-1}(t) = \frac{t_m - t}{t_m - t_{m-1}}, \quad \psi^m(t) = \frac{t - t_{m-1}}{t_m - t_{m-1}}.$$

Further, it holds:

$$u'_k|_{I_m} = \frac{u_k^m - u_k^{m-1}}{t_m - t_{m-1}}.$$

The test-function ϕ_k is piece-wise constant and taken as $\phi_k|_{I_m} \equiv 1$. Hence:

$$\int_{I_m} f_k u'_k g_k dt = \frac{u_k^m - u_k^{m-1}}{t_m - t_{m-1}} \int_{I_m} (f_k^{m-1}\psi^{m-1} + f_k^m\psi^m)(g_k^{m-1}\psi^{m-1} + g_k^m\psi^m) dt$$

We evaluate:

$$\int_{I_m} (\psi^{m-1})^2 dt = \int_{I_m} (\psi^m)^2 dt = \frac{t_m - t_{m-1}}{3}, \quad \int_{I_m} \phi^{m-1}\psi^m dt = \frac{t_m - t_{m-1}}{6},$$

and result in an equivalent time-stepping formulation

$$\int_{I_m} f_k u'_k g_k dt = (u_k^m - u_k^{m-1}) \left(\frac{1}{3} f_k^{m-1} g_k^{m-1} + \frac{1}{6} f_k^{m-1} g_k^m + \frac{1}{6} f_k^m g_k^{m-1} + \frac{1}{3} f_k^m g_k^m \right)$$

We have derived three different approaches for the time-discretization of the ALE-formulation of fluid-structure interaction problems. All these approaches are second order accurate and are somehow related to the Crank-Nicolson method.

4.2 Linearizations of fluid-structure interactions in the ALE framework

Newton: FernandezMoubachir, Exact Jacobian mit Literatur

Discretization in time results in a sequence of quasi-stationary systems of partial differential equations. These are highly nonlinear. Nonlinearities arise from material laws, convective terms, but in the case of fluid-structure interactions in particular due to the motion of the domain. Considering the strict ALE formulation with mapping of the complete variational system to a reference domain, this domain nonlinearity is represented by the domain map T , its gradient \mathbf{F} and determinant J . In the following paragraphs, we will discuss different ways of linearization of these quasi-stationary systems. First of all, a straightforward way to linearize the set of equations would be the use of explicit time-stepping schemes. This however is not

feasible due to several reasons: first of all, the incompressibility constraint of the Navier-Stokes equations (or of incompressible structures) cannot be taken care of by explicit methods. A choice of approximation would be to apply projection schemes. We do not follow this approach, but refer to the literature [176, 91]. Another drawback of explicit discretization schemes is the limited stability, that will call for very strict step-size conditions. By using very small time-steps, we would however loose all possible benefits, that strong monolithic methods can bring along. Instead, we will – for the following and for simplicity – consider time-discretization with the backward Euler method. Given velocity \mathbf{v}^{old} and deformation \mathbf{u}^{old} at the old time-step we find (see Lemma 35):

$$\mathbf{v} \in \mathcal{V}, \quad \mathbf{u} \in \mathcal{W}, \quad p_f \in \mathcal{L}_f,$$

such that

$$\begin{aligned} & \left(\rho_f J \left(k^{-1}(\mathbf{v} - \mathbf{v}^{\text{old}}) + \mathbf{F}^{-1}(\mathbf{v} - k^{-1}(\mathbf{u} - \mathbf{u}^{\text{old}})) \cdot \nabla \mathbf{v} \right), \phi \right)_{\mathcal{F}} \\ & \quad + (J\sigma_f \mathbf{F}^{-T}, \nabla \phi)_{\mathcal{F}} = (J\rho_f \mathbf{f}, \phi)_{\mathcal{F}} \\ & \quad (J\mathbf{F}^{-1} : \nabla \mathbf{v}^T, \xi)_{\mathcal{F}} = 0 \\ & (\rho_s^0 k^{-1}(\mathbf{v} - \mathbf{v}^{\text{old}}), \phi)_{\mathcal{S}} + (\mathbf{F}\Sigma_s, \nabla \phi)_{\mathcal{S}} = (\rho_s^0 \mathbf{f}, \phi)_{\mathcal{S}} \\ & (k^{-1}(\mathbf{u} - \mathbf{u}^{\text{old}}) - \mathbf{v}, \psi_s)_{\mathcal{S}} = 0 \\ & (\nabla \mathbf{u}, \nabla \psi_f)_{\mathcal{F}} = 0, \end{aligned} \tag{4.4}$$

for all

$$\phi \in \mathcal{V}, \quad \psi_f \in \mathcal{W}_f, \quad \psi_s \in \mathcal{L}_s, \quad \xi_f \in \mathcal{L}_f,$$

and with the fluid's stress tensor σ_f in ALE coordinates and the 2nd Piola Kirchhoff stress tensor of the St. Venant Kirchhoff material

$$\begin{aligned} \sigma_f &:= -pI + \rho_f \nu_f (\mathbf{F}^{-1} \nabla \mathbf{v} + \nabla \mathbf{v}^T \mathbf{F}^{-T}) \\ \Sigma_s &:= 2\mu_s \mathbf{E}_s + \lambda_s \text{tr}(\mathbf{E}_s) I, \end{aligned} \tag{4.5}$$

with the Green-Lagrangian Strain tensor

$$\mathbf{E}_s := \frac{1}{2}(\mathbf{F}^T \mathbf{F} - I),$$

and the material parameters $\rho_f, \rho_s^0, \nu_f, \mu_s$ and λ_s , describing density of fluid and solid, kinematic viscosity, shear modulus and Lamé coefficient.

We skipped all “hat's” denoting the use of reference coordinates. Still, \mathcal{F} and \mathcal{S} stand for the non-moving reference domains of fluid- and solid-domain. The function spaces \mathcal{V} and \mathcal{W} are basically the space $H^1(\Omega)$ differing only in the type of boundary values. While $\mathcal{W} = H_0^1(\Omega)$ has Dirichlet boundary values all around $\partial\Omega$, the velocity space $\mathcal{V} = H_0^1(\Omega; \Gamma^D)^d$ can have a Neumann outflow boundary $\Gamma_f^{\text{out}} \subset \partial\Omega$. The pressure space $\mathcal{L}_f = L^2(\mathcal{F})$ is defined on the fluid-domain only. The test-space $\mathcal{W}_f = H_0^1(\mathcal{F})^d$ for the definition of the ALE-map has homogenous Dirichlet values all around the fluid-domain. The test-space of the deformation-velocity relation is $\mathcal{L}_s = L^2(\mathcal{S})^d$ only.

4.2.1 Linearization by fixpoint-iterations

A simple approach to linearization of (4.4) is to apply fixpoint-iterations. Starting with

$$\mathbf{v}^{(0)} = \mathbf{v}^{\text{old}}, \quad \mathbf{u}^{(0)} = \mathbf{u}^{\text{old}},$$

we search for approximations $\mathbf{v}^{(l)}$ and $\mathbf{u}^{(l)}$ that converge to \mathbf{v} and \mathbf{u} for $l \rightarrow \infty$. We define

$$\mathbf{F}^{(l)} := I + \nabla \mathbf{v}^{(l)}, \quad J^{(l)} := \det \mathbf{F}^{(l)},$$

and solve the sequence of linearized systems

$$\begin{aligned} & \left(\rho_f J^{(l-1)} \left(k^{-1} (\mathbf{v}^{(l)} - \mathbf{v}^{\text{old}}) + \mathbf{F}^{(l-1)-1} (\mathbf{v}^{(l-1)} - k^{-1} (\mathbf{u}^{(l-1)} - \mathbf{u}^{\text{old}})) \cdot \nabla \mathbf{v}^{(l)} \right), \phi \right)_{\mathcal{F}} \\ & + (J^{(l-1)} \sigma_f(\mathbf{v}^{(l)}, p^{(l)}) \mathbf{F}^{(l-1)-T}, \nabla \phi)_{\mathcal{F}} = (J^{(l-1)} \rho_f \mathbf{f}, \phi)_{\mathcal{F}} \\ & (J^{(l-1)} \mathbf{F}^{(l-1)-1} : \nabla \mathbf{v}^T, \xi)_{\mathcal{F}} = 0 \\ & (\rho_s^0 k^{-1} (\mathbf{v}^{(l)} - \mathbf{v}^{\text{old}}), \phi)_{\mathcal{S}} + (\mathbf{F}^{(l-1)} \boldsymbol{\Sigma}_s^{(l)}, \nabla \phi)_{\mathcal{S}} = (\rho_s^0 \mathbf{f}, \phi)_{\mathcal{S}} \\ & (k^{-1} (\mathbf{u}^{(l)} - \mathbf{u}^{\text{old}}) - \mathbf{v}^{(l)}, \psi_s)_{\mathcal{S}} = 0 \\ & (\nabla \mathbf{u}^{(l)}, \nabla \psi_f)_{\mathcal{F}} = 0, \end{aligned} \tag{4.6}$$

with an ad hoc linearization of the solid's stress tensor (here, given for the St. Venant Kirchhoff material):

$$\begin{aligned} \boldsymbol{\Sigma}_s^{(l)} &:= 2\mu_s \mathbf{E}_s^{(l)} + \lambda_s \text{tr}(\mathbf{E}_s^{(l)}) I, \\ \mathbf{E}_s^{(l)} &:= \frac{1}{2} \left(\nabla \mathbf{u}^{(l)} + \nabla \mathbf{u}^{(l)T} + \nabla \mathbf{u}^{(l-1)} \nabla \mathbf{u}^{(l)T} \right). \end{aligned}$$

Other choices are possible. This fixed-point linearization of the fsi system is similar to the Oseen linearization of the Navier-Stokes system, see Section 3.4.1. A theoretical analysis on the convergence of this fixed-point iteration is difficult, but we will add numerical tests using the benchmark problem fsi-3 of Hron and Turek [134], see Remark ??.

4.2.2 Newton linearization for fluid-structure interactions in Arbitrary Lagrangian Eulerian formulation

In Section 3.4, we have seen, that general fixed-point iterations for the linearization of the Navier-Stokes system usually show very slow convergence properties, see Figure 3.8. Only by using Newton scheme for approximation of the nonlinear systems, we could establish a robust and very fast converging scheme. This section will now describe Newton linearization for fluid-structure interactions in ALE formulation. The main difficulty will again be the handling of the domain motion, that is hidden in the ALE mapping T , its gradient \mathbf{F} and determinant J . By consulting Section 3.4.2, the general Newton method for a (quasi-)stationary system of partial differential equations in variational formulation was given as (compare (3.34)):

$$\mathbf{W} \in \mathcal{X} : \quad A'(\mathbf{U}^{(l-1)})(\mathbf{W}^{(l)}, \Phi) = F(\Phi) - A(\mathbf{U}^{(l-1)})(\Phi), \quad \forall \Phi \in \mathcal{Y}, \tag{4.7}$$

with

$$\mathbf{U}^{(l)} := \mathbf{U}^{(l-1)} + \omega^{(l)} \mathbf{W}^{(l)}. \tag{4.8}$$

In the context of fluid-structure interactions in ALE formulation, discretized in time with the backward Euler method, the known last approximation $\mathbf{U}^{(l-1)} \in \mathcal{X}$ is given by

$$\mathbf{U}^{(l-1)} := \{\mathbf{v}^{(l-1)}, \mathbf{u}^{(l-1)}, p_f^{(l-1)}\} \in \mathcal{X} = \mathcal{V} \times \mathcal{W} \times \mathcal{L}_f,$$

and we denote the unknown update by

$$\mathbf{W}^{(l)} = \{\mathbf{z}, \mathbf{w}, q_f\} \in \mathcal{X} = \mathcal{V} \times \mathcal{W} \times \mathcal{L}_f.$$

Remark 28 (Initial value). *Newton convergence highly depends on a good choice of an initial approximation $\mathbf{U}^{(0)}$. In the context of non-stationary problems, a good choice is always to use the old solution at time t_{n-1} , hence $\mathbf{U}^{(0)} = \mathbf{U}(t_{n-1}) = \mathbf{U}^{\text{old}}$. This initial choice could even be enhanced by using a linear extrapolation of the two last approximations, by choosing*

$$\mathbf{U}^{(0)} = \mathbf{U}(t_{n-1}) + (t_n - t_{n-1}) \frac{\mathbf{U}(t_{n-1}) - \mathbf{U}(t_{n-2})}{t_{n-1} - t_{n-2}}.$$

Considering the backward Euler discretization, the semilinear form $A(\cdot)(\cdot)$ is given by (compare 4.4)

$$\begin{aligned} A(\mathbf{U})(\Phi) = & \left(\rho_f J \left(k^{-1}(\mathbf{v} - \mathbf{v}^{\text{old}}) + \nabla \mathbf{v} \mathbf{F}^{-1} \left(\mathbf{v} - k^{-1}(\mathbf{u} - \mathbf{u}^{\text{old}}) \right) \right), \phi \right)_{\mathcal{F}} \\ & + (J \sigma_f \mathbf{F}^{-T}, \nabla \phi)_{\mathcal{F}} - (J \rho_f \mathbf{f}, \phi)_{\mathcal{F}} \\ & + (\mathbf{J} \mathbf{F}^{-1} : \nabla \mathbf{v}^T, \xi)_{\mathcal{F}} \\ & + (\rho_s^0 k^{-1} \mathbf{v}, \phi)_{\mathcal{S}} + (\mathbf{F} \boldsymbol{\Sigma}_s, \nabla \phi)_{\mathcal{S}} \\ & + (k^{-1} \mathbf{u} - \mathbf{v}, \psi_s)_{\mathcal{S}} + (\nabla \mathbf{u}, \nabla \psi_f)_{\mathcal{F}} \end{aligned} \quad (4.9)$$

and the right hand side $F(\cdot)$ by

$$F(\Phi) = (\rho_s^0 \mathbf{f}, \phi)_{\mathcal{S}} + (\rho_s^0 k^{-1} \mathbf{v}^{\text{old}}, \phi)_{\mathcal{S}} + (k^{-1} \mathbf{u}^{\text{old}} \psi_s)_{\mathcal{S}}. \quad (4.10)$$

To simplify the representation of the derivatives of the convective term, we have – in (4.9) – used the relation

$$((\mathbf{F}^{-1} \mathbf{v}) \cdot \nabla) \mathbf{w} = \nabla \mathbf{v} \mathbf{F}^{-1} \mathbf{w}.$$

The data term $(J \rho_f \mathbf{f}, \phi)_{\mathcal{F}}$ must reside in the form $A(\cdot)(\cdot)$, as the deformation determinant J depends on the unknown deformation \mathbf{u} . The same applies to the old solution \mathbf{v}^{old} appearing in the momentum equation of the fluid problem.

The derivative $A'(\mathbf{U}^{(l-1)})(\mathbf{W}^{(l)}, \Phi)$ in (4.7) is the Gâteaux derivative of the semilinear form $A(\cdot)(\cdot)$, which can be seen as the directional derivative at $\mathbf{U}^{(l-1)}$ in direction $\mathbf{W}^{(l)}$, tested with Φ . It is defined as

$$A'(\mathbf{U})(\mathbf{W}, \Phi) := \lim_{s \rightarrow 0} \frac{d}{ds} A(\mathbf{U} + s\mathbf{W})(\Phi) \Big|_{s=0}. \quad (4.11)$$

The semilinear form $A(\cdot)(\cdot)$ is given in variational formulation. On a fixed domain, we can exchange the order of differentiation and integration, such that it holds

$$\int_{\Omega} f(\mathbf{u} + s\mathbf{w}) \phi \, d\mathbf{x} \Big|_{s=0} = \int_{\Omega} \left(\frac{d}{ds} f(\mathbf{u} + s\mathbf{w}) \Big|_{s=0} \right) \phi \, d\mathbf{x}.$$

Hence,

$$\frac{d}{ds} (f(\mathbf{u} + s\mathbf{w}), \phi)_{\Omega} \Big|_{s=0} = (f'(\mathbf{u}) \mathbf{w}, \phi)_{\Omega}.$$

In the case of fluid-structure interaction, this situation is more involved, as the motion of the domain depends on the solution. Formally, variational formulations of fluid-structure interactions are defined on domains, that depend on the solution. Here, differentiation and integration may not be exchanged:

$$\frac{d}{ds} (f(\mathbf{u} + s\mathbf{w}), \phi)_{\Omega(\mathbf{u})} \Big|_{s=0} \neq (f'(\mathbf{u}) \mathbf{w}, \phi)_{\Omega(\mathbf{u})},$$

instead, the derivative with respect to the domain of integration must be considered.

A straightforward and simple way for computing the derivative $A'(\cdot)(\cdot, \cdot)$ is by means of finite differences:

$$A'(\mathbf{U})(\mathbf{W}, \Phi) \approx \epsilon^{-1} (A(\mathbf{U} + \epsilon \mathbf{W})(\Phi) - A(\mathbf{U})(\Phi)), \quad \epsilon > 0. \quad (4.12)$$

This approach is widely used for complex simulations [109, ?]. The main difficulty of finite difference approximations is the choice of ϵ . This parameter must be small enough, such that the approximation accuracy of the Jacobian (4.12) is high. On the other hand, a too small value of ϵ may cause cancellation effects and will give rise to a substantial truncation error. An optimal choice based on a priori information is usually not possible, see [27], where the authors investigated finite difference approximations in the context of gradient based optimization.

If the derivatives (4.11) are to be evaluated exactly, we need to manage the domain deformation. It will turn out, that our very strict form of the *Arbitrary Lagrangian Eulerian* framework, that works on a fixed reference system for the complete variational form, see (4.9) and (4.10), helps to avoid all difficulties, as all domains are fixed, such that we can exchange orders of differentiation and integration. Using the alternative formulation on updated meshes, motion of the domains must be carefully included. In [94], the authors use shape derivatives to include these derivatives with respect to the mesh motion. Van der Zee and co workers [255, 256] describe two different approaches for differentiation of the variational formulation. The first approach [255] is very similar to our strict interpretation of the ALE method: the equations are mapped to the fixed reference domain, and all differentiation is carried out here. The second approach [256] is based on the theory of *shape calculus*, see [216, 257], where the derivative with respect to the domain motion is explicitly computed: let $T(t) : \Omega \rightarrow \Omega(t)$ be a sufficiently regular domain map. Then, the following fundamental formula holds:

$$\frac{d}{ds} \int_{\Omega(s)} f(x) dx = \int_{\partial\Omega(s)} \langle \vec{n} \cdot \partial_s T(s) \rangle f(o) do,$$

where \vec{n} is the outward facing unit normal at the boundary of $\Omega(s)$. We will have to get back to this approach, when dealing with the Fully Eulerian approach in Section 5.4. Here, we can rely on the strict variant of the ALE method, where all domains are fixed.

The following theorem gives the full Jacobian of the fluid-structure interaction problem in ALE coordinates, discretized with the backward Euler equation, that is, the directional derivative of (4.9):

Theorem 11 (Jacobian for fluid-structure interactions in Arbitrary Lagrangian Eulerian coordinates). *Let $\mathbf{U} = \{\mathbf{v}, \mathbf{u}, p_f\} \in \mathcal{X}$, $\mathbf{W} = \{\mathbf{z}, \mathbf{w}, q_f\} \in \mathcal{X}$ and $\Phi = \{\phi, \psi_f, \psi_s, \xi_f\}$. For the*

directional derivative of (4.9) at \mathbf{U} in direction of \mathbf{W} , it holds:

$$\begin{aligned}
 A'(\mathbf{U})(\mathbf{W}, \Phi) = & \left(\rho_f J \left(k^{-1} \mathbf{z} + \nabla \mathbf{z} \mathbf{F}^{-1} \left(\mathbf{v} - \frac{\mathbf{u} - \mathbf{u}^{old}}{k} \right) + \nabla \mathbf{v} \mathbf{F}^{-1} \mathbf{z} \right), \phi \right)_{\mathcal{F}} \\
 & + \left(J \frac{d\sigma_f}{d\mathbf{v}}(\mathbf{W}) \mathbf{F}^{-T}, \nabla \phi \right)_{\mathcal{F}} - (J \mathbf{F}^{-T} q_f, \nabla \phi)_{\mathcal{F}} \\
 & + ((J \mathbf{F}^{-1} : \nabla \mathbf{z}^T, \xi)_{\mathcal{F}} \\
 & + \left(\rho_f J \operatorname{tr} (\mathbf{F}^{-1} \nabla \mathbf{w}) \left(k^{-1} (\mathbf{v} - \mathbf{v}^{old}) + \right. \right. \\
 & \quad \left. \left. \nabla \mathbf{v} \mathbf{F}^{-1} \left(\mathbf{v} - k^{-1} (\mathbf{u} - \mathbf{u}^{old}) \right) \right), \phi \right)_{\mathcal{F}} \\
 & - \left(\rho_f J \nabla \mathbf{v} \mathbf{F}^{-1} \nabla \mathbf{w} \mathbf{F}^{-1} \left(\mathbf{v} - k^{-1} (\mathbf{u} - \mathbf{u}^{old}) \right), \phi \right)_{\mathcal{F}} \\
 & - (\rho_f J \nabla \mathbf{v} \mathbf{F}^{-1} k^{-1} \mathbf{w}, \phi)_{\mathcal{F}} \\
 & + (J \operatorname{tr} (\mathbf{F}^{-1} \nabla \mathbf{w}) \sigma_f \mathbf{F}^{-T}, \nabla \phi)_{\mathcal{F}} - (J \sigma_f \mathbf{F}^{-T} \nabla \mathbf{w}^T \mathbf{F}^{-T}, \nabla \phi)_{\mathcal{F}} \\
 & + \left(J \frac{d\sigma_f}{d\mathbf{u}}(\mathbf{W}) \mathbf{F}^{-T}, \nabla \phi \right)_{\mathcal{F}} \\
 & + (J (\mathbf{F}^{-T} : \nabla \mathbf{w}) (\mathbf{F}^{-1} : \nabla \mathbf{v}^T), \xi)_{\mathcal{F}} - (J \mathbf{F}^{-1} \nabla \mathbf{w} \mathbf{F}^{-1} : \nabla \mathbf{v}^T, \xi)_{\mathcal{F}} \\
 & + (\rho_s^0 k^{-1} \mathbf{z}, \phi)_{\mathcal{S}} + \left(\nabla \mathbf{w} \boldsymbol{\Sigma}_s + \mathbf{F} \frac{d\boldsymbol{\Sigma}_s}{d\mathbf{u}}(\mathbf{W}), \nabla \phi \right)_{\mathcal{S}} \\
 & - (\mathbf{z}, \psi_s)_{\mathcal{S}} + (k^{-1} \mathbf{w}, \psi_s)_{\mathcal{S}} \\
 & + (\nabla \mathbf{w}, \nabla \psi_f)_{\mathcal{F}},
 \end{aligned} \tag{4.13}$$

where the directional derivatives of the Navier-Stokes stress tensor are given by

$$\begin{aligned}
 \frac{d}{d\mathbf{v}} \sigma_f(\mathbf{U})(\mathbf{z}) &= \rho_f \nu_f (\mathbf{F}^{-1} \nabla \mathbf{z}_f + \nabla \mathbf{z}_f^T \mathbf{F}^{-T}), \\
 \frac{d}{d\mathbf{u}} \sigma_f(\mathbf{U})(\mathbf{w}) &= -\rho_f \nu_f (\mathbf{F}^{-1} \nabla \mathbf{w} \mathbf{F}^{-1} \nabla \mathbf{v} + \nabla \mathbf{v}^T \mathbf{F}^{-T} \nabla \mathbf{w}^T \mathbf{F}^{-T}),
 \end{aligned}$$

and where the directional derivatives of the St. Venant Kirchhoff material's tensor are given by

$$\begin{aligned}
 \frac{d\boldsymbol{\Sigma}_s}{d\mathbf{u}}(\mathbf{U})(\mathbf{w}) &= 2\mu_s \frac{d\mathbf{E}_s}{d\mathbf{u}}(\mathbf{W}) + \lambda_s \operatorname{tr} \left(\frac{d\mathbf{E}_s}{d\mathbf{u}}(\mathbf{W}) \right), \\
 \frac{d\mathbf{E}_s}{d\mathbf{u}}(\mathbf{W}) &= \frac{1}{2} (\nabla \mathbf{w}^T \mathbf{F} + \mathbf{F}^T \nabla \mathbf{w})
 \end{aligned}$$

Proof. The proof is split into different part by a partitioning of the semilinear form (4.9) into subparts for Navier-Stokes momentum equation

$$\begin{aligned}
 A^{m,f}(\mathbf{U})(\Phi) = & \left(\rho_f J \left(k^{-1} (\mathbf{v} - \mathbf{v}^{old}) + \mathbf{F}^{-1} (\mathbf{v} - k^{-1} (\mathbf{u} - \mathbf{u}^{old})) \cdot \nabla \mathbf{v} \right), \phi \right)_{\mathcal{F}} \\
 & + (J \sigma_f \mathbf{F}^{-T}, \nabla \phi)_{\mathcal{F}} - (J \rho_f \mathbf{f}, \phi)_{\mathcal{F}}, \tag{4.14}
 \end{aligned}$$

the equation for divergence freeness

$$A^{div,f}(\mathbf{U})(\Phi) = (J \mathbf{F}^{-1} : \nabla \mathbf{v}^T, \xi_f)_{\mathcal{F}}, \tag{4.15}$$

the momentum equation of the solid problem and the velocity deformation relation

$$A^{m,s}(\mathbf{U})(\Phi) = (\rho_s^0 k^{-1} \mathbf{v}, \phi)_S + (\mathbf{F} \boldsymbol{\Sigma}_s, \nabla \phi)_S, \quad A^{uv,s}(\mathbf{U})(\Phi) = (k^{-1} \mathbf{u} - \mathbf{v}, \psi_s)_S, \quad (4.16)$$

and finally the (harmonic) extension of the deformation that defines the ALE mapping

$$A^{ale,f}(\mathbf{U})(\Phi) = (\nabla \mathbf{u}, \nabla \psi_f)_{\mathcal{F}}. \quad (4.17)$$

The full variational form $A(\mathbf{U})(\Phi)$ is given as the sum of $A^{m,f}(\mathbf{U})(\Phi) + A^{div,f}(\mathbf{U})(\Phi) + A^{m,s}(\mathbf{U})(\Phi) + A^{uv,s}(\mathbf{U})(\Phi) + A^{ale,f}(\mathbf{U})(\Phi)$.

Calculation of the different derivatives of these forms with respect to \mathbf{v} , \mathbf{u} and p_f is done in the following lemmas: first, in Lemma 71 we deal with the derivatives of $A^{NS}(\cdot)(\cdot)$ and $A^{div}(\cdot)(\cdot)$ (the Navier-Stokes part). The Jacobian for the harmonic ALE extension (a linear operator) is directly available. Then, Lemma 73 shows the directional derivatives of the structure equation. And finally, Lemma 74 takes care of the derivatives of the Navier-Stokes part with respect to the artificial domain motion. This part only comes from the ALE formulation and would not be present in Eulerian formulations of the Navier-Stokes problem. \square

Lemma 71 (Derivatives of the Navier-Stokes equations with respect to velocity and pressure). *For the directional derivatives of $A^{m,f}$ and $A^{div,f}$ in direction of velocity \mathbf{v} and pressure p_f it holds:*

$$\begin{aligned} A_{\mathbf{v}}^{m,f}(\mathbf{U})(\mathbf{W}, \Phi) &= \left(\rho_f J \left(k^{-1} \mathbf{z} + \nabla \mathbf{z} \mathbf{F}^{-1} \left(\mathbf{v} - \frac{\mathbf{u} - \mathbf{u}^{old}}{k} \right) + \nabla \mathbf{v} \mathbf{F}^{-1} \mathbf{z} \right), \phi \right)_{\mathcal{F}} \\ &\quad + \left(J \frac{d\sigma_f}{d\mathbf{v}}(\mathbf{W}) \mathbf{F}^{-T}, \nabla \phi \right)_{\mathcal{F}}, \\ A_{p_f}^{m,f}(\mathbf{U})(\mathbf{W}, \Phi) &= - (J \mathbf{F}^{-T} q_f, \nabla \phi)_{\mathcal{F}}, \\ A_{\mathbf{v}}^{div,f}(\mathbf{U})(\mathbf{W}, \Phi) &= (J \mathbf{F}^{-1} : \nabla \mathbf{z}^T, \xi_f)_{\mathcal{F}}, \end{aligned}$$

The derivative of the fluid's stress tensor is given by

$$\frac{d\sigma_f}{d\mathbf{v}}(\mathbf{W}) = \rho_f \nu_f (\mathbf{F}^{-1} \nabla \mathbf{z}_f + \nabla \mathbf{z}_f^T \mathbf{F}^{-T}).$$

Proof. By the definition of the Gâteaux derivative (4.11), calculation of the derivatives is simply given by standard scalar differentiation, as the order of integration and differentiation can be exchanged. For the derivatives of the stress tensor, consult its ALE form (4.5). For basics on the linearization of the navier-Stokes equations, see Section 3.4.2. \square

Before proceeding with the St. Venant Kirchhoff material and the derivatives of the ALE formulation with respect to the deformation, we gather some useful relations:

Lemma 72 (Derivatives of the transformation gradient). *Let $\mathbf{F} := I + \nabla \mathbf{u}$ and $J := \det \mathbf{F}$ its*

gradient. It holds:

- (i) $\frac{d\mathbf{F}}{d\mathbf{u}}(\mathbf{w}) = \nabla \mathbf{w},$
- (ii) $\frac{d\mathbf{F}^T}{d\mathbf{u}}(\mathbf{w}) = \nabla \mathbf{w}^T,$
- (iii) $\frac{d\mathbf{F}^{-1}}{d\mathbf{u}}(\mathbf{w}) = -\mathbf{F}^{-1} \nabla \mathbf{w} \mathbf{F}^{-1},$
- (iv) $\frac{d\mathbf{F}^{-T}}{d\mathbf{u}}(\mathbf{w}) = -\mathbf{F}^{-T} \nabla \mathbf{w}^T \mathbf{F}^{-T},$
- (v) $\frac{dJ}{d\mathbf{u}}(\mathbf{w}) = J \mathbf{F}^{-T} : \nabla \mathbf{w} = J \operatorname{tr}(\mathbf{F}^{-1} \nabla \mathbf{w})$

Proof. Relations (i) and (ii) are directly available. For relation (iii) we use differentiate the identity $\mathbf{F}^{-1}\mathbf{F} = I$ and use (i):

$$\frac{d}{d\mathbf{u}} (\mathbf{F}^{-1}\mathbf{F}) = \frac{d}{d\mathbf{u}} I = 0 \quad \Rightarrow \quad \frac{d\mathbf{F}^{-1}}{d\mathbf{u}}(\mathbf{w})\mathbf{F} + \mathbf{F}^{-1}\frac{d\mathbf{F}}{d\mathbf{u}}(\mathbf{w}) = 0.$$

Multiplication with \mathbf{F}^{-1} gives the result:

$$\frac{d\mathbf{F}^{-1}}{d\mathbf{u}}(\mathbf{w}) = -\mathbf{F}^{-1} \nabla \mathbf{w} \mathbf{F}^{-1}.$$

(iv) directly follows by taking the transpose. Relation (v) can be shown by component-wise calculation, see Problem 44. \square

With Lemma 72, we can now compute the Jacobian of the elastic structure equations with respect to velocity and deformation:

Lemma 73 (Derivative of the structure equation with respect to velocity and deformation). *It holds for the derivatives of the elastic structure equation in reference coordinates with respect to velocity and deformation:*

$$\begin{aligned} A_{\mathbf{v}}^{m,s}(\mathbf{U})(\mathbf{W}, \Phi) &= (\rho_s^0 k^{-1} \mathbf{z}, \phi)_S \\ A_{\mathbf{u}}^{m,s}(\mathbf{U})(\mathbf{W}, \Phi) &= \left(\nabla \mathbf{w} \boldsymbol{\Sigma}_s + \mathbf{F} \frac{d\boldsymbol{\Sigma}_s}{d\mathbf{u}}(\mathbf{W}), \nabla \phi \right)_S, \\ A_{\mathbf{v}}^{uv,s}(\mathbf{U})(\mathbf{W}, \Phi) &= -(\mathbf{z}, \psi_s)_S, \\ A_{\mathbf{u}}^{uv,s}(\mathbf{U})(\mathbf{W}, \Phi) &= (k^{-1} \mathbf{w}, \psi_s)_S, \end{aligned}$$

where the derivative of the 2nd Piola Kirchhoff stress tensor $\boldsymbol{\Sigma}_s$ (of the St. Venant Kirchhoff material) is given by

$$\frac{d\boldsymbol{\Sigma}_s}{d\mathbf{u}}(\mathbf{W}) = 2\mu_s \frac{d\mathbf{E}_s}{d\mathbf{u}}(\mathbf{W}) + \lambda_s \operatorname{tr} \left(\frac{d\mathbf{E}_s}{d\mathbf{u}}(\mathbf{W}) \right),$$

and the derivative of the Green-Lagrangian strain tensor \mathbf{E}_s by

$$\frac{d\mathbf{E}_s}{d\mathbf{u}}(\mathbf{W}) = \frac{1}{2} (\nabla \mathbf{w}^T \mathbf{F} + \mathbf{F}^T \nabla \mathbf{w}).$$

Proof. These relations follow using (i) and (ii) of Lemma 72. \square .

Computing the directional derivatives of complex material laws like the Mooney-Rivlin material causes more work, but can be accomplished in similar ways, see Problem 46

Finally, it remains to gather all derivatives with respect to the ALE domain mapping. These parts are most cumbersome and are left apart in various realizations of nonlinear iterations for fluid-structure interactions, see e.g. [1]. Omitting some of the derivatives (which here correspond to the dependency of the domain motion) relates to a simplified Newton method.

Lemma 74 (Derivative of the Navier-Stokes equations with respect to the domain motion). *It holds for the derivatives of the Navier-Stokes equations in ALE coordinates with respect to the domain motion u :*

$$\begin{aligned} A_{\mathbf{u}}^{m,f}(\mathbf{U})(\mathbf{W}, \Phi) &= \left(\rho_f \operatorname{tr}(\mathbf{F}^{-1} \nabla \mathbf{w}) \left(k^{-1}(\mathbf{v} - \mathbf{v}^{old}) + \right. \right. \\ &\quad \left. \nabla \mathbf{v} \mathbf{F}^{-1} \left(\mathbf{v} - k^{-1}(\mathbf{u} - \mathbf{u}^{old}) \right) \right), \phi \Big)_{\mathcal{F}} \\ &\quad - \left(\rho_f J \nabla \mathbf{v} \mathbf{F}^{-1} \nabla \mathbf{w} \mathbf{F}^{-1} \left(\mathbf{v} - k^{-1}(\mathbf{u} - \mathbf{u}^{old}) \right), \phi \right)_{\mathcal{F}} \\ &\quad - \left(\rho_f J \nabla \mathbf{v} \mathbf{F}^{-1} k^{-1} \mathbf{w}, \phi \right)_{\mathcal{F}} \\ &\quad + \left(\operatorname{tr}(\mathbf{F}^{-1} \nabla \mathbf{w}) \sigma_f \mathbf{F}^{-T}, \nabla \phi \right)_{\mathcal{F}} - \left(J \sigma_f \mathbf{F}^{-T} \nabla \mathbf{w}^T \mathbf{F}^{-T}, \nabla \phi \right)_{\mathcal{F}} \\ &\quad + \left(J \frac{d\sigma_f}{d\mathbf{u}}(\mathbf{W}) \mathbf{F}^{-T}, \nabla \phi \right)_{\mathcal{F}}. \\ A_{\mathbf{u}}^{div,f}(\mathbf{U})(\mathbf{W}, \Phi) &= (\operatorname{div}(\operatorname{tr}(\mathbf{F}^{-1} \nabla \mathbf{w}) \mathbf{F}^{-1} \mathbf{v}), \xi_f)_{\mathcal{F}} - (\operatorname{div}(J \mathbf{F}^{-1} \nabla \mathbf{w} \mathbf{F}^{-1}), \xi_f)_{\mathcal{F}}. \end{aligned}$$

where the derivative of the stress tensor with respect to the domain motion is given by

$$\frac{d\sigma_f}{d\mathbf{u}}(\mathbf{W}) = -\rho_f \nu_f (\mathbf{F}^{-1} \nabla \mathbf{w} \mathbf{F}^{-1} \nabla \mathbf{v} + \nabla \mathbf{v}^T \mathbf{F}^{-T} \nabla \mathbf{w}^T \mathbf{F}^{-T})$$

Proof. Again, all these derivatives can be estimated by tedious calculations using Lemma 72. \square

With the Jacobian of the fluid-structure interaction system at hand, we can formulate the linear systems of partial differential equations, that define every step of the Newton approximation

$$A'(\mathbf{U}^{(l-1)})(\mathbf{W}^{(l)}, \Phi) = F(\Phi) - A(\mathbf{U}^{(l-1)})(\Phi) \quad \forall \Phi \in \mathcal{Y}. \quad (4.18)$$

The variational formulation defined by $A'(\cdot)(\cdot, \cdot)$ given in Theorem 11 is very complex, it couples all different variables, but it is a linear problem. Finite element discretization of this problem will be subject to the following section. Later on, in Chapter 6, we will discuss the solution of the resulting (after discretization) linear systems of equations.

In every step of the Newton iteration, system (4.18) is itself a coupled problem on the two domains \mathcal{F} and \mathcal{S} . On the common interface, three coupling conditions are given. First, continuity of the velocity variation \mathbf{z} , second continuity of the deformation's variation \mathbf{w} and finally, a Neumann condition that comes from the linearization of the dynamic coupling condition. For deriving its exact formulation, one would have to transform $A'(\mathbf{U})(\mathbf{W}, \Phi)$ as given in Theorem 11 back to the classical formulation.

A modern alternative to the analytical computation of the Jacobian is given by the idea of *automatic differentiation*, see Rall [178] and Griewank [110]. Automatic differentiation is an

algorithmic approach that is based on the concept, that every computer implementation, e.g. the implementation of the semilinear form $A(\cdot)(\cdot)$ will internally be split into a sequence of elementary mathematical operations (like multiplications, roots, basis functions like sine or cosine etc.). These elementary operations are then derived and set together using chain and product rule. Dunne [85] presents and implementation of a Newton method for fluid-structure interactions in ALE formulation based on automatic differentiation. In particular, if the model is not fixed, automatic differentiation will help to compute exact Jacobians in a fail-proof way. It will for instance be easy to integrate complex and changing material laws. The concept of automatic differentiation is not to be confused with finite differences, that only approximate the derivatives.

4.2.3 Numerical Study on Linearizations

Vergleich von:

- fsi-3 Benchmark
- Linearisierung mit einfacher Fixpunkt-Iteration fuer ALE-Terme
- Newton
- Finite Differenzen, verschiedene epsilon

4.3 Finite elements for fluid-structure interactions in ALE formulation

Every step of the Newton iteration requires the solution of a linear system of partial differential equations, compare (4.18)

$$\begin{aligned} \mathcal{W}^{(l)} := \{\mathbf{z}^{(l)}, \mathbf{w}^{(l)}, q_f^{(l)}\} \in \mathcal{X} := \mathcal{V} \times \mathcal{W} \times \mathcal{L}_f : \\ A'(\mathbf{U}^{(l-1)})(\mathbf{W}^{(l)}, \Phi) = G(\Phi) \\ \forall \Phi := \{\phi, \psi_f, \psi_s, \xi_f\} \in \mathcal{V} \times \mathcal{W}_f \times \mathcal{L}_s \times \mathcal{L}_f. \end{aligned}$$

In the context of the backward Euler discretization of fluid-structure interactions on a fixed ALE domain, the bilinear-form $A'(\mathbf{U})(\cdot, \cdot)$ is given as in Theorem 11. The right hand side is given by

$$G(\Phi) := F(\Phi) - A(\mathbf{U}^{(l-1)})(\Phi),$$

where $\mathbf{U}^{(l-1)}$ is the last approximation and $A(\mathbf{U}^{(l-1)})(\Phi)$ and $F(\Phi)$ are shown in (4.9) and (4.10). The trial spaces for velocity and deformation are defined on the whole domain

$$\mathcal{V} := H_0^1(\Omega; \Gamma^D)^d, \quad \mathcal{W} := H_0^1(\Omega; \partial\Omega)^d,$$

and differ by the choice of boundary values only. See Section 2.3 for a discussion.

The test-function $\phi \in \mathcal{V}$ for both momentum equations is also defined on the complete domain Ω . All further test-functions are defined sub-domain wise:

$$\mathcal{L}_f := L^2(\mathcal{F}), \quad \mathcal{W}_f := H_0^1(\mathcal{F})^d, \quad \mathcal{L}_s := L^2(\mathcal{S})^d.$$

In the following, we will focus on the finite element discretization of these linear systems, and for shortness of notation, we omit the last Newton approximation $\mathbf{U}^{(l-1)}$ and simply consider the linear system

$$\mathbf{W} \in \mathcal{X} : \quad A(\mathbf{W}, \Phi) = G(\Phi) \quad \forall \Phi \in \mathcal{Y}, \quad (4.19)$$

where $A(\cdot, \cdot)$ is bilinear on $\mathcal{X} \times \mathcal{Y}$. Discretization is accomplished by restricting solution and test-function to discrete spaces:

$$\mathbf{W}_h \in X_h : \quad A(\mathbf{W}_h, \Phi_h) + S_h(\mathbf{W}_h, \Phi_h) = G(\Phi_h) \quad \forall \Phi \in Y_h, \quad (4.20)$$

where $S_h(\cdot, \cdot)$ defines some possible stabilization terms, see Sections 3.3.2 and 3.4.3.

Remark 29 (Properties of finite element spaces). *For the choice of finite element spaces X_h and Y_h must consider the following properties:*

1. *For a conforming (Petrov)-Galerkin formulation it must holds $X_h \subset \mathcal{X}$ and $Y_h \subset \mathcal{Y}$.*
2. *The dimension of test- and trial-spaces must coincide*

$$\dim X_h = \dim Y_h.$$

3. *The velocity- and pressure-coupling $\{\mathbf{v}_h, p_h\}$ within the fluid-domain must satisfy the inf-sup condition. Otherwise, the variational formulation has to be enriched by stabilization terms $S_h(\cdot, \cdot)$, see Section 3.3.2.*
4. *For implementation reasons, it is preferable to consider finite element spaces for velocity and deformation of the same type on \mathcal{F} and \mathcal{S} .*
5. *As global velocity and deformation are continuous on the complete domain Ω , but not differentiable across the interface \mathcal{I} , it is preferable, if the interface is resolved by the triangulation. Otherwise, the order of convergence will be reduced, see Section 3.5, unless special manners are taken.*

4.3.1 Finite element triangulations for fluid-structure interactions in ALE formulation

The benefit of the formulation in Arbitrary Lagrangian Eulerian coordinates is the fixation of the sub-domains \mathcal{F} and \mathcal{S} , separated by the interface \mathcal{I} . We define:

Definition 16 (Matching Mesh). *A triangulation Ω_h of the domain Ω is called a matching mesh, if for every element $K \in \Omega_h$ it holds*

$$K \in \mathcal{S} \wedge K \cap \mathcal{F} = \emptyset,$$

or

$$K \in \mathcal{F} \wedge K \cap \mathcal{S} = \emptyset.$$

For a matching triangulation, we define the sub-triangulations

$$\Omega_{h,f} := \{K \in \Omega_h, K \in \mathcal{F}\}, \quad \Omega_{h,s} := \{K \in \Omega_h, K \in \mathcal{S}\}.$$

This definition implies, that a matching mesh always resolves the interface \mathcal{I} between fluid and solid by edges of elements, such that we can define

$$\mathcal{I}_h := \{e \in \partial K, K \in \Omega_h, e \in \mathcal{I}\},$$

and it holds

$$\bar{\mathcal{I}} = \bigcup_{e \in \mathcal{I}_h} \bar{e}.$$

This directly shows, that matching meshes in this strict sense are only possible, if the interface \mathcal{I} (in reference coordinates) is a polygonal, or if the interface can be described by low order polynomials, and if a parametric finite element triangulation is considered, see Definition 12. Here, we will always assume, that all finite element meshes are matching.

Remark 30 (Approximation of curved interfaces). *If the interface between fluid and solid is curved, such that it cannot be exactly resolved by the mesh, the strict definition of matching meshes is not applicable and will be relaxed: we will call a mesh matching, if all degrees of freedom used to define the parametric triangulation (see Definition 12) are either all part of the solid-domain \mathcal{S} or all part of the fluid-domain \mathcal{F} . See Figure 4.5 for examples of matching and non-matching triangulations.*

In the finite element error analysis, the consideration of curved interfaces, that cannot be resolved by the mesh (and hence not by the finite element spaces) is still an open problem.

It is not strictly required, that one uses matching meshes for discretizing fluid-structure interactions. The use of matching meshes just simplifies the embedding of the coupling conditions, as we can define global function spaces V_h and W_h for velocity, deformation and the momentum equation's test-function and restrict these global functions to the two sub-domains. By this approach, coupling will turn out to be as simple as in the continuous case, see Section 2.3.

The following simple lemma holds in the case of matching triangulations:

Lemma 75 (Finite elements spaces on matching meshes). *Let Ω_h be a triangulation of the domain Ω and V_h the standard space of continuous elements of degree $r \geq 1$ with Lagrangian basis $V_h = \text{span}\{\phi_h^{(i)}, i = 1, \dots, N\}$, e.g.*

$$\phi_h^{(i)}(x_j) = \delta_{ij}, \quad i, j \in \{1, \dots, N\}.$$

See Section 3.2.1. The subspaces:

$$\begin{aligned} V_{h,f} &:= \text{span}\{\phi_h^{(i)} \in V_h, x_i \in \bar{\mathcal{F}} \setminus \mathcal{I}\}, \\ V_{h,s} &:= \text{span}\{\phi_h^{(i)} \in V_h, x_i \in \bar{\mathcal{S}}\}, \end{aligned}$$

define a division of V_h ,

$$V_h = V_{h,f} + V_{h,s}, \quad \dim V_h = \dim V_{h,f} + \dim V_{h,s}, \tag{4.21}$$

and the space $V_{h,f}$ is $H_0^1(\mathcal{F}; \mathcal{I})$ conforming

$$V_{h,f} \subset H_0^1(\mathcal{F}; \mathcal{I}), \quad V_{h,s} \subset H^1(\mathcal{S}).$$

Proof. For $\phi_h^{(i)}$ with $x_i \in \bar{\mathcal{F}}$, but $x_i \notin \mathcal{I}$, it holds on matching triangulations, that

$$\text{supp } \phi_h^{(i)} \in \mathcal{F}.$$

Hence, $V_{h,f} \subset H_0^1(\mathcal{F}; \mathcal{I})$. The relation $V_{h,s} \subset H^1(\mathcal{S})$ directly follows due to the continuity of $V_h \subset C(\bar{\Omega})$. Further, the dimension formula (4.21) follows, as the partitioning of Lagrange points $x_i \in \Omega_h$ to those on the interior of solid and fluid and those on the interface is unique. \square

This lemma appears trivial, but it is essential for the following approach: if a global finite element function $\mathbf{v}_h \in V_h$ is given, we can define restrictions $\mathbf{v}_{h,f} \in V_{h,f}$ and $\mathbf{v}_{h,s} \in V_{h,s}$ in the two subspaces. This allows us to hide the coupling conditions in global trial- and test-spaces.

4.3.2 Inf-sup stable FE-spaces for fluid-structure interactions in ALE formulation

We will start by introducing some finite element triples (for velocity, deformation and pressure), that fulfill as many of the desirable properties from Remark 29. Let Ω_h be a matching triangulation. We will denote the velocity space by

$$\mathbf{v}_h \in V_h,$$

and the global deformation space by

$$\mathbf{u}_h \in W_h.$$

On the two sup-domains of the matching triangulation, we define the restrictions $\mathbf{v}_{h,f}, \mathbf{v}_{h,s}$ and $\mathbf{u}_{h,f}, \mathbf{u}_{h,s}$. We will denote the discrete pressure space by $L_{h,f}$.

As discussed in Section 3.3, the fluid's finite element pair for velocity $V_{h,f}$ and pressure $L_{h,f}$ must satisfy the inf-sup condition (in ALE coordinates):

$$\inf_{p_h \in L_{h,f}} \sup_{\mathbf{v}_h \in V_{h,f}} \frac{(p_h, \operatorname{div}(J_f \mathbf{F}_f^{-1} \mathbf{v}_h))_{\mathcal{F}}}{\|J_f^{\frac{1}{2}} p_h\|_{\mathcal{F}} \|J_f^{\frac{1}{2}} \nabla \mathbf{v}_h \mathbf{F}_f^{-T}\|_{\mathcal{F}}} \geq \hat{\gamma}_h. \quad (4.22)$$

where \mathbf{F}_f and $J = \det \mathbf{F}_f$ come from the ALE-map. In terms of a computational finite element approach, the ALE-map is not a continuous, regular function, but itself defined by means of finite element functions

$$\mathbf{F}_h := I + \nabla \mathbf{u}_h, \quad J_h := \det \mathbf{F}_h.$$

In the following however, we will skip the index “ h ”. The discussion of Section 1.5.2 has shown, that the inf-sup condition in ALE formulation (4.22) is equivalent to the standard version of the inf-sup condition on the reference domains,

$$\inf_{p_h \in L_{h,f}} \sup_{\mathbf{v}_h \in V_{h,f}} \frac{(p_h, \operatorname{div} \mathbf{v}_h)_{\mathcal{F}}}{\|p_h\|_{\mathcal{F}} \|\nabla \mathbf{v}_h\|_{\mathcal{F}}} \geq \gamma, \quad (4.23)$$

if the domain mapping sufficiently regular. The two inf-sup constants however can significantly differ,

$$\hat{\gamma} \ll \gamma,$$

if the deformation of the domain is large. An analysis of the inf-sup condition on transformed domains is given in [168]. By these considerations, we suggest the following choices of finite element triples for velocity, deformation and pressure. See also Figure 4.6:

1. The generalized Taylor-Hood space

$$[Q^k]^d \times [Q^k]^d \times Q^{k-1}, \quad k \geq 2,$$

on quadrilateral meshes and

$$[P^2]^d \times [P^2]^d \times P^1, \quad [P^k]^d \times [P^k]^d \times P^{k-2}, \quad k \geq 3,$$

on triangular meshes. These spaces are inf-sup stable. Further, they have the simple property, that deformation and velocity come from the same space. Finally, velocity and deformation spaces are the same on both parts of the domain.

2. The generalized Taylor-Hood spaces with discontinuous pressure

$$[Q^k]^d \times [Q^k]^d \times P^{k-1,dc}, \quad k \geq 2,$$

on quadrilateral meshes and the bulb-enriched space

$$[P^{2,bulb}]^d \times [P^2]^d \times P^{1,dc},$$

on triangular meshes. These combinations have all the benefit of the first choice. In addition, practical application usually shows better solutions (in particular on coarse meshes) due to local conservation properties, that come from the use of discontinuous pressures.

Another advantage comes to the fore, if incompressible materials are considered, see Section 1.2.2. These material laws require the introduction of a second pressure variable $p_s \in L^2(\mathcal{S})$. As there is no physical reason for continuity of the two pressures p_f and p_s at the interface \mathcal{I} , the two discrete variables must be separated. Using continuous finite elements, this would cause technical problems, as there is only one Lagrange point on the interface. As the discontinuous space $P^{k-1,dc}$ is defined in an element-wise manner, implementation is simplified. We can define one global pressure $p_h \in L_h$ and define fluid- and solid-pressure as restrictions:

$$p_{h,f} = p_h \Big|_{\mathcal{F}}, \quad p_{h,s} = p_h \Big|_{\mathcal{S}}.$$

Both of these choices are conforming in all three variables, deformation, velocity and pressure. For the definition of the test-spaces, we need to pay special attention to the interface. While velocity and deformation are defined in a global way, only the test-space $\phi \in \mathcal{V}$ for the momentum equation is defined on the complete domain Ω . The test-functions for extension of the deformation $\psi_f \in \mathcal{W}_f$ as well as the test-space for the deformation-velocity relation $\psi_s \in \mathcal{L}_s$ must be decoupled at the interface. Based on the second (just as example) choices of finite element spaces, we define

$$\begin{aligned} V_h &:= \text{span}\{\phi_h \in C(\Omega)^d, \phi_h^{(i)} \text{ piece-wise quadratic, } \phi_h = 0 \text{ on } \Gamma^D\}, \\ W_h &:= \text{span}\{\phi_h \in C(\Omega)^d, \phi_h^{(i)} \text{ piece-wise quadratic } \phi_h = 0 \text{ on } \partial\Omega\}, \\ L_{h,f} &:= \text{span}\{\xi_h \in L^2(\mathcal{F}), \xi_h^{(i)} \text{ piece-wise linear}\}, \\ W_{f,h} &:= \text{span}\{\phi_h \in C(\mathcal{F})^d, \phi_h^{(i)} \text{ piece-wise quadratic } \phi_h = 0 \text{ on } \partial\mathcal{F}\} \\ L_{s,h} &:= \text{span}\{\phi_h \in C(\mathcal{S})^d, \phi_h^{(i)} \text{ piece-wise quadratic}\}. \end{aligned} \tag{4.24}$$

With this construction of finite element spaces, we can define a well-posed discrete finite element approximation of the backward-Euler discretization for fluid-structure interactions in Arbitrary Lagrangian Eulerian coordinates:

System 4 (Finite Element Discretization of the fsi-system in ALE formulation). *Let $A(\cdot, \cdot)$ be given by (4.9), $F(\cdot)$ by (4.10). The Jacobian $A(\mathbf{U})(\cdot, \cdot)$ is given by Theorem 11. Given the last discrete Newton approximation $\mathbf{U}_h^{(l-1)} \in X_h$, find*

$$\mathbf{W}_h^{(l)} := \{\mathbf{v}_h, \mathbf{u}_h, p_{f,h}\} \in X_h := V_h \times W_h \times L_{h,f},$$

such that

$$A'(\mathbf{U}_h^{(l-1)})(\mathbf{W}_h^{(l)}, \Phi_h) = F(\Phi_h) - A(\mathbf{U}_h^{(l-1)})(\Phi_h) \quad (4.25)$$

for all

$$\Phi_h := \{\phi_h, \psi_{h,f}, \psi_{h,s}, \xi_{h,f}\} \in Y_h := V_h \times W_{h,f} \times L_{h,s} \times L_{h,f}.$$

The Newton update problem in step (4.25) defines a linear system of equations. Chapter 6 will be devoted to the solution of this system. First we note, that for our choice of finite element spaces (4.24), the system of equations is quadratic, i.e., the number of unknowns equals the number of equations. See also Problem 47.

4.3.3 Stabilized finite elements for fluid-structure interactions

In Section 3.3.2, we have introduced concepts for stabilizing finite element pairs, that do not satisfy the inf-sup condition. Here, we want to shortly apply this concept to the discretization of fluid-structure interactions. The basic idea was to either modify the test-space by a Petrov-Galerkin approach, or to modify the variational formulation by adding stabilization terms $S_h(\cdot, \cdot)$. This latter approach is more general and also covers Petrov-Galerkin discretizations. We shortly discuss the very simple case of the non-conforming pressure stabilization used in Lemma 65. The linearized discrete variational formulation is enriched by a pressure stabilization term

$$A'_h(\mathbf{U}_h)(\mathbf{W}_h, \Phi_h) := A(\mathbf{U}_h)(\mathbf{W}_h, \Phi_h) + S_h(\mathbf{W}_h, \Phi_h).$$

For the proper definition of the pressure stabilization in Arbitrary Lagrangian Eulerian formulation, we must transfer the standard method from Eulerian coordinates to the fixed reference system. Hence, let – just for the following discussion – $\hat{\mathcal{F}}$ be the reference fluid domain and \mathcal{F} be the current Eulerian fluid-domain in the actual time-step. Then, the pressure stabilization term in Eulerian coordinates on \mathcal{F} was defined as

$$S_h(\mathbf{U}_h, \Phi_h) := (\alpha_{\text{stab}} \nabla p_h, \nabla \xi_h)_{\mathcal{F}}, \quad (4.26)$$

with an element-wise defined stabilization parameter

$$\alpha_{\text{stab}}|_K = \alpha_0 \left(\frac{\nu_f}{h_K^2} + \frac{\|\mathbf{v}\|_{L^\infty(K)}}{h_K} \right).$$

See Section 3.3.2. The mesh-size h_K would be the mesh-size of a Eulerian mesh. The first detail, that has to be analyzed in the context of Arbitrary Lagrangian formulations is the

concept of the mesh-size h_K . Usually, for shape-regular triangulations (see Definition 13), we can define the mesh-size of the triangulation $\hat{\Omega}_h$ of the reference domain $\hat{\mathcal{F}}$ as

$$\hat{h}_K := \text{diam}(\hat{K}).$$

Another suitable definition is to define the mesh-size as an integral value

$$\hat{h}'_K := \left(\int_{\hat{K}} 1 \, d\hat{x} \right)^{\frac{1}{d}}.$$

On shape-regular triangulations, there exists a constant $c > 0$, such that

$$c^{-1}h'_K \leq h_K \leq ch'_K \quad \forall \hat{K} \in \hat{\Omega}_h, \quad (h \rightarrow 0). \quad (4.27)$$

In the following, we will use the definition by integration. Now, let $T : \hat{K} \rightarrow K$ be the ALE map and $K := T(\hat{K})$ be the Eulerian counterpart of $\hat{K} \in \hat{\Omega}_h$. It holds

$$h_K := \left(\int_K 1 \, dx \right)^{\frac{1}{d}} = \left(\int_{\hat{K}} J \, d\hat{x} \right)^{\frac{1}{d}},$$

and we can estimate

$$\min_{\hat{x} \in \hat{K}} |J(\hat{x})|^{\frac{1}{d}} \hat{h}_K \leq h_k \leq \max_{\hat{x} \in \hat{K}} |J(\hat{x})|^{\frac{1}{d}} \hat{h}_K. \quad (4.28)$$

Using this relation between Eulerian and reference mesh size, the stabilization term (4.26) can be transformed in ALE coordinates

$$S_h(\hat{\mathbf{U}}_h, \hat{\Phi}_h) = (\alpha_{\text{stab}} J \mathbf{F}^{-1} \mathbf{F}^{-T} \nabla p_h, \nabla \xi_h)_{\hat{\mathcal{F}}}.$$

with an stabilization parameter, that – expressed on the reference system $\hat{\mathcal{F}}$ – is given by

$$\alpha_{\text{stab}} = \alpha_0 \left(\frac{\nu_f J^{\frac{2}{d}}}{\hat{h}_K^2} + \frac{\|\hat{\mathbf{v}}\|_{L^2(\hat{K})} J^{\frac{1}{d}}}{\hat{h}_K} \right)^{-1}.$$

If the deformation of the mesh is moderate, it holds $J \approx 1$ and $\mathbf{F} \approx I$, such that it is suitable to just choose a standard setting of the stabilization term (4.26) also on the reference domain. This construction is also directly applicable for the stabilization by means of Local Projections, see Lemma 67:

$$S_{\text{lps}}(\hat{\mathbf{U}}_h, \hat{\Phi}_h) = (\alpha \mathbf{F}^{-1} \mathbf{F}^{-T} \nabla(p_h - \pi_h p_h), \nabla(\xi_h - \pi_h \xi_h))_{\hat{\mathcal{F}}},$$

where $\pi_h : Q_h \rightarrow \tilde{Q}_h$ is the local coarse mesh projection operator. As for the Eulerian setting, the LPS method will give optimal order of convergence, if the spaces \tilde{Q}_h and Q_h are well chosen, as weak consistency holds:

$$p_h \in \tilde{Q}_h \quad \Rightarrow \quad S_{\text{lps}}(p_h, \xi_h) = 0 \quad \forall \xi_h \in Q_h.$$

In the case of residual based stabilization techniques like PSPG (or SUPG), the correct application to the Arbitrary Eulerian Lagrangian formulation is more difficult. The success of these techniques is based on a consistent formulation: if $\mathbf{U} \in \mathcal{X}$ is the solution, it should hold

$$S_{\text{PSPG}}(\mathbf{U}, \Phi_h) = 0 \quad \forall \Phi_h \in X_h.$$

This is realized by testing the complete momentum equation of the fluid system (compare the Jacobian in Theorem 11) with the modified test-function

$$\tilde{\phi}_h := \phi_h + \alpha \nabla \xi_h.$$

This gives rise to complex coupled terms including the complete strong residual. For a discussion on a practical way of applying residual based stabilization techniques to fsi-problems in Arbitrary Lagrangian Eulerian coordinates, we refer to Wall [239].

Remark 31 (Stabilization for large deformations). *As long as the deformation and motion of the domains is small, we can apply all stabilization techniques without any modification and just omit the ALE mapping. This does not hold true, if the deformation is very large, i.e., if $J \ll 1$ or $J \gg 1$ or if simply \mathbf{F} significantly differs from the identity I . As long as the ALE mapping is isotropic, we simply need to adjust the mesh size by means of relation (4.28). If the mapping however inhibits very strong anisotropies, the concept of stabilization must be altered. In particular, it will be necessary to separate directions. On a Eulerian, cartesian anisotropic mesh, the simple pressure stabilization term in the case of the linear Stokes equations must be constructed as:*

$$S_{h,\text{aniso}}(\mathbf{U}_h, \Phi_h) = (\alpha_0 h_x^2 \partial_x p_h, \partial_x \xi_h)_\mathcal{F} + (\alpha_0 h_y^2 \partial_y p_h, \partial_y \xi_h)_\mathcal{F}.$$

For a detailed analysis of the Local Projection stabilization on anisotropic meshes, we refer to the Literature [196, 47, 40, 187] and in particular Molnar [168] in the case of fluid-structure interactions.

Besides stabilization of the pressure-velocity coupling, we need to take care of problems with dominant convection, that require stabilization of transport oscillations. Here, we can follow the same procedure: starting with a stabilization technique in Eulerian coordinate, we map the resulting stabilization terms back to the reference framework. Again, all methods work very well without modifications, if small deformations are considered. Only the case of very large deformation with substantial anisotropies is still open. See [239, 168].

4.4 Practical aspects

4.4.1 Matrix formulation of the linear systems

The finite element discretization of the linearized system, that has to be solved in every step of the Newton iteration

$$A'(\mathbf{U})(\mathbf{W}, \Phi_h) = F(\Phi) - A(\mathbf{U})(\Phi), \quad (4.29)$$

gives rise to a large linear system of equations, that can be compactly written in the form

$$\mathbf{A}_h \mathbf{x}_h = \mathbf{b}_h.$$

In this section, we will give details on the derivation and resulting structure of the system matrix. The exact form of the matrix strongly depends on the choice of finite element spaces. For discretization of

$$X_h \subset \mathcal{X}, \quad Y_h \subset \mathcal{Y},$$

we follow a simply approach and also make some additional assumptions:

- First, we assume, that the triangulation is matching the domain-partitioning.
- We assume, that both fluid and solid problem are given with Dirichlet conditions on the outer boundaries of the domain. In this case, it holds $\mathcal{V} = \mathcal{W}$ and it will also hold (in terms of (4.24)), that $V_h = W_h$.
- We consider inf-sup stable finite elements, such that no pressure-stabilization is required.
- We choose equal-order finite element spaces for velocity \mathcal{V} and deformation \mathcal{W} , as well as for the test-function of momentum equations \mathcal{V} , ALE extension \mathcal{W}_f and deformation-velocity relation \mathcal{L}_s . All these discrete spaces are based on the same set of matrix-functions.

By these assumptions, let V_h be the space of continuous finite elements on the complete domain Ω_h of degree $r \geq 2$, with strong Dirichlet-values on the complete boundary $\partial\Omega_h$ and a Lagrangian nodal basis

$$V_h := \text{span}\{\phi_h^{(i)}, i = 1, \dots, N\}.$$

Discrete velocity update and deformation update are given by

$$\mathbf{z}_h(x) = \sum_{i=1}^N \mathbf{z}_i \phi_h^{(i)}(x), \quad \mathbf{w}_h(x) = \sum_{i=1}^N \mathbf{w}_i \phi_h^{(i)}(x).$$

We define the following subsets of indices, that collect all basis functions with support in the fluid, in the solid and those, that touch the interface

$$\begin{aligned} I_f &:= \{i \in \{1, \dots, N\} \mid \text{supp } \phi_h^{(i)} \subset \mathcal{F}\}, & N_f &:= \# I_f, \\ I_s &:= \{i \in \{1, \dots, N\} \mid \text{supp } \phi_h^{(i)} \subset \mathcal{S}\}, & N_s &:= \# I_s, \\ I_I &:= \{1, \dots, N\} \setminus (I_f \cup I_s), & N_i &:= \# I_i. \end{aligned}$$

Then, the test-space of the ALE-extension is given by

$$W_{h,f} := \text{span}\{\phi_h^{(i)}, i \in I_f\},$$

and the test-space of the deformation-velocity coupling by

$$W_{h,s} := \text{span}\{\phi_h^{(i)}, i \in I_s \cup I_i\}.$$

Finally, the pressure-space $L_{h,f}$ is given by

$$L_{h,f} = \text{span}\{\xi_h^{(i)}, i = 1, \dots, N_p\}.$$

By $\xi_h^{(i)}$ a basis of either a lower-degree continuous space (e.g. $r - 1$ on quadrilaterals), or some discontinuous space can be given. The pressure update is then given by

$$q_{h,f}(x) = \sum_{i=1}^{N_p} \mathbf{q}_i \xi_h^{(i)}(x).$$

By insertion of these basis representations in (4.29), we derive the matrix formulation of the linear system. This matrix has a block-structure in multiple senses: first, parts of the equation act on the fluid-domain, parts on the solid-domain. Second, we get a natural block-structure

due to the coupled equations: momentum equation of Navier-Stokes (*NS*), divergence condition in the Navier-Stokes equations (*div*), equation for the extension of the ALE map (*ALE*), momentum equation of the elastic solid (*ES*) and finally, relation between deformation and velocity (*uv*). Each of these equations appears in the Jacobian and may appear multiple times: the momentum part of the Navier-Stokes equations (*NS*) has directional derivatives with respect to the pressure, the velocity and the deformation. We will use this terminology to denote the sub-matrices and explain this procedure based on Navier-Stokes' momentum equations including the derivatives with respect to pressure and velocity:

$$\begin{aligned} [F_p^{NS}]_{ij} &= - \left(J\mathbf{F}^{-T} \xi_{h,f}^{(j)}, \phi_h^{(i)} \right)_{\mathcal{F}} \\ &\quad \forall i \in I_f \cup I_i, \quad \forall j \in \{1, \dots, N_p\} \\ [F_{\mathbf{v}}^{NS}]_{ij} &= \left(\rho_f J \left(k^{-1} \tilde{\phi}_{h,f}^{(j)} + \nabla \tilde{\phi}_{h,f}^{(j)} \mathbf{F}^{-1} \left(\mathbf{v} - \frac{\mathbf{u} - \mathbf{u}^{\text{old}}}{k} \right) + \nabla \mathbf{v} \mathbf{F}^{-1} \tilde{\phi}_{h,f}^{(j)} \right), \phi_h^{(i)} \right)_{\mathcal{F}} \\ &\quad + \left(J \frac{d\sigma_f}{d\mathbf{v}}(\mathbf{W}) \mathbf{F}^{-T}, \nabla \phi \right)_{\mathcal{F}} - (J\mathbf{F}^{-T} q_f, \nabla \phi)_{\mathcal{F}} \\ &\quad \forall i \in I_f \cup I_i, \quad \forall j \in I_f \cup I_i \end{aligned}$$

All the remaining parts are derived in a similar way. Altogether, we derive the following matrices for fluid- and solid-problem:

$$\mathbf{F} = \begin{pmatrix} 0 & F_{\mathbf{v}}^{\text{div}} & F_{\mathbf{u}}^{\text{div}} \\ F_p^{\text{NS}} & F_{\mathbf{v}}^{\text{NS}} & F_{\mathbf{u}}^{\text{NS}} \\ 0 & 0 & F_{\mathbf{u}}^{\text{ALE}} \end{pmatrix}, \quad \mathbf{S} = \begin{pmatrix} S_{\mathbf{v}}^{\text{ES}} & S_{\mathbf{u}}^{\text{ES}} \\ S_{\mathbf{v}}^{\text{uv}} & S_{\mathbf{u}}^{\text{uv}} \end{pmatrix}, \quad (4.30)$$

with

$$\mathbf{F} \in \mathbb{R}^{(N_p+2N_f+2N_i) \times (N_p+2N_f+2N_i)}, \quad \mathbf{S} \in \mathbb{R}^{2(N_s+N_i) \times 2(N_s+N_i)}.$$

To assemble the coupled system matrix on the complete domain Ω , we must construct the sum of both parts. First, we define subsets of the coefficient vectors

$$\mathbf{z} := \{\mathbf{z}_f, \mathbf{z}_i, \mathbf{z}_s\}, \quad \mathbf{w} := \{\mathbf{w}_f, \mathbf{w}_i, \mathbf{w}_s\},$$

where \mathbf{z}_f , \mathbf{z}_i and \mathbf{z}_s denote only those indices in I_f , I_i and I_s , respectively. The same splitting is applied to \mathbf{w} and also to the test-functions ϕ_h and ψ_h . By this definition, we can give a more detailed version of the two sub-matrices, that distinguishes between degrees freedom within the domain and those on the interface

$$\begin{aligned} \mathbf{F}_h &= \begin{bmatrix} \xi_{h,f} \\ \phi_{h,f} \\ \psi_{h,f} \\ \phi_{h,i} \\ \psi_{h,i} \end{bmatrix} \begin{pmatrix} 0 & F_{\mathbf{v}}^{\text{div}} & F_{\mathbf{u}}^{\text{div}} & F_{\mathbf{v}}^{\text{div}} & F_{\mathbf{u}}^{\text{div}} \\ F_p^{\text{NS}} & F_{\mathbf{v}}^{\text{NS}} & F_{\mathbf{u}}^{\text{NS}} & F_{\mathbf{v}}^{\text{NS}} & F_{\mathbf{u}}^{\text{NS}} \\ 0 & 0 & F_{\mathbf{u}}^{\text{ALE}} & 0 & F_{\mathbf{u}}^{\text{ALE}} \\ F_p^{\text{NS}} & F_{\mathbf{v}}^{\text{NS}} & F_{\mathbf{u}}^{\text{NS}} & F_{\mathbf{v}}^{\text{NS}} & F_{\mathbf{u}}^{\text{NS}} \\ 0 & 0 & 0 & 0 & 0 \end{pmatrix} \\ \mathbf{S}_h &= \begin{bmatrix} \phi_{h,i} \\ \psi_{h,i} \\ \phi_{h,s} \\ \psi_{h,s} \end{bmatrix} \begin{pmatrix} S_{\mathbf{v}}^{\text{ES}} & S_{\mathbf{u}}^{\text{ES}} & S_{\mathbf{v}}^{\text{ES}} & S_{\mathbf{u}}^{\text{ES}} \\ S_{\mathbf{v}}^{\text{uv}} & S_{\mathbf{u}}^{\text{uv}} & S_{\mathbf{v}}^{\text{uv}} & S_{\mathbf{u}}^{\text{uv}} \\ S_{\mathbf{v}}^{\text{ES}} & S_{\mathbf{u}}^{\text{ES}} & S_{\mathbf{v}}^{\text{ES}} & S_{\mathbf{u}}^{\text{ES}} \\ S_{\mathbf{v}}^{\text{uv}} & S_{\mathbf{u}}^{\text{uv}} & S_{\mathbf{v}}^{\text{uv}} & S_{\mathbf{u}}^{\text{uv}} \end{pmatrix} \end{aligned}$$

We note, that the off-diagonal blocks that denote couplings between interface degrees of freedom with those inside the fluid-domain are mainly zero, as only very few basis functions $\phi_{h,i}$ and

$\phi_{h,f}$ have an overlapping support. The saddle-point structure of the Navier-Stokes equations is directly visible. Finally, we note, that the test-space for the ALE extension $W_{h,f}$ does not include test-functions, that live on the interface. This is the correct choice, as the ALE map is defined as an extension of the solid's deformation by using Dirichlet values. Nevertheless, this last row is included in \mathbf{F}_h to yield a quadratic matrix.

Given this detailed description of the sub-matrices, we can formulate the coupled linear system of equations by the sum of the two sub-systems:

$$\mathbf{A} = \left(\begin{array}{ccc|ccc|cc} F_p^{div} & F_v^{div} & F_u^{div} & F_p^{div} & F_v^{div} & F_u^{div} & 0 & 0 \\ F_p^{NS} & F_v^{NS} & F_u^{NS} & F_p^{NS} & F_v^{NS} & F_u^{NS} & 0 & 0 \\ 0 & 0 & F_u^{ALE} & 0 & 0 & F_u^{ALE} & 0 & 0 \\ \hline F_p^{div} & F_v^{div} & F_u^{div} & F_p^{div} & F_v^{div} & F_u^{div} & 0 & 0 \\ F_p^{NS} & F_v^{NS} & F_u^{NS} & F_p^{NS} & F_v^{NS} + S_v^{ES} & F_u^{NS} + S_u^{ES} & S_v^{ES} & S_u^{ES} \\ 0 & 0 & 0 & 0 & S_v^{uv} & S_u^{uv} & S_v^{uv} & S_u^{uv} \\ \hline 0 & 0 & 0 & 0 & S_v^{ES} & S_u^{ES} & S_v^{ES} & S_u^{ES} \\ 0 & 0 & 0 & 0 & S_v^{uv} & S_u^{uv} & S_v^{uv} & S_u^{uv} \end{array} \right) \quad (4.31)$$

Again, we note, that all the shaded matrix entries are very sparse. In every step of the Newton method we have to find the coefficient vector

$$\mathbf{x} = \begin{pmatrix} \mathbf{q} \\ \mathbf{z}_f \\ \mathbf{w}_f \\ \mathbf{z}_i \\ \mathbf{w}_i \\ \mathbf{z}_s \\ \mathbf{w}_s \end{pmatrix} \in \mathbb{R}^{N_p + 2N_f + 2N_i + 2N_s},$$

subject to the linear system of equations

$$\mathbf{A}_h \mathbf{x} = \mathbf{b},$$

where \mathbf{b} is the discrete right hand side, coming from the discretization of

$$G(\Phi) := F(\Phi) - A(\mathbf{U})(\Phi).$$

The system matrix \mathbf{A}_h lacks all desirable properties like symmetry, positivity or diagonal dominance. Solution of these linear systems is a very difficult task. Application of direct solvers is difficult due to the immense dimension of the linear system. Furthermore, we will see in Chapter 6, that the condition number of the coupled matrix can be so bad, that even modern direct solvers can fail.

4.4.2 Construction of the ALE map

In this section, we demonstrate different ways of extending the solid deformation $\mathbf{u}_{h,s}$ from the interface to the fluid domain $\mathbf{u}_{h,f}$. Such an extension is the typical way for defining the ALE mapping by means of:

$$T_{h,f}(x, t) := x + \mathbf{u}_{h,f}(x, t).$$

Here, we aim at a quantitative comparison of different mesh motion models. In Section 2.4.1, we have already discussed qualitative regularity restrictions that arise from different mesh motion models. In the literature, computational overviews are given in [254] or by Wick [242].

Here, we will analyze a simple numerical test-case, that gives rise to large rotations of a freely embedded solid in a fluid domain. This rotation causes very large deformation of the fluid domain and poses severe challenges to the construction of the ALE map. We show the configuration of the geometry in Figure 4.7a. We briefly detail the configuration. The initial domain partitioning is given as

$$\Omega = (-1, 1)^2, \hat{\mathcal{S}} = \left(-\frac{1}{2}, \frac{1}{2}\right) \times \left(-\frac{1}{8}, \frac{1}{8}\right), \hat{\mathcal{F}} = \Omega \setminus \bar{\hat{\mathcal{S}}}.$$

The boundary $\Gamma = \partial\Omega$ consists of two inflow parts of width 0.5, Γ_1^{in} in the upper left corner and Γ_2^{in} in the lower right one. Here we prescribe a Dirichlet condition for the velocity

$$\mathbf{v}_i^{\text{in}}(x, y, t) = 4\alpha(t)(x - x_i^0)(x - x_i^1)\vec{n} \text{ on } \Gamma_i^{\text{in}},$$

where the x_i^j are indicated in the sketch of the configuration and where \vec{n} is the outward facing normal vector at Γ_i^{in} . The functional $\alpha(t)$ is added for a smooth initial transition

$$\alpha(t) = \begin{cases} \frac{1}{2}(1 - \cos(\pi t/2)) & t \leq 2, \\ 1 & t \geq 2 \end{cases}.$$

The solid is modeled as St. Venant-Kirchhof, and the parameters are set to

$$\rho_f = 1, \quad \rho_s = 1\,000, \quad \mu_s = 20, \quad \lambda_s = 80, \quad \nu_f = 1.$$

In the right plot in Figure 4.7c, we show the solution at different points in time. Bright values denote large pressures, dark colors small ones. Further, we plot streamlines of the velocity field and the vector field of the solid deformation. The symmetric flow causes a rotational movement of the solid. As quantity of interest, we measure the average rotation:

$$J(\mathbf{u}_h(t)) = \frac{1}{|\hat{\mathcal{S}}|} \int_{\hat{\mathcal{S}}} \hat{x} \times \mathbf{u}_{h,s} \, d\hat{x}.$$

The value of $J(\mathbf{u}_h(t))$ is shown in Figure 4.7b. Due to very large deformation of the fluid domain and a deterioration of the ALE map, all computations will break down at some final time $t' > 0$. These points in time are indicated in Figure 4.7b. We will see, that depending on the type of extension operator, we achieve a substantial difference in the final time.

Harmonic extension

We start by defining the extension of the solid deformation $\mathbf{u}_{h,s}$ from the interface $\hat{\mathcal{I}}$ to the fluid-domain $\mathbf{u}_{h,f} \in V_{h,f}^\Gamma$, by means of an harmonic extension, given as

$$(\nabla \mathbf{u}_{h,f}, \nabla \psi_{h,f})_{\mathcal{F}} = 0 \quad \forall \psi_{h,f} \in W_{h,f}^\Gamma, \quad (4.32)$$

where $\psi_{h,f}$ has trace zero on the complete boundary of \mathcal{F} , that includes the interface. Solution $\mathbf{u}_{h,f}$ and test-function $\psi_{h,f}$ come from standard finite element space with the boundary constraints

$$\begin{aligned}\mathbf{u}_{h,f} &\in V_{h,f}^\Gamma := \{\phi_h \in V_h(\mathcal{F}), \phi_h = \mathbf{u}_{h,s} \text{ on } \mathcal{I}, \phi_h = 0 \text{ on } \partial\mathcal{F} \setminus \mathcal{I}\} \\ \psi_{h,f} &\in W_{h,f}^\Gamma := \{\phi_h \in V_h(\mathcal{F}), \phi_h = 0 \text{ on } \mathcal{I}, \phi_h = 0 \text{ on } \partial\mathcal{F} \setminus \mathcal{I}\}.\end{aligned}\quad (4.33)$$

We show results in Figure 4.8 for two different points in time. While the ALE mapping yields a nicely transformed mesh at time $t = 5$ sec, some elements are close to deterioration at time $t = 8.6$ sec. This in particular happens at the edge of the solid. Here, we also see a very strong (and non-physical) feedback from the deformation to the elasticity problems. Bad approximation due on the strongly deformed meshes give rise to artificial forces bending the solid.

This extension operator can be relaxed by varying the boundary conditions on the outer boundary

$$\Gamma_f := \partial\mathcal{F} \setminus \mathcal{I}.$$

Here, it is not strictly necessary for $\mathbf{u}_{h,f}$ to guarantee a full homogenous Dirichlet condition. If the deformation $\mathbf{u}_{h,f}$ is allowed to move freely in tangential direction, the resulting map $T_{h,f}$ will still map the reference domain to the fluid-domain. Hence, we can alter the test-space $W_{h,f}$ in such a way, that Dirichlet-conditions are only imposed in normal direction, similar to the free-slip condition that is known from fluid-dynamics

$$W_{h,f}^\Gamma := \{\phi \in C(\mathcal{F})^d, \phi_h \Big|_K \in P^r(K), \vec{n} \cdot \phi_h = 0 \text{ on } \Gamma_f, \phi_0 = 0 \text{ on } \mathcal{I}\},$$

where $P^r(K)$ is the local finite element space. In Figure 4.9 we show both different choices of boundary values. Although we choose different boundary values only on the outer boundary of the domain, we see a substantial improvement of mesh quality also at the interface. In particular, the solid's shape is not deteriorated at the edges. However, some mesh elements already start to lose regularity.

Harmonic extension with stiffening

The examples show, that we have to expect difficulties close to the solid domain, in particular close to edges. Here, stiffening of the extension can help to assure better quality of the deformed meshes. We change the extension operator by introducing a local parameter function $\alpha : \mathcal{F} \rightarrow \mathbb{R}_+$:

$$(\alpha \nabla \mathbf{u}_{h,f}, \nabla \phi_{h,f})_{\mathcal{F}} = 0 \quad \forall \psi_{h,f} \in W_{h,f}^\Gamma.$$

Given differentiability of $\alpha(x)$, this weak formulation belongs to a transport-diffusion problem

$$-\Delta \mathbf{u}_{h,f} - \alpha^{-1} \nabla \alpha \cdot \nabla \mathbf{u}_{h,f} = 0.$$

If we can choose $\alpha : \mathcal{F} \rightarrow \mathbb{R}_+$ in such a way, that the ratio

$$\frac{|\nabla \alpha|}{|\alpha|} \gg 0 \text{ at } \mathcal{I},$$

is large close to the interface, and if the transport direction points away from the interface

$$-\nabla \alpha \sim \vec{n}_s \text{ at } \mathcal{I},$$

where \vec{n}_s is the outward facing normal vector of \mathcal{S} , the extension mainly behaves like a simple transport-problem and the deformation $\mathbf{u}_{h,s}$ on \mathcal{I} is carried into the fluid-domain with as little changes as possible. Further away from the interface, the extension should take the role of a harmonic extension. The choice of $\alpha(x)$ can be based on the distance of x to the closed interface point:

$$d_{\mathcal{I}}(x) := \min_{y \in \mathcal{I}} \|x - y\|_2,$$

and then, a good choice of α is

$$\alpha(x) = 2.0 - \text{erf}(5d_{IN}(x)),$$

where erf is the Gauss error function. For this choice of α it holds

$$\frac{|\nabla \alpha(x)|}{|\alpha(x)|} > 1 \text{ if } d_{\mathcal{I}}(x) < \frac{1}{4} \text{ and } \frac{|\nabla \alpha(x)|}{|\alpha(x)|} \ll \frac{1}{100} \text{ if } d_{\mathcal{I}}(x) > \frac{1}{2}.$$

By a proper scaling of this function, the area of dominant transport can be adjusted to the specific geometry. Figure 4.10 shows the results. First, we see a significant improvement in mesh-quality. If we go on in time and rotation however, we again see deterioration of mesh elements and also a non-physical deformation of the solid.

Extension by pseudo-elasticity

Another possibility for defining the extension operator is by means of the Navier-Lamé equation, see also [204]:

$$(\mu_e(\nabla \mathbf{u}_{h,f} + \nabla \mathbf{u}_{h,f}^T) + \lambda_e \operatorname{div} \mathbf{u}_{h,f} I, \nabla \psi_{h,f})_{\mathcal{F}} = 0 \quad \forall \psi_{h,f} \in W_{h,f}^{\Gamma}.$$

The parameters μ_e and λ_e can again be chosen in such a way, that the material stiffens closer to the solid. Let $E_e(x)$ be the Young modulus, depending on the distance, and ν_e a chosen Poisson ratio. We pick the two parameters as

$$\mu_e(x) = \frac{E_e(x)}{2(1 + \nu_e)}, \quad \lambda_e(x) = \frac{\nu_e E_e(x)}{(1 + \nu_e)(1 - 2\nu_e)}.$$

The results at times $t = 11.6$ sec and $t = 14$ sec are shown in Figure 4.11. At time 11.6 sec we get a very good mesh quality (compared to the harmonic operator with stiffening). No artificial feedback to the solid problem is observed. The computations break down around $t = 14$ sec.

Using the pseudo-elasticity model, one can improve the results by using material parameters in the *auxetic* range

$$-1 < \nu_e < 0.$$

Here, we pick $\nu_e = -0.2$. The results are shown in the lower right plot of Figure 4.11. A significant improvement in mesh quality is not visible, but using material parameters in the auxetic range allows to reach a final time of $t = 14.9$ sec.

For a pseudo-elastic extension, it is possible to apply stiffening in a semi-automatic way, by coupling the Young modulus to the deformation gradient's determinant

$$J_e := \det(I + \nabla \mathbf{u}_h).$$

E_e is increased, if J_e gets large or close to zero:

$$E_e := E_e \left(J_e + \frac{1}{J_e} \right).$$

This technique is referred to as Jacobian-based stiffening, see [218].

Biharmonic extension

Finally, we consider the biharmonic operator Δ^2 for defining the extension of the deformation, see also [120]. For realization, we choose a mixed formulation by introducing a secondary variable $\mathbf{w}_f = -\Delta \mathbf{u}_f$:

$$(\nabla \mathbf{w}_{h,f}, \nabla \psi_{h,f}^1)_{\mathcal{F}} + (\nabla \mathbf{u}_{h,f}, \nabla \psi_{h,f}^2)_{\mathcal{F}} - (\mathbf{w}_{h,f}, \psi_{h,f}^2)_{\mathcal{F}} = \langle \vec{n} \cdot \nabla \mathbf{u}_{h,s}, \psi_{h,f}^2 \rangle_{\mathcal{I}},$$

where solution and test-function come from the spaces

The biharmonic extension has the benefit, that no configuration dependent parameter-tuning is necessary. Due to the fourth order character, special care has to be taken for discretization. Either, C^1 -conforming finite elements, or a mixed formulation is required. For numerical benchmark problems, a very high computational effort is reported [242], with computing times up to 10 times higher than for the simple harmonic extension. Hence, it is usually more advisable to spend some effort on parameter tuning and choose one of the previously discussed options.

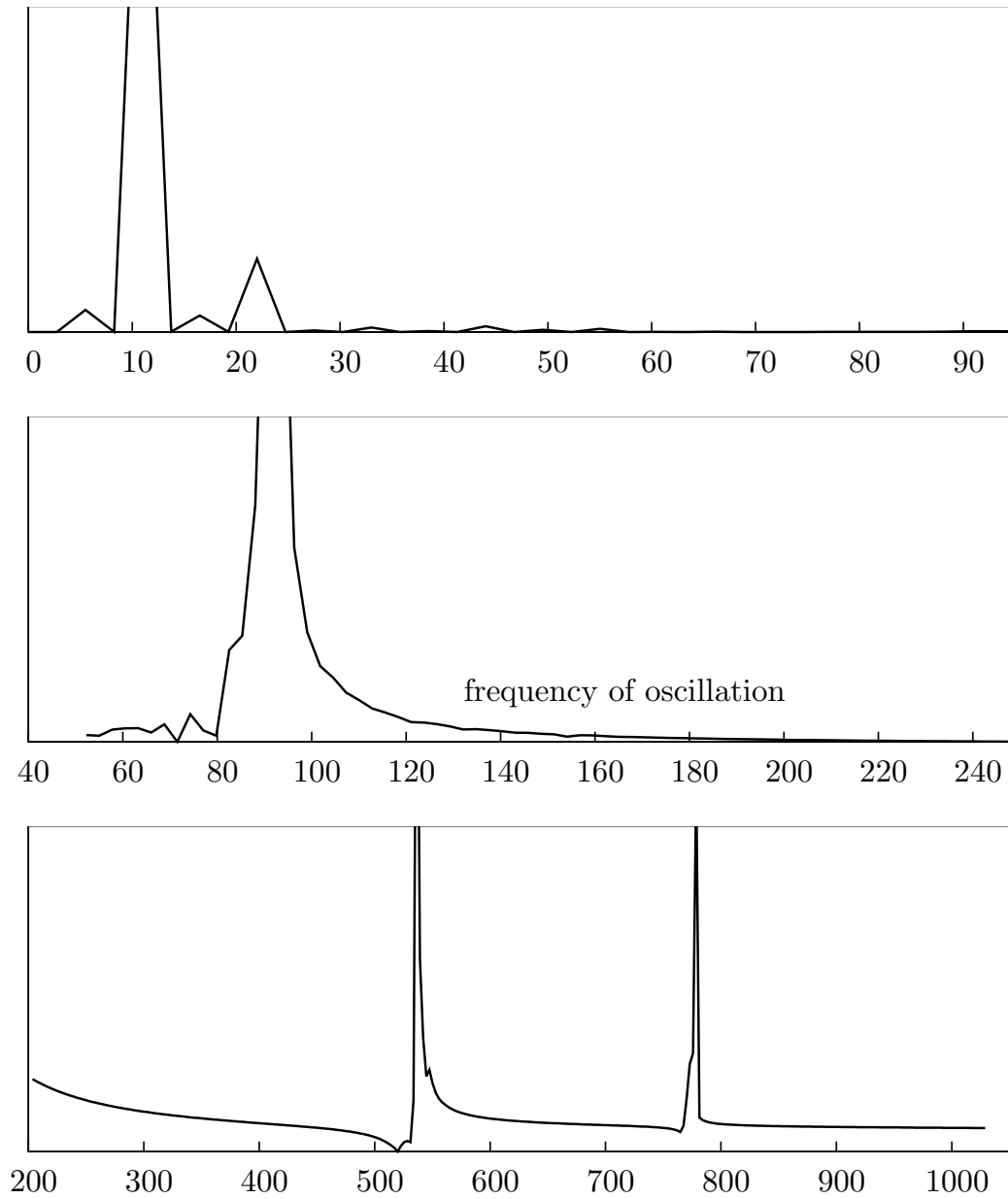


Figure 4.2: Discrete Fourier analysis of the output functional (drag) shows the dominant frequency $f_{fsi} \approx 11$ Hz and further important sub-frequencies at about $f \approx 100$ Hz and 500 Hz as well as 800 Hz. These modes are stable under temporal and spatial mesh refinement.

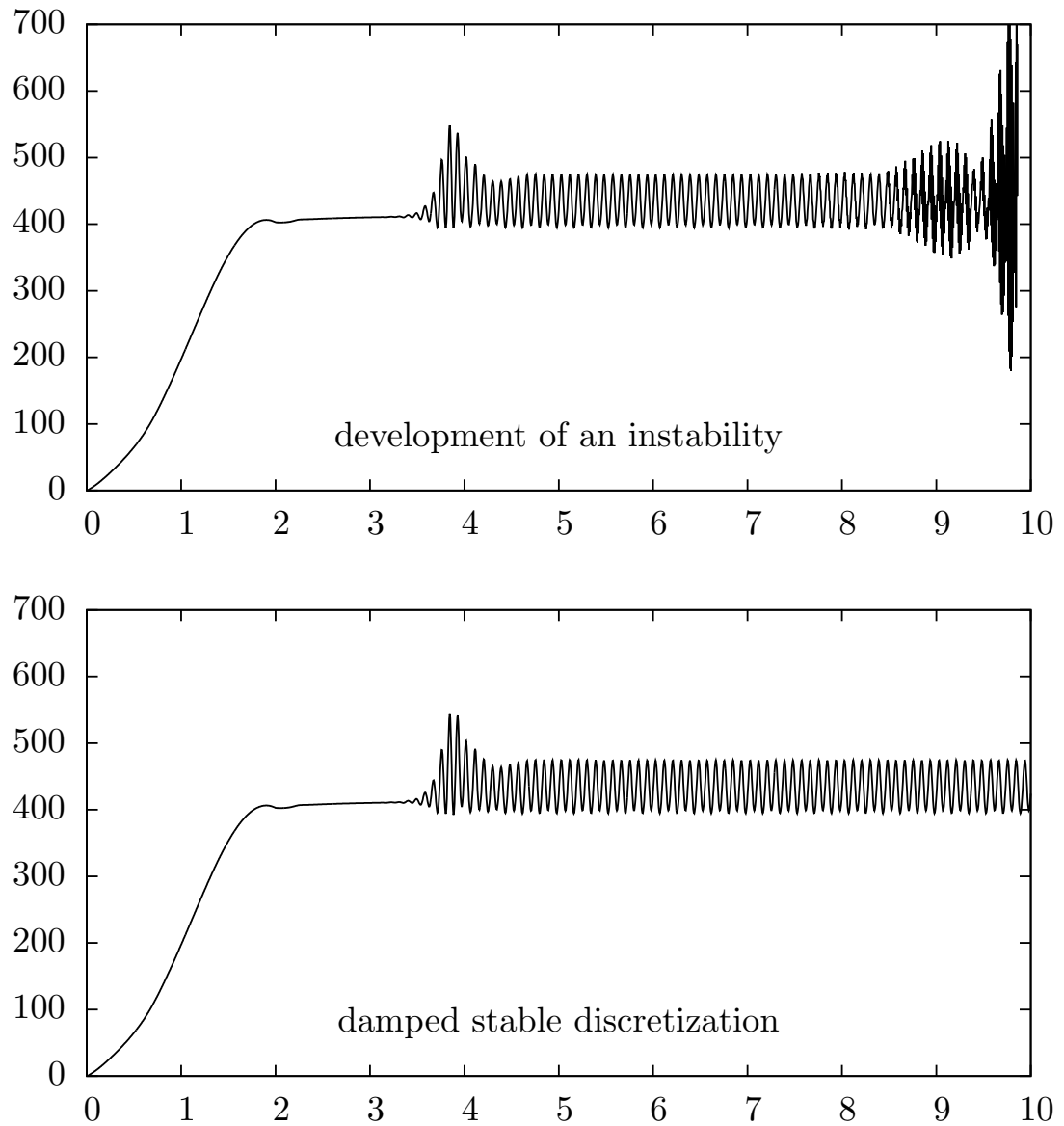


Figure 4.3: Simulation for $k = 0.005$. Top: undamped Crank-Nicolson scheme develops an instability. Bottom: implicitly shifted scheme produces a stable solution on $I = [0, 10]$.

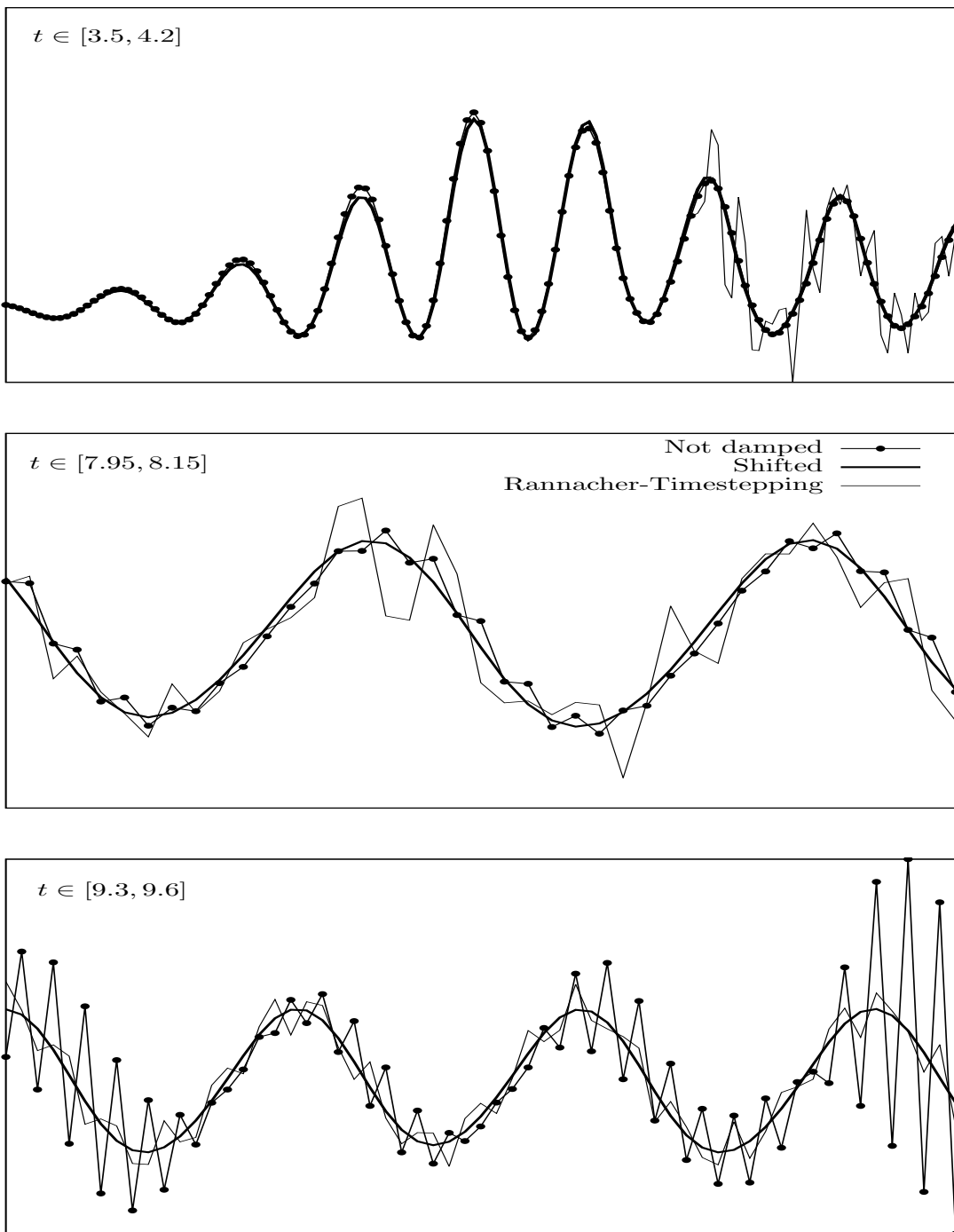


Figure 4.4: Comparison of different damping strategies: undamped Crank-Nicolson, shifted version $\frac{1}{2} + k$ and Rannacher time-marching with two backward Euler steps at every time-unit.

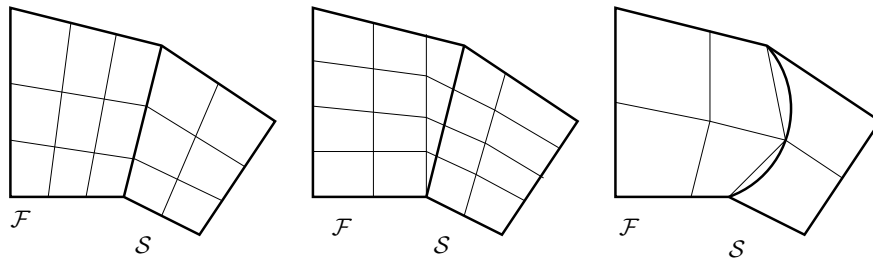


Figure 4.5: Examples for a matching mesh (left), a non-matching mesh (middle) and a matching mesh, following the relaxed definition for curved boundaries, see Remark 30.

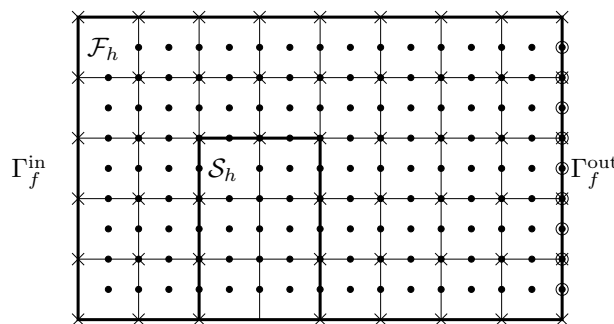
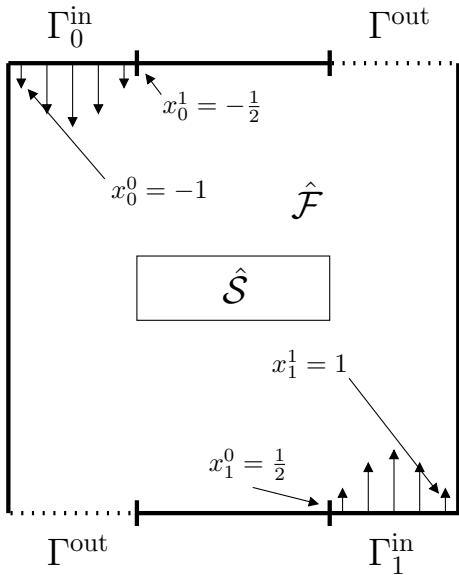


Figure 4.6: A possible finite element discretization for fluid-structure interactions in ALE coordinates. Piece-wise quadratic finite elements for velocity and deformation, piece-wise linear pressure. By \times we denote pressure degrees of freedom and by \bullet degrees of freedom in velocity and deformation. By \odot we denote velocity degrees of freedom on the outflow boundary, where no deformation degree of freedom exists.

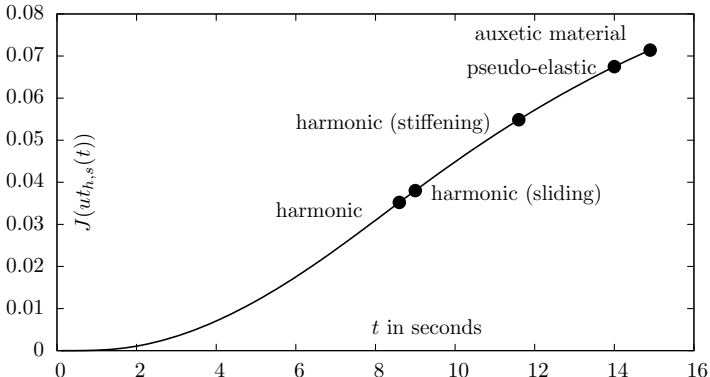


(a) Geometric configuration of the test-case. The boundary consists of two inflow, two outflow parts and a rigid wall. The solid $\hat{\mathcal{S}}$ is not supported.

The domain Ω is split into fluid $\hat{\mathcal{F}}$ and solid $\hat{\mathcal{S}}$

$$\Omega = (-1, 1)^2, \hat{\mathcal{S}} = \left(-\frac{1}{2}, \frac{1}{2}\right) \times \left(-\frac{1}{8}, \frac{1}{8}\right), \hat{\mathcal{F}} = \Omega \setminus \bar{\hat{\mathcal{S}}}.$$

On the two inflow boundary parts Γ_i^{in} ($i = 1, 2$) we prescribe parabolic Dirichlet conditions for the velocity \mathbf{v}_f .



(b) Rotation $J(\mathbf{u}_{th,s}(t))$ as function over time indicating the rigid body rotation of the solid. The points indicate the final time, where mesh elements start to deteriorate.

(c) Right: Solution at different times with streamlines and deformation vector field. Bright colors indicate large pressure, dark colors indicate small pressures.

©2013-2016 Thomas Richter, All Rights Reserved

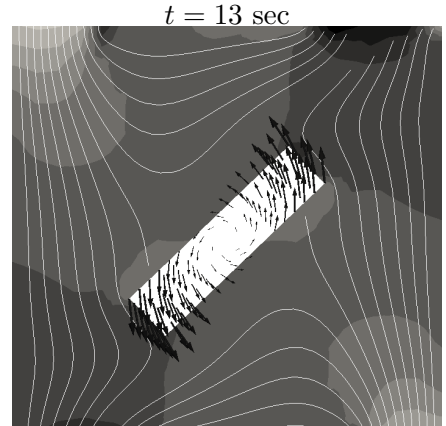
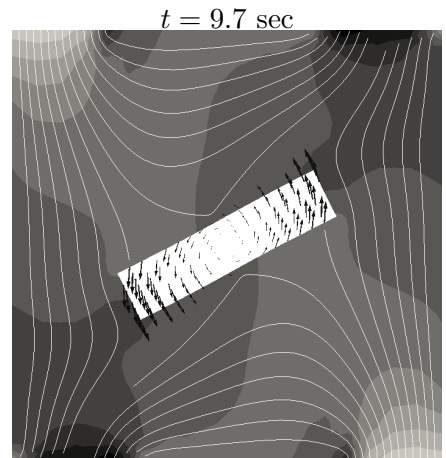
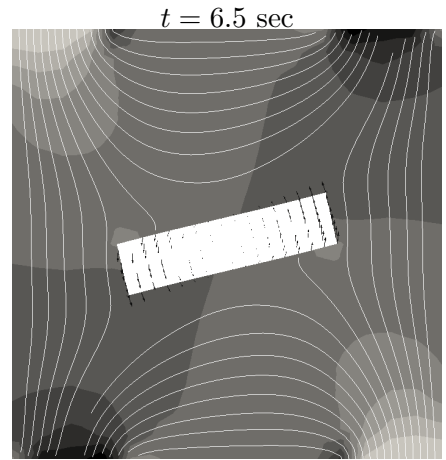
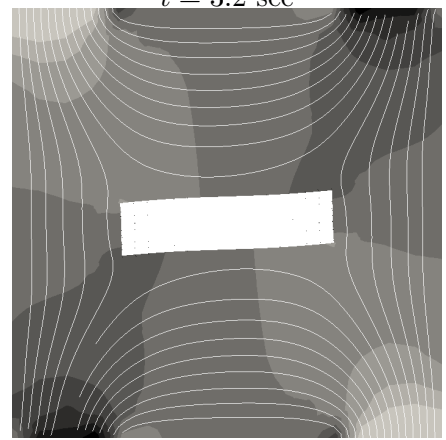


Figure 4.7: Description of the benchmark problem for testing the influence of the ALE map definition.

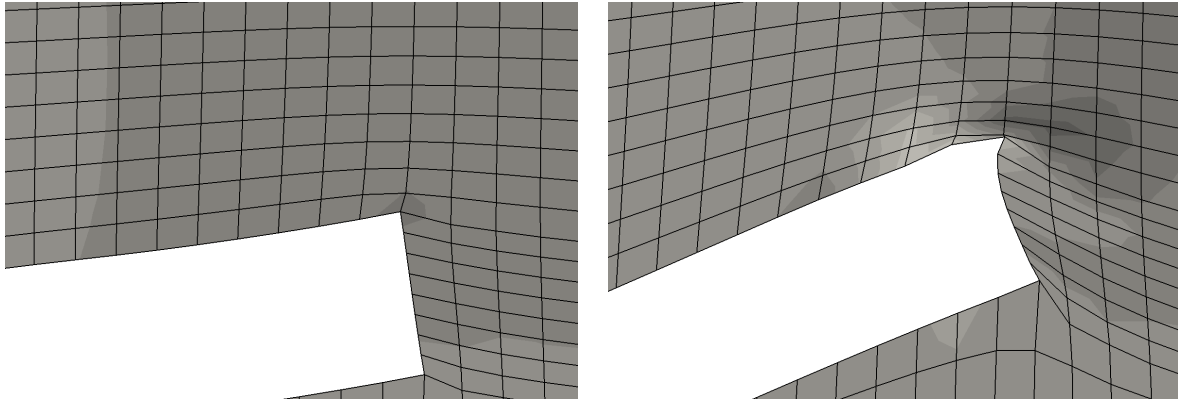


Figure 4.8: Extension with the harmonic operator. Left: $t = 5$ sec. Right: $t = 8.6$ sec close to break-down due to degeneration of map elements.

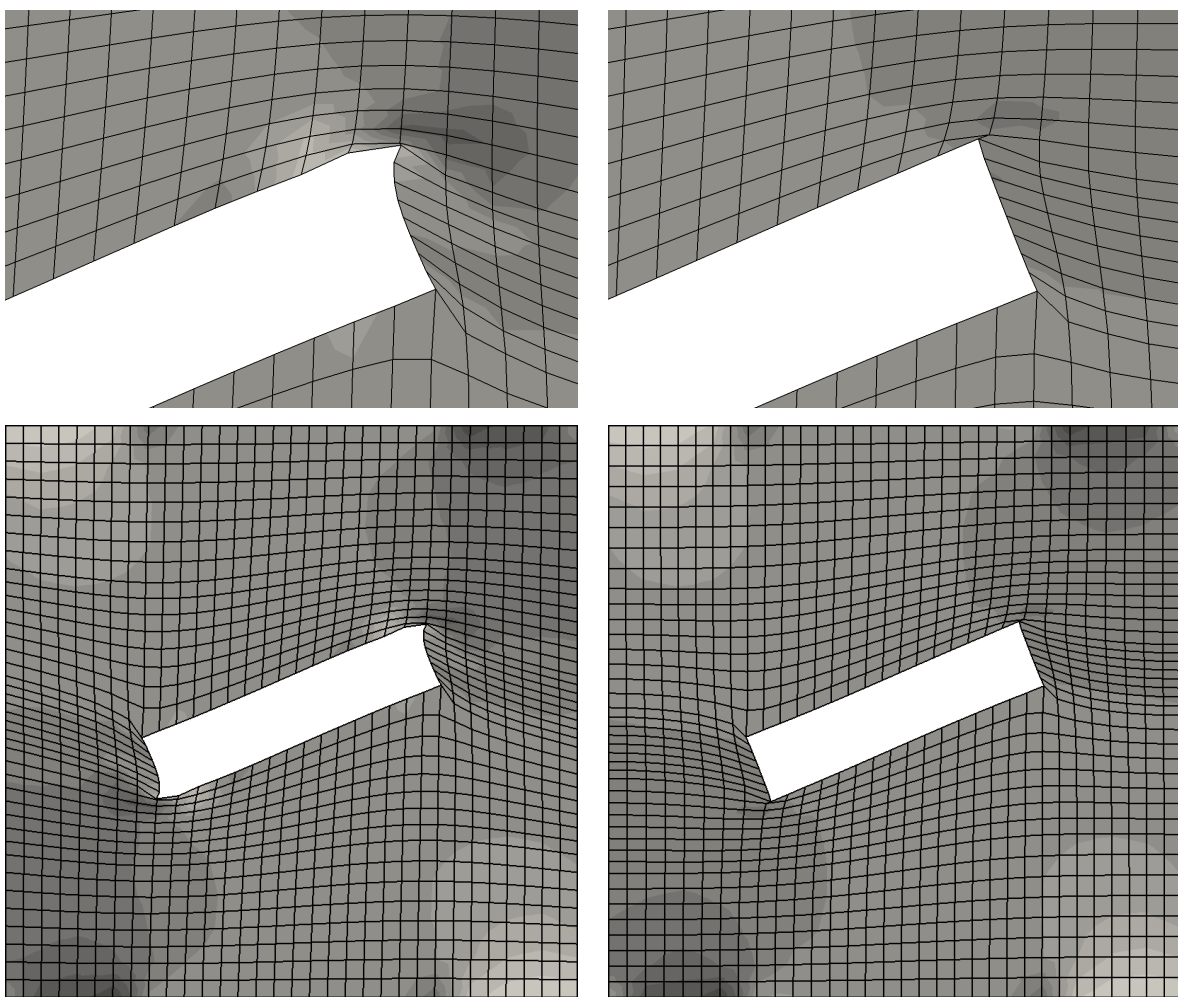
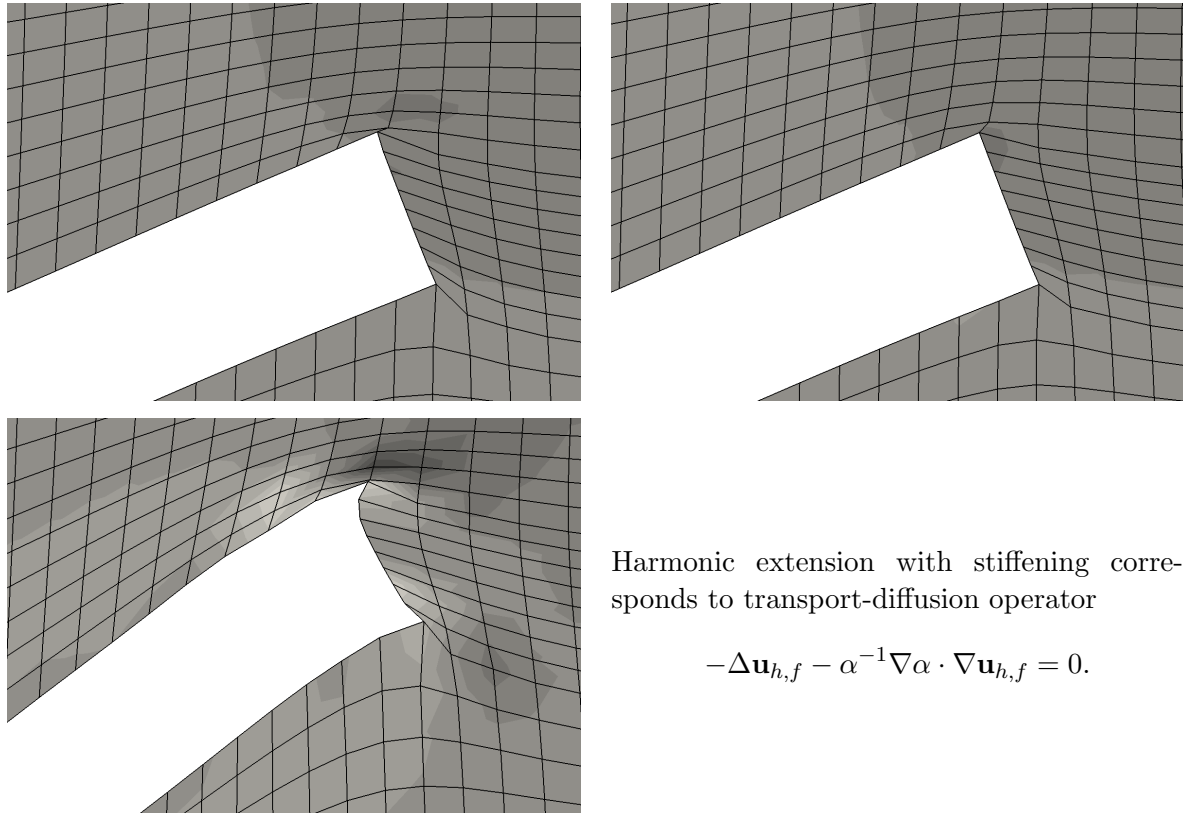


Figure 4.9: Extension with the harmonic operator. Comparison of different boundary values at the outer boundary $\partial\mathcal{F} \setminus \mathcal{I}$. Left: homogenous Dirichlet. Right: $\vec{n} \cdot \mathbf{u}_{h,f}$. Both at times $t = 8.6$ sec. In the bottom line we show the complete computational domain. Here, the effect of sliding boundary conditions gets obvious.



Harmonic extension with stiffening corresponds to transport-diffusion operator

$$-\Delta \mathbf{u}_{h,f} - \alpha^{-1} \nabla \alpha \cdot \nabla \mathbf{u}_{h,f} = 0.$$

Figure 4.10: Upper row: extension with the harmonic operator using sliding boundary conditions (left) and the harmonic operator with stiffening at the solid (right), both at time $t = 8.6$ sec. Lower row: harmonic extension with stiffening at time $t = 11.6$ sec.

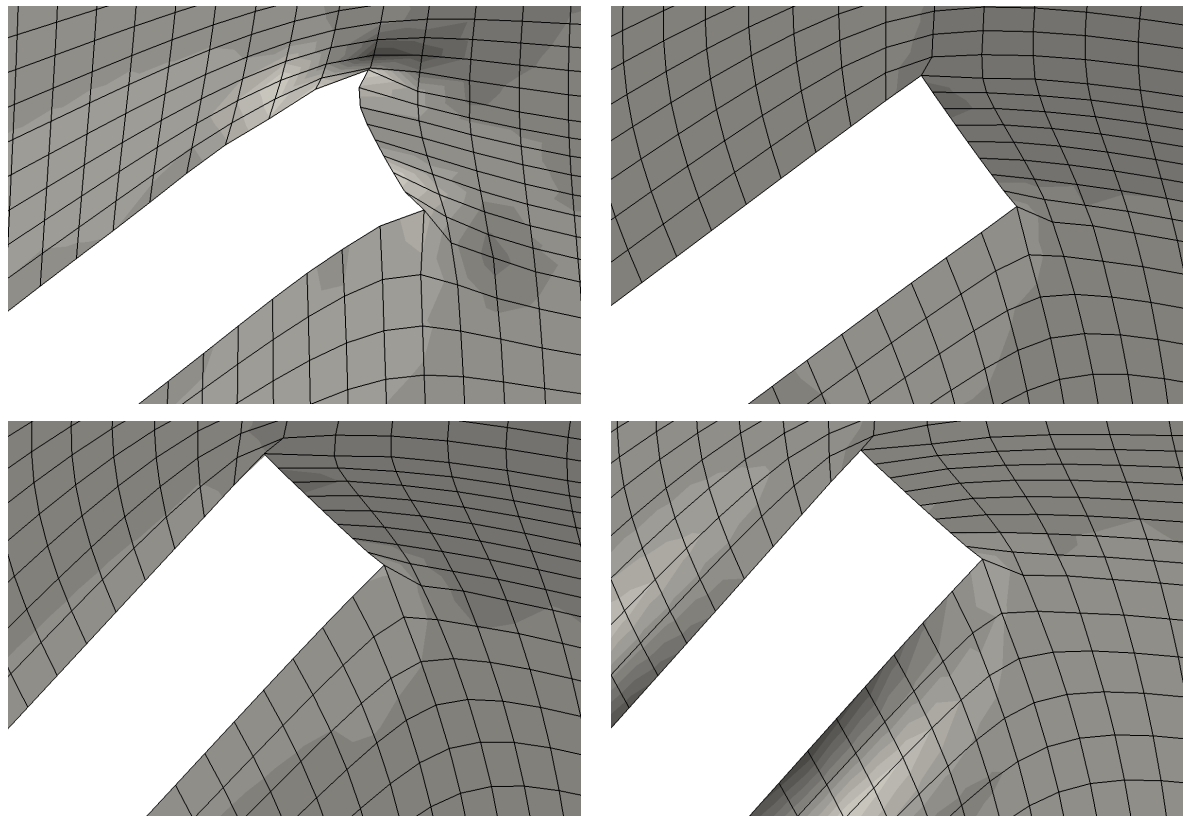


Figure 4.11: Upper row: extension with the harmonic operator using stiffening (left) and using a pseudo-elasticity model (right), both at time $t = 11.6$ sec. Lower row: pseudo-elastic extension at time $t = 14$ sec (left) and pseudo-elasticity with an auxetic material behavior (right).

Problem 41. Let $u, f, g \in C^\infty(I)$. Estimate the order of the truncation error and the leading error constant for the following time-discretization schemes:

$$(i) f(\bar{t})u'(\bar{t})g(\bar{t}) \approx \frac{1}{4} (f^{m-1} + f^m) \left(\frac{u^m - u^{m-1}}{k} \right) (g^{m-1} + g^m)$$

$$(ii) f(\bar{t})u'(\bar{t})g(\bar{t}) \approx \frac{1}{2} f^{m-1} \left(\frac{u^m - u^{m-1}}{k} \right) g^{m-1} + \frac{1}{2} f^m \left(\frac{u^m - u^{m-1}}{k} \right) g^m,$$

where

$$\bar{t} = \frac{t_{m-1} + t_m}{2}.$$

Problem 42. Let $u, f, g \in C^\infty(I)$. Estimate the order of the truncation error and the leading error constant for the following time-discretization scheme:

$$f(\bar{t})u'(\bar{t})g(\bar{t}) \approx \frac{u^m - u^{m-1}}{k} \left(\frac{1}{3} f_k^{m-1} g_k^{m-1} + \frac{1}{6} f_k^{m-1} g_k^m + \frac{1}{6} f_k^m g_k^{m-1} + \frac{1}{3} f_k^m g_k^m \right)$$

where

$$\bar{t} = \frac{t_{m-1} + t_m}{2}.$$

Problem 43. Show, that for the choice of finite element spaces introduced in Section 4.3, the discrete Galerkin formulation is

equivalent to a quadratic linear system of equations, e.g. it holds

$$N_v + N_u + N_p = N_v + N_p + N_f + N_s.$$

Problem 44. Show relation (v) in Lemma 72. (Hint: review the proof of Reynold's transport theorem.)

Problem 45. Assume, that $\mathbf{u}, \mathbf{w} \in C^2$ and $\mathbf{v}, \mathbf{F}^{-1} \in C^1$. Show, that all second derivatives with respect to \mathbf{u} and \mathbf{w} in $A_u^{\text{div}}(\mathbf{U})(\mathbf{W}, \Phi)$ will cancel out.

Problem 46. Compute the directional derivatives of the 2nd Piola-Kirchhoff stress tensor of the Mooney-Rivlin solid

$$\boldsymbol{\Sigma}_s =$$

Problem 47. Let Ω_h be a matching triangulation of $\Omega = \mathcal{F} \cup \mathcal{I} \cup \mathcal{S}$. Show, that for the choice of finite element spaces (4.24), it holds

$$\dim(V_h) + \dim(W_h) + \dim(L_{h,f}) = \dim(V_h) + \dim(W_{h,f}) + \dim(L_{h,s}) + \dim(L_{h,f}).$$

Problem 48. Show relation (4.27) on shape-regular triangular meshes.

5 Fully Eulerian Formulation for Fluid-Structure Interactions

This chapter is devoted to an alternative monolithic formulation for fluid-structure interactions. While the ALE scheme was based on a mapping of the Eulerian fluid system $\mathcal{F}(t)$ onto a fixed reference framework $\hat{\mathcal{F}}$ to be coupled with the Lagrangian solid domain, the Fully Eulerian formulation goes the other way around: both problems, fluid as well as solid are modeled on the moving Eulerian domains $\mathcal{F}(t)$ and $\mathcal{S}(t)$ connected by the moving interface $\mathcal{I}(t)$. The general approach is comparable: both sub-systems can be variationally coupled such that we arrive at a monolithic global system. A conceptual difference is in the kind of interface treatment: while the ALE interface $\hat{\mathcal{I}}$ is temporally fixed, the Eulerian interface $\mathcal{I}(t)$ is moving in time and depends on the solution. The domain motion is not any longer hidden in the artificial deformation variable \mathbf{u}_f but must be separately captured by the discretization. Here, we describe this rather new formulation, that has been introduced by Dunne in 2006 [84, 85]. Since then, similar approaches have been published [72, 187, 192, 117, 245, 189]. The underlying principle for all Eulerian formulations is to avoid the introduction of artificial coordinate systems, that can cause a break down of the coupled scheme. In ALE formulations, the fluid's reference domain does not have a physical significance. As seen in Section 4.4.2, the construction of the ALE map is – up to certain degree – arbitrary. Picking the wrong map can result in a loss of regularity or invertibility and finally to a break-down of the scheme. A Lagrangian-Eulerian mapping of the solid problem however is completely physical. Both formulations are equivalent, as long as material rupture or material overlapping is not allowed. However large the deformation or motion of the solid is, the Eulerian system will be well-posed.

5.1 Eulerian models for fluid-structure interactions

The success of the ALE formulation for fluid-structure interactions crucially depends on the quality of the fluid domain map \hat{T}_f . If this mapping loses its regularity, equivalence between the variational ALE formulation in Lemma 35 and the classical formulations of the fluid-structure interaction problem in (2.4) will not hold any more. Further, we have seen that bounds on $\hat{\nabla}\hat{T}_f$ and $\nabla\hat{T}_f^{-1}$ will enter basic inequalities like the trace inequality, Poincaré inequality and also the inf-sup inequality. Even if the derivatives of \hat{T}_f and \hat{T}_f^{-1} are bound, the constants, that will finally enter stability and error estimates can be very large.

Some configurations will necessarily lead to a degeneration of the ALE mapping. The most prominent example is given for contact problems, as a C^1 -diffeomorphism between two domains with different topology cannot exist. In this section, we will introduce an alternative variational formulation for the coupled fluid-structure interaction problem that goes the opposite way: instead of mapping the moving fluid domain onto a fixed reference domain $\hat{T}_f(t) : \hat{\mathcal{F}} \rightarrow \mathcal{F}(t)$ we use an inverse map to transform the Lagrangian solid reference domain onto the Eulerian

moving solid domain $\hat{T}_s(t) : \hat{\mathcal{S}} \rightarrow \mathcal{S}(t)$. Like the ALE map \hat{T}_f , this transformation is defined by the deformation $\hat{\mathbf{u}}_s$:

$$\hat{T}_s(\hat{x}, t) := \hat{x} + \hat{\mathbf{u}}_s(\hat{x}, t).$$

There is one fundamental difference between \hat{T}_s and \hat{T}_f . While the ALE map \hat{T}_f is arbitrary and $\hat{\mathcal{F}}$ does not play a physical role, the solid domain map \hat{T}_s is given by physical principles. It maps between Lagrangian and Eulerian coordinates. If the solid problem is well-posed, both formulations are valid and it holds, that

- the mapping \hat{T}_s is a bijection between $\hat{\mathcal{S}}$ and $\mathcal{S}(t)$,
- mapping \hat{T}_s and inverse \hat{T}_s^{-1} are differentiable,
- the determinants $\hat{J}_s := \det(\hat{\nabla}\hat{T}_s)$ and $\hat{J}_s^{-1} = \det(\nabla\hat{T}_s^{-1})$ satisfy

$$c_1 < \hat{J}_s < c_2,$$

where $c_1 > 0$ and $c_2 < \infty$.

Problem 49. Motivate the properties of \hat{T}_s and its inverse \hat{T}_s^{-1} with physical reasoning.

The well-posedness of an Eulerian formulation for fluid-structure interactions is obvious, since the Eulerian coordinates are the physical coordinates, where all governing equations (the conservation laws) have been derived. The transition to the Lagrangian reference system was mainly for practical reasons, as deformation stresses can best be modeled in a particle centered viewpoint. For structure mechanics both viewpoints, the Lagrangian and the Eulerian are physically relevant and the mapping between them is simply given by the deformation.

5.1.1 Elastic structures in Eulerian coordinates

In Section 1.1.6, we derived the basic conservation principles for moving volumes, that were based on conservation of mass, momentum and angular momentum. Here, we will derive the Eulerian formulation for the structure problem on the moving solid domain $\mathcal{S}(t)$, that is given by the Lagrangian deformation of $\hat{\mathcal{S}}$:

$$\mathcal{S}(t) = \{\hat{x} + \hat{\mathbf{u}}_s(\hat{x}, t), \hat{x} \in \hat{\mathcal{S}}\}.$$

By mass and momentum conservation, we derived the non-conservative formulation of the momentum equation (1.14)

$$\rho_s \partial_t \mathbf{v}_s + \rho_s \mathbf{v}_s \cdot \nabla \mathbf{v}_s - \nabla \cdot \boldsymbol{\sigma}_s = \rho_s \mathbf{f} \text{ in } \mathcal{S}(t),$$

where $\rho_s(x, t)$ is the Eulerian density of the solid at time t in point $x \in \mathcal{S}(t)$, $\mathbf{v}_s(x, t)$ is the Eulerian velocity and $\boldsymbol{\sigma}_s$ the Eulerian Cauchy-Stress tensor of the solid problem, also given in the Eulerian coordinate system. Here, it is necessary to remember, that the transformation to Lagrangian or to an arbitrary reference system in ALE coordinates only touches the domain $\mathcal{S}(t)$ and $\hat{\mathcal{S}}$, not the image, e.g. it holds

$$\mathbf{v}(x, t) = \hat{\mathbf{v}}(\hat{x}, t),$$

for a pair $x = \hat{T}(\hat{x}, t)$. For defining a Eulerian representation σ_s of the Cauchy stress tensor, we must introduce a Eulerian counterpart \mathbf{u}_s of the Lagrangian deformation $\hat{\mathbf{u}}_s$. We define

$$\mathbf{u}_s(x, t) = \hat{\mathbf{u}}_s(\hat{x}, t),$$

for a point $x = \hat{x} + \hat{\mathbf{u}}_s(\hat{x}, t)$. Then, it holds

$$\hat{x} = x - \hat{\mathbf{u}}_s(\hat{x}, t) = x - \mathbf{u}_s(x, t),$$

which defines the inverse mapping $T_s(t) : \mathcal{S}(t) \rightarrow \hat{\mathcal{S}}$:

$$T_s(x, t) := x - \mathbf{u}_s(x, t), \quad T_s = \hat{T}_s^{-1}.$$

Further, considering Lemma 4 and (2.25), it holds

$$T_s \circ \hat{T}_s = \text{id} \quad \Rightarrow \quad \nabla T_s =: \mathbf{F}_s = \hat{\mathbf{F}}_s^{-1} = (\hat{\nabla} \hat{T}_s)^{-1}, \quad J_s = \hat{J}_s^{-1}. \quad (5.1)$$

And with $\hat{T}_s := \hat{x} + \hat{\mathbf{u}}_s$ and $T_s := x - \mathbf{u}_s$ it finally follows, that

$$[I - \nabla \mathbf{u}_s] = [I + \hat{\nabla} \hat{\mathbf{u}}_s]^{-1} \quad \Leftrightarrow \quad \nabla \mathbf{u}_s = I - [I + \hat{\nabla} \hat{\mathbf{u}}_s]^{-1} = I - \hat{\mathbf{F}}_s^{-1}.$$

Using these relations, we can transform the Cauchy stress tensor $\hat{\sigma}_s$ from Lagrangian to Eulerian coordinates:

Lemma 76 (Cauchy stress tensor for the St. Venant Kirchhoff material in Eulerian coordinates). *The Cauchy stress tensor of the St. Venant Kirchhoff material in Eulerian coordinates is given by*

$$\sigma_s = J_s \mathbf{F}_s^{-1} (2\mu \mathbf{E}_s + \lambda_s \text{tr}(\mathbf{E}_s) I) \mathbf{F}_s^{-T}, \quad \mathbf{E}_s := \frac{1}{2} (\mathbf{F}_s^{-T} \mathbf{F}_s^{-1} - I).$$

Proof. The second Piola Kirchhoff stress tensor $\hat{\Sigma}_s$ of the St. Venant Kirchhoff material is given by (see Definition 4)

$$\hat{\Sigma}_s = 2\mu_s \hat{\mathbf{E}}_s + \lambda_s \text{tr}(\hat{\mathbf{E}}_s) I,$$

with the Green-Lagrangian strain tensor

$$\hat{\mathbf{E}}_s := \frac{1}{2} (\hat{\mathbf{F}}_s^T \hat{\mathbf{F}}_s - I).$$

The relation between Cauchy stress tensor and 2nd Piola Kirchhoff stress tensor is given by the Piola transformation in Definition 3:

$$\hat{\sigma}_s = \hat{J}_s^{-1} \hat{\mathbf{F}}_s \hat{\Sigma}_s \hat{\mathbf{F}}_s^T.$$

Then, by (5.1), we get the its Eulerian representation as

$$\sigma_s = J_s \mathbf{F}_s^{-1} \Sigma_s \mathbf{F}_s^{-T},$$

with the 2nd Piola Kirchhoff tensor in Eulerian coordinates

$$\Sigma_s = 2\mu_s \mathbf{E}_s + \lambda_s \text{tr}(\mathbf{E}_s) I,$$

where the Eulerian Green-Lagrangian strain tensor is given by

$$\mathbf{E}_s := \frac{1}{2}(\mathbf{F}_s^{-T}\mathbf{F}_s^{-1} - I).$$

□

The derivation of the Cauchy stress tensor σ_s in Eulerian coordinates completes the description of the momentum equation. It remains to add an equation for the unknown Eulerian density ρ_s . By defining

$$\rho_s(x, t) = \hat{\rho}_s(\hat{x}, t),$$

and using (1.27), it holds

$$\rho_s(x, t) = J_s \hat{\rho}_s^0(\hat{x}), \quad (5.2)$$

where $\hat{\rho}_s^0$ is the density of the solid at time $t = 0$ in the corresponding reference coordinate. Usually one considers homogenous materials, such that relation (5.2) simplifies to

$$\rho_s(x, t) = J_s \hat{\rho}_s^0. \quad (5.3)$$

In the Eulerian coordinate framework, we must also transform the relation between deformation and velocity, compare Lemma Lemma 5:

$$d_t \hat{\mathbf{u}}_s = \partial_t \mathbf{u}_s + \mathbf{v}_s \cdot \nabla \mathbf{u}_s, \quad d_t \hat{\mathbf{v}}_s = \partial_t \mathbf{v}_s + \mathbf{v}_s \cdot \nabla \mathbf{v}_s.$$

Combining the foregoing discussion it holds:

Lemma 77 (Solid problem in Eulerian coordinates). *The elastic deformation of a St. Venant Kirchhoff material in Eulerian coordinates is given by*

$$J_s \hat{\rho}_s (\partial_t \mathbf{v}_s + \mathbf{v}_s \cdot \nabla \mathbf{v}_s) - \nabla \cdot \sigma_s = J_s \hat{\rho}_s \mathbf{f}, \quad \partial_t \mathbf{u}_s + \mathbf{v}_s \cdot \nabla \mathbf{u}_s = \mathbf{v}_s,$$

with the Eulerian formulation of the Cauchy stress tensor

$$\sigma_s := J_s \mathbf{F}_s^{-1} (2\mu_s \mathbf{E}_s + \lambda_s \text{tr}(\mathbf{E}_s) I) \mathbf{F}_s^{-T}, \quad \mathbf{E}_s := \frac{1}{2} (\mathbf{F}_s^{-T} \mathbf{F}_s^{-1} - I),$$

and the Eulerian deformation gradient

$$\mathbf{F}_s = I - \nabla \mathbf{u}_s.$$

Apart from the complex nonlinear form of the stress tensor, the solid problem is naturally given in Eulerian coordinates. The immediate drawback of this Eulerian formulation is twofold:

- The problem is formulated on the moving domain $\mathcal{S}(t)$, that is a priori unknown and part of the solution. For defining a standard variational formulation of the solid equation in Eulerian coordinates, all difficulties already discussed in Section 1.5 must be tackled again.
- By transformation to Eulerian coordinate, convective terms are introduced:

$$d_t \hat{\mathbf{v}} = \partial_t \mathbf{v} + \mathbf{v} \cdot \nabla \mathbf{v}, \quad d_t \hat{\mathbf{u}} = \partial_t \mathbf{u} + \mathbf{v} \cdot \nabla \mathbf{u}.$$

A discretization of this convective term will cause numerical stability problems, as known for the transport term in the Navier-Stokes equations. Numerical methods must introduce artificial stabilization terms that will cause loss of conservation principles.

Finally, we introduce a variational formulation of the structure problem in Eulerian coordinates, derived by multiplication with suitable test-functions. Find

$$\{\mathbf{v}_s, \mathbf{u}_s\} \in \mathcal{V}_s(t) \times \mathcal{W}_s(t),$$

such that

$$\begin{aligned} (J_s \hat{\rho}_s (\partial_t \mathbf{v}_s + \mathbf{v}_s \cdot \nabla \mathbf{v}_s), \phi_s)_{\mathcal{S}(t)} + (\sigma_s, \nabla \phi_s)_{\mathcal{S}(t)} &= (J_s \hat{\rho}_s^0 \mathbf{f}, \phi)_{\mathcal{S}(t)} \quad \forall \phi_s \in \mathcal{V}_s^{\text{test}} \\ (\partial_t \mathbf{u}_s + \mathbf{v}_s \cdot \nabla \mathbf{u}_s - \mathbf{v}_s, \psi_s)_{\mathcal{S}(t)} &= 0 \quad \forall \psi_s \in \mathcal{W}_s^{\text{test}}, \end{aligned} \quad (5.4)$$

While the Lagrangian velocity $\hat{\mathbf{v}}_s \in L^2(\hat{\mathcal{S}})^d$ is defined as L^2 -projection, the Eulerian counterpart requires some control over the derivative in direction of \mathbf{v}_s .

5.1.2 Fluid-structure interaction in Eulerian coordinates

Given the variational formulation of the Eulerian structure problem, it is straightforward to formulate the coupled fluid-structure interaction problem in Eulerian coordinates. We simple combine (5.4) with the incompressible Navier-Stokes equations (1.48) on the moving domain $\mathcal{F}(t)$ by adding appropriate interface conditions

$$\begin{aligned} (\rho_f (\partial_t \mathbf{v}_f + \mathbf{v}_f \cdot \nabla \mathbf{v}_f), \phi_f)_{\mathcal{F}(t)} + (\sigma_f, \nabla \phi_f)_{\mathcal{F}(t)} &= (\rho_f \mathbf{f}, \phi_f)_{\mathcal{F}(t)} \\ (\nabla \cdot \mathbf{v}_f, \xi_f)_{\mathcal{F}(t)} &= 0 \\ (J_s \hat{\rho}_s (\partial_t \mathbf{v}_s + \mathbf{v}_s \cdot \nabla \mathbf{v}_s), \phi_s)_{\mathcal{S}(t)} + (\sigma_s, \nabla \phi_s)_{\mathcal{S}(t)} &= (J_s \hat{\rho}_s^0 \mathbf{f}, \phi)_{\mathcal{S}(t)} \\ (\partial_t \mathbf{u}_s + \mathbf{v}_s \cdot \nabla \mathbf{u}_s - \mathbf{v}_s, \psi_s)_{\mathcal{S}(t)} &= 0 \\ \mathbf{v}_f &= \mathbf{v}_s && \text{on } \Gamma_i(t), \\ \sigma_f n &= \sigma_s n && \text{on } \Gamma_i(t) \end{aligned} \quad (5.5)$$

Variational coupling of these equations on $\mathcal{F}(t)$ and $\mathcal{S}(t)$ is easily possible following the guidelines introduced in Section 2.3. As the two domain $\mathcal{F}(t)$ and $\mathcal{S}(t)$ match and share a common interface $\Gamma_i(t) = \partial \mathcal{F}(t) \cap \partial \mathcal{S}(t)$, we can combine the trial space to embed continuity of velocities into the variational formulation

$$\mathbf{v} \in \mathcal{V}, \quad \mathbf{v}_f = \mathbf{v}|_{\mathcal{F}(t)}, \quad \mathbf{v}_s = \mathbf{v}|_{\mathcal{S}(t)}.$$

For realizing the dynamic coupling condition, we combine the test-spaces of the momentum equations:

$$\phi \in \mathcal{V}, \quad \phi_f = \phi|_{\mathcal{F}(t)}, \quad \phi_s = \phi|_{\mathcal{S}(t)}.$$

Then, it holds:

Lemma 78 (Variational formulation of the Eulerian fluid-structure interaction problem). *Let $\{\mathbf{v}, p_f, \mathbf{u}_s\}$ be the solution of the variational problem*

$$\begin{aligned} &(\rho_f (\partial_t \mathbf{v}_f + \mathbf{v}_f \cdot \nabla \mathbf{v}_f), \phi)_{\mathcal{F}(t)} + (\sigma_f, \nabla \phi)_{\mathcal{F}(t)} \\ &+ (J_s \hat{\rho}_s (\partial_t \mathbf{v}_s + \mathbf{v}_s \cdot \nabla \mathbf{v}_s), \phi)_{\mathcal{S}(t)} + (\sigma_s, \nabla \phi)_{\mathcal{S}(t)} = (\rho_f \mathbf{f}, \phi)_{\mathcal{F}(t)} + (J_s \hat{\rho}_s^0 \mathbf{f}, \phi)_{\mathcal{S}(t)} \\ &(\nabla \cdot \mathbf{v}_f, \xi_f)_{\mathcal{F}(t)} = 0 \\ &(\partial_t \mathbf{u}_s + \mathbf{v}_s \cdot \nabla \mathbf{u}_s - \mathbf{v}_s, \psi_s)_{\mathcal{S}(t)} = 0. \end{aligned} \quad (5.6)$$

Given sufficient regularity, a transformation of $\{\mathbf{v}, p_f, \mathbf{u}_s\}$ to Lagrangian coordinates (in the solid domain) also solves the fluid-structure interaction problem in classical formulation (2.4).

Apparently, the Eulerian formulation of the fluid-structure interaction problem has a simpler structure than the ALE formulation. No mapping, at least no artificial mapping between domains is necessary. Hence, there is no obvious reason, while the Eulerian formulation should show limits when treating problems with very large deformation, motion or even contact. All this is true, the simplicity of the variational formulation in Lemma 78 however hides one essential vagueness: the deformation of the domains $\mathcal{F}(t)$ and $\mathcal{S}(t)$ is given by the solution, to be precise, by the deformation of the solid domain:

$$\text{id} + \hat{\mathbf{u}}_s : \hat{\mathcal{S}} \rightarrow \mathcal{S}(t).$$

The formulation in Eulerian coordinates is based on the inverse of this relation:

$$\text{id} - \mathbf{u}_s : \mathcal{S}(t) \rightarrow \hat{\mathcal{S}},$$

the so-called *backward characteristic*. The complete derivation of the eulerian method leaves out one dilemma, that is inherent to fluid-structure interaction problems: the domains $\mathcal{F}(t)$ and $\mathcal{S}(t)$ are moving and depend on the solution. However, for assembling the Eulerian formulation (5.6), we must - for every point $x \in \Omega$ - know its affiliation to the fluid-domain $x \in \mathcal{F}(t) \subset \Omega$ or solid domain $x \in \mathcal{S}(t) \subset \Omega$. This appears to be an irreconcilable barrier for implicit monolithic formulations of the Eulerian model, as the domain affiliation is prerequisite for setting up the equations, whose solution is required for defining the affiliation.

5.2 Interface Capturing and the Initial Point Set Method

To work around this dilemma, we need to enrich the system of equations by a variable used to capture the location of the two domains. Multi-phase methods that live on a fixed background system and where the interface between the phases in freely moving are called *interface-capturing* techniques. One of the most prominent *interface-capturing* methods is the *Level-Set method* by Sethian [210].

Remark 32 (Level-Sets). *Assume, that $\mathcal{F}(0) \cup \mathcal{I}(0) \cup \mathcal{S}(0)$ is the initial partitioning of the domain. We define a level-set function $\Psi(x, 0)$ as the signed distance function belonging to this partitioning:*

$$\Psi(x, 0) := \begin{cases} \text{dist}(x, \mathcal{I}(0)) & x \in \mathcal{S}(0), \\ 0 & x \in \mathcal{I}(0), \\ -\text{dist}(x, \mathcal{I}(0)) & x \in \mathcal{F}(0). \end{cases}$$

We assume, that the domain-partitioning is moving with velocity field \mathbf{v} . Then, the level-set function is advected with this field by

$$\frac{\partial \Psi}{\partial t} + \mathbf{v} \cdot \nabla \Psi,$$

or, if motion is restricted to the normal direction by

$$\frac{\partial \Psi}{\partial t} + \mathbf{v} |\nabla \Psi| = 0.$$

This allows for a level set representation of the interface

$$\mathcal{I}(t) = \{x \in \mathbb{R}^d, \Psi(x, t) = 0\}.$$

Normal vectors and curvatures can be calculated based on the level set function. Some problems of level set formulations is the need of reinitialization if distances are to be discovered. An auxiliary equation is introduced at time t' to normalize the gradient $\nabla\Psi$ to one, e.g. by

$$\partial_\tau \Psi + \text{sgn}(\Psi(t')) (|\nabla\Psi| - 1) = 0, \quad \tau > 0.$$

Numerical schemes for the advection of the level set function will introduce diffusion. This will cause a smearing of sharp corners, that cannot be well approximated as zero lines of level sets. Nevertheless, level sets are one of the most established methods for capturing interfaces in Eulerian based simulations, see [210, 175].

One of the disadvantages connected to the Level-Set method is a degeneration of edges. Due to numerical dissipation and due to the reinitialization procedure, edges will be smoothed. While this does not pose a major problem for multiphase flows, the conservation of sharp edges (e.g. of the solid subdomain) is crucial in fluid-structure interaction applications. He and Qiao introduced a Eulerian formulation for fluid-structure interactions, where the interface was captured with the help of three Level-Set functions [117].

Here, we describe the *Initial Point Set method* for capturing the interface between fluid- and solid-domain. To be precise: instead of capturing the interface location, we will capture the complete reference coordinate system. We know, that at time $t \geq 0$, a spatial coordinate $x \in \Omega$ belongs to the solid domain $x \in \mathcal{S}(t)$, if it holds

$$T_s(x, t) = \hat{x} - \mathbf{u}_s(x, t) \in \hat{\mathcal{S}},$$

if the coordinate $x \in \Omega$ is the location of the particle $\hat{x} \in \hat{\mathcal{S}}$ at time t . This construction will be transferred to the fluid-domain. Assume, that $\mathbf{u}_f(x, t)$ is a vector field, such that:

$$x - \mathbf{u}_f(x, t) \in \hat{\mathcal{F}} \Leftrightarrow x \in \mathcal{F}(t).$$

By \mathbf{u}_f we denote the Eulerian deformation of the fluid-domain. Similar to the fluid domain map $\hat{\mathbf{u}}_f$ in the ALE formulation, this deformation \mathbf{u}_f does not describe the physical motion of a particle. We use \mathbf{u}_f to define the inverse fluid-map $T_f(x, t) = x - \mathbf{u}_f(x, t)$. Next, we assume, that there is a continuous transition from T_f to T_s on the interface $\Gamma_i(t)$. Then, we can define one global inverse mapping

$$T(x, t) := \begin{cases} T_s(x, t) & x \in \mathcal{S}(t) \\ T_s(x, t) = T_f(x, t) & x \in \Gamma_i(t) \\ T_f(x, t) & x \in \mathcal{F}(t). \end{cases}$$

Based on this mapping, we can decide the domain affiliation for every spatial coordinate $x \in \Omega$:

$$\begin{aligned} x \in \mathcal{S}(t) &\Leftrightarrow T(x, t) \in \hat{\mathcal{S}}, \\ x \in \mathcal{F}(t) &\Leftrightarrow T(x, t) \in \hat{\mathcal{F}}. \end{aligned}$$

This inverse map $T(x, t)$ is exactly the *backward-characteristic* $Y(x, t)$ used in the formulations of Milcent and Maitre [72, 165].

It remains to define the Eulerian fluid-domain deformation \mathbf{u}_f in an implicit way. To derive a continuous transition between T_f and T_s , the deformations \mathbf{u}_f and \mathbf{u}_s will need to be continuous. We can define \mathbf{u}_f simply by an extension of \mathbf{u}_s to $\mathcal{F}(t)$.

Remark 33 (Initial Point Set). *This construction looks very similar to the construction of the ALE-map in the context of the Arbitrary Lagrangian Eulerian model and one could argue, that the same difficulties are introduced. As we define an arbitrary extension \mathbf{u}_f of the solid's deformation \mathbf{u}_s , numerical artifacts come into place. There are however two fundamental differences: first, the inverse map $T(x, t)$ inside the fluid domain is not used for any kind of mapping. We do not require its inverse or its derivatives. Instead, it is for look-up purposes only. Second, we do not even require, that $T_f(x, t) \in \hat{\mathcal{F}}$ for $x \in FL(t)$. It is completely sufficient, that $x \in \mathcal{F}(t)$ is mapped outside of the solid domain. Therefore, we can relax the definition of the extension \mathbf{u}_f , i.e. by requiring Dirichlet values only on the interface and by relaxing the look-up property. Instead of requiring $T(x, t) \in \hat{\mathcal{F}}$ for $x \in \mathcal{F}(t)$, we simply demand $T(x, t) \notin \hat{\mathcal{S}}$ for such fluid points.*

Definition 17 (Initial Point Set). *A vector field $\Phi_{IPS} \in C(I; C(\Omega))$ is called Initial Point Set, if for $x \in \Omega$ and $t \geq 0$ it holds:*

$$\begin{aligned}\Phi_{IPS}(x, t) &= x - \mathbf{u}_s(x, t) & x \in \bar{\mathcal{S}}(t) \\ \Phi_{IPS}(x, t) &\notin \hat{\mathcal{S}} & x \in \mathcal{F}(t)\end{aligned}$$

Finally, we can indicate possibilities for the construction of \mathbf{u}_f . One simple option is to choose one more a harmonic extension of \mathbf{u}_s :

$$-\Delta \mathbf{u}_f = 0 \text{ in } \mathcal{F}(t), \quad \mathbf{u}_f = \mathbf{u}_s \text{ on } \Gamma_i(t), \quad \partial_n \mathbf{u}_f = 0 \text{ on } \partial\Omega_f(t) \setminus \Gamma_i(t).$$

Here, we have chosen homogenous Neumann boundary conditions on the outer boundary of the fluid-domain. This deformation \mathbf{u}_f will not define a mapping back to a reference domain, but as discussed, this property is not necessary. Finally, we can close the formulation of the coupled fluid-structure interaction problem in Eulerian coordinate:

Lemma 79 (Initial Point Set formulation of the Eulerian fluid-structure interaction problem). *Let $\{\mathbf{v}, p_f, \mathbf{u}\}$ be the solution of the variational problem [Raeume](#)*

$$\begin{aligned}& (\rho_f(\partial_t \mathbf{v} + \mathbf{v} \cdot \nabla \mathbf{v}), \phi)_{\mathcal{F}(t)} + (\sigma_f, \nabla \phi)_{\mathcal{F}(t)} \\ &+ (J_s \hat{\rho}_s(\partial_t \mathbf{v} + \mathbf{v} \cdot \nabla \mathbf{v}), \phi)_{\mathcal{S}(t)} + (\sigma_s, \nabla \phi)_{\mathcal{S}(t)} = (\rho_f \mathbf{f}, \phi)_{\mathcal{F}(t)} + (J_s \hat{\rho}_s^0 \mathbf{f}, \phi)_{\mathcal{S}(t)} \\ & \quad (\nabla \cdot \mathbf{v}, \xi_f)_{\mathcal{F}(t)} = 0 \\ & \quad (\partial_t \mathbf{u} + \mathbf{v} \cdot \nabla \mathbf{u} - \mathbf{v}, \psi_s)_{\mathcal{S}(t)} = 0 \\ & \quad (\nabla \mathbf{u}, \nabla \psi_f)_{\mathcal{F}(t)} = 0.\end{aligned}$$

Given sufficient regularity, a transformation of $\{\mathbf{v}, p_f, \mathbf{u}_s\}$ to Lagrangian coordinates (in the solid domain) also solves the fluid-structure interaction problem in classical formulation (2.4).

Remark 34 (Eulerian FSI and multiphase-flows). *The Fully Eulerian formulation for fluid-structure interactions is closely connected to Eulerian models for multiphase flows, where one conservation law is given on a domain Ω*

$$\rho(\partial_t \mathbf{v} + \mathbf{v} \cdot \nabla \mathbf{v}) - \sigma = 0,$$

and where the material parameters, such as density or viscosity depend on the location

$$\rho(x) = \begin{cases} \rho_1 & x \in \mathcal{F}_1(t), \\ \rho_2 & x \in \mathcal{F}_2(t) \end{cases}.$$

The fundamental difference to fluid-structure interactions however is, that only one type of differential operator is defined. In fluid-structure interactions, we have a transition from a hyperbolic equation in the solid domain to a parabolic equation in the fluid domain. This brings along the already discussed regularity problems on the interface. For multiphase flows, there exist approaches, that work with a smoothing of the parameters (density and viscosity) at the interface, such that it does not need to be sharply resolved.

By introducing the characteristic functions with respect to fluid- and solid-domain χ_f and χ_s

$$\chi_s(x, t) := \begin{cases} 1 & x - \mathbf{u}(x, t) \in \hat{\mathcal{S}}, \\ 0 & x - \mathbf{u}(x, t) \notin \hat{\mathcal{S}} \end{cases}, \quad \chi_f(x, t) := 1 - \chi_s(x, t),$$

the coupled momentum equations is shortly written as

$$\begin{aligned} (\rho(\partial_t \mathbf{v} + \mathbf{v} \cdot \nabla \mathbf{v}), \phi) + (\sigma, \nabla \phi) &= (\rho \mathbf{f}, \phi), \\ \rho &= \chi_f \rho_f + \chi_s J_s \hat{\rho}_s, \\ \sigma &= \chi_f \sigma_f + \chi_s \sigma_s. \end{aligned} \tag{5.7}$$

The introduction of such a characteristic function simplified the formulation, it however simply hides the difficulty behind the notation.

5.3 Time-Discretization of the Fully Eulerian Framework

In the spirit of Section 3.6, the Fully Eulerian Formulation leads to an interface problem with an interface, that is moving in time. A straightforward discretization of the Eulerian momentum equation (5.7) with the backward Euler method

$$(\rho(k^{-1} \mathbf{v}^n + \mathbf{v}^n \cdot \nabla \mathbf{v}^n), \phi) + (\sigma(\mathbf{v}^n, p^n), \nabla \phi) = (\rho k^{-1} \mathbf{v}^{n-1} + \rho \mathbf{f}^n, \phi),$$

would result in a reduction of the convergence order, as the solution must not be differentiable in time, i.e.

$$\frac{\mathbf{v}^n(x) - \mathbf{v}^{n-1}(x)}{k},$$

may refer to a point $x \in \Omega$, which is solid $x \in \mathcal{S}(t_{n-1})$ at the old point in time and fluid $x \in \mathcal{F}(t_n)$ at the new time-step.

To derive a simple first order scheme, it is sufficient, to properly evaluate the projection of the old time-step to the new domain partitioning. Let

$$\Omega^n = \mathcal{F}^n \cup \mathcal{I}^n \cup \mathcal{S}^n,$$

and

$$T_n : \Omega^{n-1} \rightarrow \Omega^n,$$

be given by the deformation \mathbf{u}^n

$$T_n(x) := x + \mathbf{u}^n(x) - \mathbf{u}^{n-1}(x), \quad T_n^{-1}(x) = x - \mathbf{u}^n(x) + \mathbf{u}^{n-1}(x).$$

With help of this mapping, which is available by the Initial Point Set method, a function \mathbf{v}^{n-1} from time-step t_{n-1} can be approximated on the partitioning Ω^n via

$$F(\phi) = (\rho \mathbf{f}^n, \phi) + ((\rho \circ T_n^{-1})(\mathbf{v}^{n-1} \circ T_n^{-1}), \phi).$$

As T_n and so T_n^{-1} implicitly depends on the new deformation \mathbf{u}^n , which is unknown in a fully coupled Eulerian fluid-structure interaction setting, the evaluation of this right hand side is an implicit part of the equation.

The theoretical analysis of high order accurate time-stepping methods for moving interface problems, where the interface-motion comes from the solution itself is still open. Transferring the parabolic setting from Section 3.6 to the Eulerian Framework for fluid-structure interactions experimentally gives the correct order, see [100].

All higher order accurate schemes will require an implicit iteration on the domain partitioning, as $\Omega^n = \mathcal{F}^n \cup \mathcal{I}^n \cup \mathcal{S}^n$ is only available, when \mathbf{u}^n itself is available. In a Newton like procedure, this will call for derivatives with respect to the domain motion, see the following Section 5.4.

To avoid such an effort, reduced order approximation could be used. In [189], non-stationary problems in the Eulerian Framework have been approximated by a fully explicit treatment of the interface location, i.e. by decoupling the geometry problem from the momentum equations. Better results can be expected by using higher order extrapolations. If problems with possible contact are considered, explicit handling of the interface motion will result in restrictive time-step conditions - at least, if the interface is close to contact. Such situations can efficiently be handled by means of adaptive time-step control

5.4 Linearizations of the Fully Eulerian coordinates

One of the benefits of an Eulerian formulation for fluid-structure interactions is the ease of the variational setting, see Lemma 79. The complete system is given as

$$\begin{aligned} A(U)(\Phi) &= (\rho_f(\partial_t \mathbf{v} + \mathbf{v} \cdot \nabla \mathbf{v}), \phi)_{\mathcal{F}(t)} + (\sigma_f, \nabla \phi)_{\mathcal{F}(t)} + (\nabla \cdot \mathbf{v}, \xi_f)_{\mathcal{F}(t)} \\ &\quad + (J_s \hat{\rho}_s(\partial_t \mathbf{v} + \mathbf{v} \cdot \nabla \mathbf{v}), \phi)_{\mathcal{S}(t)} + (\sigma_s, \nabla \phi)_{\mathcal{S}(t)} \\ &\quad + (\partial_t \mathbf{u} + \mathbf{v} \cdot \nabla \mathbf{u} - \mathbf{v}, \psi_s)_{\mathcal{S}(t)} + (\nabla \mathbf{u}, \nabla \psi_f)_{\mathcal{F}(t)}, \end{aligned} \tag{5.8}$$

with

$$\sigma_s = J_s \mathbf{F}_s^{-1} (2\mu \mathbf{E}_s + \lambda_s \text{tr}(\mathbf{E}_s) I) \mathbf{F}_s^{-T}, \quad \mathbf{E}_s = \frac{1}{2} (\mathbf{F}_s^{-T} \mathbf{F}_s^{-1} - I).$$

Most of the terms appearing in this formulation are linear or have a quadratic nonlinearity. Only the inverse deformation gradient's determinant J_s and the solid's stresses require closer attention. The characteristic difficulty however will be the dependency of the integrals on the domains $\mathcal{F}(t)$ and $\mathcal{S}(t)$, which are moving in time. Hence, geometric derivatives must be considered. For the following derivation we closely follow the approach in Section 4.2.2, in particular Theorem 11 and Lemma 72.

Lemma 80 (Derivatives of the Eulerian deformation gradient). *Let $\mathbf{F} = I - \nabla \mathbf{u}$, $J := \det(\mathbf{F})$ and $\mathbf{E} := \frac{1}{2}(\mathbf{F}^{-T}\mathbf{F}^{-1} - I)$*

$$\begin{aligned}
 (i) \quad & \frac{d\mathbf{F}}{d\mathbf{u}}(\mathbf{w}) = -\nabla \mathbf{w}, \\
 (ii) \quad & \frac{d\mathbf{F}^T}{d\mathbf{u}}(\mathbf{w}) = -\nabla \mathbf{w}^T, \\
 (iii) \quad & \frac{d\mathbf{F}^{-1}}{d\mathbf{u}}(\mathbf{w}) = \mathbf{F}^{-1} \nabla \mathbf{w} \nabla \mathbf{F}^{-1}, \\
 (iv) \quad & \frac{d\mathbf{F}^{-T}}{d\mathbf{u}}(\mathbf{w}) = \mathbf{F}^{-T} \nabla \mathbf{w}^T \nabla \mathbf{F}^{-T}, \\
 (v) \quad & \frac{dJ(\mathbf{u})}{d\mathbf{u}}(\mathbf{w}) = -J \mathbf{F}^{-T} : \nabla \mathbf{w} = -J \operatorname{tr}(\mathbf{F}^{-1} \nabla \mathbf{w}), \\
 (vi) \quad & \frac{d\mathbf{E}(\mathbf{u})}{d\mathbf{u}}(\mathbf{w}) = \frac{1}{2} \mathbf{F}^{-T} (\nabla \mathbf{w}^T \nabla \mathbf{F}^{-T} + \mathbf{F}^{-1} \nabla \mathbf{w}) \mathbf{F}^{-1}
 \end{aligned}$$

Proof. We refer the reader to Lemma 72. \square

By these derivation rules most of the terms in the Jacobian of the Eulerian formulation (5.8) can be expressed.

What remains, is the handling of the formulation's dependency on the domain motion. Here, the concept of geometric derivatives, *shape calculus* must be considered. It holds

Theorem 12 (Directional Shape Derivatives). *Let $\hat{\Omega}$ be a domain with piece-wise C^1 boundary, $\hat{T}(\hat{x}) := \hat{x} + \hat{\mathbf{u}}$ be a smooth domain map $\hat{T} : \hat{\Omega} \rightarrow \Omega(\mathbf{u})$, such that $\hat{T} \in W^{1,1}(\hat{\Omega})$. Further, let $f \in W^{1,1}(\Omega(\mathbf{u}))$. It holds*

$$\frac{d}{ds} \int_{\Omega(\mathbf{u}+s\mathbf{w})} f \, dx \Big|_{s=0} = \int_{\partial\Omega(\mathbf{u})} (\vec{n} \cdot \mathbf{w}) f \, do, \quad (5.9)$$

where \vec{n} is the outward facing normal vector on $\partial\Omega(\mathbf{u})$.

Proof. Let \mathbf{u}, \mathbf{w} be given with Lagrangian counter-part $\hat{\mathbf{u}}(\hat{x}, t) = \mathbf{u}(x, t)$ and $\hat{\mathbf{w}}(\hat{x}, t) = \mathbf{w}(x, t)$. It holds

$$\frac{d}{ds} \int_{\Omega(\mathbf{u}+s\mathbf{w})} f \, dx = \int_{\hat{\Omega}} \frac{d}{ds} \hat{J}(\hat{\mathbf{u}} + s\hat{\mathbf{w}}) f(\hat{x} + \hat{\mathbf{u}} + s\hat{\mathbf{w}}) \, d\hat{x} \quad (5.10)$$

where

$$\hat{J}(\hat{\mathbf{u}} + s\hat{\mathbf{w}}) = \det(I + \hat{\nabla}(\hat{\mathbf{u}} + s\hat{\mathbf{w}})). \quad (5.11)$$

Then, by Lemma 72, it holds

$$\frac{d}{ds} \hat{J}(\hat{\mathbf{u}} + s\hat{\mathbf{w}}) f(\hat{x} + \hat{\mathbf{u}} + s\hat{\mathbf{w}}) \Big|_{s=0} = \hat{J}(\hat{\mathbf{u}}) f(\hat{x} + \hat{\mathbf{u}}) \hat{\mathbf{F}}^{-T}(\mathbf{u}) : \hat{\nabla} \hat{\mathbf{w}} + \hat{J}(\hat{\mathbf{u}}) \nabla f(\hat{x} + \hat{\mathbf{u}}) \cdot \hat{\mathbf{w}}.$$

Therefore, by mapping back to $\Omega(\mathbf{u})$ and with help of integration by parts:

$$\begin{aligned}
 \frac{d}{d\mathbf{u}} \int_{\Omega(\mathbf{u}+s\mathbf{w})} f \, dx \Big|_{s=0} &= \int_{\Omega(\mathbf{u})} f I : \nabla \mathbf{w} \, dx + \int_{\Omega(\mathbf{u})} \nabla f \cdot \mathbf{w} \, dx \\
 &= \int_{\partial\Omega(\mathbf{u})} (\vec{n} \cdot \mathbf{w}) f \, dx - \int_{\Omega(\mathbf{u})} \operatorname{div}(f I) \cdot \mathbf{w} \, dx + \int_{\Omega(\mathbf{u})} \nabla f \cdot \mathbf{w} \, dx.
 \end{aligned} \quad (5.12)$$

□This result is specially adapted to our requirements. For more general results and an introduction to the area of shape calculus with application to partial differential equations, we refer to Simon [214] or [216, 76].

This theorem can directly be applied to calculate the Jacobian of the variational formulations. Formula (5.9) must be considered as a simple tool for evaluation of the derivatives. This formula however requires high regularity of the function f at the boundary. For example, we consider the variational formulation of Laplace's equation

$$A(\mathbf{u})(\phi) = \int_{\Omega} \nabla \mathbf{u} \cdot \nabla \phi \, dx.$$

Now, assume, that $\Omega = \Omega(\mathbf{u})$ as stated in Theorem 12. The variational formulation has a double dependency on \mathbf{u} , appearing as trial function itself and by the domain's dependency. Formula (5.9) gives

$$A'(\mathbf{u})(\mathbf{w}, \phi) = \int_{\Omega} \nabla \mathbf{w} \cdot \nabla \phi \, dx + \int_{\partial\Omega} (\vec{n} \cdot \mathbf{w}) \nabla \mathbf{u} \cdot \nabla \phi \, do.$$

For this expression to be well-defined, we need traces of $\nabla \mathbf{u}$ and $\nabla \phi$. For H^1 -functions, this regularity is not given. The crucial step in Theorem 12 is hidden in (5.12) using integration by parts. While the volume-formulation of the derivative is well-defined, the boundary integral formally requires higher regularity. See [214] for a discussion.

By the combination of Theorem 12 and Lemma 80, we can derive the complete Jacobian of the Fully Eulerian fluid-structure interaction problem.

Theorem 13 (Jacobian of the Fully Eulerian Formulation of Fluid-Structure interactions). *For the directional derivative of formulation (5.8) in $\mathbf{U} = \{\mathbf{v}, \mathbf{u}, p\}$ in direction of $\mathbf{W} = \{\mathbf{z}, \mathbf{w}, q\}$ it holds*

$$\begin{aligned} A'(\mathbf{U})(\mathbf{W}, \Phi) &= \left(\rho_f (\partial_t \mathbf{z} + \mathbf{z} \cdot \nabla \mathbf{v} + \mathbf{v} \cdot \nabla \mathbf{z}), \phi \right)_{\mathcal{F}(t)} \\ &\quad + \left(\frac{d\sigma_f}{d\mathbf{v}}(\mathbf{z}) + \frac{d\sigma_f}{dp_f}(q_f), \nabla \phi \right)_{\mathcal{F}(t)} \\ &\quad + \left(\frac{dJ_s}{d\mathbf{u}}(\mathbf{w}) \hat{\rho}_s (\partial_t \mathbf{v} + \mathbf{v} \cdot \nabla \mathbf{v}) + J_s (\partial_t \mathbf{z} + \mathbf{z} \cdot \nabla \mathbf{v} + \mathbf{v} \cdot \nabla \mathbf{z}), \phi \right)_{\mathcal{S}(t)} \\ &\quad + \left(\frac{d\sigma_s}{d\mathbf{u}}(\mathbf{w}), \nabla \phi \right)_{\mathcal{S}(t)} + (\nabla \cdot \mathbf{z}, \xi_f)_{\mathcal{F}(t)} \\ &\quad + \left(\partial_t \mathbf{w} + \mathbf{v} \cdot \mathbf{w} + \mathbf{z} \cdot \mathbf{u} - \mathbf{z}, \psi_s \right)_{\mathcal{S}(t)} + \left(\nabla \mathbf{w}, \nabla \psi_f \right)_{\mathcal{F}(t)} \\ &\quad + \langle \rho_f (\partial_t \mathbf{v}_f + \mathbf{v}_f \cdot \nabla \mathbf{v}_f), (\mathbf{w}_f \cdot \vec{n}_f) \phi \rangle_{\mathcal{I}(t)} + \langle \sigma_f, \nabla \phi (\mathbf{w}_f \cdot \vec{n}_f) \rangle_{\mathcal{I}(t)} \\ &\quad + \langle \nabla \cdot \mathbf{v}_f, \xi_f (\mathbf{w}_f \cdot \vec{n}_f) \rangle_{\mathcal{I}(t)} + \langle J_s \hat{\rho}_s (\partial_t \mathbf{v}_s + \mathbf{v}_s \cdot \nabla \mathbf{v}_s), \phi (\mathbf{w}_s \cdot \vec{n}_s) \rangle_{\mathcal{I}(t)} \\ &\quad + \langle \sigma_s, \nabla \phi_s (\mathbf{w}_s \cdot \vec{n}_s) \rangle_{\mathcal{I}(t)} + \langle \partial_t \mathbf{u}_s + \mathbf{v}_s \cdot \nabla \mathbf{u}_s - \mathbf{v}_s, \psi_s (\mathbf{w}_s \cdot \vec{n}_s) \rangle_{\mathcal{I}(t)} \\ &\quad + \langle \nabla \mathbf{w}_f, \nabla \psi_f (\mathbf{w}_f \cdot \vec{n}_f) \rangle_{\mathcal{I}(t)}, \end{aligned}$$

where the directional derivatives of the deformation gradient, the stresses and the strains are defined in Lemma 80.

For the computations of the boundary terms, it must be considered, that the gradients of \mathbf{v} and \mathbf{u} are not continuous across $\mathcal{I}(t)$. Therefore, we denote the correct side by adding the subscripts "f" and "s" where necessary.

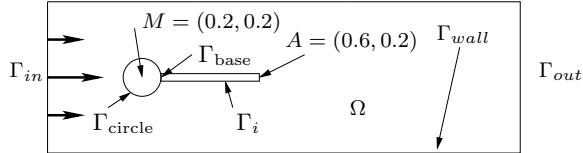


Figure 5.1: Configuration of the *csm-1* and *fsi-1* benchmark problems as published by Hron & Turek [134].

Remark 35. Including shape derivatives in the computation of the Jacobian significantly complicates the implementation work. In [84, 85], it is noted, that computational approaches for linearization and also for sensitivity based optimization work well, if these shape derivatives are neglected. At the latest when optimization problems are considered, it will be necessary to include these terms, as they will be crucial for the determination of the adjoint information transport across the interface, see also Section 8.1.

5.5 Finite Elements for the Fully Eulerian Framework

The Fully Eulerian framework for fluid-structure interactions leads to an interface problem. The interface $\mathcal{I}(t)$ must be captured and across this interface, the solution $\{\mathbf{u}, \mathbf{v}\}$ suffers from a lack of accuracy. As has been discussed in Section 3.5, we must expect a breakdown in convergence rates, if we do not accurately treat the are around this interface.

The parametric finite element scheme proposed in Section 3.5 can directly be applied to this more complex coupled problem. As velocity and deformation are globally defined as continuous functions, no special adjustments are necessary. Only the coupling between velocity and pressure must be carefully considered. In [100], Frei discusses several alternatives to stabilize the inf-sup condition on meshes resulting from the parametric interface resolution. None of the techniques however is fully satisfactory. Instead, the definition and implementation of an inf-sup stable finite element pair remains an open topic.

Away from the moving interface $\mathcal{I}(t)$, standard finite element pairs can be used for the discretization of velocity, pressure and also for the deformation. To simplify a direct variational coupling of velocities and deformations across the interface, and to avoid local changes of basis functions, the same function spaces should be used within the fluid and the solid domain. For details, we refer to Sections 3.3 and 4.3.

5.6 Numerical Study

For validation of the Eulerian model, we first consider two simple fluid-structure interaction benchmarks, the *csm-1* problem and the *fsi-1* problem as proposed by Hron and Turek [134]. Both benchmark problems use the configuration as shown in Figure 5.1, where an incompressible fluid flows around a circular obstacle and an elastic beam that is attached to this rigid obstacle. In the *csm-1* benchmark configuration the fluid is initially at rest and the beam undergoes a deformation caused by a gravity force. In the *fsi-1* benchmark problem no gravity force is acting, but the flow is driven by an inflow profile. Both problems have a

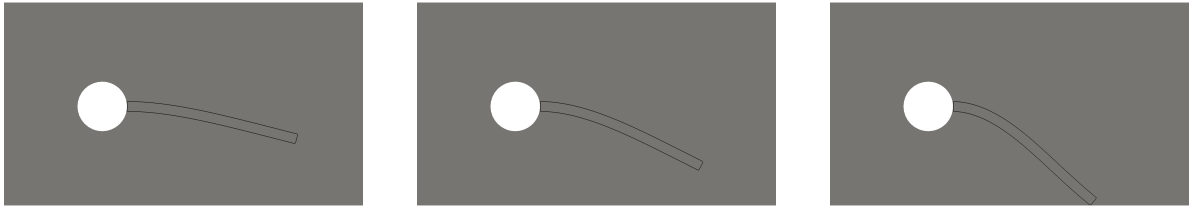


Figure 5.2: Configuration of the *csm-1* benchmark problem and modifications with larger gravity force. Left $g_s = -2$, middle $g_s = -4$ and right $g_s = -8$.

stationary solution and highly accurate results for different functional values are available in literature [134, 135]. Finally, we describe a more challenging test-case, where an elastic ball falls in an container filled with an incompressible fluid. The ball touches the bottom of the container and rebounces. Here we focus on modeling this collision of elastic structure with the domain's boundary.

5.6.1 Stationary structure benchmark problem

In this first test-case, a gravity force is acting on the elastic structure and causes a deflection, see Figure 5.1. In the original benchmark configuration [134] $g_s = 2$ has been used, Wick [242] also published results for $g_s = 4$ yielding a larger deformation. To exploit the possibilities of very large deformation with the Eulerian approach, we add a further test-case using $g_s = 8$. We measure the deflection \mathbf{u}_s in the tip of the beam $A = (0.6, 0.2)$ in the stationary limit. In Table 5.1 we present the deflections in this measurement point on different meshes with decreasing mesh sizes under three different gravity forces. For comparison, we indicate the reference values are stated in [134, 135] and [242, 244]. The complete set of parameters used in this configuration is:

$$\begin{aligned} \rho_f = \hat{\rho}_s &= 10^3, & \nu_f &= 10^{-3}, & \mu_s &= 5 \cdot 10^5, \\ \lambda_2 &= 2 \cdot 10^6, & \mathbf{f}_s &= -g_s J_s \hat{\rho}_s \chi_s. \end{aligned} \quad (5.13)$$

It is clearly seen, that the Full Eulerian method yields accurate values which are very close to the reference values cited from the literature. Further, the Eulerian framework is able to increase the gravity force up to a point ($g_s = 8$) where the beam touches the rigid bottom of the flow-channel, see Figure 5.2. Here, no results for comparison are available in the literature.

5.6.2 Stationary fluid-structure interaction problem

As a second test-case of the benchmark-suite published by Hron & Turek we refer to the *fsi-1* problem. The flow is driven by a parabolic inflow profile on the boundary Γ_{in} :

$$\mathbf{v}_{\text{in}} = \frac{y(H-y)}{4H^2} v_{\text{max}}, \quad H = 0.41, \quad v_{\text{max}} = 0.3.$$

Due to a slight unbalance in the configuration (see Figure 5.1) the elastic beam undergoes a small deflection. Apart from this modification, the material constants are taken as described in (5.13). Besides measuring the deflection of the beam, drag- and lift-values of the obstacle

mesh size	$g_s = 2$		$g_s = 4$		$g_s = 8$	
	$u^x(A)$	$u^y(A)$	$u^x(A)$	$u^y(A)$	$u^x(A)$	$u^y(A)$
$h_{\min} \approx 0.008$	6.372	61.84	21.22	114.54	59.846	189.74
$h_{\min} \approx 0.004$	7.116	64.70	25.02	121.25	65.760	192.03
$h_{\min} \approx 0.002$	7.149	66.07	25.10	122.16	66.857	192.35
Hron & Turek [134]	7.187	66.10	n/a		n/a	
Wick [242, 244]	7.150	64.90	25.33	122.30	n/a	

Table 5.1: Results for the CSM-1 benchmark problem using increasing volume forces. Functional values on a sequence of meshes. Comparison to reference values taken from the literature using the ALE framework.

(rigid circle & beam) where to be estimated. Let $\Gamma_{\text{obs}} := \Gamma_i \cup \Gamma_{\text{circle}} \setminus \Gamma_{\text{base}}$ be the complete outer boundary of the obstacle. Here, we consider the drag-value:

$$J_{\text{drag}} = \int_{\Gamma_{\text{obs}}} \vec{n}_f \sigma_f \mathbf{e}_1 \, ds.$$

Evaluation of these integrals is accomplished by rewriting the boundary integrals over the moving interface $\mathcal{I}(t)$ into integrals over the fixed boundary around the rigid circle, followed by a reformulation into volume integrals. Finally, we can compute the drag force as a residual evaluation. We first modify the functionals by using the dynamic coupling condition and inserting zero:

$$\begin{aligned} J_{\text{drag}} &= \int_{\Gamma_{\text{circle}} \setminus \Gamma_{\text{base}}} \vec{n}_f \sigma_f \mathbf{e}_1 \, ds + \int_{\Gamma_i} \underbrace{\vec{n}_f \sigma_f}_{=-\vec{n}_s \sigma_s} \mathbf{e}_1 \, ds \pm \int_{\Gamma_{\text{base}}} \vec{n}_s \sigma_s \mathbf{e}_1 \, ds \\ &= \int_{\Gamma_{\text{circle}} \setminus \Gamma_{\text{base}}} \vec{n}_f \sigma_f \mathbf{e}_1 \, ds + \int_{\Gamma_{\text{base}}} \vec{n}_s \sigma_s \mathbf{e}_1 \, ds - \int_{\partial \Omega_s} \vec{n}_s \sigma_s \mathbf{e}_1 \, ds. \end{aligned}$$

In the stationary limit (and in the absence of external forces) it holds for the exact solution $\int_{\partial \Omega_s} \vec{n} \sigma \, ds = - \int_{\Omega_s} \operatorname{div} \sigma_s \, dx = 0$ and hence:

$$J_{\text{drag}} = \int_{\Gamma_{\text{circle}}} \vec{n} \sigma \mathbf{e}_1 \, ds,$$

where by \vec{n} we denote the outward facing normal vector (whether in Ω_f or Ω_s) and by σ the corresponding acting tensor. Evaluation of this boundary integral is straightforward, since the boundary Γ_{circle} is fixed, even in the Eulerian setting. The accuracy of this functional evaluation can be further enhanced by expressing it in terms of variational residuals (*Babuška-Miller-Trick*) [8, 60, 188]. In Table 5.2 we gather the drag-value as obtained with the Eulerian approach. For evaluation of the functional we consider both the boundary integrals as well as the reformulation into residual terms. A good reference value $J_{\text{drag}} = 14.2940 \pm 10^{-5}$ is available in the literature [135, 188]. In Figure 5.3 we show the error slopes of the drag approximation. Here we observe linear order of convergence (in the mesh-size h) for the boundary integral and quadratic convergence for the residual reformulation. Using piece-wise linear finite elements one would expect (at least for a pure incompressible flow problem) the double order of convergence. Here, order reduction will take place due to the limited discretization accuracy close at the

mesh-size	dof's	Boundary	Variational
0.1	53 450	15.1052	14.9004
0.05	176 790	15.2333	14.5971
0.025	640 490	14.7836	14.4062
0.0125	2 466 390	14.5118	14.3280

Table 5.2: *fsi-1* benchmark results. Drag-coefficient $J_{\text{drag}}(U_h)$ evaluates as boundary integral and reformulated as residual expression. The reference value taken from literature is given by $J_{\text{drag}} = 14.2940 \pm 10^{-5}$.

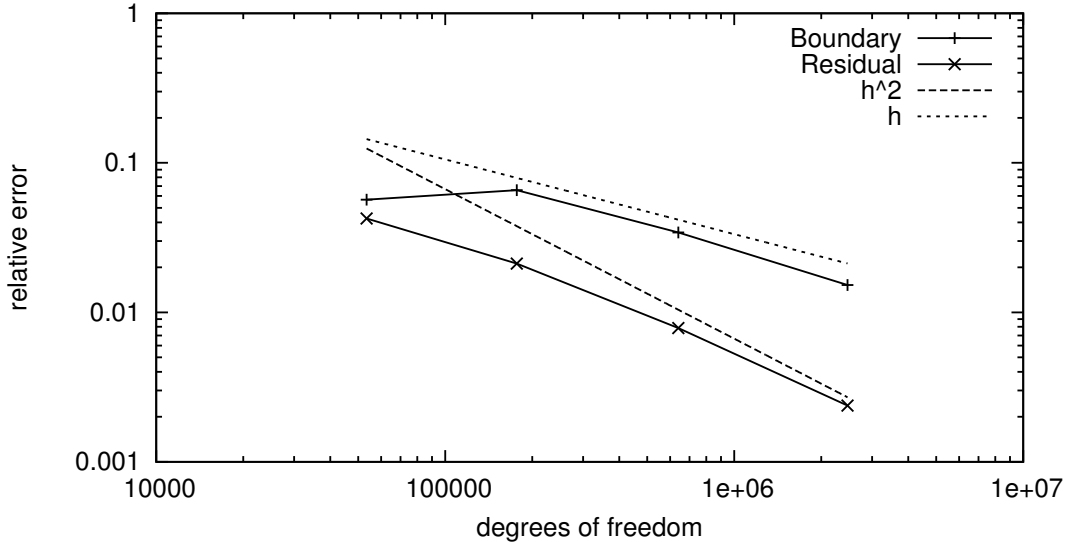


Figure 5.3: Convergence of the drag-approximation with the Eulerian coordinate framework. Evaluated as boundary integral (linear convergence) and as residual term (quadratic convergence).

elements that are cut by the moving interface. Remedy could be found by using local mesh adaptation close to the interface or considering the extended finite element method [66] for better accuracy in the interface region.

5.6.3 Contact problem

Finally, we model the “free fall” of an elastic ball Ω_s with radius $r_{\text{ball}} = 0.4$ in a container $\Omega = (-1, 1)^2$ filled with a viscous fluid Ω_f . The container is closed at the bottom boundary $\Gamma_{\text{bot}} = \partial\Omega_{y=-1}$ but open at the top and the sides. Here, by open we refer to the “do-nothing” boundary condition

$$\nu \partial_n \mathbf{v} - p \vec{n} = 0,$$

which allows free in- and outflow of the fluid, see [124].

Figure 5.4 shows the configuration of this test-case. At time $t = 0$, the midpoint of the ball is at $x_0 = (0, 0)$. Since gravity is the only acting force on the solid, the ball will accelerate and

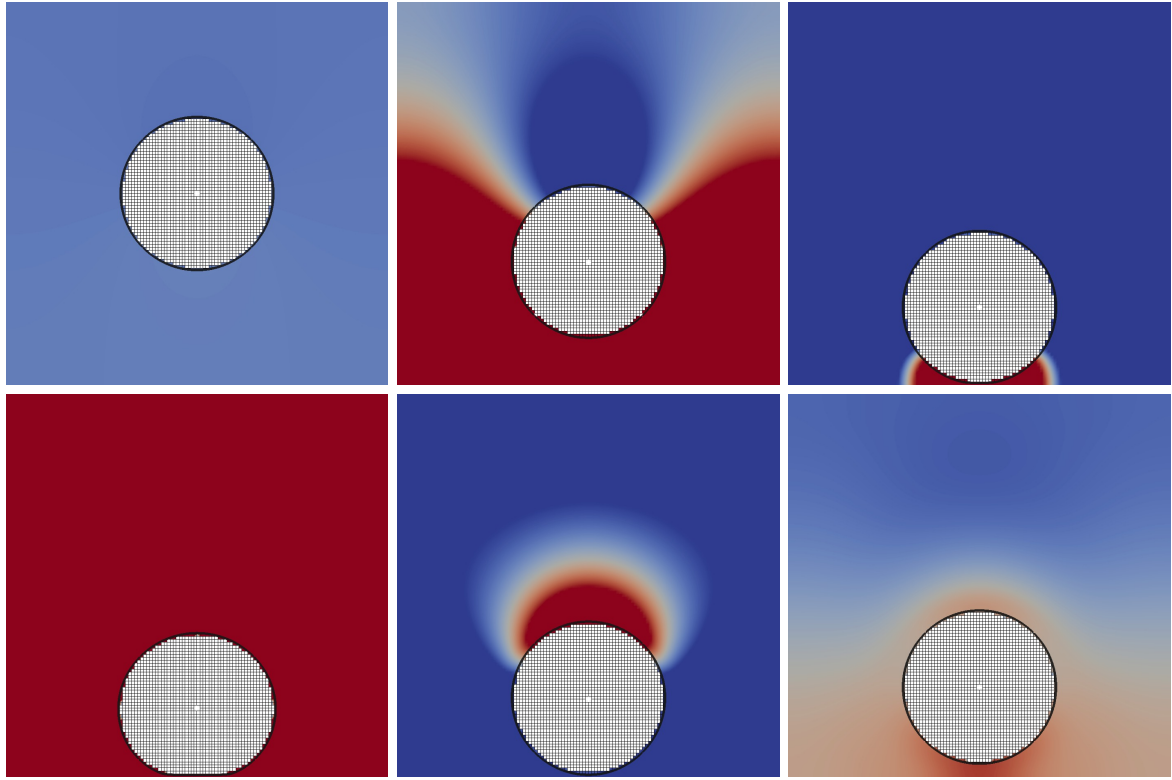


Figure 5.4: Falling ball bouncing of the bottom wall. Snapshots of the solution at times $t = 0$, $t = 0.71$, $t = 0.96$ (first contact), $t = 1.035$ (biggest deformation), $t = 1.125$ (breaking contact) and $t = 1.38$ (highest bounce-off).

fall to the bottom

$$\Gamma_{\text{bot}} = \{(x, -1), x \in (-1, 1)\}.$$

At this rigid wall with homogenous Dirichlet condition $\mathbf{v}_f = 0$, the ball stops and due to elasticity it will bounce off again. The parameters used for this test-case are given by

$$\begin{aligned} \rho_f &= 10^3, & \hat{\rho}_s &= 10^3, & \nu_f &= 10^{-2} \\ \mu_s &= 10^4, & \lambda_s &= 4 \cdot 10^4, & \mathbf{f} &= -J_s \hat{\rho}_s \chi_s. \end{aligned} \quad (5.14)$$

To get a closer look at the processes during “contact”, we show in Figure 5.5 a zoom into the area close to the lower boundary. We note, that these computations have been done with a standard finite element basis, without using the parametric approach described in Section 3.5. Figure 5.5 shows simulation results for the time, where the structure enters the last layer of elements at the boundary, the time, where the ball gets closest to the boundary (here, a significant deformation of the structure is visible) and at a time, where the ball starts to release and finally, a snap-shot of the simulation, where the ball is completely detached. The Fully Eulerian formulation does not model real contact, as solid and boundary never touch.

Remark 36 (Contact in Fluid-Structure Interactions). *It is a widely discussed topic, if contact in the case of the coupled dynamics of the incompressible Navier-Stokes equations and a solid body is possible at all. First of all, physical observation, i.e. a steel ball touching the ground, tells us, that contact is established. On the other hand, theoretical results, considering the fall*

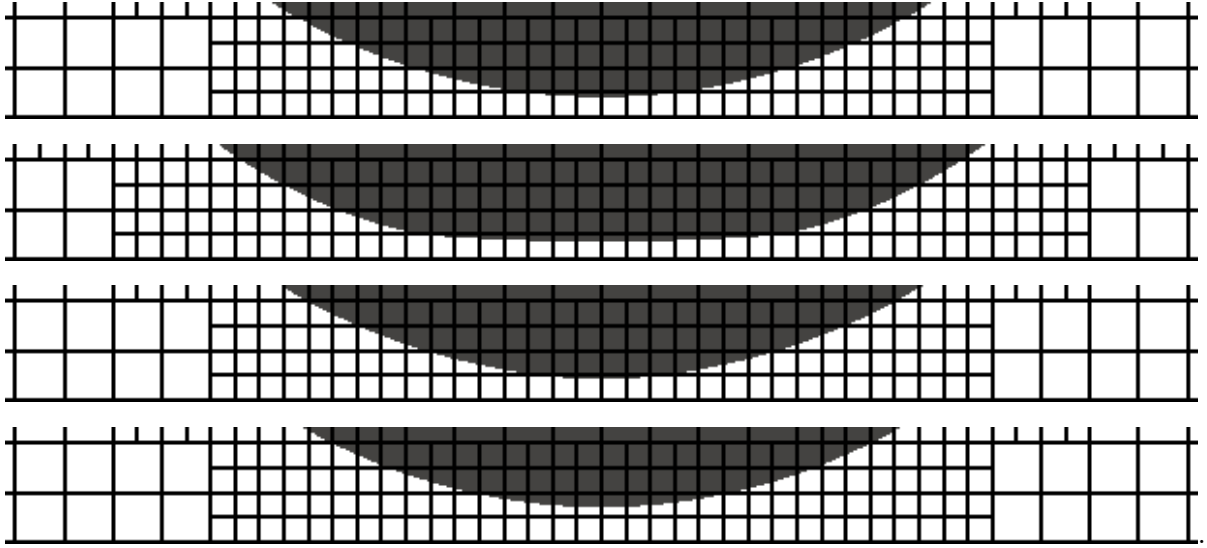


Figure 5.5: Close ups of the contact problem. From top to bottom: simulation at times, where the ball first gets into the last layer of elements at the contact boundary, shortest distance to the boundary, beginning of release and full detachment.

of an rigid body with smooth boundary in an incompressible fluid show, that contact (in the usual variational sense) will not be reached in finite time, see e.g. [77, 89, 125, 164, 126]. To the best knowledge of the author, no theoretical analysis has been done for collision problems of elastic structures in viscous fluids.

For the interaction of an elastic solid with smooth boundaries and a viscous fluid, one hypothesis is, that a finite layer of fluid will always remain. In numerical simulations based on strong local adaptivity, this could however not be assured (neither disproved) so far.

From a modeling point of view, the use of the incompressible Navier-Stokes equations is questionable for such limiting applications. First of all, also water will not behave strictly incompressible, if very large forces act on a very thin film. Secondly, the continuum hypothesis must be queried in the transmission to contact.

To shed further light on the mechanism acting at “close contact”, we consider the following functional outputs measuring stresses in fluid and solid: We measure the wall stress acting on the lower boundary and the elastic stress stored in the solid:

$$J_{\text{fluid}}(U) = \int_{\Gamma_{\text{bot}}} \sigma_f \vec{n}_f \cdot \vec{n} - f \, \text{d}\omega, \quad J_{\text{solid}}(U) = \left(\int_{S(t)} \sigma_s : \sigma_s \, \text{d}x \right)^{\frac{1}{2}}. \quad (5.15)$$

The results - together with the distance of the ball from the lower boundary - are shown in Figure 5.6. Forces are transmitted through the remaining small liquid film and elastic energy is stored in the solid.

Finally, to measure the quality of the approximation we indicate some further output functionals of the solution. First, as the Eulerian model does not have exact conservation properties,

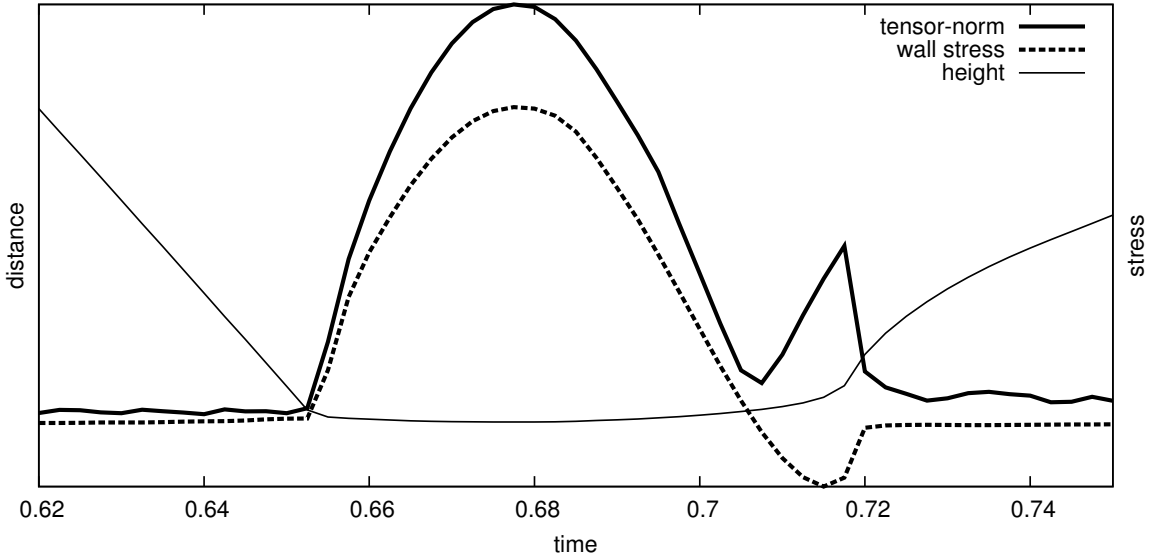


Figure 5.6: Wall stress on the lower boundary and stresses in the solid during “contact”.

we analyze the solid’s mass, measured as

$$J_{\text{mass}}(U) = \int_{S(t)} J_s \hat{\rho}_s^0 \, dx.$$

In Table 5.3 we show the error in mass conservation

$$\|j_{\text{mass}}(t) - \hat{\rho}_s \pi r_{\text{ball}}^2\|_{L^2([0,2])},$$

depending on the accuracy of the spatial and temporal discretization. The time-interval $I = [0, 2]$ is so large, that the ball hits the bottom boundary twice. We observe $O(h^2)$ convergence, even if we did not use the modified finite element approach described in Section 3.5. The time-discretization parameter k appears to be too small to have a substantial influence on the accuracy. strictly guarantee this conservation.

h/k	0.0100	0.0050	0.0025
2^{-5}	$2.68 \cdot 10^{-3}$	$2.66 \cdot 10^{-3}$	$2.69 \cdot 10^{-3}$
2^{-6}	$7.82 \cdot 10^{-4}$	$6.95 \cdot 10^{-4}$	$6.72 \cdot 10^{-4}$
2^{-7}	$2.63 \cdot 10^{-4}$	$1.92 \cdot 10^{-4}$	$1.68 \cdot 10^{-4}$

Table 5.3: Error in mass conservation for the falling ball.

Finally, we show in Figure 5.7 two further output functionals measuring the average vertical velocity of the ball and the volume of ball, both as functions over time:

$$J_{\mathbf{v}}(t) := \int_{\Omega_s(t)} \mathbf{v}_s^y(t) \, dx, \quad J_{\text{vol}}(t) := \int_{\Omega_s(t)} 1 \, dx. \quad (5.16)$$

Note, that mass should be conserved, the volume of the elastic obstacle however is subject to change, as $\nu_s = 0.4$, compare (5.14).

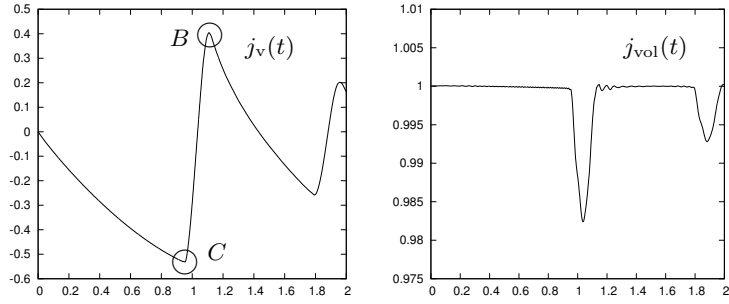


Figure 5.7: Falling ball: functionals as plot over time. Left: solid's average velocity. Right: Right: solid's relative volume. The two turning points of the velocity for contact (C) and maximum bounce-off (B) are indicated in the middle plot.

h/k	0.0100	0.0050	0.0025	h/k	0.0100	0.0050	0.0025
2^{-5}	-0.4977	-0.4990	-0.5006	2^{-5}	0.320	0.348	0.365
2^{-6}	-0.5248	-0.5286	-0.5298	2^{-6}	0.318	0.369	0.396
2^{-7}	-0.5402	-0.5311	-0.5315	2^{-7}	0.357	0.388	0.404

Table 5.4: Left: maximum (negative) velocity reached in free fall. Right: maximum average velocity after bounce-off. Calculations on three different spatial and temporal meshes.

Figure 5.7 shows the progress of the functionals (5.16) as function over time. The left sketch shows the average velocity. Here, acceleration by gravity and acceleration due to bounce off are clearly visible. The boundary of height is smaller (due to viscous damping). The right sketch shows the volume of the ball. Due to the compression at impact-time, the volume gets reduced during the contact. Reduction of volume is possible, since the flow-container is open on the upper, left and right boundaries.

Finally, in Table 5.4 we indicate the maximum (negative) velocity that is reached at the time of first contact $t_C \approx 0.952$, as well as the maximum velocity that is reached after the first bounce-off $t_B \approx 1.105$, see Figure 5.7. Computations are done using three different temporal and spatial discretization parameters h and k . All meshes are uniform in space and time. While the time-step has only a very small influence on the functional values we observe convergence under mesh-refinement.

6 Linear Solvers for Fluid-Structure Interactions

This chapter is devoted to different algebraic solution techniques for discretized fluid-structure interaction problems. We will consider discretizations in time and space as discussed in the previous chapters. The main focus will be put to fluid-structure interactions in Arbitrary Lagrangian Eulerian coordinates, as described in Chapter 4. Solution techniques for the alternative Eulerian approach from Chapter 5 will be mentioned, where standard approaches fail.

From finite element discretization and discretization in time, we derived nonlinear systems of algebraic equations, that can - in short - be written as to find $\mathbf{U}_h \in X_h$, such that

$$A_h(\mathbf{U}_h)(\Phi_h) = F(\Phi_h) \quad \forall \Phi_h \in Y_h,$$

where U_h is the unknown solution, $\Phi_h \in Y_h$ the finite element test-function and $F(\cdot)$ is the right hand side, that depends – in the case of non-stationary problems – on the old solution at the previous time-step. In Section 4.2 and 5.4 we have discussed the linearization of this system by fixed-point iterations or by means of the Newton method. In any way, linearization results in the necessity to solve linear systems of equations of the type

$$\mathbf{A}_h \mathbf{x} = \mathbf{b}.$$

These systems are huge, usually very ill-conditioned and without structures, such as symmetry or positivity. In the following sections, we will give an overview over different solution techniques for these linear systems of equations arising from the finite element discretization of fluid-structure interactions. The main focus will be on solution techniques for fluid-structure interactions in Arbitrary Eulerian Lagrangian coordinates.

Remark 37 (Partitioned Solvers). *The traditional way of solving fluid-structure interactions is to choose partitioned approaches, where the problem is split into the Navier-Stokes system and into the elastic structure system. Both problems are solved separately and the coupling is realized by means of boundary conditions. Partitioned methods are in contrast to monolithic formulations. The system is not only broken for the solution of it, instead, one starts with two separated formulations. Strongly implicit discretization techniques, like a backward Euler for the coupled problem, are not possible.*

The huge benefit of partitioned methods is the great flexibility in using two different meshes, two different discretization techniques, even two different software packages for the realization. A lot of research goes into the design of coupling methods, that use two separate modules for fluid and solid - nearly as blackboxes. See [1].

In partitioned methods one distinguishes between weakly coupled approaches and strongly coupled ones. Weakly coupled approaches can be considered as semi-explicit time-stepping schemes:

in every time-step, the coupling in one direction is neglected, such that fluid and solid can be solved in a row. There is usually no control over the realization of the coupling conditions. Only for timestep $\delta t \rightarrow 0$, one can hope, that the coupled system of fluid, solid and coupling conditions is really solved. Strongly coupled approaches iterate between fluid and solid until the error in the coupling conditions is reduced.

Weakly coupled partitioned approaches are reported to show instabilities, if the coupling is stiff, i.e., if the added mass effect acts, strongly coupled methods may call for many sub-iterations [64, 119], see also Section 2.2.

A comprehensive survey on partitioned methods is out of the scope of this book. Partitioned approaches are in contrast to the use of strongly coupled implicit discretization and solution techniques as proposed in this work. Further, the realization of gradient based error estimation and optimization methods calls for implicit monolithic coupling .

For many applications like wind turbine simulation [18], where the added-mass effect does not act strongly, partitioned approaches can be very efficient computational tools. Recent research often aims at increasing the stability and robustness of strongly coupled partitioned. For an overview on partitioned methods, we refer to [158, 159, 57, 93, 177, 119, 144, 58, 145, 105, 232, 131, 153] and many more.

6.1 Direct solution of linear systems

Let

$$\mathbf{A}_h \mathbf{x} = \mathbf{b}, \quad (6.1)$$

be the linear system arising from the discretization of a coupled fluid-structure interaction problem. We assume, that the matrix $\mathbf{A} \in \mathbb{R}^{n \times n}$ is very large $n \gg 10^3 - 10^8$ but sparse, i.e. for every row $i \in \{1, \dots, n\}$ the set of non-zero entries $\mathcal{A}_i := \{j, a_{ij} \neq 0\}$ is small, $\#\mathcal{A}_i = O(1)$. Solution of linear systems is very sensitive to error propagation from errors in the data \mathbf{A}_h and \mathbf{b} . The following (pessimistic) bound holds for the propagation of errors:

$$\frac{\|\mathbf{x} - \tilde{\mathbf{x}}\|}{\|\mathbf{x}\|} \leq \frac{\text{cond}(\mathbf{A}_h)}{1 - \text{cond}_2(\mathbf{A}_h) \frac{\|\delta \mathbf{A}_h\|}{\|\mathbf{A}_h\|}} \left(\frac{\|\delta \mathbf{b}\|}{\|\mathbf{b}\|} + \frac{\|\delta \mathbf{A}_h \mathbf{x}\|}{\|\mathbf{A}_h\|} \right),$$

if $\delta \mathbf{A}_h$ is a small perturbation of the system matrix \mathbf{A}_h , $\delta \mathbf{b}$ a perturbation of the right hand side, and where by

$$\text{cond}(\mathbf{A}_h) := \|\mathbf{A}_h\| \|\mathbf{A}_h^{-1}\|,$$

we denote the condition number of the matrix \mathbf{A}_h . For discretizations of partial differential equations, the condition number is usually very large. For elliptic problems, it holds

$$\text{cond}(\mathbf{A}_h) = O\left(\frac{1}{h^2}\right),$$

such we must – in general – expect a very strong error amplification. In Section 6.2.2, we will see, that the condition numbers of coupled fluid-structure interactions in ALE coordinates is even far worse than that, of the single systems.

Without special knowledge and usage of the matrix structure, a direct solution of the linear systems is always a possibility. For general matrices $\mathbf{A}_h \in \mathbb{R}^{n \times n}$, direct solvers have a very

Mesh Level (2d)	2	3	4	5	6	7
Unknowns	5 260	20 640	80 960	320 640	1 276 160	5 091 840
Avg. conv. rate	0.14	0.29	> 0.99	> 0.99	> 0.99	> 0.99
Memory usage	19 MB	48 MB	—	—	—	—
Avg. Time	0.12 sec	0.72 sec	—	—	—	—

Mesh Level (3d)	2	3	4	5
Unknowns	18 711	131 495	983 367	7 600 775
Avg. conv. rate	0.086	0.067	0.094	0.33
Memory usage	156 MB	1.0 GB	7.8 GB	64 GB
Avg. Time	1.23 sec	10.17 sec	120.15 sec	2399 sec

Table 6.1: Number of unknowns, average convergence rates (see Remark 38), memory usage and average computational time for linear solution with monolithic geometric multigrid solver using a fully coupled block-wise incomplete decomposition of the smoother. In the 2D case, there was no convergence starting from mesh-level 4.

great demand in computational time and also in memory use. The numerical effort scales by $O(nm^2)$, where m is the bandwidth of the sparsity pattern of the matrix. The memory usage scales by $O(nm)$. Problem on two dimensional meshes can usually be rearranged, such that $m \ll n$, making direct solvers a good option, see [163]. For three dimensional problems however, the sparsity is so excessive, that the success of reordering is limited. See [163, 74, 150, 146] for an overview of powerful packages for the direct solution of linear systems. Considering three-dimensional problems, most direct solvers however lack efficiency. Finite element discretization of three dimensional problems leads to matrices with significantly more unknowns per matrix row, than their two dimensional counterparts. Here, modern and problem-adapted iterative solvers are usually preferable.

6.2 Analysis of benchmark-problems

To start the discussion, we first present two different test problems to be used throughout this article. First, we consider the non-stationary *fsi-3 benchmark* problem of Hron and Turek [134], a 2d test case featuring large deformation and stability problems caused by the *added-mass effect*. Second, we choose a three dimensional test case [188, 190] with smaller deformation. In the following, we describe the full configuration including all problem parameters for both test cases.

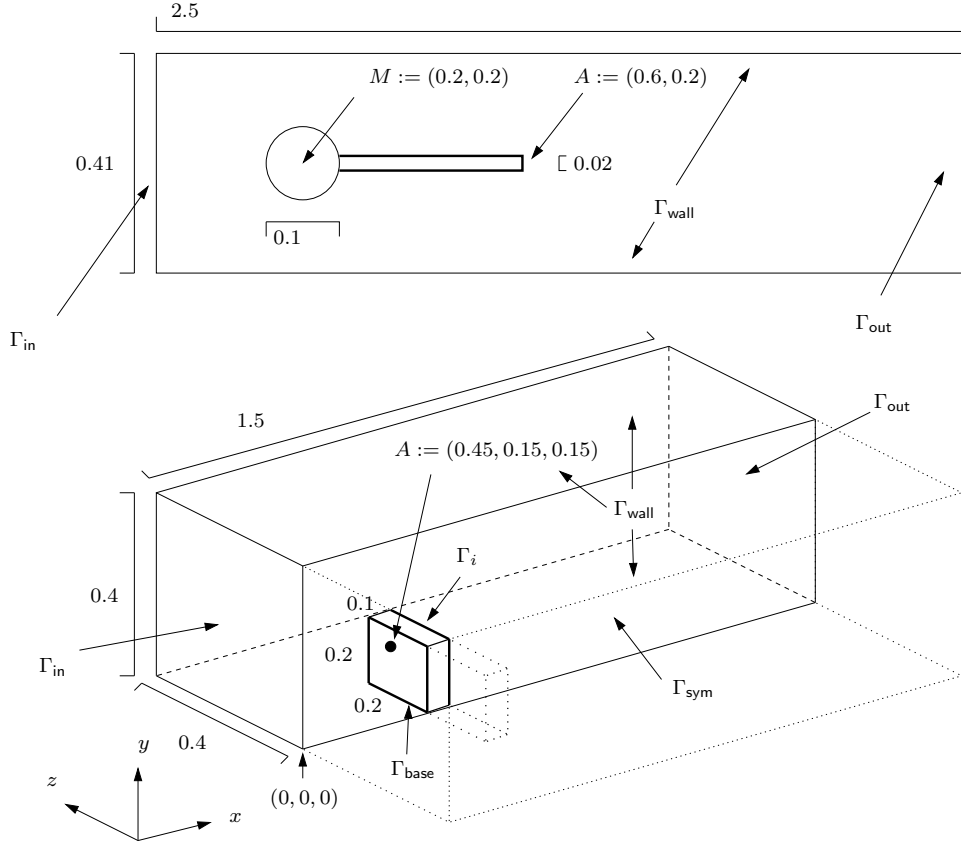


Figure 6.1: Configuration of the two test cases.

6.2.1 Configuration of the benchmark problems

Figure 6.1 shows a sketch of the geometry describing both problems. Both configurations are driven by an inflow condition $\mathbf{v}_f = \mathbf{v}_{\text{in}}$ for the velocity on Γ_{in} :

$$\mathbf{v}_{\text{in}}^{2d}(y) = \frac{y(H-y)}{(H/2)^2} \cdot \frac{3}{2} \bar{\mathbf{v}}_{\text{mean}}^{2d}, \quad \mathbf{v}_{\text{in}}^{3d}(y, z) = \frac{9}{8} \frac{y(H-y)(H^2-z^2)}{(H/2)^2 H^2} \cdot \frac{9}{8} \bar{\mathbf{v}}_{\text{mean}}^{3d},$$

with average inflow velocities of $\bar{\mathbf{v}}_{\text{mean}}^{2d} = 2 \text{ m/s}$ and $\bar{\mathbf{v}}_{\text{mean}}^{3d} = 1 \text{ m/s}$. Both profiles are temporally smoothed to give a smooth transition from $\mathbf{v} = 0$ at $t = 0$ to the maximum velocity at time $t = 2s$, by multiplying with $\alpha(t) \in \mathbb{R}$ given by

$$\alpha(t) = \begin{cases} \frac{1}{2} (1 - \cos(\pi t/2)) & t < 2 \\ 1 & t \geq 2 \end{cases}.$$

On the outflow boundary Γ_{out} we prescribe the do-nothing condition

$$\rho_f \nu_f \vec{n} \cdot \nabla \mathbf{v}_f - p \vec{n} = 0, \quad (6.2)$$

see [124], on the walls Γ_{wall} a no-slip condition $\mathbf{v}_f = 0$. In the case of the 3d-configuration, we consider a symmetry condition at Γ_{sym} . In both cases, the solid is firmly attached to the

Problem configuration	2D	3D
Fluid density ρ_f	10^3 kg/m^3	10^3 kg/m^3
Kinematic viscosity ν_f	$10^{-3} \text{ m}^2/\text{s}$	$10^{-3} \text{ m}^2/\text{s}$
Average inflow velocity \bar{v}_{mean}	2 m/s	1 m/s
Solid density ρ_s	10^3 kg/m^3	10^3 kg/m^3
Shear modulus μ_s	$2 \cdot 10^6 \text{ kg/ms}^2$	$5 \cdot 10^5 \text{ kg/ms}^2$
Poisson ratio ν_s	0.4	0.4

Table 6.2: Description of the two benchmark problems

boundary at Γ_{base} by prescribing Dirichlet conditions for velocity and deformation $\mathbf{v}_s = \mathbf{u}_s = 0$. In Table 6.2, we collect all parameters, that completely describe the settings.

The 2d-case is challenging due large deformations, that makes up about 50% of the fluid domain. The 3d-case is less demanding in this respect, as deformations are small. This reduces the effects of nonlinearities as well as the role of the ALE-mapping of the fluid problem. We start by collecting convergence rates of a fully monolithic multigrid solver in Table 6.1 for both problems.

Remark 38 (Estimation of convergence rate and time, computational setup). *As the coupled fsi problem is highly nonlinear with time-dependent dynamics, we always estimate convergence rates and computational time as averages over a sequence of time-steps. Furthermore, as the number of Newton steps may vary from time-step to time-step, we fix the averaging by the following algorithm: in the case of the 2d-problem, we compute averages over 100 time-steps and we include 5 Newton steps per time-step into the averaging. Furthermore, we use an approximate Newton scheme by reusing the Jacobian: only every tenth time-step, a new Jacobian is assembled. In the case of the 3d-problem we choose the same procedure, but averaging is limited to 20 time-steps. To sum up: all results belonging to the 2d test case contain averages over 500 steps of the linear solver, including 10 assemblies of the system matrix. In the 3d test cases, we average over 100 runs of the linear solver including 2 assemblies of the Jacobian (and the necessary preparation of the smoother or preconditioner).*

This fixation allows for a fair comparison scaling over the mesh levels. All computations have been carried out on a Xeon E5-2690 cpu at 2.90 GHz with 256 GB of memory. Single core performance only is used for all computations.

The results in Table 6.1 present the performance of a standard geometric multigrid solver, used as preconditioner in an outer GMRES iteration. Coarse mesh problems are solved with help of a direct solver, and smoothing is done by a blockwise incomplete decomposition of the coupled system matrix. This solver is the standard technique in the software library GASCOIGNE 3D[23] and is highly efficient for problem in fluid-dynamics (compressible and incompressible), solid mechanics and various coupled multiphysics problems, see [142]. Here however, we see that the convergence rates quickly deteriorate on fine meshes. Already starting with about 81 000 unknowns, this solvers ceases to work in the (more difficult) 2d-case. In terms of material parameters and deformation, the three dimensional test case is easier. This explains the better convergence rates. Besides the computational times, we see that memory consumption is a severe issue, in particular for the three dimensional benchmark configuration.

6.2. Analysis of benchmark-problems

Although multigrid convergence rates are worsening for large problem sizes, the robustness of this standard solver must be highly appreciated.

A straight-ahead alternative to coupled multigrid solvers is the solution via direct solvers. In Table 6.3 we give indications of the convergence rates, memory usage and computational time for the two benchmark problems using the direct solver UMFPACK [74]. Memory consumption quickly goes beyond feasible limits. Computations on the finest meshes have not been possible. Furthermore, solution times increase in a similar fashion, such that direct solution - in particular for 3d problems - is no alternative. It is surprising, that the direct solver (using double precision arithmetic) shows very bad error reduction, giving only one or two digits in every step. We will see, that this behavior is due to the very bad conditioning of the coupled matrix.

Mesh Level (2d)	2	3	4	5	6	7
Avg. conv. rate	0.015	0.011	0.019	0.043	0.069	—
Memory usage	36 MB	135 MB	527 MB	2.9 GB	18.1 GB	> 256 GB
Avg. Time	0.042 sec	0.21 sec	1.18 sec	8.75 sec	47.74 sec	—

Mesh Level (3d)	2	3	4	5
Avg. conv. rate	0.084	0.048	0.14	—
Memory usage	307 MB	7.3 GB	132 GB	> 256 GB
Avg. Time	0.92 sec	36.25 sec	2472 sec	—

Table 6.3: Convergence rates, memory usage and average computation time for linear solution with a monolithic direct solver.

6.2.2 Condition number analysis of the system matrices

In this section, we will analyze the condition numbers of the Jacobian \mathbf{A} and its different sub-parts. For this analysis, we consider the two benchmark problems introduced in Section 6.2. For a derivation of the system matrix, we refer to Section 4.4. Here, we shortly repeat the notation. The coupled problem consists of two matrices, \mathbf{F} for the fluid-problem and \mathbf{S} for the solid-problem, that overlap on the interface degrees of freedom. The two sub-matrices can be written as

$$\mathbf{F} = \begin{pmatrix} F_p^{div} & F_v^{div} & F_u^{div} \\ F_p^{NS} & F_v^{NS} & F_u^{NS} \\ 0 & 0 & F_u^{ALE} \end{pmatrix}, \quad \mathbf{S} = \begin{pmatrix} S_v^{ES} & S_u^{ES} \\ S_v^{uv} & S_u^{uv} \end{pmatrix}, \quad (6.3)$$

the coupled system matrix is given by

$$\mathbf{A} = \left(\begin{array}{ccc|ccc|cc} F_p^{div} & F_v^{div} & F_u^{div} & F_p^{div} & F_v^{div} & F_u^{div} & 0 & 0 \\ F_p^{NS} & F_v^{NS} & F_u^{NS} & F_p^{NS} & F_v^{NS} & F_u^{NS} & 0 & 0 \\ 0 & 0 & F_u^{ALE} & 0 & 0 & F_u^{ALE} & 0 & 0 \\ \hline F_p^{div} & F_v^{div} & F_u^{div} & F_p^{div} & F_v^{div} & F_u^{div} & 0 & 0 \\ F_p^{NS} & F_v^{NS} & F_u^{NS} & F_p^{NS} & F_v^{NS} + S_v^{ES} & F_u^{NS} + S_u^{ES} & S_v^{ES} & S_u^{ES} \\ 0 & 0 & 0 & 0 & S_{uv}^{uv} & S_u^{uv} & S_v^{uv} & S_u^{uv} \\ \hline 0 & 0 & 0 & 0 & S_v^{ES} & S_u^{ES} & S_v^{ES} & S_u^{ES} \\ 0 & 0 & 0 & 0 & S_v^{uv} & S_u^{uv} & S_v^{uv} & S_u^{uv} \end{array} \right) \quad (6.4)$$

compare also (4.31). This coupled matrix is given as the prolongation of the two sub-matrices:

$$\mathbf{A} = \mathcal{R}_f^T \mathbf{F} \mathcal{R}_f + \mathcal{R}_s^T \mathbf{S} \mathcal{R}_s.$$

The first lines of Table 6.4 show the condition number of the coupled matrix

$$\text{cond}(\mathbf{A}) = \|\mathbf{A}\|_1 \|\mathbf{A}^{-1}\|_1,$$

in the 1-norm (maximum column sum). Furthermore, we indicate the condition numbers for the solid matrix \mathbf{S} in (6.3), the main part of the Navier-Stokes system

$$\mathbf{F}^{NS} = \begin{pmatrix} F_p^{div} & F_v^{div} \\ F_p^{NS} & F_v^{NS} \end{pmatrix},$$

and the ALE extension matrix F_u^{ALE} . The latter two matrices implement homogenous Dirichlet values on the fluid-structure interface \mathcal{I} . A separate discussion of \mathbf{F}^{NS} and F_u^{ALE} is reasonable, as the system naturally decouples. All condition numbers are approximated with Matlab [222]. To avoid scaling effects (from the size of mesh elements or from problem parameters), we apply diagonal scaling before computing the condition numbers. For both benchmark problems we show the resulting condition numbers on a sequence of uniform meshes.

A first glance at the numbers in Table 6.4 reveals the expected results with a proper scaling in terms of the mesh-size. This analysis however puts forward the dramatic effect of the monolithic coupling on the conditioning of the coupled system matrix \mathbf{A} , that finally causes standard coupled multigrid solvers (with coupled multigrid smoothers) to cease work, see the introduction and Table 6.1. By a decoupling, all condition numbers are within reasonable limits. This observation will guide the design of the partitioned multigrid smoother in Section 6.4.

6.3 Krylov space solvers for fluid structure interactions

Most of the versatile and efficient iterative solution methods are Krylov subspace methods like the *Conjugate Gradient* (CG) or the *Generalized Minimum Residual Method* (GMRES) or the *Biconjugate Gradient Stabilized Method* (BiCGStab). See [203] for a general overview.

The basic idea of these methods is to approximate the solution of $\mathbf{A}_h \mathbf{x} = \mathbf{b}$ rewritten as a minimization problem

$$\|\mathbf{b} - \mathbf{A}_h \mathbf{x}^{(l)}\| \rightarrow \min,$$

Mesh Level (2d)	1	2	3	4	5
cond(\mathbf{A})	$3.30 \cdot 10^{12}$	$9.85 \cdot 10^{12}$	$4.36 \cdot 10^{13}$	$1.76 \cdot 10^{14}$	$7.40 \cdot 10^{14}$
cond(\mathbf{S})	$4.19 \cdot 10^7$	$1.49 \cdot 10^8$	$5.54 \cdot 10^8$	$1.45 \cdot 10^9$	$5.26 \cdot 10^9$
cond(\mathbf{F}^{NS})	$3.12 \cdot 10^8$	$5.78 \cdot 10^8$	$1.15 \cdot 10^9$	$2.27 \cdot 10^9$	$4.34 \cdot 10^9$
cond($F_{\mathbf{u}}^{ALE}$)	$1.85 \cdot 10^3$	$7.67 \cdot 10^3$	$2.95 \cdot 10^4$	$1.16 \cdot 10^5$	$4.59 \cdot 10^5$

Mesh Level (3d)	1	2	3
cond(\mathbf{A})	$5.25 \cdot 10^{12}$	$3.52 \cdot 10^{13}$	$1.80 \cdot 10^{14}$
cond(\mathbf{S})	$3.48 \cdot 10^5$	$2.22 \cdot 10^6$	$8.36 \cdot 10^6$
cond(\mathbf{F}^{NS})	$1.43 \cdot 10^7$	$3.25 \cdot 10^7$	$5.39 \cdot 10^7$
cond($F_{\mathbf{u}}^{ALE}$)	$7.74 \cdot 10^1$	$2.86 \cdot 10^2$	$1.62 \cdot 10^3$

Table 6.4: Condition numbers of the 2d (top) and 3d (bottom) benchmark problems for the full system matrix \mathbf{A} , the solid part \mathbf{S} , the Navier-Stokes part \mathbf{F}^{NS} and the matrix of the ALE extension $F_{\mathbf{u}}^{ALE}$ (considering harmonic extension).

in the Krylov subspaces, given by

$$K^l(\mathbf{A}, \mathbf{r}) = \{\mathbf{r}, \mathbf{A}_h \mathbf{r}, \dots, \mathbf{A}_h^{l-1} \mathbf{r}\}, \quad \mathbf{r} = \mathbf{b} - \mathbf{A} \mathbf{x}^{(0)}.$$

Krylov subspace techniques can be very efficient. The minimization problems are usually solved - or approximated - based on an orthogonalization of the Krylov spaces. The convergence rate however strongly depends on the condition number of the system matrix $\text{cond}(\mathbf{A}_h)$. For acceleration, the concept of preconditioning is applied. Instead of approximating $\mathbf{A}_h \mathbf{x} = \mathbf{b}$, one tries to solve the system

$$\mathbf{P}_h \mathbf{A}_h \mathbf{x} = \mathbf{P}_h \mathbf{b},$$

where by $\mathbf{P}_h : \mathbb{R}^n \rightarrow \mathbb{R}^n$ we denote the *preconditioner*, an operator (most often a matrix), which should be spectrally similar to \mathbf{A}_h^{-1} , such that

$$\text{cond}(\mathbf{P}_h \mathbf{A}_h) \ll \text{cond}(\mathbf{A}_h).$$

There exist general purpose preconditioners like Jacobi, Gauss-Seidel [] or incomplete decompositions of the system matrix \mathbf{A}_h . All these techniques are however not very successful in the context of fluid-structure interactions, see [] and Table 6.1 in Section 6.2, where an incomplete decomposition is not used as a preconditioner, but as a smoother within a multigrid solver.

Regarding fluid-structure interactions, a preconditioner should consider the structure of the system. Assume, that the general linear system of fsi can be written in the compact form

$$\begin{pmatrix} \mathbf{F} & \mathbf{C}_{fs} \\ \mathbf{C}_{sf} & \mathbf{S} \end{pmatrix} \begin{pmatrix} \mathbf{x}_f \\ \mathbf{x}_s \end{pmatrix} = \begin{pmatrix} \mathbf{b}_f \\ \mathbf{b}_s \end{pmatrix},$$

with a splitting into fluid-part, solid-part as well as the coupling parts. Then, the basic idea of a preconditioner would be to neglect some of the off-diagonal coupling

$$\mathbf{P} = \begin{pmatrix} \mathbf{F} & 0 \\ \mathbf{C}_{sf} & \mathbf{S} \end{pmatrix}^{-1} = \begin{pmatrix} \mathbf{F}^{-1} & 0 \\ -\mathbf{S}^{-1} \mathbf{C}_{sf} \mathbf{F}^{-1} & \mathbf{S}^{-1} \end{pmatrix}$$

Application of the preconditioner now requires multiplication with the matrix \mathbf{P} . This itself requires the solution of linear systems coming from the solid-equation \mathbf{S} and the fluid-equation \mathbf{F} . These again must be approximated with a suitable method. The large benefit of this approach however is, that smaller systems with a well known character and better conditioning have to be approximated [98]. Furthermore, by applying the partitioning in the preconditioner, it is possible to break the very bad conditioning of the coupled system, see again Section 6.2.2.

Preconditioned Krylov subspace methods (usually it is GMRES) are among the most powerful solution methods for monolithic fluid-structure interactions. For increasing robustness and efficiency, a careful design of the preconditioner is crucial. The main guideline on how to setup the matrix \mathbf{P} is given in the following Section 6.4.2 where a similar concept is analyzed in the context of multigrid solvers. Furthermore, we refer to the extensive literature on this topic [118, 240, 57, 119, 58, 15, 170].

Remark 39 (Literature on Solvers). *Most is 2d-1d or 3d-2d!!!*

6.4 Multigrid solvers for the Arbitrary Lagrangian Eulerian formulation

Another class of very efficient solvers is the multigrid method. Classic geometric multigrid methods [111, 241] are based on an approximation of the linear system on a hierarchy of levels, coming from the finite element discretization of the differential equation on a hierarchical sequence of meshes

$$\Omega_0, \Omega_1, \dots, \Omega_L = \Omega_h,$$

with its own hierarchical sequence of finite element spaces

$$V_0 \subset V_1 \subset \dots \subset V_L = V_h.$$

Geometric multigrid solvers are based on the observation, that typical iterative methods like Jacobi or Gauss-Seidel do a very bad job in solving the problem, they however are very efficient and quick in removing all high frequent error contributions. Hence, instead of “solving” the problem on the finest mesh level $\Omega_L = \Omega_h$, only high frequent error parts are removed in very few iterations of a simple iterative algorithm. The remaining error (i.e. the residual) is then restricted to the next coarse mesh level Ω_{L-1} , where this strategy is repeated. Finally, arriving at the coarsest mesh level, the remaining problem is that small, that it can efficiently be solved with help of a direct solver or a standard Krylov subspace method. So far the theory (and the reality for simple elliptic problems). In the practical application to complex multiphysics problems, several challenges appear:

1. Very often a hierarchy of meshes is not available. It is never difficult to get finer meshes (simply by refinement), if however the only mesh at hand is already very complex, e.g. coming from a mesh generator, and no coarse mesh is available, the idea of geometric multigrid fails. There are strategies of generating coarse meshes, this however is not standard [].
2. Simple iterations like Gauss-Seidel or Jacobi fail to work as smoother for problems without an elliptic character. There are robust options like iterations based on incomplete decompositions [19, 26, 142]. These however are costly and may fail for problems such

as fluid-structure interactions, see Section 6.2. For saddle-point problems, the class of Vanka smoothers [233], based on solving local subproblems is very successful. Hron, Turek and coworkers used Vanka-based smoothers in a geometric multigrid iteration with good success for 2d fluid-structure interactions [133, 185], considering 3d problems however, efficiency was reported to be lost [132].

Very often, multigrid iterations are not directly used as solvers, instead, they serve as preconditioners in outer Krylov subspace methods. This approach is promising, as multigrid iterations - due to the hierarchical setup - allow to lessen the effect of small mesh sizes on the conditioning of the system matrix, see [111]. This is also the approach, that we follow in this section. We develop a multigrid iteration for fluid-structure interactions in ALE coordinates, this iteration however will only be used as preconditioner in a Krylov subspace method as introduced in Section 6.3.

Remark 40 (Algebraic Multigrid). *A possible solution for the first issue is the concept of algebraic multigrid methods, where the hierarchy of problems is generated on the algebraic level by agglomeration of matrix entries [220]. In theory, these new methods are very robust and versatile and could serve as black-box solvers. For complex applications however, specially adapted smoothers and also agglomeration techniques must be developed.*

Gee, K  ttler and Wall [105] presented a monolithic algebraic multigrid as preconditioner for Krylov subspace iterations. Here, Gauss-Seidel splitting is applied as smoother and not for preconditioning. This change of order can help to get access to the full power of linear multigrid convergency.

This section will be devoted to the derivation of an efficient multigrid method for the preconditioning of the linear systems, that arise from the finite element discretization of fluid-structure interaction problems in Arbitrary Lagrangian Eulerian coordinates. Here, we have the setting of Chapter 4 in mind and in particular, the linear systems of equations described in Section 4.4.

The main focus will be on the design of a robust smoother, that takes the special structure of fluid-structure interactions into account.

Brummelen, et al. [55] analyzed a simplified problem with potential flow and a lower dimensional solid. Here, the authors argued, that a monolithically coupled multigrid iteration with a decoupling within the multigrid smoother only would serve as an optimal solver (convergence rates going to zero for increasing mesh-levels), if the two sub-problems in the smoother are solved exactly. In the following we want to follow this approach. The use of Vanka-type smoothers [233, 134, 133, 185] is promising, as a splitting into small subproblems is naturally given and the design and implementation is straightforward. While they show good efficiency and robustness for 2d problems [133, 185, 213], problems are reported for 3d applications [132].

Before coming to the specific solvers, we will present numerical studies on two benchmark problems.

6.4.1 GMRES multigrid iteration

In this section, we present the general layout of a multigrid preconditioned GMRES iteration for the coupled system

$$\mathbf{A}\mathbf{x} = \mathbf{b},$$

where $\mathbf{x} = (\mathbf{v}, \mathbf{u}, \mathbf{p})$ with $\mathbf{v}, \mathbf{u} \in \mathbb{R}^{2dN}$ and $\mathbf{p} \in \mathbb{R}^{N_f + N_i}$ is the vector of solution coefficients. By $\mathbf{v}_f, \mathbf{u}_f \in \mathbb{R}^{2d(N_f + N_i)}$ and $\mathbf{v}_s, \mathbf{u}_s \in \mathbb{R}^{2d(N_i + N_s)}$ we denote the overlapping (on the interface) restrictions of these vectors to the fluid- and solid degrees of freedom. \mathbf{A} is the coupled system matrix 6.4. The philosophy of the linear solver is to treat the coupled system in a monolithic manner as long as possible. The analysis in Section 6.2.2 shows, that the condition number $\text{cond}_1(\mathbf{A})$ is very large. This large condition number not only stems from the second order character of the partial differential equations, but also from the different numerical scales acting in fluid- and solid-problem. Just to highlight one example: the viscosity of water is about $10^{-3} \text{ Pa} \cdot \text{s}$, the Young's modulus of steel is $2 \cdot 10^{11} \text{ Pa}$. At the interface degrees of freedom, both equations are coupled in \mathbf{A} . Diagonal preconditioning does not significantly help to improve the condition number, see Section 6.2.2. Hence, whenever it is necessary to compute the inverse of \mathbf{A} , we will apply a splitting into fluid- and solid-part. The general outline of the solver is as follows:

1. As outer iteration to solve $\mathbf{Ax} = \mathbf{b}$ we employ a monolithic GMRES iteration, see Section 6.3.
2. The GMRES solver is preconditioned by a geometric monolithic multigrid solver.
3. The multigrid smoother is constructed as a domain decomposition iteration with a Dirichlet-Neumann coupling on the interface into solid-problem governed by \mathbf{S} and fluid-problem governed by \mathbf{F} (formulated as Dirichlet problem).
4. Each of these sub-problems is smoothed with some steps of a simple iteration, e.g. Richardson or BiCGStab [203] preconditioned with solvers of Vanka type [233, 185], or of block-ILU type [26, 142].
5. The coarse-mesh problem will be treated by a direct solution of the monolithic coupled system.

The reason for applying the partitioning in the multigrid smoother and not as outer preconditioner is motivated by two arguments: first, it has been shown by Brummelen and coworkers [55], that a partitioned smoother with exact solution of the two sub-problems is a perfect smoother for a certain class of fluid-structure interactions. Perfect here implies, that the convergence rate will go to zero for increasing number of mesh-levels. Second, it is the simple observation, that the role of the multigrid smoother is not that of finding a global solution, but it's only intend is to locally smooth high frequent error contributions. Here, global coupling conditions must not be resolved.

We assume, that a hierarchy of finite element meshes Ω_l and finite element spaces X_l is given. The classical multigrid iteration is given in a recursive fashion: the iteration itself is used to approximate the coarse mesh problems.

Algorithm 1 (Geometric Multigrid). *By Ω_l and X_l for $l = 1, \dots, L$ we denote a hierarchy of multigrid meshes and finite element spaces, by \mathbf{A}_l the hierarchy of system matrices. Let $\mathbf{x}^{(0)}$ be the initial guess and \mathbf{b} be the right hand side. Iterate for $i = 1, 2, \dots$*

$$\mathbf{x}^{(i)} = \mathcal{MG}(L, \mathbf{x}^{(i-1)}),$$

where the multigrid iteration on level l is given by

$$\begin{aligned}
 \mathbf{y} &= \mathcal{MG}(l, \mathbf{A}_l, \mathbf{b}_l, \mathbf{x}_l) : \\
 (1) \quad &\text{Pre-Smooth} & \mathbf{s}_l &= \mathcal{S}(\mathbf{A}_l, \mathbf{b}_l, \mathbf{x}_l, \nu^1), \\
 (2) \quad &\text{Residual} & \mathbf{r}_l &= \mathbf{b}_l - \mathbf{A}_l \mathbf{s}_l, \\
 (3) \quad &\text{Restrict} & \mathbf{r}_{l-1} &= \mathcal{R}(l, \mathbf{r}_l), \\
 (4) \quad &\text{Coarse-Mesh} & \mathbf{c}_{l-1} &= \mathcal{MG}(l-1, \mathbf{A}_{l-1}, \mathbf{r}_{l-1}, 0) \\
 (5) \quad &\text{Prolongate} & \mathbf{x}'_l &= \mathbf{s}_l + \mathcal{P}(l, \mathbf{c}_{l-1}) \\
 (6) \quad &\text{Post-Smooth} & \mathbf{s}'_l &= \mathcal{S}(\mathbf{A}_l, \mathbf{b}_l, \mathbf{x}', \nu^2), \\
 (7) \quad &\text{return} & \mathbf{s}'_l &.
 \end{aligned}$$

The coarse mesh problem for $l = 0$ is solved exactly

$$\mathcal{MG}(0, \mathbf{A}_0, \mathbf{b}_0, \mathbf{x}_0) := \mathbf{A}_0^{-1} \mathbf{b}_0.$$

Remark 41 (Multigrid variants). Algorithm 1 shows the so called *V-cycle*, where the multigrid iteration in step (4) is called only once to approximate the coarse mesh problem. Variants are the *W-cycle*, where two calls are applied or the *F-cycle*. See [111] or [241]. The mesh prolongation and restriction operators in steps (3) and (5) are defined as the L^2 -projections of the solution onto the next mesh level. In terms of the prolongation, this is simply the embedding and can be computed by local algebraic modifications of the coefficient vectors. Regarding the restriction, the L^2 -projection $v_l \mapsto v_{l-1}$ is - at first - a global operation, calling for an inversion of the system matrix. As however, we always restrict residuals, restriction is simplified by the following observation:

$$(r_{l-1}, \phi_i^{l-1}) = (r_l, \phi_i^{l-1}) = (b_l, \phi_i^{l-1}) - a(x_l, \phi_i^{l-1}).$$

As $V_{l-1} \subset V_l$, every test-function ϕ_i^{l-1} can be linearly combined by test-functions $\phi_{i'}^l$, such that the residual can first be evaluated on the fine mesh

$$\mathbf{r}_i^l = (b_l, \phi_i^l) - a(x_l, \phi_i^{l-1}),$$

and afterwards be transferred to the coarse mesh by local algebraic operations.

Finally, regarding locally refined meshes, different concepts of generating the multigrid hierarchy exist. In order to obtain an algorithm with optimal linear run-time, it is common to start the mesh-hierarchy in a bottom-up way: while the coarsest level Ω_0 covers the complete domain, finer mesh levels Ω_l only cover those parts, where local refinement is added. The advantage of this procedure is the reduced complexity on every mesh level. As the single mesh-levels do not cover the complete domain, it is not easily possible to treat the intermediate levels as approximations to the full problem. Furthermore, it is not trivial to realize global constraints (such as a pressure with average zero), see [19]. As an alternative, meshes can be generated in a top-down procedure, where Ω_L , the finest level is the actual finite element mesh of Ω , and where the coarser levels Ω_l are generated by coarsening. Apart from very localized refinements, this procedure is able to give optimal runtimes. As every mesh level can be considered as an approximation to the global problem, implementation and analysis is strongly simplified [19, 196, 142].

6.4.2 Partitioned multigrid smoother

Every smoothing step of the multigrid algorithm requires the approximation of the system

$$\mathbf{A}_l \mathbf{x}_l = \mathbf{b}_l.$$

For the following, we can skip the level index, as all levels cover the complete domain and can be treated in the same way. The smoothing operator

$$\mathbf{x}^{(i)} = \mathcal{S}(\mathbf{x}^{(i-1)}, \mathbf{b}), \quad i = 1, \dots, \nu,$$

is realized as a preconditioned iteration with Gauss-Seidel coupling:

1. Calculate residual of the solid problem

$$\mathbf{r}_s^{(i)} = \mathcal{R}_s(\mathbf{b} - \mathbf{A}\mathbf{x}^{(i-1)})$$

2. Solve solid problem

$$\mathbf{S}\mathbf{w}_s^{(i)} = \mathbf{r}_s^{(i)}$$

3. Update

$$\mathbf{x}^{(i-\frac{1}{2})} = \mathbf{x}^{(i-1)} + \mathcal{R}_s^T \mathbf{w}_s^{(i)}$$

4. Calculate residual of the fluid problem

$$\mathbf{r}_f^{(i)} = \mathcal{R}_f(\mathbf{b} - \mathbf{A}\mathbf{x}^{(i-\frac{1}{2})})$$

5. Solve fluid problem

$$\bar{\mathbf{F}}\mathbf{w}_f^{(i)} = \bar{\mathbf{r}}_f^{(i)}$$

6. Update

$$\mathbf{x}^{(i)} = \mathbf{x}^{(i-\frac{1}{2})} + \mathcal{R}_f^T \mathbf{w}_f^{(i)}$$

The two subproblems for solid and fluid are treated by a Dirichlet-Neumann coupling with homogenous Dirichlet values realized for velocity and deformation on the interface \mathcal{I} in the fluid matrix $\bar{\mathbf{F}}$ and the right hand side $\bar{\mathbf{r}}_f^{(i)}$ (indicated by the bar). This corresponds to assigning the kinematic coupling condition to the fluid problem and the dynamic condition to the solid problem, see Section 6.4.2. An alternative would be to treat the interface in a balanced way with a Robin condition for both subproblems. This however could deteriorate the condition numbers of the sub matrices by canceling the strict partitioning into fluid and solid. Matrix entries belonging to the interface variables would be mixed, see (6.4).

We start by describing the single fields. In a first step, we assume, that the local subproblems are solved exactly with help of a direct solver. By this intermediate construction, we will validate the smoothing property of the partitioning.

The solid problem.

The solid part in the smoothing operation asks for an approximation to the system

$$\mathbf{Sw} = \mathbf{r} \Leftrightarrow \begin{pmatrix} S_{\mathbf{v}}^{ES} & S_{\mathbf{u}}^{ES} \\ S_{\mathbf{v}}^{uv} & S_{\mathbf{u}}^{uv} \end{pmatrix} \begin{pmatrix} \mathbf{v}_{s+i} \\ \mathbf{u}_{s+i} \end{pmatrix} = \mathbf{r}_s := \mathcal{R}_s(\mathbf{b} - \mathbf{Ax}^{\text{old}}), \quad (6.5)$$

where \mathbf{x}^{old} is the old approximation. We start by analyzing the effect of this solid problem on the interface condition. Acting on the interface unknowns \mathbf{v}_i and \mathbf{u}_i only, the solid problem relates to (omitting the right hand side \mathbf{b}):

$$S_{\mathbf{v}}^{ES} \underbrace{(\mathbf{v}_i + \mathbf{v}_i^{\text{old}})}_{\mathbf{v}_i^{\text{new}}} + S_{\mathbf{u}}^{ES} \underbrace{(\mathbf{u}_i + \mathbf{u}_i^{\text{old}})}_{\mathbf{u}_i^{\text{new}}} = F_p^{NS} \mathbf{p}_i^{\text{old}} - F_{\mathbf{v}}^{NS} \mathbf{v}_i^{\text{old}} - F_{\mathbf{u}}^{NS} \mathbf{u}_i^{\text{old}}.$$

The dynamic condition constitutes itself as boundary terms in $S_{\mathbf{u}}^{ES}$, $F_{\mathbf{v}}^{NS}$ and F_p^{NS} . Hence, this iteration corresponds to the dynamic coupling condition

$$\sigma_s(\mathbf{u}^{\text{new}}) \vec{n}_s + \sigma_f(\mathbf{v}^{\text{old}}, p^{\text{old}}) \vec{n}_f = 0.$$

Alternative approaches are possible. By adding fluid-interface parts to the solid-matrix $S_{\mathbf{v}}^{ES}$, the dynamic condition would include an intermediate fluid-velocity. Gee, K  ttler and Wall [105] shift the complete interface treatment to the fluid-subproblem. Here, we strictly decouple both problems in a Dirichlet-Neumann sense in order to separate different parameter scales.

Problem (6.5) can be decoupled, as both $S_{\mathbf{v}}^{ES}$ and $S_{\mathbf{v}}^{uv}$ correspond to the mass matrix, see Section 4.4. It holds

$$a_v^{ES}(\mathbf{w}, \phi) = k^{-1}(\rho_s^0 \mathbf{w}, \phi), \quad a_v^{uv}(\mathbf{w}, \psi_s) = -(\mathbf{w}, \psi_s) \Rightarrow S_{\mathbf{v}}^{ES} = -\rho_s^0 k^{-1} S_{\mathbf{v}}^{uv}.$$

Hence, instead of solving (6.5) as one coupled system, we can approximate the solution in two sub-steps:

$$\begin{aligned} [\rho_s^0 k^{-1} S_{\mathbf{u}}^{uv} + S_{\mathbf{u}}^{ES}] \mathbf{u}_{s+i} &= \mathbf{r}_{s,\mathbf{v}} + \rho_s^0 k^{-1} \mathbf{r}_{s,\mathbf{u}}, \\ S_{\mathbf{v}}^{ES} \mathbf{v}_{s+i} &= \mathbf{r}_{s,\mathbf{v}} - S_{\mathbf{u}}^{ES} \mathbf{u}_{s+i}. \end{aligned} \quad (6.6)$$

In Section 6.4.3 we describe, how these problems can be approximated by an iterative scheme.

The fluid problem.

The fluid step

$$\bar{\mathbf{F}}\mathbf{w} = \mathbf{r} \Leftrightarrow \begin{pmatrix} F_p^{div} & \bar{F}_{\mathbf{v}}^{div} & \bar{F}_{\mathbf{u}}^{div} \\ \bar{F}_p^{NS} & \bar{F}_{\mathbf{v}}^{NS} & \bar{F}_{\mathbf{u}}^{NS} \\ 0 & 0 & \bar{F}_{\mathbf{u}}^{ALE} \end{pmatrix} \begin{pmatrix} \mathbf{p}_{f+i} \\ \mathbf{v}_{f+i} \\ \mathbf{u}_{f+i} \end{pmatrix} = \bar{\mathbf{r}}_f := \bar{\mathcal{R}}_f(\mathbf{b} - \mathbf{Ax}^{\text{old}}),$$

is modified to carry homogenous Dirichlet values for velocity and deformation on all interface nodes. This problem decouples into the ALE extension part

$$\bar{F}_{\mathbf{u}}^{ALE} \mathbf{u}_{f+i} = \bar{\mathbf{r}}_{f,\mathbf{u}}, \quad (6.7)$$

followed by the Navier-Stokes part

$$\begin{pmatrix} F_p^{div} & \bar{F}_{\mathbf{v}}^{div} \\ \bar{F}_p^{NS} & \bar{F}_{\mathbf{v}}^{NS} \end{pmatrix} \begin{pmatrix} \mathbf{p}_{f+i} \\ \mathbf{v}_{f+i} \end{pmatrix} = \begin{pmatrix} \mathbf{r}_{f,p} - \bar{F}_{\mathbf{u}}^{div} \mathbf{u}_{f+i} \\ \mathbf{r}_{f,\mathbf{v}} - \bar{F}_{\mathbf{u}}^{NS} \mathbf{u}_{f+i} \end{pmatrix}. \quad (6.8)$$

Again, we first assume, that these two problems (6.7) and (6.8) are inverted with help of a direct solver. An approximative approach is described in Section 6.4.3.

Numerical analysis of the partitioned smoother with exact subproblems.

Before presenting the final multigrid solver that avoids all direct matrix inversions, we show in Table 6.5 convergence rates, memory usage and computational times for the multigrid iteration with a partitioned smoother. On every mesh level, we use one single smoothing iteration. The different subproblems (6.6), (6.7) and (6.8), are solved with help of the direct solver UMFPACK [74]. Comparing to the results given in Table 6.3, that correspond to a monolithic direct solver for the coupled problem, we first observe, that only about half the memory is used. Further on, the average convergence rates of the linear solver are even better than those obtained with a monolithic direct solver. This is only due to the very bad conditioning, that causes significant loss of digits in applying direct inversion. Actually, we observe better convergence rates for finer meshes. This result is in accordance to the theoretical observations of Brummelen and coworkers [55].

Mesh Level (2d)	2	3	4	5	6	7
Avg. conv. rate	0.049	0.034	0.018	0.016	0.019	0.014
Memory usage	21 MB	71 MB	292 MB	1.2 GB	5.2 GB	49 GB
Avg. Time	0.07 sec	0.27 sec	1.18 sec	5.90 sec	35.93 sec	345 sec

Mesh Level (3d)	2	3	4	5
Avg. conv. rate	< 0.01	< 0.01	< 0.01	–
Memory usage	194 MB	2.1 GB	44 GB	> 256 GB
Avg. Time	2.51 sec	37.03 sec	1217 sec	–

Table 6.5: Convergence rates, memory usage and average computation time for linear solution with splitting smoother and exact subproblems.

In Table 6.5 we collect the results for the two benchmark problems. It is well seen, that the convergence rates are stable under mesh-refinement. Furthermore, convergence is very fast, in particular compared to the rates of the monolithic multigrid smoother given in Table 6.1. However we note, that the separate problems within the smoother are solved with a direct solver. Nevertheless, compared to a direct solution of the monolithic system, we could already substantially reduce the effort, as (in 3d) separate and smaller systems with three unknowns (extension) and four unknowns (Navier-Stokes and elasticity) are solved instead of one global system with seven unknowns.

6.4.3 Approximation of the subproblems

The different sub-steps described in the previous section ask for the approximation (smoothing) of subproblems for the structure (6.6), the ALE extension (6.7) and the Navier-Stokes equations in ALE formulation (6.8). For all of these problems of type $\mathbf{Ax} \approx \mathbf{b}$, we choose a simple preconditioned Richardson iteration

$$\mathbf{x}^k = \mathbf{x}^{k-1} + \mathbf{P}(\mathbf{A}^{-1})(\mathbf{b} - \mathbf{Ax}^{k-1}), \quad k = 1, 2, \dots, K,$$

Mesh Level (2d)	2	3	4	5	6	7
Avg. conv. rate	0.078	0.042	0.043	0.040	0.048	0.054
Memory usage	17 MB	42 MB	142 MB	540 GB	2.1 GB	8.8 GB
Avg. Time	0.10 sec	0.43 sec	1.89 sec	8.47 sec	38.22 sec	171.92 sec

Mesh Level (3d)	2	3	4	5
Avg. conv. rate	0.049	0.052	0.059	0.068
Memory usage	115 MB	510 MB	4.5 GB	27 GB
Avg. Time	0.48 sec	4.10 sec	42.90 sec	401.2 sec

Table 6.6: Convergence rates, memory usage and average computation time for linear solution with splitting smoother and iterative smoother in subproblems.

with $\mathbf{x}^0 = 0$ and usually with $K = 4$. As preconditioner we choose a stabilized incomplete lower-upper decomposition of the Matrix \mathbf{A} . This decomposition is performed in a block-wise sense. All degrees of freedom coupling in one node are strongly coupled. For the Navier-Stokes part (in three dimensions), this corresponds to small 4×4 blocks coupling pressure and the three velocities. For stabilization, we strengthen the diagonal by adding the weighted sum of all off-diagonals. This approximation is well suited as smoothing operation for various complex problems, see [20, 25, 26, 49, 142] for description of the smoother and application to different problems. It is possible to use stronger iterations for enhancing the smoothing process.

The idea of this smoother can be seen as a mixture of Vanka-smoother and ILU-smoother. It is stronger, than a Vanka-smoother with Jacobi- or Gauss-Seidel coupling, as the inversion of the local blocks is embedded into an incomplete decomposition of the matrix. On the other hand, we use smaller block-sizes coupling only the degrees of freedom in single nodes (and not even those of one element). It will be worthwhile to analyze different smoothers for the sub-problems, as standard Vanka-smoothers will be better suited for parallelization [185, 213].

Lastly, we use the final iteration algorithm with the outer GMRES iteration, a geometric multigrid iteration with a partitioned Dirichlet-Neumann smoother using iterative approximation for the subproblems to solve both benchmark problems.

In Table 6.6, we report on the performance of the multigrid solver with split smoothing and approximate solution of the subproblems as described in Section 6.4.3. The first glance shows three desired effects: the convergence rates are nearly robust with respect to the mesh size, memory usage is optimal (linear), and the computational time is nearly linear. Comparing the results of Table 6.6 with those for the standard multigrid solver in Table 6.1 or those using the direct solver in Table 6.3, we see a substantial improvement in both memory consumption and computational costs.

In Figure 6.2 we show a comparison of the memory performance of the different approaches. Here, we observe a great benefit of the splitting approach within the smoother and the avoidance of direct solvers, that always bring along fill-ins. Regarding the 3d problems, we observe a substantial improvement of the final multigrid solver with regard to the standard multigrid solver of GASCOIGNE 3D [23, 142]. This stems from the reduction of the overall matrix size: instead of one global 7×7 matrix, we only deal with smaller sub-matrices on either the fluid-

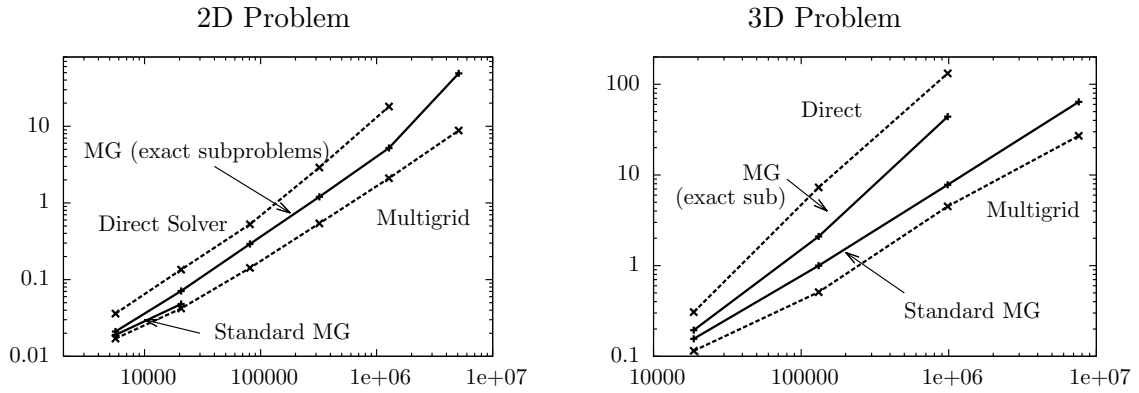


Figure 6.2: Memory usage in Gigabyte for the different solvers. 2D problem in left column and 3D problem in right one. The final multigrid solver shows linear memory consumption of about 1.8 Kilobyte per unknown for the 2d-problem and 4 Kilobyte per unknown in the 3d-case.

or the solid-domain. The memory savings compared to direct solvers are dramatic, both for 2d and 3d problems.

Figure 6.3 shows a similar comparison regarding the average computational time required for solving the linear systems. Here, the similar performance of all methods in case of the 2d problem is a striking result. In particular the excellent performance of the direct solver UMFPACK [74] must be appreciated. This result is even more surprising, as Figure 6.2 does show a significant and non-optimal increase of memory usage. Regarding the 3d test case, there is a substantial discrepancy between the different solver's performance. Direct inversion of the global matrix or use of direct solvers within the smoother process immediately ruins the performance. The standard multigrid solver of GASCOIGNE 3D [23, 142] shows a good performance, that is however sub-optimal, as the convergence rates deteriorates on fine meshes, see Table 6.1. Only the final multigrid solver based on partitioned smoothing operations shows a nearly optimal (linear) scaling.

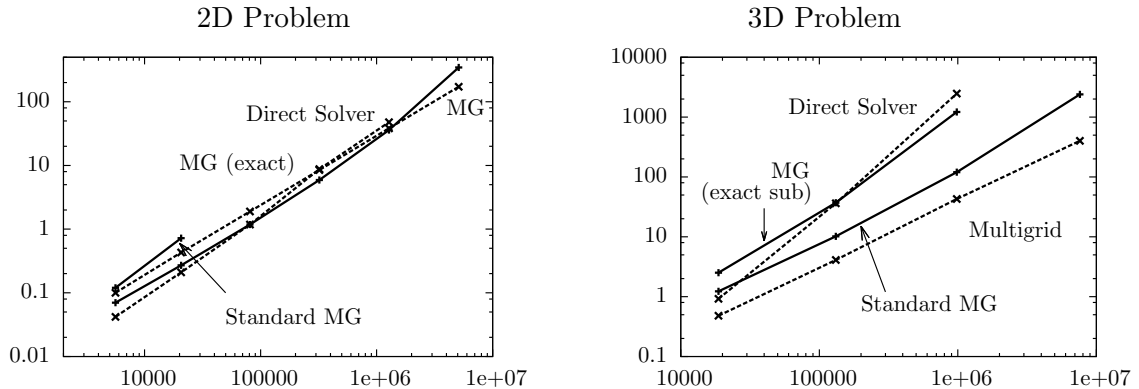


Figure 6.3: Computational time in seconds (lower row) for the different solvers. 2D problem in left column and 3D problem in right one. Nearly linear run-time for the final multigrid solver in 3D. In 2d, similar performance of all solvers.

In Figure 6.4 we show a detailed analysis on the number of Newton- and GMRES-steps required in every time-step for two different meshes. Both iteration counts do not depend on the mesh-level. In most of the iterations, exactly four Newton-steps are required. About 6 GMRES iterations are needed in every cycle of the Newton method, such that we totally use about 25 step of the linear solver in every time-step.

Remark 42 (Numerical studies in the literature). *The two dimensional example discussed by Gee, K ttler and Wall in Section 8.2 of [105] is comparable to the 2d-benchmark problem. Both configurations describe the self-excited motion of a flexible beam in a laminar flow. The authors [105] used a discretization with about 80 000 degrees of freedom, similar to mesh-level 4, see Table 6.1. On this mesh, the geometric multigrid solver with partitioned smoother requires an average of 1.89 seconds in every time-step. An average of 5 Newton steps in every time-steps results in 9.5 seconds per time-step compared to an average of 7 seconds taken from [105]. In Figure 6.4, we show the number of Newton steps and GMRES iterations required in each time-step. Here, we show the results belonging to the discretization with 80 960 and the discretization with 320 640 degrees of freedom. A direct comparison is difficult, as the authors of [105] used a Newton tolerance of 10^{-4} vs. 10^{-8} in my work. Furthermore, the results in [105] have been obtained by a parallel solver on 4 cores, whereas the present results use single core performance only.*

In [170] (Section 4.3.1) the authors investigate a partitioned scheme as preconditioned for a monolithic GMRES iteration. Comparable to Section 6.4.2, the authors investigate the performance of their solver, if all sub-systems are solved by direct inversion. They show nearly robust and good convergence rates. However, in contrast to the results shown in Table 6.5, convergence does not improve on finer meshes. This supports the assumption, that a multigrid solver with a partitioned smoother (with exact solution of the subproblem) shows better robustness as preconditioner to a GMRES iteration, than a preconditioner, that is based on a partitioned iteration. Again, we refer to [55], where exactly this relation was shown for a linear model problem.

6.4.4 Robustness versus problem parameters

Next, we have a look at the robustness of the partitioned smoother with regard to different problem parameters. For example variations in the density ratio ρ_f/ρ_s could lead to instabilities due to the *added-mass effect* [231, 232, 64]. In Table 6.7, we modify different parameters in separate computations. All remaining settings are kept as in the standard configuration, see Table 6.2. All computations are carried out on mesh-level three with 131 495 unknowns. We indicate the average linear convergence rate over a total of 20 time steps. The results collected in Table 6.7 show good robustness of the multigrid smoother. It is able to handle large variations of the density ratio as well as variations in the fluid velocity (that will lead to variation of the Reynolds number). Further, we are able to cover nearly incompressible materials without breakdown of the smoother. This will stem from the fact, that the partitioned smoother operation is based on incomplete block-wise decomposition of the matrices, that initially was designed for incompressible flows, see [20, 142]. A dramatic effect on the convergence rate is only found for the very small shear modulus $\mu_s = 1.4 \cdot 10^5$, that belongs to a very soft material. This choice results in very large deformation at the base Γ_{base} , where the elastic obstacle is attached to the fluid domain, see Figure 6.1.

Fluid density ρ_f	0.001	0.01	0.1	1
Convergence rate	0.047	0.050	0.046	0.047
Average inflow velocity \bar{v}_{in}	1 m/s	2 m/s	4 m/s	8 m/s
Convergence rate	0.047	0.045	0.045	0.046
Shear modulus μ_s	$2 \cdot 10^5$	$2 \cdot 10^6$	$2 \cdot 10^7$	$2 \cdot 10^8$
Convergence rate	0.092	0.047	0.045	0.045
Poisson's ratio ν_s	0.1	0.2	0.4	0.49
Convergence rate	0.048	0.049	0.047	0.046

Table 6.7: Convergence rate of the multigrid solver with partitioned smoother depending on variation of different problem parameters. 3d-benchmark problem on a mesh with 131 495 unknowns.

pre - post	0	1	2
0	—	0.047	0.048
1	0.052	0.039	0.023
2	0.050	0.022	0.031

Table 6.8: 3d-benchmark problem on a mesh with 131 495 unknowns. Convergence rates of the multigrid solver depending on the number of pre- and post-smoothing steps.

6.4.5 Analysis of the iterative smoother

In this section, we will take a closer look at the performance of the iterative smoothing process. Altogether, the solution strategy requires a multitude of different parameters. In the previous analysis we chose the values

1. Newton tolerance of 10^{-8} and assembly of system matrix, if Newton's reduction rate is worse than 10^{-1} .
2. Relative tolerance of linear solver of 10^{-4} .
3. Multigrid with direct solution on the coarse mesh. One step of post-smoothing and no pre-smoothing in case of the splitting smoother, four steps of pre- and post-smoothing for the standard monolithic ILU smoother.
4. In the case of the iterative approximation of the subproblems, four steps of an ILU-preconditioned Richardson iteration for each of the three subproblems.

Table 6.8 compares different numbers of pre- and post-smoothing steps in the multigrid iteration. Here, this corresponds to the number of Gauss-Seidel iterations described in Section 6.4.2. The effect of increasing the number of iterations in the smoother is very little. This result corresponds to the findings of Brummelen and coworkers [55] and the results presented in Section 6.4.2, dealing with the partitioned smoother based on exact solution of the subproblems: if these are approximated with sufficient accuracy, one step of post-smoothing is sufficient to yield good and robust convergence, see Table 6.5.

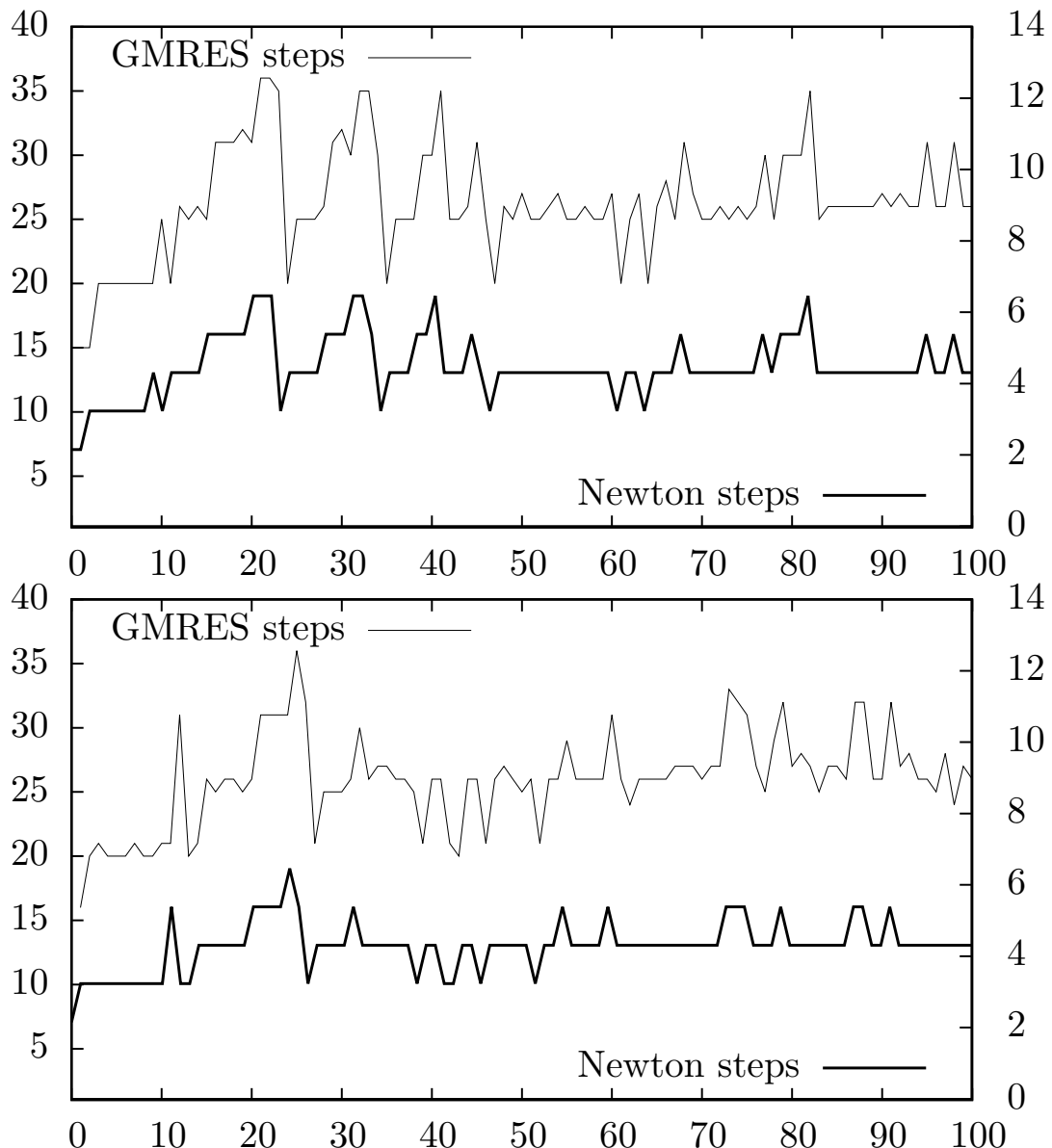


Figure 6.4: Number of GMRES (left) and Newton (right) iterations in every time-step. Upper figure: problem with 80 960 unknowns on mesh level 4. Lower figure: problem with 320 640 unknowns on mesh level 5.

7 Error Estimation and Adaptivity

This chapter is devoted to a posteriori error estimation and adaptivity. Error estimators can help to judge the quality of simulation results and serve as stopping criteria for our algorithms. In the following Section 7.1 we will start by gathering the basics of a posteriori error estimation in the finite element method. As we aim at the application to complex problems like fluid-structure interactions, the main target will be efficiency and ease of realization. Error estimation will be based on the *Dual Weighted Residual Method*, that has been developed by Becker and Rannacher [28, 29] as a very flexible tool to estimate errors in *goal functionals* of the solution, that can be any kind of output values, such as the deformation of a solid-point, the wall stress on an elastic obstacle or the vorticity in a flow field. What follows in Section 7.2 is an overview of methods that can be used to control the quality of the spatial discretization. In the finite element method, this refers to the refinement (or the coarsening) of the underlying triangulation. Control of the temporal discretization, i.e. the choice of optimal time-step sizes is the topic of Section 7.1.2. Finally, in Section 7.3, we describe the application of all these methods to coupled fluid-structure interaction problems.

7.1 A posteriori error estimation

We start by discussing estimators for the discretization error $u - u_h$ of finite element solution. Such error estimators are important to guarantee, that a computed solution $u_h \in X_h$ satisfies a required error bound, e.g. a relative error of

$$\frac{\|u - u_h\|}{\|u\|} \leq 1\%,$$

one percent. The *a priori* estimators derived in Section 3.2.2 or 3.3 have the drawback of involving constants, from interpolation estimates, trace inequality or inverse inequalities, whose values are usually not known. If an error bound of one percent is to be reached, it will make a considerable difference, if such a constant is 10 or 0.1.

The aim of *a posteriori* error estimates is to derive error bounds, that involve as few unknown quantities as possible. Instead, a posteriori estimates make use of the already computed discrete approximation $u_h \in X_h$.

A posteriori error estimation in the context of Finite Elements has a long history. At the beginning, mostly the Laplace equation

$$-\Delta u = f \text{ in } \Omega, \quad u = 0 \text{ on } \Gamma = \partial\Omega,$$

has been studied, which allows direct access to estimating the error in the energy norm with help of the residual

$$\|\nabla(u - u_h)\| = \sup_{\phi \in H_0^1(\Omega)} \frac{R(u_h)(\phi)}{\|\nabla\phi\|}, \quad R(u_h)(\phi) := (f, \phi) - (\nabla u_h, \phi).$$

Using this error representation, the following simple *residual based energy norm estimator* can be derived

$$\|\nabla(u - u_h)\| \leq c_i \left(\sum_{K \in \Omega_h} h_K^2 \|f + \Delta u_h\|_K^2 + \frac{h_K}{4} \|[\vec{n} \cdot \nabla u_h]\|_{\partial K}^2 \right)^{\frac{1}{2}}, \quad (7.1)$$

where by h_K we denote the diameter of the element $K \in \Omega_h$ and by $[\vec{n} \cdot \nabla u_h]_e$ the jump of the (discontinuous) normal derivative $\vec{n} \cdot \nabla u_h$ across the elements edge $e \subset \partial K$. The constant $c > 0$ mainly depends on the constant of the interpolation operator and the topological layout of the finite element mesh. This estimator is proven to be *robust*, which means that the estimator

$$\eta_h(u_h) := \left(\sum_{K \in \Omega_h} h_K^2 \|f + \Delta u_h\|_K^2 + \frac{h_K}{4} \|[\vec{n} \cdot \nabla u_h]\|_{\partial K}^2 \right)^{\frac{1}{2}},$$

really bounds the error (up to the constant c)

$$\|\nabla(u - u_h)\| \leq c \eta_h(u_h),$$

and furthermore, it is sharp up to higher order oscillations in the data

$$\eta_h(u_h) \leq c \|\nabla(u - u_h)\| + c \left(\sum_{K \in \Omega_h} h_K^2 \|f - f_K\|_K^2 \right)^{\frac{1}{2}}, \quad f_K = \frac{1}{|K|} \int_K f(x) \, dx.$$

By $f_K \in \mathbb{R}$ we denote a piece-wise constant approximation to f . This *data oscillation* term is of higher order. If $f \in H^1(\Omega)$, we can expect $\|f - f_K\|^2 \leq ch^2$. For details on residual based error estimators for elliptic problems, we refer to the literature [11, 6, 1, 235]

Estimators of residual type have been extended to different problems including transport, to flow problems [2] to general conservation laws [140], to Eigenvalue problems [173] to elasto-plasticity [183] and many more.

Classical residual estimators are based on the estimation in the energy norm. By means on duality, the *Aubin Nitsche Trick*, an estimation in the L^2 -norm is at hand:

$$-\Delta z = \frac{u - u_h}{\|u - u_h\|} \quad \Rightarrow \quad \|u - u_h\| = R(u_h)(z),$$

where by $R(u_h)(z)$ we again denote the residual. This approach has been carried over to a more general setting by [87]. Adjoint solutions, which are introduced to express the error in different functionals $j : H^1(\Omega) \rightarrow \mathbb{R}$,

$$-\Delta z = j,$$

are further on estimated to achieve computable error bounds. Becker and Rannacher [28, 29] then advanced this technique to a computational method, where adjoint solutions to arbitrary functionals are not analytically estimated, but where they are approximated by means of finite element discretizations and enter the error estimate as weights, such that the computable estimator for a functional error takes the form

$$|J(u - u_h)| \leq c \eta_h(u_h, z_h).$$

In the following, we will outline this error estimation technique, that is very versatile and has found much attention in literature [2, 155, 182, 24, 106, 234, 30, 116] and many more.

In the following, we shortly recapitulate the idea behind the *Dual Weighted Residual Method* (DWR) for error estimation. In Section 7.1.1 we start by discussing the linear case and quickly proceed to general nonlinear problems. Then, in Section 7.1.1 we show, how this idea can be transferred to non-stationary problems, that first have to be cast into a Galerkin formulation, see also Section 3.1.3.

7.1.1 The Dual Weighted Residual Method

Considering linear problems, the Dual Weighted Residual method for error estimation is a direct application of the Aubin Nitsche Trick to general linear error functional on the right hand side of the adjoint problem. The nonlinear theory, that gives us an error approximation for general nonlinear problems and nonlinear functions is based on an optimization approach. We start with the linear case.

Linear Problems

For the beginning, we consider an elliptic diffusion-reaction-transport equation given by the variational formulation

$$u \in \mathcal{V} := H_0^1(\Omega) : \quad A(u, \phi) = F(\phi) \quad \forall \phi \in \mathcal{V}, \quad (7.2)$$

where

$$A(u, \phi) = (\nabla u, \nabla \phi) + (\beta \cdot \nabla u, \phi) + (\alpha u, \phi), \quad F(\phi) = (f, \phi), \quad (7.3)$$

with a constant $\alpha \geq 0$ and a differentiable transport field $\beta \in C^1(\Omega)^d$ that satisfies

$$\|\operatorname{div} \beta\|_{L^\infty(\Omega)} \leq 2\alpha. \quad (7.4)$$

For every $f \in H^{-1}(\Omega)$, this equation has a unique solution, that satisfies $\|\nabla u\| \leq c\|f\|_{-1}$. Higher regularity of f , the domain and the transport field carries over to higher regularity in the solution. We aim at estimating the error $u - u_h$ not in global norms, but rather different functionals of the solution like the error in a single point of interest

$$J_a(u - u_h) = u(a) - u_h(a), \quad a \in \Omega, \quad (7.5)$$

the average error in the complete domain

$$J_\Omega(u - u_h) = \int_\Omega u(x) - u_h(x) \, dx, \quad (7.6)$$

or the average over a subdomain $\Omega_1 \subset \Omega$

$$J_{\Omega_1}(u - u_h) = \int_{\Omega_1} u(x) - u_h(x) \, dx, \quad (7.7)$$

or many more. Such error functionals can be very general, they should however be well-defined on the solution space $\mathcal{V} = H_0^1(\Omega)$, i.e., the functional should be an element of the dual space

$J \in \mathcal{V}^* = H^{-1}(\Omega)$. In two or more spatial dimensions, point-values are not well-defined, such that a functional like (7.5) has to be regularized

$$J_{a,\epsilon}(u - u_h) = \frac{1}{\pi\epsilon^2} \int_{B_\epsilon(a)} u(x) - u_h(x) dx, \quad B_\epsilon(a) = \{x \in \Omega, |x - a| < \epsilon\}. \quad (7.8)$$

Remark 43 (Point Errors). *From a analytical point of view, point functionals are not well-posed in an H^1 -sense and should be regularized in terms of (7.8). In practical realizations however, the evaluation of such an integral for ϵ very small is cumbersome. Hence, usual implementations simply evaluate in the single point. Given sufficient regularity of the data, e.g. $f \in H^1(\Omega)$, solutions to elliptic problems will have sufficient regularity (away from the boundary), such that point values are well defined.*

Lemma 81 (Adjoint problem). *Let $J \in H^{-1}(\Omega)$. The adjoint problem*

$$z \in \mathcal{V} : \quad A(\phi, z) = J(\phi) \quad \forall \phi \in \mathcal{V}, \quad (7.9)$$

where $A(\cdot, \cdot)$ is given as in (7.3), (7.4) has a unique solution $z \in \mathcal{V}$ with

$$\|\nabla z\| \leq c\|J\|_{H^{-1}(\Omega)}.$$

Given sufficient regularity $z \in \mathcal{V} \cap H^2(\Omega)$ and $J \in L^2(\Omega)^*$, the adjoint solution is given by the classical formulation

$$-\Delta z - \beta \cdot \nabla z + (\alpha - \operatorname{div} \beta)z = j,$$

where $j \in L^2(\Omega)$ is defined as

$$(j, \phi) = J(\phi) \quad \forall \phi \in L^2(\Omega).$$

Proof. As $z \in H_0^1(\Omega)$ has homogenous Dirichlet values, for $\phi = z$ it holds

$$A(z, z) = \|\nabla z\|^2 + \left(\alpha - \frac{\operatorname{div} \beta}{2} \right) \|z\|^2 \geq c\|\nabla z\|^2,$$

where we used the identity $(\beta \cdot \nabla z, z) = -(\beta \cdot \nabla z, z) - ((\operatorname{div} \beta)z, z)$, as boundary terms are zero. Together with the continuity of the form $A(\cdot, \cdot)$ we get existence of unique solutions with Lax Milgram. Integration of parts further gives

$$A(\phi, z) = (\phi, -\Delta z - \beta \cdot \nabla z + (\alpha - \operatorname{div} \beta)z)$$

the classical formulation. \square

The regularity of the adjoint solution z depends on the regularity of the domain Ω , the problem data, here α and β , and the regularity of the right hand side j , or J . We have already discussed, that for the point error it holds $J_a \notin H^{-1}(\Omega)$. For the regularized point error with $\epsilon > 0$ fixed and for the subdomain functional, we can write

$$J(\phi) = \frac{1}{\pi\epsilon^2} \int_{B_\epsilon(a)} \phi(x) dx = \frac{1}{\pi\epsilon^2} \int_{\Omega} \chi_{B_\epsilon(a)}(x) \phi(x) dx,$$

where by $j = \chi_{\Omega_1}$ we denote the characteristic function with respect to a subdomain

$$\chi_{\Omega_1}(x) = \begin{cases} 1 & x \in \Omega_1 \\ 0 & x \notin \Omega_1 \end{cases}.$$

Given sufficient regularity of Ω_1 's boundary, e.g. being Lipschitz, it holds $\chi_{\Omega_1} \in L^2(\Omega)$, but in general, for $\Omega_1 \neq \Omega$ we have $\chi_{\Omega_1} \notin H^1(\Omega)$. Hence, for subdomain-type functionals, we can conclude

$$J_{\Omega_1}, J_{a,\epsilon} \in L^2(\Omega)^*, \quad j_{\Omega_1}, j_{a,\epsilon} \in L^2(\Omega).$$

With sufficient regularity of the domain, α and β , we can expect

$$z \in H^2(\Omega), \quad \|z\|_{H^2(\Omega)} \leq c_s \|j\|_{L^2(\Omega)}. \quad (7.10)$$

For the subdomain- or the point-functional it holds

$$\|j_{a,\epsilon}\|_{L^2(\Omega)} = \frac{1}{\sqrt{\pi\epsilon}}, \quad \|j_{\Omega_1}\|_{L^2(\Omega)} = \sqrt{|\Omega_1|}. \quad (7.11)$$

The global average corresponds to the adjoint right hand side $j_\Omega = 1$ with $j_\Omega \in C^\infty(\Omega)$. Given sufficient regularity of the problem data, we can expect any regularity of z

$$\|z\|_{H^{k+2}(\Omega)} \leq c_s \|j_\Omega\|_{H^k(\Omega)} = c_s \sqrt{|\Omega|}. \quad (7.12)$$

Following [28, 29] the following simple error identities for the functional error hold:

Theorem 14 (Dual Weighted Residual Method for linear problems). *Let $J \in H^{-1}(\Omega)$ be a given error functional. Let $u \in \mathcal{V}$ and $u_h \in V_h$ be solutions to*

$$A(u, \phi) = F(\phi) \quad \forall \phi \in \mathcal{V}, \quad A(u_h, \phi_h) = F(\phi_h) \quad \forall \phi_h \in V_h,$$

and $z \in \mathcal{V}$ and $z_h \in V_h$ be the adjoint solutions

$$A(\phi, z) = J(\phi) \quad \forall \phi \in \mathcal{V}, \quad A(\phi_h, z_h) = J(\phi_h) \quad \forall \phi_h \in V_h,$$

The following error identities hold for arbitrary $\phi_h \in V_h$:

$$\begin{aligned} J(u - u_h) &= F(z - \phi_h) - A(u_h, z - \phi_h), \\ J(u - u_h) &= J(u - \phi_h) - A(z_h, u - \phi_h). \end{aligned} \quad (7.13)$$

Proof. We choose $\phi = u - u_h$ in (7.9) to get with Galerkin orthogonality and with (7.3)

$$J(u - u_h) = A(u - u_h, z) = A(u - u_h, z - \phi_h) = F(z - \phi_h) - A(u_h, z - \phi_h).$$

The second estimate follows, by using Galerkin orthogonality of the adjoint problem:

$$A(u - u_h, z) = A(u - u_h, z - z_h) = A(u - \phi_h, z - z_h) = J(u - \phi_h) - A(u - \phi_h, z_h).$$

□

If we analytically know details about the adjoint solution like (7.10), (7.11) or (7.12), we can use the error identity to estimate

$$\begin{aligned} J(u - u_h) &\leq A(u - u_h, z - i_h z) \leq c_A \|\nabla(u - u_h)\| \|\nabla(z - i_h z)\| \\ &\leq c_A h^r \|f\|_{H^{r-1}(\Omega)} c h^k \|z\|_{H^{k+1}(\Omega)}, \end{aligned}$$

where $c_A > 0$ is the constant of the continuity estimate, r the degree of the finite element approach (assuming maximum regularity of u) and where k depends on the regularity of the adjoint solution. For the cases above, we get

$$|J_{\Omega_1}(u - u_h)| \leq c(\Omega_1)h^{r+1}\|f\|_{H^{r-1}(\Omega)}, \quad |J_{\Omega}(u - u_h)| \leq ch^{2r}\|f\|_{H^{r-1}(\Omega)}.$$

Such an estimate however does not consider the local structure of the adjoint solution. In case of the point error, this coarse estimate would result in $|J(u - u_h)| \rightarrow \infty$ for $\epsilon \rightarrow \infty$ (which in most cases is wrong). In further cases, where an a priori estimate of the adjoint solution is not easily possible, one can just approximate the estimator weight by computing a numerical approximation to the adjoint solution \tilde{z}_h .

Considering the estimate in Theorem 14, direct use of the primal finite element space $z_h \in V_h$ is no option, as this would result in the approximation

$$J(u - u_h) = F(z - \phi_h) - A(u_h, z - \phi_h) \approx F(z_h - \phi_h) - A(u_h, z_h - \phi_h) = 0.$$

In literature [29, 196, 194], various approaches for the approximation of the weights $z - \phi_h$ are discussed. One straightforward and often used possibility is to compute the discrete adjoint solution in a finer finite element space, e.g.

$$\tilde{z}_h = z_h^{(2)} \in V_h^{(2)}, \quad \tilde{z}_h = z_{h/2} \in V_{h/2},$$

the spaces of double polynomial degree or the same-degree space on a finer mesh. In both cases the approximation $z - \phi_h \approx \tilde{z}_h - i_h \tilde{z}_h$, where i_h is the interpolation into V_h gives very satisfactory results [] and leads to the fully computable error approximation

$$J(u - u_h) \approx \eta_h(u_h, \tilde{z}_h) := F(\tilde{z}_h - i_h \tilde{z}_h) - A(u_h, \tilde{z}_h - i_h \tilde{z}_h).$$

The DWR method is not an error estimator, but must be regarded as an error approximation. We cannot guarantee $|J(u - u_h)| \leq c|\eta_h|$. Furthermore, which is unusual in the context of error estimation, the DWR method approximates also the sign of the error. To measure the quality of the DWR estimator, we introduce the *effectivity index* eff_h as the ratio between error estimate and error :

$$\text{eff}_h := \frac{\eta_h}{J(u - u_h)}. \tag{7.14}$$

In the limit $h \rightarrow 0$, a good error approximation should give $\text{eff}_h \rightarrow 1$. For any approximation \tilde{z}_h to z , we get the estimate

$$\text{eff}_h = \frac{\eta_h}{J(u - u_h)} = 1 + \frac{\eta_h - J(u - u_h)}{J(u - u_h)} = 1 + \frac{F(z - \tilde{z}_h) - A(u_h)(z - \tilde{z}_h)}{F(z - z_h) - A(u_h)(z - \tilde{z}_h)},$$

and the effectivity depends on the ratio

$$\frac{\|\nabla(z - \tilde{z}_h)\|}{\|\nabla(z - z_h)\|} = O(h^\alpha).$$

If we can show convergence with $\alpha > 0$, the estimator is asymptotically exact.

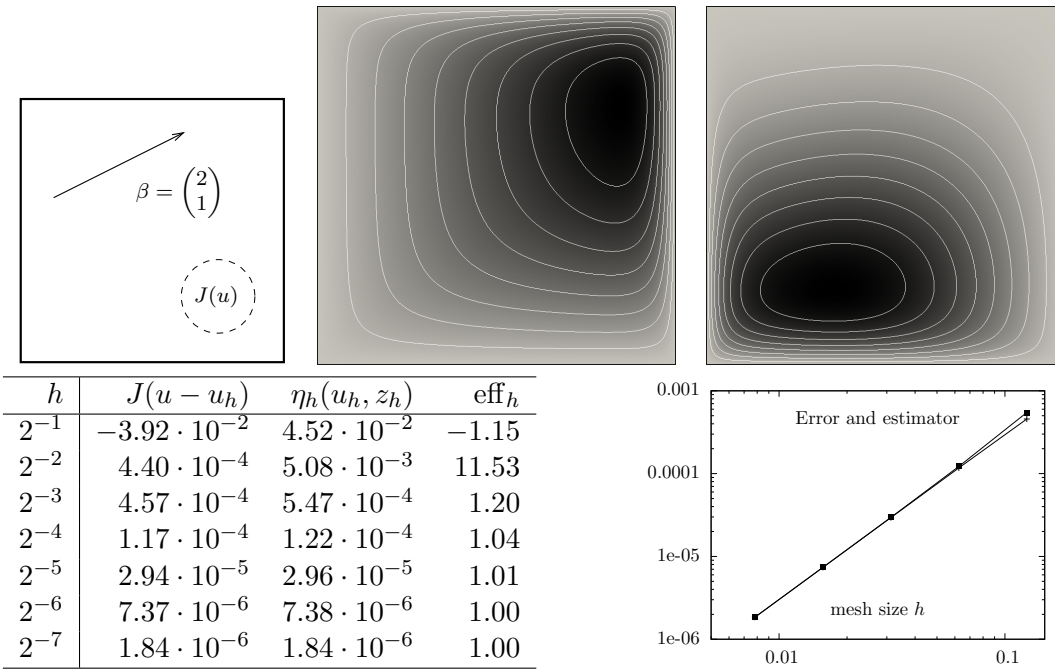


Figure 7.1: Example ???. Upper row: configuration (left), primal solution u_h (middle) and adjoint solution z_h (right). Lower row: error, estimator values and effectivity index on a sequence of meshes.

Example 2 (DWR method for elliptic problems). We consider the diffusion transport equation

$$u \in H_0^1(\Omega) : \quad (\nabla u, \nabla \phi) + (\beta \cdot \nabla u, \phi) = (f, \phi) \quad \forall \phi \in H_0^1(\Omega),$$

on the unit square $\Omega = (0, 1)^2$, with the transport field

$$\beta = \begin{pmatrix} 2 \\ 1 \end{pmatrix},$$

and the right hand side $f \equiv 1$. By $X_h \subset H_0^1(\Omega)$ we denote the space of linear finite element on a uniform mesh with mesh size h and by $u_h \in X_h$ the discrete solution. As error quantity, we consider the average of the solution over a subdomain $\Omega_0 \subset \Omega$

$$J(\phi) = \int_{\Omega_0} \phi \, dx, \quad \Omega_0 = \left\{ (x, y) \in \Omega, \left| x - \frac{1}{2} \right| < \frac{1}{8}, \quad \left| y - \frac{1}{4} \right| < \frac{1}{8} \right\}$$

The adjoint problem is given by

$$z \in H_0^1(\Omega) : \quad (\nabla \phi, \nabla z) + (\beta \cdot \nabla \phi, z) = J(\phi) \quad \forall \phi \in H_0^1(\Omega),$$

and it corresponds to the diffusion transport problem with opposite transport direction

$$z \in H_0^1(\Omega) : \quad (\nabla z, \nabla \phi) - (\beta \cdot \nabla z, \phi) = J(\phi) \quad \forall \phi \in H_0^1(\Omega).$$

By $z_h^{(2)} \in X_h^{(2)}$ we denote the Galerkin solution of the adjoint problem with polynomials of degree two. In Figure 7.1, we show both the solution u_h and adjoint solution $z_h^{(2)}$ of this problem. Further, we show the values of true error $J(u - u_h)$, error estimator $\eta_h(u_h, z_h^{(2)})$ and effectivity index eff_h . It can be well seen, that the error estimator is highly accurate.

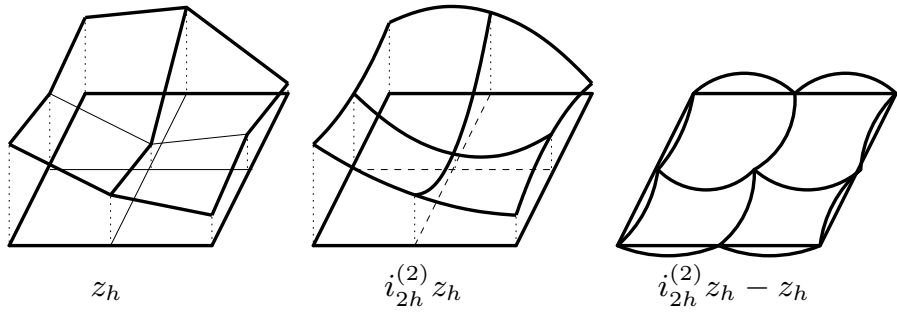


Figure 7.2: Approximation of the weights $z - I_h z \approx \tilde{z}_h - I_h \tilde{z}_h$ by a higher order reconstruction of the adjoint solution $z_h \in V_h$ be means of interpolation into a higher-order coarse-mesh space $i_{2h}^{(2)} : V_h \rightarrow V_{2h}^{(2)}$.

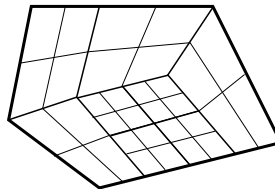


Figure 7.3: Mesh with a patch-structure: four adjacent elements each arise from uniform refinement of one father-element.

While this estimator shows very good performance, its usability is doubtful, as the effort for evaluation of the error estimator is higher than the effort for solving the problem itself. If one solves the adjoint problem with double polynomial degree, this high accuracy is also desirable for the primal solution u_h itself. Then however, we need an even higher order in the adjoint problem to get good estimator accuracy.

An alternative scheme for getting higher order approximation of $z \in V$ is by enriching $z_h \in V_h$ with local sub-problems on small parts of the mesh:

$$z_h^i \in V_h^*(P_i), \quad a(\phi_h^i, z_h + z_h^i) = J(\phi_h^i) \quad \forall \phi_h^i \in V_h^*(P_i),$$

where P_i is a set of some mesh elements $P_i = \{K_i^1, \dots, K_i^m\}$ of the mesh Ω_h . One possibility for choosing these patches is to combine all elements, that have one common node $x_i \in \Omega_h$ in common. On the outer boundary of P_i the sub-problem can be solved with either homogenous Neumann or Dirichlet boundary conditions for the enrichment z_h^i . For details, we refer to the literature [121]. One benefit of this local approach is that the small sub-problems can be solved in parallel, and that high order polynomials can be considered without large additional costs. As for $\phi_h := I_h z$ the weights can be regarded as interpolation errors $z - I_h z$, which are local error quantities only, a local enrichment by small sub-problems is well justified.

A third possibility for approximating $z - I_h z$ frequently used in literature [44, 188] is by a local reconstruction procedure. First, the discrete adjoint problem is solved in the primal trial-space $z_h \in V_h$. Then, mesh-elements of Ω_h are combined to larger patches, e.g. 2×2 elements $K \in \Omega_h$ form one patch $P \in \Omega_{2h}$. The discrete adjoint solution z_h is reinterpreted as a higher order solution $z_{2h}^{(2)} \in V_{2h}$ on a coarser mesh Ω_{2h} . If the mesh already features this

patch-structure, see e.g. Figure 7.3, this reconstruction is simply done by a local replacement of the basis functions

$$z_h(x) = \sum_{i=1}^N \vec{z}_i \phi_h^i(x) \xrightarrow{z_{2h}^{(2)} = I_{2h}^{(2)} z_h} z_{2h}^{(2)}(x) = \sum_{i=1}^N \vec{z}_i \phi_{2h}^{(2),i}(x).$$

See Figure 7.2 for this construction. A theoretical justification of this reconstruction process is by super-approximation only. Given a mesh with an - at least - locally uniform structure, we can hope for higher order accuracy in the mesh-nodes, that then can be used for reconstructing a higher order solution. See [36, 35]. Extensive studies in the literature have shown, that this higher order reconstruction operator $I_{2h}^{(2)}$ is highly accurate for a large class of problems [30, 42, 188]. Even if the mesh is completely unstructured and lacks such a patch structure, a higher order reconstruction can be undertaken, see [62].

The DWR method estimates the error in arbitrary functionals, not only in norms. This concepts brings along a number of possible pitfalls. First, a functional error $J(u - u_h)$ has a sign. It can hold $J(u - u_h) > 0$ or $J(u - u_h) < 0$ and very often, the sign changes under mesh-refinement. When such a zero-crossing happens, the absolute error $|J(u - u_h)|$ can be small beyond reasonable bounds. Then, going to even finer meshes, the absolute error will increase again.

As the functional error can change the sign and as convergence must not be monotone, the dual weighted residual estimator is not suitable for the concept of convergent finite element schemes, where error estimation and adaptivity is combined in such a way, that strict convergence of the solution (with fixed rates) can be certified [82, 169, 219, 63].

One approach for getting a bound of the functional error is to combination of primal and adjoint energy error. Considering the error identity, we have

$$J(u - u_h) = A(u - u_h)(z) = A(u - u_h)(z - z_h) \leq c_A \|\nabla(u - u_h)\| \|\nabla(z - z_h)\|. \quad (7.15)$$

In [129], the authors use this bound to combine convergence results for both error contributions. In [172], the authors combine the DWR method with robust energy norm estimators to derive a *safeguarded* DWR estimator that is robust even if the effectivity index is very bad on coarse meshes.

Nonlinear problems

The theory as presented in the last section is based on a simple duality argument linking error functional to the variational formulation. Here, we will consider general nonlinear equations described by the form $A : \mathcal{V} \times \mathcal{V} \rightarrow \mathbb{R}$, which is supposed to be linear in the second argument and three times differentiable in the first. By $J : \mathcal{V} \rightarrow \mathbb{R}$ we denote the error functional, will now also can be nonlinear and which is supposed to be three times differentiable. Nonlinear functionals can be used to measure the vorticity of a velocity field

$$J_{\times} = \int_{\Omega} (x \times \mathbf{v})^2 dx, \quad (7.16)$$

wall stress induced by nonlinear material laws

$$J_{\Sigma} = \int_{\Gamma} \mathbf{F} \boldsymbol{\Sigma} \vec{n} \cdot \mathbf{e} dx,$$

7.1. A posteriori error estimation

and many more quantities. Again, by $F \in V^*$ we denote a right hand side, and by $V_h \subset \mathcal{V}$ the discrete subspace. Following the approach by Becker & Rannacher [29], we define the Lagrange functional

$$\mathcal{L}(u, z) = J(u) + F(z) - A(u)(z). \quad (7.17)$$

Given, that $u \in V$ is the solution to $A(u)(\phi) = F(\phi)$ for all $\phi \in V$, the error in the functional is given by

$$J(u) - J(u_h) = \mathcal{L}(u, z) - \mathcal{L}(u_h, z_h),$$

for all $z \in V$ and $z_h \in V_h$. Note, that the functional error is given by $J(u) - J(u_h)$ and not by $J(u - u_h)$. These two expressions coincide for linear functionals only. It holds:

Theorem 15 (Dual Weighted Residual Method for nonlinear problems). *Let $u \in V$ and $u_h \in V_h$ be the solutions to*

$$A(u)(\phi) = F(\phi) \quad \forall \phi \in V, \quad A(u_h)(\phi_h) = F(\phi_h) \quad \forall \phi_h \in V_h.$$

and $z \in V$ and $z_h \in V_h$ be the adjoint solutions to

$$A'(u)(\phi, z) = J'(u)(\phi) \quad \forall \phi \in V, \quad A'(u_h)(\phi_h, z_h) = J'(u_h)(\phi_h) \quad \forall \phi_h \in V_h,$$

where by $A'(\cdot)(\cdot, \cdot)$ and $J'(\cdot)(\cdot)$ we denote the Gateaux derivatives

$$A'(u)(\phi, z) = \frac{d}{ds} A(u + s\phi)(z) \Big|_{s=0}, \quad J'(u)(\phi) = \frac{d}{ds} J(u + s\phi) \Big|_{s=0}.$$

For the functional error it holds

$$\begin{aligned} J(u) - J(u_h) &= \frac{1}{2} \left\{ (f, z - I_h z) - A(u_h)(z - I_h z) \right\} \\ &\quad + \frac{1}{2} \left\{ J'(u_h)(u - I_h u) - A'(u_h)(u - I_h u, z_h) \right\} + \mathcal{R}^{(3)}, \end{aligned}$$

with a remainder $\mathcal{R}^{(3)}$ of third order in the error $e_h = \{u - u_h, z - z_h\}$ and where $I_h : \mathcal{V} \rightarrow V_h$ is an arbitrary interpolation operator.

Proof. For simplicity, we introduce the notation $x := (u, z) \in \mathcal{V} \times \mathcal{V}$ and $x_h := (u_h, z_h) \in V_h \times V_h$. It holds:

$$J(u) - J(u_h) = \mathcal{L}(x) - \mathcal{L}(x_h) = \int_0^1 \frac{d}{ds} \mathcal{L}(x + s(x - x_h)) \, ds.$$

We approximate this integral by the trapezoidal rule to get

$$J(u) - J(u_h) = \frac{1}{2} \mathcal{L}'(x)(x - x_h) + \frac{1}{2} \mathcal{L}'(x_h)(x - x_h) + \mathcal{R}^{(3)},$$

where the remainder $\mathcal{R}^{(3)}$ is given by (see [29])

$$\mathcal{R}^{(3)} = \int_0^1 s(1-s) \mathcal{L}'''(x + s(x - x_h))(x - x_h, x - x_h, x - x_h) \, ds.$$

As our Galerkin approach is conforming, it holds $\mathcal{L}'(x)(x - x_h) = 0$. Further, by Galerkin orthogonality it holds

$$J(u) - J(u_h) = \frac{1}{2} \mathcal{L}'(x_h)(x - I_h x) + \mathcal{R}^{(3)},$$

and the final estimate follows by using the definition of $\mathcal{L}(\cdot)(\cdot)$, see (7.17) and its derivatives:

$$\mathcal{L}'_z(u, z)(\phi) = F(\phi) - A(u)(\phi), \quad \mathcal{L}'_u(u, z)(\phi) = J'(u)(\phi) - A'(u)(\phi, z).$$

□

The DWR method is a general concept that can be applied to all different Galerkin methods. The remainder $\mathcal{R}^{(3)}$ only appears by the application of the trapezoidal rule. If we consider linear problems only, the estimator of Theorem 15 is equivalent to the estimators of Theorem 14. As in the linear case, the error approximation depends on the unknown weights $z - i_h z$ and also the primal weight $u - i_h u$. For approximation of $z \in \mathcal{V}$ and $u \in \mathcal{V}$, the same procedures are in the preceding Section 7.1.1 can be utilized.

Remark 44 (Adjoint solution to the Navier-Stokes equations). *To discuss the linearized adjoint used for the nonlinear DWR method, we consider the Navier-Stokes equations, given by*

$$\mathbf{U} \in \mathcal{X} = \mathcal{V} \times \mathcal{L} : \quad A(\mathbf{U})(\Phi) = F(\Phi) \quad \forall \Phi \in \mathcal{X},$$

where $\mathcal{V} = H_0^1(\Omega)^d$, $\mathcal{L} = L^2(\Omega) \setminus \mathbb{R}$ and

$$\begin{aligned} A(\mathbf{U})(\Phi) &:= (\rho_f \mathbf{v} \cdot \nabla \mathbf{v}, \phi) + (\rho_f \nu_f \nabla \mathbf{v}, \nabla \phi) - (p, \nabla \cdot \phi) + (\operatorname{div} \mathbf{v}, \xi) \\ F(\Phi) &:= (\mathbf{f}, \phi) \end{aligned}$$

The Gateaux derivative at $\mathbf{U} \in \mathcal{X}$ in direction $\mathbf{Z} = \{\mathbf{z}, q\} \in \mathcal{X}$ is given as

$$A'(\mathbf{U})(\mathbf{Z}, \Phi) = \left(\rho_f (\mathbf{v} \cdot \nabla \mathbf{z} + \mathbf{z} \cdot \nabla \mathbf{v}), \phi \right) + (\rho_f \nu_f \nabla \mathbf{z}, \nabla \phi) - (q, \nabla \cdot \phi) + (\operatorname{div} \mathbf{z}, \xi)$$

The adjoint solution is determined by the linearized adjoint form $A'(\mathbf{U})(\Phi, \mathbf{Z})$:

$$A'(\mathbf{U})(\Phi, \mathbf{Z}) = \left(\rho_f (\mathbf{v} \cdot \nabla \phi + \phi \cdot \nabla \mathbf{v}), \mathbf{z} \right) + (\rho_f \nu_f \nabla \phi, \nabla \mathbf{z}) - (\xi, \nabla \cdot \mathbf{z}) + (\operatorname{div} \phi, q) \quad (7.18)$$

As functional of interest, we consider the vorticity (7.16). Its derivative is given by

$$J'(\mathbf{U})(\Phi) = 2 \int_{\Omega} (\mathbf{x} \times \mathbf{v}) \cdot (\mathbf{x} \times \phi) \, dx.$$

This right hand side, together with the adjoint variational formulation corresponds to the classical formulation of the Adjoint Navier-Stokes system

$$\rho_f \left(\nabla \mathbf{v}^T \mathbf{z} - \mathbf{v} \cdot \nabla \mathbf{z} \right) + \nabla q = j, \quad \operatorname{div} \mathbf{z} = 0.$$

The transport direction is switched and an additional reaction term appears. Furthermore, the new ‘‘pressure variable’’ $q \in \mathcal{L}$ appears with a positive sign. The appearance of the reaction term can lead to stability problems, as its sign cannot be controlled.

Theorem 15 covers the case of conforming and consistent finite element schemes. It can directly be applied to many different configurations and equations. We simply need a Galerkin structure in such a way, that a solution $u \in \mathcal{X}$ is given by

$$A(u)(\phi) = F(\phi) \quad \phi \in \mathcal{X},$$

7.1. A posteriori error estimation

and an approximation in a subspace $X_h \subset \mathcal{X}$ that defines $u_h \in X_h$ such that

$$A(u_h)(\phi_h) = F(\phi_h) \quad \forall \phi_h \in X_h.$$

Finally, we present a modification of this theorem that can be applied to non-conforming discretizations, i.e. problems, where the discrete solution $u_h \in X_h$ is defined as

$$A_h(u_h)(\phi_h) = F_h(\phi_h),$$

where A_h and F_h are modifications of A and F , respectively.

One possible situation is the use of stabilization techniques, e.g. in the context of the Navier-Stokes equations

$$A_h(\mathbf{U}_h)(\Phi_h) := A(\mathbf{U}_h)(\Phi_h) + S_h(\mathbf{U}_h)(\Phi_h),$$

where $\mathbf{U}_h = \{\mathbf{v}_h, p_h\}$ and where $A(\cdot)(\cdot)$ is given as in Remark 44. Considering simple pressure stabilization in the context of Section 3.3.2 and artificial diffusion like in Section 3.4.3, this stabilization term is given as

$$S_h(\mathbf{U}_h)(\Phi_h) = (\alpha \nabla p_h, \nabla \xi_h) + (\delta \nabla \mathbf{v}_h, \nabla \phi_h).$$

Theorem 16 (DWR method for non-conforming discretizations). *Let $u \in V$ and $u_h \in V_h$ be the solution to*

$$A(u)(\phi) = F(\phi) \quad \forall \phi \in V, \quad A_h(u_h)(\phi_h) = F(\phi_h) \quad \forall \phi_h \in V_h,$$

and $z \in V$ and $z_h \in V_h$ be solutions to

$$A'(u)(\phi, z) = J'(u)(\phi) \quad \forall \phi \in V, \quad A'_h(u_h)(\phi_h, z_h) = J'(u_h)(\phi_h) \quad \forall \phi_h \in V_h.$$

Then, it holds

$$\begin{aligned} J(u) - J(u_h) &= \frac{1}{2} \left\{ F(z - I_h z) - A_h(u_h)(z - I_h z) \right\} \\ &\quad + \frac{1}{2} \left\{ J'(u_h)(u - I_h u) - A'_h(u_h)(u - I_h u, z_h) \right\} \\ &\quad + S(u_h)(z) + S'(u_h)(u - u_h, z_h) + \mathcal{R}^{(3)} \end{aligned} \quad (7.19)$$

Proof. First, we define $\mathcal{L}_h(u_h, z_h) = J(u_h) + F(z_h) - A_h(u_h)(z_h)$. It holds

$$\mathcal{L}_h(u_h, z_h) = \mathcal{L}(u_h, z_h) - S(u_h, z_h).$$

Using $x := (u, z)$ and $x_h := (u_h, z_h)$ the error is given as

$$J(u) - J(u_h) = \mathcal{L}(x) - \mathcal{L}_h(x_h) = \mathcal{L}(x) - \mathcal{L}(x_h) + S(u_h, z_h).$$

Again, by using an integral representation and approximation with the trapezoidal rule it holds

$$J(u) - J(u_h) = \frac{1}{2} \mathcal{L}'(x)(x - x_h) + \frac{1}{2} \mathcal{L}'(x_h)(x - x_h) + S(u_h, z_h) + \mathcal{R}^{(3)},$$

where, $\mathcal{L}'(x)(x - x_h) = 0$. We cannot immediately use Galerkin orthogonality in the second part. Instead,

$$\begin{aligned} J(u) - J(u_h) &= S(u_h, z_h) \\ &+ \frac{1}{2} \left\{ F(z - I_h z) - A(u_h)(z - I_h z) - S(u_h)(z - I_h z) \right\} + S(u_h)(z - z_h) \\ &+ \frac{1}{2} \left\{ J'(u_h)(u - I_h u) - A'(u_h)(u - I_h u, z_h) - S'(u_h)(u - I_h u, z_h) \right\} \\ &\quad + S'(u_h)(u - u_h, z_h) + \mathcal{R}^{(3)} \end{aligned}$$

□

To evaluate this error estimator we must approximate the remainders given by the stabilization term. This will depend on the specific type of stabilization scheme. As example, we consider a simple stabilization of the Stokes equations

Example 3 (DWR for the Stokes equations with pressure stabilization). *Let $\Omega = (0, 1)^2$ and $\{\mathbf{v}, p\} \in H_0^1(\Omega)^2 \times L_0^2(\Omega)$ be the solution to the Stokes equations*

$$(\nabla \mathbf{v}, \nabla \phi) - (p, \nabla \cdot \phi) + (\nabla \cdot \mathbf{v}, \xi) = (\mathbf{f}, \phi) \quad \forall \phi \in H_0^1(\Omega)^2 \times L_0^2(\Omega).$$

The finite element solution $\{\mathbf{v}_h, p_h\} \in V_h \times Q_h$ is given using the simple pressure stabilizations scheme, see Lemma 65:

$$(\nabla \mathbf{v}_h, \nabla \phi_h) - (p_h, \nabla \cdot \phi_h) + (\nabla \cdot \mathbf{v}_h, \xi_h) + \sum_K h_K^2 (\nabla p_h, \nabla \xi_h) = (\mathbf{f}, \phi_h) \quad \forall \phi \in V_h \times Q_h.$$

Here, the stabilization is linear, symmetric and of the form

$$S(p, \xi) = \sum_K h_K^2 (\nabla p, \nabla \xi).$$

The discrete adjoint solution $\{\mathbf{z}_h, q_h\} \in V_h \times Q_h$ is given as

$$(\nabla \mathbf{z}_h, \nabla \phi_h) + (q_h, \nabla \cdot \phi_h) - (\nabla \cdot \mathbf{z}_h, \xi_h) + \sum_K h_K^2 (\nabla q_h, \nabla \xi_h) = J'(\mathbf{v}_h, p_h)(\phi_h, \xi_h).$$

Then, the exact form of estimator (7.19)

$$\begin{aligned} J(\mathbf{v}) - J(\mathbf{v}_h) &= \frac{1}{2} \left\{ (f, \mathbf{z} - I_h \mathbf{z}) - (\nabla \mathbf{v}_h, \nabla(\mathbf{z} - I_h \mathbf{z})) \right. \\ &\quad \left. + (p_h, \nabla \cdot (\mathbf{z} - I_h \mathbf{z})) - (\nabla \cdot \mathbf{v}_h, q - I_h q) - S(p_h, q - I_h q) \right\} \\ &\quad + \frac{1}{2} \left\{ J'(\mathbf{v}_h)(\mathbf{v} - I_h \mathbf{v}, p - I_h p) - (\nabla \mathbf{z}_h, \nabla(\mathbf{v} - I_h \mathbf{v})) \right. \\ &\quad \left. - (q_h, \nabla \cdot (\mathbf{v} - I_h \mathbf{v})) + (\nabla \cdot \mathbf{z}_h, q - I_h q) - S(p - I_h p, q_h) \right\} \\ &\quad - S(p - p_h, q - q_h) + S(p, q) \end{aligned}$$

For evaluation, the term $S(p - p_h, q - q_h)$ is of higher order and can be neglected. The second stabilization term can be approximated as

$$S(p, q) \approx S(I_{2h}^{(2)} p_h, I_{2h}^{(2)} q_h),$$

using the higher order interpolation operator.

The DWR method has been applied to a large variety of equations and coupled systems of equations ranging from reactive flows [41, 49], general conservation laws [115], plasticity [182] to applications like model error analysis [174, 44] or optimization and parameter identification problems [30, 236]. We will continue with the extension of the DWR method to time-dependent problems.

7.1.2 The DWR Method for Galerkin time-stepping schemes

Techniques for estimating the error due to time-discretization are usually based on an estimation of the truncation error [1]. Here, we shortly want to present a technique to apply the Dual Weighted Residual method to error control in time. We loosely follow the extensive study by Schmich, Vexler, Rannacher [207, 206, 34].

In Section 3.1.3, we have presented Galerkin methods for time-discretization, compare Lemma 44, where the following variational formulation for the heat equation was derived:

$$\begin{aligned} u \in X_I^1 : \quad & \sum_{m=1}^M \int_{I_m} \left\{ (u'(t), \phi(t))_\Omega + A(u(t))(\phi(t)) \right\} dt + ([u]_{m-1}, \phi(t_{m-1})^+) \\ & = \sum_{m=1}^M \int_{I_m} (f(t), \phi(t)) dt \quad \forall \phi \in X_I^0, \end{aligned}$$

where X_I^1 is the space of piece-wise (on $I_m = [t_{m-1}, t_m]$, linear, globally on $I = [0, T]$ continuous functions and X_I^0 the space of piece-wise constant functions. For linear and autonomous problems, this $cG(1)$ -Formulation is equivalent to the Crank-Nicolson scheme. In the general setting however, the Galerkin error must be considered as a new time-discretization scheme, that differs from the Crank-Nicolson method by an error of order $O(k^2)$, where $k = \max_m |t_m - t_{m-1}|$ is the step-size. This is exactly the same convergence order as the order of the Crank-Nicolson's truncation error.

For the following, we define

$$A_I(u)(\phi) = \sum_{m=1}^M \int_{I_m} \left\{ (u'(t), \phi(t))_\Omega + A(u(t))(\phi(t)) \right\} dt + ([u]_{m-1}, \phi(t_{m-1})^+).$$

The solution $u \in W(I)$ is given as

$$A_I(u)(\phi) = F(\phi) \quad \forall \phi \in W(I). \quad (7.20)$$

Given discrete trial and test-spaces X_I and Y_I , the discrete solution is defined as

$$u_k \in X_I : \quad A_I(u_k)(\phi_k) = F(\phi_k) \quad \forall \phi_k \in Y_I. \quad (7.21)$$

We assume, that Y_I is globally discontinuous. Then, the Galerkin formulation decouples to a time-stepping scheme for $m = 1, \dots, M$

$$\begin{aligned} & \int_{I_m} (\partial_t u_k, \phi_k)_\Omega + A(u_k)(\phi_k) dt + (u_k^+(t_{m-1}), \phi_k^+(t_{m-1}))_\Omega \\ & = (u^0, \phi_k^-(t_0)) + (u_k^-(t_{m-1}), \phi_k^+(t_{m-1}))_\Omega + \int_{I_m} (f, \phi_k) dt, \end{aligned}$$

where $u_k^-(t_0) = u^0$ and $\phi_k^-(t_0)$ is introduced to include the initial value. As error functional we consider values at final time T and distributed values

$$J(u) = J_T(u(T)) + \int_I J_I(t, u(t)) dt, \quad (7.22)$$

where $J_T \in H^{-1}(\Omega)$ and $J_I : I \rightarrow H^{-1}(\Omega)$.

With these preparations, we can define the adjoint non-stationary solution $z \in W(I)$ as

$$A'_I(u)(\phi, z) = J'(u)(\phi) \quad \forall \phi \in W(I), \quad (7.23)$$

and the discrete counterpart $z_k \in Y_I$ by

$$A'_I(u_k)(\phi_k, z_k) = J'(u_k)(\phi_k) \quad \forall \phi_k \in X_I, \quad (7.24)$$

where the role of trial and test-spaces are switched. The adjoint solution “runs backward in time”, as by switching test- and trial-functions partial integration gives:

$$\int_I (\partial_t \phi, z) dt = \int_I (\phi, -\partial_t z) dt + \phi(T)^- z(T)^- - \phi(0)^+ z(0)^+. \quad (7.25)$$

Right hand side of the adjoint problem, as well as initial data at time $t = T$ are given by the functional (7.22). The distributed part defines the right hand side, and the part J_T together with (7.25) gives

$$(\phi(T)^-, z(t)^-) = J'_T(u(T))(\phi(T)^-).$$

Lemma 82. *The discrete adjoint problem decouples to a time-stepping method running backward in time.*

Proof. It holds with integration by parts and reordering:

$$\begin{aligned} A'_I(u)(\phi, z) &= \sum_{i=1}^M \int_{I_m} \{(\phi'(t), z(t)) + A'(u(t))(\phi(t), z(t))\} dt \\ &\quad + \sum_{i=1}^M (\phi(t_{m-1})^+, z(t_{m-1})^+) - \sum_{i=2}^M (\phi(t_{m-1})^-, z(t_{m-1})^+) \\ &= \sum_{i=1}^M \int_{I_m} \{(-z'(t), \phi(t)) + A'(u(t))(\phi(t), z(t))\} dt \\ &\quad + \sum_{i=1}^M (z(t_m)^-, \phi(t_m)^-) - (z(t_{m-1})^+, \phi(t_{m-1})^+) \\ &\quad + \sum_{i=1}^M (\phi(t_{m-1})^+, z(t_{m-1})^+) - \sum_{i=2}^M (\phi(t_{m-1})^-, z(t_{m-1})^+) \\ &= \sum_{i=1}^M \int_{I_m} \{(-z'(t), \phi(t)) + A'(u(t))(\phi(t), z(t))\} dt \\ &\quad + (z(t_M)^-, \phi(t_M)^-) + \sum_{i=1}^{M-1} (z(t_m)^- - z(t_m)^+, \phi(t_m)^-) \end{aligned}$$

Coupling takes place via the jump-terms only. Here, it is the adjoint solution, which in most discrete realizations will be discontinuous

$$z_k(t_m)^- \neq z_k(t_m)^+,$$

while the test-function ϕ_k is often chosen continuously. For the adjoint problem, the first and the last step often take a different form. Here, in the general setting, on $I_M = [t_{M-1}, t_M]$ it holds

$$\begin{aligned} (z_k(T)^-, \phi(T)^-) + \int_{I_M} (-z'_k(t), \phi_k(t)) + A'_I(u_k(t))(\phi_k(t), z_k(t)) dt \\ = J'_T(u(T))(\phi(T)) + \int_{I_M} J'_I(t, u(t))(\phi(t)) dt. \end{aligned}$$

The, for $m = M-1, \dots, 1$ we have

$$\begin{aligned} (z_k(t_m)^-, \phi(t_m)^-) + \int_{I_m} (-z'_k(t), \phi_k(t)) + A'_I(u_k(t))(\phi_k(t), z_k(t)) dt \\ = (z_k(t_m)^+, \phi(t_m)^-) \int_{I_m} J'_I(t, u(t))(\phi(t)) dt, \end{aligned}$$

and in the final step. \square

Theorem 17 (DWR method for temporal Galerkin methods). *Let $u \in W(I)$ be solution to (7.20), $u_k \in X_I \subset W(I)$ solution to (7.21). Let J be an error functional in the sense of (7.22). Let $z_k \in Y_I$ be the adjoint solution to (7.24), $z \in W(I)$ the continuous counterpart given by (7.23). Then, it holds*

$$\begin{aligned} J(u - u_k) &= \frac{1}{2} \left\{ F(z - i_k^* z) - A_I(u_k)(z - i_k^* z) \right\} \\ &\quad + \frac{1}{2} \left\{ J'(u_k)(u - i_k u) - A'_I(u_k)(u - i_k u, z_k) \right\} + \mathcal{R}^3(u - u_k, z - z_k), \end{aligned}$$

where \mathcal{R}^3 is the third order remainder and $i_k : W(I) \rightarrow X_I$ and $i_k^* : W(I) \rightarrow Y_I$ are projection operators in time.

Proof. The proof directly follows by applying Theorem 15 to the Galerkin-in-time setting. \square

Remark 45 (Galerkin time-integration). *There are various realizations of the Dual Weighted Residual method for error estimation in space and time based on Galerkin approximations of the time-dependent problem [206, 34]. The benefit of Galerkin time-discretization is, that the non-stationary problem is cast into a variational setting that allows for the application of analytical tools known from the finite element method. The method is universal and various continuous or discontinuous trial- test-spaces can be combined.*

It is well known, that the dG(0)-method corresponds to the backward Euler and the cG(1)-discretization (that is cG(1) for X_I and dG(0) for Y_I) to the Crank-Nicolson method. But what exactly is the meaning of “corresponds”? For linear autonomous problems, the two methods are exactly equivalent. For all other problems, that time-stepping method can be derived by numerical quadrature from the Galerkin method. However, this quadrature error is usually not

of higher order, but of the same order as the Galerkin method's approximation order. Hence, we must speak of two separate methods.

One big problem of Galerkin time-discretizations is the higher effort. For setting up the system matrix, the term

$$\int_{I_m} A'_I(u_k)(w_k, \phi_k) dt,$$

must be evaluated. For an accurate (higher order) approximation of the integral, Gauss quadrature rules must be considered. This quickly doubles the usual effort for assembling the matrix. Considering coupled problems like fluid-structure interactions, such an effort is impractical. If even higher order time-discretizations are used, e.g. a dG(1)-method, each time-step couples two separate states. This increases the size of the system-matrix (and the effort) by a factor of 4. Nevertheless, Galerkin methods are often used, whenever the Galerkin structure is of importance, as it is in the context of gradient based optimization [27, 191, 217].

Finally, we shortly want to address the question of error control for efficient time-stepping methods like the shifted Crank-Nicolson scheme or the Fractional-Step Theta method. These methods cannot be exactly written as Galerkin formulations. Instead, error estimation is based on the following principle:

1. Solve the forward problem u_k by time-stepping, e.g. with the Crank-Nicolson method
2. Estimate the error in two steps

$$|u - u_k| \leq |u - u_k^G| + |u - u_k^G|,$$

where u_k^G is a Galerkin solution, that however will not be numerically distributed.

Here, the first error is distributed into a contribution of the Galerkin error, and the discrepancy between Galerkin solution and time-stepping scheme, a quadrature error. The first error can be approximated with help of Theorem 17. We give details for the application to the shifted Crank-Nicolson scheme:

Theorem 18 (DWR method for the Crank-Nicolson time-stepping method). *Let u, z be solution and adjoint solution given by (7.20) and (7.23). Let $u_k = \{u_1, \dots, u_M\} \in \mathcal{X}^M$ be the approximation by the shifted Crank-Nicolson method*

$$A_{I,k}(u_k)(\phi_k) = F_k(\phi_k),$$

where

$$A_{I,k}(u_k)(\phi_k) = \dots$$

Proof. Ausformulieren, diskrete Raeume, Fehlerschaetzer. Klarmachen: 2 probleme, time-stepping & Galerkin \square

Details on how to extend this method to the fractional step theta method are found in [160, 161, 209].

7.2 Adaptivity

The accuracy of the discretization is controlled by the mesh size h and the time step size k . For $k \rightarrow 0$ and $h \rightarrow 0$ we expect, that the discretization error will then converge to zero. The efficiency of a discretization can be measured in error versus effort, where the effort depends on the discrete problem size. In the context of finite elements, we can measure the problem size in $N \cdot M$, where $N = \dim(V_h)$ is the dimension of the discrete function space and $M = T/k$ is the number of time-steps. Given an optimal algorithm, where all parts have a linear run-time, the effort is proportional to $N \cdot M$.

For many problems it is not appropriate to use uniform meshes in space and time to get the most efficient discretization. Instead, different spatial and temporal regions may ask for a different resolution of the discretization. The general problem for adaptivity is to find the optimal distribution of spatial and temporal mesh points which gives the smallest error. We first consider spatial adaptivity only and formulate two optimization problems:

$$\min |J(u) - J(u_h)|, \text{ for all } u_h \in V_h \text{ with } \dim(V_h) = N_0,$$

i.e., find that best discretization with N_0 unknowns, such that the resulting error is smallest. A second viewpoint is to optimize

$$\min \{ \dim(V_h) \}, \text{ such that } |J(u) - J(u_h)| < TOL,$$

i.e., find the most efficient mesh, such that the error is below a given bound. Both settings are important for application. The second optimization problem aims at satisfying a guaranteed error bound, while the first problem tries to get the best possible result for given resources, e.g. the available memory. See [3].

The construction of new meshes Ω_h and finite element spaces V_h can either be done by *refinement* of existing elements $K \in \Omega_h$ into smaller elements, or by a complete *remeshing* of Ω_h to a new mesh Ω'_h . A complete remeshing gives greater flexibility, as the mesh elements can be distributed arbitrarily in the domain, it however brings along the drawback of having no relationship between two finite element spaces V_h and V'_h . If the new mesh Ω'_h is constructed by mesh refinement, every mesh element $K \in \Omega'_h$ is either element of the preceding mesh $K \in \Omega_h$ or it results from refinement of a *father-element* $P \in \Omega_h$. In Figure 7.4 we show typical refinements used for the splitting of elements. If only parts of the mesh are refined, it is necessary to assure the structural regularity of the mesh. This is needed to allow for conformity $V_h \subset H^1(\Omega)$, mainly for the continuity of the discrete functions. Basically, two different options exist: first, one can introduce temporary elements (the right sketches in Figure 7.4). This are simply introduced to ensure structural adaptivity. Using such elements usually demands for meshes with mixed element types, i.e. mixing quadrilaterals with triangles. This additional effort can be circumvented by the concept of *hanging nodes*. These are nodes, that belong to a refined element, but not to the coarse element. In these nodes, no real degrees of freedom exist. Instead, the values at such a node are replaced by an interpolation between to neighboring nodes. See [14, 196].

Another advantage of refinement based adaptivity is the availability of a natural hierarchy of meshes and function spaces. Starting on a coarse mesh Ω_0

$$\Omega_0 \rightarrow \Omega_1 \rightarrow \dots \rightarrow \Omega_l,$$

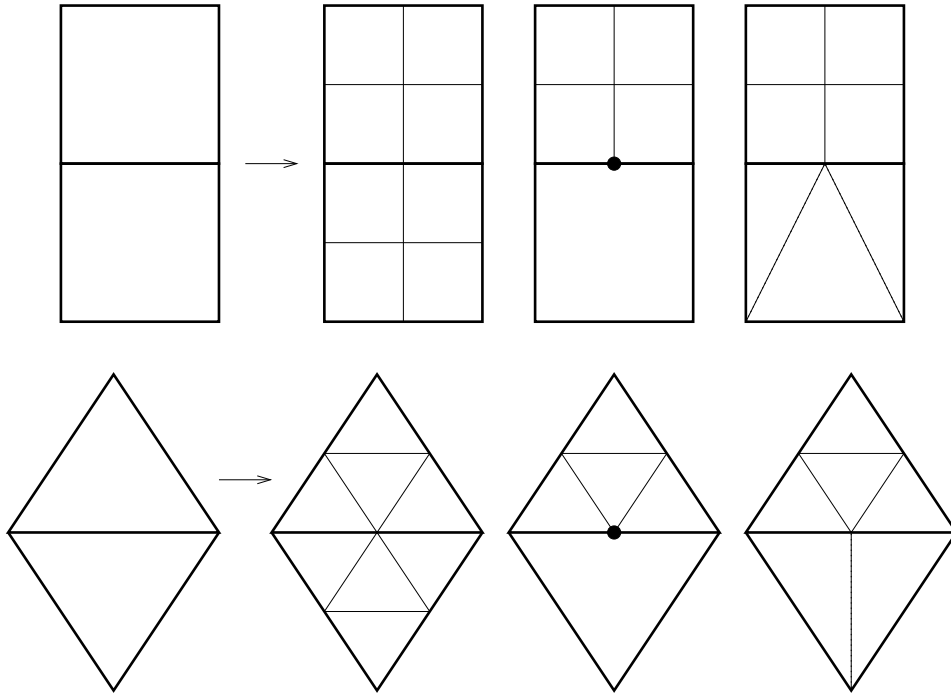


Figure 7.4: Different refinement ways for splitting mesh-elements. Both rows: uniform refinement, local refinement with *hanging nodes* and local refinement using temporary elements for assuring structural regularity.

we construct a sequence of hierarchical finite element spaces

$$V_0 \subset V_1 \subset \cdots \subset V_l.$$

This sequence of spaces is a natural starting point for hierarchical multigrid solvers. The usually very difficult step of creating a coarse mesh hierarchy is easily established based on the already existing history, see [111, 16, 20].

For both refinement and remeshing, local error contributions must be available. The error estimators presented in the preceding section give global error measures

$$J(u) - J(u_h) \approx \eta_h(u_h, z_h).$$

To use such quantities for mesh refinement, we need a splitting into local contributions

$$\eta_h(u_h, z_h) = \sum_i \eta_i(u_h, z_h).$$

How to derive such localizations is topic of the following section.

7.2.1 Localization of a posteriori error estimators

The choice, whether or not to refine a mesh element $K \in \Omega_h$, will be based on local error indicators that measure the error contribution of some small area. Here, we will describe

7.2. Adaptivity

different ways for a localization of the dual weighted residual error $J(u) - J(u_h)$ as

$$J(u) - J(u_h) \approx \sum_i \eta_i,$$

where the sum \sum_i usually is a localization into element-wise contributions η_K or node-wise values η_i . Then, areas are picked for refinement, if the local indicator $|\eta_i|$ is large compared to the other indicators. Techniques for picking elements for refinement are presented in the next section, Section 7.2.2.

In the following, we only discuss discretizations of the Laplace equation

$$A(u)(\phi) := (\nabla u, \nabla \phi) = F(\phi) := (f, \phi) \quad \forall \phi \in \mathcal{V} = H_0^1(\Omega).$$

For a reliable refinement based on the local indicators η_i , we will ask for robustness and effectivity of the indicators, e.g. for the existence of constants $c_1, c_2 > 0$

$$|J(u - u_h)| \leq c_1 \sum_i |\eta_i|, \quad \sum_i |\eta_i| \leq c_2 |J(u - u_h)|.$$

We have already discussed, that the second inequality cannot hold for general functionals $J(\cdot)$, as the functional error can be very small or zero even for substantial discretization errors, see Section 7.1.1. Hence, we weaken the effectivity assumption to

$$\sum_i |\eta_i| \leq c_2 \|\nabla(u - u_h)\| \|\nabla(z - z_h)\|,$$

such that the error indicators are bound by the product of the energy errors, that themselves are a bound for the functional error $|J(u - u_h)|$. For measuring the effectivity of error indicators, we define the *indicator index*

$$\text{ind}_h := \frac{\sum_i |\eta_i|}{|\eta_h|}$$

as the fraction of absolute indicator values by the error estimator, compare the definition of the effectivity index (7.14).

$$\text{eff}_h := \frac{\eta_h}{J(u - u_h)}.$$

If it holds

$$\text{ind}_h \cdot \text{eff}_h \rightarrow 1,$$

we can assume, that the refinement based on the localization η_i of the error estimator η_h will give highly reliable results. In the following, we will describe and shortly analyze different localization techniques for the DWR error identities given in Theorems 14 and 15. For details on the analysis and further possibilities for localization we refer to [194].

Localization by restriction to elements

The most simple approach for a localization by restricting the weak residual in an element-wise manner

$$\eta_K = (f, z - i_h z)_K - (\nabla u_h, \nabla(z - i_h z))_K$$

fails. Locally, it holds for every η_K

$$\eta_K = (f + \Delta u_h, z - i_h z)_K - \int_{\partial K} \partial_n u_h \cdot (z - i_h z) \, ds.$$

While the volume term itself yields optimal order

$$|(f + \Delta u_h, z - i_h z)_K| \leq \|\Delta(u - u_h)\|_K \|z - i_h z\|_K,$$

the boundary term lacks the sufficient approximation order as can be seen using interpolation estimates and the trace inequality:

$$\begin{aligned} \left| \int_{\partial K} \partial_n u_h \cdot (z - i_h z) \, ds \right| &\leq c_{\text{tr}} h_K^{-1} (\|\nabla u_h\|_K + h_K \|\nabla^2 u_h\|_K) \\ &\quad (\|z - i_h z\|_K + h_K \|\nabla(z - i_h z)\|_K). \end{aligned}$$

While the adjoint solution enters the estimate with the proper local order, the boundary term does show convergence with respect to the primal residual. This result is well-known in literature, and the typical remedy is given by balancing boundary terms with adjacent finite elements, as shown in the following paragraph.

Localization based on the classical (strong) formulation

The typical localization procedure for residual based error estimators is based on the classical formulation of residual estimators [235]. For the functional error it holds (considering linear problems)

$$\begin{aligned} J(u - u_h) &= \sum_{K \in \Omega_h} \frac{1}{2} \left\{ (f, z - i_h z)_K - (\nabla u_h, \nabla(z - i_h z))_K \right\} \\ &\quad + \sum_{K \in \Omega_h} \frac{1}{2} \left\{ (j, u - i_h u)_K - (\nabla(u - i_h u), \nabla z_h)_\Omega \right\} \\ &= \sum_{K \in \Omega_h} \frac{1}{2} \left\{ (f + \Delta u_h, z - i_h z)_K - \langle \partial_n u_h, z - i_h z \rangle_{\partial K} \right\} \\ &\quad + \sum_{K \in \Omega_h} \frac{1}{2} \left\{ (j + \Delta u_h)_K - \langle \partial_n z_h, u - i_h u \rangle_{\partial K} \right\} \\ &= \sum_{K \in \Omega_h} \frac{1}{2} \left\{ (f + \Delta u_h, z - i_h z)_K - \frac{1}{2} - \langle [\partial_n u_h], z - i_h z \rangle_{\partial K} \right\} \\ &\quad + \sum_{K \in \Omega_h} \frac{1}{2} \left\{ (j + \Delta u_h)_K - \frac{1}{2} \langle [\partial_n z_h], u - i_h u \rangle_{\partial K} \right\}, \end{aligned} \tag{7.26}$$

where by $[\cdot]$ we denote the jump of the (discontinuous) normal derivative ∂u_h across the edge $e \subset \partial K$

$$[\partial_n u_h](x) \Big|_e := \lim_{h \downarrow 0} \partial_n u_h(x + h\vec{n}) - \lim_{h \downarrow 0} \partial_n u_h(x - h\vec{n}),$$

with a normal vector \vec{n} facing outward of K . Now, (7.26) can be estimated to

$$|J(u - u_h)| \leq \sum_{K \in \Omega_h} \rho_K(u_h) \omega_K(z_h) + \rho_K^*(z_h) \omega_K^*(u_k), \tag{7.27}$$

with the residuals and weights

$$\begin{aligned}\rho_K(u_h) &= \|f + \Delta u_h\|_K + \frac{1}{2} h_K^{-\frac{1}{2}} \|\partial_n u_h\|_{\partial K} \\ \rho_K^*(z_h) &= \|j + \Delta z_h\|_K + \frac{1}{2} h_K^{-\frac{1}{2}} \|\partial_n z_h\|_{\partial K} \\ \omega_K(z_h) &= \|z - i_h z\|_K + h_K^{\frac{1}{2}} \|z - i_h z\|_{\partial K} \\ \omega_K^*(u_h) &= \|u - i_h u\|_K + h_K^{\frac{1}{2}} \|u - i_h u\|_{\partial K}.\end{aligned}\tag{7.28}$$

Half a power of h_K was introduced, such that edge and volume residuals and weights, respectively, have the same order. The benefit of this estimation is, that positive local error quantities are directly available

$$\eta_h = \sum_{K \in \Omega_h} \eta_K, \quad \eta_K = \rho_K \omega_K + \rho_K^* \omega_K^*.$$

Based on η_K , refinement or remeshing can be pursued. By using Cauchy Schwarz estimate, possible orthogonality is lost. As this estimate is used locally, we still get good effectivity of the indicators.

Lemma 83 (Effectivity of the localization based on the classical residual). *Let $u, z \in V$ be the solution and adjoint solution to the Laplace equation with sufficient regularity. For the primal error estimator*

$$|J(u - u_h)| \leq \sum_K 2\rho_K(u_h)\omega_K(z_h),$$

where ρ_K and ω_K are defined in (7.28) it holds

$$\sum_{K \in \Omega_K} 2\rho_K \omega_K \leq \|u - i_h u\|_h \|z - i_h z\|_h,$$

where – given sufficient regularity – the norm $\|\cdot\|_h$ is equivalent to energy norm

$$\|u\|_h^2 = \|\nabla(u - u_h)\|^2 + \sum_{K \in \Omega_h} h_K^2 \|\nabla^2(u - u_h)\|_K^2 + h_K^{-2} \|u - u_h\|_K^2.\tag{7.29}$$

Proof. See [194]. □

This localization technique is often used and well documented in literature. It has two severe drawbacks: as it is based on Cauchy-Schwarz estimates in an early stage, orthogonality effects are lost. Considering general differential operators $\mathcal{L}(u) = f$, the strong residuals $f - \mathcal{L}(u)$ and $j - \mathcal{L}'(u)(z)$ must be available. Such a computation can be very costly as we will discuss in Section 7.3 for fluid-structure interactions. Finally, the classical estimator requires the evaluation of jump-terms at the element edges, which is possibly costly.

Localizations based on the variational formulation

We can circumvent both problems, the strong residual as well as edge jump terms, if we base the localization on the variational formulation. Braack and Ern [45] introduced a localization of the DWR method based on a patch-wise filtering approach. Very good effectivities are obtained at the little cost of additional patch-structures in the mesh, see Figure 7.3. Let V_h be the finite

element space with $V_{2h} \subset V_h$ being the coarse space on the patches. By $\pi_{2h} : V_h \rightarrow V_{2h}$ we denote the embedding into this coarse space. By $i_{2h}^{(2)} : V_h \rightarrow V_{2h}^{(2)}$ we denote the higher order reconstruction introduced in Section 2, see Figure 7.2. We can write

$$z_h(x) = \sum_{i=1}^N \mathbf{z}_i \phi_h^{(i)}(x), \quad i_{2h} z_h(x) = \sum_{i=1}^N \mathbf{z}_i i_{2h} \phi_h^{(i)}(x), \quad i_{2h}^{(2)} z_h(x) = \sum_{i=1}^N \mathbf{z}_i i_{2h}^{(2)} \phi_h^{(i)}(x),$$

and approximate the error identity as

$$\begin{aligned} J(u - u_h) &= F(z - i_h z) - A(u_h)(z - i_h z) \\ &= F(z - i_h z - \pi_{2h}(z - i_h z)) - A(u_h)(z - i_h z - \pi_{2h}(z - i_h z)) \\ &\approx F\left(i_{2h}^{(2)}(z_h - i_{2h} z_h) - (z_h - i_{2h} z_h)\right) \\ &\quad - A(u_h)\left(i_{2h}^{(2)}(z_h - i_{2h} z_h) - (z_h - i_{2h} z_h)\right) \\ &= \sum_{i=1}^N \left(F(i_{2h}^{(2)} \phi_h^{(i)} - \phi_h^{(i)}) - A(u_h)(i_{2h}^{(2)} \phi_h^{(i)} - \phi_h^{(i)})\right) (\mathbf{z}_i - (i_{2h} z_h)_i) \\ &=: \sum_{i=1}^N \eta_i. \end{aligned}$$

By this localization, a node-wise indicator is derived. Due to the filtering $z_h - i_{2h} z_h$, the error indicators are zero on all coarse mesh-nodes causing a strong oscillation of the indicators, see [194]. For this local values, we can also show effectivity

$$\sum_{i=1}^N |\eta_i| \leq c \|u - u_h\|_h \|z - i_h z\|_h.$$

Finally, we introduce a new localization approach based on the variational formulation that combines the simplicity of the filtering approach - as it will be given in terms of variational residuals - with an easy interpretation possibility, as the local estimators η_i can be regarded as coefficient of a discrete error function. Let $\{\psi_i \in V, i = 1, \dots, N\}$ be a partition of unity (POU) with $\sum_i \psi_i \equiv 1$, where we usually consider $\psi_i := \phi_i$ the basis functions of the finite element space V_h . Then, it holds:

$$\begin{aligned} J(u - u_h) &= F(z - i_h z) - A(u_h)(z - i_h z) \\ &= \sum_{i=1}^N F((z - i_h z) \psi_i) - A(u_h)((z - i_h z) \psi_i) \\ &\approx \sum_{i=1}^N F((i_{2h}^{(2)} z_h - z_h) \psi_i) - A(u_h)((i_{2h}^{(2)} z_h - z_h) \psi_i) =: \sum_{i=1}^N \eta_i. \quad (7.30) \end{aligned}$$

Again, we derived node-wise indicators for the local error. The partition of unity ψ_i is independent of the finite element space V_h . It is however reasonable to choose the standard space of piece-wise linear finite elements to define ψ_i .

Lemma 84 (Effectivity of the POU localization). *Let $u \in \mathcal{V}$ be the solution to the Laplace equation, $z \in \mathcal{V}$ be the adjoint solution. $u_h, z_h \in V_h$ their discrete counter-part. Further, let*

7.2. Adaptivity

$\sum \psi_i$ be a POU with $\|\nabla \psi_i\|_\infty = O(h^{-1})$. The error indicators given by (7.30) are effective, i.e.,

$$\sum_{i=1}^N |\eta_i^P| \leq c \|\nabla(u - u_h)\| \|z - i_h z\|_h.$$

Proof. See [194]. □

7.2.2 Techniques for spatial mesh refinement

We assume, that a reliable and effective localization of the error estimator is given

$$c_1 \sum_K |\eta_K| \leq |\eta_h| \leq c_2 \sum_K |\eta_K|.$$

For simplicity, we assume, that this localization is element-wise. Node-wise values can easily be averaged to element-wise contributions. Our goal is to pick a subset of elements $\{K_1, \dots, K_m\} \subset \Omega_h$ for refinement. Most strategies for DWR-type refinement are highly heuristically and based on assumptions that can only be proven under restrictive regularity assumptions, see e.g. [235, 3, 29]:

1. The most efficient discretization have balanced error indicators

$$\eta_K \approx \eta_{K'} \quad \forall K, K' \in \Omega_h.$$

2. Once all error indicators are balanced, it is optimal perform uniform steps of mesh-refinement.
3. It is always best to refine elements with largest indicator value.

The third assumption is the basic guideline for designing refinement strategies, and the most common used are

1. *fixed-number*: Refine the $p\%$ elements with the largest error

$$\text{refine } \{K_1, \dots, K_{p \cdot \#\Omega_h}\}, \text{ for } \eta_{K_1} \geq \eta_{K_2} \cdots \geq \eta_{K_{\#\Omega_h}}$$

2. *fixed-fraction*: Refine those elements with largest error, that sum up to $p\%$ of the overall error

$$\text{refine } \{K_1, \dots, K_l\}, \text{ for } \min \arg_l \sum_{i=1}^l |\eta_{K_i}| \geq p \sum_{i=1}^{\#\Omega_h} |\eta_{K_i}|.$$

3. *equilibration*: Refine all element with error indicator larger than α -times the average

$$\text{refine } K, \text{ if } |\eta_K| \geq \frac{\alpha}{\#\Omega_h} \sum_K |\eta_K|.$$

All three strategies require a parameter p , or α that control the amount of refinement done in every step. The two first techniques will never satisfy assumption 2., as even for completely balanced error indicators, only a subset of some $p\%$ elements will be refined. The equilibration strategy does satisfy all three assumptions, if $\alpha \leq 1$. Such a small value of α however can lead to very excessive over-refinement.

In practical applications, most refinement strategies will give similar results. Further, the parameters p and α must often be tuned to specific problem sets, and it is not possible to pick one optimal strategy. For more insight to refinement strategies and theoretical analysis of the three assumptions, see [3, 186].

7.3 Application to fluid-structure interactions in ALE formulation

In Section 7.1 and 7.2 we have introduced a general framework for a posteriori error estimation and mesh adaptivity. Here, we apply this concept to fluid-structure interaction problems given in ALE coordinates. Again, we want to allow for error estimation with respect to general functionals depending on the solution of the coupled problem. Error estimator and adaptive mesh refinement are driven by the general nonlinear DWR formulation, see Section 7.1.1. We start with the fully stationary case and closely follow [188]. The variational formulation of the FSI system in ALE coordinates is given by

$$A(\mathbf{U})(\Phi) = (J(\mathbf{F}^{-1}\mathbf{v} \cdot \nabla)\mathbf{v}, \phi)_{\mathcal{F}} + (J\sigma_f \mathbf{F}^{-T}, \nabla\phi)_{\mathcal{F}} + (J\mathbf{F}^{-1} : \nabla\mathbf{v}^T, \xi)_{\mathcal{F}} \\ + (\mathbf{F}\boldsymbol{\Sigma}_s, \nabla\phi)_{\mathcal{S}} + (\nabla\mathbf{u}, \nabla\psi_s)_{\mathcal{F}}, \quad (7.31)$$

where (taking $\mathbf{v}|_{\mathcal{S}} = 0$ into account)

$$\mathbf{U} = \{\mathbf{v}, \mathbf{u}, p\} \in \mathcal{X} = H_0^1(\mathcal{F})^d \times H_0^1(\mathcal{F} \cup \mathcal{I} \cup \mathcal{S})^d \times L_0^2(\mathcal{F}).$$

We repeat the notation of the stresses σ_f and $\boldsymbol{\Sigma}_s$ of the St. Venant Kirchhoff material

$$\boldsymbol{\Sigma}_s := 2\mu_s \mathbf{E}_s + \lambda \text{tr}(\mathbf{E}_s), \quad \mathbf{F} := I + \nabla\mathbf{u}, \quad \mathbf{E}_s := \frac{1}{2} (\mathbf{F}^T \mathbf{F} - I), \\ \sigma_f = \rho_f \nu_f (\nabla\mathbf{v} \mathbf{F}^{-1} + \mathbf{F}^{-T} \nabla\mathbf{v}^T) - pI \quad (7.32)$$

The most important step for estimating goal oriented errors is the computation of an adjoint solution with respect to a given error functional $J(\cdot)$. In fluid-structure interactions, these sensitivities must properly include the correct adjoint coupling conditions between the fluid-problem and the solid problem. It is not sufficient to compute sensitivities for each fluid- and solid-problem and neglect the coupling. Such a strategy is only possible for problems with very weak coupling, see [32].

7.3.1 Sensitivities for stationary fluid-structure interactions in ALE coordinates

Given a differentiable error functional $J : \mathcal{X} \rightarrow \mathbb{R}$, the adjoint problem is defined as

$$\mathbf{Z} \in \mathcal{X} : \quad A'(\mathbf{U})(\Phi, \mathbf{Z}) = J'(\mathbf{U})(\Phi) \quad \forall \Phi \in \mathcal{X},$$

where $A'(\mathbf{U})(\Phi, \mathbf{Z})$ is the adjoint of the the directional Gâteaux derivative, the Jacobian, which is defined by

$$A'(\mathbf{U})(\mathbf{W}, \Phi) := \frac{d}{ds} A(\mathbf{U} + s\mathbf{W})(\Phi) \Big|_{s=0}.$$

This Jacobian has already derived in Section 4.2.2 for the ALE formulation and in Section 5.4 for the Fully Eulerian model. Here, we only need to transpose the resulting matrix for obtaining the coupled system matrix of the adjoint problem.

For denoting solution $\mathbf{U} \in \mathcal{X}$, direction $\mathbf{W} \in \mathcal{X}$ and test-function $\Phi \in \mathcal{X}$, we use

$$\mathbf{U} := \begin{pmatrix} \mathbf{v}_f \\ \mathbf{u} \\ p_f \end{pmatrix}, \quad \mathbf{W} := \begin{pmatrix} \mathbf{z}_f \\ \mathbf{w} \\ q_f \end{pmatrix}, \quad \Phi := \begin{pmatrix} \psi_f \\ \phi \\ \xi_f \end{pmatrix}$$

Then, from Section 4.2.2 we copy the stationary parts of (4.13)

$$\begin{aligned} A'(\mathbf{U})(\mathbf{W}, \Phi) &= (\rho_f J (\nabla \mathbf{z} \mathbf{F}^{-1} \mathbf{v} + \nabla \mathbf{v} \mathbf{F}^{-1} \mathbf{z}), \phi)_{\mathcal{F}} \\ &\quad + \left(J \frac{d\sigma_f}{d\mathbf{v}}(\mathbf{W}) \mathbf{F}^{-T}, \nabla \phi \right)_{\mathcal{F}} - (J \mathbf{F}^{-T} q_f, \nabla \phi)_{\mathcal{F}} \\ &\quad + ((J \mathbf{F}^{-1} : \nabla \mathbf{z}^T, \xi)_{\mathcal{F}} \\ &\quad + (\rho_f J \operatorname{tr}(\mathbf{F}^{-1} \nabla \mathbf{w}) (\nabla \mathbf{v} \mathbf{F}^{-1} \mathbf{v}), \phi)_{\mathcal{F}} - (\rho_f J \nabla \mathbf{v} \mathbf{F}^{-1} \nabla \mathbf{w} \mathbf{F}^{-1} \mathbf{v}, \phi)_{\mathcal{F}} \\ &\quad + (J \operatorname{tr}(\mathbf{F}^{-1} \nabla \mathbf{w}) \sigma_f \mathbf{F}^{-T}, \nabla \phi)_{\mathcal{F}} - (J \sigma_f \mathbf{F}^{-T} \nabla \mathbf{w}^T \mathbf{F}^{-T}, \nabla \phi)_{\mathcal{F}} \\ &\quad + \left(J \frac{d\sigma_f}{d\mathbf{u}}(\mathbf{W}) \mathbf{F}^{-T}, \nabla \phi \right)_{\mathcal{F}} \\ &\quad + (J (\mathbf{F}^{-T} : \nabla \mathbf{w}) (\mathbf{F}^{-1} : \nabla \mathbf{v}^T), \xi)_{\mathcal{F}} - (J \mathbf{F}^{-1} \nabla \mathbf{w} \mathbf{F}^{-1} : \nabla \mathbf{v}^T, \xi)_{\mathcal{F}} \\ &\quad + \left(\nabla \mathbf{w} \boldsymbol{\Sigma}_s + \mathbf{F} \frac{d\boldsymbol{\Sigma}_s}{d\mathbf{u}}(\mathbf{W}), \nabla \phi \right)_{\mathcal{S}} \\ &\quad + (\nabla \mathbf{w}, \nabla \psi_f)_{\mathcal{F}}, \end{aligned}$$

Transposition of this bilinear form gives the adjoint system. Here, this simply means switching of \mathbf{W} against Φ and \mathbf{Z} :

Lemma 85 (Adjoint problem for fluid-structure interactions). *Let $\mathbf{U} \in \mathcal{X}$. The linearized adjoint problem is given as to find $\mathbf{Z} = \{\mathbf{z}_f, \mathbf{w}, q_f\} \in \mathcal{Y}$, such that*

$$A'(\mathbf{U})(\Phi, \mathbf{Z}) = J'(\mathbf{U})(\Phi) \quad \forall \Phi \in \mathcal{X},$$

where

$$\begin{aligned}
 A'(\mathbf{U})(\mathbf{W}, \Phi) = & (\rho_f J (\nabla \psi \mathbf{F}^{-1} \mathbf{v} + \nabla \mathbf{v} \mathbf{F}^{-1} \psi), \mathbf{w})_{\mathcal{F}} \\
 & + \left(J \frac{d\sigma_f}{d\mathbf{v}}(\Phi) \mathbf{F}^{-T}, \nabla \mathbf{w} \right)_{\mathcal{F}} - (J \mathbf{F}^{-T} \xi_f, \nabla \mathbf{w})_{\mathcal{F}} \\
 & + ((J \mathbf{F}^{-1} : \nabla \psi^T, q_f)_{\mathcal{F}} \\
 & + \left(\rho_f J \operatorname{tr}(\mathbf{F}^{-1} \nabla \phi) (\nabla \mathbf{v} \mathbf{F}^{-1} \mathbf{v}), \mathbf{w} \right)_{\mathcal{F}} - (\rho_f J \nabla \mathbf{v} \mathbf{F}^{-1} \nabla \phi \mathbf{F}^{-1} \mathbf{v}, \mathbf{w})_{\mathcal{F}} \\
 & + (J \operatorname{tr}(\mathbf{F}^{-1} \nabla \phi) \sigma_f \mathbf{F}^{-T}, \nabla \mathbf{w})_{\mathcal{F}} - (J \sigma_f \mathbf{F}^{-T} \nabla \phi^T \mathbf{F}^{-T}, \nabla \mathbf{w})_{\mathcal{F}} \quad (7.33) \\
 & + \left(J \frac{d\sigma_f}{d\mathbf{u}}(\Phi) \mathbf{F}^{-T}, \nabla \mathbf{w} \right)_{\mathcal{F}} \\
 & + (J (\mathbf{F}^{-T} : \nabla \phi) (\mathbf{F}^{-1} : \nabla \mathbf{v}^T), q_f)_{\mathcal{F}} - (J \mathbf{F}^{-1} \nabla \phi \mathbf{F}^{-1} : \nabla \mathbf{v}^T, q_f)_{\mathcal{F}} \\
 & + \left(\nabla \phi \Sigma_s + \mathbf{F} \frac{d\Sigma_s}{d\mathbf{u}}(\Phi), \nabla \mathbf{w} \right)_{\mathcal{S}} \\
 & + (\nabla \phi, \nabla \mathbf{z}_f)_{\mathcal{F}},
 \end{aligned}$$

This adjoint problem is linear in $\mathbf{Z} \in \mathcal{Y}$ and $\Phi \in \mathcal{X}$. The assembly of the adjoint system matrix is computationally intense. If the nonlinear fluid-structure interaction problem will be solved by a Newton's method, see Section 4.2.2 and the Jacobian is required in every step of the Newton iteration. Then, solving the adjoint problem simply corresponds to the effort required for transposing the matrix and performing one additional Newton-like step.

Although this formulation indicates the exact linearized adjoint of the fsi-problem in variational formulation, it does not give insight into the adjoint coupling conditions. Here, it would be required to derive a classical adjoint formulation and adjoint boundary conditions for \mathbf{z}, \mathbf{w}_f and q_f on Γ_i which is demanding due to the complex structure of the linearized adjoint. It would be necessary to remove all derivatives from the test-functions. Considering single terms in (7.33) like

$$\left(\rho_f J \operatorname{tr}(\mathbf{F}^{-1} \nabla \phi) \nabla \mathbf{v} \mathbf{F}^{-1}, \mathbf{w} \right)_{\mathcal{F}},$$

this task is rather complex. Considering this difficulty, the value of approximations and linearizations to error estimators that do not require the strong residual nor edge terms, that have been derived in Section 7.2.1 gets obvious.

7.3.2 Numerical examples: error estimation and adaptivity

In this section, we study two problems and show the efficiency of the dual weighted residual method. First we consider the stationary FSI-1 benchmark as proposed by Hron, Turek et. al. in [135]. In this two-dimensional problem, a laminar flow around a circular obstacle with an attached elastic beam is considered, see Figure 7.5. Quantity of interest is the drag coefficient of the obstacle as well as the deformation of the tip of the beam.

Secondly, as a three-dimensional benchmark problem, the laminar flow over an elastic obstacle mounted on the wall is considered. As quantities of interest we again evaluate the deformation in a point within the elastic structure and the drag coefficient of the obstacle.

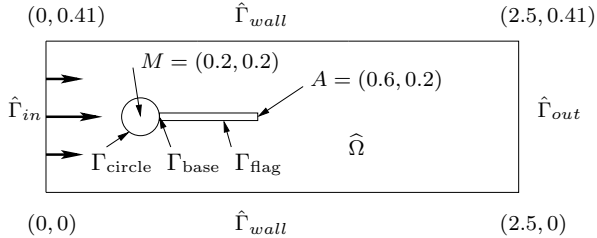


Figure 7.5: Flow around cylinder with elastic beam with circle-center $M = (0.2, 0.2)$ and radius $r = 0.05$.

The FSI-1 benchmark problem

First, we consider the stationary benchmark problem FSI-1 [57, 58]. Here, the laminar flow around a cylinder, with an attached elastic beam is simulated. Figure 7.5 shows a sketch of the configuration.

Problem configuration Three benchmark problems have been proposed by Hron & Turek [135]. We limit the considerations to the stationary FSI-1 test-case. The flow is laminar with Reynolds-number $Re = 20$ and driven by a parabolic inflow profile with average velocity $\bar{v}_f = 0.2$. For the structural problem, the St. Venant-Kirchhoff material law is used in a slightly compressible setting with Poisson ratio $\nu_s = 0.4$:

$$\rho_f = \rho_s = 1000, \quad \nu_f = 10^{-3}, \quad \mu_s = 5 \cdot 10^5, \quad \lambda_s = 2 \cdot 10^6, \quad \bar{v}_f = 0.2$$

As quantities of interest, we measure the horizontal and vertical deflection of the structure in the point $A = (0.6, 0.2)$ on the tip of the beam, as well as the drag- and lift- coefficient of the complete obstacle (including rigid circle and the elastic beam):

$$\begin{aligned} J_{\text{drag}}(\mathbf{U}) &:= \int_S (J\sigma_f \mathbf{F}^{-T}) \vec{n}_f \cdot e_1 \, ds & J_{\text{lift}}(\mathbf{U}) &:= \int_S (J\sigma_f \mathbf{F}^{-T}) \vec{n}_f \cdot e_2 \, ds \\ J_x(\mathbf{U}) &:= \mathbf{u}_1(A) & J_y(\mathbf{U}) &:= \mathbf{u}_2(A), \end{aligned}$$

where $e_i := (\delta_{i1}, \delta_{i2})$ are the Cartesian unit vectors and $S := \Gamma_{\text{flag}} \cup (\Gamma_{\text{circle}} \setminus \Gamma_{\text{base}})$.

Evaluation of the surface integral For easier evaluation, we modify the functional expression. Let Γ_{circle} be the boundary, $\Gamma_{\text{base}} \subset \Gamma_{\text{circle}}$ that part of the circle, where the solid domain \mathcal{S} is attached. Then, by using the dynamic coupling condition on Γ_i it holds:

$$J_{\text{drag}}(\mathbf{U}) = \int_{\Gamma_{\text{circle}} \setminus \Gamma_{\text{base}}} (J\sigma_f \mathbf{F}^{-T}) \vec{n}_f \cdot e_1 \, ds - \int_{\Gamma_i} (J\sigma_s \mathbf{F}^{-T}) \vec{n}_s \cdot e_1 \, ds$$

Further, using $\text{div}(J\sigma_s \mathbf{F}^{-T}) = 0$ since no right hand side is given in this benchmark configuration, the surface integral can be transformed into an integral over the complete circle Γ_{circle} :

$$J_{\text{drag}}(\mathbf{U}) = \int_{\Gamma_{\text{circle}} \setminus \Gamma_{\text{base}}} (J\sigma_f \mathbf{F}^{-T}) \vec{n}_f \cdot e_1 \, ds + \int_{\Gamma_{\text{base}}} (J\sigma_s \mathbf{F}^{-T}) \vec{n}_s \cdot e_1 \, ds$$

An evaluation of this surface integral with higher accuracy is possible by expressing it in terms of residuals (the *Babuska-Miller-Trick*) [8, 9, 10, 60, 48] tested with a non-conforming test-function $\hat{\mathbf{Z}}^{\text{drag}} \notin X$

$$J_{\text{drag}}(\mathbf{U}) = A(\mathbf{U})(\hat{\mathbf{Z}}^{\text{drag}}), \quad \hat{\mathbf{Z}}^{\text{drag}} := \{0, 0, \hat{\chi}^u\}, \quad (7.34)$$

where

$$\hat{\chi}_y^u := 0, \quad \hat{\chi}_x^u := \begin{cases} 1 & : x \in \Gamma_{\text{circle}} \\ \text{extended to } 0 & : x \notin \Gamma_{\text{circle}} \cup \Gamma_{\text{base}} \end{cases}.$$

Given sufficient regularity, the evaluation of the drag- and lift-coefficients using this technique yields a higher order of convergence [48], namely second order for linear finite elements. In the case of the lift-coefficients, the components $\hat{\chi}_y^u$ and $\hat{\chi}_x^u$ must be switched.

Obtaining Reference values of the FSI-1 benchmark problem This benchmark problem is well analyzed in the collections [57, 58]. In Table 7.1 we collect reference values for all four functionals used in this work. These results are obtained by reviewing the cited references and extrapolating results using higher order finite elements on uniform meshes. The values are in very good agreement with those identified by Turek and coworkers [228].

functional	reference value	accuracy
drag	14.294	$\pm 5 \cdot 10^{-4}$
lift	0.7648	$\pm 5 \cdot 10^{-5}$
x -deformation	$2.268 \cdot 10^{-5}$	$\pm 5 \cdot 10^{-9}$
y -deformation	$8.190 \cdot 10^{-4}$	$\pm 5 \cdot 10^{-7}$

Table 7.1: Reference values for the FSI-1 benchmark.

Error estimation and results on locally refined meshes For error estimation with the dual weighted residual method we need to approximate the adjoint problems:

$$\mathbf{Z}_h \in X_h : \quad A'_h(\mathbf{U}_h)(\Phi_h, \mathbf{Z}_h) = J'(\mathbf{U}_h)(\Phi_h) \quad \forall \Phi_h \in X_h.$$

Detail on the adjoint bilinear-form are given in the previous section. For the two deflection functionals J_x, J_y , the right hand side of the adjoint problems is a Dirac and lacks the necessary regularity $J'_x, J'_y \notin H^{-1}(\Omega)$. Hence, these functionals should be regularized with a small parameter $\epsilon > 0$:

$$J_{x/y}(\mathbf{U}) = \frac{1}{|B_\epsilon(A)|} \int_{B_\epsilon(A)} u_{x/y} \, d\mathbf{x}, \quad B_\epsilon(A) := \{x \in \Omega : |x - A| < \epsilon\}.$$

In the case of the drag- and lift-coefficients, the right hand side of the adjoint problems is defined by using $\hat{\mathbf{Z}}^{\text{drag}}$ from (7.34)

$$J'_{\text{drag}}(\mathbf{U})(\Phi) = A'(\mathbf{U})(\Phi, \hat{\mathbf{Z}}^{\text{drag}}).$$

Since $\hat{\mathbf{Z}}^{\text{drag}}$ is a extension of (non-conforming) Dirichlet-values into the domain, this problem is related to solving a problem with homogenous right hand side and non-homogenous Dirichlet values on Γ_{circle} :

$$\hat{\mathbf{Z}}_h \in \hat{\mathbf{Z}}^{\text{drag}} + X_h : \quad A'_h(\mathbf{U}_h)(\Phi_h, \hat{\mathbf{Z}}_h) = 0 \quad \forall \Phi_h \in X_h.$$

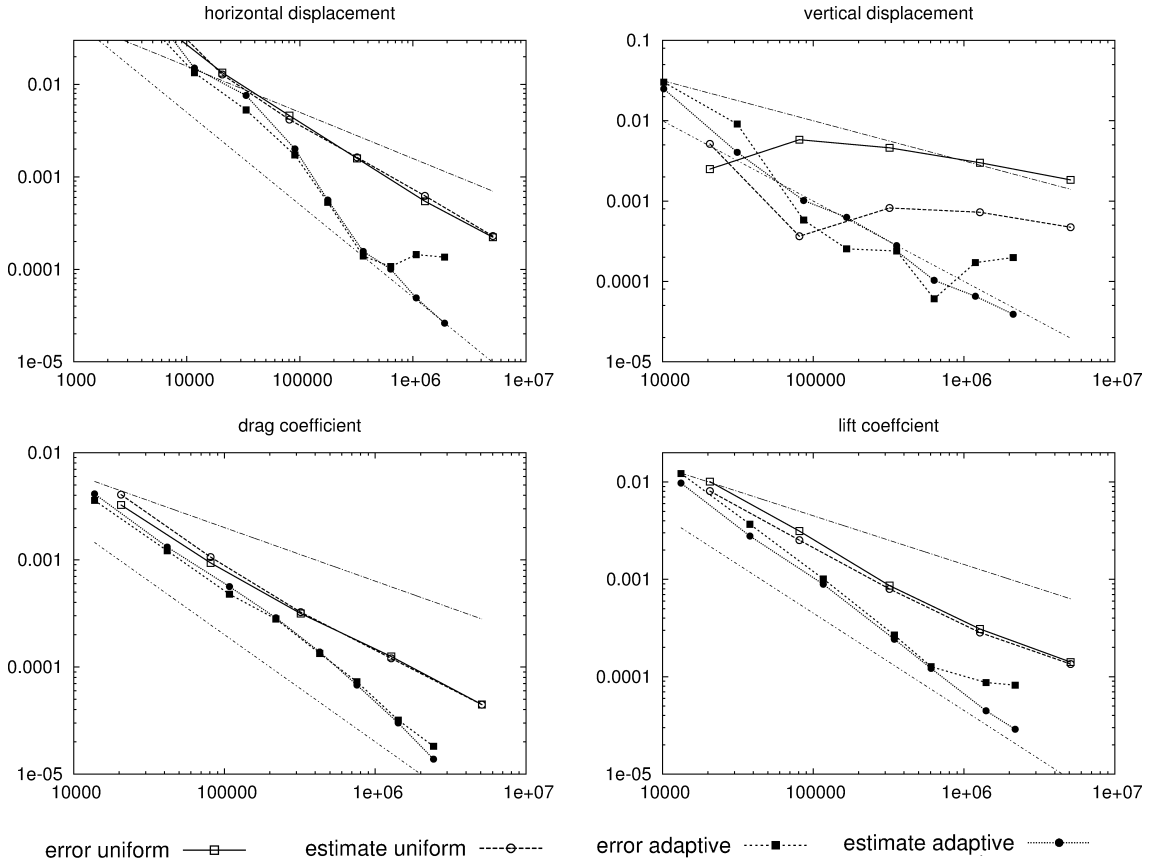


Figure 7.6: Error and estimator for the different functionals on uniform meshes and locally refined meshes. Top left to bottom right: error in horizontal and vertical deflection, drag- and lift-coefficient. For comparison: slopes with linear and quadratic convergence.

In Figure 7.6, we compare the convergence history of all four error-functionals. In each sketch we compare the relative errors using uniform mesh refinement with those obtained on locally refined meshes using the dual weighted residual method. Further, on both sequences of meshes we plot the values of the error estimator. Finally, for comparison we give sketches of the error slopes corresponds to linear convergence $h \approx N^{-\frac{1}{2}}$ and quadratic convergence $h^2 \approx N^{-1}$. Note, that apparent loss of convergency on fine meshes (in particular for the lift-coefficient and the two displacement functionals) is due to limited accuracy of the reference values, see Table 7.1.

Next, in the left plot in Figure 7.7 we show the effectivities of the error estimator, namely

$$\text{eff}_h := \frac{\eta_h(\mathbf{U}_h, \mathbf{Z}_h)}{J(\mathbf{U}) - J(\mathbf{U}_h)},$$

on a sequence of uniform meshes for all four error functionals. A value of one indicates error estimation with optimal accuracy. In the right half of this Figure 7.7 we show the composition of the error estimator split into the primal residual $F(\mathbf{Z} - i_h \mathbf{Z}) - A_h(\mathbf{U}_h)(\mathbf{Z} - i_h \mathbf{Z})$, the adjoint residual $J'(\mathbf{U}_h)(\mathbf{U} - i_h \mathbf{U}) - A'_h(\mathbf{U}_h)(\mathbf{U} - i_h \mathbf{U}, \mathbf{Z}_h)$ and the stabilization part $S_h(\mathbf{U}_h)(\mathbf{Z}_h)$ considering the drag-coefficient.

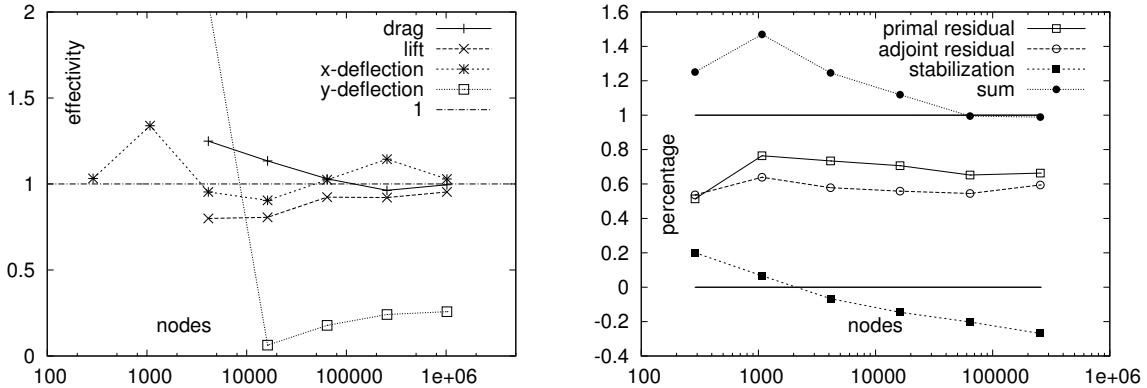


Figure 7.7: Effectivity of the dual weighted residual method on uniform meshes. Left: effectivities for all four functionals values on uniform meshes. Right: composition of the estimator into primal residual, adjoint residual and stabilization part for the drag coefficient w.r.t the exact error.

In Figure 7.8 we show the adjoint solutions with regard to the drag-evaluation. In the top-row the two components of the adjoint variable $\mathbf{w}_f \in \mathcal{V}_f$ which is only defined in \mathcal{F} and in the bottom-row the two components of the variable $\mathbf{u} \in \mathcal{V}$ are shown. In the lower left plot one sees the Dirichlet-values $\hat{\mathbf{Z}}^{\text{drag}}$ on the obstacle used to evaluate the drag coefficient.

Discussion of the results We start by discussing the results obtained on uniform meshes. Using piecewise linear finite elements, all four functionals should converge with second order (in the mesh size), given sufficient regularity of the solution. Figure 7.6 however depicts linear convergence only. This order reduction is due to limited regularity induced by the reentrant edges at the interface Γ_i as seen from the fluid domain. Similar results are observed for pure fluid dynamics benchmark problems [205, 48]. When comparing the estimator value with the real error in Figures 7.6 and 7.7, one observes very good effectivities $\text{eff}_h \xrightarrow[h \rightarrow 0]{} 1$ for the drag- and lift-coefficient (even if the regularity of the problem is not sufficient to guarantee higher order convergence of the remainders $\mathcal{R}^{(3)}$). In the case of the two deflection functionals - and in particular for the vertical deflection functional J_y - the quality of the estimator is less. This is explained by additional regularity limitations due to the Dirac structure of the functionals J_x and J_y .

The right sketch in Figure 7.7 shows that all three parts of the error estimator are essential. It is well known [29] that for linear problems primal and adjoint parts in the error estimator coincide (in the limit $h \rightarrow 0$). For nonlinear problems all parts must be taken into account. Further, we see that the stabilization part cannot be neglected. In Figure 7.9 we show some meshes with local mesh refinement obtained during the simulation.

3D fluid-structure interaction

Finally, we present numerical simulations of a three dimensional test-case. In the domain $\Omega := (0, 1.5) \times (0, 0.4) \times (-0.4, 0.4)$ an elastic structure $\mathcal{S} := (0.4, 0.5) \times (0, 0.2) \times (-0.2, 0.2)$

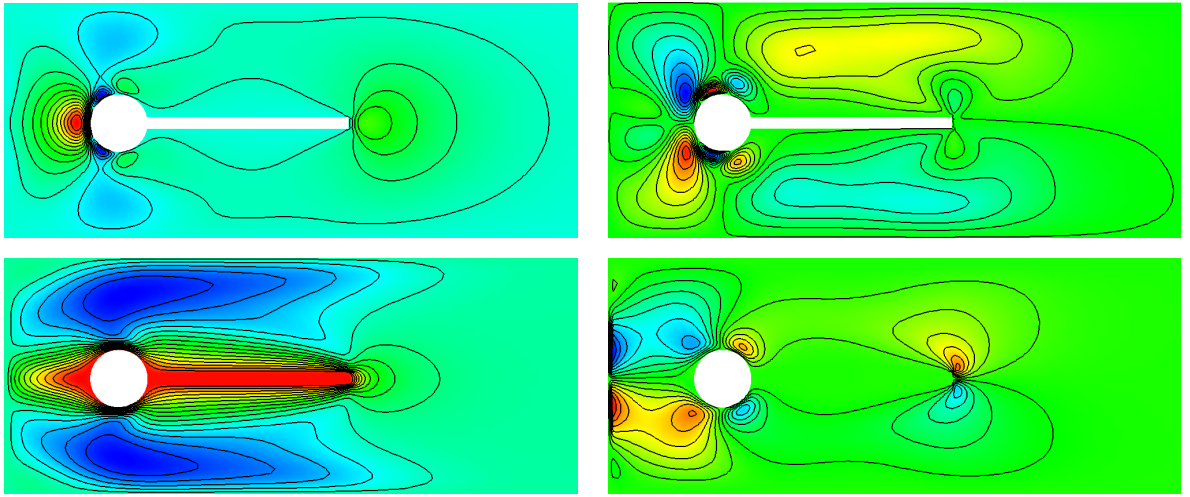


Figure 7.8: Adjoint solution with regard to the drag-coefficient. Top row: adjoint horizontal velocity \mathbf{w}_f , bottom row, adjoint deformation \mathbf{z} .

is inscribed, see Figure 7.10. The problem is considered to be symmetric in the x/y -plane. Hence, we run the simulation only in one half of the domain. On the inflow boundary $\Gamma_{\text{in}} = (0, 0.4) \times (-0.4, 0.4)$, a parabolic velocity profile is given as Dirichlet condition with peak velocity $\mathbf{v}_{\max} = 0.3$. On the inner symmetry plane, we prescribe $\mathbf{v}_f \cdot \vec{n} = 0$ as Dirichlet condition, on the outflow boundary Γ_{out} the *do-nothing* condition for velocity and pressure. The no-slip condition is used on the remaining boundaries Γ_{wall} . The solid is fixed by a homogenous Dirichlet condition $\mathbf{u}_s = 0$ on the bottom Γ_{base} . Deformation in normal-direction is prohibited $\mathbf{u}_s \cdot \vec{n} = 0$ on the symmetry-plane Γ_{sym} . On the remaining boundaries $\Gamma_{\text{wall}}, \Gamma_{\text{out}}$ and Γ_{in} the fluid's deformation is extended with homogenous Dirichlet values $\mathbf{u}_f = 0$.

The fluid is incompressible with $\rho_f = 10^3$ and $\nu_f = 10^{-3}$. The solid's density is $\rho_s = 10^3$, its Poisson ratio $\nu_s = 0.4$ with a shear modulus of $\mu_s = 5 \cdot 10^5$. With an average inflow velocity of $\bar{\mathbf{v}}_{\text{in}} \approx 0.15$, and an obstacle of size 0.2, the Reynolds number is $Re \approx 25$ and the flow is in the laminar regime. For the LPS stabilization, we use the parameter $\delta_0 = 0.25$.

As quantities of interest, we measure the x -deflection of the obstacle at the coordinate $A = (0.45, 0.15, 0.15)$ close to the outer corner of the structure, as well as the force of the fluid on the structure in the dominant flow direction:

$$J_x(\mathbf{U}) := \mathbf{e}_1 \cdot \mathbf{u}(A), \quad J_{\text{drag}}(\mathbf{U}) := \int_{\Gamma_i} (J \sigma_f \mathbf{F}^{-T}) \vec{n}_f \cdot \mathbf{e}_1 \, d s.$$

Like in the two-dimensional case, the surface integral is first transformed using the structure equation and then expressed as a residual term $J_{\text{drag}}(\mathbf{U}) = A(\mathbf{U})(\hat{\mathbf{Z}}^{\text{drag}})$ using a function $\hat{\mathbf{Z}}^{\text{drag}} \notin \mathcal{X}$ with non-conforming boundary values at Γ_{base} , compare (7.34).

For obtaining reference values we estimate the two error quantities on a sequence of meshes using uniform refinement. Table 7.2 we collect the results. By extrapolating, using the values on the finest three meshes, we define reference values in Table 7.3.

We believe these values to be exact to a relative error of about 1%. Further refinements using parallel computers and higher order finite elements on adapted meshes are necessary to

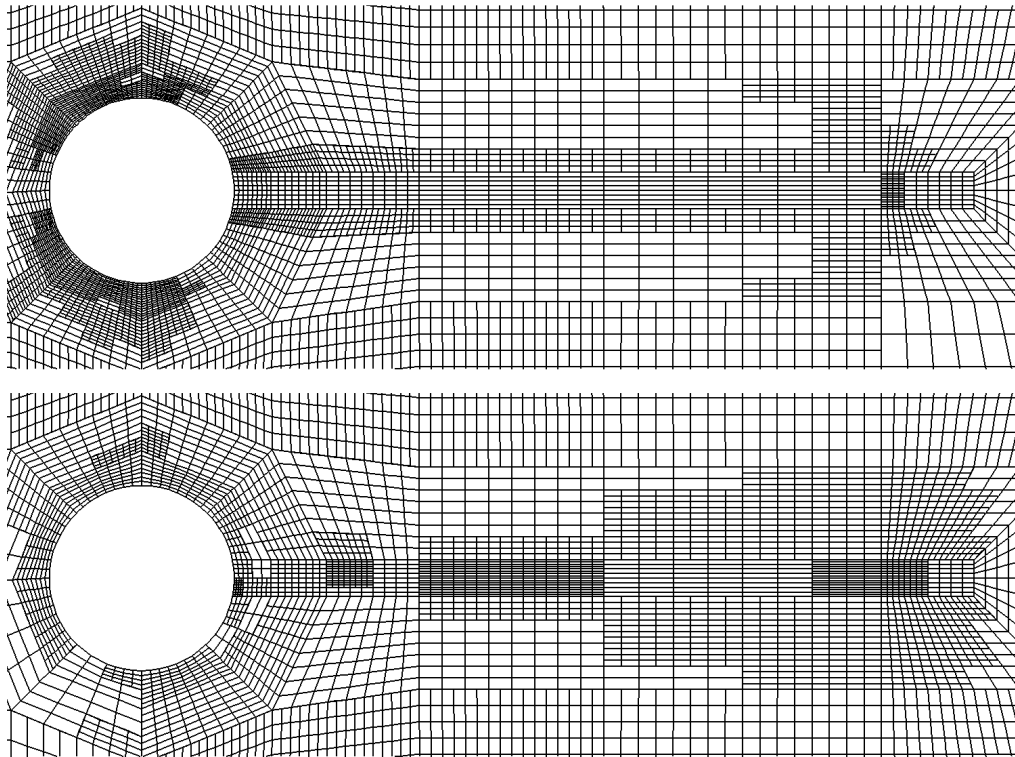


Figure 7.9: Cut-out of locally refined meshes used to approximate the drag-coefficient (top) and the horizontal displacement functional (bottom).

generate reference values with a higher accuracy. Here however we refrain from using higher order finite elements, since the reconstruction method for evaluating the error estimator in Section 2 would require an even larger patch structures of the mesh which is not feasible without parallel computers, see Figure 7.3.

In Figure 7.11 we plot the convergence history on uniform and locally refined meshes, both for the drag-coefficient and the horizontal displacement functional.

This three dimensional test-case has the same regularity limitations as the FSI-1 benchmark problem. The elastic obstacle induces corner singularities in the solution and the horizontal deflection functional J_x lacks regularity. In both cases, the computational effort necessary to reach a certain error tolerance is reduced significantly by using adaptive finite elements. Considering the complexity of three dimensional simulations these savings are substantial. In order to resolve the singularities caused by the reentrant corners of the embedded structure, it was essential to run the adaptation process very slowly by choosing $\alpha = 8$ in the equilibration procedure described in Section 7.2.2.

Finally, Figure 7.12 shows a visualization of a numerical solution. Here, adaptation is driven in order to optimize the functional value $J_x(\mathbf{U}_h)$. Deformation of the structure is scaled by 100 for better visualization.

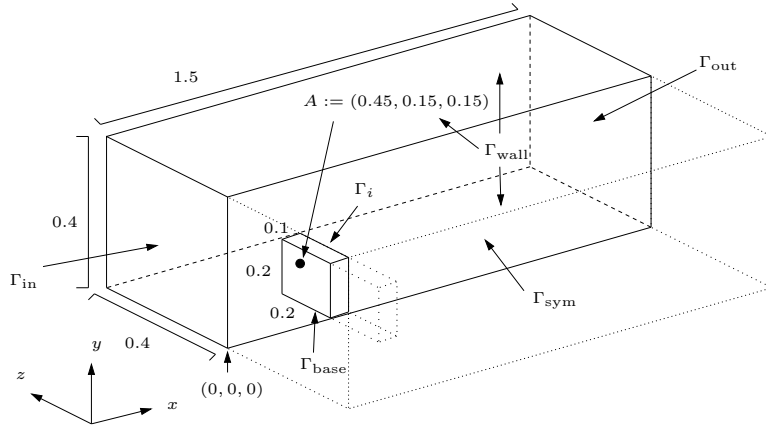


Figure 7.10: Configuration of the three-dimensional test-case. Domain and solution are symmetric in z -direction.

dof's	$J_{\text{drag}}(\mathbf{U}_h)$	error (abs)	$J_x(\mathbf{U}_h)$	error (abs)
2 975	1.5249	$1.98 \cdot 10^{-1}$	$4.9337 \cdot 10^{-5}$	$9.90 \cdot 10^{-6}$
18 711	1.4763	$1.49 \cdot 10^{-1}$	$5.5686 \cdot 10^{-5}$	$3.55 \cdot 10^{-6}$
131 495	1.4038	$7.68 \cdot 10^{-2}$	$5.8529 \cdot 10^{-5}$	$7.11 \cdot 10^{-7}$
983 367	1.3563	$2.93 \cdot 10^{-2}$	$5.9075 \cdot 10^{-5}$	$1.65 \cdot 10^{-7}$
7 600 775	1.3380	$1.10 \cdot 10^{-2}$	$5.9202 \cdot 10^{-5}$	$3.80 \cdot 10^{-8}$

Table 7.2: Convergence history of the three dimensional fsi test-case using piece-wise linear finite elements. The bold lines indicate, that an error below 1% has been reached.

7.3.3 Adaptivity for time-periodic fsi problems

7.3.4 Anisotropic mesh refinement

functional	reference value	accuracy
drag	1.33	1%
x -deflection	$5.95 \cdot 10^{-5}$	1%

Table 7.3: Reference values for the three dimensional benchmark problem.

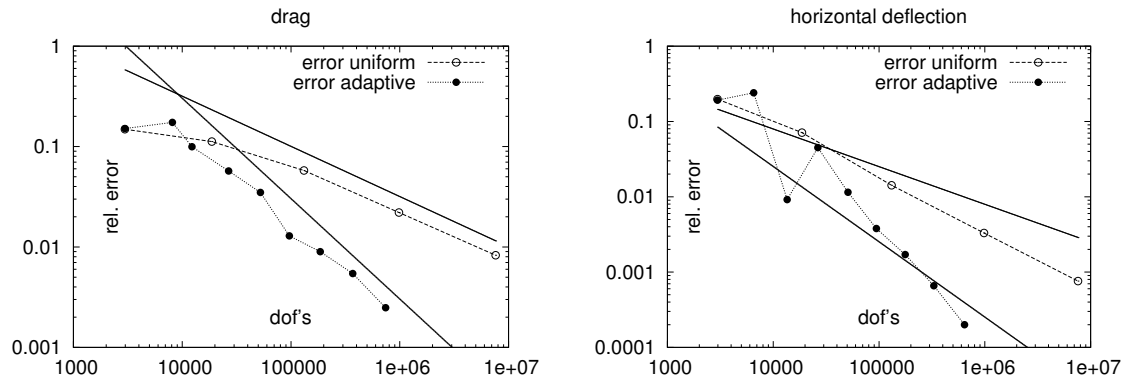


Figure 7.11: Error history for the drag-coefficient (left) and horizontal displacement (right) on uniform and adaptively refined meshes. Linear and quadratic error slopes for comparison.

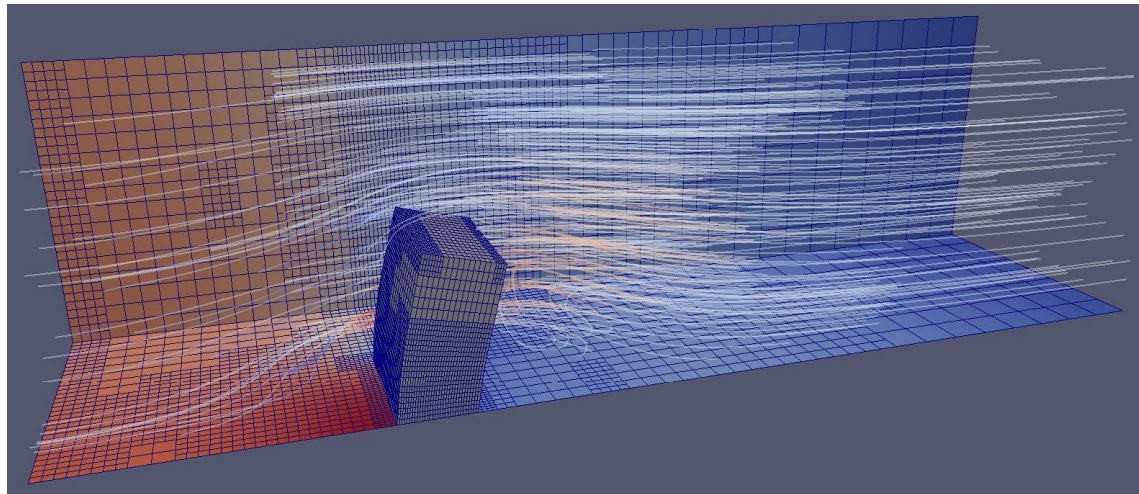


Figure 7.12: Sketch of the numerical solution on locally refined meshes. The domain is cut at the symmetry plane Γ_{sym} in the front.

8 Applications

In this last chapter, we will present different applications of fluid-structure interactions. Common to all of them is a special kind of demand for strong coupling, monolithic formulations and implicit discretizations and solvers. Among the vast diversity of applications, this presentation is only a very small subset with a focus on large deformation, laminar flows and a very strong coupling between the phases.

8.1 Optimization with fluid-structure interactions

Many applications require the approximation of inverse problems. The simulation is only a tools for predicting the behavior of the coupled system. Typical optimization problems could be the control of inflow to reduce the vorticity or to stabilize the dynamics of a fluid-structure interaction system. A related problem is the identification of parameters like Lamé coefficients by indirect measurements.

In this section, some basic principles for the optimization with partial differential equations and the application to simple, stationary fluid-structure interaction problems will be collected. For an intensive introduction to optimization and parameter identification with partial differential equations, we refer to the literature [225, 226, 162, 127]. On optimization with fluid-structure interactions, there is only little literature [57, 58, ?]. From the large variety of different optimization techniques, we solely consider gradient based methods. The contents of this section have mainly been taken from [193], a collaboration with Thomas Wick.

For gradient based optimization of coupled problems, it is necessary to assemble gradients of the fully coupled model. The adjoint solutions, based on these gradients, are sensitivities that show the impact of the control on the target functional. In partitioned methods, where the coupling is realized by an iterative algorithm only, this is a very difficult step. In general, it is easily possible to perform a sensitivity analysis within the subproblems, the correct transportation of adjoint information across the interface however is not easily possible.

8.1.1 The optimization problem

We consider optimization problems, where the optimal solution is solution to a stationary fluid-structure interaction problem. For simplicity, we will consider the ALE formulation from Chapter 4 only, such that $\mathbf{U} \in \mathbf{U}^D + \mathcal{X}$ is constraint to

$$\begin{aligned} A(\mathbf{U})(\Phi) = & (\rho_f J (\nabla \mathbf{v} \mathbf{F}^{-1} \mathbf{v}), \phi)_{\mathcal{F}} + (J \sigma_f \mathbf{F}^{-T}, \nabla \phi)_{\mathcal{F}} - (J \rho_f \mathbf{f}, \phi)_{\mathcal{F}} \\ & + (J \mathbf{F}^{-1} : \nabla \mathbf{v}^T, \xi)_{\mathcal{F}} + (\mathbf{F} \boldsymbol{\Sigma}_s, \nabla \phi)_{\mathcal{S}}, \end{aligned} \quad (8.1)$$

8.1. Optimization with fluid-structure interactions

where \mathbf{U}^D is an extension of the Dirichlet data and where $\mathbf{U} = \{\mathbf{v}, \mathbf{u}, p\}$ is found in

$$\mathcal{X} = H_0^1(\mathcal{F}; \Gamma_f^D)^d \times H_0^1(\mathcal{F} \cup \mathcal{I} \cup \mathcal{S}; \Gamma^D)^d \times L_0^2(\mathcal{F}).$$

We consider the following setting: by $K : \mathcal{X} \rightarrow \mathbb{R}$ we denote a given functional of interest. One example could be the outflow rate at a boundary part Γ_f^{out}

$$K_{\text{out}}(\mathbf{U}) = \int_{\Gamma_f^{\text{out}}} (\mathbf{v} \cdot \vec{n})^2 \, d\sigma, \quad (8.2)$$

or a functional of tracking type measuring the deflection of the solid

$$K_A(\mathbf{U}) = |\mathbf{u}(A) - \mathbf{u}^A|^2, \quad (8.3)$$

where $A \in \bar{\mathcal{S}}$ is a point within the solid, $\mathbf{u}^A \in \mathbb{R}^d$ a prescribed deflection. Regarding the discussion in Section 7.1.1, such a functional of point-type must be regularized to fit into the theoretical framework. We assume, that $K(\cdot)$ is two times Fréchet differentiable.

Furthermore, by $\mathbf{q} \in \mathbf{Q}_d$, we denote the control, coming from the control space \mathbf{Q}_d . Typical examples could be the Lamé coefficients $\mathbf{q} = \{\mu_s, \lambda_s\}$, a two-dimensional control space, the inflow profile $\mathbf{q} = \mathbf{v}^{\text{in}}$, where $\mathbf{Q}_d = H^{\frac{1}{2}}(\Gamma_f^{\text{in}})$, a mean inflow pressure $\mathbf{q} = P^{\text{in}}$, where $\mathbf{Q}_d = \mathbb{R}$. Often, such controls are constrained, e.g. by allowing only for positive pressures up to a certain limit or by requiring the Lamé coefficients to satisfy some physical relations. Here, we will not consider any control constraints.

The control \mathbf{q} can enter the problem in various ways. We introduce the modified variational formulation

$$\mathbf{U} \in \mathbf{U}^D + \mathcal{X} : \quad A(\mathbf{q}, \mathbf{U})(\Phi) := A(\mathbf{U})(\Phi) + B(\mathbf{q}, \mathbf{U})(\Phi) = F(\Phi) \quad \forall \Phi \in \mathcal{X},$$

where by $B(\cdot, \cdot)(\cdot)$ we denote the *control form*. We specify this control form for two examples: first, we consider the case of controlling the average inflow pressure on the boundary Γ_f^{in} . Then, the velocity is found in

$$\mathbf{v} \in \mathbf{v}^D + H_0^1(\mathcal{F}; \Gamma_f^D \setminus \Gamma_f^{\text{in}})^d,$$

such that natural boundary conditions act. Together with

$$B(\mathbf{q}, \mathbf{U})(\Phi) = -\langle \rho_f \nu_f J \nabla \mathbf{v}^T \mathbf{F}^{-T} \mathbf{F}^{-T} \vec{n}, \phi \rangle_{\Gamma_f^{\text{in}}} - \langle \mathbf{q} J \mathbf{F}^{-T} \vec{n}, \phi \rangle_{\Gamma_f^{\text{in}}}, \quad (8.4)$$

integration by parts reveals on Γ_f^{in} the condition

$$\rho_f \nu_f J \mathbf{F}^{-1} \nabla \mathbf{v}^T \mathbf{F}^{-T} \vec{n} - p J \mathbf{F}^{-T} \vec{n} = \mathbf{q} J \mathbf{F}^{-T} \vec{n},$$

which corresponds to an average inflow pressure of \mathbf{q} , see Section 1.4.2. Second, we consider the control of the parameter μ_s in the material law by introducing the control form

$$B(\mathbf{q}, \mathbf{U})(\Phi) = (\mathbf{F} \boldsymbol{\Sigma}_s(\mathbf{q}) - \mathbf{F} \boldsymbol{\Sigma}_s(\mu_s^0), \nabla \phi)_{\mathcal{S}}, \quad (8.5)$$

where (for the St. Venant Kirchhoff material)

$$\boldsymbol{\Sigma}_s(\mathbf{q}) := 2\mathbf{q}\mathbf{E}_s + \lambda_s \text{tr}(\mathbf{E}_s)I, \quad \mathbf{E}_s := \frac{1}{2}(\mathbf{F}^T \mathbf{F} - I). \quad (8.6)$$

By μ_s^0 we denote an initial guess. The goal of our optimization problem is to determine the optimal parameters $\mathbf{q} \in \mathbf{Q}_d$ such that the functional of interest $K(\cdot)$ gets minimal. This quantity of interest is completed by a regularization term of Tikhonov type, which involves a regularization parameter $\alpha > 0$:

$$K(\mathbf{q}, \mathbf{U}) := K(\mathbf{U}) + \frac{\alpha}{2} \|\mathbf{q} - \bar{\mathbf{q}}\|_Q^2, \quad (8.7)$$

with a reference control $\bar{\mathbf{q}} \in \mathbf{Q}_d$ and a suitable norm $\|\cdot\|_Q$ in the control-space. With these preparations we can formulate the constrained optimization problem:

System 5 (Constrained optimization problem). *Find $\mathbf{U} \in \mathbf{U}^D + \mathcal{X}$ and $\mathbf{q} \in \mathbf{Q}_d$, such that*

$$K(\mathbf{q}, \mathbf{U}) \rightarrow \min, \text{ where } A(\mathbf{q}, \mathbf{U})(\Phi) = F(\Phi) \quad \forall \Phi \in \mathcal{X}.$$

Introducing the Lagrangian

$$L(\mathbf{q}, \mathbf{U}, \mathbf{Z}) = K(\mathbf{q}, \mathbf{U}) + F(\mathbf{Z}) - \mathbf{A}(\mathbf{q}, \mathbf{U})(\mathbf{Z}),$$

a minimum to System 5 must satisfy the first order optimality condition

$$L'(\mathbf{q}, \mathbf{U}, \mathbf{Z})(\delta \mathbf{q}, \delta \mathbf{U}, \delta \mathbf{Z}) = 0 \quad \forall \delta \mathbf{q} \in \mathbf{Q}_d, \forall \delta \mathbf{U} \in \mathcal{X}, \forall \delta \mathbf{Z} \in \mathcal{X},$$

which corresponds to the following system of equations, the *Karush-Kuhn-Tucker conditions* (KKT):

$$\begin{aligned} A(\mathbf{q}, \mathbf{U})(\Phi) &= F(\Phi) & \forall \Phi \in \mathcal{X}, \\ A'_U(\mathbf{q}, \mathbf{U})(\Phi, \mathbf{Z}) &= K'_U(\mathbf{q}, \mathbf{U})(\Phi) & \forall \Phi \in \mathcal{X}, \\ A'_q(\mathbf{q}, \mathbf{U})(\chi, \mathbf{Z}) &= K'_q(\mathbf{q}, \mathbf{U})(\chi) & \forall \chi \in \mathbf{Q}_d. \end{aligned} \quad (8.8)$$

The first equation is called the *state equation*, the second the *adjoint equation* and the last one the *gradient equation*.

The adjoint equation is exactly the equation for the adjoint problem in the context of the *Dual Weighted Residual method*, that has been introduced in Section 7.1.1 and which is detailed in (7.33). The specific form of the gradient equation strongly depends on the way, that the control enters the problem. In the case of the pressure control on the inflow boundary (8.4), this gradient equation reads

$$-\chi \langle J\mathbf{F}^{-T} \vec{n}, \mathbf{z} \rangle_{\Gamma_f^{\text{in}}} = \chi \alpha (\mathbf{q} - \bar{\mathbf{q}}) \quad \forall \chi \in \mathbb{R}. \quad (8.9)$$

This allows to express the control \mathbf{q} in terms of the other variables

$$\mathbf{q} = \bar{\mathbf{q}} - \frac{1}{\alpha} \langle J\mathbf{F}^{-T} \vec{n}, \mathbf{z} \rangle_{\Gamma_f^{\text{in}}}, \quad (8.10)$$

which reduces the KKT system (8.8) to a coupled system of the state and the adjoint equation. Regarding the identification of the Lamé coefficient (8.5), the gradient equation gets

$$\chi (2\mathbf{F}\mathbf{E}_s, \nabla \mathbf{z})_{\mathcal{S}} = \chi \alpha (\mathbf{q} - \bar{\mathbf{q}}) \quad \forall \chi \in \mathbb{R}, \quad (8.11)$$

where we directly computed the derivative of $\Sigma_s(\mathbf{q})$ in direction of \mathbf{q} , compare (8.6). Again, we can explicitly compute the control $\mathbf{q} \in \mathbb{R}$ from this equation

$$\mathbf{q} = \bar{\mathbf{q}} + \frac{2}{\alpha} (2\mathbf{F}\mathbf{E}_s, \nabla \mathbf{z})_{\mathcal{S}}. \quad (8.12)$$

8.1.2 Reduced formulation of the optimization problem

On drawback of the direct discretization of the KKT system (8.8) is the very large coupled system of equations, that has to be solved. Even if an explicit formula for the computation of the control \mathbf{q} can be used, a coupled system in $\{\mathbf{U}, \mathbf{Z}\} \in \mathcal{X} \times \mathcal{X}$ remains to be solved. In terms of fluid-structure interaction, this refers to a coupled system of 10 (in 2d) and 14 (in 3d) equations. Instead, we first introduce a *reduced formulation* of the optimization problem [225, 226, 27, 162, 127] and [193] in the context of fsi:

System 6 (Unconstrained optimization problem). *Find $\mathbf{q} \in \mathbf{Q}_d$, such that*

$$k(\mathbf{q}) := K(\mathbf{q}, S(\mathbf{q})) \rightarrow \min, \quad (8.13)$$

where the solution operator $S : \mathbf{Q}_d \rightarrow \mathcal{X}$ is defined as

$$A(\mathbf{q}, S(\mathbf{q}))(\Phi) = F(\Phi) \quad \forall \Phi \in \mathcal{X}.$$

The solution of this unconstrained optimization problem is characterized by the first order necessary condition

$$k'(\mathbf{q})(\chi) = 0 \quad \forall \chi \in \mathbf{Q}_d, \quad (8.14)$$

a local minimum is guaranteed by the second-order optimality condition

$$k''(\mathbf{q})(\chi, \chi) \geq 0 \quad \forall \chi \in \mathbf{Q}_d.$$

To approximate the solutions of (8.14), we employ a Newton's method. Starting with $\mathbf{q}^0 \in \mathbf{Q}_d$ (one possibility is $\mathbf{q}^0 = \bar{\mathbf{q}}$) we iterate

$$k''(\mathbf{q}^l)(\delta \mathbf{q}^l, \chi) = -k'(\mathbf{q}^l)(\chi) \quad \forall \chi \in \mathbf{Q}_d, \quad \mathbf{q}^{l+1} = \mathbf{q}^l + \omega^l \delta \mathbf{q}^l,$$

where $\omega^l \in \mathbb{R}$ is a possible relaxation parameter. Every step of this Newton loop requires the evaluation of the residual and the solution of the Hessian. As the solution $\mathbf{U} = S(\mathbf{q})$ is implicitly given, this involves some effort.

Lemma 86 (Residual of the Newton iteration). *Let $\mathbf{q}^l \in \mathbf{Q}$ be given. Then, the residual is given by*

$$-k'(\mathbf{q}^l)(\chi) := -\alpha(\mathbf{q}^l - \bar{\mathbf{q}}, \chi) + A'_\mathbf{q}(\mathbf{q}^l, \mathbf{U}^l)(\chi, \mathbf{Z}^l),$$

where the solution $\mathbf{U}^l \in \mathcal{X}$ and the adjoint solution $\mathbf{Z}^l \in \mathcal{X}$ are given by

$$(1) \quad A(\mathbf{q}^l, \mathbf{U}^l)(\Phi) = F(\Phi) \quad \forall \Phi \in \mathcal{X},$$

$$(2) \quad A'_U(\mathbf{q}^l, \mathbf{U}^l)(\Phi, \mathbf{Z}^l) = K'_U(\mathbf{q}^l, \mathbf{U}^l)(\Phi) \quad \forall \Phi \in \mathcal{X}.$$

Proof. Let $\mathbf{U}^l = S(\mathbf{q}^l)$ be the solution to (1) and $\mathbf{Z}^l \in \mathcal{X}$ be the solution to (2). Then, formal derivation of $k(\mathbf{q})$ yields

$$k'(\mathbf{q}^l)(\chi) = K'_\mathbf{q}(\mathbf{q}^l, S(\mathbf{q}^l)) + K'_U(\mathbf{q}^l, S(\mathbf{q}^l))(S'(\mathbf{q}^l)\chi).$$

Deriving the state equation to \mathbf{q} gives a relation for $S'(\mathbf{q}^l)\chi$

$$A'_q(\mathbf{q}^l, S(\mathbf{q}^l))(\Phi) = -A'_U(\mathbf{q}^l, S(\mathbf{q}^l))(S'(\mathbf{q}^l)\chi, \Phi) \quad \forall \Phi \in \mathcal{X}. \quad (8.15)$$

Then, by using (8.7), the adjoint equation and this relation (8.15)

$$\begin{aligned} k'(\mathbf{q}^l)(\chi) &= \alpha(\mathbf{q} - \bar{\mathbf{q}}, \chi)_{\mathbf{Q}} + A'_{\mathbf{U}}(\mathbf{q}^l, S(\mathbf{q}^l))(S'(\mathbf{q}^l)\chi, \mathbf{Z}^l) \\ &= \alpha(\mathbf{q} - \bar{\mathbf{q}}, \chi)_{\mathbf{Q}} - A'_q(\mathbf{q}^l, S(\mathbf{q}^l))(\mathbf{Z}^l). \end{aligned}$$

□

For estimation of the residual, we must first solve the *state equation*, followed by a solution of the *adjoint equation*. These equations can be solved independently. Once the residual is given, the Hessian equation must be solved.

Lemma 87 (Hessian of the Newton iteration). *Let $\mathbf{q}^l \in \mathbf{Q}$ be given, \mathbf{U}^l and \mathbf{Z}^l be the adjoint solutions defined in Lemma 86. Let $\{\chi_1, \dots, \chi_{\#q}\}$ be a basis of \mathbf{Q} . Then, solve the $\#q$ tangent equations and adjoint for hessian equations for $\mathbf{U}_1^l, \dots, \mathbf{U}_{\#q}^l$ and $\mathbf{Z}_1^l, \dots, \mathbf{Z}_{\#q}^l$ for $i = 1, \dots, \#q$*

$$\begin{aligned} A'_{\mathbf{U}}(\mathbf{q}^l, \mathbf{U}^l)(\mathbf{U}_i^l, \Phi) &= -A'_{\mathbf{q}}(\mathbf{q}^l, \mathbf{U}^l)(\chi_i, \Phi) & \forall \Phi \in \mathcal{X} \\ A'_{\mathbf{U}}(\mathbf{q}^l, \mathbf{U}^l)(\Phi, \mathbf{Z}_i^l) &= K''_{\mathbf{UU}}(\mathbf{q}^l, \mathbf{U}^l)(\mathbf{U}_i^l, \Phi) \\ &\quad - A''_{\mathbf{qU}}(\mathbf{q}^l, \mathbf{U}^l)(\chi_i, \Phi, \mathbf{Z}^l) \\ &\quad - A''_{\mathbf{UU}}(\mathbf{q}^l, \mathbf{U}^l)(\mathbf{U}_i^l, \Phi, \mathbf{Z}^l) & \forall \Phi \in \mathcal{X}. \end{aligned} \tag{8.16}$$

Then, the Hessian (in the Basis $\{\chi_i\}$) is given as

$$\begin{aligned} \mathbf{k}_{ij}(\mathbf{q}^l) &:= \alpha(\chi_i, \chi_j)_{\mathbf{Q}} - A''_{\mathbf{qq}}(\mathbf{q}^l, \mathbf{U}^l)(\chi_i, \chi_j, \mathbf{Z}^l) \\ &\quad - A''_{\mathbf{qU}}(\mathbf{q}^l, \mathbf{U}^l)(\chi_i, \mathbf{U}_j^l, \mathbf{Z}^l) - A'_{\mathbf{q}}(\mathbf{q}^l, \mathbf{U}^l)(\chi_i, \mathbf{Z}_j^l). \end{aligned}$$

Proof. Derivation of the residual gives

$$\begin{aligned} k''(\mathbf{q}^l)(\chi, \tau) &= \alpha(\chi, \tau)_{\mathbf{Q}} - A''_{\mathbf{qq}}(\mathbf{q}^l, \mathbf{U}^l)(\chi, \tau, \mathbf{Z}^l) \\ &\quad - A''_{\mathbf{qU}}(\mathbf{q}^l, \mathbf{U}^l)(\chi, S'(\mathbf{q}^l)\tau, \mathbf{Z}^l) - A'_{\mathbf{q}}(\mathbf{q}^l, \mathbf{U}^l)(\chi, Z'(\mathbf{q})\tau). \end{aligned} \tag{8.17}$$

The first two terms can be evaluated with the knowledge of $\mathbf{q}^l, \mathbf{U}^l$ and \mathbf{Z}^l . By derivation of the state equation we obtain the *tangent equation* which we solve for $\mathbf{U}_\tau^l := S'(\mathbf{q}^l)\tau$

$$A'_{\mathbf{U}}(\mathbf{q}^l, \mathbf{U}^l)(\mathbf{U}_\tau^l, \Phi) = -A'_{\mathbf{q}}(\mathbf{q}^l, \mathbf{U}^l)(\tau, \Phi) \quad \forall \Phi \in \mathcal{X}.$$

This allows to evaluate the third term $A''_{\mathbf{qu}}$ in (8.17). For evaluation of the last term we solve for $\mathbf{Z}_\tau^l = Z'(\mathbf{q}^l)\tau$ given by the derivative of the adjoint equation

$$\begin{aligned} A'_{\mathbf{U}}(\mathbf{q}^l, \mathbf{U}^l)(\Phi, \mathbf{Z}_\tau^l) &= K''_{\mathbf{UU}}(\mathbf{q}^l, \mathbf{U}^l)(\mathbf{U}_\tau^l, \Phi) \\ &\quad - A''_{\mathbf{qU}}(\mathbf{q}^l, \mathbf{U}^l)(\tau, \Phi, \mathbf{Z}^l) - A''_{\mathbf{UU}}(\mathbf{q}^l, \mathbf{U}^l)(\mathbf{U}_\tau^l, \Phi, \mathbf{Z}^l). \end{aligned}$$

□

Compared to the residual, the assembly of the Hessian calls for the additional effort of solving $\#q$ tangent equations and $\#q$ adjoint for hessian equations. Each of these problems is linear and has the same dimension as the adjoint problem. The overall effort appears to be rather large, by using the reduced solution approach, one however circumvents the introduction of large systems, where state and adjoint solution are coupled. For the discussed examples with a one-dimensional control space \mathbf{Q}_d , one Newton iteration requires the solution of the nonlinear state equation, the solution of one linear adjoint, one tangent and one adjoint for hessian equation.

8.1. Optimization with fluid-structure interactions

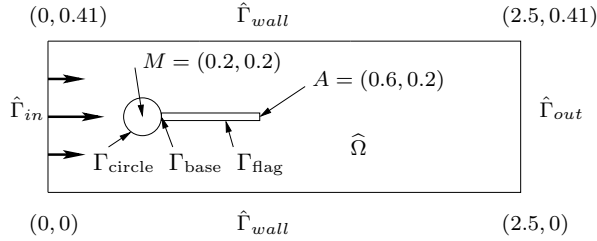


Figure 8.1: Configuration of the parameter identification test-case with the modified fsi-1 benchmark configuration.

8.1.3 Realization with fluid-structure interactions

The described Newton iteration for the optimization problem requires the evaluation of several further derivatives of the variational formulation. We have already derived the Jacobian in Section 4.2.2, which is the system matrix of the tangent equation (8.16). Its inverse is the system matrix of the adjoint equation and further the system matrix of the adjoint for hessian equation, also shown in (8.16). All the remaining derivatives are required on different right hand sides of the problems. Their evaluation is partially simple, e.g. $A'_{\mathbf{q}}$, $K''_{\mathbf{U}\mathbf{U}}$ or $A''_{\mathbf{q}\mathbf{U}}$. Only the second derivative of $A(\cdot)(\cdot)$ with respect to the solution \mathbf{U} will give rise to excessive terms due to the ALE mapping. Here, given \mathbf{U}_i^l we propose the approximation by finite differences

$$A''_{\mathbf{U}\mathbf{U}}(\mathbf{q}^l, \mathbf{U}^l)(\mathbf{U}_i^l, \Phi, \mathbf{Z}^l) \approx \frac{A'_{\mathbf{U}}(\mathbf{q}^l, \mathbf{U}^l + \epsilon \mathbf{U}_i^l)(\Phi, \mathbf{Z}^l) - A'_{\mathbf{U}}(\mathbf{q}^l, \mathbf{U}^l)(\Phi, \mathbf{Z}^l)}{\epsilon},$$

where $\epsilon > 0$ is a parameter that has to be carefully chosen.

8.1.4 Parameter identification test

Based on the benchmark problem fsi-1 by Hron & Turek [134], see also Section 5.6, we formulate a parameter identification test-case. According to [229, 228], the geometry has been changed by slightly widening the beam, compare Figure 8.1. *Wie breit ist der denn genau?*

We initially “forget” the Lamé coefficient μ_s and try to reconstruct it based on measurement of the deformation of the beam in the point $A = (0.6, 0.2)$. We introduce the regularized cost functional

$$K(\mathbf{q}, \mathbf{U}) = |\mathbf{u}_y(A) - \mathbf{u}_y^{\text{ref}}|^2 + \frac{\alpha}{2} |\mathbf{q} - \bar{\mu}|^2,$$

where $\bar{\mu} \in \mathbb{R}$ is an initial guess and $\alpha = 10^{-3}$ the Tikhonov parameter. The control $\mathbf{q} \in \mathbb{R}$ enters in form of a material parameter, such that the control form is given by (8.5).

The flow is driven by a parabolic inflow profile on Γ_{in} with maximum velocity $\bar{\mathbf{v}}^{\text{in}} = 1.5 \text{ m/s}$ and the remaining parameters used in this test-case are given by

$$\varrho_f = \varrho_s = 10^3 \frac{\text{kg}}{\text{m}^3}, \quad \nu_f = 10^{-3} \frac{\text{m}^2}{\text{s}}, \quad \nu_s = 0.4.$$

On the outflow boundary Γ_f^{out} we prescribe the *do-nothing* outflow condition, see Section 1.4.2. All computations in this sections have been carried out by Thomas Wick [193, 247] using the software library deal.II [13]. e

DoF	μ^{ref}	$\mathbf{u}_y^{\text{ref}}$
19 488	500 000	$8.2747 \cdot 10^{-4}$
76 672	500 000	$8.2289 \cdot 10^{-4}$

Table 8.1: Forward computation for obtaining reference values $\mathbf{u}^{\text{ref}}(A)$ using the exact Lamé coefficient $\mu^{\text{opt}} = 500\,000$ on two subsequent meshes.

Step	μ	$\mathbf{u}_y(A)$	$ \mathbf{u}_y(A) - \mathbf{u}_y^{\text{ref}} $	Residual
1	5 000	$2.0118 \cdot 10^{-3}$	$1.18 \cdot 10^{-3}$	$1.00 \cdot 10^{-0}$
2	188 133	$1.1992 \cdot 10^{-3}$	$3.72 \cdot 10^{-4}$	$5.90 \cdot 10^{-1}$
3	498 310	$8.2884 \cdot 10^{-4}$	$1.37 \cdot 10^{-6}$	$2.76 \cdot 10^{-3}$
4	499 767	$8.2770 \cdot 10^{-4}$	$2.30 \cdot 10^{-7}$	$4.01 \cdot 10^{-6}$
5	499 769	$8.2768 \cdot 10^{-4}$	$2.10 \cdot 10^{-7}$	$6.58 \cdot 10^{-9}$

(a) Results on a mesh with 19 488 unknowns, $\mathbf{u}_y^{\text{ref}} = 0.00082747$

Step	μ	$\mathbf{u}_y(A)$	$ \mathbf{u}_y(A) - \mathbf{u}_y^{\text{ref}} $	Residual
1	5 000	$2.000 \cdot 10^{-3}$	$1.18 \cdot 10^{-3}$	$1.00 \cdot 10^{-0}$
2	118 309	$1.347 \cdot 10^{-3}$	$5.24 \cdot 10^{-4}$	$7.23 \cdot 10^{-1}$
3	493 626	$8.279 \cdot 10^{-4}$	$5.01 \cdot 10^{-6}$	$1.16 \cdot 10^{-2}$
4	499 756	$8.232 \cdot 10^{-4}$	$3.10 \cdot 10^{-7}$	$2.27 \cdot 10^{-5}$
5	499 768	$8.231 \cdot 10^{-4}$	$2.10 \cdot 10^{-7}$	$2.70 \cdot 10^{-8}$

(b) Results on a mesh with 76 672 unknowns, $\mathbf{u}_y^{\text{ref}} = 0.00082289$

Table 8.2: *fsi 1* parameter estimation problem. Results of the optimization loop for two different meshes, using the reference values as collected in Table 8.1. Showing iteration, control $\mathbf{q}^l = \mu^l$, deformation $\mathbf{u}_y(A)$, absolute error in deformation and Newton residual.

In Table 8.1 we determine the deformation $\mathbf{u}_y(A)$ in the tip of the beam considering the Lamé coefficient $\mu^{\text{ref}} = 500\,000$ on a sequence of two meshes in forward simulations. These values act as reference values $\mathbf{u}_y^{\text{ref}}$ for each optimization test-case.

We start the actual optimization look with the initial control $\mathbf{q}^0 = 5\,000$ far away from the optimal state $\mathbf{q}^{\text{opt}} = \mu^{\text{opt}} = 500\,000$. In Table 8.2 we indicate the results of the optimization algorithm on two meshes, using the corresponding reference deformation $\mathbf{u}_y^{\text{ref}}(A)$ on each level. Here, it shows, that the presented Newton optimization scheme with the exactly derived adjoint problems for the monolithic variational formulation yields a very efficient (quadratic) convergence to the optimal state.

In Figure 8.2, we show plots of x -velocity and the corresponding adjoint solution component for the solution of this optimization problem.

8.1.5 Optimal control test

Beschriftung anpassen, auch oben, Rawnder

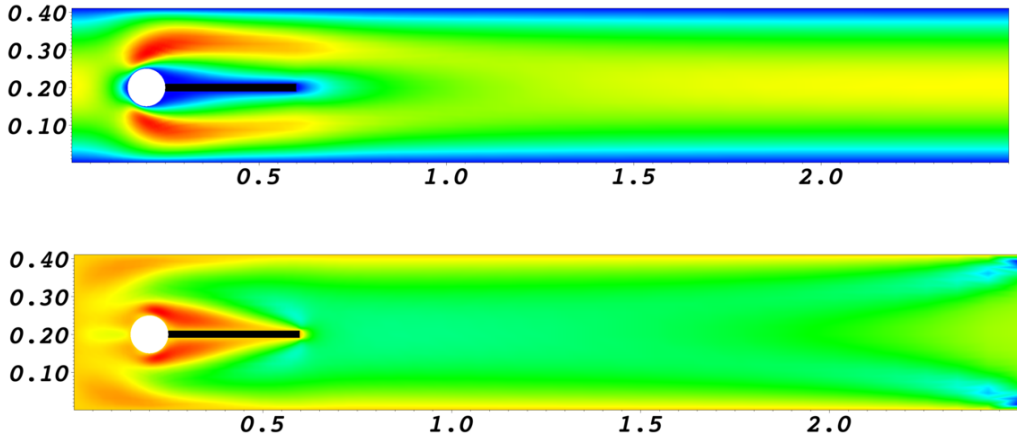


Figure 8.2: *fsi-1* parameter estimation: x-velocity profile \mathbf{v}_x (top) and corresponding adjoint solution \mathbf{z}_x (bottom).

As second problem we consider an optimal control test. Figure 8.3 shows the configuration. By controlling the inflow pressure on Γ_f^{in} by $\mathbf{q} = p_f^{\text{in}} \in \mathbb{R}$ we aim at maximizing the outflow at Γ_f^{out} . An elastic obstacle \mathcal{S} is embedded in the flow domain. At increased velocities, this obstacle will be sucked to the top of the domain and closes the channel, such that the flow rate will decrease again.

Control is realized by the pressure control form 8.4, the target function is given by

Both problems are constructed such that the optimal solution can be easily verified by forward simulations to offer suitable test-cases for the optimization routines and in particular for the derivation of the adjoint formulations.

$$K_{\text{out}}(\mathbf{q}, \mathbf{U}) = - \int_{\Gamma_f^{\text{out}}} (\vec{n} \cdot \mathbf{v})^2 \, ds + \frac{\alpha}{2} |\mathbf{q} - \bar{\mathbf{q}}|^2, \quad (8.18)$$

where $\alpha > 0$ is the regularization parameter. We changed the sign to obtain a minimization problem. The material parameters are chosen as

$$\varrho_f = \varrho_s = 10^3 \frac{kg}{m^3}, \quad \nu_f = 10^{-3} \frac{m^2}{s}, \quad \nu_s = 0.4, \quad \mu_s = 500 \frac{kg}{ms}.$$

Velocity and deformation as set to zero on all outer boundaries Γ^{wall} .

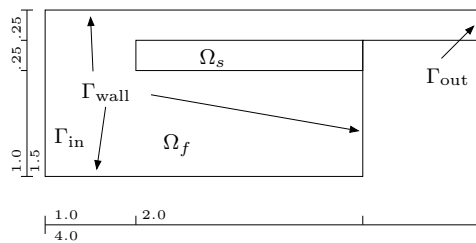


Figure 8.3: Configuration of the optimal control test-case. beam.

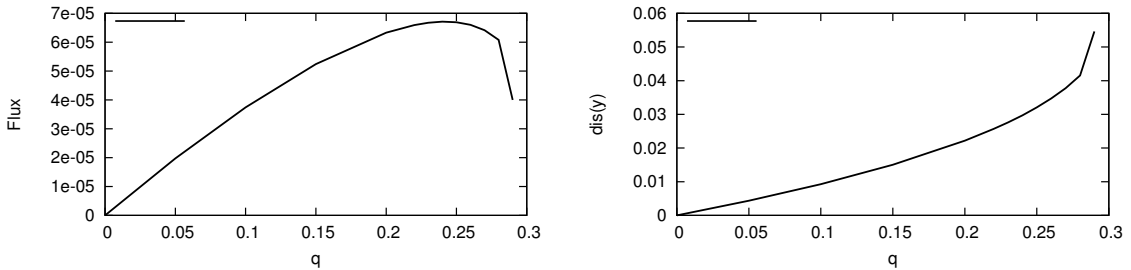


Figure 8.4: Forward simulations for varying inflow pressures \mathbf{q} . Left: outflow rate $K_{\text{out}}(\mathbf{q}, \mathbf{U}(\mathbf{q}))$. Right: deformation of the tip of the beam $\mathbf{u}_y(A)$. The outflow rate goes down after some $\mathbf{q} > 0.25$. Here, we expect the optimal control.

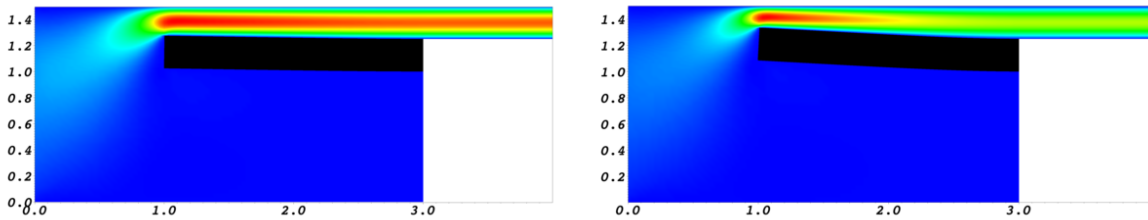


Figure 8.5: Maximization of the outflow rate. Left: velocity for the initial control $\mathbf{q}^0 = 0.1$ and close to the optimal control $\mathbf{q}^{\text{opt}} \approx 0.23$.

Figure 8.4 shows results of forward simulation for different values of the control \mathbf{q} , i.e. the average inflow pressure on Γ_f^{in} . Considering higher pressures, the beam will narrow the channel and reduce the outflow rate; we refer the reader to Figure 8.5 for snapshots of the solution for different inflow pressures $\mathbf{q} = p_{\text{in}}$. From the forward simulation we estimate $\mathbf{q}^{\text{opt}} \in [0.23, 0.24]$.

Both control and target functional are living within the fluid problem. Without the interaction to the solid however, no effect could be observed. This example asks for a careful analysis of the adjoint information transport through the structural problem.

To approximate this problem, we use an updated Tikhonov parametrization, where both the parameter α and the parameter $\bar{\mathbf{q}}$ in

$$K(\mathbf{q}, \mathbf{U}) = K_{\text{out}}(\mathbf{U}) + \frac{\alpha}{2} |\mathbf{q} - \bar{\mathbf{q}}|^2,$$

are updated. We start with $\bar{\mathbf{q}}^0 = \mathbf{q}^0 = 0.1$ and take the last available optimum in each step. Furthermore, the parameter α is reduced step by step. In Table 8.3, we show the convergence of this iterated Tikhonov scheme, together with the chosen values for α^i and the obtained controls p_{opt}^i . As expected by the forward computation, the maximal flux is reached for $p_{\text{opt}} \sim 0.23 - 0.24$. Indeed, it can be observed that the channel is narrowed in the maximized solution as illustrated in Figure 8.5. Here, in the unloaded reference configuration, the gap has a width of 0.125. Using the initial control $\bar{p}_{\text{in}}^0 = 0.1$, the gap is narrowed to 0.115 and in the optimum state, for $p_{\text{opt}} \approx 0.24$, the size of the gap is reduced to 0.095. This is an overall reduction of about 25%. Finally, Figure 8.6 illustrates the three components $\mathbf{z}_v, z_p, \mathbf{z}_n$ of the adjoint solution.

DoF	\bar{p}_{in}	α	$u_y(A)$	$K_{\text{out}}(U)$	p_{opt}
12 612	0.1000	$1.0 \cdot 10^{-5}$	$0.97 \cdot 10^{-2}$	$3.87 \cdot 10^{-5}$	0.1038
	0.1038	$7.5 \cdot 10^{-6}$	$1.02 \cdot 10^{-5}$	$4.04 \cdot 10^{-5}$	0.1090
	0.1090	$5.0 \cdot 10^{-6}$	$1.11 \cdot 10^{-5}$	$4.29 \cdot 10^{-5}$	0.1170
	0.1170	$2.5 \cdot 10^{-6}$	$1.30 \cdot 10^{-5}$	$4.78 \cdot 10^{-5}$	0.1335
	0.1335	$1.0 \cdot 10^{-6}$	$1.85 \cdot 10^{-5}$	$5.87 \cdot 10^{-5}$	0.1759
	0.1759	$7.5 \cdot 10^{-7}$	$2.43 \cdot 10^{-5}$	$6.53 \cdot 10^{-5}$	0.2254
	0.2254	$5.0 \cdot 10^{-7}$	$2.72 \cdot 10^{-5}$	$6.67 \cdot 10^{-5}$	0.2280
49 540	0.1759	$1.0 \cdot 10^{-6}$	$2.46 \cdot 10^{-5}$	$6.52 \cdot 10^{-5}$	0.2135
	0.2135	$7.5 \cdot 10^{-7}$	$2.84 \cdot 10^{-5}$	$6.70 \cdot 10^{-5}$	0.2330
196 356	0.1759	$1.0 \cdot 10^{-6}$	$2.42 \cdot 10^{-5}$	$6.50 \cdot 10^{-5}$	0.2111
	0.2111	$7.5 \cdot 10^{-7}$	$2.92 \cdot 10^{-5}$	$6.71 \cdot 10^{-5}$	0.2367

Table 8.3: Maximizing the outflow rate $K_{\text{out}}(\mathbf{U})$ by controlling the inflow pressure $q = p_{\text{in}}$ on three globally refined meshes using an iterated Tikhonov regularization with Tikhonov parameter α and reference control \bar{p}_{in} .

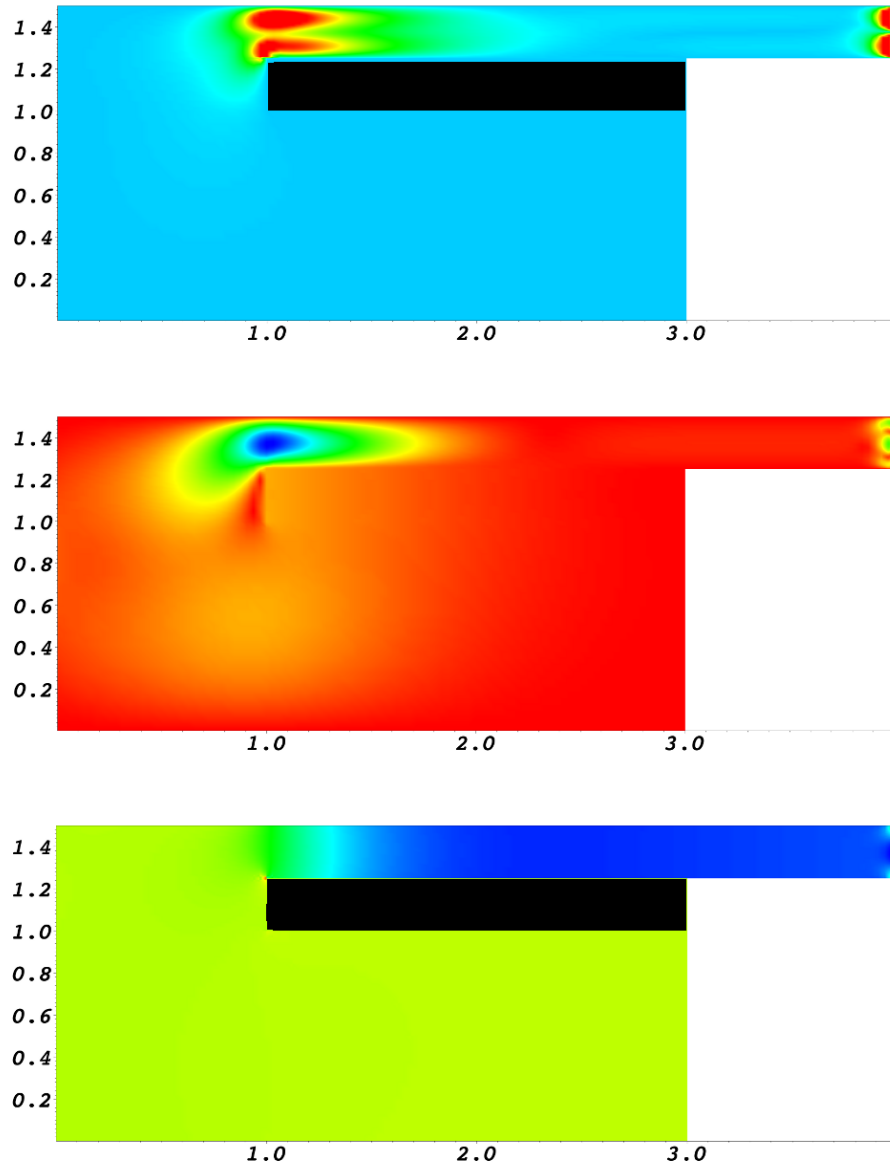


Figure 8.6: Maximization of the outflow rate. Adjoint solution with respect to the velocity (top), displacement (middle) and pressure (bottom). All solutions are displaced in the undeformed reference configuration in ALE coordinates.

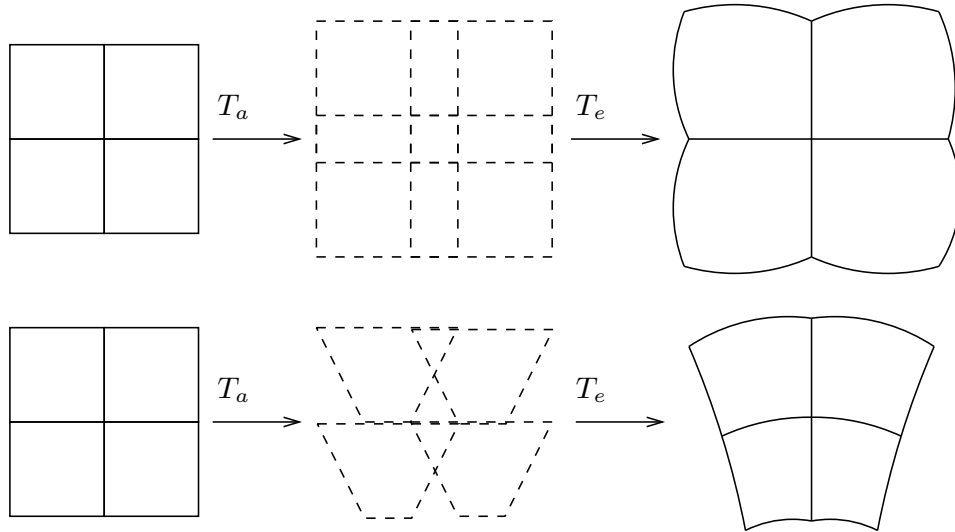


Figure 8.7: Two different kinds of active material deformation. Top row: isotropic growth. Bottom: constriction of volume elements. The intermediate configuration is grown and stress-free but not physical.

8.2 Mechano-chemical fluid structure interactions and active material growth

Many aspects in solid dynamics cannot be explained by an elastic response of the material. In some applications, the material undergoes active change, e.g. by growth, swelling or generation of material, by chemically induced contractions or bending. In other situations, the reference state is not stress-free. If a log of wood is cut into two pieces, these will afterwards deform and spread.

One model for the realization of active material modification is the introduction of an intermediate material configuration, the *grown configuration*, that is assumed to include the active growth or change of material, a configuration that is stress-free but non-physical, see Rodriguez et al [198] and [141] for further examples. We call this configuration $\hat{\mathcal{S}}_a$, the active one. Further, we introduce a mapping, that describes only this growth process

$$\hat{T}_a(t) : \hat{\mathcal{S}} \rightarrow \hat{\mathcal{S}}_a(t),$$

and maps the Lagrangian reference state to the grown on. In Figure 8.7 we show two possible models for active material growth, isotropic growth of control volumes and a volume-conserving constriction of control volumes. The grown state is understood to be stress-free but non-physical, as control volumes overlap.

In a second step, the material elastically reacts on this intermediate configuration. We denote by

$$\hat{T}_e(t) : \hat{\mathcal{S}}_a(t) \rightarrow \mathcal{S}(t),$$

the mapping of this elastic response. The overall material deformation is given by the nesting

$$\hat{T}(t) : \hat{\mathcal{S}} \rightarrow \mathcal{S}(t), \quad \hat{T}(t) = \hat{T}_e(t) \circ \hat{T}_a(t). \quad (8.19)$$

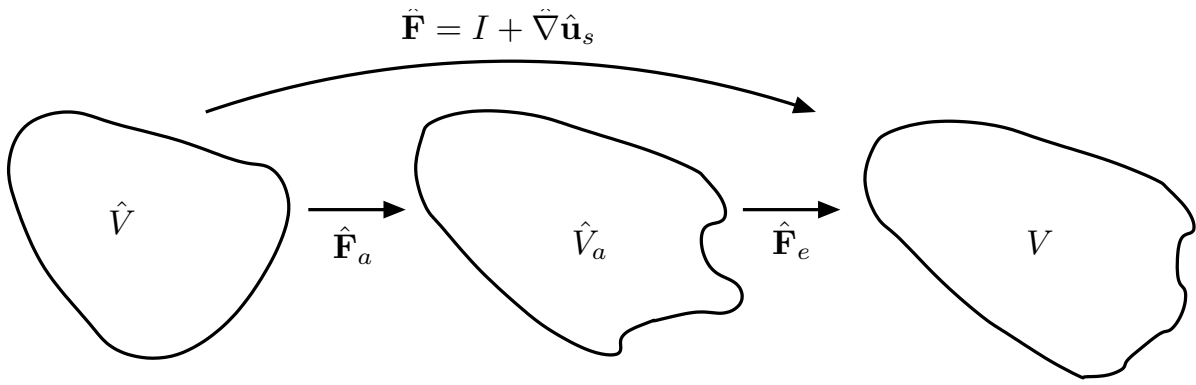


Figure 8.8: Multiplicative decomposition of the deformation gradient into active part $\hat{\mathbf{F}}_a$ and elastic response $\hat{\mathbf{F}}_e$.

In numerical simulations, we model by the deformation $\hat{\mathbf{u}}$ the complete deformation from $\hat{\mathcal{S}}$ to $\hat{\mathcal{S}}(t)$, including growth and response, such that

$$p\hat{T}(\hat{x}, t) = \hat{x} + \hat{\mathbf{u}}(\hat{x}, t),$$

and as usual, we introduce the deformation gradient and its determinant

$$\hat{\mathbf{F}} := \hat{\nabla}\hat{T}, \quad \hat{J} := \det \hat{\mathbf{F}}. \quad (8.20)$$

The splitting into growth and elastic response is done on the level of the deformation gradient, see Figure 8.8. We introduce

$$\hat{\mathbf{F}}_a := \hat{\nabla}\hat{T}_a, \quad \hat{J}_a := \det \hat{\mathbf{F}}_a, \quad (8.21)$$

and

$$\hat{\mathbf{F}}_e := \hat{\nabla}\hat{T}_e, \quad \hat{J}_e := \det \hat{\mathbf{F}}_e, \quad (8.22)$$

By means of (8.19), it holds

$$\hat{\mathbf{F}} = \hat{\mathbf{F}}_e \hat{\mathbf{F}}_a, \quad \hat{J} = \hat{J}_e \hat{J}_a.$$

If we now assume, that \hat{T}_a and hence $\hat{\mathbf{F}}_a$ is given by some external mechanism, we can compute the elastic deformation gradient based on the deformation \mathbf{u} and this growing part

$$\hat{\mathbf{F}}_e = \hat{\mathbf{F}} \hat{\mathbf{F}}_a^{-1} = (I + \hat{\nabla} \hat{\mathbf{u}}) \hat{\mathbf{F}}_a^{-1}.$$

Now, stresses will depend solely on this elastic part. In terms of Definition 4, the first Piola Kirchhoff stress tensor of the St. Venant Kirchhoff material is given by

$$\hat{\mathbf{P}}_e = \hat{\mathbf{F}}_e \hat{\Sigma}_e = 2\mu_s \hat{\mathbf{F}}_e \hat{\mathbf{E}}_e + \lambda_s \text{tr}(\hat{\mathbf{E}}_e) \hat{\mathbf{F}}_e, \quad \hat{\mathbf{E}}_e := \frac{1}{2}(\hat{\mathbf{F}}_e^T \hat{\mathbf{F}}_e^T - I). \quad (8.23)$$

8.2.1 Growth models

“Growth” can come in various forms. It is possible, that new material is added. Then, material can simply swell while conserving its mass. Finally, “growth” can also be a shear change of configuration, without change of volume or mass.

We first consider the case, where the same type of material is locally added in an isotropic fashion. Let \hat{V} be a control volume and $\hat{x}_0 \in \hat{V}$ be a reference point. We assume, that this control volume isotropically growing

$$\hat{V} \rightarrow V_a(t), \quad V_a(t) := \{\hat{x}_0 + \alpha t(\hat{x} - \hat{x}_0), \hat{x} \in \hat{V}\},$$

where by $\alpha \in \mathbb{R}$ we denote the *growth rate*, see Figure 8.7. By

$$\hat{T}_a(\hat{x}, t) = \hat{x} + \alpha t(\hat{x} - \hat{x}_0), \quad \hat{\mathbf{F}}_a = \hat{\nabla} \hat{T}_a = (1 + \alpha t)I = \hat{J}_a = (1 + \alpha t)^d, \quad (8.24)$$

we can express the active mapping and deformation gradient, where $d > 0$ is the spatial dimension. We assume, that the new material has the same density $\hat{\rho}^0$, such that mass is added (or decreased for $\alpha < 0$)

$$m(V_a(t)) = \int_{V_a(t)} \rho^0 dx = \int_{\hat{V}} \hat{J}_a \rho^0 d\hat{x} =: \int_{\hat{V}} \hat{\rho}_a d\hat{x},$$

such that by

$$\hat{\rho}_a := \hat{J}_a \hat{\rho}^0 = (1 + \alpha t)^d \hat{\rho}^0, \quad (8.25)$$

we denote the grown density in the reference configuration.

Second, we consider the swelling of material, that is isotropic growth while the mass is conserved. The growth map is given as in (8.7), the mass however is conserved from \hat{V} to $V_a(t)$:

$$m(\hat{V}) = \int_{\hat{V}} \hat{\rho}^0 d\hat{x} \stackrel{!}{=} \int_{V_a(t)} \rho_a dx = \int_{\hat{V}} \hat{J}_a \hat{\rho}_a d\hat{x} = \int_{\hat{V}} (1 + \alpha t)^d \hat{\rho}_a d\hat{x},$$

such that

$$\hat{\rho}_a = (1 + \alpha t)^{-d} \hat{\rho}^0.$$

Third, we consider the case of a constriction, where both mass and volume of the control volumes stays the same, see the bottom row of Figure 8.7. Let \hat{V} be a reference volume and $\hat{x}^0 \in V$ be its center of mass. In two spatial dimensions, the active map is given by

$$\hat{T}_a(\hat{x}, t) = \begin{pmatrix} \hat{x}_1^0 + (\hat{x}_1 - \hat{x}_0^1)(1 + \alpha t(\hat{x}_2 - \hat{x}_0^2)) \\ \hat{x}_2 \end{pmatrix},$$

with deformation gradient

$$\hat{\mathbf{F}}_a(\hat{x}, t) = \begin{pmatrix} 1 + \alpha t(\hat{x}_2 - \hat{x}_0^2) & (\hat{x}_1 - \hat{x}_0^1)\alpha t \\ 0 & 1 \end{pmatrix}, \quad \hat{J}_a = 1 + \alpha t(\hat{x}_2 - \hat{x}_0^2).$$

8.2.2 Mechano-chemical fluid-structure interactions

We consider the coupled dynamics of an incompressible fluid, an elastic structure that undergoes active growth or deformation and the dynamics of chemical species, that are transported, that react and that cause solid growth. This model is a generalization of a detailed model for the dynamics of the formation and growth of plaques in blood vessels, that has been discussed in [251, 252, 253].

We introduce a simplified model that describes the formation and growth of plaques in large blood vessels. For simplicity, we denote by $\Omega(t) \subset \mathbb{R}^2$ a two-dimensional domain, split into the vessel wall $\mathcal{S}(t) \subset \mathbb{R}^2$ and the fluid domain $\mathcal{F}(t) \subset \mathbb{R}^2$, occupied by blood. The interface between fluid and solid is denoted by $\mathcal{I}(t)$, see Figure 8.9. We model blood as an incompressible Newtonian and homogenous fluid. The vessel wall is described by the St. Venant Kirchhoff material as stated above.

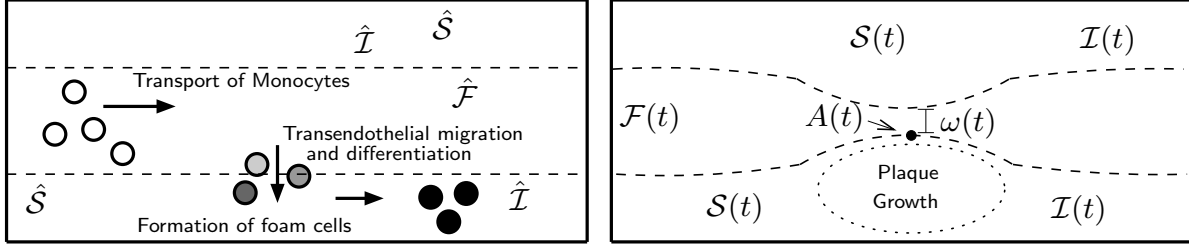


Figure 8.9: Configuration of the domain and mechanism of plaque formation. Left: Domain in reference configuration split into fluid part $\hat{\mathcal{F}}$ and solid $\hat{\mathcal{S}}$ divided by the interface $\hat{\mathcal{I}}$. Right: domain in the current (Eulerian) description with plaque formation and narrowing of vessel.

In short, the biological mechanism is evolving as follows (compare Figure 8.9): First, monocytes (concentration called c_f) are transported by an advection-diffusion process within the blood flow. Secondly, they penetrate damaged parts of the vessel wall (in damaged areas) where they are transformed to macrophages (called c_s). The migration rate depends on the difference of monocyte and macrophage concentration ($c_f - c_s$) on the interface, on the wall stress and the damage condition of the wall. Thirdly, within the vessel wall, the macrophages are again transported by an advection-diffusion process and transformed into foam cells (called c_s^*). Finally, accumulation of foam cells leads to plaque growth.

This problem is coupled to the dynamics of the fluid-structure interaction problem. Due to hemodynamical forces driven by the pulsating flow, the geometry deforms substantially. Furthermore, the formation of plaques significantly changes the domains. Finally, the hemodynamical forces influence the penetration of monocytes into the vessel wall and therefore a two-way coupled problem must be considered. The complete set of equations is given by

$$\left. \begin{array}{l} \rho_f(\partial_t \mathbf{v}_f + \mathbf{v}_f \cdot \nabla \mathbf{v}_f) - \operatorname{div} \boldsymbol{\sigma}_f = 0 \\ \operatorname{div} \mathbf{v}_f = 0 \\ \partial_t c_f + \mathbf{v}_f \cdot \nabla c_f - D_f \Delta c_f = 0 \\ \rho_s(\partial_t \mathbf{v}_s + \mathbf{v}_s \cdot \nabla \mathbf{v}_s) - \operatorname{div} \boldsymbol{\sigma}_s = 0 \\ \partial_t c_s + \mathbf{v}_s \cdot \nabla c_s - D_s \Delta c_s = -\beta c_s \\ \partial_t c_s^* + \mathbf{v}_s \cdot \nabla c_s^* = \beta c_s \\ \boldsymbol{\sigma}_f \vec{n}_f + \boldsymbol{\sigma}_s \vec{n}_s = 0 \\ \mathbf{v}_f = \mathbf{v}_s \\ D_f \nabla c_f \vec{n}_f + D_s \nabla c_s \vec{n}_s = 0 \\ D_s \nabla c_s \vec{n}_s = \zeta(c_f - c_s) \end{array} \right\} \begin{array}{l} \text{in } \mathcal{F}(t) \\ \text{in } \mathcal{S}(t) \\ \text{on } \mathcal{I}(t) \end{array} \quad (8.26)$$

Here, \mathbf{v}_f and \mathbf{v}_s stand for the fluid and solid velocity. By ρ_f and ρ_s we denote the densities of blood and vessel wall and by \vec{n}_f and \vec{n}_s the outer normals of the fluid and solid domain,

respectively. D_f and D_s are diffusion coefficients for monocytes and macrophages. In particular D_s depends on the concentration of foam cells c_s^* [252]. The coefficient ζ describes the migration of monocytes through the vessel wall. This parameter will depend on the hemodynamical stress $\zeta = \zeta(\sigma_f \vec{n})$. The parameter β , usually depending on the concentration of foam cells, controls the transformation of macrophages to foam cells.

One of the major challenges in plaque modeling is the huge variety of temporal scales: while the heart beats once in about every 1s, plaque growth takes place in a time span of months, i.e. $T \gg 1\,000\,000s$. Although all scales have a significant influence on the coupled dynamics, a numerical simulation will not be able to resolve each detail while following the long-term process. Instead, we – as most approaches – consider an averaged flow problem and focus on the long-scale dynamics. Effective model parameters controlling the migration of monocytes through the vessel walls will be obtained by local (in time) small-scale simulations.

Rather than developing a quantitative model, we concentrate in this paper on a robust numerical framework for the coupled long-term dynamics of fluid-structure interaction with active growth processes and large deformation. Hence, the approximation of the chemical dynamics play a minor role. We therefore strongly simplify Model (8.26) and replace the complete chemical dynamics by a simple ODE modeling the total concentration of foam cells

$$\partial_t c_s^*(t) = \gamma(\sigma_{WS}, t), \quad c_s^*(0) = 0, \quad (8.27)$$

where the functional γ specifies the rate of foam cell accumulation. Here, this function depends on the wall stress in main stream direction σ_{WS} to include the coupling of fluid-dynamical forces

$$\gamma(\sigma_{WS}, t) = \gamma_0 \left(1 + \frac{\sigma_{WS}(t)}{\bar{\sigma}}\right)^{-1}, \quad \bar{\sigma} = 50 \frac{g}{cm \cdot s^2}, \quad \gamma_0 = 5 \cdot 10^{-7}. \quad (8.28)$$

For details on models of the dependency of the monocyte migration rate on the wall stress we refer to [56]. The scalar concentration $c_s^* : [0, T] \rightarrow \mathbb{R}_+$ will directly determine the active growth. The exact role and influence of the wall stress on the migration rate is not yet completely understood. For further discussion, we refer to [69]. Growth will take part in the middle parts of the vessel walls, see Figure 8.9.

Accurate handling of the different time-scales is an open problem. Most approaches use an averaging in time and focus on the long-scale dynamics only [65, 252]. A two-scale approach has been suggested in [102]. Here, we simply consider an averaged long-scale model. We neglect the pulsating flow and instead choose one constant inflow-rate. We fully acknowledge, that this approach will result in enormous modeling errors and refer to [102] for a detailed discussion.

System 7 (Long-Scale Growth). *In $I = [0, T]$, find fluid-velocity \mathbf{v}_f , pressure p_f , solid deformation \mathbf{u}_s and foam cell concentration c_s^* , given by*

$$\begin{aligned} \rho_f \mathbf{v}_f \cdot \nabla \mathbf{v}_f - \operatorname{div} \sigma_f &= 0, \quad \operatorname{div} \mathbf{v}_f = 0 \quad \text{in } \mathcal{F}(t) \\ - \operatorname{div} \sigma_s(c_s^*(t)) &= 0 \quad \text{in } \mathcal{S}(t) \\ \mathbf{v}_f &= 0, \quad \sigma_f \vec{n}_f + \sigma_s(c_s^*(t)) \vec{n}_s = 0 \quad \text{on } \mathcal{I}(t) \\ \partial_t c_s^*(t) &= \gamma(\sigma_{WS}), \quad c_s^*(0) = 0 \quad \text{in } \mathcal{S}(t). \end{aligned} \quad (8.29)$$

The boundary data is given by

$$\mathbf{v}_f(t) = \bar{\mathbf{v}}^{in}(t) \text{ on } \Gamma_f^{in}, \quad \rho_f \nu_f \vec{n} \cdot \nabla \mathbf{v}_f - p \vec{n} = 0 \text{ on } \Gamma_f^{out}, \quad \mathbf{u}_s = 0 \text{ on } \Gamma_s, \quad (8.30)$$

where \vec{n} is the outward facing normal vector and $\bar{\mathbf{v}}^{in}$ is an averaged inflow profile that depends on the width of the blood vessel.

8.2.3 Monolithic schemes for the coupled problem

In this section, we derive monolithic variational formulations for System 7 in ALE and in Fully Eulerian coordinates. Growth can lead to substantial deformations of the solid up to a full closure of the vessel. Together with the stiff coupling between blood and tissue, this is a prototypical application for the Eulerian framework introduced in Chapter 5.

System 8 (Long-Scale problem in ALE formulation). *Find the fluid velocity $\hat{\mathbf{v}}_f \in \bar{\mathbf{V}}^{in}(t) + \mathcal{V}_f$, deformation $\hat{\mathbf{u}} \in \mathcal{W}$ and the pressure $\hat{p}_f \in \mathcal{L}_f$, such that*

$$(\hat{\rho}_f \hat{J}_f \hat{\mathbf{v}}_f \cdot \hat{\mathbf{F}}_f^{-1} \hat{\nabla} \hat{\mathbf{v}}_f, \hat{\phi}_f)_{\hat{\mathcal{F}}} + (\hat{J}_f \hat{\sigma}_f \hat{\mathbf{F}}_s^{-T}, \hat{\nabla} \hat{\phi})_{\hat{\mathcal{F}}} + (\hat{\mathbf{F}}_e \hat{\Sigma}_e, \hat{\nabla} \hat{\phi})_{\hat{\mathcal{S}}} = 0 \quad \forall \hat{\phi} \in \mathcal{W}, \\ (\widehat{\operatorname{div}}(\hat{J} \hat{\mathbf{F}}_s^{-1} \hat{\mathbf{v}}_f), \hat{\xi}_f)_{\hat{\mathcal{F}}} = 0 \quad \forall \hat{\xi} \in \mathcal{L}_f,$$

where the extension $\hat{\mathbf{u}}_f$ is defined as

$$(\hat{\nabla} \hat{\mathbf{u}}_f, \hat{\nabla} \hat{\psi}_f)_{\hat{\mathcal{F}}} = 0 \quad \forall \hat{\psi}_f \in \mathcal{W}_f,$$

in the case of the harmonic extension. For the biharmonic extension we use:

$$(\hat{\mathbf{w}}_f, \hat{\chi}_f)_{\hat{\mathcal{F}}} - (\hat{\nabla} \hat{\mathbf{u}}_f, \hat{\nabla} \hat{\chi}_f)_{\hat{\mathcal{F}}} + (\hat{\nabla} \hat{\mathbf{w}}_f, \hat{\nabla} \hat{\psi}_f)_{\hat{\mathcal{F}}} = 0 \quad \forall \{\hat{\psi}_f, \hat{\chi}_f\} \in \tilde{\mathcal{W}}_f \times \mathcal{W}_f$$

The elastic deformation gradient is defined as in (8.22) depending on the concentration of foam cells. The latter one is defined by the ODE

$$\partial_t c_s^* = \gamma(\sigma_{WS}, t), \quad c_s^*(0) = 0.$$

The function spaces are given by

$$\begin{aligned} \mathcal{V}_f &= [H_0^1(\hat{\mathcal{F}}; \hat{\mathcal{I}} \cup \hat{\Gamma}_f^{in})]^2, & \mathcal{L}_f &= L^2(\hat{\mathcal{F}}), \\ \mathcal{W} &= [H_0^1(\hat{\Omega}; \hat{\Gamma}_f^{in} \cup \hat{\Gamma}_s)]^2, & \mathcal{W}_f &= [H_0^1(\hat{\mathcal{F}})]^2, \quad \tilde{\mathcal{W}}_f &= [H^1(\hat{\mathcal{F}})]^2. \end{aligned}$$

Remark 46 (Biharmonic mesh model). We have chosen a mixed formulation for the biharmonic extension, such that an efficient discretization with simple C^0 -conforming finite elements is possible.

To express the coupled model including growth in Fully Eulerian coordinates, we must carry over the decomposition of the deformation gradients into the current system. We denote the inverse mappings of \hat{T}_a and \hat{T}_e by T_a and T_e and their gradients by F_a and F_e respectively. Using $\mathbf{F} = \hat{\mathbf{F}}^{-1}$, we have

$$\mathbf{F}_s = \hat{\mathbf{F}}_s^{-1} = \hat{\mathbf{F}}_a^{-1} \hat{\mathbf{F}}_e^{-1} =: \mathbf{F}_a \mathbf{F}_e. \quad (8.31)$$

Although a direct modeling in Eulerian coordinates is possible, we derive the Eulerian solid model by a mapping of the Lagrangian formulation to the Eulerian system:

$$\begin{aligned} J_s \hat{\rho}_s^0 (\partial_t \mathbf{v}_s + \mathbf{v}_s \cdot \nabla \mathbf{v}_s) - \operatorname{div}(J \mathbf{F}_e^{-1} \Sigma_e \mathbf{F}_s^{-T}) &= 0 & \text{in } \mathcal{S}(t), \\ \partial_t \mathbf{u}_s + \mathbf{v}_s \cdot \nabla \mathbf{u}_s &= \mathbf{v}_s \end{aligned} \quad (8.32)$$

where the Eulerian description of the 2nd Piola-Kirchhoff stress is given by

$$\Sigma_e := 2\mu_s \mathbf{E}_e + \lambda_s \operatorname{tr}(\mathbf{E}_e) I, \quad \mathbf{E}_e := \frac{1}{2}(\mathbf{F}_e^{-T} \mathbf{F}_e^{-1} - I). \quad (8.33)$$

Remark 47 (Piola Transform and Growth). In (8.32), we have used the Piola transform $\operatorname{div}(J\mathbf{F}_e^{-1}\boldsymbol{\Sigma}_e\mathbf{F}_s^{-T})$ of $\hat{\mathbf{F}}_e\hat{\boldsymbol{\Sigma}}_e$. The determinant J_s as well as the deformation gradient \mathbf{F}_s^{-T} stem from transformation from the Lagrangian to the Eulerian coordinate system. The Piola transformation can be derived by integral transformation of the variational formulation to the Eulerian system using $\hat{T}(t) : \hat{V} \rightarrow V(t)$:

$$(\hat{\mathbf{F}}_e\hat{\boldsymbol{\Sigma}}_e, \hat{\nabla}\hat{\phi})_{\hat{\mathcal{S}}} = (J\mathbf{F}_e^{-1}\boldsymbol{\Sigma}_e, \nabla\phi\mathbf{F}_s^{-1})_{\mathcal{S}(t)}. \quad (8.34)$$

By the relations $J = J_e J_a$ and $\mathbf{F}_s^{-1} = \mathbf{F}_e^{-1} \mathbf{F}_a^{-1}$, we can define the symmetric Eulerian Cauchy stress tensor of the Saint Venant Kirchhoff solid

$$J_s \mathbf{F}_e^{-1} \boldsymbol{\Sigma}_e \mathbf{F}_s^{-T} = J_a \underbrace{J_e \mathbf{F}_e^{-1} \boldsymbol{\Sigma}_e \mathbf{F}_e^{-T}}_{=: \sigma_e} \mathbf{F}_a^{-T} = J_a \sigma_e \mathbf{F}_a^{-T}. \quad (8.35)$$

Solid growth in Eulerian coordinates

Next, we carry over the growth model to the Eulerian representation. We will use again the simple isotropic growth model

$$\hat{\mathbf{F}}_a = \hat{g} I \quad (8.36)$$

and define the Eulerian growth function g by setting $g(x, t) = \hat{g}(\hat{x}, t)$. By the relation $\hat{\mathbf{F}}_a = \mathbf{F}_a^{-1}$, it holds that

$$\mathbf{F}_a = g^{-1} I. \quad (8.37)$$

By the decomposition (8.31) it follows that

$$\mathbf{F}_e = \mathbf{F}_a^{-1} \mathbf{F}_s = g \mathbf{F}_s, \quad J_e = g^2 J_s. \quad (8.38)$$

The complete Eulerian stresses are given by

$$J_a \sigma_e \mathbf{F}_a^{-T} = J_s \mathbf{F}_e^{-1} \boldsymbol{\Sigma}_e \mathbf{F}_s^{-T} = g^{-1} J_s \mathbf{F}_s^{-1} (2\mu_s \mathbf{E}_e + \lambda_s \operatorname{tr}(\mathbf{E}_e) I) \mathbf{F}_s^{-T}, \quad (8.39)$$

with the Eulerian elastic strain tensor

$$\mathbf{E}_e = \frac{1}{2} (g^{-2} \mathbf{F}_s^{-T} \mathbf{F}_s^{-1} - I). \quad (8.40)$$

Finally, we derive the equation of mass conservation in Eulerian coordinates. We assume, that homogenous material with the same parameters is added, such that the density is constant $\hat{\rho}_a = \hat{\rho}_s$. Hence, if $m(\hat{V})$ is the mass of the reference state, $m(\hat{V}_a)$ is the mass of the grown material, which is conserved in the current configuration V

$$m(\hat{V}) = \int_{\hat{V}} \hat{\rho}_s^0 d\hat{x}, \quad m(\hat{V}_a) = \int_{\hat{V}_a} \hat{\rho}_a d\hat{x}^g = \hat{\rho}_s^0 \int_{\hat{V}} \hat{J}_a d\hat{x} = \hat{\rho}_s^0 \int_V \hat{J}_a J_s dx, \quad (8.41)$$

where $\hat{J}_a := \det(\hat{\mathbf{F}}_a) = \hat{g}^2$ is the determinant of the growth part, such that for the density ρ of the current configuration it holds

$$\rho = \hat{\rho} = g^2 \hat{\rho}_s^0 J_s. \quad (8.42)$$

System 9 (Long-Scale problem in Fully Eulerian coordinates). *Find velocity $\mathbf{v}_f(t) \in \bar{\mathbf{v}}^{\text{in}} + \mathcal{V}_f$, deformation $\mathbf{u} \in \mathcal{W}$ and pressure $p_f \in \mathcal{L}_f$, such that*

$$\begin{aligned} (\rho_f \mathbf{v}_f \cdot \nabla \mathbf{v}_f, \phi_f)_{\mathcal{F}(t)} + (\sigma_f, \nabla \phi)_{\mathcal{F}(t)} + (J_a \sigma_e \mathbf{F}_a^{-T}, \nabla \phi)_{\mathcal{S}(t)} &= 0 \quad \forall \phi \in \mathcal{W} \\ (\operatorname{div} \mathbf{v}_f, \xi_f)_{\mathcal{F}(t)} &= 0 \quad \forall \xi_f \in \mathcal{L}_f, \\ (\nabla \mathbf{u}_f, \nabla \psi_f)_{\mathcal{F}(t)} &= 0 \quad \forall \psi_f \in \mathcal{W}_f. \end{aligned}$$

The elastic deformation gradient is defined in (8.38). Accumulation of foam cells is described by the ODE

$$\partial_t c_s^* = \gamma(\sigma_{WS}, t).$$

The function spaces are defined as

$$\begin{aligned} \mathcal{V}_f &= [H_0^1(\mathcal{F}(t); \Gamma_i(t) \cup \Gamma_f^{\text{in}})]^2, & \mathcal{L}_f &= L^2(\mathcal{F}(t)), \\ \mathcal{W} &= [H_0^1(\Omega(t); \Gamma_f^{\text{in}} \cup \Gamma_s)]^2, & \mathcal{W}_f &= [H_0^1(\mathcal{F}(t))]^2. \end{aligned}$$

8.2.4 Numerical Tests

We compare results obtained with the ALE approach against the fully Eulerian method.

Problem setting

As geometry we use a channel with length 10 cm and an initial width $\omega(0)$ of 2 cm as illustrated in Figure 8.9. The solid parts on the top and bottom have an initial thickness of 1 cm each. Fluid density and viscosity are given by $\rho_f = 1 \text{ g/cm}^3$ and $\nu_f = 0.3 \text{ cm}^2/\text{s}$. The solid parameters are given by $\rho_s = 1 \text{ g/cm}^3$ and the Lamé parameters $\nu_s = 10^4$ and $\lambda_s = 4 \cdot 10^4 \text{ dyn/cm}^2$. We prescribe a pulsating velocity inflow profile on Γ_f^{in} given by

$$\mathbf{v}^{\text{in}}(t, x, y) = \frac{3}{2} \begin{pmatrix} \mathbf{v}^{\text{in}}(t)(1 - y^2) \\ 0 \end{pmatrix}, \quad \mathbf{v}^{\text{in}}(t) = (\varepsilon_\omega + 5\omega(t))(1 + \sin(2\pi t)) \text{ cm/s}, \quad (8.43)$$

depending on the width of the channel $\omega(t)$ (see Figure 8.9). The parameter ε_ω is used to control the minimum flow rate and will be specified below. These parameters are similar to a real plaque growth configuration. The remaining boundary conditions are specified in (8.30). For the growth, we specify a function that depends on the concentration of foam cells c_s^* that is defined by the ODE (8.28). Growth is centered around the middle part of the vessel

$$\hat{g}(\hat{x}, \hat{y}, t) = 1 + c_s^*(t) \exp(-\hat{x}^2)(2 - |\hat{y}|), \quad \hat{\mathbf{F}}_g(\hat{x}, \hat{y}, t) := \hat{g}(\hat{x}, \hat{y}, t) I. \quad (8.44)$$

Growth \hat{g} and inflow rate $\mathbf{v}^{\text{in}}(t)$ implicitly depend on the solution. As the configuration is symmetric in the vertical direction, we can use the lower half of the geometry for the simulation only.

The problem is driven by a parabolic inflow profile with an average inflow rate $\bar{\mathbf{v}}^{\text{in}}(t)$. We use the averaged inflow profile of (8.43)

$$\bar{\mathbf{v}}^{\text{in}}(t) = (\varepsilon_\omega + 5\omega(t)) \text{ cm/s}. \quad (8.45)$$

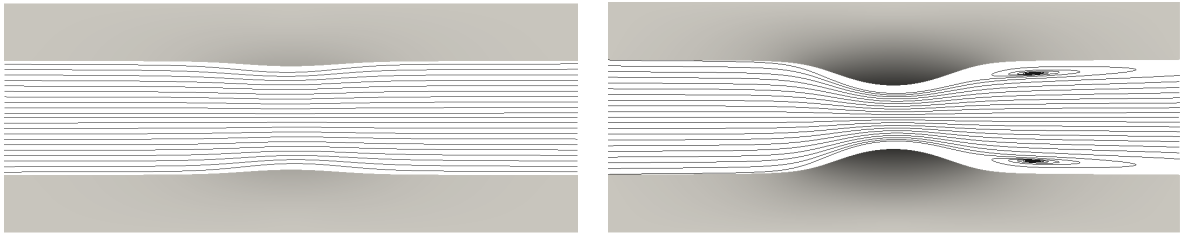


Figure 8.10: Solution after 10 days (left) and 50 days (right). Streamlines of the fluid and the deformation of the vessel wall are shown.

We discretize the coupled system by a splitting in time and approximate by the following iteration:

Mechano-Chemical Iteration

Initialize $\mathbf{v}^0 = 0$, $\mathbf{u}^0 = 0$, $g^0 = 0$ and the vessel-width $\omega^0 = 2$. Set time-step $k_l = 0.1$ day = 8 640 s. Iterate for $n = 1, 2, \dots$:

1. Solve quasi-stationary Long-Scale System 7:

$$\{c_s^{*,n-1}, \omega^{n-1}\} \mapsto \{\mathbf{v}^n, \mathbf{u}^n, p^n\}$$

2. Compute wall stress in main stream direction

$$\sigma_{WS}^n = \int_{\Gamma_i} |\sigma_f(\mathbf{v}^n, p^n) \vec{n} \cdot \vec{e}_1| \, d\Omega \quad (8.46)$$

3. Update the foam cell concentration

$$c_s^{*,n} = c_s^{*,n-1} + k_l \gamma_0 \left(1 + \sigma_{WS}^n / \bar{\sigma}\right)^{-1}$$

4. Compute width of vessel in point $A(t_n)$

$$\omega^n = 2 - 2\mathbf{u}_2^n(A(t_n), t_n)$$

First, we choose a minimum inflow velocity of $\varepsilon_\omega = 0.1$ cm/s. In Figure 8.10, the streamlines of the fluid and the deformed vessel walls at times $t = 10$ days and $t = 50$ days are shown.

In Figure 8.11 we show the course of different output functionals over time: the wall stress in main stream direction on the vessel wall Γ_i (8.46), the channel width $\omega(t) = 2 - 2\mathbf{u}_2(A(t_n))$ in the middle point $A(t_n)$ (see Figure 8.9), the vorticity of the solution in the L^2 -norm and the outflow at the right boundary defined by

$$J_{\text{vort}} = \int_{\mathcal{F}(t)} (\partial_y \mathbf{v}_1 - \partial_x \mathbf{v}_2)^2 \, dx, \quad J_{\text{out}} = \int_{\Gamma_{f,\text{out}}} \mathbf{v} \cdot \mathbf{n}. \quad (8.47)$$

The functional values for the ALE method (harmonic and biharmonic extension) and the fully Eulerian approach show very good agreement. Using the harmonic extension, the ALE method

broke down at $t = 63.2$ days due to degeneration of mesh cells, with the biharmonic extension, we were able to get results up to $t = 109.3$ days.

The fully Eulerian method, on the other hand, was able to yield reliable results until the channel was almost closed. As the inflow velocity is bounded from below by $\varepsilon_\omega = 0.1$ cm/s and as the fluid is incompressible, a passage must always remain. As higher wall stresses slow down plaque growth, see (8.28), the vertical displacement approaches a limit. However, increasing fluid-dynamical forces cause strong horizontal deflections that finally result in a break-down of the simulation.

As the results for the ALE method with harmonic and biharmonic extension are nearly identical until time $t = 63.1$ days, we will not show the harmonic variant anymore in the following tests.

In Figure 8.12, we present the deformed meshes at time $t = 109.3$ days for the ALE approach with biharmonic mesh deformation and the fully Eulerian approach. In the case of the biharmonic ALE approach, this was the last mesh before the calculation broke down.

Next, we study convergence with respect to the spatial grid size h for both the fully Eulerian and the ALE technique in Table 8.4. For the fully Eulerian approach, we use Q_1 equal-order elements and meshes with 256, 1024 and 4096 patch elements. For the ALE approach we use Q_2^c/P_1^{dc} elements and choose slightly coarser meshes for a fair comparison.

We evaluate the functionals at $t = 50$ days. The functional values for the ALE and the fully Eulerian approach converge roughly against the same values. Small differences are due to time discretization (the time step has been chosen 0.1 days) and the fact that in the ALE method, the deformation enters implicitly which means that the deformation u^n at time t_n defines the domains $\mathcal{F}^n, \mathcal{S}^n$, while in the fully Eulerian method, we apply the deformation explicitly, which means that the deformation u^n at time t_n determines the domains $\mathcal{F}^{n+1}, \mathcal{S}^{n+1}$ in the next time step.

Furthermore, we estimated the convergence order for all of the functionals, see Table 8.4. Besides the wall stress, all estimated convergence orders lie between linear and quadratic convergence order and the ALE and the fully Eulerian approach converge similarly. The ALE approach, however, seems to yield better values already on very coarse grids. Furthermore, the ALE approach shows faster convergence in the wall stress functional. The reason for this better performance is the use of inf-sup stable Q_2 elements in the case of ALE, which is not yet possible with the parametric interface approximation scheme described in Section 3.5, where stabilized $Q_1 - Q_1$ elements are utilized.

An interesting aspect from a modeling point of view is the question if the channel closes completely or if there will remain a small layer of fluid between the vessel walls. As discussed before, a complete closure of the channel is not possible as long as the inflow rate ε_ω is positive.

To study closure, we decrease the minimal inflow velocity ε_ω from 0.1 to 0 and the velocity inflow by a factor of 10 to

$$\mathbf{v}_1^{\text{in}} = 0.15 \cdot (5\omega(t))(1 - y^2) \text{ cm/s} \quad (8.48)$$

in a second configuration. This means that the flow through the narrow part of the channel will decrease considerably when the channel is almost closed. This has two important effects: First, the fluid forces acting against the growth of the solid are much smaller. Secondly, the wall stress becomes smaller which has a strengthening impact on the solid growth in our model.

#patches	Wall Stress	Width	Vorticity	Outflow
Euler	$1.033 \cdot 10^2$	1.092	$3.408 \cdot 10^3$	9.251
	$1.050 \cdot 10^2$	1.064	$3.457 \cdot 10^3$	9.547
	$1.060 \cdot 10^2$	1.052	$3.472 \cdot 10^3$	9.648
Extrapol.	$1.074 \cdot 10^2$	1.047	$3.479 \cdot 10^3$	9.700
	Conv.	0.77	1.81	1.71
ALE	$1.087 \cdot 10^2$	1.033	$3.527 \cdot 10^3$	9.892
	$1.076 \cdot 10^2$	1.037	$3.515 \cdot 10^3$	9.849
	$1.073 \cdot 10^2$	1.038	$3.510 \cdot 10^3$	9.834
Extrapol.	$1.072 \cdot 10^2$	1.039	$3.506 \cdot 10^3$	9.826
	Conv.	1.87	1.49	1.26
				1.52

Table 8.4: Convergence of functional values at $t = 50$ days on three different grids for the fully Eulerian and the ALE approach. We indicate estimated convergence rates and extrapolated limits.

Altogether, this has the effect that in our simulation the channel closes completely at time $t = 55.8$ days.

In Figure 8.13, we show plots of the channel width and the vorticity over time. In contrast to the larger inflow velocity studied above, the fluid forces (e.g. the vorticity) decrease after $t \approx 40$ days which makes the closure of the channel possible. In Figure 8.14, we show the last mesh obtained with the fully Eulerian approach ($t = 55.8$ days) where the channel is completely closed. The ALE calculation (with biharmonic extension) broke down at time $t = 40.6$ days.

These simplified simulations consider an averaged inflow velocity only. The main mechanical forcing however is due to the pulsating blood flow. In [102] a two-scale approach has been suggested, where effective parameters for the wall stress are computed from isolated short-scale simulations, that resolve the pulsation. It is shown, that substantial variations in plaque growth up to 20% exist.

8.3 Simulation of high performance ball-bearings

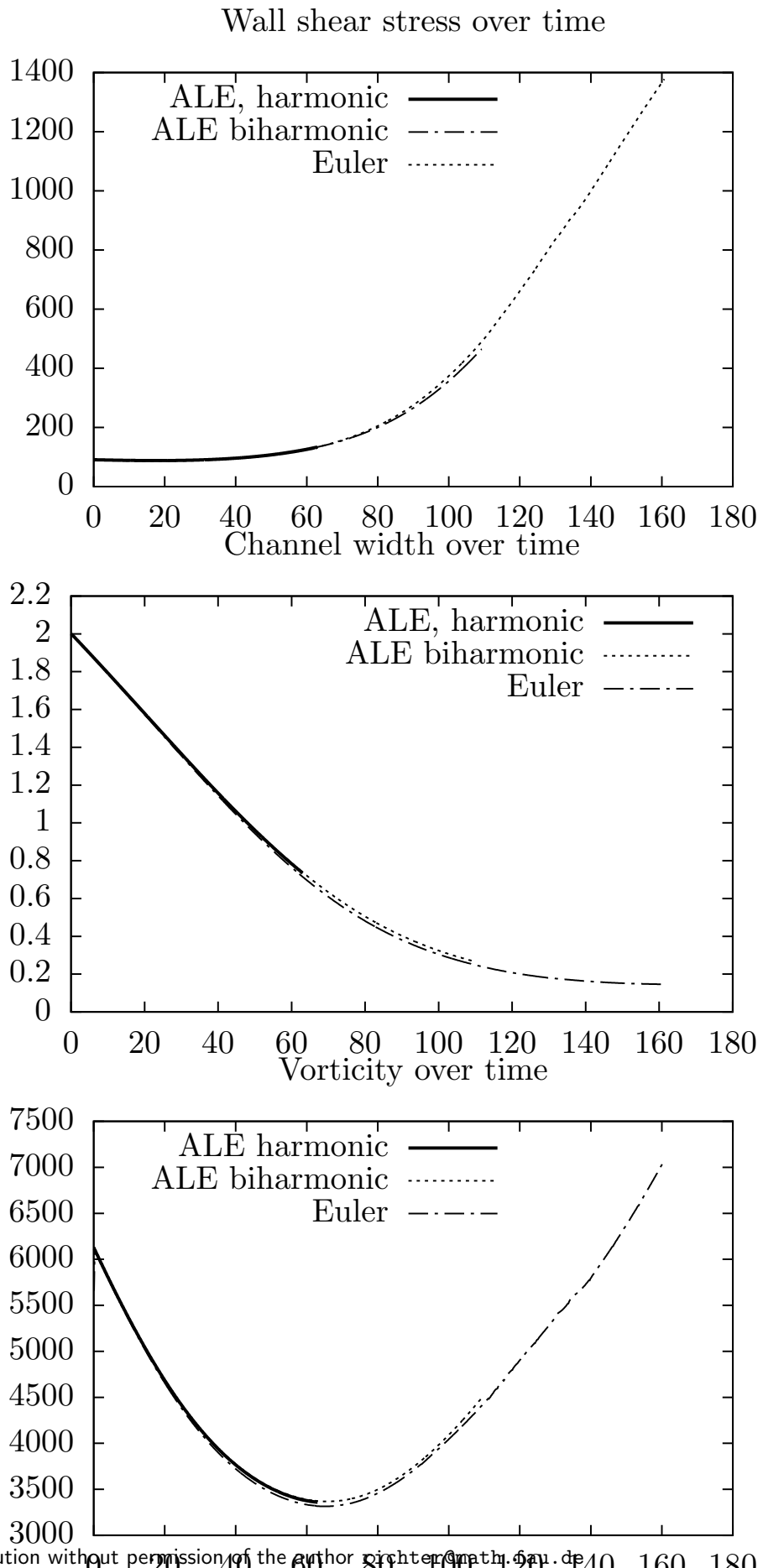


Figure 8.11: Course of different output functionals over time during closing of channel. For small deformations, the three different modeling approaches give similar results. Once the deformation gets larger, the two ALE approaches with harmonic and biharmonic extensions will fail.

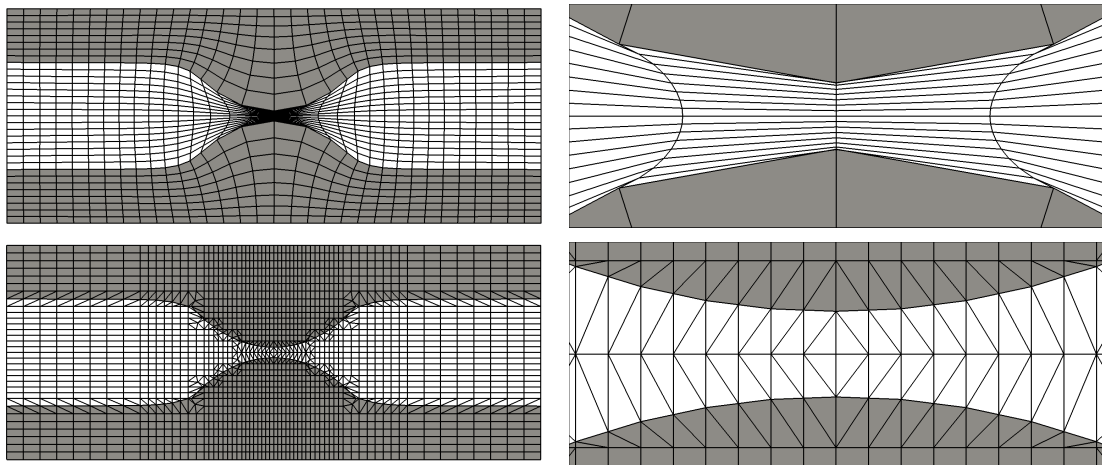


Figure 8.12: Biharmonic deformation (on top) close to break-down at $t = 109.3$ days and zoom-in at right. On the bottom the corresponding meshes at the same time instance $t = 109.3$ days for the fully Eulerian approach are provided.

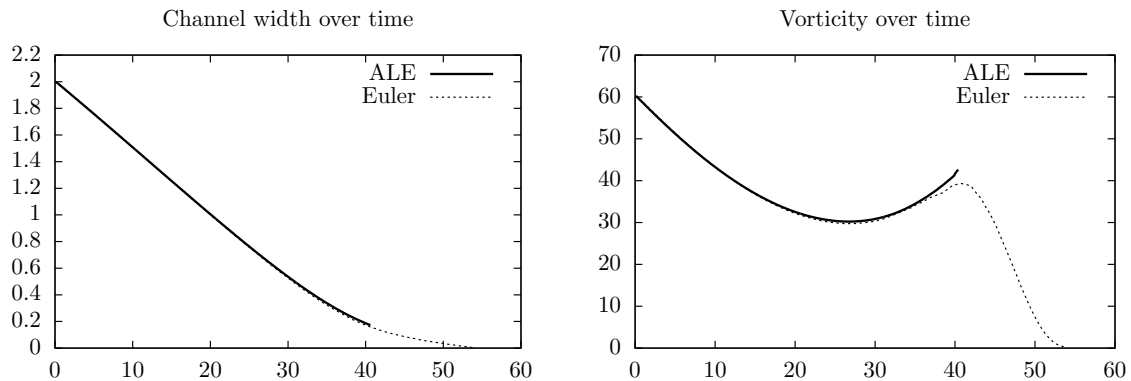


Figure 8.13: Channel width and vorticity for a long-scale simulation with reduced inflow velocity. The inflow velocity goes to zero when the channel closes. This makes the complete closure of the channel possible.

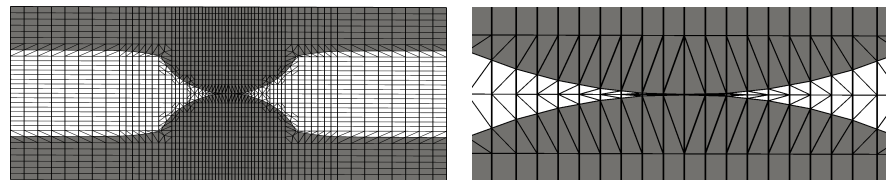


Figure 8.14: Fully Eulerian deformation when the channel is completely closed at $t = 55.8$ days.

Bibliography

- [1] M. Ainsworth and J. T. Oden. A unified approach to a posteriori error estimation using element residual methods. *Numer. Math.*, 65(1):23–50, 1993.
- [2] M. Ainsworth and J. T. Oden. A posteriori error estimation in finite element analysis. *Computer Methods in Applied Mechanics and Engineering*, 142(1-2):1–88, 1997.
- [3] An Adaptive Finite Element Method for Reactive Flow Problems. *M. Braack*. PhD thesis, Universität Heidelberg, 1998.
- [4] T. Apel. *Anisotropic finite elements: Local estimates and applications*. Advances in Numerical Mathematics. Teubner, Stuttgart, 1999.
- [5] I. Babuška. The finite element method for elliptic equations with discontinuous coefficients. *Computing*, 5:207–213, 1970.
- [6] I. Babuška. Feedback, adaptivity and a posteriori estimates in finite elements, aims, theory, and experience. In I. Babuška et al., editor, *Accuracy Estimates and Adaptive Refinements in Finite Element Computations*, pages 3–23. Wiley, New York, 1986.
- [7] I. Babuška, U. Banarjee, and J.E. Osborn. Generalized finite element methods: Main ideas, results, and perspective. *Int. J. of Comp. Methods*, 1:67–103, 2004.
- [8] I. Babuška and A.D. Miller. The post-processing approach in the finite element method. I. calculations of displacements, stresses and other higher derivatives of the displacements. *Int. J. Numer. Meth. Engrg.*, 20:1085–1109, 1984.
- [9] I. Babuška and A.D. Miller. The post-processing approach in the finite element method. II. the calculation of stress intensity factors. *Int. J. Numer. Meth. Engrg.*, 20:1111–1129, 1984.
- [10] I. Babuška and A.D. Miller. The post-processing approach in the finite element method. III. a posteriori error estimation and adaptive mesh selection. *Int. J. Numer. Meth. Engrg.*, 20:2311–2324, 1984.
- [11] I. Babuška and W.C. Rheinboldt. Error estimates for adaptive finite element computations. *SIAM J. Numer. Anal.*, 15:736–754, 1978.
- [12] W. Bangerth, M. Geiger, and R. Rannacher. Adaptive galerkin finite element methods for the wave equation. *Comp. Meth. Appl. Math.*, 10:3–48, 2010.
- [13] W. Bangerth, T. Heister, L. Heltai, G. Kanschat, M. Kronbichler, M. Maier, and B. Turcksin. The `deal.II` library, version 8.3. *preprint*, 2015.
- [14] R.E. Bank, A.H. Sherman, and A. Weiser. Some refinement algorithms and data structures for regular local mesh refinement. volume 1 of *Transactions on Scientific Computing*. 1983.

- [15] A. Barker and X.-C. Cai. Scalable parallel methods for monolithic coupling in fluid-structure interaction with application to blood flow modeling. *J. Comp. Phys.*, 229(3):642 – 659, 2010.
- [16] P. Bastian. Parallel adaptive multigrid methods. Technical Report 93–60, Interdisziplinäres Zentrum für Wissenschaftliches Rechnen, 1993.
- [17] Y. Bazilevs, V.M. Calo, T.J.R Hughes, and Y. Zhang. Isogeometric fluid-structure interaction: theory, algorithms, and computations. *Comput Mech*, 43:3–37, 2008.
- [18] Y. Bazilevs, K. Takizawa, and T.E. Tezduyar. *Computational Fluid-Structure Interaction: Methods and Applications*. Wiley, 2013.
- [19] R. Becker and M. Braack. Multigrid techniques for finite elements on locally refined meshes. *Numerical Linear Algebra with Applications*, 7:363–379, 2000. Special Issue.
- [20] R. Becker and M. Braack. Solution of a benchmark problem for natural convection at low mach number natural convection at low mach number. *SFB Preprint*, 30, 2000.
- [21] R. Becker and M. Braack. A finite element pressure gradient stabilization for the Stokes equations based on local projections. *Calcolo*, 38(4):173–199, 2001.
- [22] R. Becker and M. Braack. A two-level stabilization scheme for the Navier-Stokes equations. In et. al. M. Feistauer, editor, *Numerical Mathematics and Advanced Applications, ENUMATH 2003*, pages 123–130. Springer, 2004.
- [23] R. Becker, M. Braack, D. Meidner, T. Richter, and B. Vexler. The finite element toolkit GASCOIGNE. [HTTP://WWW.GASCOIGNE.UNI-HD.DE](http://WWW.GASCOIGNE.UNI-HD.DE).
- [24] R. Becker, M. Braack, and R. Rannacher. On error control for reactive flow problems. In *Computational Fluid Dynamics, Reaction Engineering, and Molecular Properties*, volume 1, pages 320–327. Scientific Computing in Chemical Engineering II, Springer, Berlin, 1999.
- [25] R. Becker, M. Braack, R. Rannacher, and C. Waguet. Fast and reliable solution of the Navier-Stokes equations including chemistry. *Comput. Visual. Sci.*, 2(2 and 3):107–122, 1999.
- [26] R. Becker, M. Braack, and Th. Richter. Parallel multigrid on locally refined meshes. In R. Rannacher, et. al., editor, *Reactive Flows, Diffusion and Transport*. Springer, Berlin, 2006.
- [27] R. Becker, D. Meidner, and B. Vexler. Efficient numerical solution of parabolic optimization problems by finite element methods. *Optimization Methods and Software*, 22(5):813–833, 2007.
- [28] R. Becker and R. Rannacher. Weighted a posteriori error control in FE methods. In et al. H. G. Bock, editor, *ENUMATH'97*. World Sci. Publ., Singapore, 1995.
- [29] R. Becker and R. Rannacher. An optimal control approach to a posteriori error estimation in finite element methods. In A. Iserles, editor, *Acta Numerica 2001*, volume 37, pages 1–225. Cambridge University Press, 2001.
- [30] R. Becker and B. Vexler. A posteriori error estimation for finite element discretization of parameter identification problems. *Numer. Math.*, 96(3):435–459, 2004.

- [31] T. Belytschko. Fluid-structure interaction. *Comput. Struct.*, 12:459–469, 1980.
- [32] F. Bengzon and M.G. Larson. Adaptive finite element approximation of multiphysics problems: A fluid-structure interaction model problem. *Int. J. Numer. Meth. Engrg.*, 84:1451–1465, 2010.
- [33] F. Bertrand, S. Mnzenmaier, and G. Starke. First-order system least squares on curved boundaries: Lowest-order raviart–thomas elements. *SIAM J. Numer. Anal.*, 52(2):880–894, 2014.
- [34] M. Besier and R. Rannacher. Goal-oriented space-time adaptivity in the finite element galerkin method for the computation of nonstationary incompressible flow. *Int. J. Numer. Math. Fluids.*, 70(9):1139–1166, 2012.
- [35] H. Blum. Asymptotic error expansion and defect correction in the finite element method. Habilitationsschrift, Institut für Angewandte Mathematik, Universität Heidelberg, 1991. SFB-123 Preprint 640.
- [36] H. Blum, Q. Lin, and R. Rannacher. Asymptotic error expansion and richardson extrapolation for linear finite elements. *Numer. Math.*, 49:11–37, 1986.
- [37] H. Blum and R. Rannacher. On the boundary value problem for the biharmonic operator on domains with angular corners. *Math. Meth. in the Appl. Sci.*, 2:556–581, 1980.
- [38] O. Boiarkine, D. Kuzmin, S. Canic, G. Guidoboni, and A. Mikelic. A positivity-preserving ale finite element scheme for convection-diffusion equations in moving domains. *J. Comp. Phys.*, 230:2896–2914, 2011.
- [39] C. Börgers. A triangulation algorithm for fast elliptic solvers based on domain imbedding. *SIAM J. Numer. Anal.*, 27:1187–1196, 1990.
- [40] M. Braack. A stabilized finite element scheme for the Nnavier Stokes equations on anisotropic meshes. *M2AN*, 2007. submitted.
- [41] M. Braack, R. Becker, and R. Rannacher. Adaptive finite elements for reactive flows. In *ENUMATH-97, Second European Conference on Numerical Mathematics and Advanced Applications*, pages 206–213. Enumath, World Scientific Publ., Singapore, 1998.
- [42] M. Braack, R. Becker, and R. Rannacher. The dual-weighted residual method applied to three-dimensional flow problems. submitted to AMIF 2002 Proc., Computer & Fluids, 2002.
- [43] M. Braack, E. Burman, V. John, and G. Lube:. Stabilized finite element methods for the generalized oseen problem. *Comput. Methods Appl. Mech. Engrg.*, 196:853–866, 2007.
- [44] M. Braack and A. Ern. A posteriori control of modeling errors and discretization errors. *Multiscale Model. Simul.*, 1(2):221–238, 2003.
- [45] M. Braack and A. Ern. Adaptive computation of reactive flows with local mesh refinement and model adaptation. In et. al. M. Feistauer, editor, *Numerical Mathematics and Advanced Applications, ENUMATH 2003*, pages 159–168. Springer, 2004.
- [46] M. Braack and P.B. Mucha. Directional do-nothing condition for the navier-stokes equations. *J. Comp. Math.*, 32(5):507–521, 2014.

- [47] M. Braack and T. Richter. Local projection stabilization for the stokes system on anisotropic quadrilateral meshes. In Bermudez de Castro et al, editor, *Enumath*, pages 770–778. Springer, 2005.
- [48] M. Braack and T. Richter. Solutions of 3D Navier-Stokes benchmark problems with adaptive finite elements. *Computers and Fluids*, 35(4):372–392, May 2006.
- [49] M. Braack and T. Richter. Stabilized finite elements for 3-d reactive flows. *Int. J. Numer. Math. Fluids.*, 51:981–999, 2006.
- [50] D. Braess. *Finite Elemente*. Springer, 1997.
- [51] J.H. Bramble and J.T. King. A finite element method for interface problems in domains with smooth boundaries and interfaces. *Advances in Computational Mathematics*, 6:109–138, 1996.
- [52] F. Brezzi and M. Fortin. *Mixed and Hybrid Finite Element Methods*. Springer-Verlag, Berlin, 1991.
- [53] M.O. Bristeau, R. Glowinski, and J. Periaux. Numerical methods for the navier-stokes equations. *Comput. Phys. Rep.*, 6:73–187, 1987.
- [54] A.N. Brooks and T.J.R. Hughes. Streamline upwind Petrov-Galerkin formulation for convection dominated flows with particular emphasis on the incompressible Navier-Stokes equations. *Comput. Methods Appl. Mech. Engrg.*, 32:199–259, 1982.
- [55] E.H. van Brummelen, K.G. van der Zee, and R. de Borst. Space/time multigrid for a fluid-structure-interaction problem. *Applied Numerical Mathematics*, 58(12):1951–1971, 2008.
- [56] M.A.K. Bulelzai and J.L.A. Dubbeldam. Long time evolution of atheroscelrotic plaques. *J. Theor. Biol.*, 297:1–10, 2012.
- [57] H.-J. Bungartz and M. Schäfer, editors. *Fluid-Structure Interaction. Modelling, Simulation, Optimisation*, volume 53 of *Lecture Notes in Computational Science and Engineering*. Springer, 2006. ISBN-10: 3-540-34595-7.
- [58] H.-J. Bungartz and M. Schäfer, editors. *Fluid-Structure Interaction II. Modelling, Simulation, Optimisation*. Lecture Notes in Computational Science and Engineering. Springer, 2010.
- [59] E. Burman. Consistent supg-method for transient transport problems: Stability and convergence. *Comput. Methods Appl. Mech. Engrg.*, 199:1114–1123, 2010.
- [60] G.F. Carey, S.S. Chow, and M.K. Seager. Approximate boundary-flux calculations. *Comput. Methods Appl. Mech. Engrg.*, 50:107–120, 1985.
- [61] J. Carlson, A. Jaffe, and A. Wiles, editors. *Millenium Prize Problems*. CMI/AMS, 2006. ISBN-13: 978-0-8218-3679-8.
- [62] J. Carpio, J.L. Prieto, and R. Bermejo. Anisotropic “goal-oriented” mesh adaptivity for elliptic problems. *SIAM Journal on Scientific Computing*, 35(2):A861–A885, 2013.
- [63] C. Carstensen. Convergence of adaptive finite element methods in computational mechanics. *Appl. Numer. Math.*, 59:2119–2130, 2009.

- [64] P. Causin, J.F. Gereau, and F. Nobile. Added-mass effect in the design of partitioned algorithms for fluid-structure problems. *Computer Methods in Applied Mechanics and Engineering*, 194:4506–4527, 2005.
- [65] C.X. Chen, Y. Ding, and J.A. Gear. Numerical simulation of atherosclerotic plaque growth using two-way fluid-structural interaction. *ANZIAM J.*, 53:278–291, 2012.
- [66] J. Chessa, P. Smolinski, and T. Belytschko. The extended finite element method (xfem) for solidification problems. *Int. J. Numer. Meth. Engrg.*, 53:1959–1977, 2002.
- [67] P.G. Ciarlet. *Mathematical Elasticity, Vol. I: Three-dimensional Elasticity*. North-Holland, Amsterdam., 1991.
- [68] P.G. Ciarlet. On korn’s inequality. *Chin. Ann. Math.*, 31:607–618, 2010.
- [69] M. Cilla, E. Pe na, and M.A. Martínez. Mathematical modelling of atheroma plaque formation and development in coronary arteries. *J. R. Soc. Interface*, 11(90), 2013.
- [70] P. Clément. Approximation by finite element functions using local regularization. *R.A.I.R.O. Anal. Numer.*, 9:77–84, 1975.
- [71] B. Cockburn, G.E. Karniadakis, and C.-W. Shu, editors. *Discontinuous Galerkin methods. Theory, computation and applications*. Lecture Notes in Computational Science and Engineering 11. Springer, Berlin, 2000.
- [72] G.-H. Cottet, E. Maitre, and T. Milcent. Eulerian formulation and level set models for incompressible fluid-structure interaction. *ESAIM: M2AN*, 42(3):471–492, 2008.
- [73] D. Coutand and S. Shkoller. Motion of an elastic solid inside an incompressible viscous fluid. *Arch. Ration. Mech. Anal.*, pages 25–102, 2005.
- [74] T.A. Davis. Umfpack, an unsymmetric-pattern multifrontal method. *ACM Transactions on Math. Soft.*, 30(2):196–199, 2014.
- [75] G. de Rham. *Variétés différentiables*. Hermann, Paris, 1960.
- [76] M.C. Delfour and J.-P. Zolésio. *Shapes and Geometries: Metrics, Analysis, Differential Calculus and Optimization*. Advances in Design and Control. SIAM, 2nd edition edition, 2011.
- [77] B. Desjardins and M.J. Esteban. Existence of weak solutions for the motion of rigid bodies in a viscous fluid. *Arch. Rational Mech. Anal.*, 146:59–71, 1999.
- [78] P. Deuflhard and F. Bornemann. *Numerische Mathematik II*. Walter de Gruyter, Berlin, 1994.
- [79] Peter Deuflhard. *Newton Methods for Nonlinear Problems*. Springer, 2005. ISBN-13: 978-3540210993.
- [80] M. Dobrowolski. On the lbb constant on stretched domains. *Math. Nachr.*, 254-255:64–67, 2003.
- [81] J. Donea. An arbitrary lagrangian-eulerian finite element method for transient dynamic fluid-structure interactions. *Comput. Methods Appl. Mech. Engrg.*, 33:689–723, 1982.
- [82] W. Dörfler. A convergent adaptive algorithm for Poisson’s equation. *SIAM J. Numer. Anal.*, 33(3):1106–1124, 1996.

- [83] J.J. Droux and T. J. R. Hughes. A boundary integral modification of the galerkin least squares formulation for the Stokes problem. *Comput. Methods Appl. Mech. Engrg.*, 113(173-182), 1994.
- [84] T. Dunne. An eulerian approach to fluid-structure interaction and goal-oriented mesh refinement. *Int. J. Numer. Math. Fluids.*, 51:1017–1039, 2006.
- [85] T. Dunne. *Adaptive Finite Element Approximation of Fluid-Structure Interaction Based on Eulerian and Arbitrary Lagrangian-Eulerian Variational Formulations*. PhD thesis, University of Heidelberg, 2007. urn:nbn:de:bsz:16-opus-79448.
- [86] K. Eriksson, D. Estep, P. Hansbo, and C. Johnson. Introduction to adaptive methods for differential equations. In A. Iserles, editor, *Acta Numerica 1995*, pages 105–158. Cambridge University Press., 1995.
- [87] D. Estep. A posteriori error bounds and global error control for approximation of ordinary differential equations. *SIAM J. Numer. Anal.*, 32(1):1–48, 1995.
- [88] X. Fang. An isoparametric finite element method for elliptic interface problems with nonhomogeneous jump conditions. *WSEAS Transactions on Mathematics*, 12, 2013.
- [89] E. Feireisl. On the motion of rigid bodies in a viscous incompressible fluid. *J. Evol. Equ.*, 3(3):419–441, 2003.
- [90] M. Feistauer and V. Sobotíková. Finite element approximation of nonlinear problems with discontinuous coefficients. *Modél. Math. Anal. Numér.*, 24:457–500, 1990.
- [91] M.A. Fernández. Coupling schemes for incompressible fluid-structure interaction: implicit, semi-implicit and explicit. *SeMA Journal*, 55(1):59–108, 2013.
- [92] M.A. Fernández and J.-F. Gerbeau. Algorithms for fluid-structure interaction problems. In L. Formaggia, A. Quarteroni, and A. Veneziani, editors, *Cardiovascular Mathematics: Modeling and simulation of the circulatory system*, volume 1 of *MS & A*, pages 307–346. Springer, 2009.
- [93] M.A. Fernández, J.-F. Gerbeau, and C. Grandmont. A projection semi-implicit scheme for the coupling of an elastic structure with an incompressible fluid. *Int. J. Numer. Meth. Engrg.*, 69(4):794–821, 2007.
- [94] M.A. Fernández and M. Moubachir. A newton method using exact jacobians for solving fluid-structure coupling. *Computers and Structures*, 83:127–142, 2005.
- [95] Luca Formaggia and Fabio Nobile. A stability analysis for the arbitrary Lagrangian Eulerian formulation with finite elements. *East-West Journal of Numerical Mathematics*, 7:105 – 132, 1999.
- [96] Luca Formaggia and Fabio Nobile. Stability analysis of second-order time accurate schemes for ALE-FEM. *Comp. Methods Appl. Mech. Engrg.*, 193(39-41):4097 – 4116, 2004.
- [97] Luca Formaggia, Alfio Quarteroni, and Alessandro Veneziani. *Cardiovascular Mathematics: Modeling and simulation of the circulatory system*. Springer-Verlag, Italia, Milano, 2009.

- [98] C. Förster, W. Wall, and E. Ramm. Artificial mass instabilities in sequential staggered coupling of nonlinear structures and incompressible viscous flows. *Computer methods Applied Mechanics and Engineering*, 196:1278–1293, 2007.
- [99] R.L. Fosdick and E.G. Virga. A variational proof of the stress theorem of cauchy. *Archive for Rational Mechanics and Analysis*, 105(2):95–103, 1989.
- [100] S. Frei. *Eulerian*. PhD thesis, Universität Heidelberg, 2016.
- [101] S. Frei and T. Richter. A locally modified parametric finite element method for interface problems. *SIAM J. Numer. Anal.*, 52(5):2315–2334, 2014.
- [102] S. Frei, T. Richter, and T. Wick. Long-term simulation of large deformation, mechano-chemical fluid-structure interactions in ale and fully eulerian coordinates. *submitted to J. Comp. Physics.*, 2015.
- [103] G. P. Galdi. *An Introduction to the Mathematical Theory of the Navier-Stokes Equations, Vol. I, Steady-State Problems*. Springer, New York, 2011.
- [104] F. Gazzola and M. Squassina. Global solutions and finite time blow up for damped semilinear wave equations. *Ann. I.H. Poincaré*, 23:185–207, 2006.
- [105] M.W. Gee, U. Küttler, and W.A. Wall. Truly monolithic algebraic multigrid for fluid-structure interaction. *Int. J. Numer. Meth. Engrg.*, 85:987–1016, 2010.
- [106] M.B. Giles and E. Süli. Adjoint methods for pdes: a posteriori error analysis and post-processing by duality. *Acta Numerica 2002*, pages 145–236, 2002. A. Iserles, ed.
- [107] V. Girault and P.-A. Raviart. *Finite Elements for the Navier Stokes Equations*. Springer, 1986.
- [108] R. Glowinski. Finite element methods for the numerical simulation of incompressible viscous flow. introduction to the control of the Navier-Stokes equations. *Lect. Appl. Math.*, 28:219–301, 1991.
- [109] T. Grätsch and K.J. Bathe. Goal-oriented error estimation in the analysis of fluid flows with structural interactions. *Computer Methods in Applied Mechanics and Engineering*, 195:5673–5684, 2006.
- [110] A. Griewank. On automatic differentiation. In M. Iri and K. Tanabe, editors, *Mathematical Programming: Recent Developments and Applications*, pages 83–108. Kluwer Academic Publishers, 1989.
- [111] W. Hackbusch. *Multi-Grid Methods and Applications*. Springer, 1985.
- [112] E. Hairer and G. Wanner. *Solving Ordinary Differential Equations II. Stiff and Differential-Algebraic Problems*.
- [113] A. Hansbo and P. Hansbo. An unfitted finite element method, based on Nitsche’s method, for elliptic interface problems. *Comput. Methods Appl. Mech. Engrg.*, 191(47-48):5537–5552, 2002.
- [114] A. Hansbo and P. Hansbo. A finite element method for the simulation of strong and weak discontinuities in solid mechanics. *Comput. Methods Appl. Mech. Engrg.*, 193:3523–3540, 2004.

- [115] R. Hartmann. Adaptive FE-methods for conservation equations. In G. Warnecke, editor, *Eighth International Conference on Hyperbolic Problems. Theory, Numerics, Applications (HYP2000)*, 2000.
- [116] Ralf Hartmann. Multitarget error estimation and adaptivity in aerodynamic flow simulations. *SIAM J. Sci. Comput.*, 31(1):708–731, 2008.
- [117] P. He and R. Qiao. A full-eulerian solid level set method for simulation of fluid?structure interactions. *Microfluidics and Nanofluidics*, 11:557–567, 2011.
- [118] M. Heil. An efficient solver for the fully coupled solution of large-displacement fluid-structure interaction problems. *Comput. Methods Appl. Mech. Engrg.*, 193:1–23, 2004.
- [119] M. Heil, A.L. Hazel, and J. Boyle. Solvers for large-displacement fluid-structure interaction problems: Segregated vs. monolithic approaches. *Computational Mechanics*, 43, 2008.
- [120] B.T. Helenbrook. Mesh deformation using the biharmonic operator. *Int. J. Numer. Meth. Engrg.*, pages 1–30, 2001.
- [121] V. Heuveline and R. Rannacher. Duality-based adaptivity in the hp-finite element method. *J. of Num. Math.*, 11(2):95–113, 2003.
- [122] J. Heywood and R. Rannacher. Finite element approximation of the nonstationary Navier-Stokes problem. iii. smoothing property and higher order error estimates for spatial discretization. *SIAM J. Numer. Anal.*, 25(3):489–512, 1988.
- [123] J. Heywood and R. Rannacher. Finite element approximation of the nonstationary Navier-Stokes problem. iv. error analysis for second-order time discretization. *SIAM J. Numer. Anal.*, 27(3):353–384, 1990.
- [124] J.G. Heywood, R. Rannacher, and S. Turek. Artificial boundaries and flux and pressure conditions for the incompressible Navier-Stokes equations. *Int. J. Numer. Math. Fluids.*, 22:325–352, 1992.
- [125] M. Hillairet. Lack of collision between solid bodies in a 2d incompressible viscous flow. *Comm. Partial Differential Equations*, 32:1345–1371, 2007.
- [126] M. Hillairet and T. Takahashi. Collisions in 3d fluid structure interactions problems. *SIAM J. Math. Anal.*, 40(6):2341–2377, 2009.
- [127] Michael Hinze, René Pinnau, Michael Ulbrich, and Stefan Ulbrich, editors. *Optimization with PDE constraints*. Number 23 in Mathematical modelling: theory and applications ; 23 ; Mathematical modelling: theory and applications. Springer, [Dordrecht u.a.], 2009.
- [128] M. Holst and S. Pollock. Convergence of goal-oriented adaptive finite element methods for nonsymmetric problems. *Num. Meth. Part. Diff. Eq.*, 2015. online.
- [129] C.O. Horgan. Korn’s inequalities and their applications in continuum mechanics. *SIAM Review*, 37:491–511, 1995.
- [130] G. Hou, J. Wang, and A. Layton. Numerical methods for fluid-structure interactions - a review. *Comm. Comp. Phys.*, 12(2):337–377, 2012.
- [131] J. Hron. personal communication. , 2014.

- [132] J. Hron and S. Turek. A monolithic fem solver for an ale formulation of fluid-structure interaction with configuration for numerical benchmarking. In P. Wesseling, E. Onate, and J. Périaux, editors, *European Conference on Computational Fluid Dynamics ECCOMAS CDF 2006*, pages 1–21. TU Delft, 2006.
- [133] J. Hron and S. Turek. A monolithic fem/multigrid solver for an ale formulation of fluid-structure interaction with applications in biomechanics. In H.-J. Bungartz and M. Schäfer, editors, *Fluid-Structure Interaction: Modeling, Simulation, Optimization*, Lecture Notes in Computational Science and Engineering, pages 146–170. Springer, 2006.
- [134] J. Hron, S. Turek, M. Madlik, M. Razzaq, H. Wobker, and J.F. Acker. Numerical simulation and benchmarking of a monolithic multigrid solver for fluid-structure interaction problems with application to hemodynamics. In H.-J. Bungartz and M. Schäfer, editors, *Fluid-Structure Interaction II: Modeling, Simulation, Optimization*, Lecture Notes in Computational Science and Engineering, pages 197–220. Springer, 2010.
- [135] T.J.R. Hughes, J.A. Cottrell, and Y. Bazilevs. Isogeometric analysis: Cad, finite elements, nurbs, exact geometry and mesh refinement. *Computer Methods in Applied Mechanics and Engineering*, 194(3941):4135 – 4195, 2005.
- [136] T.J.R. Hughes, L.P. Franca, and M. Balestra. A new finite element formulation for computational fluid dynamics: V. circumvent the Babuska-Brezzi condition: A stable Petrov-Galerkin formulation for the Stokes problem accommodating equal order interpolation. *Computer Methods in Applied Mechanics and Engineering*, 59:89–99, 1986.
- [137] C. Johnson. *Numerical Solution of Partial Differential Equations by the Finite Element Method*. Dover Publications, 2009. ISBN-13: 978-0-486-46900-3.
- [138] C. Johnson and A. Szepessy. Adaptive finite element methods for conservation laws based on a posteriori error estimates. *Comm. Pure Appl. Math.*, 48(3):199–234, 1995.
- [139] G.W. Jones and S.J. Chapman. Modeling growth in biological materials. *SIAM Review*, 54(1):52–118, 2012.
- [140] M. Kimmritz and T. Richter. Parallel multigrid method for finite element simulations of complex flow problems on locally refined meshes. *Numerical Linear Algebra with Applications*, 2010. doi: 10.1002/nla.744.
- [141] S. Knauf, S. Frei, T. Richter, and R. Rannacher. Towards a complete numerical description of lubricant film dynamics in ball bearings. *Computational Mechanics*, 53:239–255, 2014.
- [142] U. Kuettler and W.A. Wall. Fixed-point fluid-structure interaction solvers with dynamic relaxation. *Computational Mechanics*, 43(1):61–72, 2008.
- [143] U. K”uttler, M.W. Gee, Ch. Förster, A. Comerford, and W.A. Wall. Coupling strategies for biomedical fluid-structure interaction problems. *International Journal for Numerical Methods in Biomedical Engineering*, 26(3-4):305–321, 2010.
- [144] A. Kuzmin, M. Luisier, and O. Schenk. Fast methods for computing selected elements of the greens function in massively parallel nanoelectronic device simulations. In F. Wolf, B. Mohr, and D. Mey, editors, *Euro-Par 2013 Parallel Processing*, volume 8097 of *Lecture Notes in Computer Science*, pages 533–544. Springer Berlin Heidelberg, 2013.

- [145] D. Kuzmin. On the design of general-purpose flux limiters for implicit fem with a consistent mass matrix. i. scalar convection. *J. Comp. Phys.*, 219:513–531, 2006.
- [146] D. Kuzmin, R. Löhner, and S. Turek, editors. *FLux-Corrected Transport: Principles, Algorithms and Applications*. Scientific Computation. Springer, 2005.
- [147] P. Le Tallec and J. Mouro. Fluid structure interaction with large structural displacement. *Comput. Methods Appl. Mech. Engrg.*, 190:3039–3067, 2001.
- [148] Xiaoye S. Li. An overview of SuperLU: Algorithms, implementation, and user interface. *ACM Trans. on Math. Software*, 31(3):302–325, 2005.
- [149] A. Linke, G. Matthies, and L. Tobiska. Robust arbitrary order mixed finite element methods for the incompressible stokes equations with pressure independent velocity errors. *ESAIM: Math. Mod. and Num. Anal.*, 2015. in press.
- [150] A. Linke, C. Merdon, and W. Wollner. Optimal L2 velocity error estimate for a modified pressure-robust Crouzeix-Raviart Stokes element. *submitted*, 2015.
- [151] M. Lukáčová-Medvid'ová, G. Rusnáková, and A. Hundertmark-Zaušková. Kinematic splitting algorithm for fluidstructure interaction in hemodynamics. *Comput. Methods Appl. Mech. Engrg.*, 265:83 – 106, 2013.
- [152] M. Luskin and R. Rannacher. On the smoothing propoerty of the crank-nicholson scheme. *Applicable Anal.*, 14:117–135, 1982.
- [153] L. Machiels, A.T. Patera, and J. Peraire. Output bound approximation for partial differential equations; application to the incompressible Navier-Stokes equations. In S. Bir ingen, editor, *Industrial and Environmental Applications of Direct and Large Eddy Numerical Simulation*. Springer, Berlin-Heidelberg-New York, 1998.
- [154] R.J. MacKinnon and G.F. Carey. Treatment of material discontinuities in finite element computations. *Int. J. Numer. Meth. Engrg.*, 24:393–417, 1987.
- [155] K.-A. Mardal, J. Schöberl, and R. Winther. A uniformly stable fortin operator for the taylor-hood element. *Numer. Math.*, 123(3):537–551, 2012.
- [156] H.G. Matthies and J. Steindorf. Partitioned but strongly coupled iteration schemes for nonlinear fluid-structure interactions. *Comp. Struct.*, 80:1991–1999, 2002.
- [157] H.G. Matthies and J. Steindorf. Partitioned strong coupling algorithms for fluid-structure interaction. *Comp. Struct.*, 81:805–812, 2003.
- [158] D. Meidner and T. Richter. Goal-oriented error estimation for the fractional step theta scheme. *Comp. Meth. Appl. Math.*, 14:203–230, 2014.
- [159] D. Meidner and T. Richter. A posteriori error estimation for the fractional step theta discretization of the incompressible navier-stokes equations. *Comp. Meth. Appl. Mech. Engrg.*, 288:45–59, 2015.
- [160] Dominik Meidner. *Adaptive Space-Time Finite Element Methods for Optimization Problems Governed by Nonlinear Parabolic Systems*. PhD thesis, University of Heidelberg, 2008.
- [161] Metis. Serial graph partitioning, <http://www-users.cs.umn.edu>.

- [162] Eberhard Michel. *On the motion of rigid bodies submerged in incompressible fluids*. PhD thesis, University of Heidelberg, 2008. urn:nbn:de:bsz:16-opus-85761.
- [163] T. Milcent and E. Maitre. Eulerian model of immersed elastic surfaces with full membrane elasticity. *submitted*, 2015.
- [164] M. Mitrea and S. Monniaux. Maximal regularity for the lam system in certain classes of non-smooth domains. *Journal of Evolution Equations*, 10(4):811–833, 2010.
- [165] N. Moës, J. Dolbow, and T. Belytschko. A finite element method for crack growth without remeshing. *Int. J. Numer. Meth. Engrg.*, 46:131–150, 1999.
- [166] M. Molnar. Stabilisierte Finite Elemente für Strömungsprobleme auf bewegten Gebieten. Master’s thesis, Universität Heidelberg, 2015.
- [167] P. Morin, R.H. nochetto, and K.G. Siebert. Convergence of adaptive finite element methods. *SIAM Rev.*, 44(4):631–658, 2002.
- [168] R.L. Muddle and M. Mihajlović. An efficient preconditioner for monolithically-coupled large-displacement fluid-structure interaction problems with pseudo-solid mesh updates. *J. Comp. Phys.*, 231:7315–7334, 2012.
- [169] J. Nečas. *Equations aux dérivées partielles*. Presses de Université de Montréal, Montréal, 1965.
- [170] R.H. Nochetto, A. Veerani, and M. Verani. A safeguarded dual weighted residual method. *IMA Journal of Numerical Analysis*, 29(1):126–140, 2009.
- [171] C. Nystedt. A priori and a posteriori error estimates and adaptive finite element methods for a model eigenvalue problem. Technical Report Preprint NO 1995-05, Department of Mathematics, Chalmers University of Technology, 1995.
- [172] J. T. Oden and K. Vemaganti. Estimation of local modeling error and goal-oriented modeling of heterogeneous materials; Part II: A computational environment for adaptive modeling of heterogeneous elastic solids. *Comput. Methods Appl. Mech. Engrg.*, 190, 2001.
- [173] S. Osher and R. Fedkiw. *Level set methods and dynamic implicit surfaces*. Applied Mathematical Sciences. Springer, 2003.
- [174] A. Prohl. *Projection and Quasi-COmpressibility Methods for Solving the Incompressible Navier-Stokes Equations*. Advances in Numerical Mathematics. Springer, 1997.
- [175] A. Quarteroni and A. Quaini. A semi-implicit approach for fluid-structure interaction based on an algebraic fractional step method. *Math. Models Meth. Appl. Sciences*, 17:957–983, 2007.
- [176] L.B. Rall. *Automatic Differentiation - Techniques and Applications*, volume 20 of *Lecture Notes in Computer Science*. Springer, 1981.
- [177] R. Rannacher. Finite element solution of diffusion problems with irregular data. *Numer. Math.*, 43:309–327, 1984.
- [178] R. Rannacher. *Numerik partieller Differentialgleichungen*. Universität Heidelberg, <http://numerik.uni-hd.de/~lehre/notes/>, 2008. Vorlesungsskriptum.

- [179] R. Rannacher and T. Richter. A priori estimates for the stokes equations with slip boundary conditions on curved domains. submitted, 2015.
- [180] R. Rannacher and F.-T. Suttmeier. A posteriori error control in finite element methods via duality techniques: Application to perfect plasticity. *Computational Mechanics*, 21:123–133, 1998.
- [181] R. Rannacher and F.-T. Suttmeier. A posteriori error estimation and mesh adaptation for finite element models in elasto-plasticity. *Comput. Methods Appl. Mech. Engrg.*, 176:333–361, 1999.
- [182] Rolf Rannacher. On the stabilization of the Crank-Nicolson scheme for long time calculations. Preprint, August 1986.
- [183] M. Razzaq, H. Damanik, J. Hron, A. Ouazzi, and S. Turek. {FEM} multigrid techniques for fluid-structure interaction with application to hemodynamics. *Applied Numerical Mathematics*, 62(9):1156 – 1170, 2012.
- [184] T. Richter. Funktionalorientierte gitteroptimierung bei der finite-elemente approximation elliptischer differentialgleichungen. Diplomarbeit, Universität Heidelberg, June 2001.
- [185] T. Richter. A fully eulerian formulation for fluid-structure-interaction problems with large deformations and free structure movement. In J.C.F. Pereira and A. Sequira, editors, *V. European Conference on Computational Fluid Dynamics ECCOMAS CFD*, Lisbon, Portugal, 2010.
- [186] T. Richter. Goal oriented error estimation for fluid-structure interaction problems. *Comput. Methods Appl. Mech. Engrg.*, 223-224:28–42, 2012.
- [187] T. Richter. A fully eulerian formulation for fluid-structure interactions. *J. Comp. Phys.*, 223:227–240, 2013.
- [188] T. Richter. A monolithic geometric multigrid solver for fluid-structure interactions in ale formulation. *Int. J. Numer. Meth. Engrg.*, 104(5):372–390, 2015.
- [189] T. Richter, A. Springer, and B. Vexler. Efficient numerical realization of discontinuous galerkin methods for temporal discretization of parabolic problems. *Numer. Math.*, 2012. to appear.
- [190] T. Richter and T. Wick. Finite elements fo fluid-structure interaction in ale and fully eulerian coordinates. *Computer Methods in Applied Mechanics and Engineering*, 2010. doi: 10.1016/j.cma.2010.04.016).
- [191] T. Richter and T. Wick. Optimal control and parameter estimation for stationary fluid-structure interaction problems. *SIAM J. Sci. Comput.*, 35(5):B1085–B1104, 2013.
- [192] T. Richter and T. Wick. Variational localizations of the dual weighted residual method. *J. Comput. Appl. Math.*, 279:192–208, 2015.
- [193] T. Richter and T. Wick. On time discretizations of fluid-structure interactions. In T. Carraro, M. Geiger, S. Körkel, and R. Rannacher, editors, *Multiple Shooting and Time Domain Decomposition Methods*, volume 9 of *Contributions in Mathematical and Computational Science*, pages 377–400. Springer, to appear 2015.

- [194] Th. Richter. *Parallel Multigrid for Adaptive Finite Elements and its Application to 3D Flow Problem*. PhD thesis, Universität Heidelberg, 2005.
- [195] R.S. Rivlin and J.L. Ericksen. Stress-deformation relations for isotropic materials. *J. of Rational Mech. and Anal.*, 4:323–425, 1955. Reprinted in Rational Mechanics of Materials. International Science Review Series, New York: Gordon & Breach, 1965.
- [196] E.K. Rodriguez, A. Hoger, and A.D. McCulloch. Stress-dependent finite growth in soft elastic tissues. *J. Biomechanics*, 4:455–467, 1994.
- [197] A. Rössle. Corner singularities and regularity of weak solutions for the two-dimensional lamé equations on domains with angular corners. *Journal of Elasticity*, 60:57–75, 2000.
- [198] W. Rudin. *Functional Analysis*. International Series in Pure and Applied Mathematics. McGraw-Hill, 1991.
- [199] T. Richter S. Frei. Second order time-stepping for parabolic interface problems with moving interfaces. *SIAM J. Numer. Anal.*, submitted, 2014.
- [200] T. Wick S. Frei, T. Richter. Solid growth and clogging in fluid-structure interaction in ale and fully eulerian coordinates. *J. Comp. Physics*, submitted, 2014.
- [201] Y. Saad. *Iterative Methods for Sparse Linear Systems*. PWS Publishing Company, 1996.
- [202] P. Sackinger, P. Schunk, and R. Rao. A newton-raphson pseudo-solid domain mapping technique for free and moving boundary problems: a finite element implementation. *J. Comp. Phys.*, 125(1):83–103, 1996.
- [203] M. Schäfer and S. Turek. Benchmark computations of laminar flow around a cylinder. (With support by F. Durst, E. Krause and R. Rannacher). In E.H. Hirschel, editor, *Flow Simulation with High-Performance Computers II. DFG priority research program results 1993-1995*, number 52 in Notes Numer. Fluid Mech., pages 547–566. Vieweg, Wiesbaden, 1996.
- [204] M. Schmich. *Adaptive Finite Element Methods for Computing Nonstationary Incompressible Flows*. PhD thesis, Universität Heidelberg, 2009. urn:nbn:de:bsz:16-opus-102001.
- [205] M. Schmich and B. Vexler. Adaptivity with dynamic meshes for space-time finite element discretizations of parabolic equations. *SIAM J. Sci. Compu.*, 30(1):369–393, 2008.
- [206] L.R. Scott and S. Zhang. Finite element interpolation of nonsmooth functions satisfying boundary conditions. *Math. Comp.*, 54(190):483–493, 1990.
- [207] A. Seitz. Vergleich von Teilschritt-Theta-Verfahren, 2013. Diploma's thesis, Universität Heidelberg.
- [208] J.A. Sethian. *Level Set Methods and Fast Marching Methods Evolving Interfaces in Computational Geometry*. Fluid mechanics, COnputer Vision and Material Science. Cambridge University Press, 1999.
- [209] P. Shi and S. Wright. $w^{2,p}$ -regularity of the displacement problem for the lamé system on $w^{2,s}$ domains. *J. Math. Anal. Appl.*, 239(2):291 – 305, 1999.
- [210] G.R. Shubin and J.B. Bell. An analysis of grid orientation effect in numerical simulation of miscible displacement. *Comput. Math. Appl. Mech. Eng.*, 47:47–71, 1984.

- [211] T. Siekmann. Parallelisierte vanka-glätter für komplexe strömungsprobleme. Master's thesis, Universität Heidelberg, 2015.
- [212] J. Simon. Differentiation with respect to the domain in boundary value problems. *Numer. Fun. Anal. and Opt.*, 2(7-8):649–687, 1980.
- [213] H. Sohr. *The Navier-Stokes Equations. An Elementary Functional Analytic Approach.* Birkhäuser Advanced Texts. Birkhäuser, 2001.
- [214] J. Sokółowski and J.-P. Zolésio. *Introduction to shape optimization*, volume 16 of *Computational Mathematics*. Springer, 1992.
- [215] A. Springer. *Efficient Higher Order Discontinuous Galerkin Time Discretizations for Parabolic Optimal Control Problems*. PhD thesis, Technische Universität München, 2015. urn:nbn:de:bvb:91-diss-20150519-1237294-1-6.
- [216] K. Stein, T.E. Tezduyar, and R. Benney. Mesh moving techniques for fluid-structure interactions with large displacements. *J. Appl. Math.*, 70:58–63, 2003.
- [217] R. Stevenson. An optimal adaptive finite element method. *SIAM J. Numer. Anal.*, 42(5):2188–2217, 2005.
- [218] K. Stben. A review of algebraic multigrid. *J. Comput. Appl. Math.*, 128(12):281 – 309, 2001.
- [219] R. Temam. *Navier-Stokes Equations: Theory and Numerical Analysis*. AMS, 2000.
- [220] Inc The MathWorks. Matlab and statistics toolbox release 2012b. Natick, Massachusetts, United States.
- [221] V. Thomée. *Galerkin Finite Element Methods for Parabolic Problems*. Number 25 in Springer Series in Computational Mathematics. Springer, 1997.
- [222] A.N. Tikhonov and A.A. Samarskii. Homogeneous difference schemes. *USSR Comp. Math. and Math. Phys.*, 1:5–67, 1962.
- [223] F. Tröltzsch. *Optimale Steuerung partieller Differentialgleichungen - Theorie, Verfahren und Anwendungen*. Vieweg, 2005.
- [224] F. Tröltzsch. *Optimal Control of Partial Differential Equations - Theory, Methods and Applications*, volume 112 of *Graduate Studies in Mathematics*. American Mathematical Society, 2010. Translation of the second German edition by J. Sprekels.
- [225] C. Truesdell and W. Noll. *The Non-Linear Flied Theories of Mechanics*. Springer-Verlag, 2004.
- [226] S. Turek, J. Hron, M. Madlik, M. Razzaq, H. Wobker, and J. Acker. Numerical simulation and benchmarking of a monolithic multigrid solver for fluid–structure interaction problems with application to hemodynamics. Technical report, Fakultät für Mathematik, TU Dortmund, February 2010. Ergebnisberichte des Instituts für Angewandte Mathematik, Nummer 403.
- [227] S. Turek, J. Hron, M. Razzaq, H. Wobker, and M. Schäfer. Numerical benchmarking of fluid–structure interaction: A comparison of different discretization and solution approaches. In H.J. Bungartz, M. Mehl, and M. Schäfer, editors, *Fluid Structure Interaction II: Modeling, Simulation and Optimization*. Springer, 2010.

- [228] S. Turek, L. Rivkind, J. Hron, and R. Glowinski. Numerical study of a modified time-stepping theta-scheme for incompressible flow simulations. *Journal of Scientific Computing*, 28(2–3):533–547, 2006. doi: 10.1007/s10915-006-9083-y.
- [229] E van Brummelen. Added mass effects of compressible and incompressible flows in fluid-structure interaction. *J. Appl. Mech.*, 76, 2009.
- [230] E. van Brummelen. Partitioned iterative solution methods for fluid-structure interaction. *Int. J. Numer. Math. Fluids.*, 65:3–27, 2011.
- [231] S. P. Vanka. Block-implicit multigrid solution of Navier-Stokes equations in primitive variables. *J. Comp. Phy.*, 65:138–158, 1985.
- [232] D.A. Venditti and D.L. Darmofal. Anisotropic grid adaptation for functional outputs: application to two-dimensional viscous flows. *JCP*, 187:22–46, 2003.
- [233] R. Verfürth. *A Review of A Posteriori Error Estimation and Adaptive Mesh-Refinement Techniques*. John Wiley/Teubner, New York-Stuttgart, 1996.
- [234] B. Vexler and W. Wollner. Adaptive finite elements for elliptic optimization problems with control constraints. *SIAM J. Cont. Opt.*, 47:509–534, 2008.
- [235] M. von Laer. Finite elemente simulation of non-newtonian flows. Master’s thesis, Universität Heidelberg, 2013.
- [236] A. Ženíšek. The finite element method for nonlinear elliptic equations with discontinuous coefficients. *Numer. Math.*, 58:51–77, 1990.
- [237] W.A. Wall. *Fluid-Structure Interaction with Stabilized Finite Elements*. PhD thesis, University of Stuttgart, 1999. urn:nbn:de:bsz:93-opus-6234.
- [238] T. Washio, T. Hisada, H. Watanabe, and T.E. Tezduyar. A robust preconditioner for fluid?structure interaction problems. *Computer Methods in Applied Mechanics and Engineering*, 194(39?41):4027 – 4047, 2005.
- [239] P. Wesseling. *An introduction to multigrid methods*. Wiley, Chichester, 1991.
- [240] T. Wick. Fluid-structure interactions using different mesh motion techniques. *Computers and Structures*, 89:1456–1467, 2011.
- [241] T. Wick. *Adaptive Finite Element Simulation of Fluid-Structure Interaction with Application to Heart-Valve Dynamics*. PhD thesis, Universität Heidelberg, 2012. urn:nbn:de:bsz:16-opus-129926.
- [242] T. Wick. Benchmark results for fluid-structure interaction problems in ale coordinates using different mesh motion techniques. Technical report, University of Heidelberg, 2012.
- [243] T. Wick. Fully Eulerian fluid-structure interaction for time-dependent problems. *Comp. Methods Appl. Mech. Engrg.*, 255(0):14–26, 2012.
- [244] T. Wick. Coupling of fully Eulerian and arbitrary Lagrangian-Eulerian methods for fluid-structure interaction computations. *Comput. Mech.*, 2013.
- [245] T. Wick. Solving monolithic fluid-structure interaction problems in arbitrary Lagrangian Eulerian coordinates with the deal.ii library. *Archive of Numerical Software*, 1:1–19, 2013.

- [246] T. Wick. Stability estimates and numerical comparison of second order time-stepping schemes for fluid-structure interactions. In A. Cangiani, R.L. Davidchack, E. Georgoulis, A.N. Gorban, J. Levesley, and M.V. Tretyakov, editors, *Numerical Mathematics and Advanced Applications 2011*, Proceedings of ENUMATH 2011, Leicester, September 2011, pages 625–632. 2013, 2013.
- [247] J. Wloka. *Partielle Differentialgleichungen*. Teubner, Stuttgart, 1982.
- [248] H. Xie, K. Ito, Z.-L. Li, and J. Toivanen. A finite element method for interface problems with locally modified triangulation. *Contemporary Mathematics*, 466:179–190, 2008.
- [249] Y. Yang. *Mathematical modeling and simulation of the evolution of plaques in blood vessels*. PhD thesis, Universität Heidelberg, 2014.
- [250] Y. Yang, W. Jäger, M. Neuss-Radu, and T. Richter. Mathematical modeling and simulation of the evolution of plaques in blood vessels. *J. of Math. Biology*, accepted, 2015.
- [251] Y. Yang, T. Richter, W. Jaeger, and M. Neuss-Radu. An ale approach to mechano-chemical processes in fluid-structure interactions. *Int. J. Numer. Math. Fluids.*, submitted, 2015.
- [252] S. Yirgit, M. Schäfer, and M. Heck. Grid movement techniques and their influence on laminar fluid-structure interaction rproblems. *J. Fluids and Structures*, 24(6):819–832, 2008.
- [253] K.G. van der Zee, E.H. van Brummelen, and R. de Borst. Goal-oriented error estimation and adaptivity for free-boundary problems: The domain-map linearization approach. *SIAM J. on Scientific Computing*, 32(2):1074 – 1092, 2010.
- [254] K.G. van der Zee, E.H. van Brummelen, and R. de Borst. Goal-oriented error estimation and adaptivity for free-boundary problems: The shape-linearization approach. *SIAM J. on Scientific Computing*, 32(2):1093–1118, 2010.
- [255] J.-P. Zolesio and M.C. Delfour. *Shapes and Geometries: Analysis, Differential Calculus and Optimization*. SIAM, 2001.

Index

- 1st Piola Kirchhoff stress tensor, 17
- 2nd Piola Kirchhoff stress tensor, 17
- a posteriori error estimates, 225
- A-stable, 85
- absolute stability, 84
 - region, 85
- added mass operator, 62
- adjoint equation, 263
- algebraic multigrid, 213
- amplification factor, 85
- artificial diffusion, 127
- automatic differentiation, 160
- auxetic materials, 174
- BiCGStab, 212
- Cauchy stress tensor, 9
- Cauchy traction vector, 9
- CG, 211
- channel flow, 34
- checkerboard pattern, 114
- Clement-Interpolation, 103
- conforming finite element space, 102
- Conjugate Gradient Method, 211
- conservation principles, 1
- continuum, 1
- Coupling condition
 - dynamic, 55, 57
 - geometric, 55, 58
 - kinematic, 55, 56
- current configuration, 1
- def:inh, 22
- deformation, 2
- deformation gradient
 - inverse, 5
- Deformation gradient, 4
- dissipation, 89
- do-nothing condition, 34
- Domain
 - curved, 101
- Dual Weighted Residual Method, 225
- DWR, 225
- Dynamic coupling condition, 55, 57
- effectivity index, 230
- Euler-Almansi strain tensor, 7
- Eulerian coordinates, 3
- FCT, 129
- Finite Elements
 - iso-parametric, 102
 - parametric, 102
- first Piola-Kirchhoff traction vector, 9
- first order optimality condition, 263
- first Piola-Kirchhoff stress tensor, 9
- flux correction, 129
- Galerkin orthogonality, 104
- Geometric coupling condition, 55, 58
- geometric coupling condition, 55
- geometric multigrid, 213
- globally A-stable, 90
- GMRES, 211
- gradient equation, 263
- gradient-robust methods, 119
- Green deformation tensor, 6
- Green-Lagrange strain tensor, 6
- hanging nodes, 101, 242
- indicator index, 244
- inf-sup condition, 39
- Initial Point Set method, 191
- Initial Point Set method, 78
- inteface-capturing, 78, 190
- interface problem, 129
- interface-tracking, 72
- Karush-Kuhn-Tucker condition, 263
- Kinematic coupling condition, 55, 56
- KKT condition, 263

- Korn's inequality, 24
Lagrangian coordinates, 2
left Cauchy-Green tensor, 7
Level-Set, 78, 190
Local Projection Stabilization, 121
matching mesh, 162
material velocity, 2
material growth, 272
material law, 17
material laws, 1
material velocity gradient, 8
mesh refinement, 242
Method of Lines, 83
Mini-Element, 143
multigrid, 213
algebraic, 213
normal stress, 9
optimization, 261
Oseen equation, 123
parameter identification, 261
parametric triangulation, 99
Piola transformation, 15
Poiseuille flow, 34
preconditioning, 212
rate of strain tensor, 8
reference configuration, 1
Region of absolute stability, 85
remeshing, 242
residual error estimator, 226
Reynolds number, 36
Reynolds' Transport Theorem, 11
right Cauchy-Green tensor, 6
rigid body, 7
robust estimator, 226
Rothe's Method, 83
saddle-point, 26
Scott and Zhang interpolation, 104
shape regularity, 99
Shape Calculus, 156
shape calculus, 195
shear stress, 9
shear modulus, 22
Space-Time discretization, 83
spatial velocity gradient, 8
St. Venant Kirchhoff, 21
St. Venant Kirchhoff material, 21
state equations, 263
Strain rate tensor, 8
strain rate tensor, 8
Streamline Upwind Petrov Galerkin, 127
Stress, 8
stress tensor
 2nd Piola Kirchhoff, 17
stress tensor
 1st Piola Kirchhoff, 17
strong A-stability, 90
structural regularity, 99
SUPG, 127
surface tension, 9
Surface coupled problem, 55
Taylor-Hood element, 114
tensor
 Euler-Almansi strain, 7
 Green deformation, 6
 Green-Lagrange strain, 6
 left Cauchy-Green, 7
 rate of strain, 8
 right Cauchy-Green, 6
Theorem of Cosserat, 23
velocity, 2
Volume coupled problem, 55